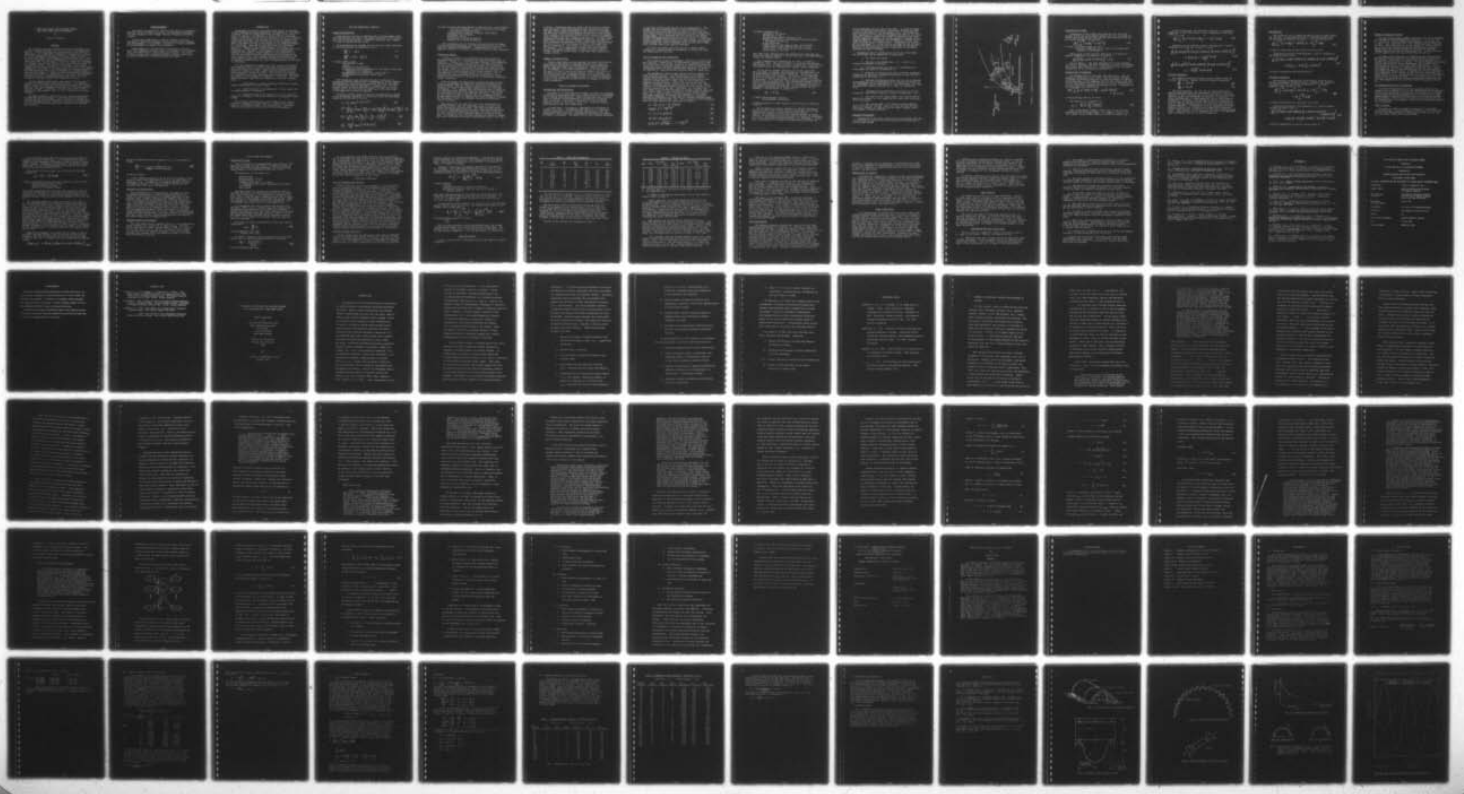
AD-A033 822 AUBURN UNIV ALA SCHOOL OF ENGINEERING F/G 14/2
1976 USAF-ASEE SUMMER FACULTY RESEARCH PROGRAM.(U)
SEP 76 J F O'BRIEN F44620-75-C-0031
UNCLASSIFIED AFOSR-TR-76-1419 NL

1 OF 9
AD A033822





(9)

1976 USAF/ASEE Summer Faculty RESEARCH PROGRAM

Conducted by
Auburn University
with Assistance from
Ohio State University
and
Other Installations
under
USAF Contract Grant F 44620-75-C-0031

PARTICIPANT'S RESEARCH REPORTS

Submitted to
Air Force Office of Scientific Research
Bolling Air Force Base
Washington, D. C.

by
J. Fred O'Brien, Jr., University Project Director
Associate Director, Engineering Extension Service
Auburn University

September 1976

DDC
RECEIVED
DEC 29 1976
A

DISTRIBUTION STATEMENT A
Approved for public release;
Distribution Unlimited

PREFACE

The 1976 USAF-ASEE Summer Faculty Research Program consisted of thirty-three members of engineering and science faculties from twenty-nine colleges and universities throughout the nation, engaged in scientific research of mutual interest and benefit to the Associate (and his university) and the USAF. These professors were assigned to various USAF research laboratories at Eglin AFB, Fla., Tyndall AFB, Fla., Arnold AF Station, TN., Griffiss AFB, NY., Hanscom Field, MS., Brooks AFB, TX., Kirtland AFB, NM., Seiler AF Academy, CO., and Williams AFB, AZ., for a ten week period of concentrated research in their selected field in collaboration with an assigned USAF colleague.

The basic program objectives were:

(1) To provide scientific and technological benefits to the USAF while enhancing the research interests and capabilities of engineering educators.

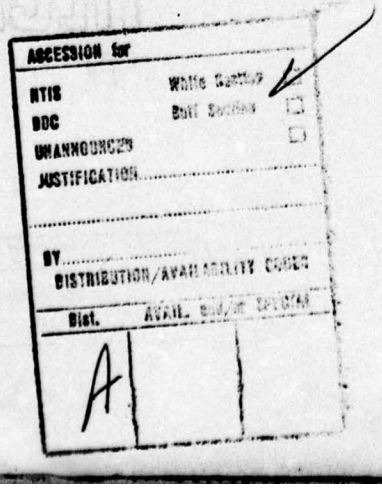
(2) To stimulate continuing relations among paricipating faculty members and their professional peers at the AFSC laboratories.

(3) To from the basis for continuing research of interest to the Air Force at the participant's institution.

(4) To sponsor research in areas of mutual interest to the USAF, the faculty member, and his institution.

The program was conducted under contract with the Air Force by the School of Engineering, Auburn University with assistance from the School of Engineering, Ohio State University. The American Society for Engineering Education is co-sponsor of the program.

This document is a compilation of each associate's report assembled by J. Fred O'Brien, Jr., Project Director, who has exercised certain administrative prerogatives to produce this report.



LIST OF PARTICIPANTS

1976 USAF/ASEE SUMMER FACULTY RESEARCH PROGRAM

AFCEC (Tyndall)	DEGREE, SPECIALTY & LAB ASSIGNMENT
Barry Arden Benedict, 34 Associate Professor Civil Engineering Department Tulane University New Orleans, LA 70118	Degree: Ph. D. Civil Eng. Specialty: Hydraulics & Fluid Mech. Assigned: AFCEC/ Colleague: Capt. Stephen P. Shelton
Lloyd C. Fitzpatrick, 39 Associate Professor Department of Biological Science North Texas State University Denton, TX 76203	Degree: Ph. D. Ecology Specialty: Ecological Energetics Assigned: AFCEC/ Colleague: Captain Stephen Shelton
Fang-Hui-Chou, Professor Department of Civil Engineering San Diego State University San Diego, CA 92182	Degree: Ph. D. Theoretical & Appl. Mech. Specialty: Structural Mechanics & Struc. Eng Assigned: AFCEC/DE Colleague: Lt. Dennis Morrison
David Kermit Holger, 27 Assistant Professor Dept. of Engineering Science and Mechanics Iowa State University Ames, IA 50011	Degree: Ph. D. Aerospace Eng. & Mech. Specialty: Fluid Dyn Sound Generation Assigned: AFCEC/DEE/21 Colleague: Major Robinson
William Henry Highter, Assistant Professor, 32 Clarkson College of Technology Civil and Environmental Engineering Potsdam, NY 13676	Degree: Ph. D. Civil Eng. Specialty: Pavements, Soil Mech. Assigned: AFCEC/EMR Colleague: L. M. Womack
AFATL (Eglin)	
William L. Oberkampf, Assistant Professor, 32 Taylor Hall 167 University of Texas at Austin Austin, TX 78712	Degree: Ph. D. Aerospace Eng. Specialty: Aerodyn. & Computational Fluid D. Assigned: AFATL/DLDL Colleague: Dr. Donald C. Daniel
Irene K. Petroff, 40 Associate Professor Division of Engineering California State University Fullerton, CA 92634	Degree: Ph. D. Engineering Specialty: Electromagnetic Theory Assigned: AFATL/DLMT Colleague: Dr. David Ebeoglu
Charles William Caldwell, 35 Assistant Professor Electrical Engineering University of Arkansas Fayetteville, AK 72701	Degree: Ph. D. Biomedical Eng. Specialty: Biomedical Instrumentation Assigned: AFATL/DLMM Colleague: Major Robert Haney
Robert A. Higgins, 50 Associate Professor Electrical Engineering Department South Dakota State University Brookings, SD 57006	Degree: Ph. D. Electrical Eng. Specialty: Computers, Control Assigned: AFATL/DLMM Colleague: Major R. L. Haney

AEDC (Arnold)

William Gregg Tiederman, Jr., 38
Professor, School of Mech & Aerosp. Eng.
EN 218
Oklahoma State University
Stillwater, OK 74074

Degree: Ph. D. Mechanical Eng.
Specialty: Fluid Mechanics
Assigned: AEDC/ARO
Colleague: C. F. Lo

Kent Friedley Palmer, 35
Assistant Professor
Department of Physics
University of Kentucky
Lexington, KY 40506

Degree: Ph. D. Physics
Specialty: Atomic & Molecular Spectroscopy
Assigned: AEDC/DYR
Colleague: Herman E. Scott

Grant T. Patterson, 32
Assistant Professor
Department of Mech. & Aerospace Eng.
University of Tennessee
Knoxville, TN 37916

Degree: Ph. D. Aerospace Eng.
Specialty: Thermodynamics
Assigned: AEDC/ETF-TAB
Colleague: Glenn R. Lazarlier

Robert C. Nelson, 33
Assistant Professor
Aerospace and Mechanical Engineering
P.O. Box 537
Notre Dame, IN 46556

Degree: Ph. D. Aerospace Eng.
Specialty: Aerodynamics, Stability & Contr l
Assigned: AEDC
Colleague: William B. Baker, Jr.

RADC (Griffis)

Melvin Miles Drossman, 39
Professor and Chairman
Computer Science and Elec. Eng. Tech
New York Institute of Technology
Wheatley Road
Old Westbury, NY 11804

Degree: Ph. D. Electrical Eng.
Specialty: Computer Science
Assigned: RADC/ISI
Colleague: Rocco F. Iuorno

Robert Dean Strattan, 40
Associate Professor
Electrical Engineering
600 South College
University of Tulsa
Tulsa, OK 74104

Degree: Ph. D. Electrical Eng.
Specialty: Electromagnetics, Radar, Gamoufl ge
Assigned: RADC/OCTM
Colleague: Fred Demma

Henry Allen Wiebe, 39
Associate Professor
Engineering Management Department
University of Missouri-Rolla
Rolla, MO 65401

Degree: Ph. D. Industrial Eng.
Specialty: Economic Analysis
Assigned: RADC/RBRT
Colleague: Jerry Klion

*Shreedhar G. Lele, 45
Associate Professor
Electrical Engineering Department
Tennessee Tech. University
Box 5-04 Tech Station
Cookeville, TN 38501

Degree: Ph. D.. Electrical Engineering
Specialty: Microwave Tubes
Assigned: RADC/ETE
Colleague: Dr. Charles J. Drane, Jr.

*located at Hanscom AFB, Mass.

AFGL (Hanscom)

George C. Sherman, 38
Assistant Professor
The Institute of Optics
University of Rochester
Rochester, NY 14627

Degree: Ph. D. Meteorology
Specialty: Physical & Meteorological Optics
Assigned: AFGL/OPA
Colleague: Robert W. Fenn

Louise Gray Young, 41
Research Scientist
Physics Department
Texas A&M University
College State, TX 77843

Degree: Ph. D. Engineering Science
Specialty: Infrared Molecular Spectroscopy
Assigned: AFGL/OPI
Colleague: Robert McClatchey/Laurance Rothman

ESD (Hanscom)

John D. Spragins, 41
Associate Professor
Electrical & Computer Engineering
Oregon State University
Corvallis, OR 97331

Degree: Ph. D. Electrical Eng.
Specialty: Computer Communications
Assigned: ESD/XR
Colleague: Dr. Donald Brick

USAFSAM (Brooks)

Bruce Kendall Colburn, 28
Assistant Professor
Electrical Engineering Department
Texas A&M University
College Station, TX 77843

Degree: Electrical Eng.
Specialty: Modern Control Theory
Assigned: USAFAM/BRM
Colleague: Dr. Sherwood Samn

James Joseph Freeman, 36
Associate Professor
University of Detroit
4001 W. McNichols Road
Detroit, MI 48221

Degree: Ph. D. Electrical Eng.
Specialty: Medical Instrumentation
Assigned: SAM/VNB
Colleague: Dr. Kent Gillingham

Carole D. Hansult, 37
Assistant Professor
Department of Psychology
State University of New York at Binghamton
Binghamton, NY 13901

Degree: Ph. D. Biopsychology
Specialty: Behavior Genetics
Assigned: USAFAM/RAW
Colleague: Dr. Donald N. Farrer

AFWL (Kirtland)

John Jay Wright, 33
Assistant Professor of Physics
DeMeritt Hall
University of New Hampshire
Durham, NH 03824

Degree: Ph. D. Atomic Physics
Specialty: Atomic Physics
Assigned: AFWL/ALC
Colleague: Steve Davis

David Y. L. Wang, 41
Associate Professor
Department of Civil Engineering
University of Wisconsin-Platteville
Platteville, WI 35818

Degree: Ph. D. Engineering Mechanics
Specialty: Mech. & Elastic Solids
Assigned: AFWL/DES-S
Colleague: Dr. Maynard A. Plamondon

AFWL (Kirtland) continued

Donald A. Smith, 40
Associate Professor
Department of Electrical & Elec
North Dakota State University
Fargo, ND 58102

Degree: Ph. D. Electrical Eng.
Specialty: Communications & Electronics
Assigned: AFWL/ELN
Colleague: John H. Darrah

Ping W. Chan, 38
Associate Professor, Colorado State University
Department of Electrical Engineering
Fort Collins, CO 80523

Degree: Ph. D. Physics
Specialty: Plasma Dynamics
Assigned: AFWL/ALE
Colleague: Dr. D. Drummond/L. Schlie

SEILER (AF Academy)

Craig S. Sims, 33
Associate Professor
Electrical Engineering
Oklahoma State University
Stillwater, OK 74074

Degree: Ph. D. Electrical Eng.
Specialty: Estimation Theory
Assigned: FJSRL/AMS/Applied Math
Colleague: Captain Robert Ahser

William D. Closson, 42
Professor
Department of Chemistry
State University of New York at Albany
Albany, NY 12222

Degree: Ph. D. Organic Chemistry
Specialty: Organic Reaction
Assigned: FJSRL/NC
Colleague: Capt. Scott A. Shackelford

AFRPL (Edwards)

David Dean Chesak, 43
Associate Professor and Chairman of Math
and Physics Department
St. Joseph's College
Rensselaer, IN 47978

Degree: Ph. D. Electrical Eng.
Specialty: Power System Analysis
Assigned: AFRPL
Colleague: Franklin Mead

Amos J. Leffler, 51
Professor, Inorganic Chemistry
Villanova University
Villanova, PA 19085

Degree: Ph. D. Inorganic Chemistry
Specialty: Inorg. Chem. of Light Element
Assigned: AFRPL/MKPA
Colleague: Dr. Claude Merrill

John Roger Dodd, 33
Assistant Professor
Chemistry Department
Emory University
Atlanta, GA 30322

Degree: Ph. D. Organic Chemistry
Specialty: ESR 7 NMR Spectroscopy etc.
Assigned: AFRPL/DYC
Colleague: John T. Nakamura

AFHRL (Williams) Ariz.

Edward D. McDowell, 34
Assistant Professor
Department of Industrial & General Engineering
Oregon State University
Corvallis, Oregon 97331

Degree: Ph. D. Industrial & Systems E[illegible].
Specialty: Humans Factors
Assigned: AFHRL/FT
Colleague: Edward E. Eddows

RESEARCH REPORTS

Report No.	Title	Research Associates
1	A Near Field Model for Dissolved Oxygen and Other Water Quality Parameters	Dr. Barry A. Benedict
2	Ecological Considerations for Development of a Water Quality Assessment Model	Dr. Lloyd C. Fitzpatrick
3	Dynamic Responses of Aircraft Shelters	Dr. Fang-Hui-Chou
4	A Sensitivity Study of Noisemap Power Offset Profiles (DSELs)	Dr. D. K. Holger
5	Determination of Unloaded and Loaded Pavement Profiles Used for Prediction of Dynamic Response of Aircraft	Dr. William H. Highter
6	Wind Tunnel Experiment Program for Aerodynamics of Missiles at High Angle of Attack	Dr. William L. Oberkampf
7	Analysis of Millimeter Wave Signatures of Snow and Ice	Dr. Irene K. Petroff
8	Configuration Specifications for a Digital Guided Weapon Flight Control Module	Dr. C. W. Caldwell
9	Sensor and Navigation System Processing Requirements for Digital Guided Missiles	Dr. Robert A. Higgins
10	Interpretation of Laser Velocimeter Measurements in Transonic Turbulent Boundary Layers	Dr. William G. Tiederman
11	Methods to Quantify Constituents in Binary Component Cryodeposits	Dr. Kent F. Palmer
12	Engine Test Cell Acoustics	Dr. G. T. Patterson
13	High Angle of Attack Support Interference	Dr. Robert C. Nelson
14	Development of a Nested Virtual Machine, Data-Structure Oriented Software Design Methodology and Procedure for its Evaluation	Dr. M. M. Drossman
15	Real-World Limitations of Radar Signatures for Target Identification	Dr. Robert D. Strattan
16	Confidence Intervals for Life Cycle Cost Analysis	Dr. H. A. Wiebe

RESEARCH REPORTS (continued)

Report No.	Title	Research Associates
17	Computer Aided Decision of Special Monopole and Dipole Antennas	Dr. Shreedhar G. Lele
18	Satellite Based Remote Probing of Atmospheric Visibility: A Bibliography of Relevant Literature	Dr. George C. Sherman
19	Analysis of Spectroscopic Data for Trace Gases in the Earth's Atmosphere	Dr. Louise Gray Young
20	Potential Technology Breakthroughs in Next Generation Radars	Dr. John Spragins
21	Pilot Transfer Function Identification	Dr. Bruce K. Colburn
22	Modeling of Eye Level Blood Pressure and Flow as a Function of G_z	Dr. James J. Freeman
23	Effect of Radiofrequency Radiation (RFR) on Performance and Retention of a Delayed Response Task	Dr. Carole D. Hansult
24	Time-Resolved Fluorescence of the $a^3II_0^+$ State of BrCL	Dr. John J. Wright
25	Dynamic Response of an Aboveground Arch Subjected to a Blast Load	Dr. David Y. L. Wang
26	Optical Fiber Explosion-Initiation System	Dr. Donald A. Smith
27	Density and Temperature Dependence Studies of the Thallium Mercury Excimer System	Dr. P. W. Chan
28	Signal Processing for Optics Progress as of July 1, 1976	Dr. Craig S. Sims
29	Syntheses and Decomposition Mechanisms of New Nitroaliphatic and Polycyclic Triazoline Compounds	Dr. William D. Closson
30	Electrode Erosion in Pulsed Plasma Thrusters	Dr. D. D. Chesak
31	Preparation of Solid Propellant Burning Rate Modifiers	Dr. Amos J. Leffler
32	Electrochemical Studies in Anhydrous Liquid Hydrazine	Dr. John R. Dodd
33	The Transfer Effectiveness of Platform Motion and Field of View in Training Selected UPT Maneuvers	Dr. Edward D. McDowell

1976 USAF-ASEE Summer Faculty Research Program

29 Universities

Tulane University
San Diego University
Clarkson College
California State University
South Dakota State University
University of Notre Dame
University of Tulsa
Tennessee Tech, University
Texas A&M University
University of New Hampshire
North Dakota State University
St. Josph's College
Emory University
University of Kentucky
University of Detroit

North Texas State University
Iowa State University
University of Texas
University of Arkansas
Oklahoma State University
University of Tennessee
New York Institute of Tech
University of Missouri-Rolla
University of Rochester
Oregon State University
State University of New York
University of Wisconsin
Colorado State University
Villanova Universtiy

1976 USAF-ASEE SUMMER FACULTY RESEARCH PROGRAM
sponsored by
THE AIR FORCE OFFICE SCIENTIFIC RESEARCH
CONDUCTED BY
AUBURN UNIVERSITY AND OHIO STATE UNIVERSITY

PARTICIPANT'S FINAL REPORT

A NEAR-FIELD MODEL FOR DISSOLVED OXYGEN AND OTHER WATER QUALITY PARAMETERS

Prepared by:	Barry A. Benedict, Ph.D.
Academic Rank:	Associate Professor
Department and University:	Department of Civil Engineering Tulane University
Assignment:	Tyndall AFB Air Force Civil Engineering Center Directorate of Environics Water and Solid Resources
USAF Research Colleague:	Capt Stephen P. Shelton, Ph.D.
Date:	August 20, 1976
Contract No.:	F44620-75-C-0031

A NEAR FIELD MODEL FOR DISSOLVED OXYGEN AND OTHER WATER QUALITY PARAMETERS

by

Barry A. Benedict

ABSTRACT

The standard approach to many water quality problems, e.g., dissolved oxygen (DO) and BOD, is to utilize a one-dimensional analysis. In some streams, the discharge may not become one-dimensional for a substantial distance. In addition, a variety of outfall strategies may exist for a given waste loading. To assess the impact of different discharge schemes and to evaluate the adequacy of the one-dimensional (1-D) analysis a near-field model has been developed. The model treats the discharge as a surface jet issuing from one bank at an arbitrary angle to the ambient current. The model is an integral type, using assumed similar lateral profiles of velocity and the water quality parameters. The model is two-dimensional and currently includes only BOD and DO as water quality parameters, although others can easily be added. A system of seven simultaneous differential equations is solved by a Runge-Kutta technique on the computer to yield values of 7 unknowns defining jet width, velocity, trajectory, and BOD and DO levels along the jet axis.

Initial computer runs reveal some trends, but more work is necessary to define functional relationships. For example, higher degrees of early jet mixing tend to decrease the critical deficit. Any such discharge has regions with deficits greater than the critical 1-D deficit. The receiving water volume affected by these greater deficits may be significant in some instances.

The model provides a useful tool for assessing the impact of different outfall designs, but further work is needed to overcome current shortcomings, such as failure to account for stream bank interference. Extensive numerical experimentation and verification with existing data is necessary to provide full results.

ACKNOWLEDGEMENT

The author is grateful to the Air Force Office of Scientific Research and to the American Society for Engineering Education for their support of this summer research through an excellent program.

A very warm thanks goes to Captain Stephen P. Shelton, the author's research colleague, who provided technical counsel and encouragement. The flexible, intellectually free atmosphere he provided made the summer very worthwhile.

Other members of the Environics Directorate of the Air Force Civil Engineering Center made life pleasant for the author's stay, with Major Emil C. Frein being very helpful. The staff of the Air Force Civil Engineering Center Computer Center also provided considerable assistance during the summer.

INTRODUCTION

Discharges of material with some oxygen demand in the form of BOD (biochemical oxygen demand) may be damaging to the oxygen resources of the receiving water body, whether it is a lake, river, or estuary. In addition to oxygen and BOD, other substances, both conservative and non-conservative, may be contained within the discharge. The ability to project the behavior of these substances and their distribution in the receiving water body is an essential step in assessing the environmental impact of a discharge. Analyses of this kind have been performed for years, spurred by the pioneering work of Streeter and Phelps (1). These studies usually assume a one-dimensional (1-D) condition and, therefore, only changes in the longitudinal direction are studied. This assumes that all properties of interest are fully mixed both laterally and vertically at any river cross-section. This assumes further that the BOD or any other property associated with the discharge from an outfall is completely mixed across the river instantaneously at the point of discharge.

The one-dimensional assumption is most nearly correct when the discharge takes place from a submerged diffuser extending across the full river width. However, many discharges do not meet this criterion and may require some substantial distance to mix laterally across the river. The question then arises as to whether or not this condition may in some cases invalidate the results of the standard 1-D approach to analysis. The work described herein addresses this question, with these ultimate goals:

1. Development of a model enabling projection of water quality conditions in the near field.

2. Identification of circumstances, if any, where the 1-D approximation is inadequate.

3. Identification of the sensitivity of the physical system to the manner in which the material is discharged to the stream.

All of these investigations will be made for the case of a surface discharge from one bank of a stream, with initial emphasis on dissolved oxygen - BOD interactions. The model itself is described in the section of Model Development.

THE ONE-DIMENSIONAL APPROACH

Oxygen Sag Equations

Much has been written on modeling the dissolved oxygen (DO) - BOD relationship, and only a few points pertinent to the current work will be presented here. Numerous references (for example, 1, 2 and 3) present further detail.

Both substances are assumed subject to first order reactions of the type outlined in Equations 1 and 2.

$$\frac{dL}{dt} = -K_1 L \qquad (1)$$

$$\frac{dD}{dt} = K_1 L - K_2 D \qquad (2)$$

in which L=BOD in mg/l
D=DO deficit in mg/l
$=C_s - C$
C=actual DO concentration
C_s=saturation DO concentration of the water at the same temperature and pressure
K_1=deoxygenation coefficient, units time $^{-1}$
K_2=reaeration coefficient, units time $^{-1}$
t=time

These equations quite obviously do not include all the sources and sinks of BOD and DO. Sedimentation, benthal demand, photosynthesis, dispersion, and two-stage BOD decay are among the factors which may be important in a given case. For the current study, initially only the K_1 and K_2 terms will be included, but it will be seen that addition of the other terms to the model will present no problem.

Solution of these equations for the one-dimensional, steady-state, continuous discharge of a BOD load yields the following equations for BOD and DO (2,3,4).

$$L = L_A \exp(-K_1 x/U) \qquad (3)$$

$$D = \frac{K_1 L_A}{K_2 - K_1}\left[\exp\left(-\frac{K_1 x}{U}\right) - \exp\left(-\frac{K_2 x}{U}\right)\right] + D_A \exp\left(-\frac{K_2 x}{U}\right) \qquad (4)$$

$$X_c = \frac{U}{K_2 - K_1} \ln\left\{\frac{K_2}{K_1}\left[1 - \left(\frac{K_2}{K_1} - 1\right)\frac{D_A}{L_A}\right]\right\} \qquad (5)$$

$$D_c = \frac{L_A K_1}{K_2} \exp(-K_1 X_c / U) \qquad (6)$$

in which L_A=total BOD load (weight or mass per unit time) divided by river discharge - can also include any existing BOD received from upstream.
X=longitudinel distance, measured from outfall
U=average river velocity
D_A=deficit at X=O
X_C=location of critical deficit
D_C=value of critical DO deficit

These equations are the standard ones used where the other sources and sinks mentioned, as well as dispersion and unsteadiness, are considered unimportant. Comparisons which will be made will refer to 1-D values calculated by use of these equations.

Transverse Mixing

A number of studies have addressed the question of the distance required for a discharge to become one-dimensional in character. Holley, et al (5), use the solution to the diffusion equation for a discharge from one bank to estimate distances to (1) the point where the discharge reaches the far bank and (2) the point where the material has become well mixed across the stream. Ward (6) made similar analyses for discharges into the river from various points in the cross-section, e.g., at the midpoint, at the quarter point, or at the bank. It is required that some percentage of variation across the river section be specified as a criterion for establishing "completely mixed" conditions.

Rood and Holley (7) have drawn on diffusion equation solutions to investigate the effect of transverse mixing on the DO-BOD problem. Here it should be noted that the diffusion equation is really a mass balance equation for the substance of interest. It is assumed that the discharge has no impact on the receiving water velocity field and that all mixing is due to turbulence existing in the ambient flow field. Therefore, any jet action or initial mixing, and its subsequent effect on the oxygen problem, is neglected by these diffusion solutions. See References 8 and 9 for further discussion of diffusion versus jet mixing.

Rood and Holley (7) deal with case of a two-dimensional discharge problem, with the discharge being a vertical line source located on the bank (y=o). The term two-dimensional means that longitudinal advection and lateral mixing are going on, but no vertical mixing is occuring. For this situation, an exact solution to the diffusion equation for BOD is available, including the bank influence through the method of images. BOD values calculated from this solution must then be fed into

a finite - difference model to obtain the DO deficit solution. Road and Holley concerned themselves only with results along the bank (y=o), which corresponds to the location of the maximum BOD value and hence the greatest DO deficit at each stream cross section. They present results from a variety of computer runs, categorizing their results by use of a set of dimensionless parameters obtained from a dimensional analysis. Certain cases gave values for the critical deficit essentially the same as those obtained from Equation 6, while other cases yielded values for the critical deficit as much as four or more times that given by Equation 6. The reader is referred to their paper for details. It is important to realize that the increased deficit they predict represents a value at a point, and no attempt is made to define areas of the water body affected by a given deficit.

Summary of Earlier Work

Briefly, most water quality analyses in rivers and estuaries have been one-dimensional, although some work now exists to suggest that the neglect of near-field jet mixing conditions may be important under some circumstances. This fact led to the development of the model described in the next section. The goal is first to assess the need for models other than 1-D, and second to provide an adequate model if one is needed. It is realized that this assessment process will require consideration of water areas and volumes exposed to certain DO deficits, as well as an evaluation of sensitivity to changes in the pertinent parameters.

NEAR-FIELD MODEL DEVELOPMENT

Introduction and Limitations

The model to be developed will attempt to accurately describe the hydraulic interactions which occur when material is discharged into a moving receiving body. Much work has been done in recent years to develop an understanding of the behavior of heated water discharges. This work is summarized in such works as Benedict, et al (8) and Jirka, et al (10). This work forms a good foundation for the current work.

To begin with, a non-buoyant discharge will be treated to simplify the study. In addition, BOD and DO will be the only quality parameters included, although temperature, other non-conservative substances, and conservative substances can easily be added to the model. The model will be for a surface discharge

at one bank of the stream and will be two-dimensional. This assumes that the discharge pipe or canal discharges over essentially the entire depth of the stream or that some density stratification exists which prevents vertical mixing from taking place. It is believed that the review of the effect of near-field mixing and dilution can most easily be studied without the added complication of vertical mixing. If the study reveals a need for such an addition, some current three-dimensional models for heated discharges could be utilized or modified to study other water quality problems.

In short, the model initially will be a simpler model looking at a limited number of parameters to assess the need for future work in the area.

Basic Formulation and Assumptions

The technique of model development used here is called integral analysis. Essentially, in this method, mathematical forms are selected for the lateral variation of important properties within the jet, or discharge plume; these profile forms are then integrated within the basic conservation equations to reduce the problem to a one-dimensional problem along the plume axis.

The mathematical form of the lateral profiles remains the same along the jet axis, and these profiles are therefore called similar profiles. Many investigators have chosen a Gaussian form (bell-shaped curve) for all profiles due to the good fit of this profile to data taken on discharges into stagment receiving bodies. Morton (12) points out that the effect of assuming similar profiles and the form of the inflow velocity is to suppress analytic solution of the details of the lateral structure of the jet. Therefore, any reasonable profile shape can be assumed although all evidence implies that some sort of bell shape is more descriptive of the lateral profile than, say, a top-hat profile (values constant across plume). The forms chosen for this model are polynomials, originally proposed by Abramovich (12) and used in a heated discharge model by Stolzenbach and Harleman (13). They are given in the following equations and schematically indicated in Figure 1.

$$u = U_a \cos\beta + \tilde{u}_c f(\eta/b) \tag{7}$$

$$f(\eta/b) = [1 - (\eta/b)^{3/2}]^2 \tag{8}$$

$$L = L_a + L_c g(\eta, b) \tag{9}$$

$$D = D_a + D_c g(\eta, b) \tag{10}$$

$$g(\eta, b) = \sqrt{f(\eta/b)} = 1 - (\eta/b)^{3/2} \tag{11}$$

in which L_a=ambient BOD
D_a=ambient DO deficit
u=velocity in jet
u_c=centerline excess velocity in jet
η=lateral distance in jet measured from axis (η=0) and normal to the axis
b=jet half-width
L=BOD excess at any point in jet cross section
L_c=BOD excess (above ambient BOD) at jet axis
D=DO excess at any point in jet cross section
D_c=DO excess at jet axis

Note that these profiles have the advantage over Gaussian profiles that they do approach a finite jet limit, such that ambient values are reached at η=b.

The f expression in Equation 8, as noted, is based on Abramovich work. The use of $g=\sqrt{f}$, as noted by Stolzenbach and Harleman (13) is based on Taylor's theory that scalar properties (heat, e.g.) are diffused more rapidly than is momentum.

In the use of integral analysis, one of two approaches must be taken to consider the changing jet characteristics due to entrainment of ambient fluid by the jet. Either one must be based on empirical evidence. One method is to assume the form of an expression describing the rate of change of width of the plume. The second method is the entrainment formulation, which is the one chosen here. This formulation assumes that the rate of fluid entrainment into the jet is proportional to the jet centerline excess velocity, u_c. An entrainment velocity is postulated, representing an inflow velocity across the jet boundary. This velocity is assumed to be

$$V_e = E\,\tilde{u}_c \qquad (12)$$

in which Ve=entrainment velocity
E=entrainment coefficient

Further discussion on this approach can be found in references 8 and 10.

The assumption of similar profiles is usually considered valid only after some initial region, called the zone of flow establishment (ZOFE), during which mixing proceeds from the jet boundaries to the axis and the profile is established. An excellent discussion appears in a paper by Albertson, et al (15), and further discussion exists in reference 8. Therefore, the portion of the model assuming similar profiles can

only be employed from the end of the ZOFE. As shown in figure 1, the jet may have experienced considerable bending and some dilution and widening. Two approaches exist, (1) solving the basic equations for conditions throughout the ZOFE or (2) using empirical evidence coupled with simple conservation relations. In this beginning studies, the latter approach is being used to simplify matters. Few people have attempted a solution in the ZOFE, and none really satisfactorily. Treatment of the ZOFE will be discussed in a later section, showing how the jet angle, β_o, and half-width, b_o, at the end of the ZOFE are determined and used as the starting point for integration of the model equations to find a solution.

Assumptions basic to formulation of the near-field model for this study can be summarized as shown below.

1. All flows are steady.

2. The jet is two-dimensional, i.e., there is no vertical entrainment occurring.

3. Turbulent mixing into the jet is represented by entrainment as indicated in Equation 12.

4. Profiles of velocity and other pertinent parameters normal to the jet axis are similar along the jet axis and are prescribed by Equations 7-11.

5. Pressure differential across the jet due to ambient flow separation can be represented by a drag force (similar to Fan (14)) which can be described by a drag coefficient, C_D, times an appropriate ambient velocity head, times an exposed jet area.

6. Deoxygenation and reaeration processes can be described as first order reactions, similar to Equations 1 and 2.

7. The zone of flow establishment can be described by empirical evidence for the length and the angle, β_o, resulting at its end point.

8. The initial model will assume a uniform ambient velocity field and constant values of E and C_D along the jet. These can, however, be made to vary by simple changes within the computer solution routines.

Equation Development

Integration of the basic conservation relationships over the cross section of the jet will yield the necessary equations to describe the system.

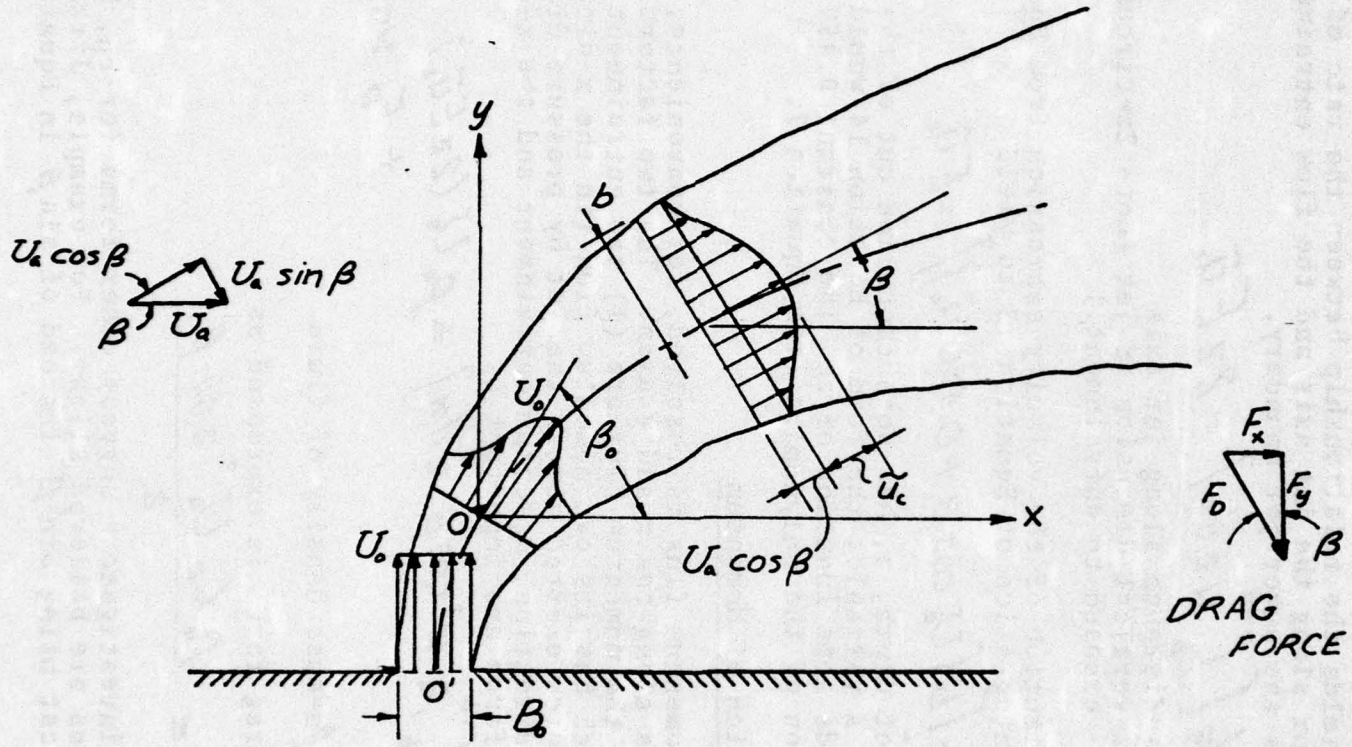


FIGURE 1 - SCHEMATIC FOR ANALYSIS OF SURFACE JET

Conservation of Mass

Integration of the volume flux equation over the cross section yields the relationship between the rate of change of volume flux along the jet axis and the flow entrained into the jet across the outer jet boundary.

$$\frac{d}{ds}\left[\int_{-b}^{+b} u z \, d\eta\right] = 2z E \tilde{u}_c \qquad (13)$$

in which s=distance along jet axis
z=vertical dimension of jet (note 2z=circumference exposed to entrainment.)

Substitution of the velocity expression from Equation 7 enables integration of Equation 13 to yield

$$\frac{d}{ds}\left[b\left\{U_a \cos\beta + 0.450\,\tilde{u}_c\right\}\right] = E\tilde{u}_c \qquad (14)$$

The jet depth, z, has been cancelled out of the equation. If z were a variable, the form of Equation 14 would be different and include some function of z. The constant 0.450 represents integration of the polynomial from Equation 7.

Conservation of Momentum

The momentum flux is resolved, for convenience, into its components along the x and y axes. The two factors tending to change the momentum flux are (1) the entrainment of ambient fluid which has its own momentum flux (in the x-direction) and (2) the force exerted across the jet by pressure differentials. In the x-direction, momentum entrainment and the x-component of the drag force are important, or

$$\frac{d}{ds}\left[\int_{-b}^{+b} \rho_a u^2 \cos\beta \; z \, d\eta\right] = \rho_a U_a (2zE\tilde{u}_c) + F_D \sin\beta \qquad (15)$$

in which ρ_a=mass density of fluid

The drag force is expressed as

$$F_D = \frac{\rho_a C_D U_a^2 z \sin\beta}{2} \qquad (16)$$

Some investigators suggest other forms for F_D, but the differences are believed slight. For example, Jirka, et al (10) suggest using $\sin^2\beta$ instead of $\sin\beta$ in Equation 16.

In the y direction, the entrained fluid has no y-momentum component, so the only factor is the y-component of the drag force, or

$$\frac{d}{ds}\left[\int_{-b}^{+b} \rho_a u^2 \sin\beta \, z \, d\eta\right] = -F_D \cos\beta \tag{17}$$

Insertion of the velocity profile from Equation 7 enables integration of Equations 15 and 17 to yield

$$\frac{d}{ds}\left[b\cos\beta\left\{U_a^2\cos^2\beta + 0.900\,\tilde{u}_c\,U_a\cos\beta + 0.316\,\tilde{u}_c^2\right\}\right] = E\tilde{u}_c U_a + \frac{C_D U_a^2 \sin^2\beta}{4} \tag{18}$$

$$\frac{d}{ds}\left[b\sin\beta\left\{U_a^2\cos^2\beta + 0.900\,\tilde{u}_c\,U_a\cos\beta + 0.316\,\tilde{u}_c^2\right\}\right] = -\frac{C_D U_a^2}{4}\sin\beta\cos\beta \tag{19}$$

Geometry Equations

The geometric relations between length changes along the jet axis and x and y changes yield two geometry equations.

$$\frac{dx}{ds} = \cos\beta \tag{20}$$

$$\frac{dy}{ds} = \sin\beta \tag{21}$$

The five equations - 14, 18, 19, 20, and 21-which have been developed describe the hydrodynamic behavior of the jet. Solution of these equations as a unit yield the jet trajectory, velocity, width, and therefore the dilution it undergoes. To these equations must be added equations for any water quality parameters of interest. The BOD and DO deficit equations to be used here are uncoupled from these first five equations in that the BOD and DO equations do not feed back into the hydrodynamic equations. If parameters such as temperature or high suspended solids were included which significantly affected density characteristics and hence flow behavior, feedback would exist. Very clearly, in all instances the first five equations feed information into the DO and BOD equations.

BOD Equation

Two processes act to change the BOD flux as one moves along the jet axis - entrainment of fluid at the ambient BOD level, La, and decay as shown in Equation 1. This is expressed as

$$\frac{d}{ds}\left[\int_{-b}^{+b} uL'z\,d\eta\right] = 2zE\tilde{u}_c L_a - K_1\int_{-b}^{+b} L'z\,d\eta \qquad (22)$$

in which L' =BOD value at any point in cross section

Insertion of profiles from Equations 7 and 9, integration, and simplification yield

$$\frac{d}{ds}\left[b\left\{U_a L_a \cos\beta + 0.450 L_a \tilde{u}_c + 0.600 L U_a \cos\beta + 0.368\tilde{u}_c L\right\}\right] = E\tilde{u}_c L_a - K_1 b\left[L_a + 0.600L\right] \qquad (23)$$

in which L=centerline BOD excess above La

DO Deficit Equation

The processes changing flux of DO deficit along the axis include entrainment of ambient fluid of deficit Da, oxygen use to reduce BOD, and reaeration as indicated in Equation 2. Combining these effects yields

$$\frac{d}{ds}\left[\int_{-b}^{+b} uD'z\,d\eta\right] = 2zE\tilde{u}_c D_a + K_1\int_{-b}^{+b} L'z\,d\eta - K_2\int_{-b}^{+b} D'z\,d\eta \qquad (24)$$

in which D' =DO deficit at any point in section

Insertion of profiles from Equations 7, 9, and 10 enables integration which leads to

$$\frac{d}{ds}\left[b\left\{U_a D_a \cos\beta + 0.450\tilde{u}_c D_a + 0.600 D U_a \cos\beta + 0.368\tilde{u}_c D\right\}\right] = E\tilde{u}_c D_a + K_1 b\left[L_a + 0.600L\right] - K_2 b\left[D_a + 0.600D\right] \qquad (25)$$

in which D=centerline DO deficit excess above Da

Summary of Equation System

The near-field oxygen dynamics problem has now been described by a system of seven differential equations - 14, 18, 19, 20, 21, 23, and 25 - which contain seven unknowns - $\tilde{u}_c$, b, β, x, y, L, and D - all a function of s, the distance measured along the jet axis. Note than once any of the centerline values (such as $\tilde{u}_c$, L, or D) are predicted from this equation set, values at points other than on the centerline are obtained from the assumed lateral profiles of those properties. In the Equations are two empirically obtained coefficients, E and C_D.

A review of the procedure in formulating the equations for BOD and DO deficit shows that any other parameters could easily be included. Other source or sink terms can be included in the BOD and DO equations if desired. If the reactions representing sources and sinks for other constituents can be identified, then equations can be written for those constituents. If the constituent of interest is conservative, then the only item on the right hand side of the equation would be the term showing entrainment of ambient fluid. If quantities of this constituent were negligible in the ambient fluid, then the right-hand side would reduce to zero, indicating that the flux of that constituent along the jet axis was constant. It is expected that the left hand side of the equation for most constituents would have much the same appearance as the left-hand sides of Equations 23 and 25.

Non-dimensionalization of Equations

In order to more easily solve the equation system on the computer, it is helpful to try to non-dimensionalize the equations to the extent possible, with the goal of reducing the left hand side of each of the seven equations to a derivative of a single dimensionless variable taken with respect to a non-dimensional axial distance. The full set of steps in this process will not be presented here, but Appendix A contains the non-dimensionalized set of equations.

ZOFE Treatment

As noted, in order to obtain a solution it is necessary to provide values of the parameters bo and β_o at the end of the zone of flow establishment, in addition to values u_o, Lo, and Do, the excess values at the end of ZOFE.

For the reduced angle, β_o, the data presented by Motz and Benedict (16) will be utilized. It is expected that these values will provideangles sufficiently close to actual to give useful results. Ultimately, sensitivity of the model to input angle will have to be reviewed, but these existing data will be used for current modeling efforts.

The initial velocity excess, u_o, at the end of the ZOFE is defined by

$$u_o = U_o - U_a \cos\beta_o \qquad (26)$$

in which u_o=initial excess centerline velocity at end of ZOFE
U_o=discharge velocity = Qp/A_D
Qp=total plant discharge
A_D=area of discharge ovifice

This merely recognizes that the total jet centerline velocity at the end of the ZOFE is still that which existed at jet discharge, or U_o. Values for L_o and D_o are simply found by subtracting ambient values La and Da from discharge values L_o' and D_o'.

The remaining parameter needed at the end of the ZOFE is b_o, the jet half-width. The initial discharge half width is b_o'. It has been stated that different lateral profiles were chosen for the scalar properties than for velocity due to the faster lateral diffusion of the former. This has the effect of causing the ZOFE based on L, e.g., to end before the ZOFE based on velocity. This would mean that when this latter point was reached, the BOD would already be below Lo. However, little is known about this behavior in discharges into moving streams. Therefore, for the time being it will be assumed that the ZOFE has the same length by either definition. Fan (14) notes that this has the effect of underestimating the dilution of the scalar property, in this case BOD, probably by about 10 percent. Further refinement in this approach may be sought in the future, but the accuracy here is believed consistent with goals of the current work.

Using this assumption, and neglecting any decay of BOD in the ZOFE, the flux of BOD in the jet from the orifice can be equated to the flux of BOD in the jet at the end of the ZOFE. If ambient BOD, La, is assumed zero, this conservation equation becomes

$$2U_o b_o' z L_o' = 2b_o z L_o \{0.60 U_a \cos\beta_o + 0.368 u_o\} \qquad (27)$$

Using the definition given in Equation 27, it is possible to obtain

$$\frac{b_o}{b_o'} = \frac{1}{0.368 + 0.232\, A \cos \beta_o} \qquad (28)$$

in which $A = Ua/U_o$

A more complete expression for b_o will be developed in the future to also cover cases where L_o' is of the same order of magnitude as La. In addition, if evidence becomes available to suggest a decrease of centerline BOD by the end of the velocity ZOFE, this can be incorporated.

Selection of Coefficients

The coefficients to be specified for the model are the entrainment coefficient, E, and the drag coefficient, C_D. Values for these coefficients are somewhat dependent on the profiles used. However, previous work suggests that C_D is similar to values for solid bodies and is in the range 0.5 - 1.0. Stolzenbach and Harleman (13) who used the same profile forms for heated discharges, have been successful using the same E value for all cases, on the order of 0.05. Prych's model (17), as fitted to extensive data by Shirazi and Davis (18) has employed a single E value, also equal to 0.05 but using Gaussian profiles, for all cases. While some uncertainty exists on these coefficients, it is believed that use of E=0.05 and C_D=0.5 will provide a sound beginning point for analysis, and these values will be employed here.

Computer Solution Techniques

The seven dimensionless equations must be solved numerically on the computer for a given set of input values. Physical values which must be known include these: b_o, β_o, Uo, A=Ua/Uo, Lo, La, Do, Da, K_1, K_2, E, and C_D. Details of input format are included with the computer program. With the input data provided, the program solves the equation system by a fourth-order Runge-Kutta technique.

TYPICAL RUNS AND RESULTS

Selection of Cases

Runs to evaluate the reasonableness and utility of the model must be made for some cases. A beginning point is the case considered by Rood and Holley (7), who selected, among others, a case presented by Velz (3, p 215).

The parameters of the system are:

Ua=0.6 ft/sec
B=river width = 473 ft
H=river depth = 4 ft
L_A=mixed river BOD = 12.15 mg/1
(loading of population equivalent of 311,000)
K_1=0.416/day
K_2=1.38/day

Rood and Holley (7) analyzed this situation with no upstream BOD (La=0) and no upstream deficit (Da=0), which will also be done here. One thing that is noteworthy in Velz' book is that he makes no mention of the way in which the material is discharged to the receiving stream. There are, therefore, a multitude of possible schemes for such a discharge, and several will be investigated here.

As a beginning case this situation had several nice features. First, it is a shallow receiving stream so the two-dimensional assumption of the model is reasonable. Second, the value of K_2 is very high, leading to a critical deficit point further upstream, possibly closer to or in the region where the jet model may be expected to still be valid. As the depth is so shallow, only the case Z=H will be considered.

For La=0, the mixed concentration in the river can be calculated by

$$L_A = \frac{Q_p}{Q_r} L_o \qquad (29)$$

in which Qp=plant flow rate
Qr=river flow rate

Solution of Equation 29 for Qp and insertion into the expression for initial discharge velocity, Uo, gives

$$B_o = \frac{Q_r (L_A/L_o)}{U_o H} \qquad (30)$$

in which Bo=discharge width

In this expression are three variables, any two of which can be selected; the value of the third is then fixed by Equation 30. Essentially, any combination of Uo, Lo, and Bo which satisfies this equation for the given L_A, Q_R, and H will discharge the same amount of BOD into the river. Therefore, Equation 30 was used as a basis for selecting several alternatives to review. It was also felt that if this was considered to be primarily domestic waste, then a population equivalent of 311,000 would result in a flow of from about 31.1 MGD - 62.2 MGD (based on 100-200 gallons per capita per day), or about 48-96 cfs. Therefore, discharge flows, Qp, should probably be in this range.

COMPARISON TECHNIQUES

Critical Deficit and Location

Several different means of estimating the critical deficit and its location now exist. Three immediate ones are the 1-D method represented by Equations 3-6, the 2-D diffusion model by Rood and Holley (7), and the jet model of this paper. A fourth one which will be used here to provide a comparison will be a coupling of the jet model and the 1-D approach. Jet model results will be applied until some cutoff point is reached where the so-called far field (region where discharge characteristics no longer have any real influence and the dominant factor is the ambient current and ambient turbulence) begins. The criterion here is that recommended by Jirka, et al (10) who suggest ending the jet region when the centerline velocity excess $\tilde{u}_c$, is less than 10 percent of the original excess, u_o. When this point is reached, some lateral distribution of BOD and DO deficit will be shown by the model. To tie immediately to the 1-D model it will then be necessary to evaluate the average BOD (this will be L_A in Equations 3-6) and average deficit (this will be D_A in Equations 3-6) and then apply the 1-D equations downstream. The location of the critical deficit would then be the distance predicted by the 1-D method (Equation 5) plus the distance at the jet cutoff point. Obviously, the adequacy of this technique is dependent upon the degree to which the distribution remaining from the jet solution approaches a laterally mixed condition. It may, however, provide some further insight to the results.

Area and Volume Influenced

Another useful piece of information which can be extracted from the two-dimensional models is the area and hence volume of the receiving stream affected by deficits greater than some chosen level. For example, it might be desirable to estimate what part of the river is exposed to deficits greater than the

critical deficit if predicted by Equation 6. The portion of the cross-sectional area of the river so affected may be of interest also. These concepts have been widely applied in evaluation of impact of thermal discharges.

Equation 10 describes the lateral variation of the deficit Dc is known. For a specified deficit of interest, say D', the lateral distance to that contour (of equal DO deficit) can be calculated using this equation to yield (with some manipulation)

$$\eta' = \left[1 - \frac{D' - D_a}{\bar{D} L_o} \right]^{2/3} W b_o \qquad (31)$$

in which D=Dc/Lo
W=b_c/b_o
b_c=jet half width at section of interest
η'=lateral distance (from jet axis) to location of deficit value D

Note that this expression is only valid for locations where the centerline deficit is greater than the deficit of interest. If it is not, it merely means that no point in the cross-section has a deficit that large.

If the deficit first reaches D' on the axis at S_1, and continues greater than D' until location S_2, the surface area within the D' contour can be found from

$$A_c = \frac{b_o^2}{E} \int_{S_1}^{S_2} W \left[1 - \frac{D' - D_a}{\bar{D} L_o} \right]^{2/3} dS \qquad (32)$$

in which Ac=area within D contour
S= $\frac{sE}{b_o}$

For the two-dimensional case being studied here, the volume affected would simply be Ac multiplied by the stream depth. The portion of the stream cross section affected at any point can be determined by comparison of the contour widths to stream width.

RUNS AND RESULTS

Table 1 presents basic information on the runs made for initial evaluation.

TABLE 1 - BASIC RUN PARAMETERS

RUN	A= Ua/Uo	β'_o	β_o, deg	Bo, ft	B, ft	Lo', mg/l
1	0.5	90	50	14.4	473	200
2	0.5	0	0	28.8	473	200
3	0.2	90	72	14.4	473	80
4	0.25	90	65	7.2	473	200
5	0.25	0	65	14.4	473	200
6	0.8	90	27	23.04	473	200
7	0.8	0	0	46.1	473	200
8	0.8	0	0	184.3	473	50
9	0.8	90	27	9.6	197	200
10	0.8	0	0	19.2	197	200

For all these runs, except No 9, K_1 = 0.416/day and K_2 = 1 38/ day; for Run 9, K_2 - 0.138/day. Also, for Runs 9 and 10, a check will reveal that the total BOD loading on the river has been decreased by a factor 2.4 (proportional to decrease of the width, B) because the mixed concentration L_A was retained constant.

One other point should be mentioned concerning those discharges at an angle of zero degrees (Runs 2, 5, 7, 8 and 10). In all cases the value of Bo is twice what would be shown from Equation 30. This is because these discharges have been schematized by treating them as discharges of twice the physical width with the centerline on the bank. Therefore, the actual physical discharge width in the stream is one-half that shown in Table 1 for the runs cited, making the total discharge correct.

Results of the analyses are presented in Table 2.

TABLE 2 - RESULTS OF RUNS

RUN	Dc, mg/l ROOD	1-D	JET +1-D	JET only	Xc, miles ROOD	1-D	JET +1-D	JET only
1	9.55	2.18	2.18	3.12	5.6	12.2	12.46	6.16
2	9.55	2.18	a	3.50	5.6	12.2	a	6.90
3	9.55	2.18	2.13	0.89	5.6	12.2	12.51	7.64
4	9.55	2.18	2.18	1.65	5.6	12.2	12.40	6.95
5	9.55	2.18	2.18	1.92	5.6	12.2	14.55	7.64
6	9.55	2.18	2.19	6.96	5.6	12.2	12.33	6.23
7	9.55	2.18	a	7.03	5.6	12.2	a	6.56
8	9.55	2.18	a	3.23	5.6	12.2	a	7.21
9	b	7.00	7.04	8.35	b	39.1	39.1	18.96
10	3.94	2.18	a	4.64	5.6	12.2	a	15.2

a: critical deficit in jet model occurs before cut off point
b: No comparable run

A number of preliminary observations can be made based on results shown in Table 2.

First, note that the critical deficit given by the jet + 1-D approximation is essentially identical to that by 1-D equations alone. In fact, using the same value of K_1, the decay of BOD from the stream cross-section will be the same if the total quantity of BOD in the section is the same, regardless of the distribution. Therefore, the total amount of BOD remaining at any point downstream will be the same. In fact, all the jet + 1-D values should identically match the 1-D critical deficit, but there are a few anomalies due to the predicted jet size exceeding the actual stream width.

Bank effects can be observed by looking at Runs 3-5. Note that the critical deficit is less than the 1-D value. This occurs because the jet model predicts jet spreading which causes the jet to extend past the actual physical bank. Because of its inability to account for the finite limit placed by the bank, the jet model overestimates the total dilution which the plume achieves. Physically, once a bank is reached, entrainment would cease, but the model does not account for this at this time.

It is apparent that jet-induced mixing brings about a more rapid dilution than predicted by the diffusion model of Rood and Holley. Runs 1 and 2, where bank effects are not significant, illustrate this point. The discharge velocity is 2 times the ambient velocity in these runs, and the maximum deficit is substantially reduced due to the more rapid early dilution.

Both the jet and diffusion models predict a smaller distance to the critical deficit than the 1-D model does. In a case where the stream is of constant section, this location may not be too important. However, in streams of varying section, where segmenting is necessary in modeling, it could be very important.

Higher values of A imply that the jet discharge velocity approaches the ambient velocity in magnitude. These cases approach the diffusion case more closely for the degree of jet-induced dilution early in the jet is reduced. Runs 6 and 7 show critical deficits considerable higher than those for Runs 1 and 2, and they approach the diffusion values.

Run 8 shows a somewhat artificial case showing the approach to 1-D results. To form the case for Run 8, the discharge of Run 7 was made 4 times wider with a BOD concentration of one-fourth, thereby heeping the total BOD loading constant. Note the reduction in the critical deficit to something which approaches the 1-D value. This corresponds to a discharge extending about 20 percent of the stream width. This condition could be obtained by a diffuser pipe of that length.

The angle of the discharge, $\beta o'$, is clearly important in determining impingement on near or far banks, but it may be less important in dilution calculations. Note that the critical deficit in Runs 1 and 2 do not differ by much despite the discharge angle difference. This effect is even more pronounced in Runs 6 and 7, where the deficit differs by only about one percent. In this latter case, it is easy to see why such is the case, as the high A value leads to a substantial decrease in the initial angle within the ZOFE. Note that the angle drops from 90° to 27° in this short distance. If further investigation confirms this preliminary finding, then some analyses might be simplified by use of a different angle.

Area Calculations

The computer program currently does not contain the area calculations represented by Equation 32. However, a hand calculation was made for Run 7, using the computer output values for jet half width and deficits along the jet axis. The contour of 2.18 mg/1 was chosen as this corresponds to the 1-D critical value. For this case the deficit first reaches 2.18 mg/1 on the jet axis (along the bank in this case) at about 0.44 miles (downstream from the outfall) and would continue greater than 2.18 mg/1, according to the model, until about 33.6 miles downstream. The iso-deficit contour of 2.18 mg/1 has a maximum extent into the river of about 230 ft. The total area encompassed by this contour (i.e., the area with deficits greater than or equal to 2.18 mg/1) is predicted as 35.1 acres. Obviously, extension of results to

33 miles is foolish, but as experience is gained with the model and as full knowledge of characteristics of a given river exist, it will be possible to evaluate which portions of the projected contours are applicable.

Organization of Results

An attempt has been made to organize results using dimensionless groupings from a dimensional analysis of the near-field problem. Rood and Holley (7) found that they were able to present their findings in a very useful format this way. It is believed that the same can be accomplished here, possibly negating the need for computer runs in some applications. However, many more runs are needed to establish the proper relationships. The problem here also has more variables than the diffusion solution by Rood and Holley (7) because of the variety of discharge combinations possible with the jet model. Preliminary reviews indicate that Dcr/Lo (where Dcr = critical deficit) is a function of, at least A $_o$, K_2/K_1, and $K_{01} = boK_1/EU_o$. It is believed that sufficient numerical experimentation with the model will develop some relationships which will enable, in most cases, a first assessment without need for running the computer program. Further work is needed to define this possibility.

MODEL LIMITATIONS

It is appropriate to review some of the major model limitations which have been identified, most of which are common to integral models. The first obvious limitation is the inability to cope with interference by stream banks. The case of a zero angle discharge is fairly easily schematized, as shown earlier. Ways to treat other cases of near and far bank impingement and the resultant reduction of entrainment (and possible re-entrainment) are less clear cut. Benedict, et al (8) have suggested using reduced values of the entrainment coefficient when bank interference is obvious. Also, Jirka, et al (10) suggest that meaningful results can still be obtained by modification of model results to account for bank interference, although only gross attempts have been made to date. This problem needs more attention in the current model and similar discharge models.

Diffusion due to ambient turbulence is a process separate from the jet-induced entrainment of ambient fluid. As the jet proceeds downstream and the excess velocity gets smaller, the magnitude of mixing due to turbulent diffusion will be of the same order as jet entrainment and ultimately be larger. Failure to account for this diffusion further downstream may cause the jet model to underpredict the incremental dilution in those reaches.

An obvious limitation exists due to the fact that few streams will retain constant hydraulic conditions (width, depth, velocity, etc.) long enough for the full application of the model to the far-field, completely mixed situation. The example from Run 7 in excess of 30 miles is a case in point. Work needs to be done to tie the model to other components to handle the problem of changing channel hydraulics.

MODEL UTILITY

Full model utility has not yet been identified. However, it seems clear that it provides a tool for assessment of the impact of the particular discharge strategy chosen for a given waste loading. One thing that should be made clear is that the model should not only be applicable to lakes, it should provide a useful tool for input into various lake models. While the two-dimensional character of the model might have to be modified for some lake systems, the possibility of less bank interference enhances the use of this model.

The role of the model in assessing adequacy of the 1-D approach needs more testing. Ultimately, the model may help sort out another of the physical processes which are so often all lumped together in best fit coefficients. Also, the coupling of the model with other components (diffusion, 1-D model, etc.) may help better depict the stages of the oxygen dynamics as one moves downstream.

RECOMMENDATIONS FOR FUTURE WORK

Initial study has suggested a number of possible steps to be taken in the future. Several are summarized here.

1. Many more runs must be made varying the important dimensionless groupings to enable organization of the results into a meaningful format. From this data, identification should be made of those cases where the 1-D model is not satisfactory.

2. The computer program should be modified to calculate desired areas influenced. Efforts should be made to also establish a functional relationship between these areas and pertinent dimensionless parameters.

3. Ways to account for bank interference should be investigated, including entrainment reduction, schematization of the discharge, and parametric estimates of recirculation on the near bank.

4. The model should be thoroughly tested as to its sensitivity to various input parameters and an error analysis made to define expected limits of accuracy and identify needed areas of refinement.

5. The addition of turbulent diffusion to the basic equations should be considered, especially in the later regions of the jet where jet-induced entrainment becomes small.

6. Better ways should be sought to tie the jet model to 1-D and/or diffusion models to carry the solution further downstream. In this context, the effect of changing channel geometry should be evaluated with possible attempts to incorporate segmenting of the river into the modeling process.

7. The addition of other source and sink terms to the DO and BOD equations should be accomplished after the impact of K_1 and K_2 interactions is fully assessed.

8. In order to verify the model, any available field and laboratory data should be reviewed to assess model applicability. This will likely be easier with the hydrodynamic aspects of the model.

9. Other water quality parameters should be added to the model as data justifies. Temperature is an obvious first addition due to the advances made in thermal modeling recently. As far as model verification, any substance which might act as a "tracer" would be useful.

10. Improve the treatment of the zone of flow-establishment, especially in describing the width of the jet.

Further work will bring forth other areas needing added investigation and refinement. It is believed that the model described in this report is a strong first step in near-field water quality modeling.

11. Morton, B.R., "On a Momentum-Mass Flux Diagram for Turbulent Jets, Plumes, and Wakes," Journal of Fluid Mechanics, 10, 1961, pp 101-112.

12. Abramovich, G.N., The Theory of Turbulent Jets, The M.I.T. Press, Massachusetts Institute of Technology, 1963.

13. Stolzenbach, K.D., and D.R.F. Harleman, "An Analytical and Experimental Investigation of Surface Discharges of Heated Water," R.M. Parsons Laboratory Report No. 135, Massachusetts Institute of Technology, 1971.

14. Fan, L.N., "Turbulent Buoyant Jets into Stratified or Flowing Ambient Fluids," Technical Report No. KH-R-15, W.M. Keck Laboratory of Hydraulics and Water Resources, California Institute of Technology, Pasadena, California, Jun 1967.

15. Albertson, M.L,, Y.B. Dai, R.A. Jensen, and H. Rouse, "Diffusion of Submerged Jets," Transactions, ASCE, 115, 1950, pp 639-697.

16. Motz, L.H., and B.A. Benedict, "Surface Jet Model for Heated Discharges, "Journal of the Hydraulics Division, ASCE, 98, HY1, Jan 1972, pp 181-199.

17. Prych, E.A., A Warm Water Effluent Analyzed as a buoyant Surface Jet, "Swedish Meteorological and Hydrological Institute, Series Hydrology Report No. 21, Stockholm, 1972.

18. Shirazi, M.A., and L.R. Davis, "Workbook of Thermal Plume Prediction - Volume 2 - Surface Discharge, "EPA-R2-72-005b, Environmental Protection Technology Series, Environmental Protection Agency, May 1974.

REFERENCES

1. Streeter, H.W., and E.B. Phelps, "A Study of the Pollution and Natural Purification of the Ohio River," Public Health Bulletin 146, U.S. Public Health Service, Washington DC, 1925.

2. Dobbins, W.E. "BOD and Oxygen Relationships in Streams," Journal of the Sanitary Engineering Division, ASCE, 90, SA3, June 1964, pp 53-78.

3. Velz, C.J., Applied Stream Sanitation, Wiley-Interscience, New York, 1970, 619pp

4. Nemerow, N.L., Liquid Wastes of Industry - Theories, Practices and Treatment, Addison-Wesley Publishing Co., Reading MA, 1971

5. Holley, E.R., J. Siemons, and G. Abraham, "Some Aspects of Analyzing Transverse Diffusion in Rivers, "Journal of Hydraulic Research, 10, 1, 1972, pp 27-57.

6. Ward, P.R.B., "Prediction of Mixing Lengths for River Flow Gaging", Journal of the Hydraulics Division, ASCE, 99, HY7, Jul 1973, pp 1069-1081

7. Rood, O.E., Jr., and E.R. Holley, "Critical Oxygen Deficit for Bank Outfall", Journal of the Environmental Engineering Division, ASCE, 100, EE3, Jun 1974, pp 661-678

8. Benedict, B.A., J.L. Anderson, and E.L. Yandell, Jr., Analytical Modeling of Thermal Discharges: A Review of the State of the Art, ANL/ES-18, Argonne National Laboratory, April 1974, 321 pp.

9. Benedict, B.A., E.M. Polk, Jr., E.L. Yandell, Jr., and F.L. Parker, "Surface Jet and Diffusion Models for Discharge of Heated Water," Proceedings, Fourteenth Congress, International Association for Hydraulic Research, Paris, September 1971, Vol 1, Paper A22, pp 183-190.

10. Jirka, G.H., G. Abraham, and D.R.F. Harleman, "An Assessment of Techniques for Hydrothermal Prediction," Report No 203, Ralph M. Parsons Laboratory, Massachusetts Institute of Technology, July 1975, pp 403.

1976 USAF-ASEE SUMMER FACULTY RESEARCH PROGRAM

Sponsored by

THE AIR FORCE OFFICE OF SCIENTIFIC RESEARCH

Conducted by

AUBURN UNIVERSITY AND THE OHIO STATE UNIVERSITY

PARTICIPANT'S FINAL REPORT

ECOLOGICAL CONSIDERATIONS FOR DEVELOPMENT OF A WATER QUALITY ASSESSMENT MODEL

Prepared by:	Lloyd C. Fitzpatrick, PhD
Academic Rank:	Associate Professor and Director Environmental Systems
Department and University:	Department of Biological Sciences and Institute of Applied Sciences North Texas State University
Assignment: (Air Force Base)	Tyndall AFB
(Laboratory)	Air Force Civil Engineering Center
(Division)	Environmental Planning Division
(Branch)	N/A
USAF Research Colleague:	Captain Stephen P. Shelton
Date:	23 July 1976
Contract Number:	F44620-75-C-0031

ACKNOWLEDGEMENT

The author expresses sincere appreciation to Colonel Iten and all the AFCEC personnel who made this report possible and his stay at Tyndall AFB profitable and enjoyable. Lt Colonel Silva and Majors Kanter and Wooten were especially helpful. The author is greatly indebted to Major Frein and Captain Shelton for their tireless assistance and patience.

The author believes that the USAF/ASEE Summer Faculty Research program will benefit both the Air Force and cooperating universities and hopes that it will enjoy continued success in the future.

LITERATURE CITED

Cardwell, R. D., D. G. Foreman, T. R. Payne and D. J. Wilbur. 1976. Acute Toxicity of Selected Toxicants to Six Species of Fish. EPA-600/3-76-008. Ecological Research Series. Environmental Research Laboratory Office of R&D. US EPA. Duluth, Minnesota.

Doudoroff, P. 1976. Toxicity to Fish of Cyanides and Related Compounds, A Review. EPA-600/3-76-038. Ecological Research Series. Environmental Research Laboratory Office of R&D. US EPA. Duluth, Minnesota.

Lefebvre, E. E. 1969. Toxic Effects of a Cutting Fluid on Biological Treatment Systems. USAF Technical Report EHL(K) 69-4.

1970. Toxic Effects of Color Photographic Processing Wastes on Biological Systems. USAF Technical Report EHL(K) 70-9.

ECOLOGICAL CONSIDERATIONS FOR DEVELOPMENT OF A WATER QUALITY ASSESSMENT MODEL

Report Submitted
to
The United States Air Force
Civil Engineering Center
Environics
Water and Solid
Resources Division

Tyndall Air Force Base
Panama City, Florida
32401

by

Lloyd C. Fitzpatrick, Ph.D.
23 July 1976

INTRODUCTION

Installations of the United States Air Force exist in vastly different environmental settings throughout the world. Many of these installations are located close to large bodies of water and have small lakes or ponds on and streams traversing their grounds. Numerous operations and missions at these installations directly or indirectly impact these surface waters. Impacts result from point and non-point effluents generated from technical/industrial operations (e.g., aircraft/AGE wash racks, vehicle wash racks, plating and metal finishing, photoprocessing, paint shops, NDI shops, degreasing heating/cooling/power generating plants); general "domestic" wastewater; runoff from runways (e.g., fuel, fire protection chemicals, foam for emergency landings), streets, and landscaping and construction projects; precipitation of airborne materials (e.g., exhaust from aircraft); landfills; and from modifications of vegetation surrounding and overhanging the waters. Some of the effluents contain substances having known or suspected toxicity to acquatic life (see, Lefebvre 1969, 1970; Doudoroff 1976; Cardwell et al. 1976). Other substances or their

derivatives may bioaccumulate in food webs/chains leading to man where they man be harmful. Often effects of effluents, landscape modification, etc., are subtle and not detectable with standard bioassay/toxicological techniques (e.g., LD_{50}'s). Minute, but chronic, levels of contaminants, increases in turbidity, alterations in stream flow, changes in substrate particle sizes, changes in thermal regimes, removal of vegetation cover, etc., can produce behavorial changes, reduction in fecundity or fertility, changes in sequencing of life history phenomena and changes in the energy-nutrient drives of the system. These may reduce a species' or several species' fitness, producing changes in community composition; overall consequence of which is difficult to predict.

The Air Force realizes its obligation to the letter and spirit of local, state and federal legislation inacted to mitigate impacts on natural systems. To fulfill this commitment, the Environics' Water and Solids Resource Division of the U.S. Air Force is developing a water quality assessment model (WQAM). This model should be able to predict and assess impacts and offer mitigative strategies for sound environmental planning of Air Force operations that could impact aquatic ecosystems. Development of an effective instrument requires much more than systems analysis and computer modeling

technology. It requires working knowledge of structure and dynamics of aquatic ecosystems and their watersheds, and adequate data bases for specific systems. Biological subsystems within ecosystems are considerably more complex and difficult to model than physical dynamics (e.g., hydrological). Air Force personnel involved in WQAM development should have an understanding of the structure and dynamics of aquatic ecosystems and their watersheds. Because aquatic systems vary considerably among eco-geographical regions, they should be cognizant of specific baseline data required to develop models of lentic and lotic dynamics. These baseline data minimally include:

1. Species and trophic (foodweb connectivities) structure throughout a year (i.e., aspectional succession).

2. Spatial array of species.

3. Life histories of species and factors that sequence them.

4. Relationship between physical structure (e.g., substrate particle size) and species.

5. Susceptability of various life history stages (i.e., egg, larval, immature and adult) of species to compounds in effluents (both LD_{50} - type data and data on subtle behavior,

fertility, fecundity, developmental, etc., effects of compounds singly and combined as in the effluents are required).

4. Similar effects of physical factors (e.g., temperature, turbidity, flow rates, sedimentation) on life history stages.

5. Standard water quality characterization including thermal and hydrological regimes throughout the year.

6. Qualitative and quantitative characterization of point and non-point effluents throughout the year.

My basic objective in this report is to introduce Air Force personnel involved in WQAM development to:

1. Nature and complexities of biotic communities.

2. Current primitive status of ecological knowledge and paucity of falsifiable theories at the biotic community-ecosystem levels.

3. Inherent difficulties of applying mathematical modeling techniques, so well-developed in engineering, to biological systems.

4. Local and regional variability and uniqueness of biotic communities.

5. Types of time-series studies required for development, interpretations, implementation, and verification of WQAM.

My approach is to review and summarize some of the contemporary literature on ecosystem structure and dynamics (specifically biotic communities in stream ecosystems), provide a reasonably comprehensive bibliography and construct a preliminary conceptual model for the biotic community in Clover Creek at McChord AFB, Washington. I deliberately avoid discussing literature on toxicology and pollutant effects.

My report is divided into four sections, each with a selected bibliography. These are:

I. General Contemporary Concepts and Theories in Community Ecology

II. Structure and Dynamics of Biotic Communities in Stream Ecosystems

III. General Comments on Modeling Biotic Communities

IV. General Conceptual Model of the Biotic Community in Clover Creek

LITERATURE CITED

Cardwell, R. D., D. G. Foreman, T. R. Payne and D. J. Wilbur. 1976. Acute Toxicity of Selected Toxicants to Six Species of Fish. EPA-600/3-76-008. Ecological Research Series. Environmental Research Laboratory Office of R&D. U.S. EPA. Duluth, Minnesota.

Doudoroff, P. 1976. Toxicity to Fish of Cyanides and Related Compounds, A Review. EPA-600/3-76-038. Ecological Research Series. Environmental Research Laboratory Office of R&D. U.S. EPA. Duluth, Minnesota.

Lefebvre, E. E. 1969. Toxic Effects of a Cutting Fluid on Biological Treatment Systems. USAF Technical Report EHL(K) 69-4.

_____. 1970. Toxic Effects of Color Photographic Processing Wastes on Biological Systems. USAF Technical Report EHL(K) 70-9.

I. GENERAL CONTEMPORARY CONCEPTS AND THEORIES IN ECOLOGY

In this section I wish to emphasize the relations between biotic community structure (e.g., spatial, species, trophic, niche) and dynamics (e.g., energy flow, material cycling, population fluctuations), and the growing controversy surrounding the diversity-stability hypothesis; particularly in reference to using species diversity indices as unbiased estimators of ecosystems "health" or to assess impacts of Air Force projects. I also wish to argue for the need for development of falsifiable theories at the community-ecosystem level and that studies designed to test them should be supported.

The concept of the biotic community (= living components of ecosystems) and ecosystem is not new to ecologists. However, there are divergent views among ecologists as to whether or not they represent the highest levels of functional biotic integration. Odum (1971) addressed this idea and pointed out the importance of the principle of functional integration. Essentially life is arrayed in a hierarchy of levels of organization, and ". . . no one level is any more or less important or any more or less deserving of scientific

study than any other level . . . furthermore, the findings at any one level aid in the study of another level, but never completely explain the phenomena occurring at that level." Odum emphasized this as " . . . an important point because persons sometimes contend that it is useless to try to work on complex populations and communities when the smaller units are not yet fully understood." The principle infers that new properties develop or emerge (emergent properties) at each level of organization as a consequence of subsystems or sublevel coupling. Thus, the whole is greater than the sum of its parts. In attempting to understand one level, we must be cognizant of what knowledge of lower levels is trivial and what is pertinent. Often work at one level directs meaningful research at lower levels. Thus, ecologists working at different levels should maintain communication. Such advice applies to all disciplines involved in environmental studies.

Smith (1975) articulately summarized, and I believe put to rest, the often semantic dichotomous views on ecosystems.

> "Two extreme views of ecosystems can be recognized. In one view, an ecosystem emerges as the sum of its parts. Any understanding of the whole must derive from studies of the species. An evolutionary understanding of ecosystems follows from studies of the ecology of each species as a product of natural selection. Such studies

> are the heart of Evolutionary Ecology, based on intimate observations and experimentation in natural history, population dynamics, population genetics, behavior, physiology, etc. This approach includes studies of co-evolution among strongly associated species. Studies on enough species in an ecosystem will, collectively, provide an evolutionary understanding of the form and function of the system. In this view the species are unique. Any uniqueness of the ecosystem derives from the uniqueness of its species.
>
> In the opposite view, ecosystems are persistent organizations, constrained to workable configurations and therefore themselves strongly constraining the evolution of its species. Much of the evolution that does occur is irrelevant in the sense that it has little if any effect on the performance of the system. Indeed, one species or set of species may be substituted for another with little disruption of the whole. This implies that the uniqueness of species may contribute little or nothing to the uniqueness of the ecosystem. In this opposite view, ecosystems have uniqueness of their own that guides the evolution of species, rather than emerging from the evolution of species."

Smith argued ". . . that both views have validity, and that they are in less conflict than may at first appear." Using concepts of the hypervolume niche, interspecific competition and natural selection, Smith concluded ". . . that ecosystems emerge as products of the evolution . . . [and] . . . These same selective forces operating through connected systems of species, exert consistent and predictable effects upon the evolution of assemblages. These are . . . systems constraints. Learning about them will be a basic contribution to ecosystem science." Smith argued that although the species is the unit for study, each species in a community affects other species. "Not only does

each species achieve balance, but they do so at the same time in the same systems. Through the food web, and through competition for other resources, one species' gain is often another species' loss." "The basic requirement of existence for each species is a general balance of inputs and outputs. . . . The array of adaptations affecting inputs and outputs is potentially very large . . . [and] . . . will usually involve trade-offs, improving some relationships at the expense of others. Thus, the equations of inputs and outputs are interconnected . . ." The relevance of the species' connectivity to modeling and systems analysis is the potential problem of solving many simultaneous differential equations. Not only do errors in one place generate errors throughout the model, but because each species is affected by all others, modeling their feedbacks is drastically complicated.

Biotic communities are composed of populations of species arrayed in space. Each community type (e.g., stream, pond, lake, forest, grassland, intertidal) has unique vertical and horizontal structure. Structure also varies within a community type over geographical and ecological space (e.g., fast mountain streams vs. slow streams in lowlands). Species are generally not arrayed randomly, (if random it is most likely to be Poisson) but are dispersed in a

contiguous (clumped) fashion. Smith (1975) stated that the struggle to occupy space is a major organizing force in many ecosystems.

Populations are connected through the food web. This trophic structure is unique among community types and also varies within community types over time and space. Although species often interact outside the food web, trophic interactions are important for modeling; they are the input-output functions. It is through the food web that matter cycles (i.e., biogeochemical cycle) and energy flows. Smith (1975) argued that trophic interaction is also a major organizing force within ecosystems.

Each species within a community occupies a niche. There is considerable literature on niche theory and niche dynamics. For this report I equate niche with the trophic role of a species in its community. That is, the qualitative and quantitative ways it processes matter and energy. Niches have been segregated and refined through interspecific (between species) competition. Niches are dynamic on three time scales. First, they change according to life history changes of a species (e.g., larval and adult stages of butterflies have different niches). Second, they change seasonally. Third, they change over evolutionary time.

Thus, the biotic community can be envisioned as a dynamic three-dimensional matrix of niches that captures and processes matter and energy. Unlike physical systems that process matter or energy or both, the community's integrity is dependent upon continuous imput of matter and energy. In fact, the concept of energy flow as an organizing force in open system thermodynamics has directly and indirectly produced several "unifying concepts" in community-ecosystem ecology. Ecologists have searched for a unified theory to account for geographic variations in community structure (principally species diversity) and biotic succession (i.e., the apparent orderly replacement of one biotic community by another). According to Prigogine's theorem, open systems have maximal structural order and efficient material cycles when energy input equals output (i.e., they are in steady state).

Thus, ecological systems should evolve structure that comes closest to equalizing energy input and output (i.e., the climax community). Since physico-chemical constraints differ across space, community structure should also differ. Succession is the local process by which the climax assemblage develops over ecological time. One stage outcompetes another until there is a persistent community. This terminal association should have the most complex and stable structure, and most efficient biogeochemical cycles because it

is closest to the steady state. Extending Smith's (1975) arguments, the internal development of this organization is through competitive trophic and spatial interactions (i.e., reciprocal or co-evolution) among species. That is, neo-Darwinian processes of adaptation and natural selection function in ecosystem evolution. The process is Markovian, each change constrains the set of next possible changes.

Observations that climax communities persist through time with apparently greater stability than earlier successional stages and that some forms of diversity (usually species) increase with succession have led to the diversity-stability hypothesis. This states that diverse systems are more stable than less diverse ones. This idea has persisted in ecology for some time and is a basis for laypersons to conceive of diverse systems as being more desirable than less diverse systems. Most guidelines for environmental impact statements, assessments and analyses require evaluation of ecosystems in terms of species diversity. However, the relations between diversity and attributes of persistence, stability, predictability, steady state energy flow, ecological efficiences, biogeochemical cycles, productivity, etc. are unclear.

Consider stability. May (1973) developed mathematical models of systems that suggest increased diversity is accomplished by increased dynamic fragility. Odum (1975) hypothesized

> " . . . that too much diversity can be destabilizing as well as too little. . . [and] . . . that optimum diversity is a function of the quality and quantity of energy flow. Low diversity may be optimum in ecosystems strongly subsidized by high quality auxillary energy flows and/or by large nutrient inputs, while a higher diversity may be optimum in ecosystems limited by the quality of energy input and/or dependent on internal nutrient recycling. Any positive correlation between diversity and stability is, therefore, a secondary rather than a primary relationship. Which is to say that quite stable systems in terms either of persistence in time or in terms of resistence to perturbation can have either a low or a high diversity, depending on the energy forcing function."

He based the above hypothesis on 150 censuses of major trophic and taxonomic components which have important roles in ecosystems representing a wide variety of natural, seminatural, managed and cultivated types. He used species diversity as measured by the reciprocal Simpson Index where Pi is the probability

$$1 - \Sigma\ (Pi)^2 \qquad (1)$$

for each species in terms of the ratio of its importance to the total of importance values. He used numbers as the basis for importance where individual sizes were comparable, but biomass or productivity where sizes varied widely. The index scales diversity from

0-1, where 0 is the lowest and 1 is the maximum. The frequency distribution of the diversity index values was bimodal, low (0.05-0.2) in one group and higher (0.7-0.85) in another. There were relatively few ecosystems with intermediate diversities (ca. 0.5) and no case where there were large numbers of species with similar importance (i.e., producing index close to unity). Low diversity systems were stressed (i.e., degraded) by external factors such as inputs to polluted aquatic systems, or were agriculturally managed croplands and forests. Systems receiving large high quality and predictable energy subsidies and nutrients (e.g., tidal marshes) also showed low diversity. High diversity was observed in ecosystems powered principally by sunlight (a low quality energy source relative to its utilization efficiency), such as grasslands, upland forests, lakes in stable or nutrient-poor watersheds.

Odum stated that

> "The strategy of nature is to diversity but not to the extent of reducing energetic efficiency . . . the quality of energy in terms of utility and low entropy is as important as the quantity . . . the optimum diversity is determined by both the kind and the level of energy input. When one or a few sources of high utility energy coupled with pumped-in growth-promoting substances are available in excess of maintenance needs, low diversity has its advantages; a concentrated and specialized structure is more efficient in exploiting the bonanza than is a dispersed structure. It is perhaps under such conditions that high diversity is destabilizing (i.e.,

> undesirable) as May's (1973) theoretical models show. High energy, low diversity systems can be quite stable both time-wise and in terms of resistance to perturbation if the input subsidies are regular or continual at the same level over long periods of time . . . . Under such conditions a low diversity of the order of 0.1-0.2 is optimum. But . . . such systems will tend to 'boom or bust' when the subsidies fluctuate irregularly where energy is limiting or of low . . . then a higher diversity of order of 0.7-0.8 appears to be optimum for the performance of the steady state."

Odum also pointed out that high diversity characterizes ecosystems in very stable physical environments (e.g., some ocean bottoms, wet tropics). This supports the stability-time hypothesis which states that diversity should be highest in regions that have been stable for the longest time. The stability-time hypothesis essentially articulates the other view of diversity-stability relations. That is, diversity does not precede or cause stability first; stable environments permit development of diverse communities. They, in turn, may become more stable internally, resisting invasion by exotic species, disease epidemics, violent population fluctuations, etc.

On the base of his data, Odum urged caution in using diversity as an index to pollution or other human effects on ecosystems; and stated "If the impacted system has high diversity, then most stresses will certainly lower the diversity. But if the system has a low diversity to begin with, then a man-made perturbation may actually increase diversity ratios."

Odum's data essentially accord with Smith's (1975) contention that trophic interaction is a major organizing force in ecosystems. The matrix of niches appears to develop as a function of energy and matter forcing functions. Thus, ecosystem structure as increased by diversity must be considered in the context of the set of forcing functions.

I have used diversity and stability without clearly defining them or discussing how to measure them. However, before doing so, I wish to conclude the diversity-stability argument with excerpts from Goodman's (1975) fine treatment of the subject

> "About twenty years ago, the belief, traditional among ecologists, that complex natural communities are more stable than simple ones was given formal expression in a way that seemed to offer promise of both precise empirical tests and further theoretical development. The elaboration of theoretical models at first yielded gratifying results suggesting reasons why complex ecological systems should indeed be more stable, but these models suffered from questionable analogies and the use of peculiar and unrealistic mathematical representations. The broad scope of the diversity-stability hypothesis, and its particular implications, elevated it to a position of importance in practical debates concerning resource management, pest control, and preservation of natural areas. Observational confirmation of the diversity-stability hypothesis never materialized . . . The social implications of the failure of diversity-stability theory involve both straightforward practical concerns and more subtle problems of conservationist ideology.
>
> The diversity-stability hypothesis has been trotted out time and time again as an argument for various preservationist and environmentalist policies. It has seemed to offer an easy way to refute the charge that these policies

represent nothing more than the subjective preferences of some minority constituencies. The burden of evidence subsumed in this review indicates that this particular defense will not be possible much longer, since continued scientific support for an untenable theory would become an embarrassment to that spirit of detached empirical sobriety which so often is held up as an ideal of scientific comportment. From a practical standpoint, the diversity-stability hypothesis is not really necessary; even if the hypothesis is completely false it remains logically possible - and, on the best available evidence, very likely - that disruption of the patterns of evolved interaction in natural communities will have untoward, and occasionally catastrophic, consequences. In other words, although the hypothesis may be false, the policies it promotes are prudent. The troubling questions for the moment are how effectively these policies will be defended with scientifically more acceptable arguments, and how smoothly this transition can occur.

The diversity-stability hypothesis may have caught the lay conservationists' fancy, not for the allure of its scientific embellishments, but for the more basic appeal of its underlying metaphor. It is the sort of thing that people like, and want, to believe. Thus, though better theories supplant it in scientific usage, we may be certain that the "hypothesis" will persist for a while as an element of folk-science. Eventually, that remnant, too, may vanish in light of discordant facts, and the essential imagery of this once-scientific hypothesis will recede to a revered position in the popular environmental ethic, where it doubtless will do much good."

Diversity can take two major forms in ecosystems: spatial heterogeneity (e.g., horizontal and vertical complexity of the physical environment, biotic structure as in foliage heights of plants) and species (niche) diversity. Although the former has direct and indi ect stabilizing effects on population dynamics (e.g., predator-prey, herbivore-plant, parasite-host relations) and

may influence species diversity (e.g., more bird species are found in woodlots with high foliage-height diversity than in those with less), species diversity is the more frequently used to measure community-ecosystem complexity. Because species represent niches (recall that one species' niche may change seasonally and according to the life history stage so that one species actually represents a "niche spectrum"), species diversity is a first approximation of, say, trophic diversity (i.e., diversity of matter and energy channels).

Species diversity has two major components, variety or richness and evenness or equitability. Richness has to do with the number of different species (S) that exist in a community, and evenness is a function of how the total number of individuals (N) is distributed among S species. Thus, maximum diversity for a 10 S community with 1000 N would be when each S has 100 N. Number of individuals per species essentially represents a numerical importance value (Ni/N) for the ith species (S_i). Use of numbers may be suitable for a set of species that are of similar sizes and physiologies. Other variables such as biomass, bio-content (caloric equivalent of biomass), productivity (grams or calories produced by species per unit time), energy flow (production + respiration per unit time), etc. can be used.

Extreme care must be used in selecting the variable and set of species for diversity measurements and in deciding what the diversity index measures beyond the obvious "importance" of each species relative to numbers, biomass or some process. If it is to reflect the possible number and relative importance of, say, energy flow channels or intertrophic connectivities, then species must be grouped according to their trophic level(s). Since many species feed in more than one level on a daily or seasonal basis or both, this becomes complicated. This difficulty faces the modeler when attempting to construct equivalence input-output classes for compartmental models of ecosystems.

Before discussing diversity in terms of trophic connectivities, I wish to list the most frequently used indices. I will not comment on their relative merits beyond saying that the optimal index should be reasonably independent of sample size and measure both components of diversity. Shannon-Weaver and Simpson's indices are the most frequently used and satisfy the requirements as well as any others. It should be kept in mind that the biological relevance, if any, of the index depends upon what ecosystem attribute is being used.

Simpson's Index is

$$D = 1 - \sum_{j=1}^{S} \frac{Nj(Nj - 1)}{N(N - 1)} \qquad (2)$$

where Nj - number (or biomass, etc.) of individuals in the jth species and N = total number of individuals in the collection of S species.

Index of dominance (variation of number 2) is

$$C = \sum_{j=1}^{S} (nj/N) \qquad (3)$$

where nj = importance value (e.g., numbers, biomass) of the ith species and N = total of importance values.

Index of Similarity between two communities

$$S = \frac{2\,C}{A + B} \qquad (4)$$

where A = number of species in community or a sample one, B = number in two and C = number common to both.

Index of Dissimilarity

$$D = 1 - S \qquad (5)$$

Varietal or richness indices

$$D = S = \text{number of species only} \qquad (6)$$

$$D = S / 1000\ N \qquad (7)$$

$$D = (S - 1) / \log N \quad (8)$$

$$D = S / \sqrt{N} \quad (9)$$

where N = total number of individuals in S species.

Indices based on the Information Theory

$$I = \log_2 S \quad (10)$$

$$I = \log_2 \frac{(N - 1)!}{(N - S)!(S - 1)!} \quad (11)$$

$$I = \log_2 N! \quad (12)$$

$$I = \frac{1}{N} \log_2 \frac{N!}{N_1!N_2! \ldots N_s!} \quad (13)$$

$$I = \log_2 (N^N) \quad (14)$$

$$I = N (\log_2 N - 1) \quad (15)$$

$$\bar{H} = - \sum_{i=1}^{S} Pi \log_2 Pi \quad (16)$$

where I = information (diversity) in bits. Number 10 gives I_{min}, based simply on the number of species. Number 11 gives information content (diversity) of knowing how N is distributed among S. Number 12 is Brillouin's index and gives total I_{max}, based on knowing where each individual is located in space. Number 13 gives I_{max} per individual. Numbers 14 and 15 use

Stirling's approximation ($\log_2 N! = N(\log_2 N - 1)$ of Brillouin's Index. Number 16 is the most frequently used index based on the Information Theory. It was recently discussed by Mulholland (1975) and Goodman (1975), who presented constrasting views as to its usefulness. The relative importance of each species is Pi.

Evenness Index

$$J = \bar{H} / \bar{H}_{max} \qquad (17)$$

where $\bar{H}_{max} = \log_2 S$ (i.e., when each S has an equal number (or biomass, etc.) of individuals.

Redundancy Index

$$b = \bar{H} / \bar{H}_{max} \qquad (18)$$

Mulholland (1975) stated that "Diversity and the complexity of food web structure, or connectivity, are central to the discussion of ecological stability and choice." Instead of simply using species diversity measured by numbers, biomass, biocontent, etc., he suggested that we "consider a definition of diversity as the effective number of choices between equally likely alternatives for the flow of energy through the ecosystem." Mulholland demonstrated that "the complexity of the food web structure, and hence the ecological stability, can be altered by changing

the initial flow vector." I find the basic concept, which predates Mulholland's paper (e.g., Odum 1953; MacArthur 1955; Margalef 1963), intuitively pleasing and compatible with Odum's (1975) hypothesis and Smith's (1975) contention that energy-nutrient drives and trophic interaction organize communities. However, Mulholland pointed out that "In order to be of practical use as a tool for ecosystem analysis, the stability index . . . must be tested in real world situations. It must also be evaluated relative to other proposed measures of ecological stability. And, with respect to theoretical studies, it must be investigated as a possible connection between the concept of ecological stability and the formal mathematical stability definition." Such an evaluation will be difficult, requiring considerable effort. Orians (1975) stated that

> "Unfortunately it will be difficult to establish causal relationships between stability and diversity because we must measure one or more concepts of stability in ecological systems differing only in some measure of diversity. The easiest ecosystems to compare cannot provide adequate proof because differences in diversity are usually associated with differences in the physical environment and other complicating factors. Rather than demonstrating greater stability in species-rich systems we may only be showing that species are more vulnerable to disturbances in marginal environments, or that environmental constancy facilitates diversity while reducing perturbations that might affect stability. In fact, we are confronted with the apparent paradox that stability in natural ecosystems seems to be associated with diversity whereas increasing the diversity of a variety of model ecosystems tends to reduce rather than enhance their stability (May, 1973).

> Another attractive option, the perturbation experiment, also confronts serious interpretational problems because the species in ecosystems are coevolved and removal or addition of one or more of the species not only changes the diversity of the system but many of the interaction parameters as well. Which of the changes should be attributed to differences in diversities and which should be attributed to changed interactive patterns is difficult to determine. If the species are allowed to adjust evolutionarily to the new association patterns, the final stabilities may be very different from the ones observed immediately after the perturbation.
>
> Theoretical developments face similar problems. Most formal analyses of concepts of stability are based on non-linear population equations. Given a system of these equations, equilibrium populations are determined by setting all growth rates equal to zero and then analyzing the effects of perturbations around the equilibrium. A common bond is the use of an m x m matrix, referred to as the interaction matrix, each element of which describes the effect of species j on species i near equilibrium. Analysis of an interaction matrix reveals whether or not the system is stable, i.e., if it returns to its original state after a perturbation, and the speed of return which can be estimated from the values of the elements. Most theoretical studies have focussed on local stability under deterministic environments and small perturbations. It is, however, also possible to construct matrices whose elements are random variables and to analyze responses to stronger perturbations (May 1973), or to considerable qualitative matrices in which only the signs of the interactions are known and not these values."

Mulholland used ". . . a piecewise linear, donor-controlled compartment type system [model]" developed for an International Biological Program (grassland biome study, Patten 1972) for a stability analysis. Although only a first approximation of this approach, I believe it demonstrated enough value for workers to pursue it. However, I suggest that simultaneous

examination of other, more easily measured, diversity parameters (e.g., species diversity) be taken. Thus, if there is high correlation between Mulholland's pathway choice index and a more easily obtained attribute, the latter could be used.

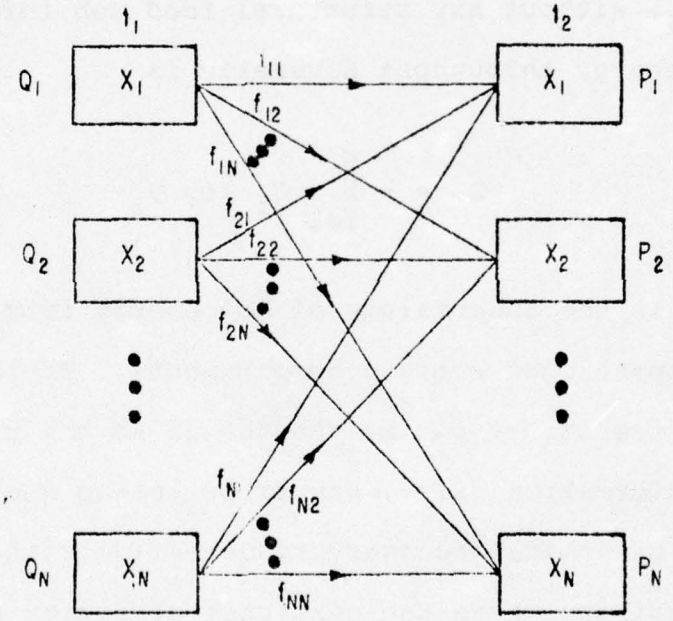
Also, as pointed out by Mulholland

> "The diversity of throughput [= compartment content, say in calories x turnover] does not completely characterize the choice of pathways for energy flow and, as has been demonstrated experimentally . . . it cannot be used exclusively as a measure of stability. The choice of pathways for energy flow, and hence the ecological stability, depends not only on the diversity of throughput but also on the complexity of the food web structure. Complexity of the food web structure, or connectivity, refers to the degree and patterns of component interdependence in an ecosystem. Maximum complexity occurs when every compartment derives energy from every other compartment in equal amounts. A [linear] food chain represents minimum complexity or connectivity."

I believe that the maximum complexity is as Mulholland stated, but do not believe that there is any reason to believe a priori that this evenness should evolve in all climax communities. The number of throughput channels and their relative importance should be a function, as Odum (1975) argued, of the quality and quantity of the forcing functions. Considerable basic research is needed on the dynamics of food web complexity and their relations to inputs (i.e., their quantity, quality, and predictability). This research is essential to developing stream models (e.g., WQAM). However,

because Mulholland's approach has merit, can be used to describe ecosystem diversity in another way and enables discussion of the Shannon-Weaver equation, I will present his model before going into what is meant by stability.

Mulholland used a compartment model (shown below; his Fig. 1) connected by energy flow channels to demonstrate his idea.



The compartments (i.e., populations of species in different trophic levels; again recall that occupancy of trophic positions by a species is time varying, something not considered by Mulholland, but must be in future work), x_1, x_2, . . . x_n, are shown at two times t_1, and t_2. The percentage of total energy flow through the system at t_1,

passing through $x_i = Q_i$ and P_j = percentage of total energy throughput at t_2 passing through x_j. The percentage of total energy flow through x_i that passes to x_j between t_1 and $t_2 = f_{ij}$. The relations among these variables are described by

$$Pj = \sum_{i=1}^{N} fij\ Qi \qquad (19)$$

At t_1, without any structural food web information, the energy throughput diversity is

$$D = - \sum_{i=1}^{N} Q_i \log Q_i \qquad (20)$$

This is the uncertainty of how energy from given sources is apportioned among n compartments. If $\log_2$ is used the uncertainty can be thought of as the number of bits of information (i.e., number of yes-no questions that must be asked) necessary to determine with unit probability where the next unit of energy passing into x_i came from. Clearly, the maximum information is required where there is equal probability that the unit of energy came from each source. Mathematically this is, for n sources, $\log_2 n$. The minimum, zero, is when there is only one source possible.

If the food web structure is known (i.e., increased information base), a quantity known in information theory as the average mutual information, I, can be

used to measure the uncertainty resolved by that knowledge.

$$I = \sum_{k=1}^{N} \sum_{j=1}^{N} f_{kj} Q_k \log \left[f_{kj} / \sum_{i=1}^{N} f_{ij} Q_i \right] \quad (21)$$

The measure of the average remaining uncertainty about energy sources at t_2 is called conditional entropy, S, and is calculated as

$$S = D - I \quad (22)$$

Mulhollan argued that S ". . . is equivalent to the effective choice of pathways for energy flow. Thus, a measure of the remaining uncertainty . . . [and] . . . a measure of effective choice, and hence a useful index of stability. It is also clear that the complexity of the food web reflects the opportunities for choice of path."

Orians (1975) listed seven meanings for stability. He pointed out that the terms were not intended as a classification system. These terms are:

1. Constancy - a lack of change in some parameter of a system . . .

2. Persistence - the survival time of a system or some component of it.

3. Inertia - the ability of a system to resist external perturbations.

4. Elasticity - the speed with which the system returns to its former state following a perturbation.

5. Amplititude - the area over which a system is stable (also known as global stability; the distance it can be displaced and still return).

6. Cyclic stability - the property of a system to cycle or oscillate around some central point or zone.

7. Trajectory stability - the property of a system to move towards some final end point or zone despite differences in starting points.

Stability of a system must be considered in terms of its environment. Ecosystems have evolved various mechanisms of stability relative to the stresses their species have encountered over evolutionary time. Thus, we should not expect stability when new forces are applied to our ecosystem (e.g., pollution).

I will conclude the comments on stability (Table 1; Orians 1975) of environmental factors and species characteristics that appear to increase stability.

A. Persistence

1. Environmental heterogeneity in space and time
2. Large patch sizes
3. Constant physical environment
4. High resource utilization thresholds of predators

B. Inertia

1. Environmental heterogeneity in space and time
2. Greater phenotypic diversity of prey
3. Multiplicity of energy pathways
4. Intraspecific variability of prey
5. High mean longevity of individuals of component species (Frank, 1968)

C. Plasticity

1. High density-dependence in birth rate
2. Short life cycles of component species
3. Capacity for high dispersal
4. Strong migratory tendencies
5. Generalized foraging patterns

D. Amplitude

1. Weak density-dependence in birth rates
2. Intraspecific variability of component species
3. Capacity for long-distance dispersal

4. Broad physical tolerances
5. Generalized harvesting capabilities
6. Defense against predators not dependent on a narrow range of hiding places

E. Cyclic Stability
1. High resource-utilization thresholds
2. Long lag times in response of species to changes in resource availability
3. Heterogeneity of environment in space and time

F. Trajectory Stability
1. Strong organism-induced modifications of the physical environment
2. All factors increasing elasticity.

Even the simplest communities and ecosystems are extremely complex in structure and behavior. Structural and behavioral attributes are also time varying. Thus, complexity has both spatial and chronological components. Modern ecology is actively addressing functional attributes of ecosystems, but in most instances, our knowledge of structure is inadequate to support development of testable theories relating to function and structure. There are numerous concepts, but relatively few falsifiable theories at the community-ecosystem levels. Development of these theories and testing them are essential prerequisites for development

of appropriate land planning and resource management strategies, and construction of predictive computer models (e.g., WQAM).

We must have time-varying baseline data on structure and dynamics of ecosystems collected under the time-varying regime of their forcing functions. The quantity, quality, and predictability of the inputs under which the systems have evolved must be studied simultaneously with the structure and benavior. Such studies should be conducted by personnel representing biological and physical sciences (e.g., chemistry, physics, hydrology, meteorology, geology), and engineering.

1976 USAF-ASEE SUMMER FACULTY RESEARCH PROGRAM
sponsored by
THE AIR FORCE OFFICE SCIENTIFIC RESEARCH
conducted by
AUBURN UNIVERSITY AND OHIO STATE UNIVERSITY

PARTICIPANT'S FINAL REPORT

DYNAMIC RESPONSES OF AIRCRAFT SHELTERS

Prepared by:	Fang-Hui Chou Ph.D
Academic Rank:	Professor
Department and University:	Department of Civil Engineering, San Diego State University
Assignment:	Tyndall AFB. Air Force Civil Engineering Center
USAF Research Colleague:	Lt. Dennis Morrison
Date:	August 6, 1976
Contract No.:	F44620-75-C-0031

DYNAMIC RESPONSES OF AIRCRAFT SHELTERS

by

Fang-Hui Chou

ABSTRACT

The dynamic response of aircraft shelters subjected to airblast is studied. The structural system of the shelter consists of a doubly corrugated, semi-cylindrical steel shell, covered with eighteen inches of concrete. The shelter is 100 feet long with a reinforced concrete door at one end and an armor steel door recessed 30 feet from the open end. The armor steel door is connected to a reinforced concrete frame inside the shelter.

A two-hinged arch representing a typical shelter element in the longitudinal direction was analyzed by the finite element method. Time varying functions representing the dynamic pressure of an airblast from a high explosive detonation was applied. The SAP IV computer program was used in computing the dynamic responses of the arch. Response time-history for both displacement components and stress components at various points were obtained.

The analysis was then extended to a two-dimensional approach. The entire shelter was treated as a semi-circular cylindrical shell supported by the hinge base, the end wall, and the concrete frame where the armor door was located. The shelter, with the doubly corrugated steel shell at its' inner face, was transformed into a shell of uniform thickness but anisotropic in nature. The equivalent thickness and the elastic constants were so chosen that they can best represent the bending stiffness of the shelter in both circumferential and longitudinal directions. Dynamic responses of this model shell due to airblast were investigated by the method of modal superposition. Numerical results of both the arch and shell analyses are compared and discussed.

3

ACKNOWLEDGEMENT

The assistance of Lt. Dennis Morrison of the Air Force Civil Engineering Center during the course of this study is gratefully acknowledged.

4

LIST OF FIGURES

Figure 1 General Configuration of Aircraft Shelter

Figure 2 Typical Cross-Section of Arch

Figure 3,4 Finite Element And Positive Forces

Figure 5a-5c Dynamic Load Function

Figure 6a-6d Time History Responses of Arch

Figure 7 Finite Element Model of Shell

Figure 8 Cross-Section For Determining Constant I

Figure 9-a Typical Shell Element

Figure 9-b Element Stress Resultants

Figure 10 Free Vibration Mode Shapes of Shell

Figure 11a-14h Time History Responses of Shell

5

1. INTRODUCTION

1.1. Background:

This report documents the results of a 10-week study (Summer Faculty Research Program) on the dynamic response of aircraft shelters subjected to airblast. The research was conducted at the Air Force Civil Engineering Center (AFCEC) at Tyndall AFB, Florida.

Investigation of structural behaviors of aircraft shelters has been a continuing effort of the Air Force Weapons Laboratory (Ref. 1, 2, and 3). Results of full scale tests of the moment-rotation relations and other structural behaviors of concrete covered corrugated arch panels were presented in Ref. 1 and Ref. 2. Ref. 3 presents the test results of dynamic pressure, structural deformation and damage of several aircraft shelters subjected to an airblast. Analytical Studies of gross structure behaviors of aircraft shelters under blast load, however, have not been made. Methods of analyzing various types of protective structures under blast loads can be found in Refs (4) (5) and (6).

1.2 Objectives

The present study is intended to achieve two objectives:

1. To establish a reasonable structural model of the aircraft shelter for computerized analysis.

2. To determine the blast load the aircraft shelter can resist within it's elastic limit.

1.3 Approaches

The structural system of the aircraft shelters under consideration consists of a doubly corrugated steel shell covered with 18 inches of concrete. The mean radius of the semicircular shell is 25 feet. The shelter is 100 feet long with a reinforced concrete wall at one end and an armor steel door recessed 30 feet from the open end. The armor steel door is connected to a reinforced concrete frame known as the door support collar. A general overview of the aircraft shelter is shown in Fig. 1.

The analysis presented in this report is based on the finite element method. Two types of structural models are considered. One, a two hinge arch with beam elements, and the other, a semi-cylindrical shell composed of thin shell elements. The SAP IV computer program is used in computing the dynamic responses of both structural models.

2. ARCH ANALYSIS

2.1 Cross-section Properties

A two-hinged arch representing a typical shelter element in the longitudinal direction was considered. Its' cross-section and reinforcement were shown in figure 2. Preliminary tests have shown that the corrugated steel has very low equivalent modulus of elasticity under uniaxial stress. Therefore, it is not justified to consider the steel liner as the reinforcement of the concrete cross-section. From a reinforced concrete design point of view, the cross-section has an extremely low steel ratio. In view of these facts and the fact that only elastic analysis will be made, the tensile capacity of the concrete will be considered. The section properties indicated in figure 2 are those of the gross cross-section neglecting the effect of the corrugated steel. The minimum concrete strength f'_c is specified to be 4,300 psi.

2.2 Finite Element Model

The arch is subdivided into sixteen beam elements each having the same cross-section properties as the arch. The numbering system for the elements and the modal points are shown in figure 3. A typical beam element and the positive directions of forces and moments acting on the element are shown in figure 4. Several comparitive computations using the SAP IV computer program and exact solutions indicate that the required accuracy can be achieved by the sixteen element model. The results of these computations are summarized as follows:

Case I. A uniform radial pressure of 7 psi.

SAP IV results show a uniform axial force of 51 kips whereas shear force and bending moment are of much smaller order. This is in agreement with the exact solution.

Case II. A uniform radial pressure of 7 psi from point 1 to point 9 and a uniform radial suction of 7 psi from point 9 to point 17.

	SAP IV Results	Exact Solution
Moment at point 5	535.8 ft-kip.	531.6 ft-kip
9	1.7 ft-kip	0

Case III. Frequencies of Free Vibration

	SAP IV	Ref. 4 Results
Period of 1st Mode	0.223 sec.	0.225 sec.
2nd Mode	0.074 sec.	0.074 sec.
3rd Mode	0.037 sec.	0.037 sec.
4th Mode	0.023 sec.	0.023 sec.

It was also found that inclusion of shear deformation in these calculations would not result in appreciable difference in either nodal displacements or important stress components.

2.3 Dynamic Load and Numerical Results

In the analysis, it is assumed that the blast wave is propagating in the direction perpendicular to the longitudinal axis of the shelter. In establishing the dynamic pressure acting on the structure, the method outlined in reference 4 (chap. 7) was followed. The total load was represented by two load cases: (1) a uniform radial pressure and (2) an antisymmetric but uniformly distributed pressure. A normalized time varying function representing an airblast of 500 T-TNT at a distance of 600 feet was chosen from reference 3 (see fig. 5a). It's equivalent dynamic pressure on the structure was shown in figures 5b and 5c. It should be noted that, due to the extremely short rise time, the peak pressure was assumed to occur at time zero. Dynamic responses of the arch are then computed by the use of the SAP IV computer program. Time response history of several nodes are shown in figures 6a-d. Maximum forces on various elements are listed in Table 1. (See figure 4 for notations and sign convention).

Table 1 Maximum Element Forces
(peak Pressure: 7 psi)

Load Case	Element Number	F(lb)	V(lb)	M_1(in-lb)
	1	-82280	5246	0
	3	-80620	-6085	327900
I	5	-81490	-7296	256400
(SYM.)	7	-80430	8653	364600
	9	-80090	5473	-491400
	1	-53000	-41800	0
	3	-58240	-21030	-4180000
	5	48580	12260	5726000
	7	-24000	33640	4249000
II	9	7961	41890	49990
	11	38940	23320	4246000
	13	54580	-11340	-5722000
	15	57620	-33290	-4181000
	17	-52970	-41790	0

It should be noted here that these maximum forces do not occur at the same time. Complete time-history responses from the computer output, however, can not be reproduced here. Considering the area and the moment of inertia of the given cross-section, it can easily be seen that the bending moment of Load Case II is the dominating factor for the purpose of design and analysis. Therefore, the maximum tensile stress in the arch is (node 5, t = 0.096 sec.)

$$f_t = \frac{5726000 \times 18.1}{46300} = 2238 \text{ psi}$$

9

This exceeds the allowable dynamic tensile stress of (Section XI, Ref. 5)

$$F_t = 7.5\sqrt{f'_c} = 7.5\sqrt{4300} = 491 \text{ psi}$$

For the purpose of comparison with the analysis of the next section, the maximum peak pressure is established by proportion without changing the dynamic pressure function.

$$p = 7 \times \frac{491}{2238} = 1.54 \text{ psi}$$

3. SHELL ANALYSIS

3.1 Finite Element Model:

The test results of reference 3 indicated that the displacement at various points of the shelter vary in the longitudinal direction as well as the circumferential direction of the shelter. The analysis is therefore, extended to a two dimensional approach. The entire shelter is treated as a semi-cylindrical shell supported by the base, the end wall and the reinforced concrete frame where tha armor steel door is located. Along the arches where the shelter is supported by the end wall and the concrete frame, respectively, the displacement and the rotation about the axis normal to the plane are restrained. The shelter is divided into 192 elements and 221 nodes as shown in figure 7. In order to treat each element as a shell element and to use the SAP IV computer program Element No. 6, a uniform thickness must be assumed for each element. To assure bending stiffness in the circumferential direction, the equivalent thickness h must be such that the moment of inertia is unchanged that is:

$$I = \frac{1}{12} bh^3 = \frac{1}{12} (24\ h^3), \text{ with } I = 46000\ \text{in}^4$$

$$h = 28.44\ \text{in.}$$

In the longitudinal direction where the depth of the shelter varies from 18 inches to 34 inches periodically, a constant moment of inertia I_1 which can best represent the moment-rotation character must be chosen. This is accomplished by first, replacing the curvature of the cross-section in the longitudinal direction by segments of straight lines (see figure 8), then determining the constant moment of inertia I, such that it will result in the same moment rotation characteristic for a typical element in the longitudinal direction. Mathematically, it can be described as follows:

$$\theta = \frac{M\ell}{EI_1} = \int_0^{\ell} \frac{M}{EI} dx = \sum \frac{M\,\Delta X}{EI}$$

$$\frac{\ell}{I_1} = \sum \frac{\Delta x}{I}$$

$$\frac{24}{I_1} = 2x\left(\frac{3x12}{18^3} + \frac{3x12}{24^3} + \frac{3x12}{32^3} + \frac{3x12}{34^3}\right)$$

$$I_1 = 1103.\ \text{in.}^4/\text{in}$$

Since a equivalent uniform thickness of 28.44 inches has already been choosen for the shell element, an artificial modulus of elasticity E_1 must be used in order that the moment-rotation character in the longitudinal direction is

preserved:

$$EI_1 = E_1 (28.44)^3/12 = 1917\ E_1$$

$$E_1 = E \frac{I_1}{1917} = 4\times10^6 \times \frac{1103}{1917} = 2.3\times10^6 \text{ psi}$$

The procedure outlined above is necessary for the numerical analysis. To compute the dynamic responses of this shell model which has a uniform thickness but anisotropic elastic characteristics, the elastic constants in the following stress-strain equation must be identified in the computer program input:

$$\begin{Bmatrix} \sigma_{xx} \\ \sigma_{yy} \\ \tau_{xy} \end{Bmatrix} = \begin{bmatrix} C_{xx} & C_{xy} & C_{xs} \\ C_{xy} & C_{yy} & C_{ys} \\ C_{xs} & C_{ys} & G_{xy} \end{bmatrix} \begin{Bmatrix} \varepsilon_{xx} \\ \varepsilon_{yy} \\ \gamma_{xy} \end{Bmatrix}$$

In the above equation, x and y are local coordinates of the element in the circumferential and longitudinal directions respectively (Fig. 9a). Element stress resultants are shown in figure 9b. Based on the stress strain relation of

$$\begin{Bmatrix} \varepsilon_{xx} \\ \varepsilon_{yy} \\ \gamma_{xy} \end{Bmatrix} = \begin{bmatrix} \frac{1}{E_x} & -\frac{\nu_{xy}}{E_y} & 0 \\ -\frac{\nu_{yx}}{E_x} & \frac{1}{E_y} & 0 \\ 0 & 0 & \frac{1}{G} \end{bmatrix} \begin{Bmatrix} \sigma_{xx} \\ \sigma_{yy} \\ \tau_{xy} \end{Bmatrix}$$

in which $E_x = 4\times10^6$ psi, $E_y = 2.3\times10^6$ psi, and $\nu_{yx}=0.2$, the following set of elastic constants are obtained;

Cxx = 4,094,000 psi

Cyy = 2,354,000 psi

Cxy = 471,000 psi

Gxy = 1,275,000 psi

Cxs = Cys = 0

3.2 Dynamic Responses and Numerical Results:

Considering the number of elements and modes of the finite element model, it is concluded that the method of modal superposition will be efficient in computing the dynamic responses of the shelter. A free vibration analysis was made. The first six frequencies and their corresponding mode shapes are shown in figure 10. Desirable accuracy of the dynamic response of the shelter should be reached by superimposing the first six modes of free vibrations. Forcing functions and dynamic pressure used in Section 2 (see Figs. 5a,b,c) are then applied to the shell and its responses are again calculated by the use of SAP IV computer program. Typical responses of several modal points are shown in figure 10. Tables 2 and 3 show the maximum element stress resultants at various locations of the model shell.

TABLE 2 MAXIMUM ELEMENT STRESSES (ABSOLUTE VALUES)

Load Case: I Peak Pressure: 7 psi

Element Number	Fxx (lb/in)	Fyy (lb/in)	Fxy (lb/in)	Mxx (in-lb/in)	Myy (in-lb/in)	Mxy (in-lb/in)
18				195	37	152
20	–	–	T	273	48	4
22	–	–	2	21	12	137
24	–	–		306	68	38
65	–	–	–	131	20	17
67	–	–	–	56	105	12
69	–	–	–	318	49	10
71	–	–	–	389	93	15
114	–	–	–	177	37	173
116	–	–	T	250	47	7
118	–	–	2	20	14	133
120	–	–		283	71	43
146	–	–	–	45	64	109
148	–	–	–	63	69	41
150	–	–	T	18	55	101
152	–	–	–	71	155	41

(NOTE: NUMBERS LESS THAN 1 ARE NOT SHOWN)

13

TABLE 3 MAXIMUM ELEMENT STRESSES (ABSOLUTE VALUES)

Load Case: 2 Peak Pressure: 7 psi

Element Number	Fxx (lb/in)	Fyy (lb/in)	Fxy (lb/in)	Mxx (in-lb/in)	Myy (in-lb/in)	Mxy (in-lb/in)
18	27	3	5	7995	902	3385
20	26	3	22	3227	1223	5053
22	18	2	70	11670	2324	1743
24	4	1	109	4070	760	3721
26	12	1	95	10280	1954	1262
28	23	3	44	7781	1994	4231
30	27	3	8	5833	617	4761
32	27	3	2	3808	444	1762
65	52	6	-	7645	895	282
67	52	6	1	11940	1292	153
69	44	5	-	15530	3799	333
71	23	3	3	20660	3952	132
73	8	1	4	8176	1540	318
75	36	4	1	23440	4698	136
77	50	6	1	6802	2379	342
79	53	6	-	16060	1829	118
114	21	3	5	7758	966	3868
116	17	2	21	3506	1416	5416
118	11	1	70	11370	2386	1755
120	3	-	11	3975	770	3477
122	7	-	94	10040	1986	1384
124	14	2	44	7513	1877	4373
126	19	2	9	6176	957	5210
128	21	3	2	3691	418	2123
146	6	-	9	3239	987	1164
148	6	-	16	1369	3700	4747
150	6	-	20	3998	4818	1742
152	2	-	59	1487	1336	4435
154	4	-	44	3691	3599	2050
156	6	-	3	2298	4766	4430
158	6	-	2	3187	2262	2485
160	5	-	1	1471	209	3365

It should again be noted that these maximum element stress resultants do not occur at the same time. Observations of stress response output indicate that Mxx is by far the dominate factor for the purpose of analysis. Based on its' maximum value of 23440 in-lb. at element 71 (t = 0.057 sec.), the maximum tensile stress due to bending moment is:

$$f_t = \frac{23440 \times 24 \times 18.1}{46000} = 221 \text{ psi}$$

Based on an allowable dynamic tensile stress of 491 psi, the safe peak pressure is established as:

$$p = 7 \times \frac{491}{221} = 15.6 \text{ psi}$$

15

4. DISCUSSION AND CONCLUSION

In the single arch analysis, the dynamic response of the structure is primarily a flexural mode response superimposed by a breathing mode of much higher frequency. In view of the existence of the end wall and the door collar, the shell-like response in Section 3 is a more reasonable approach. Neglecting the stiffness of the end wall and the concrete door collar is far too conservative an approach. In the shell analysis of Section 3, one could also consider the stiffness of the end wall and the door collar rather than consider them to be rigid. This sophication is not included due to the ten week time constraint of this project. Nevertheless, it is believed that the method outlined and the numerical values obtained in Section 3 are reasonable.

5. RECOMMENDATIONS

Test results of reference 4 (Arch 1) also show the collapse of the steel door and the occurance of large cracks in the concrete door collar when the shelter is subjected to blast waves propagating in the direction perpendicular to its' longitudinal axis. In the same test, however, no major damage of the shelter itself is observed. This indicates that the door collar and the armor steel door could be the more critical elements in the entire structural system. Therefore, it is recommended that a study on the dynamic responses of the door supporting collar and the steel door be made.

REFERENCES

1. "Analysis and Full-Scale Testing of an Aircraft Shelter", AFWL-TR-70-170, Suppl. 1, Air Force Weapons Laboratory, Kirtland AFB, N.M. Dec. 1971.

2. L. A. Walker and G. E. Lane, Jr. "Shelter Section Capacity Study". A letter report prepared for Air Force Weapons Laboratory, Kirtland AFB. June 1975.

3. M. A. Plamondon, W. H. Krueger and H. Pahl, "Response of Air Force Structures in the Mixed Company Event, Middle North Series, Project LN 319".
AFWL-TR-74-13. Air Force Weapons Laboratory, Kirtland AFB, N.M., Apr. 1973.

4. R. E. Crawford, C. J. Higgins and E. H. Bultmann. "The Air Force Manual for Design and Analysis of Hardened Structures".
AFWL-TR-74-102 Air Force Weapons Laboratory, Kirtland AFB, N.M., Oct. 1974.

5. Crawford, R.E. et al "Protection From Nonnuclear Weapons"., AFWL-TR-70-127, Air Force Weapons Laboratory, Kirtland AFB, N.M., Feb. 1971.

6. Newmark N.M. et al "Air Force Design Manual-Principles and Practices for Design of Hardened Structures",
AFSWC-TDR-62-138, Air Force Special Weapons Center, Kirtland AFB, N.M., Dec. 1962.

17

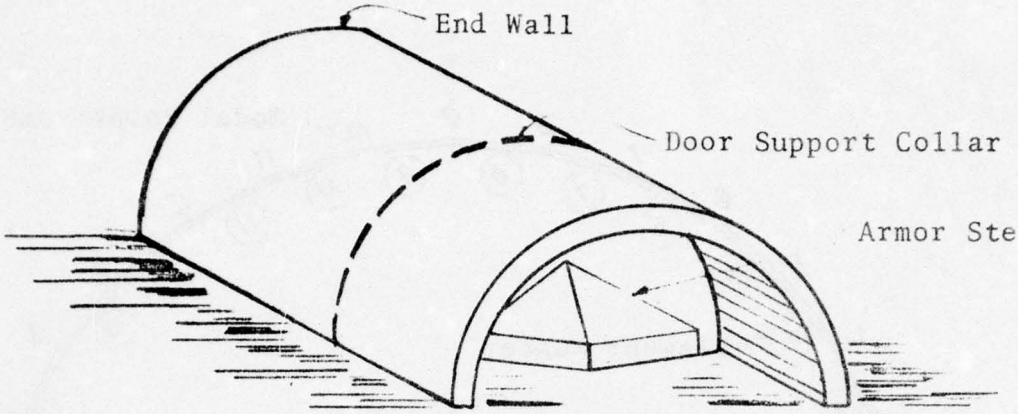


Fig. 1 General Overview of Aircraft Shelter

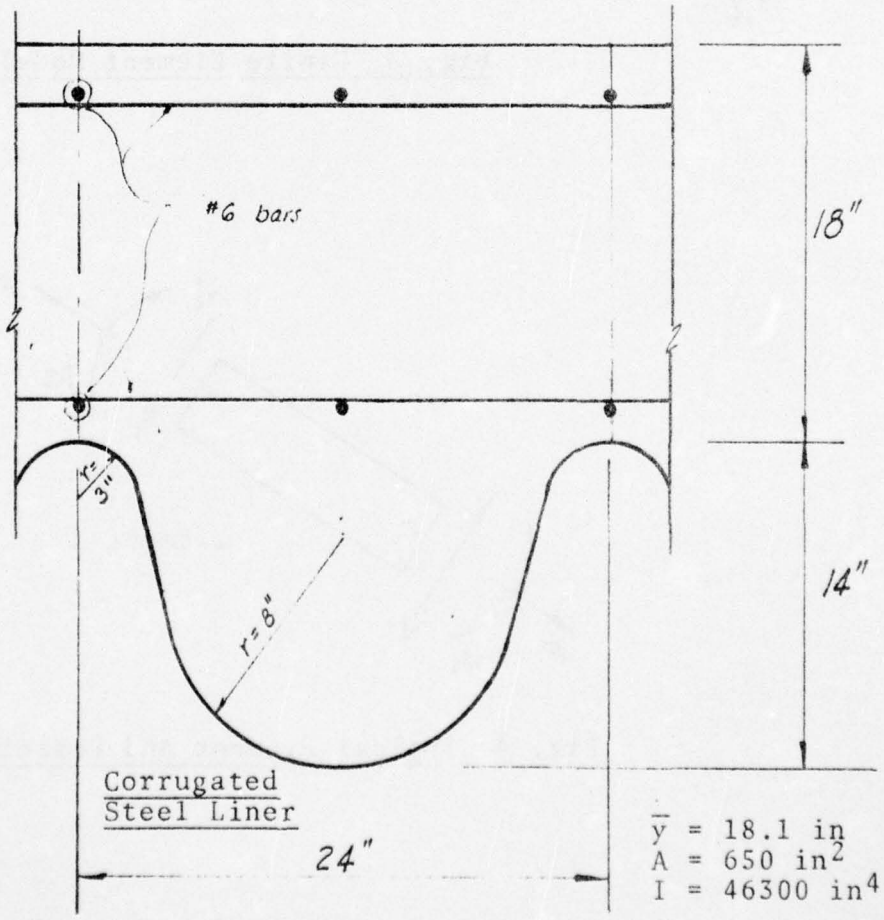


Fig. 2 Typical Cross Section of Arch

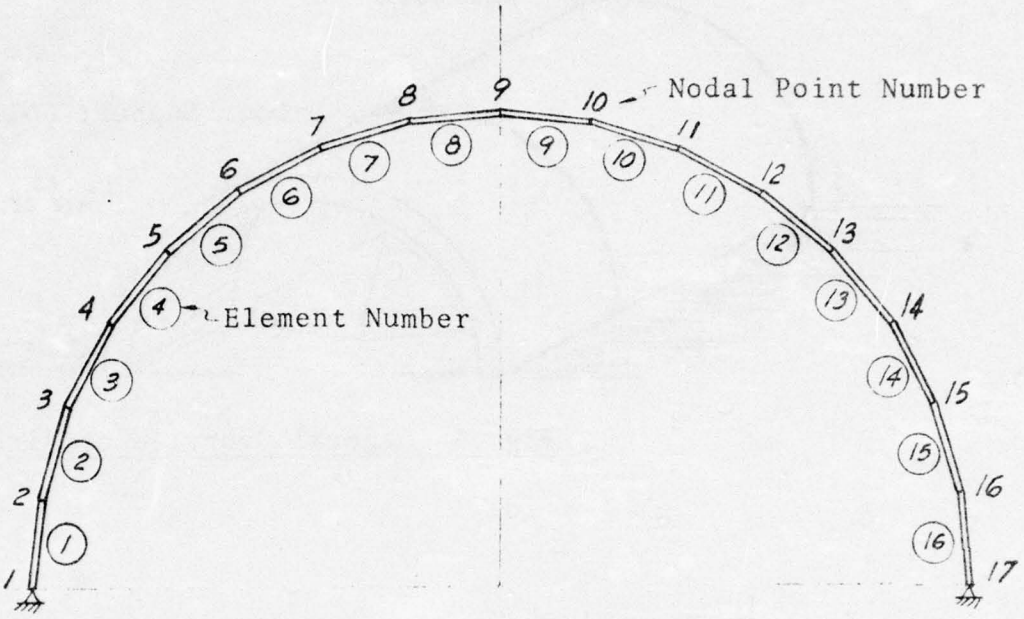


Fig. 3 Finite Element Model For Arch

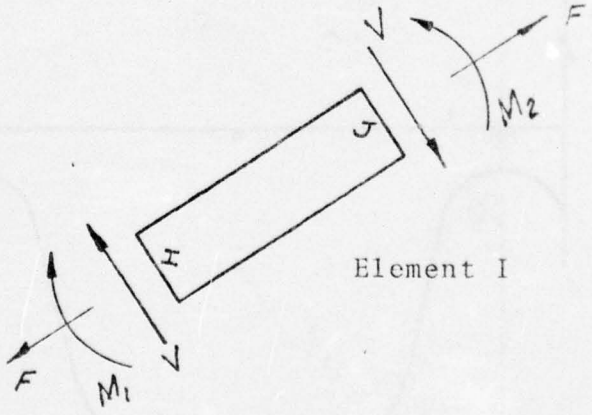


Fig. 4 Typical Element And Positive Forces

19

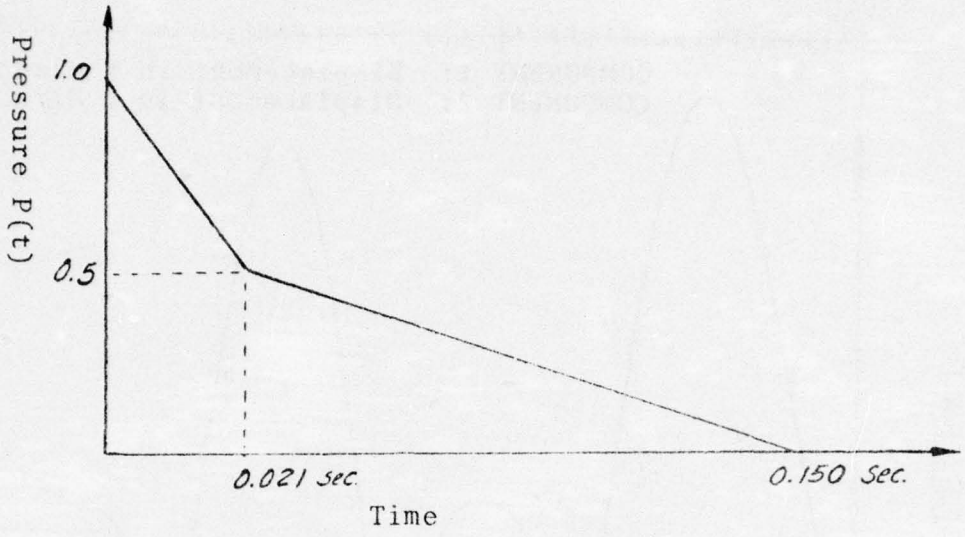


Fig. 5a Normalized Time Pressure Function

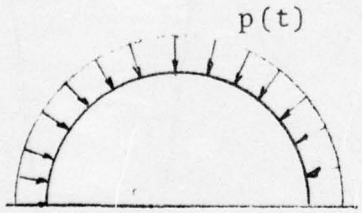


Fig. 5b Load Case II

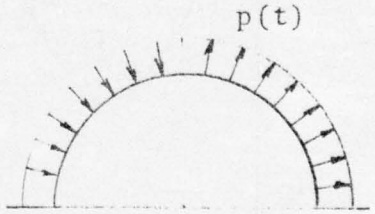


Fig. 5c Load Case II

NOTE: Time-varying concentrated forces at nodal points are required for the computer program input. In arch analysis, peak nodal force of 10,000 lb is used for computational purpose. This is equivalent to a peak pressure of 7 psi.

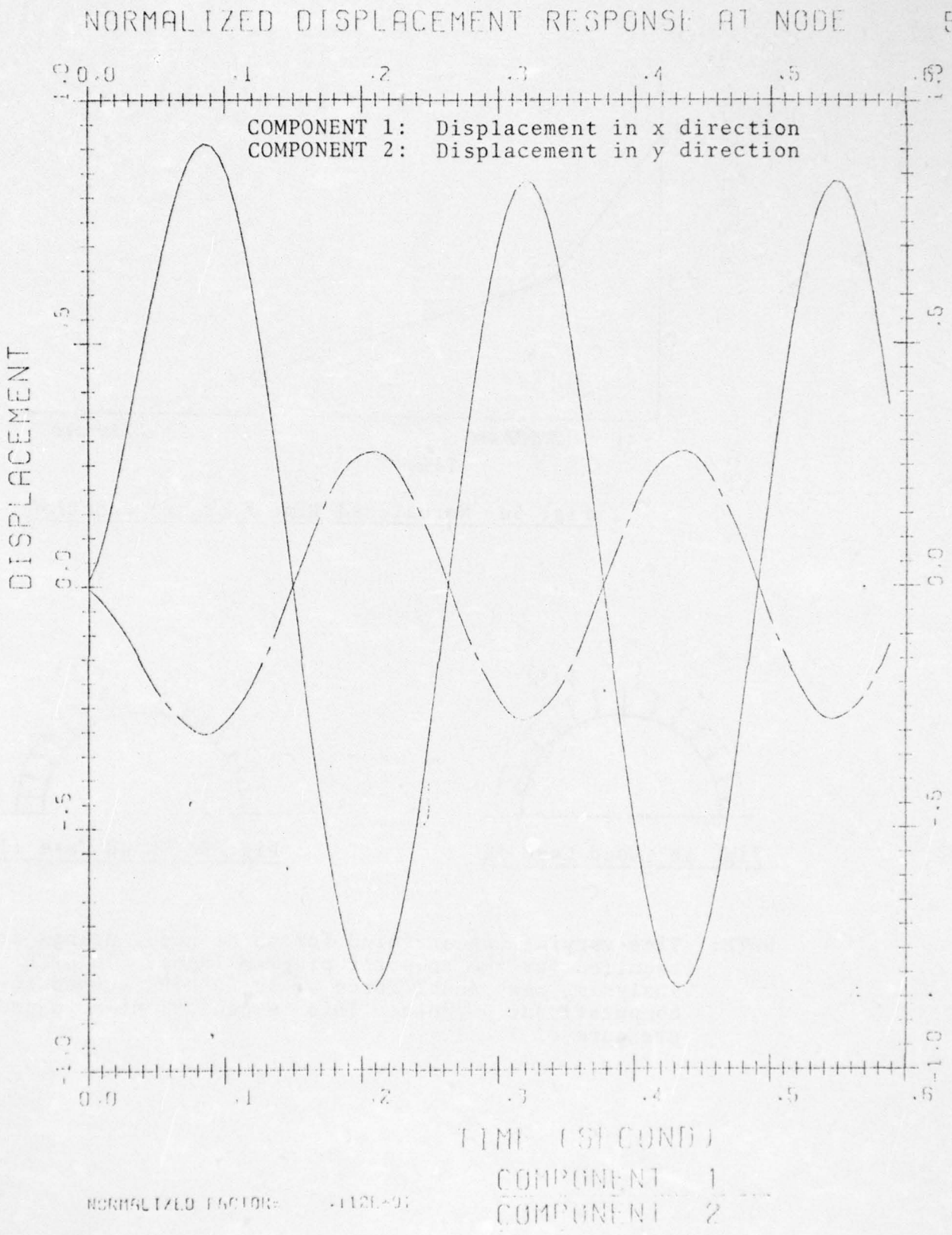
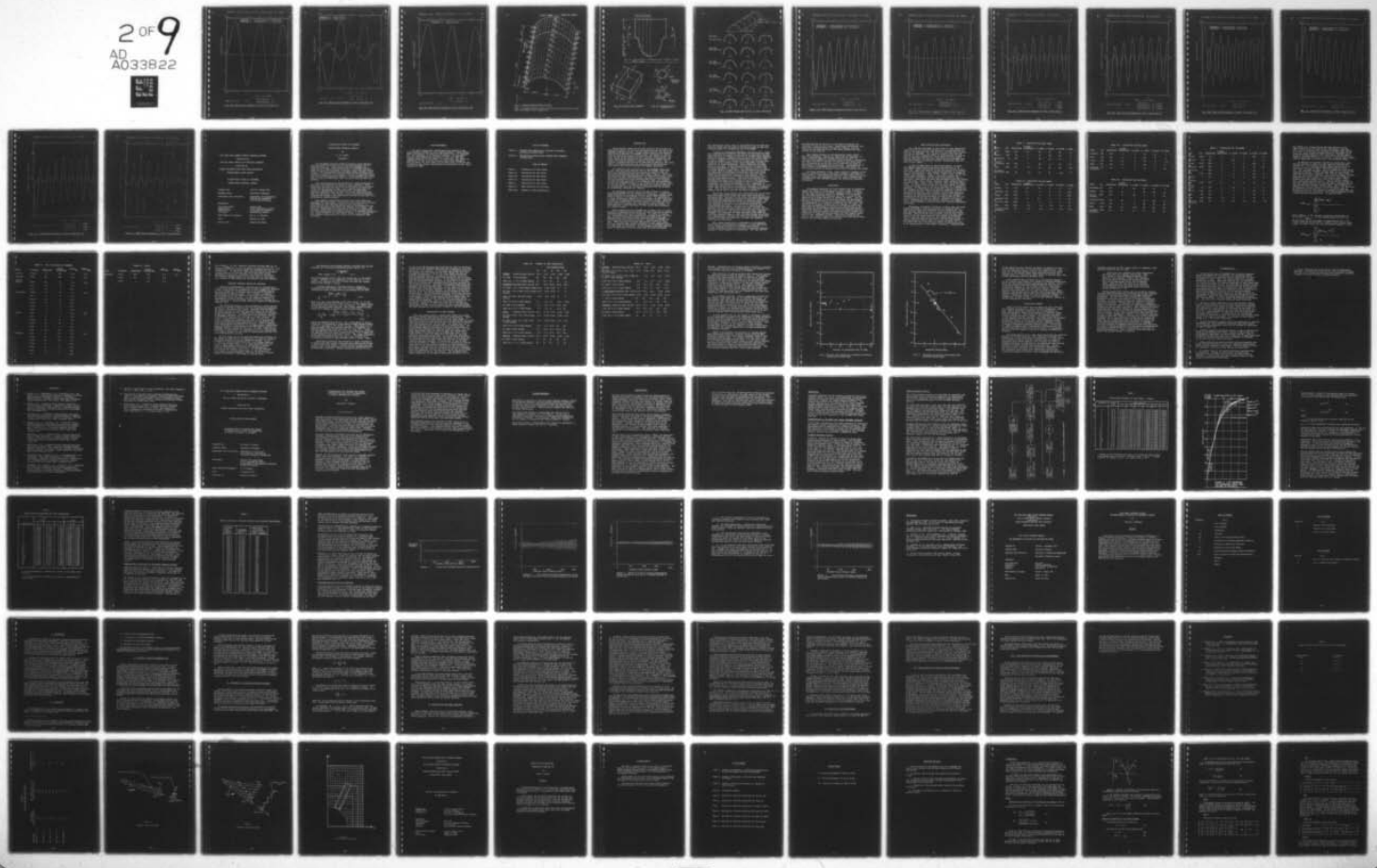


Fig. 6a Time History Response of Arch (Load Case II)

AD-A033 822 AUBURN UNIV ALA SCHOOL OF ENGINEERING F/G 14/2
1976 USAF-ASEE SUMMER FACULTY RESEARCH PROGRAM.(U)
SEP 76 J F O'BRIEN F44620-75-C-0031
UNCLASSIFIED AFOSR-TR-76-1419 NL

2 OF 9
AD
A033822



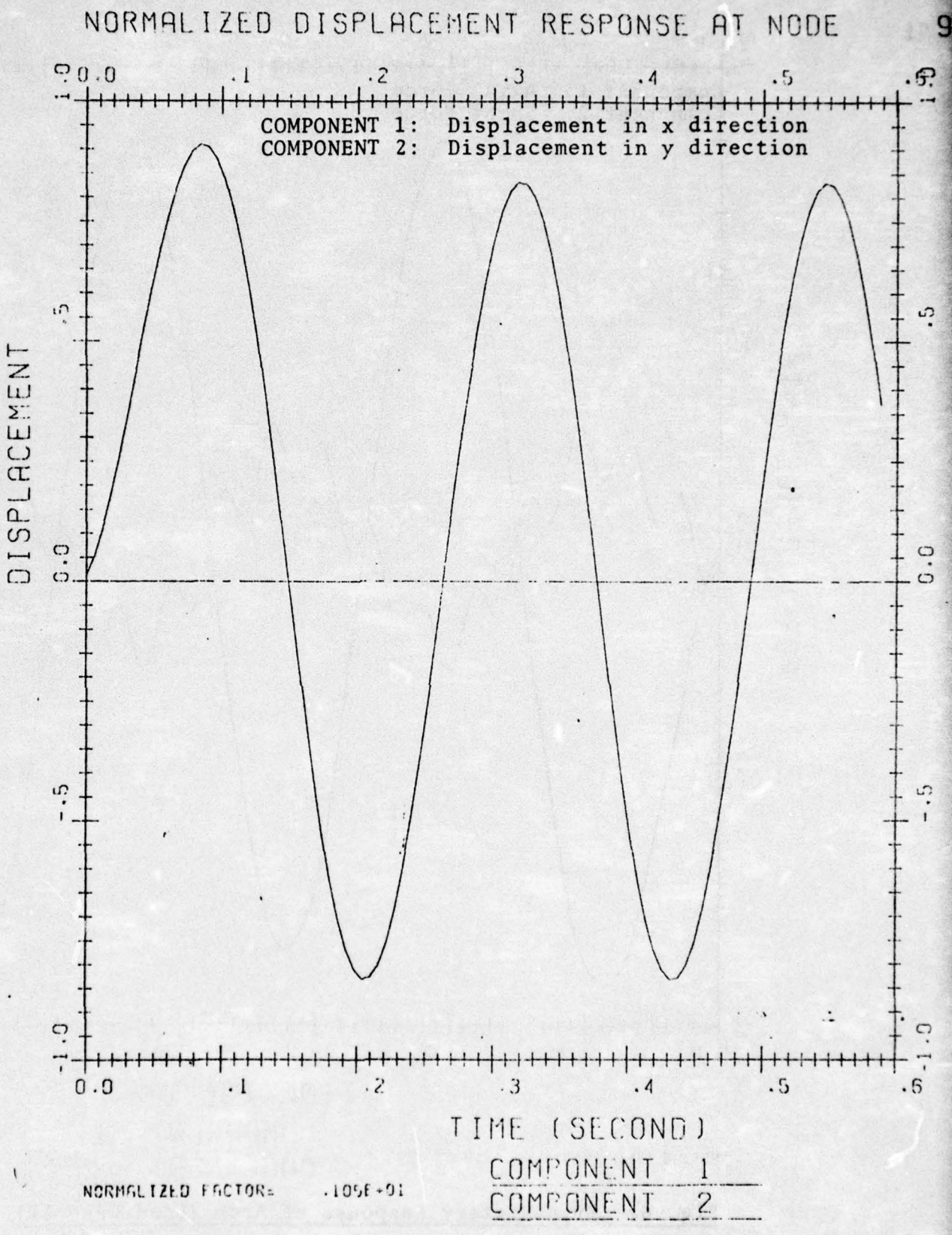


Fig. 6b Time History Response of Arch (Load Case II)

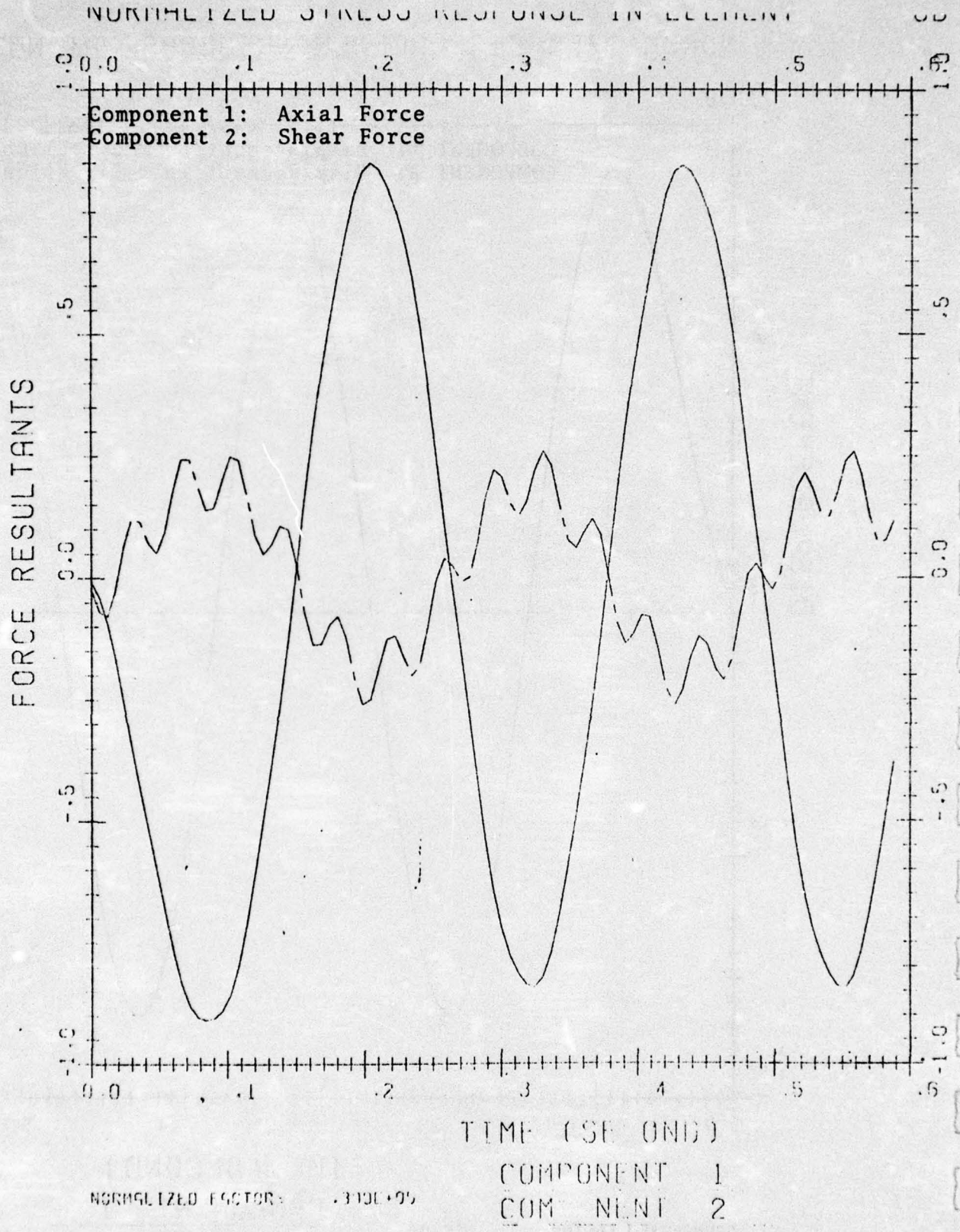


Fig. 6c Time History Response of Arch (Load Case II)

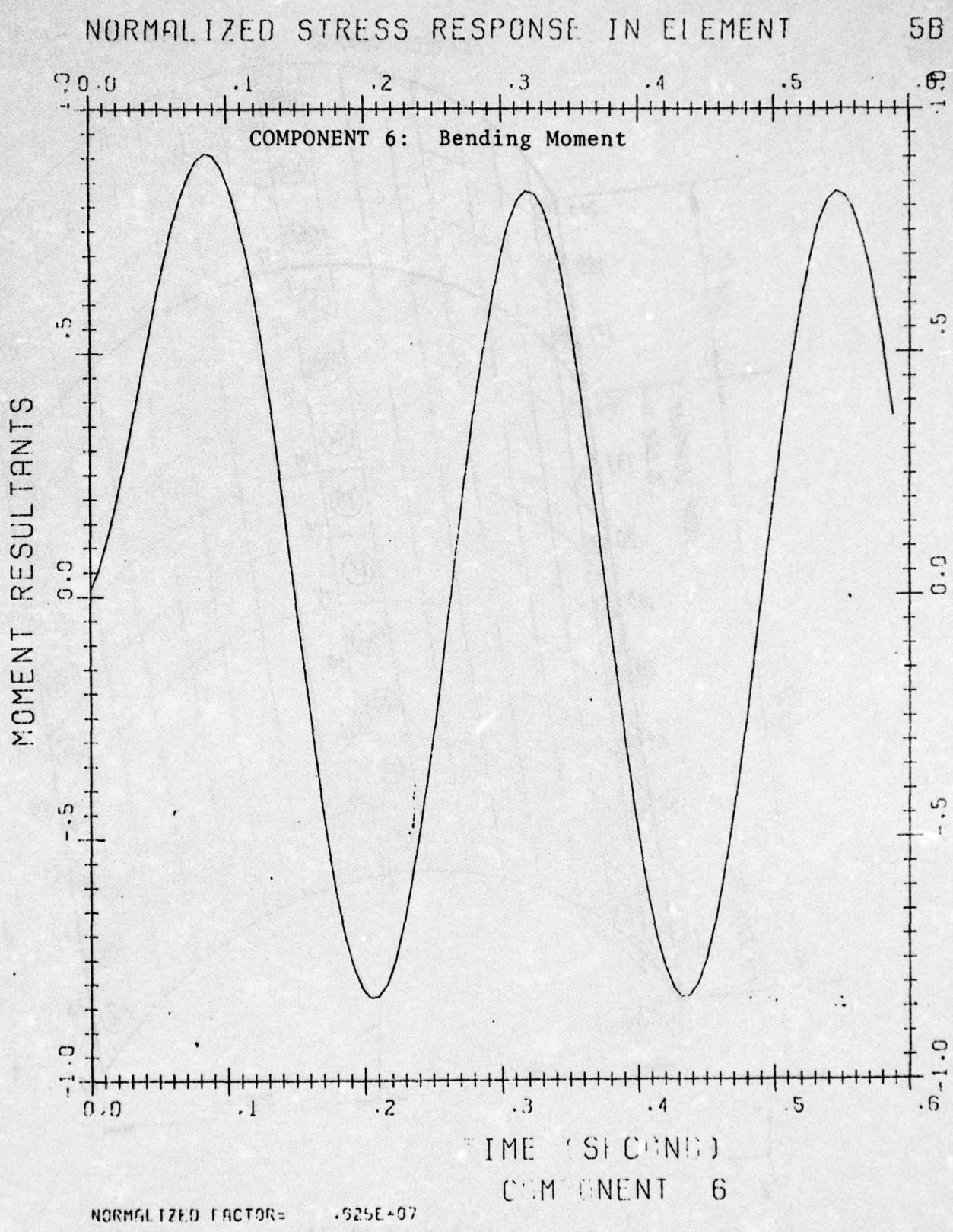


Fig. 6d Time History Response of Arch (Load Case II)

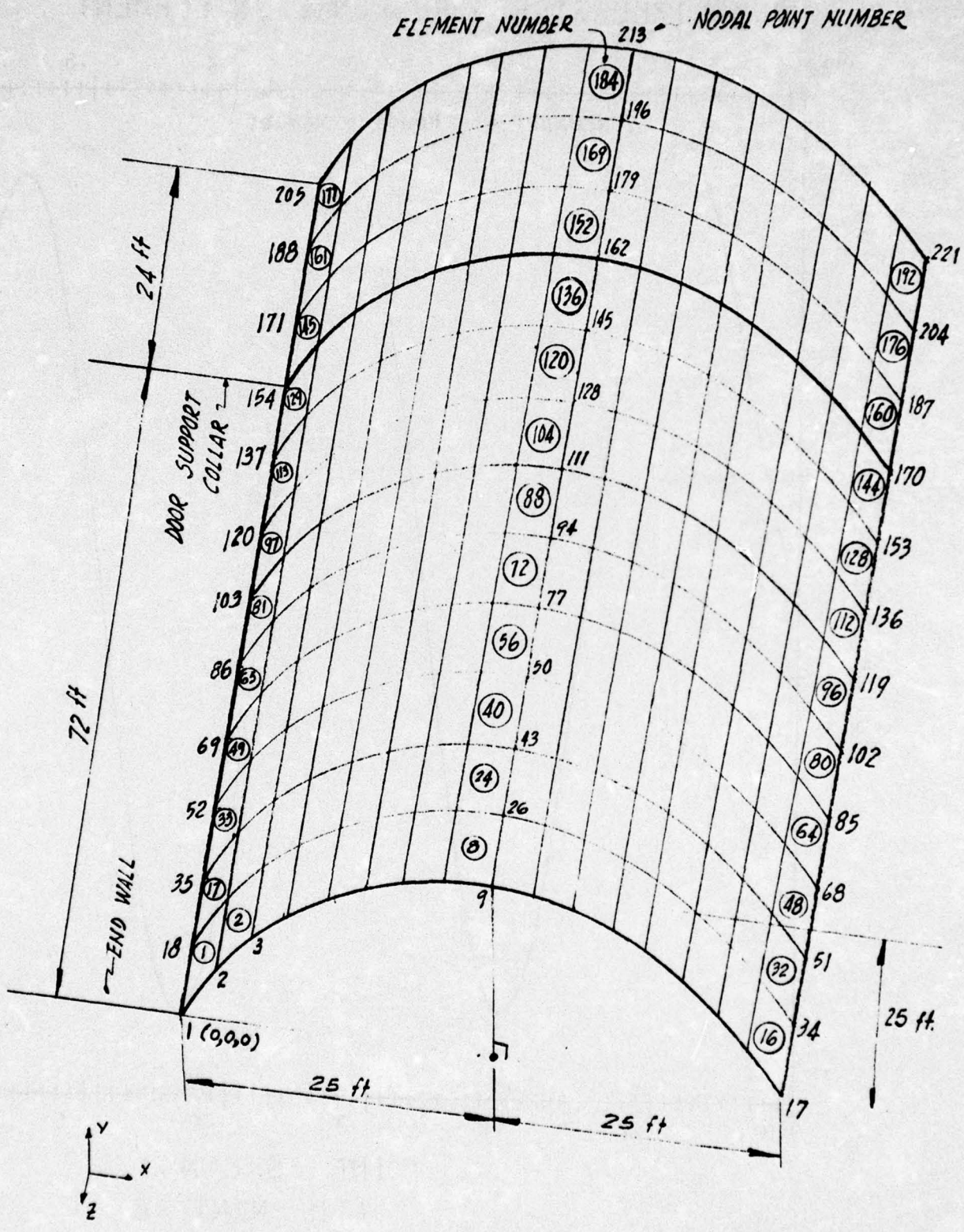


Fig. 7 Finite Element Model of Shell

NOTE: Drawing displays finite element mesh characteristics and does not display exact geometries.

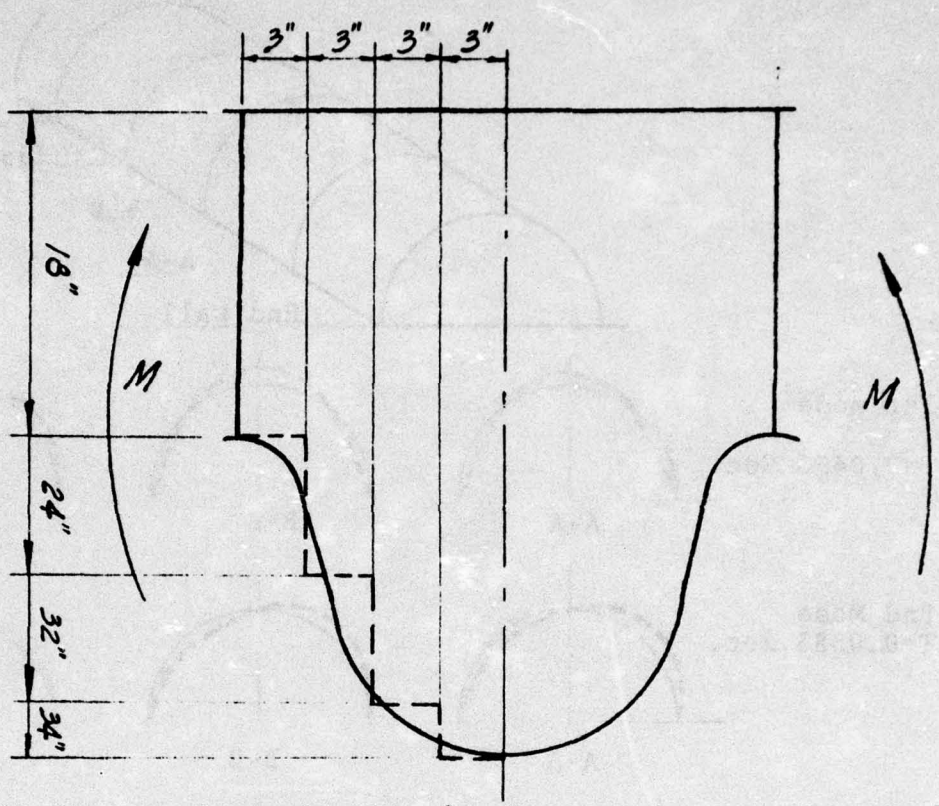


Fig. 8 Cross Section for Determining constant I about local x axis

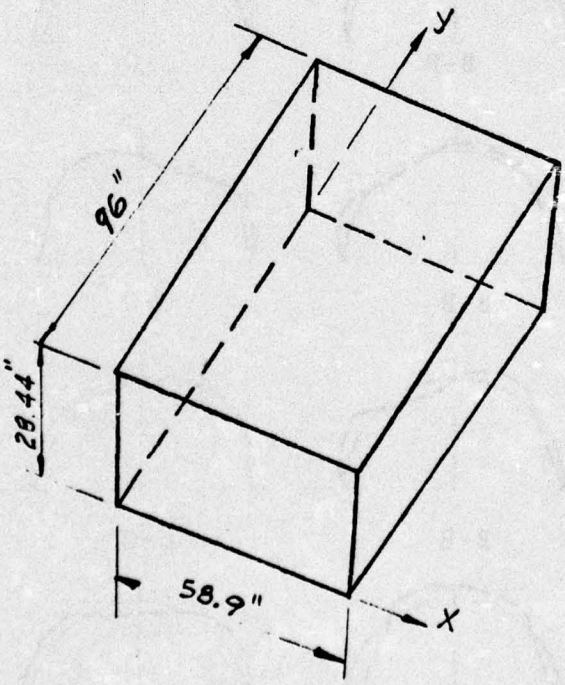
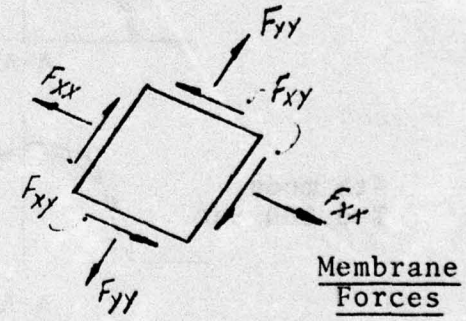


Fig. 9a Typical Shell Element



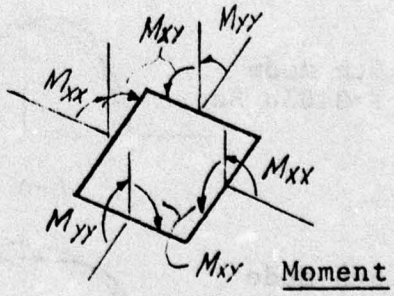


Fig. 9b Element Stress Resultants

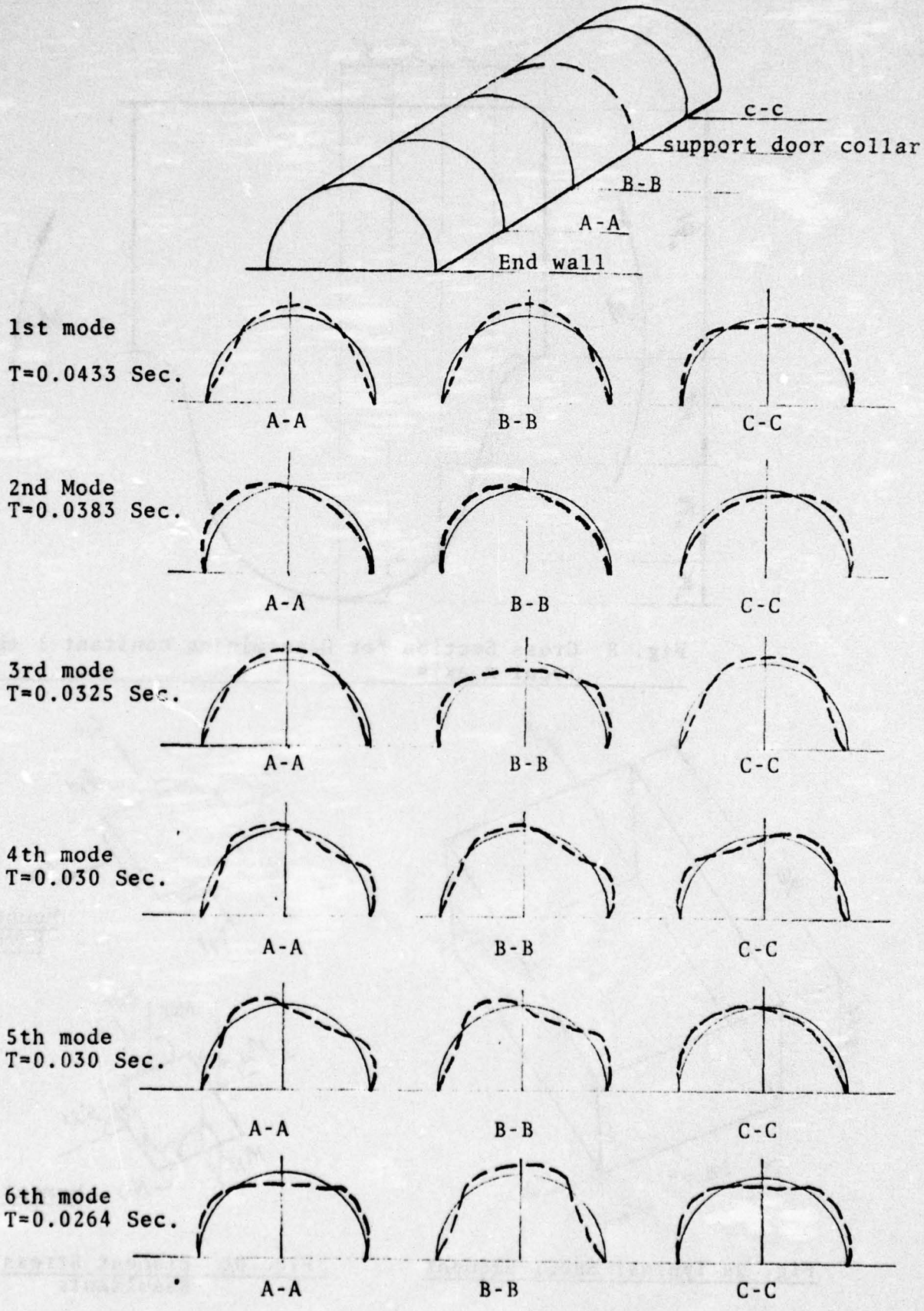


Fig. 10 Mode Shapes and Periods of Free Vibrations

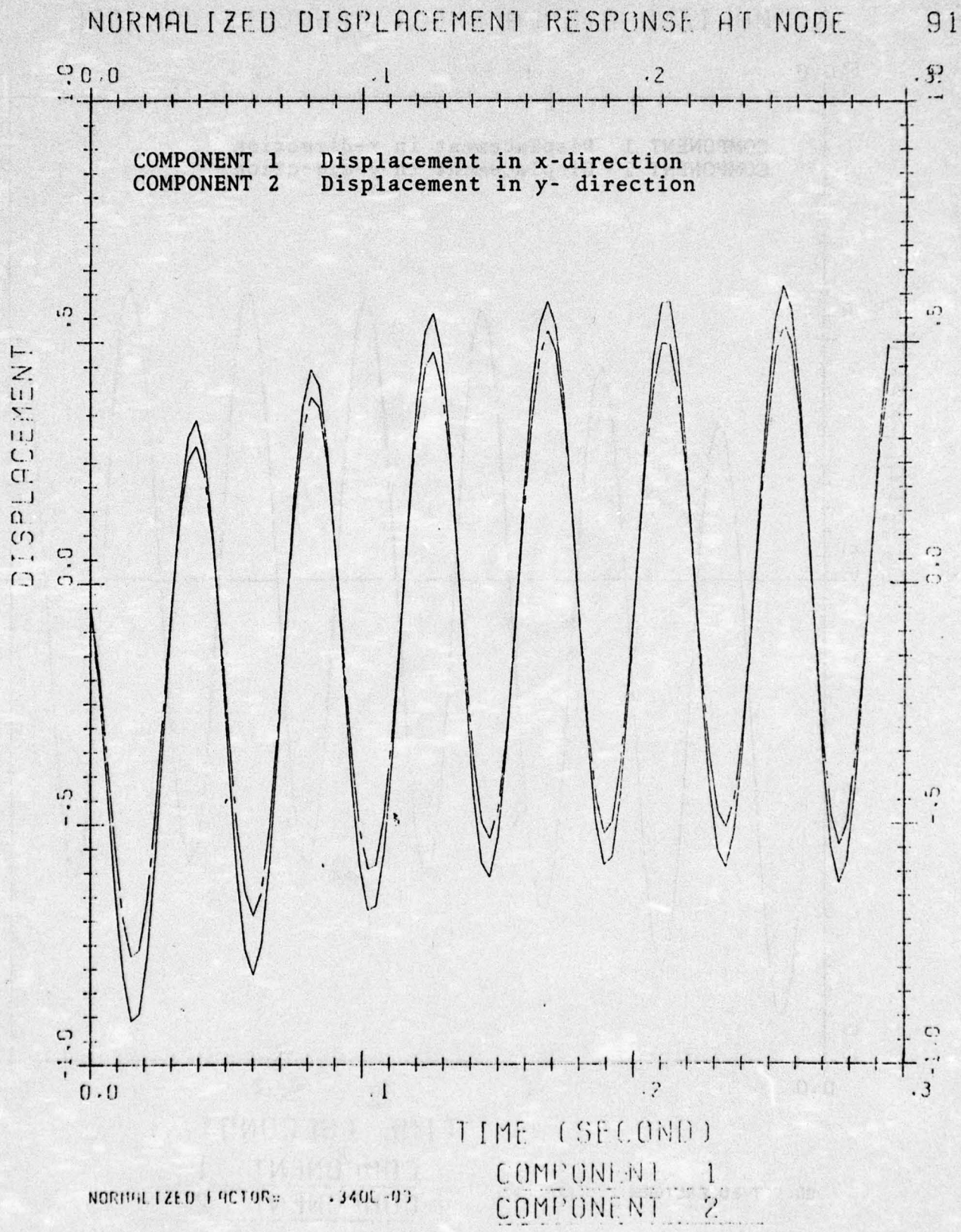


Figure 11a Time-History Response of Shell (Load Case I)

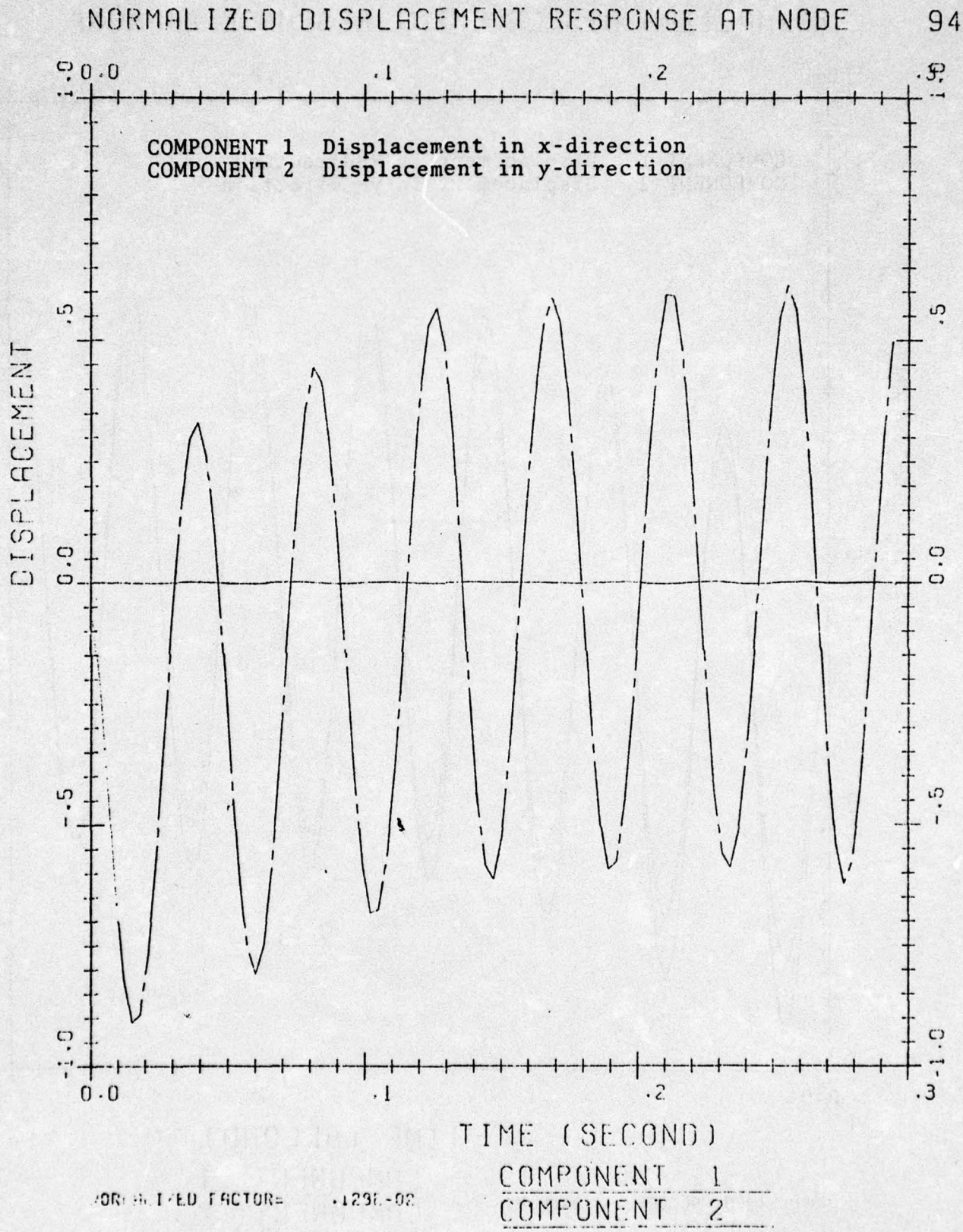


Fig. 11b Time-History Response of Shell (Load Case I)

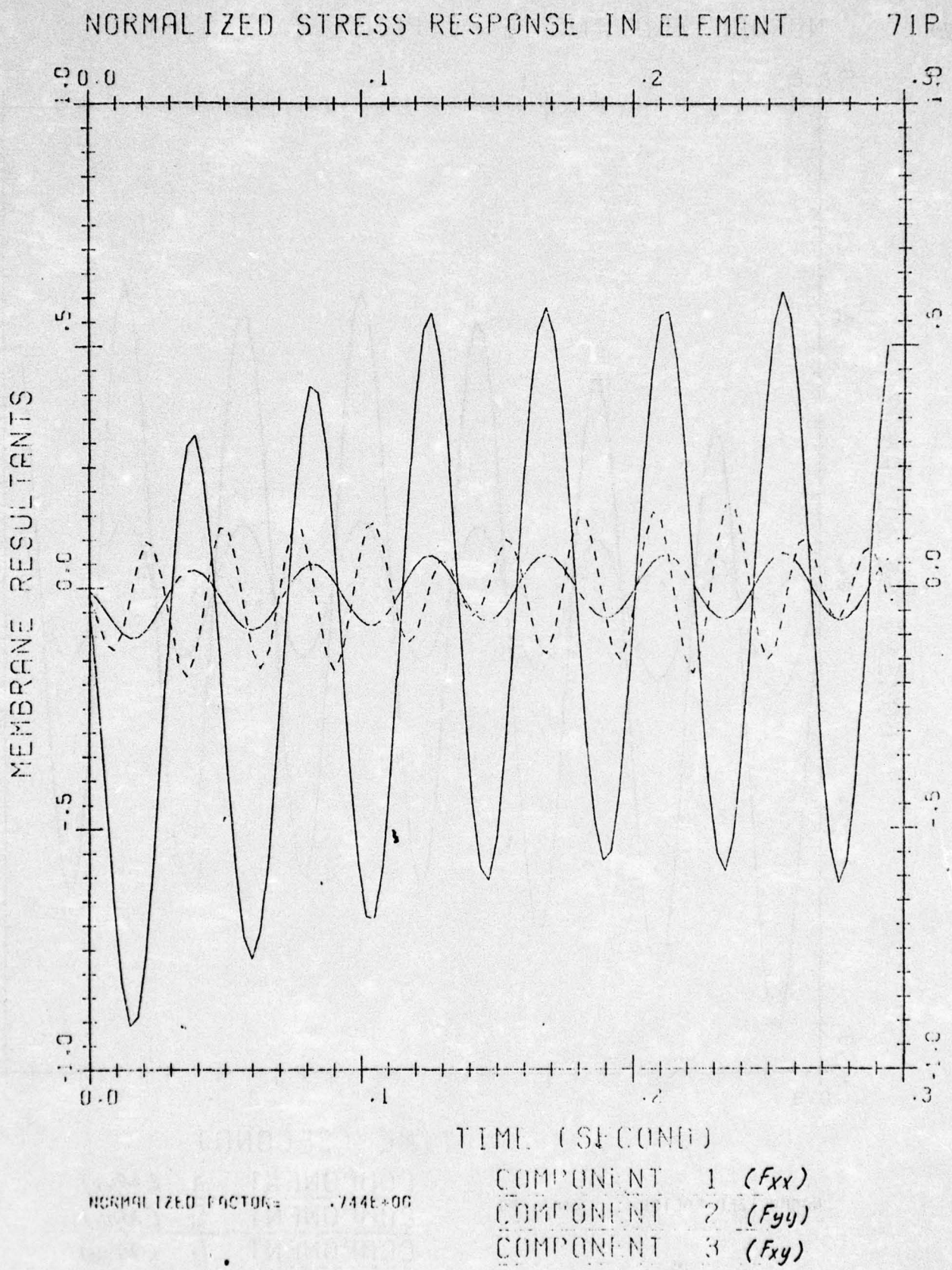


Fig. 11c Time-History Response of Shell (Load Case I)

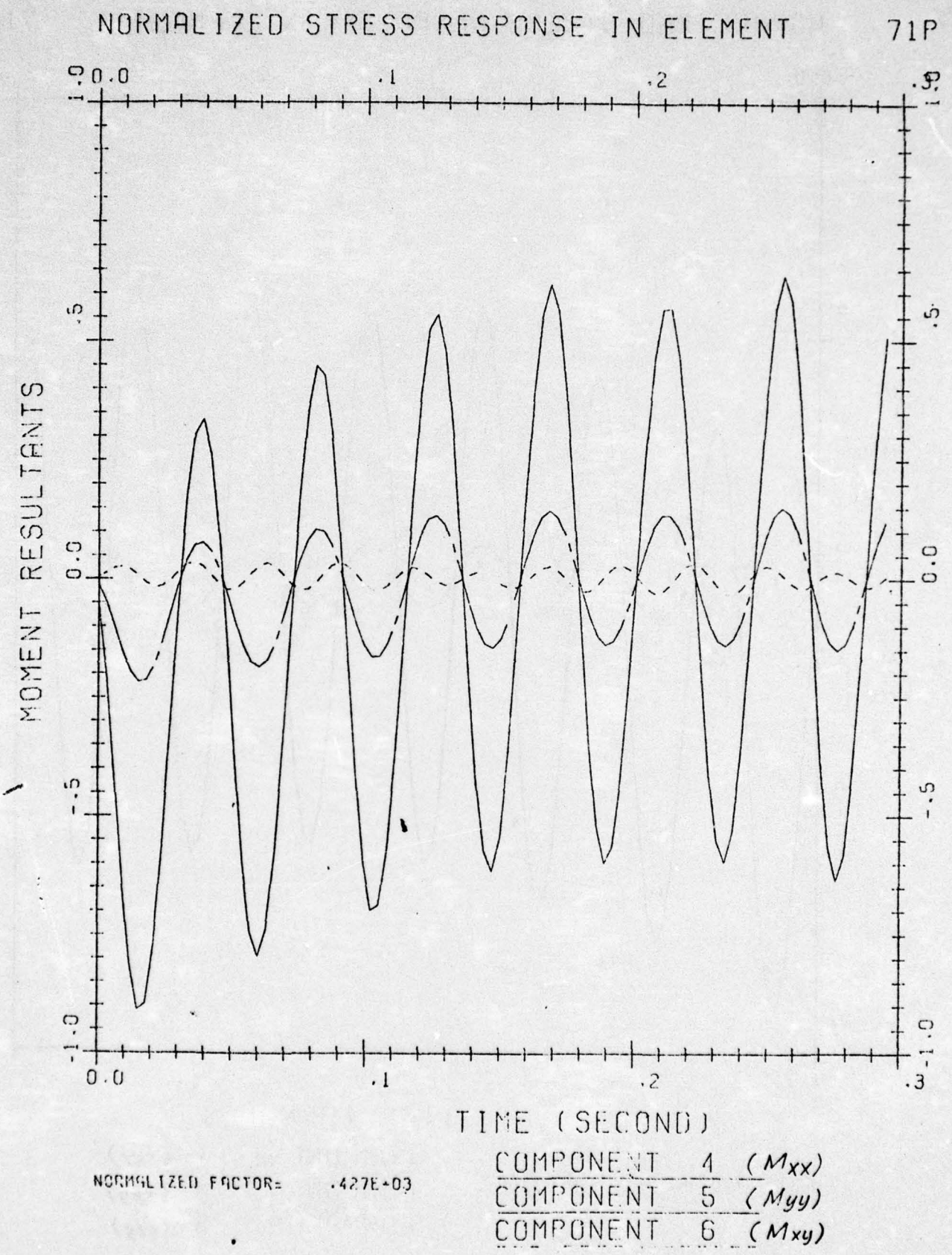


Fig. 11d Time-History Response of Shell (Load Case I)

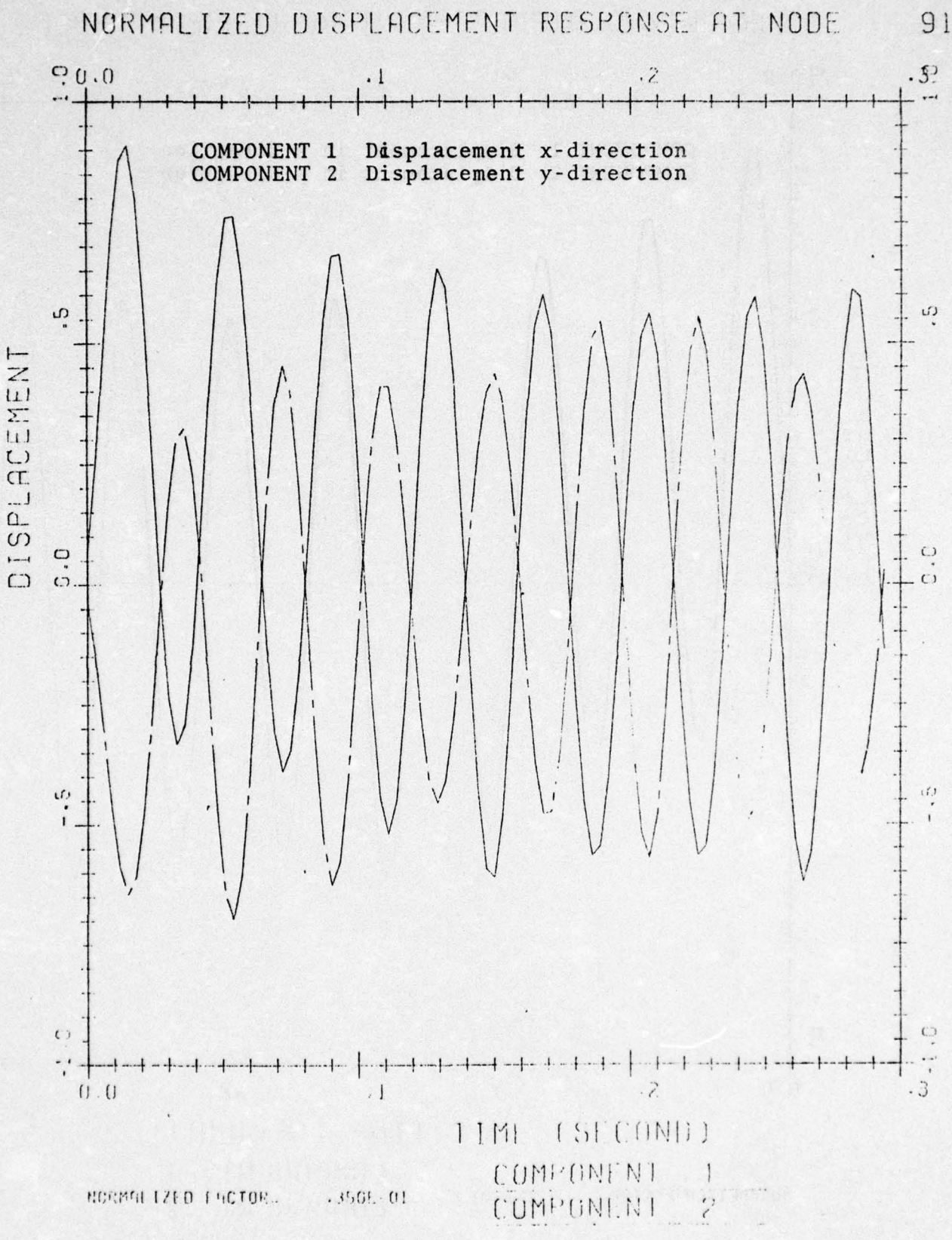


Fig. 11e Time-History Response of Shell (Load Case II)

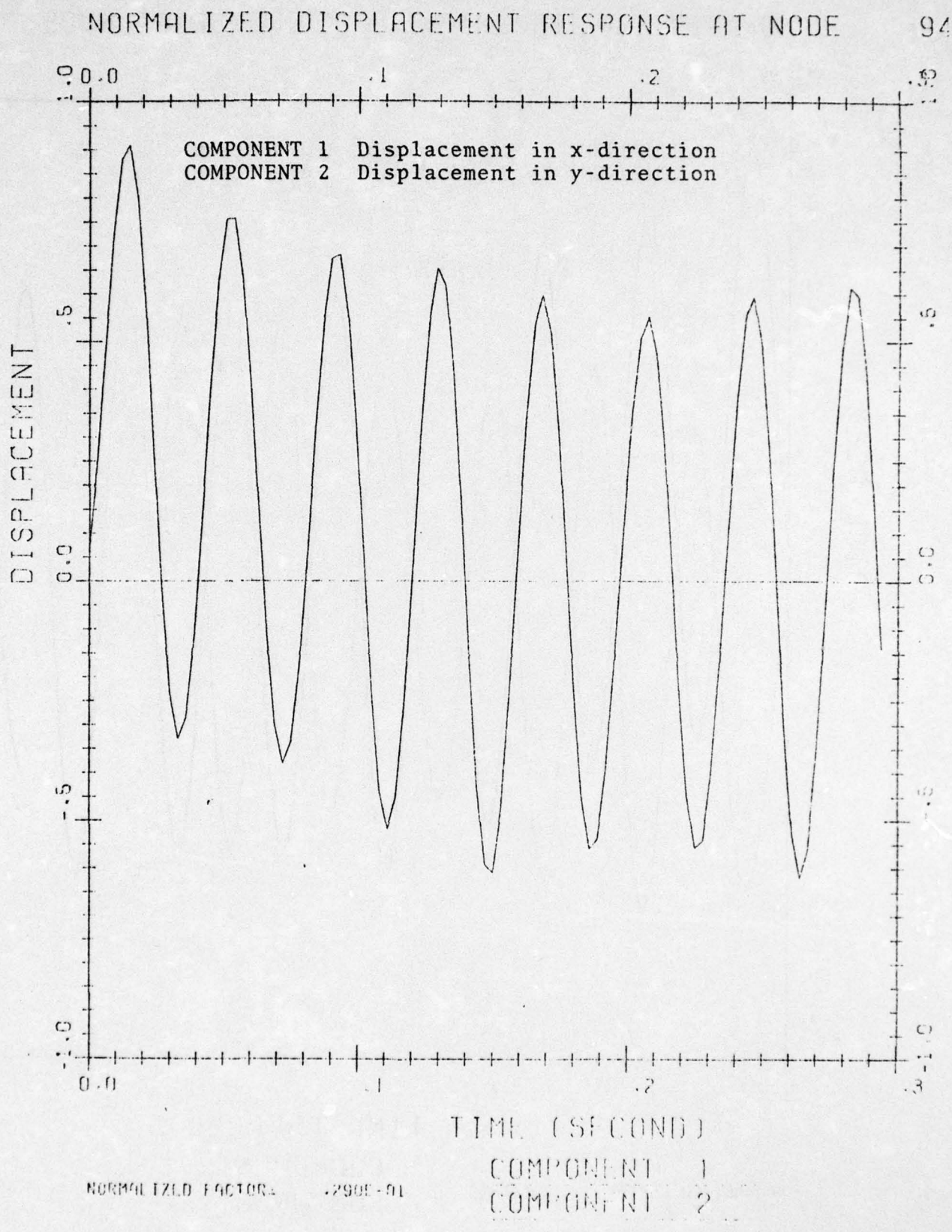


Fig. 11f Time-History Response of Shell (Load Case II)

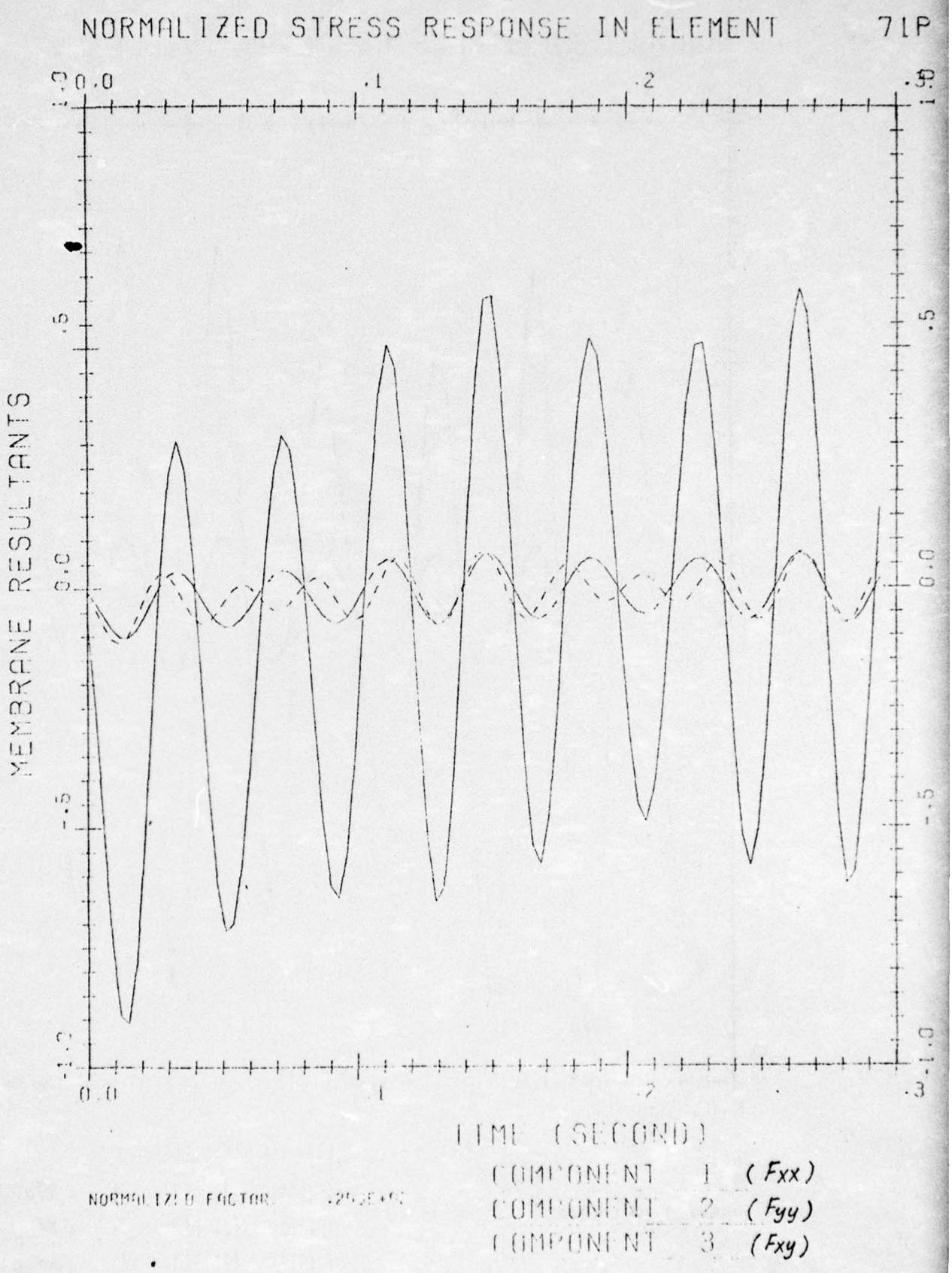


Fig. 11g Time-History Response of Shell (Load Case II)

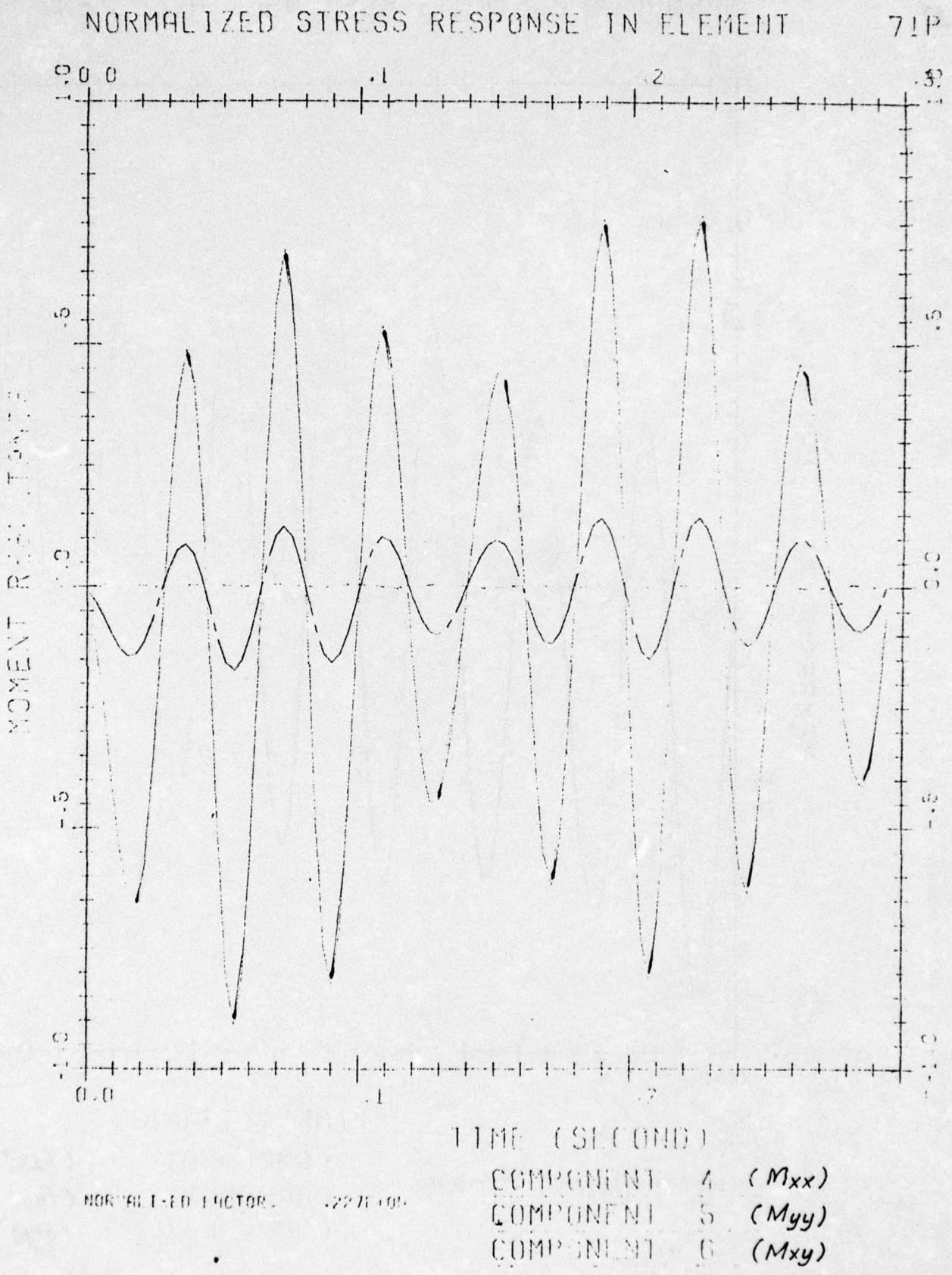


Fig. 11h Time-History Response of Shell (Load Case II)

1976 USAF-ASEE SUMMER FACULTY RESEARCH PROGRAM

Sponsored by

THE AIR FORCE OFFICE OF SCIENTIFIC RESEARCH

Conducted by

AUBURN UNIVERSITY AND OHIO STATE UNIVERSITY

PARTICIPANT'S FINAL REPORT

A SENSITIVITY STUDY OF NOISEMAP POWER OFFSET PROFILES (DSELs)

Prepared by:	David K. Holger PhD
Academic Rank:	Assistant Professor
Department and University:	Department of Engineering Science and Mechanics Iowa State University
Assignment:	
(Air Force Base)	Tyndall AFB
(Laboratory)	Civil Engineering Center
(Directorate)	Facilities and Systems
(Division)	Engineering Support
USAF Research Colleague:	Maj I. D. Robinson
Date:	August 13, 1976
Contract No.:	F44620-75-C-0031

A SENSITIVITY STUDY OF NOISEMAP POWER OFFSET PROFILES (DSELs)

by

D. K. Holger

ABSTRACT

The NOISEMAP computer program generates noise exposure contours which form a portion of the AICUZ booklet for an USAF installation. Noise computations by NOISEMAP use measured noise data for each aircraft at selected reference power settings and airspeeds to predict noise contours around a base. The contribution from aircraft flying at other than reference conditions to the noise contours is computed through the use of offset profiles (DSELs). At the present time DSELs must be input as additional data and often must be hand calculated.

This report presents the results of a study conducted to determine the influence of DSELs on noise contours. Seven bases were selected for the study on the basis of operational statistics and aircraft types. All computer runs made contained all operations for the base under consideration. Baseline, modified DSEL, no DSEL and average DSEL runs were made for each base. The change in area enclosed by selected contours was chosen as an approximate measure of the effect of modifying or deleting DSELs.

The computer simulations indicate that some DSELs are necessary for most bases. Results of the 34 runs made indicate that DSELs for the dominant aircraft are sufficient. A criterion for when DSELs should be applied is obtained on the basis of operational statistics by aircraft for a base. The criterion could result in significant savings in time during the data acquisition and handling phases of a NOISEMAP production run. There would be no significant change in the accuracy of the NOISEMAP predictions as a result of the suggested DSEL deletions.

ACKNOWLEDGEMENTS

The author gratefully acknowledges the support of Air Force Systems Command for this summer research. Fred O'Brien, Auburn University, the ASEE and the AFOSR are to be commended for the operation of an excellent program. It has been a personal and professional pleasure to work with the very capable personnel of the AFCEC. In particular, the author is indebted to Lt Col Sterling Schultz, Major Dale Robinson, MSgt Al Young, Mr. Dick Drown and Amn Bob Little of DE and DEE. In addition the author acknowledges the assistance of Mr. Jerry Speakman at AMRL.

LIST OF FIGURES

Figure 1. Percent area change as a function of percent operations without DSEL.

Figure 2. Variation of percent area change with weighted average DSEL.

LIST OF TABLES

Table I. Statistics for AFLC bases.

Table II. Statistics for ATC bases.

Table III. Statistics for MAC bases.

Table IV. Statistics for SAC bases.

Table V. Statistics for TAC bases.

Table VI. DSEL statistics by aircraft.

Table VII. Summary of DSEL sensitivity.

INTRODUCTION

Environmental impact of aircraft noise in the vicinity of USAF installations is currently estimated through the use of the NOISEMAP computer program. Proper application of the numerical prediction procedures of NOISEMAP allows evaluation of current land use practices around installations, the effect of new aircraft on the noise exposure around a present installation, the noise impact of new propulsion and suppression systems and the effect of proposed changes in present aircraft siting. The computer program permits accurate advanced estimates of the noise impact of proposed changes and acquisitions with sufficient lead time to be a major influence on command decisions.

For baseline runs the results of the NOISEMAP simulation in the form of noise exposure (Ldn at the present time) contours are combined with accident potential zones to form an Air Installation Compatible Use Zone (AICUZ) report. The report also includes USAF recommendations for changes in existing land use plans, policies and ordinances. Because of the important role of the AICUZ and other environmental impact type reports to USAF-civilian relations it is essential that the procedures used by the NOISEMAP program be as accurate as the current state of the art allows. In order to maintain the required accuracy it is essential that the technical foundations of the program be continually reviewed and updated.

An assessment approach which has been applied to several modeling parameters is the sensitivity study (1). A sensitivity study consists of a series of runs of the NOISEMAP program with varying values of the parameter under study. The sensitivity of noise contours to changes in the parameter is then quantified in terms of an appropriate measure of contour change. Previous sensitivity studies have used the change in area enclosed by a given contour or contours as a measure of contour change. In the sensitivity study discussed in this report that procedure will again be used.

Noise computations by NOISEMAP use as data a set of tables obtained by measuring noise levels for each aircraft at selected reference power settings and airspeeds. In order to compute the contribution to noise contours by aircraft flying at other than reference conditions offset profiles (DSELs) are used. Because of the data required for each aircraft a NOISEMAP run for a typical installation requires a large volume of input data. This data must be first collected at the installation and then coded by hand before execution of the computer program can take place at the AFCEC. At the present time DSELs must be input as additional data and often must be hand calculated.

This sensitivity study looks at the sensitivity of noise contours to DSELs with the hope of eliminating some of the work involving DSELs in a production run of NOISEMAP.

A review of accumulated NOISEMAP literature (2-8), along with consultations involving the staffs of the AFCEC and AMRL indicated that a computer subroutine to automatically compute DSELs is feasible. However, the volume of data input required by such a subroutine would be greater than or equal to that currently needed. As a result it is felt that if input data volume is to be reduced it must be accomplished through a reduction in input parameters. Such a reduction can come about in two ways. A more sophisticated set of algorithms could be developed to compute noise exposure contours from a reduced amount of input data. The alternative is to reduce the input data by seeking out parameters which contribute significantly to the volume of input data but have little effect on the prediction accuracy of the program. The optimization implied is to minimize input data while maintaining predictive accuracy. The best final variant of NOISEMAP will result from the application of both improved algorithms and sensitivity studies to seek out insignificant parameters. It should be emphasized that a reduction in volume and simplification in format of the input data is to be sought even at the cost of significant increases in computer time. This is because of the reduction in human errors and manhours which can be achieved by such an approach.

Thirty-two installations were considered for use in this particular sensitivity study and seven were selected for detailed study. For each of the thirty-two bases operational statistics were studied by aircraft to provide a sound basis for selecting representative bases for detailed study. The DSEL statistics for each of the seven selected bases were then analyzed in detail on an individual aircraft and installation-wide basis. In this way an operationally weighted average DSEL was obtained for each aircraft and base for use in correlating DSEL deletions with area changes for noise contours. For each of the seven bases complete NOISEMAP runs including all base operations were made for baseline, modified DSEL, no DSEL and DSEL average situations. Area computations, printed grid dumps and printer plots were produced for each run along with at least one complete chronicle for each base.

This report begins with a discussion of the specific objectives of this research followed by a brief discussion of the expected accuracy for NOISEMAP predictions. Accuracy estimates from the literature and results obtained as part of this research are considered. The next section

provides background material on the bases considered and selected for use in this study. Operational statistics, aircraft mix, characteristics of bases by command, altitude statistics and DSEL statistics for bases selected are contained in this section.

The primary results of the sensitivity study itself are then presented. Results are tabulated for baseline, no DSEL, modified DSEL and average DSEL runs in terms of enclosed area changes for selected noise contours. Indications are that a suitable criterion for deleting some DSELs without influencing noise contours may be obtained in terms of percentage of base operations by aircraft. Implementation of such criteria in NOISEMAP production runs could result in significant savings in manhours during data collection and coding.

The final sections of the report contain a summary of the results obtained and the conclusions reached on the basis of those results. Recommendations based on this research are also included along with recommendations for future research and assessments of the NOISEMAP program and underlying technical procedures.

OBJECTIVES

The primary objective for this research was to thoroughly review the theory and application of power offset profiles (DSELs) utilized by the NOISEMAP computer program. A survey of the AMRL technical reports on NOISEMAP (1-8) indicated that the most profitable approach would be a study of the sensitivity of noise contours to changes in DSELs. Thus the specific objectives for the research became the appropriate selection of installations for a sensitivity study of DSELs, the development of a suitable methodology for the study, the selection of suitable quantifiers for changes in noise contours and the generation of criteria for determining if and when DSELs may be deleted without significantly influencing predictive accuracy. These objectives are somewhat narrow in scope, but their attainment was enhanced through careful consideration of their interrelationship with the overall objectives of the NOISEMAP program. Particular attention was paid to the overall goals of minimizing and simplifying input without sacrificing predictive accuracy.

BASE SELECTION AND STATISTICS

All computer runs made in the course of this sensitivity study include all aircraft operations at an installation in exactly the same way that they would be included for a production run of NOISEMAP. As a result, studies could only be carried out for a limited number of bases because of time as well as economic constraints. This section of the report briefly describes how the seven bases for which studies were made were chosen and presents relevant statistical data for each of the bases.

Of the 107 USAF bases in the United States (9) there are complete operational statistics available for 32 at the AFCEC. These operational statistics include mix of aircraft and number and types of flight operations on an average day for each aircraft. The command distribution of these 32 bases is as follows: 4 AFLC, 5 ATC, 3 MAC, 5 SAC, 11 TAC and 4 from other commands. Tables I through V contain the operational statistics for the bases considered for use in the study. From these 28 bases the following seven were chosen for the study: Kelly (AFLC), Randolph (ATC), McChord (MAC), Fairchild (SAC), Cannon (TAC), MacDill (TAC) and Myrtle Beach (TAC). In most cases aircraft mix and total number of operations were chosen to be as close to the mean for a command as possible. In the case of TAC three bases were run because of the tendency of TAC bases to be heavily weighted to operations by a single aircraft. The altitude of a base and cost of a computer run were secondary criteria used in base selection. It should be noted that in nearly all cases the standard deviation of the data quantities is large enough so that the significance of the mean is reduced. However, the mean is still representative of the central tendency of a command and as such provides a rational basis for choosing representative bases.

Examination of Tables I through V reveals that the bases chosen represent a good cross-section of aircraft types, base size in terms of operations and base elevations. The AFLC and MAC bases have a mix of cargo, trainer and fighter aircraft. The C-130 and C-141 aircraft have the most operations at the two bases selected with number of operations and aircraft mix being close to the command mean in both cases. Randolph AFB was selected as the ATC base because it has operations by three types of trainer aircraft (T-37, T-38 and T-39) and a high enough number of operations (805) to be representative of ATC bases in general. Fairchild AFB

TABLE I. STATISTICS FOR AFLC BASES

BASE	ALT	OPERATIONS	% NIGHT OPERATIONS	% C-TYPE	% F-TYPE	% T-TYPE	% OTHER
Hill	4788	131	15	25	57	18	0
Kelly	689	84	2	38	30	31	2
McClellan	76	103	6	55	20	25	0
Wright-Patterson	824	245	3	45	6	33	15
Mean	1594	141	6.5	41	28	27	4.3
Standard Deviation	2154	72	5.9	13	22	6.8	7.2

TABLE II. STATISTICS FOR ATC BASES

BASE	ALT	OPERATIONS	% NIGHT OPERATIONS	% B-TYPE	% C-TYPE	% F-TYPE	% T-TYPE
Gather	96	226	20	12	8	1	80
Randolph	761	805	< 1	0	0	0	100
Reese	3338	1360	1	0	0	0	100
Sheppard	1015	953	2	< 1	1	0	99
Williams	1385	2140	1	0	0	5	95
Mean	1319	1097	4.8	2.6	1.8	1.2	95
Standard Deviation	1222	711	8.5	5.3	3.5	2.2	8.5

6

TABLE III. STATISTICS FOR MAC BASES

BASE	ALT	OPERATIONS	% NIGHT OPERATIONS	% B-TYPE	% C-TYPE	% F-TYPE	% T-TYPE
McChord	550	182	9	0	78	15	7
Pope	218	183	13	0	100	0	0
Scott	453	99	21	0	75	6	1.9
Mean	407	155	14	0	84	7	9
Standard Deviation	171	48	6	0	14	8	10

TABLE IV. STATISTICS FOR SAC BASES

BASE	ALT	OPERATIONS	% NIGHT OPERATIONS	% A-TYPE	% B-TYPE	% C-TYPE	% F&T TYPE
Barksdale	167	357	0	45	27	27	0
Castle	188	147	19	0	32	56	13
Davis-Monthan	2705	171	9	48	0	7	34
Fairchild	2462	140	26	0	44	48	8
March	1530	90	8	0	14	67	19
Mean	1410	181	12	18.6	23	41	14
Standard Deviation	1208	103	10	25	17	24	17

TABLE V. STATISTICS FOR TAC BASES

BASE	ALT	OPERATIONS	% NIGHT OPERATIONS	% A-TYPE	% C-TYPE	% F-TYPE	% T-TYPE
Cannon	4295	52	3	0	0	100	0
England	89	183	1	85	1	2	12
George	2875	402	1	0	0	100	0
Holloman	4000	263	0	0	0	47	53
Homestead	7	207	1	0	0	93	7
Luke	1101	362	9	0	2	98	0
MacDill	6	227	4	0	0	100	0
Mountain Home	3000	210	17	0	2	97	1
Myrtle Beach	25	408	1	92	5	0	3
Nellis	1868	513	0	6	0	78	16
Shaw	252	326	0	0	0	80	6
Mean	1593	287	3.4	17	1	72	9
Standard Deviation	1691	130	5.2	36	1.6	39	1.6

was chosen as a representative SAC base because of the high percentage of B-52 and KC-135 operations. This was felt to best represent SAC's mission in general even though it is not particularly representative of the sample of SAC bases for which statistics were available. The TAC bases selected include primarily F-4, F-111 and A-7D aircraft and range in altitude from 6 ft to 4295 ft. Activity level varies from 52 operations at Cannon AFB to 408 at Myrtle Beach.

In addition to aircraft operational statistics a statistical analysis of DSELs for each aircraft and base was carried out. The weighted average DSELs obtained will be used as an aid in quantifying the sensitivity of noise contours to changes in DSEL. Table VI summarizes this analysis. The operation weighted average DSEL for an aircraft was computed as follows. First the mean DSEL for each flight track and aircraft is computed. For a given aircraft the mean DSEL for each flight track is multiplied by the number of operations by that aircraft on that flight track. These products are then summed over all flight tracks on which that particular aircraft flies. The sum is then divided by the total operations for the aircraft under consideration to give an operation weighted average DSEL. The procedure is repeated for each aircraft at the installation. The same type of procedure is next carried out for the entire base by dividing the sum of the products of weighted average DSEL and operations over all aircraft by total base operations to give a base operation weighted DSEL. In equation form

$$(DSEL)_{wa} = \frac{\sum_{i=1}^{N} \left(\overline{DSEL_i} \times \eta_i \right)}{\sum_{i=1}^{N} \eta_i}$$

where $(DSEL)_{wa}$ is the operation weighted average DSEL for an aircraft, $\overline{DSEL_i}$ is the average DSEL for the i-th flight track, η_i is the number of operations on the i-th flight track for the aircraft in question and N is the total number of flight tracks for that particular aircraft. Also

$$(DSEL)_{bwa} = \frac{\sum_{i=1}^{M} \left[(DSEL)_{wa_i} \times M_i \right]}{\sum_{i=1}^{M} M_i}$$

TABLE VI. DSEL STATISTICS BY AIRCRAFT

BASE	AIRCRAFT	OPERATIONS	% BASE OPERATIONS	$(DSEL)_{WA}$	$(DSEL)_{BWA}$
Cannon	F-111F	52	100	3.3	3.3
MacDill	F-4E	227	100	-1.4	-1.4
Myrtle Beach	A-7D	374	92	4.9	4.5
	C-9	22	5	2.3	
	T-33	12	3	-2.7	
Fairchild	B-52G	62	44	1.1	0.4
	C-9	3	2	2.3	
	KC-135	52	37	-0.3	
	C-141	13	9	0.8	
	F-100	3	2	-4.3	
	F-111	8	6	0.2	
Kelly	B-52	2	2	0.6	0.8
	C-5	1	1	0.6	
	C-130	31	36	1.5	
	F-100	25	30	1.2	
	T-38	2	3	1.4	
	T-39	23	28	-0.5	
McChord	C-9	1	<1	2.5	0.5
	C-130	44	24	2.0	
	C-141	98	54	1.6	
	F-101	6	4	-3.1	
	F-106	21	11	-6.9	
	T-33	7	4	0.9	
	T-39	6	3	-0.9	

TABLE VI. CON'T

BASE	AIRCRAFT	OPERATIONS	% BASE OPERATIONS	$(DSEL)_{WA}$	$(DSEL)_{BWA}$
Randolph	T-37	489	61	2.0	1.8
	T-38	311	39	1.4	
	T-39	5	< 1	0.7	

Here $(DSEL)_{bwa}$ is the operation weighted average DSEL for an entire installation, M_i is the number of operations by the i-th aircraft and M is the total number of different aircraft at an installation. It should be noted that the operation weighted average DSEL for an aircraft may vary from base to base depending on operating procedures and types of operations. The weighted average DSELs will be used later in the report as a measure of DSEL change for correlation with area changes.

EXPECTED COMPUTER PREDICTION ACCURACY

Before any conclusions or criteria may be obtained from a sensitivity study it is important to have a realistic estimate of the accuracy of the predictions of the NOISEMAP program. The most direct way to estimate this accuracy is through an experimental validation study. Such a study is currently being conducted for the USAF by a contractor (10) and should be completed later this year. In the temporary absence of experimental accuracy estimates there remain two sources for such estimates -- existing AMRL technical reports or appropriate computer runs.

The percentage change in area enclosed by a noise contour caused by a change in contour value is of particular relevance for this or any sensitivity study. Together with estimates of contour prediction accuracy the area change can be used to determine whether or not a parameter has significant influence on the noise contours. The AMRL series of technical reports on NOISEMAP indicates that an error in contour value of 1 to 2 dB is to be expected (2; p.113 and 3; pp. 153 and 154). One of the reports also indicates that this is the approximate range of standard deviation encountered in experimental aircraft noise exposure measurements (4; p.A2). Thus it appears that regardless of the results of the experimental verification study in progress a lower bound on the measurable accuracy of NOISEMAP contour predictions will be 1 to 2 dB. Hence in the remainder of this report any judgements as to the significance in a contour change will be based on comparisons with the 1 to 2 dB lower bound on accuracy.

In this study, as in the previous sensitivity studies (1), the change in area within a contour will be used as a measure of contour sensitivity to the parameter changes. It is necessary to have an estimate of the area change caused by a 1 to 2 dB contour shift. It has been estimated that the linear contour shift caused by a 2 dB change in contour value is approximately 12 percent of the propagation distance to the contour (2; p. 112). If the area enclosed by a contour is roughly proportional to the square of a given linear contour dimension then this gives a 25 percent change in area for a 2 dB change in contour value.

The empirical relationship between enclosed area and NEF obtained in a previous sensitivity study (1;p.37) is

$$\text{Area (acres)} = 10^{\left[\frac{109-\text{NEF}}{18}\right]} \qquad (4\text{-}1)$$

This relationship gives a 29% area change for a 2 dB change in NEF. However, it is important to note that Eq. 4-1 is based on an average over only 9 bases and that the scatter around this average is large.

A simple theoretical analysis based on geometric spreading (inverse square law) and a single lumped excess attenuation gives an approximate relationship of the form

$$\frac{A}{A_o} = 10^{\left[\frac{\text{LDN}_o - \text{LDN} - C_a}{10}\right]} \qquad (4\text{-}2)$$

Here A is the area enclosed by the LDN contour, A_o is the area enclosed by the LDN_o contour and C_a is the lumped excess attenuation associated with the LDN contour. C_a should vary in the opposite sense from LDN. The percent change in area caused by a change in contour value is found from

$$\frac{A_1 - A_2}{A_2} = 10^{\left[\frac{(\text{LDN}_2 - \text{LDN}_1) + (C_{a_2} - C_{a_1})}{10}\right]} - 1 \qquad (4\text{-}3)$$

which was obtained from Eq 4-2. For a difference in contour values of +2 dB assuming a difference in lumped excess attenuation of -1 dB gives a 26% change in area. This result is in good agreement with the results reported by Dunderdale in a previous sensitivity study using Eq. 4-1 (1;p. 37). In Eq. 4-3 the absolute value of $(C_{a_2} - C_{a_1})$ must always be less than the absolute value of $(\text{LDN}_2 - \text{LDN}_1)$ and $(C_{a_2} - C_{a_1})$ should be of the opposite sign from $(\text{LDN}_2 - \text{LDN}_1)$. For large propagation distances the absolute value of $(C_{a_2} - C_{a_1})$ should be a significant fraction of the absolute value of $(\text{LDN}_2 - \text{LDN}_1)$.

Additional studies of the variation of area enclosed by a contour with LDN contour value were also made in the course of this sensitivity study. A larger sample of bases was considered than in the previous work since area computations for 18 bases were available. Areas enclosed by the 65, 70, 75,

80 and 85 dB LDN contours were computed for each of the bases and the mean and standard deviation were computed for the area values for each contour. In all cases the standard deviation was greater than the mean and the data spread was more than an order of magnitude. It is felt that these statistical results indicate that Eq. 4-1 may be of limited value for area predictions and that great care should be used in interpreting results obtained from it. In an attempt to circumvent some of the difficulties involved in using Eq. 4-1 the area data for all bases was normalized using the area enclosed by the 85 dB LDN contour. The mean and standard deviations were computed for the normalized data. In all cases the standard deviation was less than 34 percent of the mean and the spread of the data was greatly reduced. An empirical relationship similar to Eq. 4-2 may be obtained as an average of the normalized data. This relationship together with other features of the area-LDN studies will be discussed in more detail in a later report. Such a relationship has the drawback that the area enclosed by one of the contours must be known before others may be computed. This is not a serious problem as far as the use of the relationship in sensitivity studies is concerned. However, it does limit the use of the empirical relationship as far as area predictions are concerned unless the area enclosed by one contour is known or can be estimated.

SENSITIVITY TO DSEL CHANGES

The area change within a contour was chosen as a gross measure of contour sensitivity for this investigation. Table VII summarizes contour sensitivity for all seven bases. A baseline run area in square miles for each base gives the actual area within the contours from 65 LDN to 85 LDN with no changes from the production run for the base. All other runs for a base show percent area changes from this baseline area. Two of the bases, MacDill and Cannon, have only one aircraft so that only two non-baseline runs are shown for them. For the other bases DSELs were set equal to zero for increasingly large groups of aircraft until all DSELs were zero. As a final run for a base all DSELs were set equal to the base operation weighted average DSEL. As can be seen from Table VII using operational statistics from Table VI the DSELs have little effect on the areas except for the one or two operationally dominant aircraft. In particular it may be seen that the deletion of DSEL's for up to 50 percent of aircraft operations at an installation resulted in area changes of less than 11 percent for all installations and all contours. This means that for areas to be within 11 percent of baseline DSELs are necessary for only one aircraft at six of the seven bases studied and two at the seventh. The estimated area change caused by a 1 dB contour inaccuracy is from 12 to 16

TABLE VII. SUMMARY OF DSEL SENSITIVITY

	LDN CONTOUR VALUE				
	65	70	75	80	85
CANNON Baseline Area (sq mi)	25.5	14.4	8.22	4.28	1.84
No DSEL % Area Change	-20	-20	-25	-30	-39
DSEL Avg = 3.3; % Area Change	19	15	12	11	6
FAIRCHILD Baseline Area (sq mi)	162	95.0	46.8	26.9	15.0
No DSEL: C-9, F-100 %Area Change	0.05	0.04	0.04	0	0
No DSEL: C-9, F-100, F-111 % Area Change	0.35	0.58	0.12	0	0
DSEL for B-52, KC-135 % Area Change	0.40	0.57	0.12	0	0
DSEL for B-52 % Area Change	11	9.3	10	4.2	0.71
No DSEL % Area Change	2.7	-4.4	5.9	-6.5	-16
DSEL Avg = 0.4 % Area Change	7.3	0.3	11	-1.0	-11
KELLY Baseline Area (sq mi)	10.7	5.79	3.53	1.92	0.80
No DSEL: B-52, C-5, T-38 % Area Change	1.9	-0.16	-0.42	-0.99	-3.2
No DSEL: B-52, C-5, T-38, T-39 % Area Change	3.0	0.59	-0.34	-1.8	-3.2
DSEL for C-130 % Area Change	-3.8	-7.9	-9.5	-11	-31
No DSEL % Area Change	-4.1	-8.0	-9.7	-11.4	-31
DSEL Avg = 0.8 % Area Change	5.4	-1.5	-5.6	-6.7	-23
MACDILL Baseline Area (sq mi)	31.1	16.0	8.60	4.36	1.76
No DSEL % Area Change	73	42	32	27	17
DSEL Avg = -1.4 % Area Change	34	17	10	5	-8

TABLE VII. CON'T

MCCHORD Baseline Area (sq mi)	19.2	9.51	4.38	1.85	0.79
No DSEL: C-9, F-101, T-33, T-39 % Area Change	1.4	-0.56	-4.3	-9.6	-1.8
No DSEL: C-9, F-101, T-33, T-39, F-106, % Area Change	10	7.8	4.9	1.6	0.25
DSEL for C-141 % Area Change	9.5	7.1	4.7	1.0	0.25
No DSEL % Area Change	0.6	-4.6	-12	-21	-3.4
DSEL Avg = 0.5 % Area Change	7.5	2.5	-5	-12	-2.4
MYRTLE BEACH Baseline Area (sq mi)	71.8	32.8	16.5	9.28	4.69
No DSEL: C-9, T-33 % Area Change	0.49	0.11	-0.05	-0.16	-0.15
No DSEL % Area Change	-51	-51	-51	-61	-71
DSEL Avg = 4.5 % Area Change	24	-0.8	-10	-19	-32
RANDOLPH Baseline Area (sq mi)	23.8	11.5	5.33	2.33	0.93
DSEL for T-37 % Area Change	-2.9	-4.7	-11	-13	-20
No DSEL % Area Change	-1.6	-4.6	-14	-23	-25
DSEL Avg = 1.8 % Area Change	20	24	17	9	0

16

percent. Therefore the 11 percent change is within a conservative estimate for the area corresponding to the optimal 1 to 2 dB contour prediction accuracy of NOISEMAP.

The variation of average percent area change with percent of operations with no DSEL is shown in Fig. 1. The average percent area change appearing here is obtained by simply averaging the percent area changes for the five contours from 65 to 85 LDN. The dashed lines at 12 percent area change represent a conservative estimate of the area change corresponding to a 1 dB contour shift. The figure illustrates again that deleting DSELs for up to 60 percent of base operations causes an area change less than that caused by a 1 dB contour shift. In fact for DSELs deleted on up to 50 percent of base operations the area change is less than that caused by a 0.5 dB contour shift.

It is evident from the results summarized in Table VII and Figure 1 that DSELs may not be ignored completely. It does appear that they could be neglected for an important fraction of base operations without significantly affecting contour accuracy. In particular it seems that for most bases DSELs are necessary for only one or two operationally dominant aircraft. A working procedure stating that DSELs should be included for operationally dominant aircraft until a cumulative percentage of base operations of 60 to 70 percent is reached could significantly reduce input data.

It also appears that as the number of different aircraft at an installation increases the importance of DSELs decreases. In fact with the exception of the three TAC bases which are heavily single aircraft weighted, all bases are very near or within the 1 dB band in Fig. 1 with all DSELs deleted. This is primarily a result of the decrease in base weighted average DSEL with increasing number of aircraft types which is caused by the greater opportunity for DSEL cancellation by different aircraft.

Figure 2 illustrates the variation of average percent area change with operation weighted average deleted DSEL. The plot indicates that area change decreases linearly with increasing deleted DSEL. It further indicates that if the base operation weighted average DSEL is in the range from -1 to 1 then the expected area change is less than 12 percent. This plot could be very useful for obtaining estimates of the significance of DSELs at installations purely on the basis of operational and DSEL statistics for the base. The base weighted average DSEL will give a good estimate

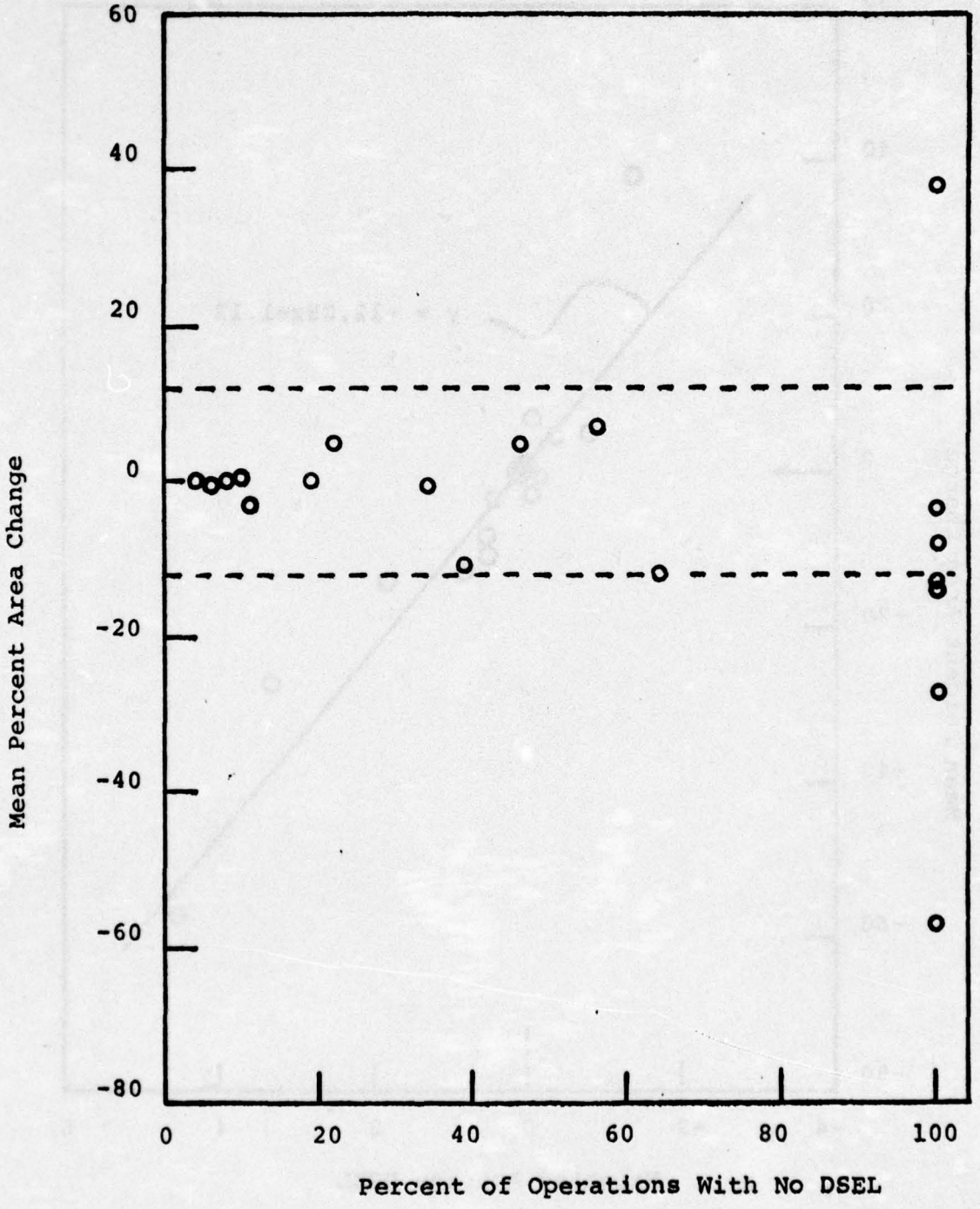


Fig. 1 Percent Area Change as a Function of Percent Operations Without DSEL.

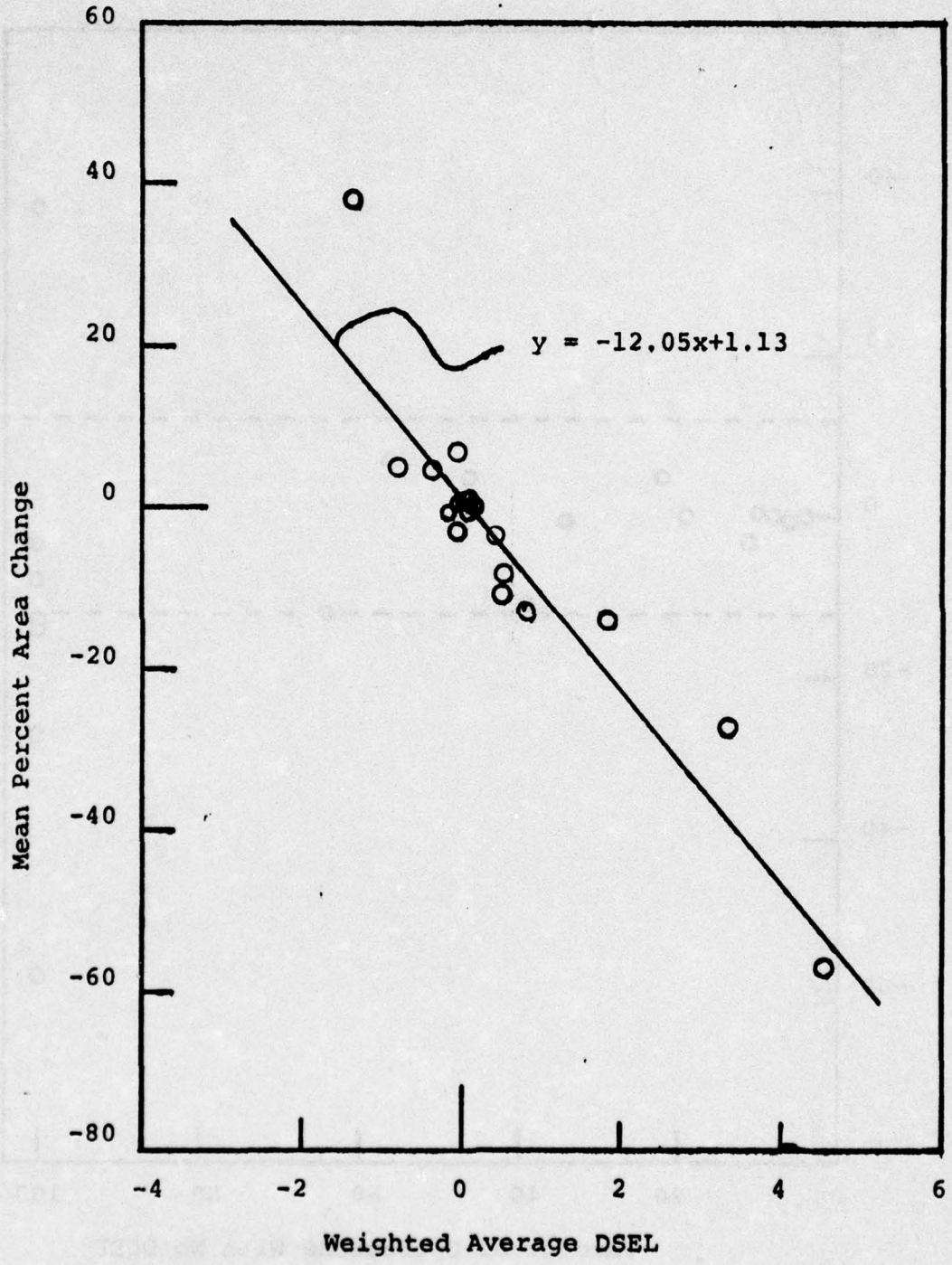


Fig. 2 Variation of Percent Area Change With Weighted Average DSEL.

of the change in area expected if DSELs are deleted via Fig. 2 alone without the need for an additional computer run. The plot is especially useful since in the range of area change from -20 to +20 percent where DSEL deletions would be considered there is a relatively small amount of scatter about the linear regression best fit straight line.

Some question may be raised as to the appropriateness of the precent area change as a measure of contour sensitivity. There are two primary reasons supporting this choice. First, it is the measure which was chosen by BBN for the previous sensitivity studies (1) and as such its use in this study facilitates comparisons with the other studies. Second, printer plots were made for all runs to study contour shape changes. The printer plots indicate that significant contour shape changes do not occur until very large area changes are present. Therefore, change in area is probably the most appropriate, as well as the most straight forward, measure of contour sensitivity available.

CONCLUDING REMARKS

There is little doubt that the DSELs for power settings and airspeed are based on a sound physical foundation. However, from a production standpoint it is undesirable to have "corrections" which must be applied to virtually every aircraft operation. This study has investigated the sensitivity of noise contours to DSELs. The results presented in the previous section indicate that DSELs have little effect on the contours for aircraft with a low percentage of base operations. There is, of course, always a question of how large an effect can be ignored before the cumulative effect of several neglected parameters becomes large. In the case of DSELs it appears that a conservative application of the results obtained in this study could result in a significant saving in man and computer time at no expense to predictive accuracy.

On a more general basis, this study along with the previous sensitivity studies indicates that continued refinement and optimization of the program can be productive. If the validation studies currently underway indicate that the computer simulation does indeed predict noise contours to within a standard deviation of experimental determinations then efforts should be directed towards program optimization. If the validation study indicates that significant improvement in the simulation is possible then sensitivity studies can help indicate where significant improvements are possible. In any such studies or further work on NOISEMAP the following

statement from one of BBN's early report on community noise exposure should be kept in mind.

> "There will be a tendency to overly complicate the input data for computer simulation. This will result in much unnecessary manpower and computer time expended. Some of the judgement as to the level of detail and complexity desirable can be quantified into a set of working rules. Much of this will have to be learned from experience with the rules and an analysis of the results of the decisions made during the course of the work." (11)

Further sensitivity studies and in particular studies of entire base situations will continue to provide important insights for future developments in NOISEMAP predictive procedures. In some cases such studies will indicate parameters which are not necessary to maintain prediction accuracy. In other cases studies will indicate parameters for which modeling techniques must be refined to improve prediction accuracy. In addition to looking at parameters singly it would be useful to also do some combined sensitivity studies for entire base situations. Such studies would help establish the cumulative effects of various parameters on noise contours. Great care must be exercised when interpreting the results of any study, particularly when deletion of input is being considered. However, it is equally important to bear in mind the limits to the accuracy of the predictive procedure due to the statistical nature of the quantities involved. It is essential that any sensitivity study consider contour change significance relative to contour inaccuracies associated with the predictions of NOISEMAP. Once the accuracy of NOISEMAP predictions has been verified to within a standard deviation of experimental determinations the primary effort should be concentrated in the area of program optimization. That is minimum input data and computer time without change in accuracy.

RECOMMENDATIONS

1. On production runs of NOISEMAP the following procedure should be adopted for the deletion of unnecessary DSELs. First determine the percentage of base operations for each aircraft at a base. Next rank them in order from highest percentage on down. DSELs are required for all operations of the aircraft with the highest percentage of base operations. If a single aircraft accounts for more than 65 percent of base operations then DSELs are not required for any other aircraft. If a single aircraft does not account for over 65 percent of base operations then DSELs are required for all operations of the two most prevalent aircraft on an operations basis. DSELs are included in this fashion for as many aircraft as are needed to cumulatively total more than 65 percent of base operations. DSELs for small percentage operation aircraft are not necessary. For most bases DSELs should be necessary for only one or two aircraft using the above criterion.

2. Because of their importance in all sensitivity studies further investigations of the relationship between enclosed area and contour value should be made. Some of the information needed for these studies is available at the AFCEC in the form of area computations for the five LDN contours from 65 to 85. Such computations have been done for most bases run since February 1976. In addition to the information available at the AFCEC it would be useful to have several bases run at 1 dB contour increments to estimate the area change caused by a 1 dB contour inaccuracy.

3. Further sensitivity studies should be conducted to identify parameters for which modeling techniques need improvement and to identify parameters which can be deleted or simplified to reduce input data.

4. Criteria should be developed through a type of sensitivity study for determining how large a change in operations may occur before significant contour changes develop. This is an especially important area since there will be many situations in the near future when decisions on whether or not bases should be rerun will need to be made.

5. Future sensitivity studies should include parameters with sound physical foundation as well as parameters about which there is some technical controversy. This is especially true for parameters involving large amounts of input data.

6. An overall look at the entire prediction procedure may be worthwhile. Perhaps a sound power and directivity approach with less input data for each aircraft would be advisable. Such an approach would probably result in more complex computational algorithms.

7. Close attention should be paid to current propagation research. In particular there may be some valuable insights into the air-to-ground ground-to-ground transition available in some of the non-aircraft oriented research.

REFERENCES

1. Bishop, D.E., Dunderdale, T.C., Horonjeff, R.D., and Mills, J.F., "Sensitivity Studies of Community Aircraft Noise Exposure (NOISEMAP) Prediction Procedure," AMRL-TR-75-115, Aerospace Medical Research Laboratory, Wright-Patterson Air Force Base, Ohio (March 1976).

2. Bishop, D.E., "Community Noise Exposure Resulting from Aircraft Operations: Application Guide for Predictive Procedure," AMRL-TR-73-105, Aerospace Medical Research Laboratory, Wright-Patterson Air Force Base, Ohio (November 1974).

3. Galloway, W.J., "Community Noise Exposure Resulting from Aircraft Operations: Technical Review," AMRL-TR-73-106, Aerospace Medical Research Laboratory, Wright-Patterson Air Force Base, Ohio (November 1974).

4. Bishop, D.E., and Galloway, W.J., "Community Noise Exposure Resulting From Aircraft Operations: Acquisition and Analysis of Aircraft Noise and Performance Data," AMRL-TR-73-107, Aerospace Medical Research Laboratory, Wright-Patterson Air Force Base, Ohio (August 1975).

5. Reddingius, N.H., "Community Noise Exposure Resulting From Aircraft Operations: Computer Program Operator's Manual," AMRL-TR-73-108, Aerospace Medical Research Laboratory, Wright-Patterson Air Force Base, Ohio (July 1974).

6. Reddingius, N.H., "Community Noise Exposure Resulting From Aircraft Operations: Appendix NOISEMAP Program Operator's Manual," AMRL-TR-73-108, Appendix, Aerospace Medical Research Laboratory, Wright-Patterson Air Force Base, Ohio (February 1976).

7. Horonjeff, R.D., Kandukuri, R.R., and Reddingius, N.H., "Community Noise Exposure Resulting From Aircraft Operations: Computer Program Description," AMRL-TR-73-109, Aerospace Medical Research Laboratory, Wright-Patterson Air Force Base, Ohio (November 1974).

8. Speakman, J.D., Powell, R.G., and Cole, J.N., "Community Noise Exposure Resulting From Aircraft Operations: Acoustic Data on Military Aircraft," AMRL-TR-73-110, Aerospace Medical Research Laboratory, Wright-Patterson Air Force Base, Ohio (to be published).

9. "Guide to USAF Bases at Home and Abroad," Air Force Magazine, 59, No. 5 (May 1976), p. 144.

10. "Validation of Aircraft Noise Exposure Prediction Procedure," Bolt Beranek and Newman, Contract F33615-76-C-5003, under the technical management of the Biodynamic Environment Branch, Aerospace Medical Research Laboratory, Wright-Patterson Air Force Base, Ohio.

11. Reddingius, N.H., "Community Noise Exposure Resulting From Aircraft Operations: Computer Facility Requirements," Report 2752, Project 11812, Directorate of Civil Engineering, Engineering Division, Headquarters USAF, Washington, D.C. (9 August 1974), p. 14.

1976 USAF-ASEE SUMMER FACULTY RESEARCH PROGRAM

Sponsored by

THE AIR FORCE OFFICE OF SCIENTIFIC RESEARCH

Conducted by

AUBURN UNIVERSITY AND OHIO STATE UNIVERSITY

PARTICIPANT'S FINAL REPORT

DETERMINATION OF UNLOADED AND LOADED PAVEMENT PROFILES USED FOR PREDICTION OF DYNAMIC RESPONSE OF AIRCRAFT

Prepared by:	William H. Highter
Academic Rank:	Assistant Professor
Department and University:	Department of Civil and Environmental Engineering Clarkson College of Technology
Assignment:	Tyndall Air Force Base Civil Engineering Center Directorate of Engineering Materials Research Division
USAF RESEARCH COLLEAGUE:	L. M. Womack
Date:	20 August 1976
Contract No:	F44620-75-C-0031

DETERMINATION OF UNLOADED AND LOADED PAVEMENT PROFILES USED FOR PREDICTION OF DYNAMIC RESPONSE OF AIRCRAFT

By

William H. Highter

A B S T R A C T

Pavement roughness affects the structural loads imposed on aircraft during ground operations and can also affect instrument readability. In some cases aircraft vertical accelarations have reached such high levels that documentation by flight crews indicate that the safety of the aircraft may be affected. Aircraft fatigue stresses and some structural deformation of aircraft have also been noted. Pavement roughness, then, is an important element in the evaluation of both rigid and flexible airfield pavements.

Aircraft response to pavement roughness can be measured by on-board instrumentation but this is an expensive and time consuming procedure because different types of aircraft respond to identical pavement profiles differently and the response is also a function of the velocity of the aircraft. For these reasons the Air Force has developed a computer code (TAXI) which simulates the response of aircraft to pavement roughness. Input to this code consists of aircraft characteristics and the pavement profile; output includes landing strut forces and displacements and vertical acceleration of the aircraft frame.

Present Air Force practice is to measure a pavement profile with a laser profilometer. The result is a series of elevations along the pavement surface which defines a pavement profile when the pavement is undeflected i.e. unloaded. This unloaded profile is different from any profile seen by aircraft because aircraft load can deflect the pavement, thus changing the profile. It is not known for certain whether the simulated response of aircraft to unloaded and loaded pavement profiles is significantly different.

To obtain the data necessary to determine if loaded and unloaded pavement profiles are enough different to be significant in the aircraft response as predicted by "TAXI", a 2100 foot pavement test section was selected on Taxiway 9 at Eglin Air Force Base, Florida. The unloaded profile was obtained by measuring the elevations of points along a straight line on the surface of the pavement at 2 foot intervals. The loaded pavement profile was obtained by measuring the deflections caused by a 25,115 pound load at the same point the unloaded elevations were obtained and subtracting these deflections from the unloaded profile. The load was applied through the same type of tire used on the main gear of an F-4 aircraft and the deflections were measured with a noncontacting deflection measuring device which uses light emitting diodes.

The unloaded profile was inputted to TAXI along with F-4 aircraft characteristics and the aircraft response to the unloaded profile at an aircraft speed of 100 ft per second are now available. The remaining steps required to complete the entire phase of the project of which this research effort is a part, is outlined in this report and summarized in a flow chart.

ACKNOWLEDGEMENTS

The author is grateful to the Air Force Systems Command, Office of Scientific Research; the Engineering Materials Directorate of the Air Force Civil Engineering Center and the American Society for Engineering Education for the technical support of this research effort. Administrative support was provided by Auburn University.

The author also wishes to acknowledge the support of his USAF Research Colleague, Mr. L.M. Womack. It has been a pleasure to work with the staff of the Engineering Materials Directorate of AFCEC. In particular, thanks are extended to Lt Col George D. Ballentine and Captain Robert F. Cauley.

The author wishes to acknowledge with thanks the assistance of CMSgt Jerome H. Bosold and Sgt J.P. Reynolds.

INTRODUCTION

The Air Force maintains some 500 million square yards of pavement at annual maintenance costs of about $400 million. These pavements were constructed at different times, under different design criteria, are subject to various types and volume of traffic, and some are located in extreme climates. With such a large and diverse inventory of pavements, two major problems face the pavement engineer; the estimation of the service life of individual pavement sections, and; an assessment of the condition of individual pavement sections at any time in the service life of the pavement.

The research described here deals with pavement roughness which is one facet of pavement condition assessment or evaluation. Pavement roughness is an important consideration because it can affect instrument readability and influence the structural loads imposed on aircraft during ground operations. Pavement roughness is defined here as the deviation of the surface of the pavement from a plane. A pavement profile is a longitudianl line which describes the surface of the pavement. The magnitude of pavement roughness is the deviation of the profile from a straight line.

The Air Force Civil Engineering Center (AFCEC) has developed a laser profilometer which can measure a pavement profile quickly with a minimum of airfield downtime. Present practice in Air Force pavement roughness evaluation is to determine the profile of airfield pavements when the pavement is unloaded and therefore undeflected. This unloaded profile is inputted into computer code TAXI along with aircraft characteristics and dynamic responses of the aircraft to pavement roughness is simulated. These responses include main gear stroke, nose gear stroke, main gear force, nose gear force, tail acceleration, center of gravity acceleration, and pilot station acceleration. Since aircraft load and deflect pavements, the profile traversed by aircraft is a loaded profile which is different from the unloaded profile presently used as input to TAXI. The aircraft roughness simulation procedure presently used by the Air Force, then, is not precise but it is not known whether or not the response of a given aircraft differs significantly if the profile transversed in the computer simulation is the unloaded profile or the loaded profile. The objective of the present research effort was to obtain the data required to make this determination, and if time allowed to make initial computer simulations of the F-4 aircraft on unloaded and loaded profiles.

If it is found that the unloaded profile affects the response of aircraft in essentially the same manner as the loaded profile, then the approach presently used by the Air Force in evaluating pavement roughness would be validated. If, however, the aircraft responses were found to be significantly different, then the Air Force would have to develop a means of measuring loaded pavement profiles quickly and accurately to serve as input to the computer code.

OBJECTIVES

A primary objective of the research program of which this research effort is a part, is to determine if the dynamic response of aircraft is significantly different when traversing unloaded and loaded pavement profiles. The primary objectives of the portion of the total research program reported here were to determine unloaded and loaded pavement profiles on at least 2000 feet of airfield pavement and to become familiar with the computer code (TAXI) that would be used to simulate aircraft response to the loaded and unloaded pavement profiles. In addition, if time allowed, initial computer simulations would be made of aircraft response to the unloaded and loaded profiles.

DETERMINATION OF UNLOADED AND LOADED PAVEMENT PROFILES

A flow chart illustrating the steps necessary to accomplish the overall research objective is shown in Figure 1. The procedures used to determine the unloaded and loaded pavement profiles is discussed in detail in this section and the results of an F-4 simulated response to the unloaded pavement profile are presented in graphical form.

Unloaded Pavement Profile

A 2100 ft. section of taxiway at Eglin Air Force Base, Florida was selected as a test section. The pavement along the test section consisted of asphaltic concrete with a sand asphalt base. Along the line of profile, the asphaltic concrete varied in thickness from 1 5/8" to 5 1/2" and the sand asphalt base was from 5" to 7 1/4" thick (Ref. 1). A 2100 ft. straight line was laid off on the taxiway and painted. The taxiway runs in a general east-west direction and distances along the line were measured from a zero point at the west end of the line. A bench mark was selected on a compass pad located about 50 ft. west of the zero point of the profile line and a local datum was established as 100.00 ft. elevation. Starting at point zero elevations to the nearest 0.001 ft were determined at 2 ft. intervals along the 2100 ft. test section. The elevations at the 1051 points determined in this manner established the unloaded pavement profile. The unloaded pavement profile data were then punched on computer cards for input to TAXI - the aircraft dynamic response computer code.

Loaded Pavement Profile

The loaded pavement profile was obtained by traversing the test section with a load cart, measuring the deflections at two foot intervals, and subtracting these deflections from the corresponding point on the unloaded pavement profile.

The load cart used was a truck with the rear axle modified so that a 25,115 pound single wheel load was applied to the pavement using an F-4 main gear wheel. The aircraft tire was inflated to the operational pressure of 250 psi. The loaded pavement profile obtained using the load cart was expected to approximate the profile actually "seen" by an F-4. Because 87.7% of the gross weight of an F-4 is carried by the main gear (Ref 2), the load cart simulated an F-4 weighing about 57,000 pounds which is close to the maximum take-off weight of 58,000 pounds (Ref. 3) of an F-4C.

Pavement deflections were measured with two different types of measuring devicees (1) linear variable differential transformers (LVDT) and (2) light emitting diodes (LED). A detailed discussion on the use of LVDT's for measuring pavement deflections can be found in Reference 4. The LED system has only recently been developed for the AFCEC and a technical report has not been published.

The LVDT system consisted of 6 gages mounted on a cantilever beam which was supported at a point outside of the deflection basin. This system was used to measure pavement deflections in a direction perpendicular to the direction of travel of the load cart. Deflections were measured at 100 ft. intervals over the 2100 ft. test section. The deflections, in inches, measured by the LVDT system are tabulated in Table 1. Inspection of this Table indicates that the position of the center of the F-4 tire with respect to the LVDT beam varied and the minimum distance from the center of the 10 inch wide tire to the closest gage was 8.5 inches at Station 2.

To predict the deflections at a point 2.5 inches from the edge of the tire (the point where the LED measured the deflections) and at the center of the tire (point of maximum deflection), regression analysis was used to fit various models to the measured LVDT deflections at Station 2. The models selected were similar to those used previously for similar purposes (Ref. 4) and those currently being used (Ref. 5). The models selected are illustrated in Figure 2 along with the LVDT deflections measured at Station 2. The broken lines in the figure indicate the area of

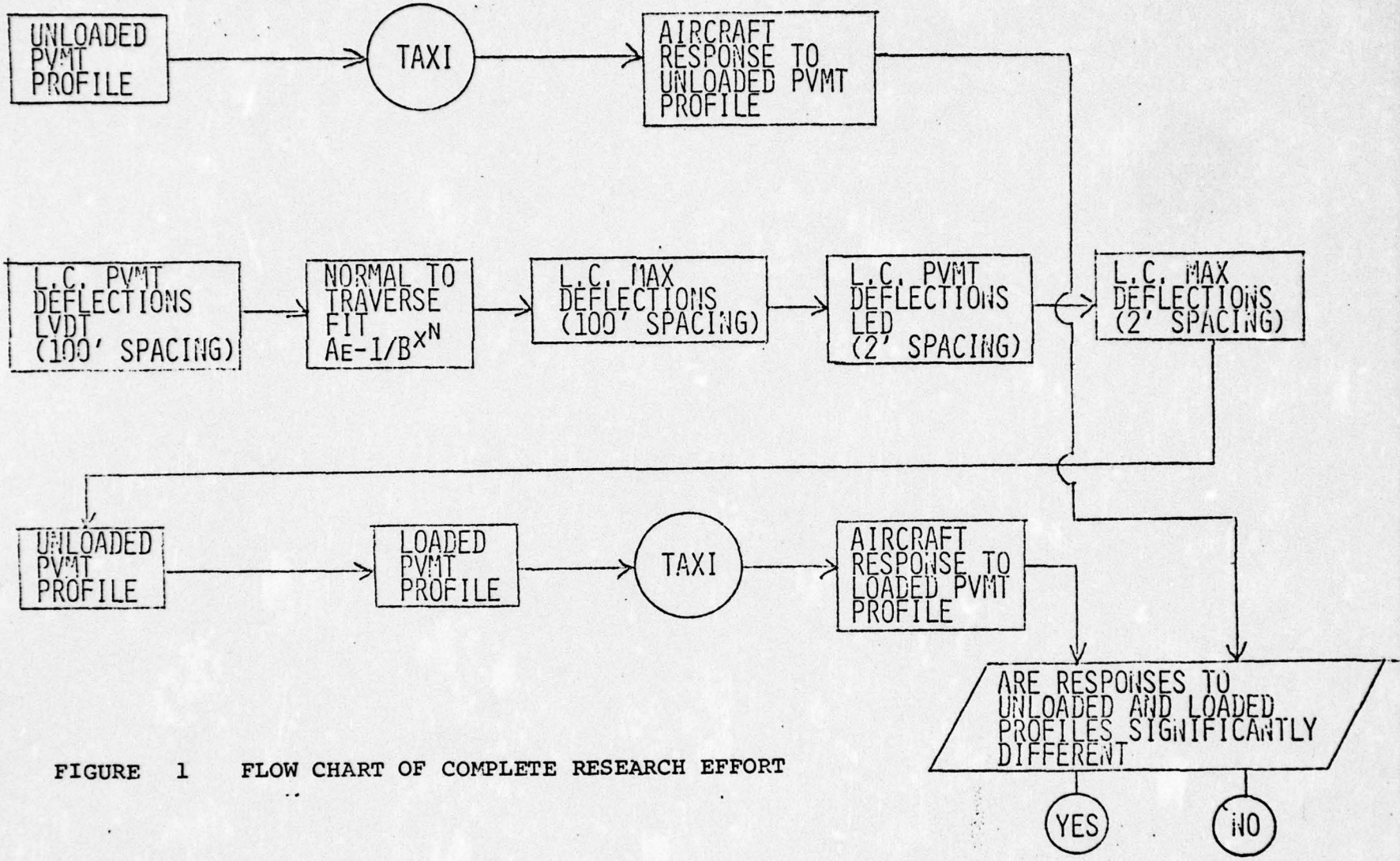


FIGURE 1 FLOW CHART OF COMPLETE RESEARCH EFFORT

TABLE 1

DEFLECTIONS MEASURED BY LVDT GAGES[1] (inches)

STATION #	OFFSET (in)	LVDT GAGE No.					
		1	2	3	4	5	6
0	14.5	0.0369	0.0294	0.0170	0.0079	0.0031	0.0011
1	12.0	0.0341	0.0268	0.0170	0.0077	0.0030	0.0008
2	8.5	0.0487	0.0379	0.0238	0.0109	0.0030	0.0008
3	15.0	0.0339	0.0267	0.0159	0.0067	0.0025	0.0007
4	10.0	0.0429	0.0311	0.0204	0.0099	0.0041	0.0014
5	10.25	0.0144	0.0131	0.0096	0.0055	0.0027	0.0010
6	12.0	0.0288	0.0238	0.0148	0.0072	0.0031	0.0013
7	10.25	0.0237	0.0197	0.0127	0.0063	0.0027	0.0027
8	9.5	0.0303	0.0237	0.0149	0.0065	0.0024	0.0009
9	10.5	0.0259	0.0197	0.0120	0.0053	0.0022	0.0009
10	10.0	0.0283	0.0210	0.0124	0.0049	0.0020	0.0007
11	9.0	0.0208	0.0172	0.0105	0.0057	0.0028	0.0014
12	11.0	0.0216	0.0176	0.0093	0.0048	0.0023	0.0009
13	10.0	0.0150	0.0120	0.0076	0.0024	0.0013	0.0007
14	10.0	0.0146	0.0119	0.0078	0.0043	0.0022	0.0010
15	9.5	0.0131	0.0117	0.0078	0.0043	0.0022	0.0010
16	8.75	0.0149	0.0110	0.0084	0.0035	0.0014	0.0005
17N	9.0	0.0172	0.0146	0.0101	0.0060	0.0031	0.0014
17S	8.6	0.0149	0.0135	0.0098	0.0061	0.0031	0.0014
18	11.0	0.0150	0.0119	0.0083	0.0049	0.0024	0.0010
19	11.5	0.0181	0.0145	0.0080	0.0039	0.0023	0.0011
20	9.74	0.0249	0.0169	0.0094	0.0040	0.0014	0.0008
21	8.9	0.0284	0.0212	0.0141	0.0075	0.0035	0.0012

[1] Offset is the distance from gage 1 to centerline of F-4 tire. Gage spacing was as follows: between gages 1 and 2, 3"; gages 3 and 4, 9"; gages 4 and 5, 10"l gage 5 and 6, 10".

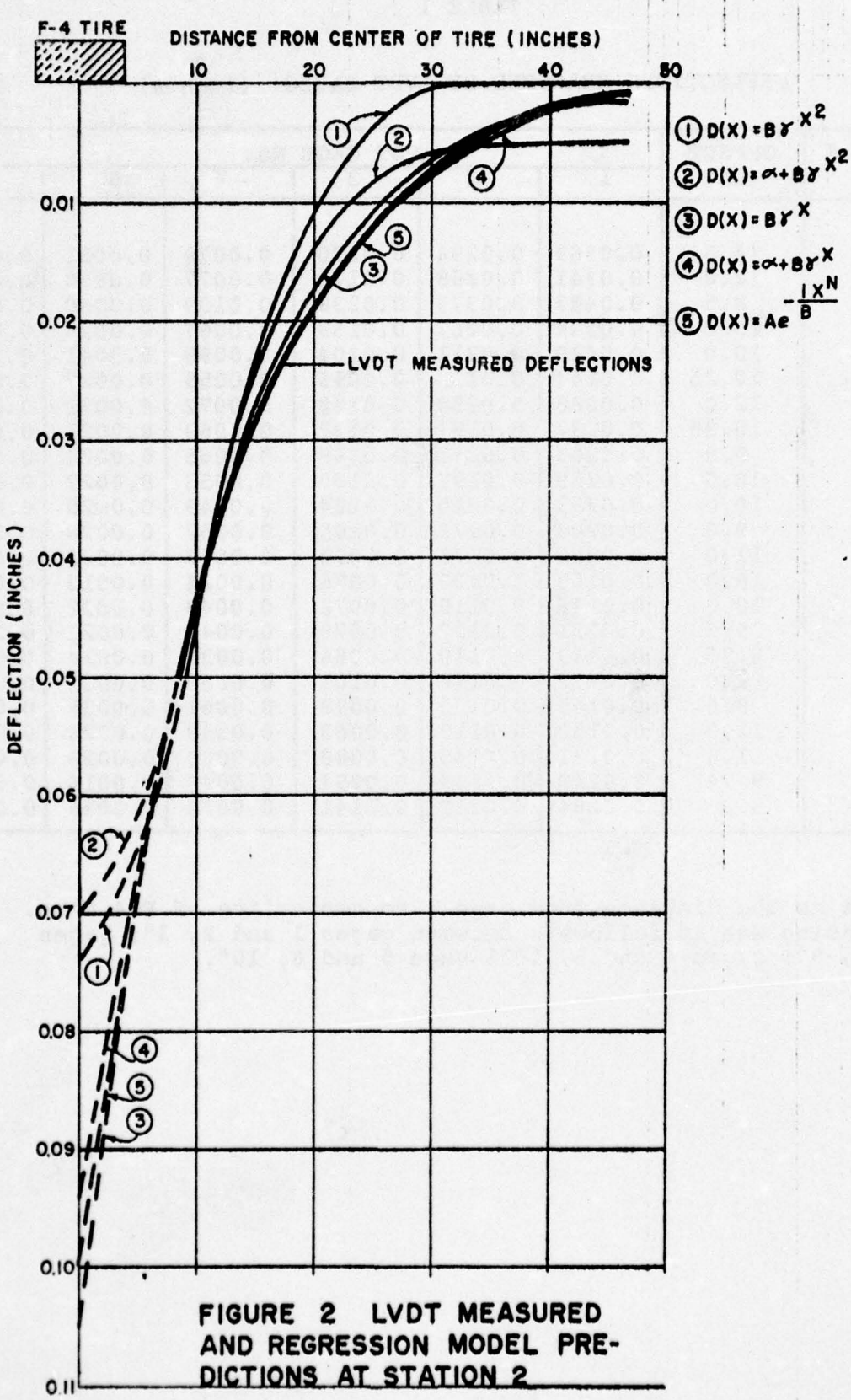


FIGURE 2 LVDT MEASURED AND REGRESSION MODEL PREDICTIONS AT STATION 2

extrapolation. Based on the analysis shown in Figure 2 and on other analyses, it was decided that the following two equations best predicted the deflections:

$$D(x)=\beta\gamma^{x^2} \qquad (1)$$

and

$$D(x)=Ae^{-B^{lx^N}} \qquad (2)$$

where

D (x) is the deflection at point x and x=0 at the center of the F-4 tire

β, γ, A, B are parameters obtained from regression analyses.

Regression analysis was carried out on both equations (1) and (2) at each station. For each station the parameters obtained from the analyses are tabulated in Table 2. By using these equations for extrapolation, an estimate can be obtained for the deflection under a wheel given the deflection at a point outside of the wheel.

Deflections along the 2100 ft. profile were needed at 2 ft. intervals. This would require 1051 different set-ups of the LVDT beam - a time consuming and expensive procedure. Because of this, it was decided to use the LED deflection measuring system which can be attached to a moving vehicle and deflections can be measured continuously.

The LED system does not measure deflections directly but requires that the actual deflection be known at some reference. This reference is an external reference and must be obtained by another independent or external measuring system. In this case, the external reference was provided by the LVDT deflection which were taken at 100 ft. intervals as described previously. The procedure used to determine deflections using the LED system was as follows: With the external reference known an LED reading was taken at the same point. The load cart was driven along the test section and the LED recorded changes in deflection at a sampling rate of 4 per second. If the external reference indicated that the deflection at a point was 0.100 inches and the LED reading at another point was -0.015 inches, then, by subtracting algebraically, the deflection at the second point as determined by the LED system was 0.115 inches.

TABLE 2

CURVE FITTING PARAMETERS FOR LVDT DEFLECTIONS

	$Ae^{-\frac{1}{B}x^N}$			$B\gamma^{x^2}$	
STATION NO.	A[1]	B	N	B[2]	γ
0	0.0632	32.658	1.273	0.1188	0.995
1	0.0580	14.557	1.050	0.0774	0.995
2	0.0661	11.102	0.976	0.0740	0.995
3	0.0636	27.470	1.237	0.1176	0.995
4	0.1161	2.613	0.594	0.0744	0.995
5	0.0155	242.503	1.757	0.0286	0.995
6	0.0394	41.957	1.325	0.0666	0.995
7	0.0300	34.810	1.271	0.0446	0.995
8	0.0423	14.821	1.067	0.0511	0.995
9	0.0365	14.566	0.945	0.0481	0.995
10	0.0469	9.580	0.981	0.0491	0.995
11	0.0253	25.823	1.181	0.0341	0.995
12	0.0320	16.757	1.051	0.0434	0.995
13	0.0202	22.500	1.185	0.0269	0.995
14	0.0200	16.853	1.038	0.0266	0.995
15	0.0143	135.306	1.636	0.0236	0.995
16	0.0273	4.188	0.699	0.0231	0.995
17N	0.0211	21.234	1.061	0.0288	0.995
17S	0.0161	87.972	1.444	0.0249	0.995
18	0.0310	4.591	0.673	0.0304	0.995
19	0.0264	26.515	1.228	0.0385	0.995
20	0.0688	2.735	0.658	0.0404	0.995
21	0.0557	3.516	0.633	0.0444	0.995

[1] A is the deflection (inches) at a point at the edge of an F-4 tire.

[2] B is the deflection (inches) of a point at the center of an F-4 tire.

Although elapsed time was not directly recorded on the magnetic tape used for recording LED readings, the sampling rate (4 per second) at which the LED data was recorded allowed elapsed time to be determined. In addition, arrows were painted on the profile line at 25 ft. intervals and as the load cart travelled over each arrow, an event marker was triggered manually on one of the tape channels. By counting the number of LED readings between successive event signals, the time it took the load cart to travel 25 ft. was obtained. Thus the average velocity of the load cast over that particular 25 ft. segment of the profile was known. With this information, individual LED readings could be coordinated with points on the profile. Using the procedure the pavement deflections at points 7.5 inches away (measured perpendicular to the direction of travel of the load cast) from points used to establish the unloaded pavement profile were determined.

Table 3 is a sample listing of the elevations at various points along the (unloaded) profile and the deflections as determined by the LED system. The unloaded profile can be directly inputted to the TAXI code to determine the response of the F-4 aircraft. Since the LED deflections are deflections at points 7.5 inches from the center of the F-4 tire, Equation (1) or (2) must first be applied to estimate the deflection at the center of the tire. Subtracting this estimate from the unloaded profile yields the loaded profile which then can be inputted to TAXI to determine the F-4 response to the loaded pavement profile.

Response of F-4 Aircraft to Unloaded Pavement Profile

Computer code TAXI (Ref. 3) simulates the dynamic response of an aircraft traversing a rigid profile i.e. the program makes no provision for pavement deflection. The user has the option of specifying either a constant speed taxi or a take-off simulation.

The length of the profile inputted to TAXI is increased by 100 ft. of horizontal pavement by the program so that the nose gear traverses the entire input profile. The input profile is normalized with respect to the first input elevation point so that the first 102 feet of the profile in the computer simulation are given elevation 0.000 feet. In addition, the elevations are normalized with respect to a straight line drawn from the first input elevation and the elevation of a point 280 feet from the end of the input profile. This feature is for output plotting purposes. The profile is

TABLE 3

SAMPLE LISTING OF UNLOADED PROFILES AND PAVEMENT DEFLECTIONS

DISTANCE ALONG PROFILE (FEET)	UNLOADED ELEVATION (FEET)	DEFLECTION 7.5 IN FROM CENTER OF F-4 TIRE (INCHES)
286.0	97.031	.060
288.0	97.017	.061
290.0	97.002	.061
292.0	96.986	.061
294.0	96.968	.061
296.0	96.952	.061
298.0	96.933	.061
300.0	96.928	.061
302.0	96.916	.061
304.0	96.897	.078
306.0	96.881	.078
308.0	96.858	.078
310.0	96.849	.078
312.0	96.839	.071
314.0	96.831	.071
316.0	96.826	.071
318.0	96.818	.072
320.0	96.803	.060
322.0	96.786	.060
324.0	96.776	.060
326.0	96.764	.060
328.0	96.742	.060
330.0	96.726	.060
332.0	96.717	.060
334.0	96.702	.060
336.0	96.694	.075
338.0	96.683	.075
340.0	96.674	.075
342.0	96.663	.075
344.0	96.650	.075
346.0	96.641	.062
348.0	96.628	.049
350.0	96.626	.050

then represented by a series of functions each of which applies to three normalized elevation points (4 ft. of pavement with input elevation at 2 ft. spacing). The slope at the beginning of each segment is set equal to the slope at the end of the previous segment thus maintaining a continuous curve between adjacent segments.

The aircraft is mathematically modeled as a flexible structure. Complete details of the mathematical basis of the code are given in Vol. 1 of Reference 1 along with aircraft characteristics which are required as input.

A simulation run of a 57,000 pound F-4C traversing the unloaded Eglin test section profile at a constant speed of 100 ft. per second was carried out and some of the results of the simulation are shown in Figures 3-6. Figure 3 is a computer plot of the normalized unloaded profile as seen by the nose gear of the aircraft in the simulation. This normalized profile is different from that which is inputted but the results of other computer runs indicate there is little difference in aircraft response if the profile is not normalized in the computer code.

Figures 4, 5, and 6 are plots of the vertical acceleration of the tail section, center of gravity, and the pilot station respectively, of an F-4 as it traverses the unloaded pavement profile at a constant speed of 100 ft. per second. These plots indicate that the tail section experienced the largest acceleration followed by the pilot station and the center of gravity. This is a characteristic of the aircraft and is not unique to this particular unloaded profile. Plots such as those shown in Figures 4-6 enable the roughest sections of the profile to be identified. If it is found that portions of the profile are too rough for safe operation, and/or unacceptably large aircraft structural loads result, then appropriate repairs can be made to the pavement. Although there is no universal agreement on what level of roughness is unacceptable, an acceptable upper limit of $\pm$ 0.4 g. has been proposed (Ref. 3).

Recommendations for Future Research

A primary objective of the research program of which the effort reported here is a part, is to determine if the dynamic response of aircraft is significantly different when traversing unloaded and loaded pavement profiles. The unloaded and loaded pavement profiles needed in making this determination have been obtained on 2100 ft. of taxiway at Eglin AFB. To meet the primary objective the following recommendations are made:

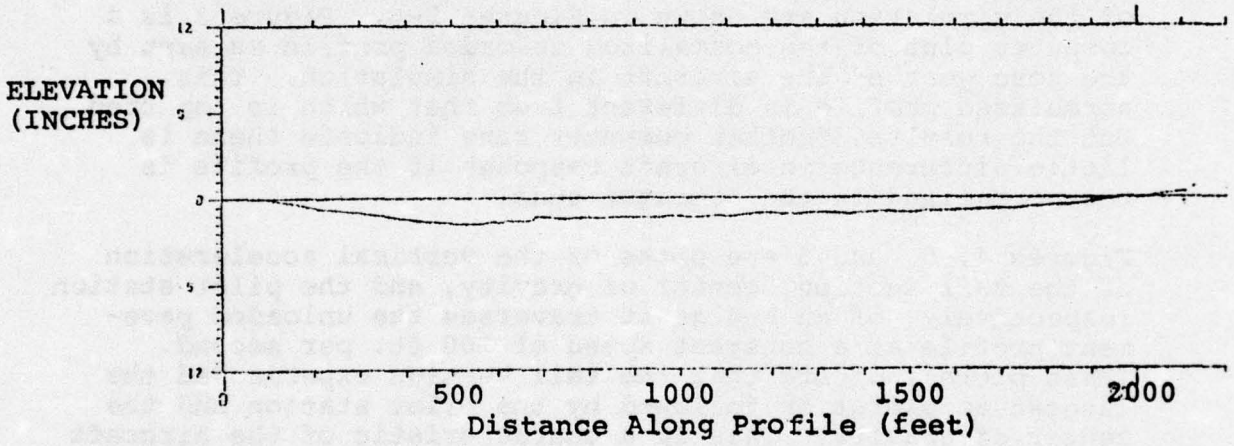


Figure 3 Normalized Unloaded Profile of Test Section

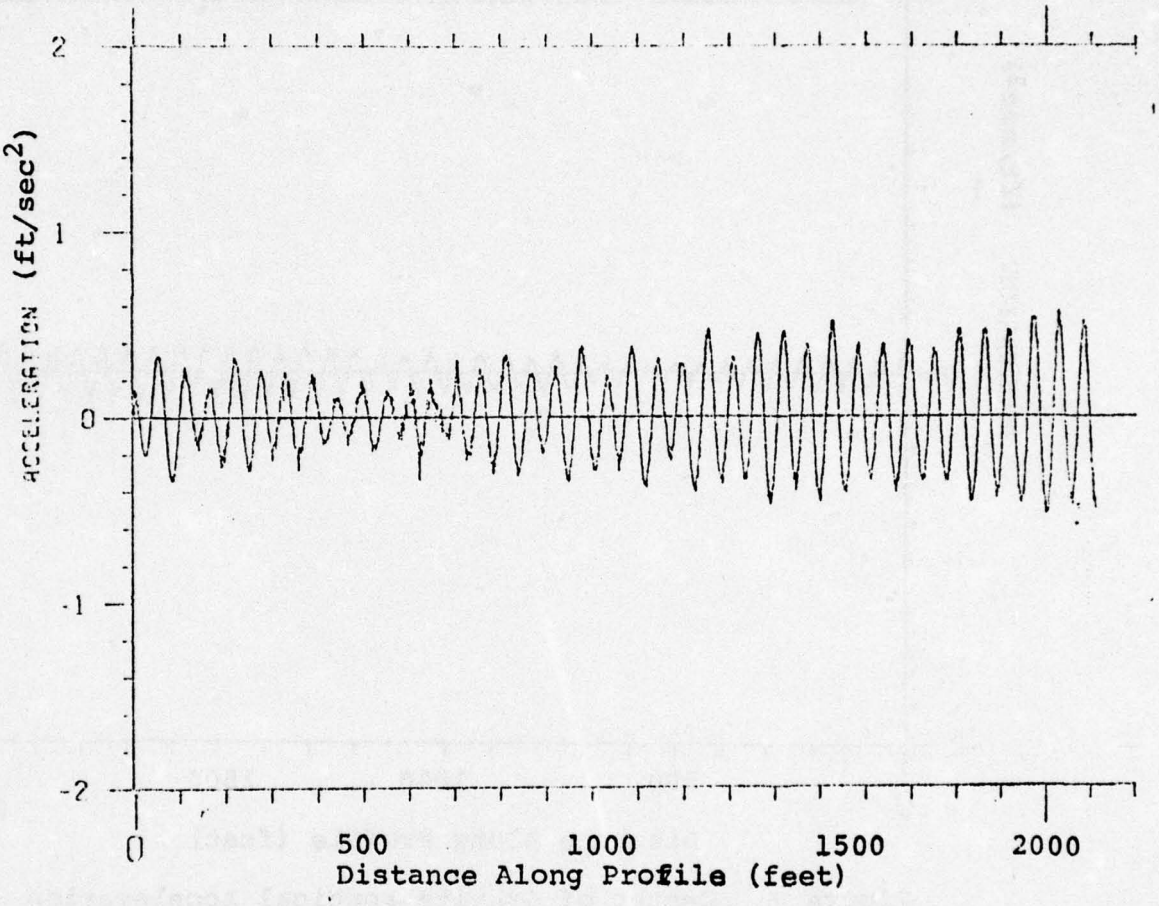


Figure 4 Tail Section Vertical Acceleration Along Unloaded Profile for F-4 Aircraft Moving at 100 ft/sec.

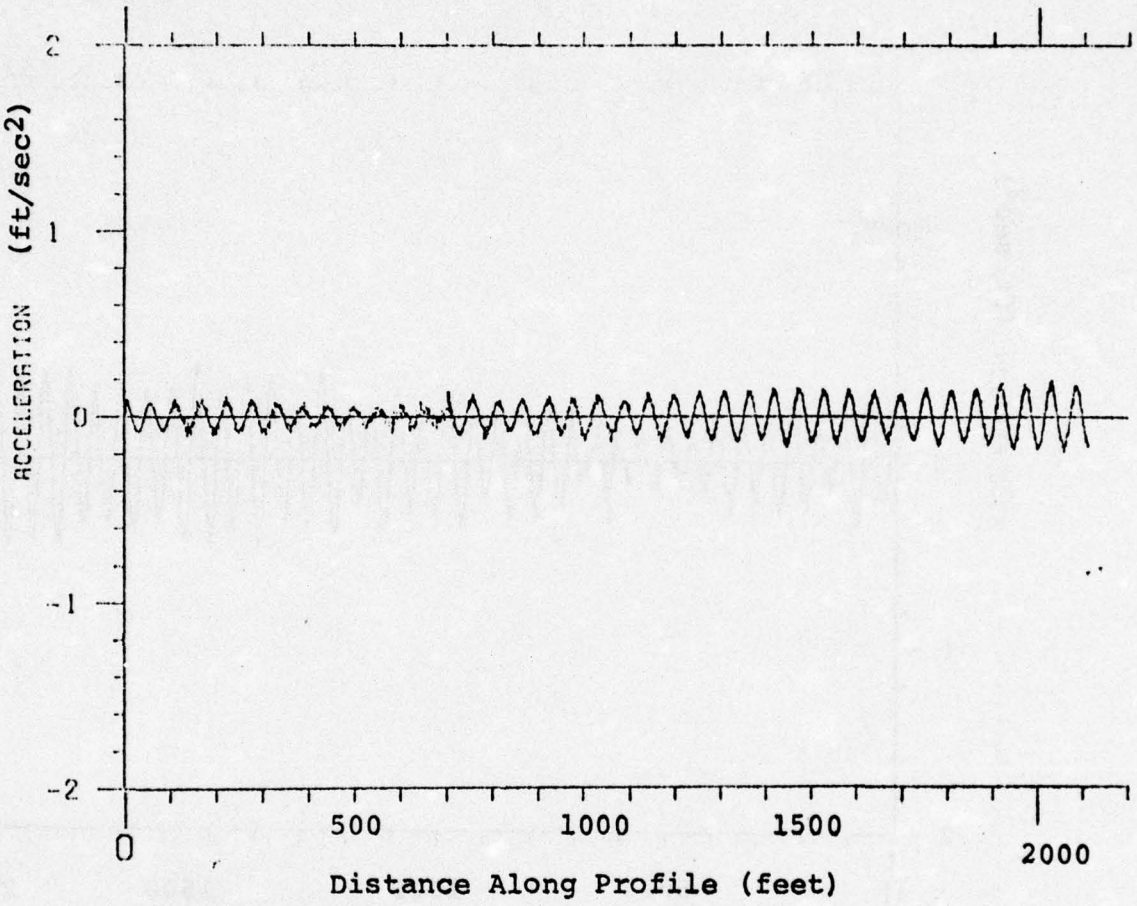


Figure 5 Center of Gravity Vertical Acceleration Along Unloaded Profile for F-4 Aircraft Moving at 100 ft/sec.

1. Run several simulations of the F-4 aircraft at different constant taxi speeds on the unloaded and loaded test section profiles.

2. For each speed make a statistical comparison between the unloaded and loaded profiles of the magnitude of pilot station, center of gravity, and tail section vertical acceleration.

3. The statistical test must be performed on the frequency of occurrance of the various levels of vertical acceleration and not on the mean value of vertical acceleration (as shown in Figures 4-6 the mean value of the acceleration is very close to zero as is expected from the oscillatory motion of the aircraft while taxiing).

4. It is suggested that the statistical tests described above be carried out on individual sections of the profile e.g. Compare the aircraft response in the first 100 ft. of the unloaded and loaded profiles and the second 100 ft. etc. This should be done because it is important to determine if there are local differences in response as well as if differences occur if the entire profiles are taken as units.

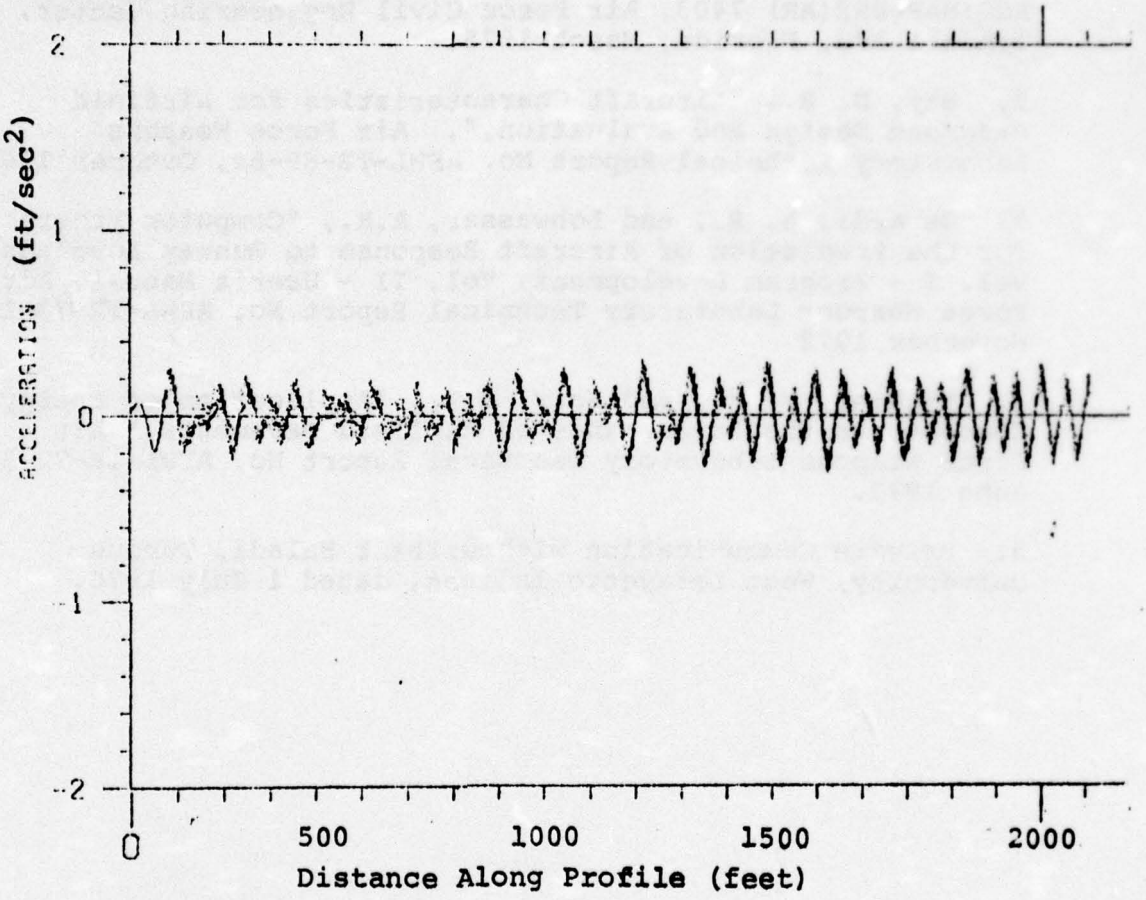


Figure 6 Pilot Station Vertical Acceleration Along Unloaded Profile for F-4 Aircraft Moving at 100 ft/sec.

REFERENCES

1. "Airfield Pavement Evaluation Report, Eglin AFB, Florida," RCS:HAF-PRE(AR) 7403, Air Force Civil Engineering Center, Tyndall AFB, Florida, March 1975.

2. Hay, D. R., "Aircraft Characteristics for Airfield Pavement Design and Evaluation,". Air Force Weapons Laboratory Technical Report No. AFWL-TR-69-54, October 1969.

3. Gerardi, A. R., and Lohwasser, A.K., "Computer Program for the Prediction of Aircraft Response to Runway Roughness," Vol. I - Program Development; Vol. II - User's Manual, Air Force Weapons Laboratory Technical Report No. AFWL-TR-73-109, November 1972.

4. Highter, W. H., and Harr, M.E., "Application of Energy Concepts to the Performance of Airfield Pavements," Air Force Weapons Laboratory Technical Report No. AFWL-TR-72-225, June 1973.

5. Private Communication with Gilbert Baladi, Purdue University, West Lafayette Indiana, dated 1 July 1976.

1976 USAF-ASEE SUMMER FACULTY RESEARCH PROGRAM
sponsored by
THE AIR FORCE OFFICE SCIENTIFIC RESEARCH
conducted by
AUBURN UNIVERSITY AND OHIO STATE UNIVERSITY

PARTICIPANT'S FINAL REPORT

WIND TUNNEL EXPERIMENT PROGRAM

FOR AERODYNAMICS OF MISSILES AT HIGH ANGLE OF ATTACK

Prepared by:	William L. Oberkampf, PhD
Academic Rank:	Assistant Professor
Department and University:	Department of Mechanical Engineering University of Texas at Austin
Assignment:	
(Air Force Base)	Eglin AFB
(Laboratory)	Armament Laboratory
(Division)	Guns, Rockets & Explosives
(Branch)	Ballistics
USAF Research Colleague:	Donald C. Daniel, PhD
Date:	August 13, 1976
Contract No.:	F44620-75-C-0031

4.

WIND TUNNEL EXPERIMENT PROGRAM FOR AERODYNAMICS OF MISSILES AT HIGH ANGLE OF ATTACK

by

William L. Oberkampf

ABSTRACT

A wind tunnel experiment program for aerodynamic measurements on a body of revolution at high angle of attack is presented. In order to determine the existing data base, a thorough literature search of unclassified documents was conducted. Experimental data in two areas of missile aerodynamics was searched; first, aerodynamic data related to the body vortex flow field, and second, forces and moments produced by body and/or fins. From a review of existing data it was determined that more complete data on body vortex strength, position, and core size for supersonic flow was needed. Wind tunnel facilities at NASA Ames Research Center, Arnold Engineering Development Center, and NASA Langley Research Center were evaluated. It was concluded that the experiments should be conducted in the Von Karman Gas Dynamics Facility 40 x 40 in. tunnel at AEDC. Details of required flow field measurements, wind tunnel operating conditions and model selection are presented.

TABLE OF CONTENTS

SECTION NO.	TITLE
	List of Figures
	List of Tables
I	Introduction
II	Objectives
III	Review of Existing Experimental Data
IV	Determination of Required Experiment Conditions
V	Evaluation of Wind Tunnel Facilities
VI	Evaluation of Wind Tunnel Models
VII	Familiarization with Weapons Systems Aerodynamics
VIII	Plans for Second and Third Year Funded Research
	References
	Tables
	Figures

4.

LIST OF FIGURES

Figure No.	Title
1	Symmetric Body Vortex Wake
2	Asymmetric Body Vortex Wake
3	Grid for Flow Field Survey

LIST OF TABLES

Table No.	Title
I	Angles of Attack and Body Stations for Flow Field Survey
II	List of Candidate Wind Tunnels

I. INTRODUCTION

Aerodynamics of missiles at high angle of attack has become increasingly important for modern design requirements. Examples of this are high maneuverability of air-to-air missiles and high launch angle of attack. For the case of low angle of attack, 0° to 5°, the flow field around a missile can be generally considered as an inviscid flow. Viscous effects are confined to the boundary layers on the wings, fins, body and in the base region of the body. These viscous effects are very important to aerodynamic drag, but are not typically important when considering flight stability. At high angle of attack viscosity produces a marked change in the forces and moments acting on the vehicle, and, consequently, on flight stability.

At angles of attack above about 10°, vortices form on the lee side of the body and these grow in strength along the length of the body (Fig 1). These body vortices affect the pressure distribution on the body, wing and tail. This typically introduces nonlinearities in the forces and moments and can cause the missile into static or dynamic instability. At angles of attack (α) less than about 25°, the body vortices are symmetric with respect to the angle of attack plane.* Above 25°, but below about 60°, the vortices become asymmetric with respect to the angle of attack plane but remain steady for a constant roll orientation of the missile (Fig 2). The particular form of the asymmetric condition depends on such tings as roll orientation, roll rate, nose shape, and minute irregularities on the nose tip. Above $\alpha = 60^{\circ}$ the body vortex wake becomes unsteady. Vortices are shed on alternate sides of the body very similar to the classical von Karman vortex street.

One of the analytical methods which has been developed to deal with high angle of attack missile aerodynamics was presented by the author in Refs 1-3. This technique addresses the problem of symmetric body vortex effects on the forces and moments produced by tail fins. Research into this topic will be continued by the author under sponsorship of the Air Force Armament Laboratory. This work will be funded beginning in October 1976 as part of the Armament Laboratory's 6.1 Basic Aerodynamics Research. The objectives of the summer research program were designed to support the overall objectives of the planned three year funded research effort.

II. OBJECTIVES

The primary objective of my summer research program is to prepare a wind tunnel test program for aerodynamic measurements on missiles at high angle of attack. The phases of this objective are:

---

* The angle of attack plane is defined as the plane passing through the velocity vector of the missile center of gravity and the centerline of the missile body. Referring to the coordinate system shown in Fig. 1, the angle of attack plane is the (x, z) plane.

6.

a. Review of existing experimental data

b. Determination of required experiment conditions

c. Evaluation of wind tunnel facilities

d. Evaluation of wind tunnel models

The secondary objective of the research program is to become acquainted with aerodynamic aspects of various weapons systems being considered by the Armament Development and Test Center.

III. REVIEW OF EXISTING EXPERIMENTAL DATA

Missile configurations which are of interest in the present work are pointed circular cylinder bodies with and without tail fins. For these configurations, aerodynamic data related to the body vortex flow field and forces and moments produced by body and/or fins was sought. The Mach number range of interest is from M = .1 to M = 4. A thorough literature search was conducted as the first step in reviewing the existing experimental data. A computerized literature search of DDC documents was conducted through the ADTC Technical Library. Using fairly broad keywords in the computer, the search yielded approximately 400 unclassified titles and abstracts. In the computer search the age of the documents was not limited so that reports dating back into the 1940's were identified. Classified documents were not searched because the funded research for AFATL will not be classified and research findings will be published in the open literature.

Of the 400 titles and abstracts reviewed, about 40 are believed to contain useful data for the present research. Many of these documents were available at the Technical Library and copies have been obtained. The remaining documents were ordered from DDC and almost all have been received to date.

Reports of interest were also suggested by colleagues working in the field. Colleagues at AFATL who assisted me in this regard were Dr. Donald Daniel (Special Assistant to the Commander), Mr. Carrol Butler (DLMA), and Mr. Mickey Rogers (DLMA). At the U.S. Army Missile Command, Huntsville, AL, Mr. Raymond Deep (RDK) and Dr. Donald Spring (RDK) were very helpful. Almost all of the reports suggested by these associates were applicable to the present research.

7.

It should be mentioned that almost all of the titles, abstracts and reports examined were new to the author. This is due to the limited distribution that most of these reports receive. The author knows the open literature fairly well but this type data rarely appears in the open literature.

About 50 documents were reviewed in detail in order to determine the status of the existing data base. Specific types of important data that were found are the following. A large amount of data on fin contribution to normal force and pitch moment was found. A fair amount of roll moment data, such as roll damping moment and induced roll moment, was found. Little data was found on fin induced side force and moment. Very important data on individual fin forces and moments in the presence of the body was found. This data exists for a large number of cruciform fin planforms. A large amount of isolated fin, i.e., single fin on a reflection plane mount, data was also found. Almost all of the above mentioned data is for α up to 30° and for Mach numbers in the range .5 to 3.0. Some of the data is for α up to 180°.

Only one report (Ref 4) was found which presented data for the strength and position of the body vortices. A laser Doppler velocimeter was used to measure the cross-flow plane velocity components for two angles of attack. Measurements were made at two body length positions and at only one speed of 61 f/s. This is very important data for analytical flow model development, but much more data of this type is needed.

IV. DETERMINATION OF REQUIRED EXPERIMENT CONDITIONS

The determination of the required experiment conditions is based on two factors: first, data needed as input to the analytical method, and second, data needed to verify the accuracy and applicability of the analytical method. For the analytical approach taken by the author in Refs. 1-3, the required input data for the theory is: body vortex strength, position, and core size; for subsonic flow, isolated fin normal force vs α ; for supersonic flow, flow separation point on the low pressure side of the fin vs α . To rigorously verify the theoretical predictions, strain gauge measurements of pitch plane and side plane forces and moments and roll moments are needed.

By comparing the existing experimental data discussed in the previous section with the theoretical requirements discussed in the last paragraph, conclusions can be made concerning the required wind tunnel experiments. The

most serious deficiency in existing data is in detailed information on the body vortex wake. In incompressible flow there have been a few investigations, Refs. 4-6, and in supersonic flow there has only been one, Ref 7, which measured vortex strength. The data on fin alone configurations appears sufficient to obtain the required input data for the theory. Concerning verification of theoretical predictions, it appears certain that sufficient data is available to validate the theory. Therefore, the wind tunnel program should concentrate solely on detailed flow measurements of the body vortices in supersonic flow.

Consider the details of what flow field data needs to be taken. Recall that the required input data for the theory is vortex strength, position, and core size. The strength of a concentrated, i.e., primary, vortex is calculated by numerically evaluating the contour integral

$$\Gamma_c = \oint_Q \vec{V} \cdot \vec{ds}$$

where Γ_c is the vortex strength, $\vec{V} = v\vec{j} + w\vec{k}$ is the cross-flow plane velocity, and $\vec{ds}$ is the differential unit vector tangent to the closed contour Q. The contour Q must only include the concentrated vortex and not vorticity from the vortex feeding sheet. Let the circulation in the feeding sheet be denoted as Γ_s, then the total circulation Γ_t in one-half plane of the wake is

$$\Gamma_t = \Gamma_c + \Gamma_s$$

The center of the concentrated vortex is defined as the point at which $v\vec{j} + w\vec{k} = \vec{0}$, that is, only the axial velocity component is nonzero. The radius of the concentrated vortex core r_c is defined as the radius of the circle on which

$$\frac{\partial V_\theta}{\partial r} = 0$$

where V_θ is the tangential velocity component of the concentrated vortex, and r is the radial position from the vortex center.

To calculate Γ_c, Γ_s and r_c from the measured cross-flow velocity components, the flow mapping grid must be relatively fine. The grid used by Mello, Ref. 7, was fairly rough. Me measured the velocity components with spatial increments $(\Delta y, \Delta z)$ of $.25\, r_b$, where r_b is the radius of

the body. Fidler, Schwind and Nielsen, Ref. 4, used a somewhat finer grid with spatial resolution of about .18 r_b. Based on these experiments, a grid resolution of .125 r_b should yield good results. A grid with .125 r_b resolution is shown in Fig. 3. Also shown in Fig. 3 is the approximate region of concentrated vortex centers for all α's and body lengths. For small α or body length the vortex center is near the bottom of the region and for large α or body length the center is near the top of the region. In order to minimize the number of grid points surveyed, three different size survey regions could be used. These are denoted in Fig. 3 as Region 1, 2, and 3. The number of grid points in each region is, respectively, 75, 147, and 291.

Based on previous experimental data, the angles of attack that should be surveyed are 10°, 15°, 20°, and 25°. This will yield sufficient data for interpolation and extrapolation for other angles of attack. At these α's, different body stations should be surveyed because the vortex strength increases with body length until asymmetry occurs. Using a 15 caliber body (including nose) the recommended combination of α's and body lengths for flow surveys is shown in Table I. Using the schedule shown in Table I, three body stations would be surveyed for each α. This would allow quadratic interpolations of data for other body stations.

If the three different size survey regions shown in Fig. 3 are used, respectively, for the three body stations shown in Table I, then a total of 513 points would be surveyed for each α. For the 4 angles of attack this would total 2052 points for each Mach number and Reynold number.

Existing data, Ref. 7, on the body vortex is for only one Mach number, M = 2, and one Reynolds number (R_d) based on body diameter. As a result, there is not experimental indication of sensitivity of vortex characteristics with M or R_d. Experience with other supersonic viscous flows indicates that the vortex parameters should not change drastically with M or R_d. Therefore, it is planned that only two Mach numbers and two Reynolds numbers be tested. One Mach number should be in the range 1.5 to 2.0 and the other should be in the range 2.5 to 3.0, depending on the particular wind tunnel used. The Reynolds numbers should be near the maximum and minimum of the wind tunnel facility in order to obtain the greatest variation.

V. EVALUATION OF WIND TUNNEL FACILITIES

Three government owned wind tunnel facilities were evaluated. These facilities were NASA Ames Research Center, Moffett Field, CA, Arnold Engineering Development Center, Arnold AF Test Station, TN, and NASA Langley Research Center, Hampton, VA. Each of these facilities was evaluated on the basis of

the following requirements: Mach number range, 1.5 to 3.0, Reynolds number (based on body diameter) greater than $.5 \times 10^6$, and detailed flow measuring instrumentation.

A facilities manual for each installation was obtained in order to determine operating characteristics of each wind tunnel. Based on the requirements listed above the candidate wind tunnels at each of the facilities are: NASA Ames, 9 x 7 ft and 6 x 6 ft; AEDC, Von Karman Gas Dynamics Facility, 40 x 40 in (tunnel A) and 12 x 12 in (tunnel D); NASA Langley, Unitary Plan 4 x 4 ft. Shown in Table II is the Mach number range and the corresponding maximum Reynolds number for the candidate tunnels. The maximum Reynolds number was calculated by making the following assumptions: $\alpha_{max} = 25^o$, body length/diameter = 15, and the body at α_{max} spanned one-half of the tunnel height.

The remaining comparison to be made between the five wind tunnels is flow field survey instrumentation. Because the least information was known about the NASA Langley 4 x 4 ft, NASA personnel at the 4 x 4 ft were contacted by telephone before a visit was planned. The flow field instrumentation of the 4 x 4 ft was discussed with Mr. W.A. Corlett. He explained that flow field surveys were done very rarely at Langley. Laser velocimeter or hot wire/hot film instrumentation was not available at Langley. The only method of making the flow field survey would be by means of a conical pressure probe. He also explained that Langley was under severe electrical power restrictions so that maximum Reynolds number operation required very high priority. For these reasons, the NASA Langley 4 x 4 ft was eliminated from the candidate list.

In order to obtain more detailed information on the instrumentation of NASA Ames and AEDC, these facilities were visited by the author. Ames was visited on July 19 and 20, and AEDC was visited on July 27 and 28. Personnel at Ames contacted concerning the flow field survey were: Dr. Gary Chapman, Dr. Kevin Owen, Dr. William Rose, and Dr. William Bachalo. During the Ames visit, three types of flow field survey instrumentation were discussed: Laser velocimeter (LV), hot wire and hot film (HW, HF), and conical pressure probe. Personnel at Ames were convinced that the best way to make the survey measurements was by means of an LV system. They reluctantly admitted, however, that there were still serious hurdles that had to be cleared before high speed vortex type flows could be probed with an LV. They felt it was possible to make accurate flow survey measurements with HW and HF systems but they were not particularly interested in pursuing this approach. Concerning the conical pressure probe, they felt that this technique was unacceptable because of the influence of the probe on the existing flow. They made these comments even without discussing specific sizes of conical probes relative to body vortex size.

Personnel at AEDC contacted concerning the flow field survey were: Mr. Jim Jacocks, Mr. William Baker, Dr. William Tiederman, Mr. Jim Uselton, Mr. Dick Matthews, Dr. Joe Donaldson, Mr. Don Gray, Mr. Andy Anerson, and Mr. Jerry Jones. The same three types of instrumentation as mentioned earlier were discussed with the personnel from AEDC. These individuals were more specific in discussing the problem areas of LV systems for high speed flow. The serious problem areas discussed are the following. First, the size of the seed particles becomes critical in highly accelerating or deccelerating flows. In a body vortex the particles will tend to be centrifuged away from the vortex. This could produce an erroneous measurement because one measures the particle speed and not the flow speed. Second, if smaller particles are seeded in the flow to avoid the centrifuge problem , then the scattered return from the particles decreases. Third, particles seeded in the freestream flow may not enter the body vortex in sufficient quantities for reliable measurements. One way of possibly eliminating this problem would be to seed the vortex core from the body. This technique has never been attempted before. Fourth, the shape of the measurement volume is typically longer for high speed flows that for low speed flows. This is due to the decrease in subtended angle betwen the laser beams for high speed flow vs low speed flow. For three dimensional flow fields such as considered here, this could produce a spatial resolution error. And fifth, two independent LV measurements must be made to obtain the three dimensional velocity components. One measurement is made to obtain (u, w) components by directing the laser in the y - direction. One measurement is made to obtain (u, v) components by directing the laser in the z-direction. These two independent measurements must be matched back together at the same spatial point in order to obtain the desired (v, w) components. This procedure has not been done before.

Because of these serious problem areas yet to be solved, it is concluded that the laser velocimeter not be used for the flow field survey. The LV technique holds considerable promise for the future but these measurements do not appear to be at hand for high speed body vortex flow.

Hot wire and hot film instrumentation was also discussed at length with AEDC personnel. VKF personnel have had limited experience with HW measurements in supersonic flow. They have made successful turbulence measurements in M=6 and 8 boundary layer flows. Some of the problem areas discussed concerning HW flow field surveys are the following. First, hot wires are extremely fragile and there could be serious problems in maintaining a hot wire in high dynamic pressure flow. Second, if a wire could be maintained then there is the problem of wire strain causing erroneous readings. Third, an HW actually measures mass flow rate per unit area, i.e., ρu. To obtain the desired velocity component, the density must be determined in the flow field survey region. This could be done by measuring static temperature and pressure and then calculating density.

12.

Considering the problem areas of HW's mentioned above, a hot film wedge probe appears to be the most promising. This type of probe occurred to the author after the visit to AEDC and has not been discussed with them. An HF wedge probe is one which has an electrically conducting film on a wedge shaped ceramic substrate. An HF wedge probe does not suffer from the first two problem areas mentioned above but still must overcome the third. The HF wedge probe is very rugged and, therefore, difficult to break. Because it is mounted on a solid ceramic backing there are no problems with signal distortion due to strain.

Conical pressure probes were also discussed with the AEDC personnel. They were certain that this technique was the simplest and most reliable technique of the three considered. They regularly use the cone probe to survey flow fields of various flight vehicles. They stated that they could measure flow angularity to a precision of $\pm$ .2°. The serious question with the cone probe is related to the size of the probe relative to the spatial velocity gradients. An accurate measurement with the cone probe assumes that the variation of the velocity field across the diameter of the cone is negligibly small. For example, suppose the radius of the vortex core is $.5r_b$ and the diameter of the cone probe is $.1r_b$. For a strong body vortex, the change in flow angularity from the vortex center to the edge of the core is typically 20°. Since in the core of the vortex the velocity profile is roughly linear, the flow angularity would change by 4° over the width of the cone. This size error is considered unacceptable for the planned experiment.

From all of the discussions with experimentalist at Ames and AEDC, it is concluded that a hot film wedge probe is the most promising technique for the flow field survey. It must be studied in more detail but it does appear to be the best compromise between speculative techniques and accuracy.

Now consider a comparison of instrumentation facilities of the Ames 9 x 7 ft and the 6 x 6 ft. As far as HF instrumentation differences between the 9 x 7 ft and the 6 x 6 ft, there is essentially none. The model sting and instrumentation support would be very similar for each tunnel. Because of the larger Reynolds number and slightly higher maximum Mach number, the 9 x 7 would be preferred over the 6 x 6.

Comparing the AEDC 40 x 40 in. to the 12 x 12 in , the 40 x 40 in. is clearly superior for the following reasons: first, the larger Reynolds number of the 40 x 40, second, the 12 x 12 is not a continuous flow tunnel, and third, the 12 x 12 does not have a captive trajectory separation (CTS) system. The CTS system was developed for studying separation of two vehicles, commonly weapons separation. The CTS system, however, is also used to mount probes of

3.

various instrumentation. For the planned experiments, the HF wedge probe would be mounted on the CTS system. Accurate spatial and angular positioning can be accomplished by means of the six-degree-of-freedom CTS. The CTS system is computer controlled so that the desired spatial and angular coordinates of the probe would be pre-programmed. It is seen that the CTS system has significant advantages over a manual or semi-automatic positioning system.

Consider a comparison of the Ames 9 x 7 ft and the AEDC 40 x 40 in. The 9 x 7 has a factor of 2 higher Reynolds number capability, depending on the Mach number. The quality of the flow, i.e., flow angularity and free stream turbulence level, in the 40 x 40 is documented in the AEDC Facilities Handbook. But no such data could be obtained on the 9 x 7. As a result, no comparisons can be made in this regard. Personnel at both facilities have experience with HW probes but not with HF wedge probes. The CTS system at AEDC is most impressive for flow field survey type work and must be weighed heavily. Personnel at Ames felt the only way in which to make the measurements was with an LV system. Combining their lack of interest in considering an HF system with the fact that they are not a service type organization as AEDC, one must be pessimistic about the outcome. Weighing all of these factors it is concluded that the wind tunnel experiments should be made in the AEDC 40 x 40 in. tunnel.

Consider an estimate of the tunnel time that would be required for the planned experiments. During my visit to AEDC, the time required by the CTS system to make the measurements was discussed. Based on their "quick look" at the measurements, they estimated that one grid point measurement would require between 10 and 20 sec. Using the number of grid points calculated earlier, 2050, this results in 6 to 12 hours per Mach number and Reynolds number. Assuming two Mach numbers and two Reynolds numbers, one has 24 to 48 hours. About 8 hours tunnel time should be allowed for such things as: HF calibration, HF replacement, model and sting adjustments, checks on the CTS system, etc. This results in an estimated tunnel time of 32 to 56 hours.

During my visit to AEDC I talked with Lt. Col. Chauncy Smith (Chief, Test Div. of VKF) concerning wind tunnel costs. For the type of wind tunnel experiments planned, he estimated that the cost of wind tunnel time in the 40 x 40 in. would be about $1500/hr. For the estimated 32 to 56 hours, this means that the planned experiments will cost from $48,000 to $84,000.

VI. EVALUATION OF WIND TUNNEL MODELS

A rather simple wind tunnel model is needed for the planned experiments. Under the model size assumptions stated earlier, it is seen from Table II

that a model diameter near 3.0" would be appropriate for the 40 x 40 in. tunnel. The length to diameter ratio would be 15. The model should be able to accept different nose shapes for possible future experiments.

The only existing model which roughly fits these requirements is the one owned by NASA Marshall Space Flight Center, Huntsville, AL. During my visit to U.S. Army Missile Command, Huntsville, AL, Dr. Donald Spring indicated that he could arrange loan of the model for the planned work. The model has a diameter of 2.0 inch and a length to diameter ratio of 10. The length of the model can be easily increased by inserting a body plug. This model has been used in the 40 x 40 in. tunnel so that all mounting fixtures are already available. The only possible problem with the model is the diameter may be smaller than necessary. This question will be resolved after discussions with personnel from AEDC. If the result of these discussions is that a 3.0 in. model could be used, then a new model will be constructed by AFATL.

VII. FAMILIARIZATION WITH WEAPONS SYSTEMS AERODYNAMICS

In order to obtain a broader understanding of the aerodynamics work conducted within ADTC, several informal meetings were set up with various individuals. Dr. Donald Daniel arranged the meetings with five individuals in the Armament Laboratory, one person in Armament Systems and one in Development Plans. An overview of ADTC aerodynamics work will enhance my ability to contribute to the long range needs of the Air Force. Mr. Ken Cobb (Ballistics Branch, DLDL) discussed various flight dynamics and flight control projects he has worked on recently. He explained some of the aerodynamics predictive techniques and 6-DOF procedures used. Mr. Charley Mathews (Aircraft Compatibility Branch, DLJC) gave an excellent overview of the work in his branch. Weapons release and aerodynamic heating problems were discussed in some detail. Mr. Fred Howard (Air-to-Air Missiles Branch, DLMI) discussed the aerodynamic and intercept aspects of air-to-air missiles. The aerodynamics of the new winged body with elliptic cross-section proved to be very fascinating. Mr. Carrol Butler (Systems Analysis Branch, DLMA) explained the short term and long term aerodynamics research trends of not only DLM but also the Armament Laboratory. His discussion concerning how the Armament Laboratory determines its basic research (6.1) and exploratory development (6.2) efforts was most interesting. Mr. Otto Heiney (Ballistics Branch, DLDL) discussed a specific problem associated with internal ballistics. A persistent problem with determining projectile friction in a gun barrel was discussed in detail. I was able to trace the problem to the data reduction procedure and thereby make a direct and immediate contribution.

15.

Mr. Mike Bouffard (GBU-15 Program Office, SD-15) explained the general operational characteristics of the GBU-15 glide bomb. Some of the aerodynamics and flight dynamics work was discussed.

Mr. Edward Bradley, (Development Plans, XR) presented an overview of the aerodynamics work conducted in Development Plans. The aerodynamic aspects of air-to-air and air-to-surface missile systems of the next ten to twenty years were discussed.

VIII. PLANS FOR SECOND AND THIRD YEAR OF FUNDED RESEARCH

By the beginning of the second year of work the status of the theoretical and experimental work should be as follows. Improvements in the body alone flow model will be completed. The theory for predicting all forces and moments on a general planform fin should be complete. The theory will be applicable to the symmetric wake problem and Mach numbers in the range .1 to .6 and 1.5 to 4. The wind tunnel experiments will be completed and the data analyzed. Wind tunnel data on the body vortices will have been incorporated in the body alone flow model.

The second year of work will extend the theory for the body alone flow field and the theory for fin forces and moments to the case of asymmetric vortices. As was mentioned in the Introduction, the case of asymmetric vortices is complicated not only by the large number of vortices in the wake but also by the fact that the flow is extremely sensitive to minute irregularities in the nose tip. This results in changes of the asymmetric flow with nose roll angle. In extending the body alone flow model to the asymmetric case, this occurence must be acounted for in some empirical fashion. The prediction of fin forces and moments will also be more difficult than the first year's work because the angle of attack of the fins will be significantly higher. These very large fin angles of attack will cause strong three-dimensional flows over the fin. In supersonic flow a complex interaction of attached and detached shock waves with separated flows will occur. The pace and success of the theoretical work during the second year is uncertain.

Depending on the success of the second year's work, the third year of work will again consider the symmetic vortex wake but for more complex missile configurations. The problem to be attacked is force and moment prediction on wing-body-fin configurations. Forces and moments on wing-body-fins at low angle of attack have been studied for many years. The proposed

16.

work for the third year will consider supersonic flow for the high angle of attack range ($10° < \alpha < 25°$). To study this problem, a major change in the theoretical approach of the first year will be required. That is, the path of the body vortices and wing-tip vortices must be calculated down the length of the body. These vortices interact with each other and with the body flow field thereby yielding a significantly more complex problem than the body alone flow field. Dillenius and Nielson (Ref. 8) have recently worked this problem (canard-body-fins) and have met with limited success. It is expected that the author's progress on this problem during the third year will also be slow.

7.

REFERENCES

1. Oberkampf, W. L. (1970), "Aerodynamics of Finned Missiles at High Angle of Attack," Ph.D. Disseration, University of Notre Dame, Notre Dame, Ind.

2. Oberkampf, W. L. and J. D. Nicolaides (1971), "Aerodynamics of Finned Missiles at High Angle of Attack", AIAA Journal, Vol. 9, No. 12, pp. 2378-2384.

3. Oberkampf, W. L. (1975), "Prediction of Roll Moments on Finned Bodies in Supersonic Flow", Journal of Spacecraft and Rockets, Vol. 12, No. 1, pp. 17-21.

4. Fidler, J. E., Schwind, R. G., and Nielsen, J. N. (1976), "An Investigation of Slender-Body Wake Vortices," Nielsen Engineering and Research, TR-108, Mountain View, Calif.

5. Fiechter, M. (1966), "On the Vortex System of High Fineness Ratio Bodies of Revolution and Their Influence on the Aerodynamic Coefficients," German-French Research Inst. of St. Louis, Rept. No. 10/66, St. Louis, France.

6. Tinling, B. E., and Allen, C. Q. 1962), "An Investigation of Normal-Force and Vortex Wake Characteristics of an Ogive-Cylinder Body at Subsonic Speeds," NASA TN D-1297.

7. Mello, J. F. (1959), "Investigation of Normal Force Distributions and Wake Vortex Characteristics of Bodies of Revolution at Supersonic Speeds," J. of Aero. Sci., vol. 26, pp. 155-168.

8. Dillenius, M. F. E. and Nielsen, J. N. (1975), "Prediction of Aerodynamics of Missiles at High Angles of Attack in Supersonic Flow," Nielsen Engineering and Research, TR-99, Mountain View, Calif.

18.

TABLE I

ANGLES OF ATTACK AND BODY STATIONS FOR FLOW FIELD SURVEY

Angle of Attack (Deg)	Body Station (x/d)
10	7, 11, 15
15	5, 10, 15
20	4, 8, 12
25	4, 7, 10

TABLE II

LIST OF CANDIDATE WIND TUNNELS

WIND TUNNEL	MACH NUMBER (Range of Interest)	MAX. REYNOLD NO. (x 10^{-6}) (Based on Missile Dia.)	APPROPRIATE MODEL DIA. (in)
NASA Ames 9' x 7'	1.5	3.55	8.5
	2.5	3.26	
NASA Ames 6' x 6'	1.5	2.08	5.7
	2.2	1.18	
AEDC VKF 40" x 40"	2.0	1.46	3.1
	3.0	2.15	
AEDC VKF 12" x 12"	2.0	1.25	.9
	3.0	.76	
NASA Langley 4' x 4'	1.5	.63	3.8
	2.5	.63	

20.

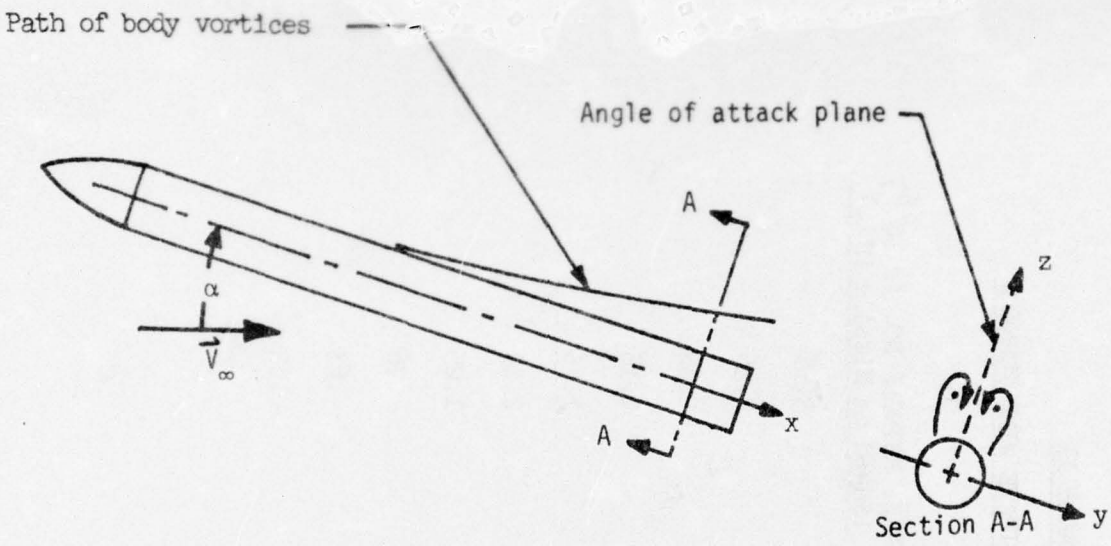


Figure 1

Symmetric Body Vortex Wake

21.

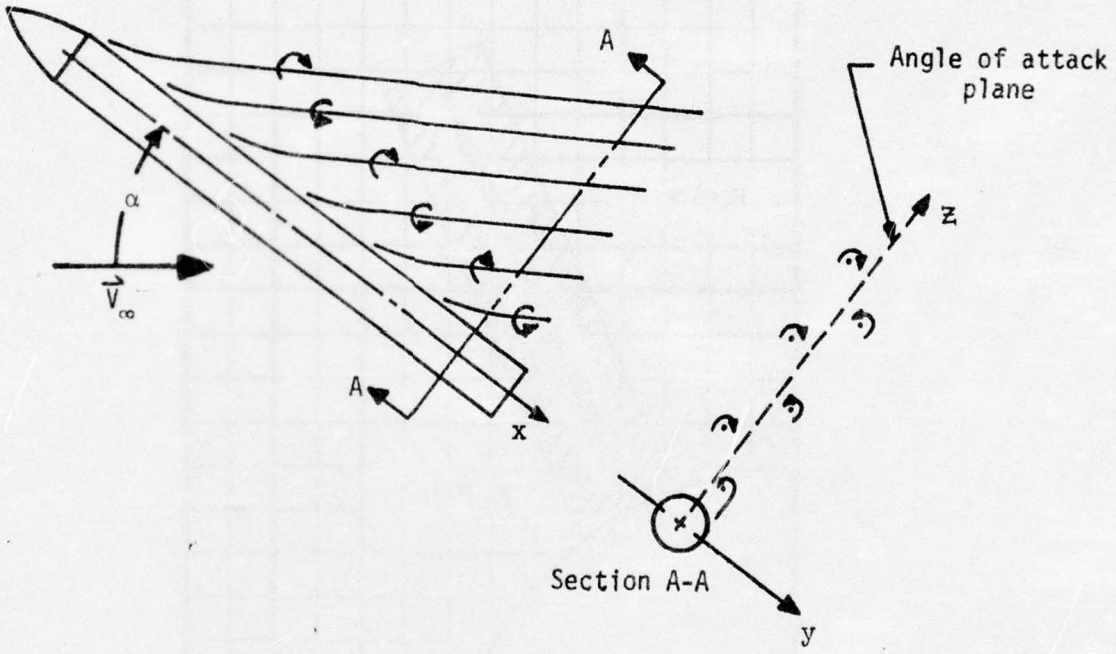


Figure 2

Asymmetric Body Vortex Wake

22.

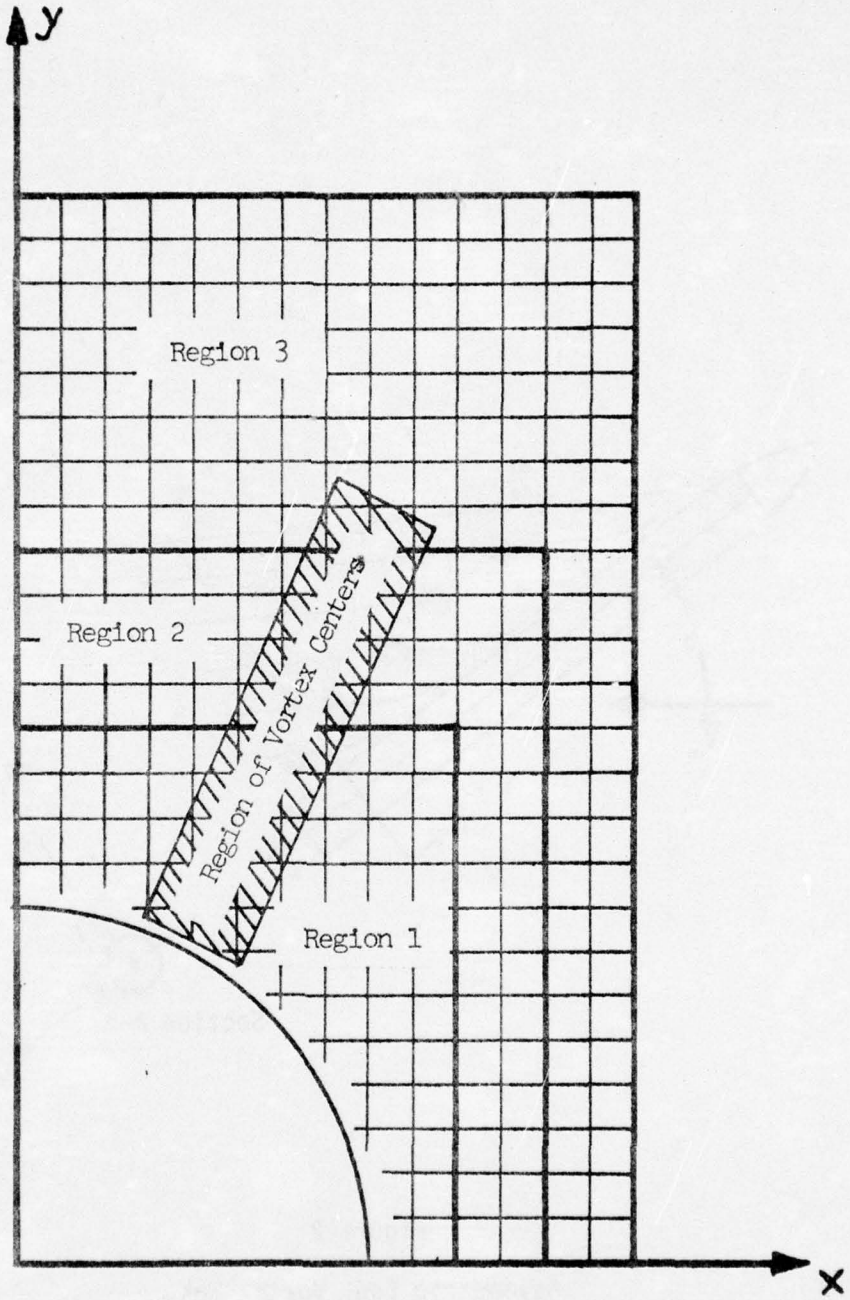


Figure 3
Grid for Flow Field Survey

1976 USAF-ASEE SUMMER FACULTY RESEARCH PROGRAM

Sponsored by

THE AIR FORCE OFFICE OF SCIENTIFIC RESEARCH

Conducted by

AUBURN UNIVERSITY AND OHIO STATE UNIVERSITY

PARTICIPANT'S FINAL REPORT

ANALYSIS OF MILLIMETER-WAVE SIGNATURES OF SNOW AND ICE

Prepared by:	Irene K. Petroff, Ph.D.
Academic Rank:	Associate Professor
University:	Division of Engineering California State University, Fullerton
Assignment:	
(Air Force Base)	Eglin AFB
(Laboratory)	Air Force Armament Laboratory
(Division)	Guided Weapons
(Branch)	Air-to-Surface Terminal Guidance
USAF Research Colleague:	Davut B. Ebeoglu, Ph.D.
Date:	August 13, 1976
Contract No.:	F44620-75-C-0031

2.

ANALYSIS OF MILLIMETER WAVE SIGNATURES OF SNOW AND ICE

by

Irene K. Petroff

ABSTRACT

A thorough understanding of the interaction of millimeter-waves with various types of snow and ice is needed before appropriate target discrimination techniques in the presence of snow covered terrain can be developed.

In this report, the reflection coefficients for vertical and horizontal polarizations are calculated for air-ice, air-snow, and air-water interfaces using representative values for the electrical parameters of snow, ice, and water, found in current literature. Further calculations are initiated for the reflection from a layer of snow, ice or water on a soil substrate.

An experiment is outlined to verify the results of the preceding calculations, and subsequent snow models which take the surface roughness into effect are proposed.

3

ACKNOWLEDGEMENTS

The author is indebted to the Air Force Office of Scientific Research, and the ASEE for support of this summer program. I deeply appreciate the assistance of the program director Mr Fred O'Brien of Auburn University and of Lt Col William Gaiser of The Armament Laboratory.

Special thanks are due to Mr Richard Sluman for his assistance and encouragement on this project, and to Mrs Barbara Brown for her assistance in the preparation of the final report.

The author also thanks Mr Charlie Brown, Major Ed Halprin, and Dr Davut Ebeoglu for useful discussions and suggestions.

4

LIST OF FIGURES

Figure 1. Geometry corresponding to reflection and refraction at an interface between two semi-infinite media.

Figure 2. Geometry corresponding to reflection and refraction in a layer.

Figure 3. Example of reflection coefficient as a function of layer thickness.

Figure 4. Experimental geometry,

Figure 5. Amplitude of reflection coefficient for low loss ice.

Figure 6. Amplitude of reflection coefficient for lossy ice.

Figure 7. Amplitude of reflection coefficient for water at $T=0^{\circ}$ C.

Figure 8. Amplitude of reflection coefficient for water at $T=10^{\circ}$ C.

Figure 9. Amplitude of reflection coefficient for water at $T=20^{\circ}$ C.

Figure 10. Amplitude of reflection coefficient for low loss snow.

Figure 11. Amplitude of reflection coefficient for lossy snow.

5

LIST OF TABLES

I. Electrical parameters of water at 35 GHz.

II. Electrical parameters of ice at 35 GHz.

III. Electrical parameters of snow at 35 GHz.

6

OBJECTIVES AND SCOPE

The main objective of the present study is to understand the effect of snow covered terrain on target signatures at Millimeter-Wave lengths.

The specific steps to achieve this objective are outlined as follows:

1. Initial calculations to investigate the scattering, the dielectric constant and the loss tangent of snow, ice, and water, using a simple geometrical configuration.

2. Formulation of more detailed models taking surface roughness into account.

3. Planning and implementation of an experiment to verify the analytical models.

7

INTRODUCTION

Recent measurements (ref. 1, 2) indicate that the presence of snow on the ground can affect millimeter-wave target signatures to a considerable extent. In some instances the target has been found to be no longer distinguishable from the background. The effect of snow, ice, and surface moisture, on target signatures must be clearly understood before appropriate discrimination techniques can be developed.

The return from snow covered terrain varies considerably with moisture content and there are indications that much of the interaction takes place in the top layer (ref.2). Therefore it is important to verify the scattering properties of the snow taking into account the condition of the surface.

Initially, the reflection coefficient will be calculated for flat air-ice, air-water and air snow interfaces, with losses taken into account. A comparison of the results should give a preliminary indication of the basic differences in the interaction of the three substances with millimeter-waves. All calculations are made for both horizontal and vertical polarizations, and for angles of incidence ranging from 0° to 90°. Calculations for water are made for three different temperatures.

THEORY

Reflection and refraction of Plane Waves at an interface (ref.3,4)

For two semi-infinite media, as shown in figure 1, the reflection coefficient is given by:

$$R_{\perp} = \frac{\cos\theta - \sqrt{(n^2-\sin^2\theta)}}{\cos\theta + \sqrt{(n^2-\sin^2\theta)}} \qquad (1)$$

$$R_{\parallel} = \frac{\sqrt{(n^2-\sin^2\theta)} - n^2\cos\theta}{\sqrt{(n^2-\sin^2\theta)} + n^2\cos\theta} \qquad (2)$$

Where $R_{\perp}$ is the reflection coefficient for waves polarized perpendicular to the plane of incidence (horizontal polarization), and $R_{\parallel}$ is the reflection coefficient for waves polarized parallel to the plane of incidence (vertical polarization).

In figure 1, the coordinate system is such that the x-y plane coincides with the boundary separating the media and the x-z plane coincides with the plane of incidence.

8

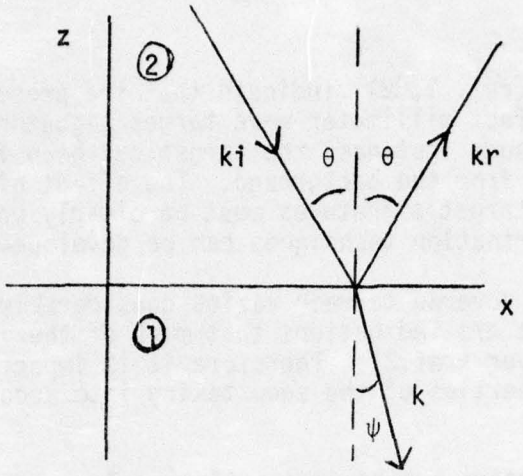


Figure 1. Geometry corresponding to reflection and refraction at an interface between two semi-infinite media.

For the geometry considered the direction of scattering is determined by the angle of incidence. The angle of scattering is the same as the angle of incidence. The angle of incidence θ and the angle of refraction ψ are related by:

$$\eta \sin\psi = \sin\theta \ , \quad \eta = \sqrt{\frac{\varepsilon^*_1}{\varepsilon^*_2}} \tag{3}$$

Where ε^*_1 and ε^*_2 are the complex dielectric constants of the two media.

Electrical parameters of ice, snow and water.

The complex permittivity is given by

$$\varepsilon^* = \varepsilon' + j\varepsilon'' \tag{4}$$

The losses are related to the imaginary part:

$$\sigma = \omega\varepsilon'' \tag{5}$$

$$\tan\delta = \frac{\varepsilon''}{\varepsilon'} \tag{6}$$

Where α is the conductivity and $\tan\delta$, the loss tangent.

The calculations of ε' and ε'' for water and ice are generally based on the Debye relaxation formula (ref. 4,5).

$$\varepsilon' - \varepsilon^{\infty} = \frac{(\varepsilon s' - \varepsilon^{\infty}_{o})}{1 + \omega^2\tau^2} \qquad (7)$$

$$\varepsilon = \frac{(\varepsilon s - \varepsilon^{\infty})\omega\tau}{1 + \omega^2\tau^2} \qquad (8)$$

Dry snow is treated as a mixture of ice and air (ref. 5) and the permittivity is calculated according to a mixture formula:

$$\frac{\varepsilon' - \varepsilon o}{3\varepsilon'} = f\,\frac{\varepsilon'_{i} - \varepsilon o}{\varepsilon'_{i} + 2\varepsilon'} \qquad (9)$$

Where f is the volume fraction of ice, and ε', ε'_{i} and εo refer to the snow, ice, and air, respectively.

WATER

The parameter values used for water are shown in Table I. The static and optical dielectric constants $\kappa'_{s} = \frac{\varepsilon'}{\varepsilon_o}$, and $\kappa'_{\infty} = \frac{\varepsilon'}{\varepsilon}$ are obtained from the Handbook of Chemistry and Physics. The relaxation time is obtained from reference 6 where $\lambda m = 2\pi c\tau$. The values of κ' and κ'' are calculated for an operating frequency of 35 GHz, from equations (7) and (8).

TABLE I

Electrical Parameters of water at 35 GHz.

T °c	λm	κ'	κ''	κs	κ'_{∞}
0	3.33	7.16	20.87	88	1.77
10	2.38	11.72	27.5		
20	1.74	18.7	34.25		

10

ICE:

The relaxation time of ice is several orders of magnitude larger than that of water (ref 5). This implies that the dielectric constant of ice is essentially independent of frequency in the microwave and millimeter wave region. High frequency measurements on ice indicate a value of κ' in the range of 3.05 to 3.2 (refs. 6,7). For the same reason, ice is theoretically a low loss material, however experimental data indicate that the loss tangent can have considerable variations. Table II shows the parameters used for ice in the initial calculations

TABLE II

Electrical parameters of ice at 35 GHz.

Ice Type	κ'	κ''	tan δ
Low Loss	3.2	$\simeq 0$	1.3×10^{-9} (ref. 6)
High Loss	3.2	0.64	2×10^{-1} (ref. 7)

SNOW

The mixture formula of equation (9) gives a dielectric constant ranging from 1 to 3.2 for dry snow. The loss tangent can vary within a range of 10^{-6} to 10^{-1} (ref.7). A mixture formula which includes water, similar to equation (9) can be used for wet snow (ref. 6). The net result is a marked increase in the dielectric constant, and the loss tangent. The actual value of these parameters falls between that of dry snow and water. For the purpose of the initial calculations, dry snow will be considered, and the results will be compared with those obtained for water. The results for wet snow can be expected to fall between these two cases. Table III shows the values used for the snow calculations.

TABLE III

Electrical Parameters of snow at 35 GHz.

Snow Type	κ'	κ''	tan δ
Low density, Low loss	1.5	1.5×10^{-4}	10^{-4}
High density, high loss	2.5	0.315	1.26×10^{-1}

RESULTS

The results of the calculations for $R_\perp$ and $R_\parallel$ as given by equations (1) and (2) are shown in figures 5 through 11 . The vertical polarization component undergoes a much higher degree of variation as a function of angle of incidence, than the horizontal component. The effect

AD-A033 822 AUBURN UNIV ALA SCHOOL OF ENGINEERING F/G 14/2
1976 USAF-ASEE SUMMER FACULTY RESEARCH PROGRAM.(U)
SEP 76 J F O'BRIEN F44620-75-C-0031
UNCLASSIFIED AFOSR-TR-76-1419 NL

3 OF 9
AD
A033822



of an increasing relative dielectric constant K' is a shift of the Brewster angle to higher values (51° for snow, 60° for ice) and a general increase in the amplitude of the reflection coefficient. As the loss component K'' increases the reflection coefficient for vertical polarization passes through a minimum at the Brewster angle, but does not decrease to zero.

Without losses, the horizontally polarized wave undergoes a phase change of 180° upon reflection. The vertically polarized wave changes phase by 180° for angles of incidence smaller than the Brewster angle, but stays in phase for incidence at angles larger than the Brewster angle.

When losses are present the phase shift is negative, in the vicinity of -180° for horizontal polarization, while the shift for vertical polarization is at first near -180° and decreases gradually toward 0° as the angle of incidence increases.

Outline of calculations for a layer of finite thickness.

In order to verify the electrical parameters experimentally the reflection coefficient should be calculated for the configuration of figure 2, where ice, dry snow or wet snow is considered to be a layer on a substrate of soil, or other appropriate material.

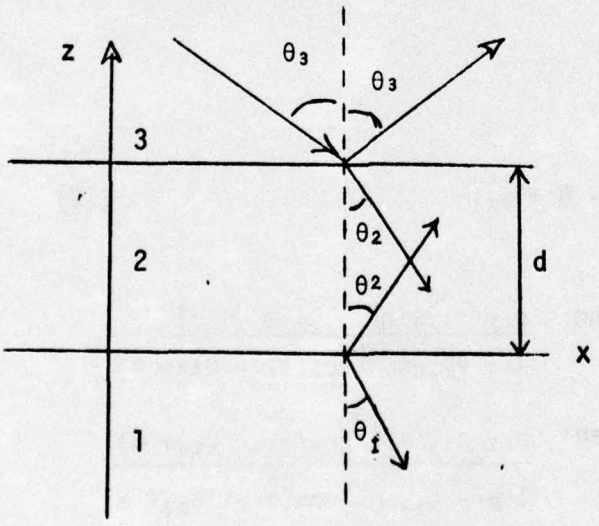


Figure 2. Geometry corresponding to reflection and refraction in a layer.

For this geometry the reflection coefficient is given by (ref. 3)

$$R = \frac{R_{23} - R_{12} \exp(2i\alpha_2 d)}{1 + R_{23} R_{12} \exp(2i\alpha_2 d)} \qquad (10)$$

R_{12} and R_{23} are the reflection coefficients for each interface as given by equations (1) and (2), where each can be calculated for horizontal or vertical polarization.

Since R_{12} and R_{23} are complex quantities they can be expressed in terms of a magnitude and phase angle:

$$R_{12} = \rho_{12} e^{i\phi_{12}} \quad , \quad R_{23} = \rho_{23} e^{i\phi_{23}}$$

In terms of these quantities, the magnitude and phase of the overall reflection coefficient $R = \rho e^{i\phi}$ are given by:

$$\rho^2 = \frac{\rho_{23}^2 + 2\rho_{12}\rho_{23} e^{-\beta}\cos(\phi_{12} - \phi_{23} + \alpha) + \rho_{12}^2 e^{-2\beta}}{1 + \rho_{12}^2 \rho_{23}^2 e^{-2\beta} + 2\rho_{12}\rho_{23} e^{-\beta}\cos(\phi_{12} + \phi_{23} + \alpha)} \qquad (11)$$

$$\phi = A - B + \phi_{23} \qquad (12)$$

where

$$A = \arctan \frac{\rho_{12} e^{-\beta}\sin(\phi_{12} - \phi_{23} + \alpha)}{\rho_{23} + \rho_{12} e^{-\beta}\cos(\phi_{12} - \phi_{23} + \alpha)}$$

$$B = \arctan \frac{\rho_{12}\rho_{23} e^{-\beta}\cos(\phi_{12} - \phi_{23} + \alpha)}{1 + \rho_{12}\rho_{23} e^{-\beta}\cos(\phi_{12} + \phi_{23} + \alpha)}$$

Finally, α and β can be evaluated in terms of the angle of incidence by:

$$\alpha + i\beta = 2k_2 \cos\theta_2 \, d = \frac{2\omega d}{c}\sqrt{n_{23}^2 - \sin^2\theta_3} \qquad (13)$$

13

For increasing thickness, or when losses are sufficiently high the expression for the reflection coefficient reduces to $R = R_{23}$. This indicates that the energy is absorbed and does not reach the second interface.

If multiple reflections take place the amplitude of the reflection coefficient can be expected to vary periodically as a function of layer thickness, due to cancellation and reinforcement effects. When losses are present the oscillations are exponentially damped as shown in Figure 3.

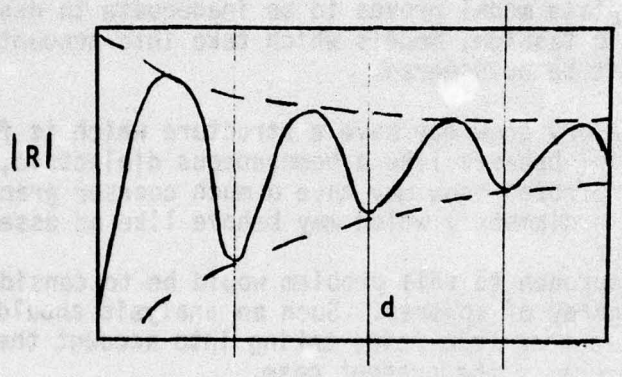


Figure 3. Example of reflection coefficient as a function of layer thickness.

EXPERIMENTAL VERIFICATION

How well the above electrical parameters represent actual snow or ice on the ground can be verified by setting up an experiment using a geometry which corresponds to the calculations, as shown in Figure 4.

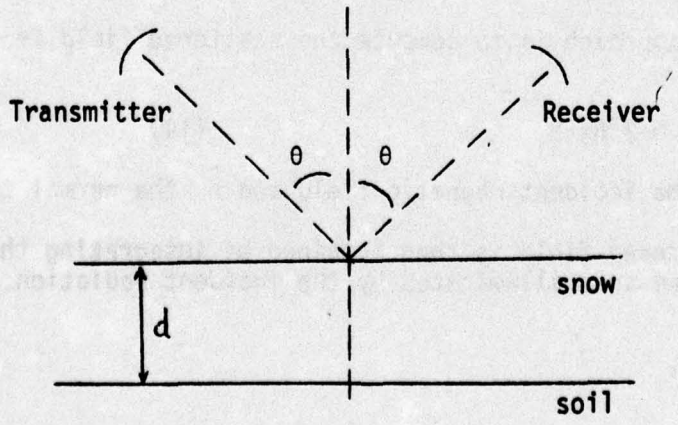


Figure 4. Experimental Geometry.

For a perfectly homogeneous dielectric , which is the point of view taken in the initial calculations, the flat plate geometry should give essentially no backscatter, all the energy being scattered forward at the same angle as the angle of incidence. A metal plate can be used for calibration in this case.

The actual scattering pattern can be easily checked once the experiment is set up, by scanning the receiver, changing both the azimuthal angle and the elevation.

ALTERNATE MODELS.

If the flat plate model proves to be inadequate to describe the snow in a realistic fashion, models which take into account surface irregularities must be considered.

Although fine dry snow may have a structure which is fine enough so that the material behaves like a homogeneous dielectric, other types of snow, such as refrozen snow may have a much coarser granular structure (up to 10mm in diameter) which may behave like an assembly of scatterers at 35GHz.

A possible approach to this problem would be to consider the scatterers as an array of spheres. Such an analysis should begin with work done on backscatter from rain, taking into account the higher density of scatterers in the present case.

The condition of the snow surface may also be an important factor affecting the amount of backscatter. The drift pattern may range from a gently undulating surface to a sharply etched small scale pattern. This problem is similar to the problem of scattering from sea surfaces. Several approaches have been used in the case of sea surfaces (ref. 8). Geometrical optics can be applied by subdividing the surface into a number of specular points where the law of reflection is satisfied for the particular set of incidence and scattering angles under consideration. The total scattered field is the sum of the fields scattered by each of the specular points.

Another approach is to compute the scattered field from the surface current,

$$J_s = 2\,\hat{n} \times H_i \qquad (14)$$

where H_i is the incident magnetic field and $\hat{n}$ the normal to the surface.

The scattered field is then obtained by integrating the current source over the area illuminated by the incident radiation.

DRAWING PAPER NO. 1280-10
TRACING PAPER NO. 1227-10
CROSS SECTION-10X10 TO 1 INCH
AQUABEE
MADE IN USA

FIGURE 5. Amplitude of reflection coefficient for low loss ice.

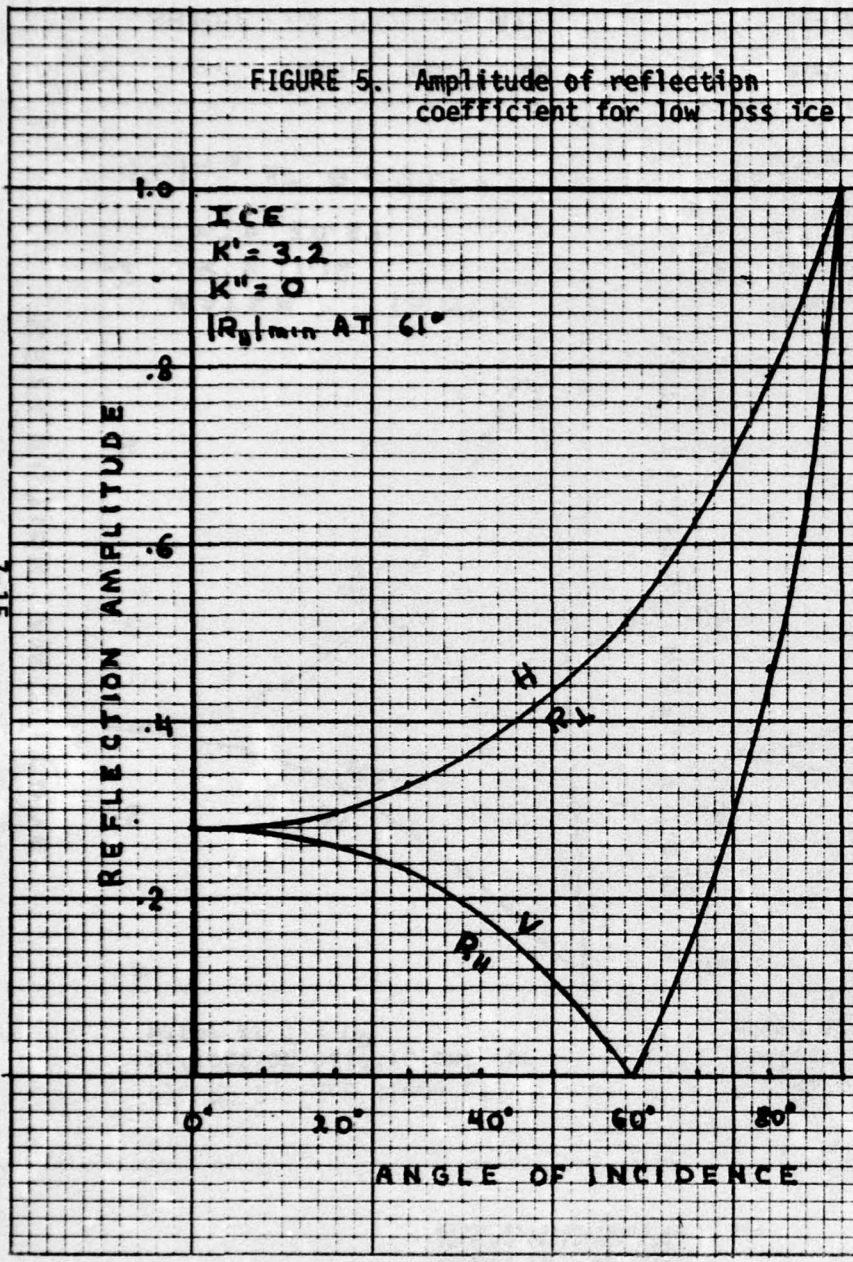
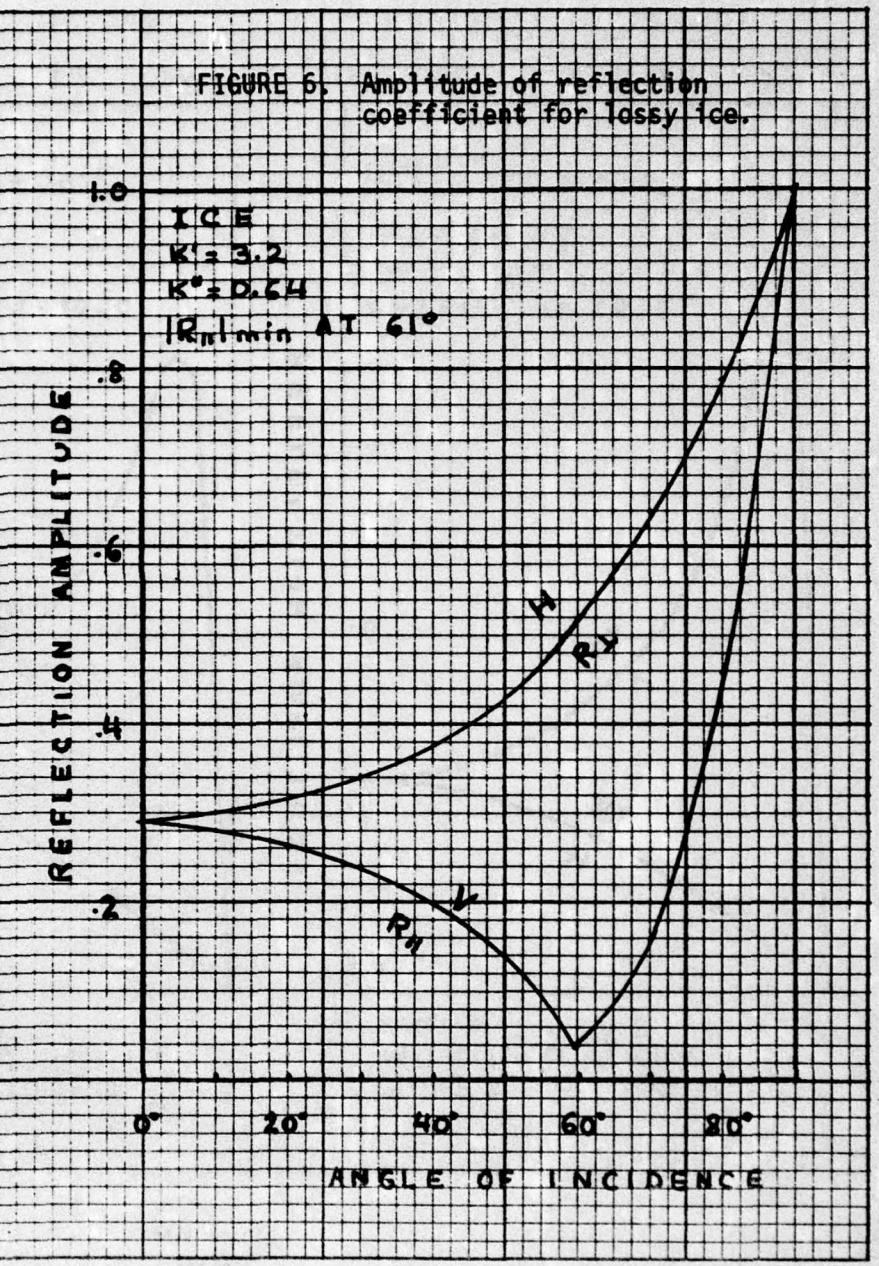


FIGURE 6. Amplitude of reflection coefficient for lossy ice.



DRAWING PAPER NO. 1220-10
TRACING PAPER NO. 1227-10
CROSS SECTION-10X10 TO 1 INCH
AQUABEE
MADE IN USA

FIGURE 7. Amplitude of reflection coefficient for water at T = 0° C.

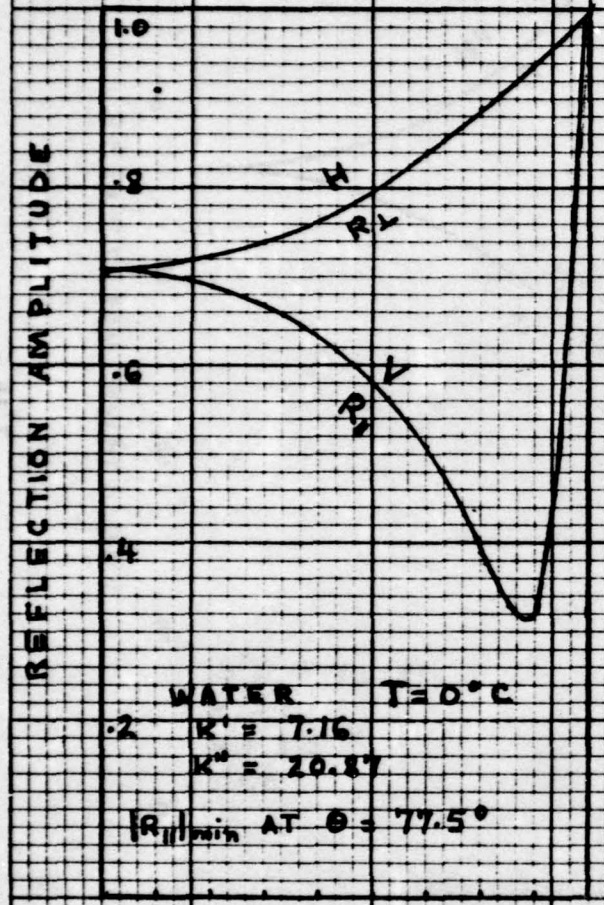


FIGURE 8. Amplitude of reflection coefficient for water at T = 10° C.

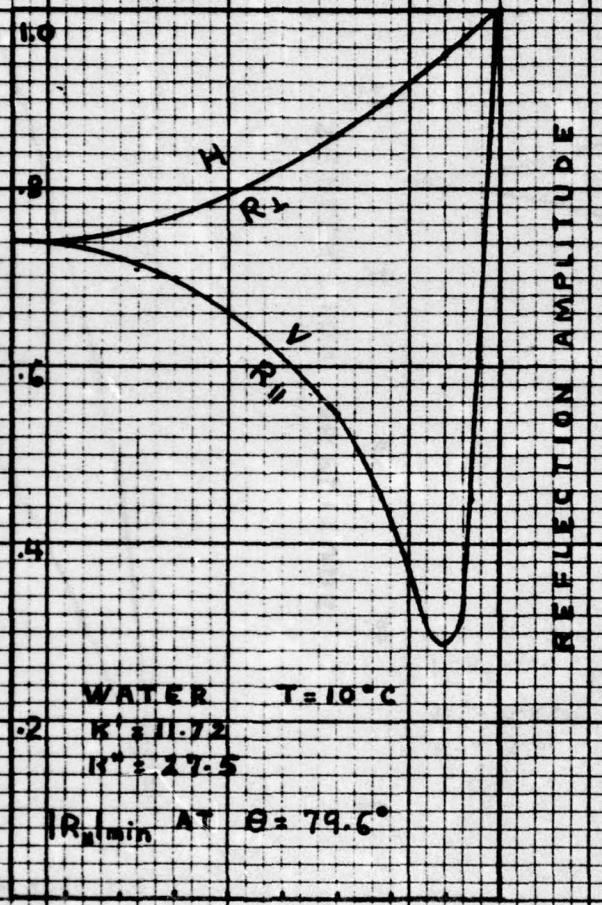
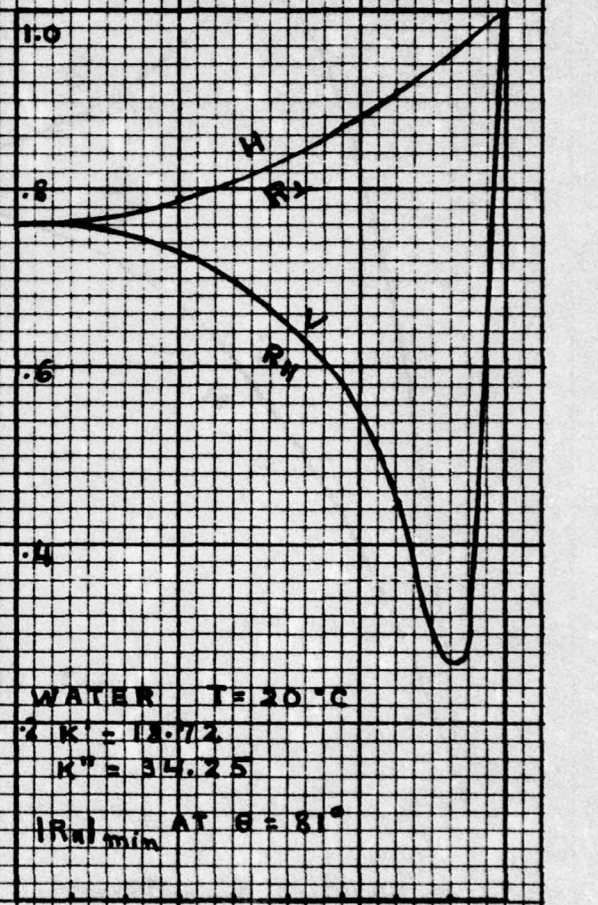


FIGURE 9. Amplitude of reflection coefficient for water at T = 20° C.



DRAWING PAPER NO. 1280-10
TRACING PAPER NO. 1227-10
CROSS SECTION-10x10 TO 1 INCH
AQUABEE
MADE IN USA

FIGURE 10. Amplitude of reflection coefficient for low loss snow.

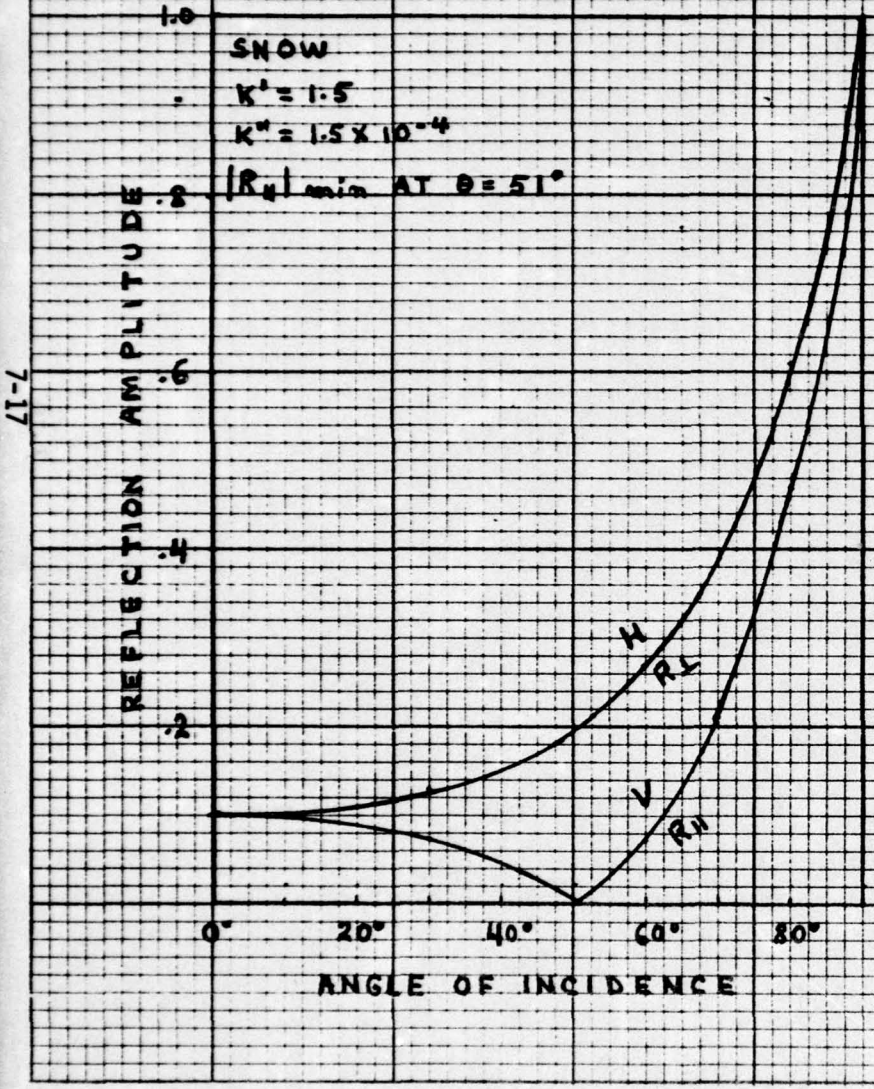
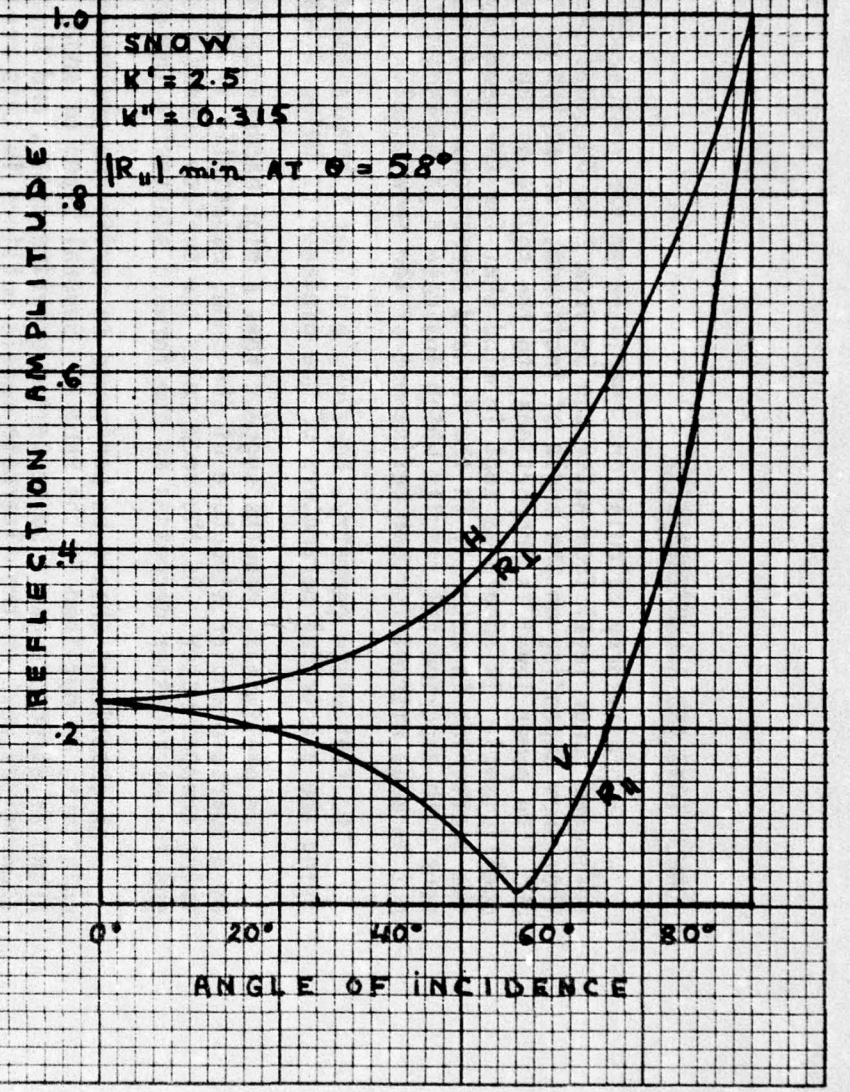


FIGURE 11. Amplitude of reflection coefficient for lossy snow.



18

CONCLUSIONS AND RECOMMENDATIONS

The preliminary calculations completed so far indicate that the reflected power level from water can be from 2 to 50 times greater than from snow depending on the angle of incidence, for angles up to about 80° (the power level is proportional to the square of the reflection coefficient). It should be kept in mind that for the geometry considered the scattering is entirely in the forward direction, and direct comparisons with experimental results which indicate high backscatter should not be made without further refinement of the snow model.

The flat plate geometry, however, provides a simple means of verifying the electrical parameters of the dielectrics being investigated.

The preliminary results suggest that a high backscatter may be caused by a coarse granular structure of the snow, especially if the snow contains trapped water. As the snow melts the surface looses its roughness and the backscatter decreases as the forward scattering increases.

An experiment should be performed to verify the preliminary calculations, as outlined in the report. Several types of snow, varying in granular structure can also be tested experimentally, and therefore theoretical work on the alternate models outlined in this report should be done in order to interpret the experimental data when it becomes available.

19

REFERENCES

1. Honeywell Inc., Systems and Research Center, Minneapolis, Minnesota, "Millimeter Wave Contrast Seeker Breadboard Flight Test", Test and Analysis Report, Contract #AF08635-75-C-0128, June 1976.

2. Currie, N.C., Dyer, F.B. and Ewell, G.W. "Radar Millimeter Backscatter Measurements from Snow", Report #1 EES/GIT Project A-1831, June 1976, Georgia Institute of Technology.

3. Brekhovskikh, L.M., Waves in Layereol Media, Academic Press, 1960.

4. Von Hippel, A.R., Dielectrics and Waves, John Wiley & Sons, Inc. 1954.

5. Hoekstra P. and Spanogle D., "Radar Cross-section measurements of Snow and Ice", CRREL Report TR235, November 1972.

6. Edgerton, A.T., Stogryn, A. and Poe, G. "Microwave Radiometric Investigations of Snowpacks", Aerojet Electrosystems Co., El Monte, California, Report #1285R-4, July 1971.

7. Linlor, W.I., "Multilayered Models for Electromagnetic Reflection Amplitudes", NASA Report TR R-438, Ames Research Center, March 1976.

8. Lentz, R.R., "A Numerical Study of Electromagnetic Scattering from Ocean-like Surfaces", NASA Contractor Report CR-2091, Ohio State University, Columbus Ohio, July 1972.

1976 USAF-ASEE SUMMER FACULTY RESEARCH PROGRAM
sponsored by
THE AIR FORCE OFFICE SCIENTIFIC RESEARCH
conducted by
AUBURN UNIVERSITY AND OHIO STATE UNIVERSITY

PARTICIPANT'S FINAL REPORT

CONFIGURATION SPECIFICATIONS FOR A DIGITAL GUIDED WEAPON FLIGHT CONTROL MODULE

Prepared by:	Charles W. Caldwell, Ph.D.
Academic Rank:	Assistant Professor
Department and University:	Department of Electrical Engineering University of Arkansas
Assignment:	Eglin AFB Armament Laboratory Guided Weapons Division Air-to-Surface Midcourse Guidance Branch
USAF Research Colleague:	Major Robert L. Haney
Date:	August 13, 1976
Contract No.:	F44620-75-C-0031

CONFIGURATION SPECIFICATIONS FOR A DIGITAL GUIDED WEAPON FLIGHT CONTROL MODULE

by
C.W. Caldwell

ABSTRACT

In order to achieve low cost weapon systems capable of accomplishing complex missions, the Air Force is incorporating state-of-the-art digital technology into a modular weapon concept. The feasibility of utilizing low cost commercially available microprocessors in a weapon flight control module is examined by analyzing the processor throughput requirements for the GBU-15 Weapon Control Unit (WCU). The sequential nature of the WCU algorithm is found to require a machine with a throughput rate of nearly 500 KOPS, which exceeds the performance characteristics of MOS processors. However, since the maximum required throughput per airframe axis is only 150 KOPS, three MOS devices could replicate the autopilot function.

A reconfiguration of the WCU autopilot function was considered which would lend itself to a distributed processor design. By processing sensor signals directly at their location outside the flight control module, the remaining functions can be carried out by a single MOS machine of current capability.

ACKNOWLEDGMENT

The author wishes to acknowledge the support provided for this project by the Air Force Office of Scientific Research and the efficient administration by Auburn University via Mr J. Fred O'Brien. Special thanks are due to the Digital Guided Weapon Technology program personnel of AFATL/DLMM. The author is indebted to Maj Robert L. Haney, Maj Larry Sokolowski, Capt James Beaumont and Lt George Beasley, Jr. for their efforts in making this project possible.

LIST OF FIGURES

Figure 1. Elements of the Weapon System

Figure 2. Weapon Bus Configuration and Interfaces

Figure 3. DP System Configuration

Figure 4. PWW Trajectory Stages

Figure 5. Sequential Execution of the Autopilot Function

Figure 6. Parallel Execution of the Autopilot Function

Figure 7. PDAP Pitch Axis Glide Mode

Figure 8. Reorganized Version of Figure 7

LIST OF TABLES

Table 1. Autopilot Flight Control System Modes

Table 2. PDAP Instruction Mix Per Axis

Table 3. Simplified Autopilot Instruction Requirements

5

INTRODUCTION

The Guided Weapons Division of the Air Force Armament Laboratory, Eglin Air Force Base, has among its responsibilities feasibility studies and advanced development of conventional tactical guided weapons systems and guided missile components. Due to rapid changes in technology and an Air Force desire to retain the maximum capability within its weapon inventory, armament systems either undergo a constant updating or are deleted in favor of next generation weapons. Most pertinent to tactical guided missile applications are the recent developments in digital integrated circuits technology and electronics packaging, which can produce increasingly sophisticated airborne electronics that are also physically smaller, consume less power and cost less. It is a facet of these applications which is addressed in this report.

The proliferation of terminal sensing and midcourse guidance schemes now permits a wide variety of tactical missions to be accomplished. In order to reduce system costs while retaining operational flexibility, current generation weapon systems are designed to be modular in nature. To facilitate the interfacing of the various weapon systems modules, the Air Force is presently designing towards an all digital weapon. The primary advantage would be that many types of missions could reside in software for a given hardware configuration. This allows the aircraft commander to have a tremendous operational flexibility, since selection of the particular mission could be delayed until just prior to weapon release. Exactly how digitization of current and future weapon systems will be accomplished is the subject of a 2-year contractual activity which is being monitored by the Digital Guided Weapons Technology (DGWT) program office at ADTC. The subject of this report concerns a parallel effort to this activity.

THE DIGITAL PROCESSOR

A block diagram of the current missile digital processor (DP) is shown in Figure 1. This design utilizes a single fast 16 bit processor which is programmed to perform all functional aspects of missile operation, such as midcourse and terminal guidance calculations, flight control, arming and fuzing, and aircraft interfacing. The DP communicates with the various I/O devices such as sensors and actuators via a shared weapons bus (Figure 2). Interfacing these devices (distributed elements (DE)) with the weapons bus is accomplished by bus interface units (BIU). Transmission of digital data and commands is performed serially along the bus. All A/D conversion of signals is performed within each DE.

Many of the missile functions must be performed simultaneously, e.g., airframe stabilization, guidance law calculations, data link decoding, etc. Since the DP is to perform nearly all such functions, it is required to have a very high processing rate. Current estimates of central processor throughput (including room for functional growth) are on the order of 2.5-3 million operations per second (MOPS). In order to achieve this speed, the brassboard version of this machine is presently constructed from Schottky-TTL technology, with a total power consumption of 160 watts. As the power of the operational version would be considerably restricted, the present contractor is proposing for the advanced device a custom LSI bipolar integrated circuit, with an estimated power consumption of 25 watts. It is not clear at this point, however, that this direction would prove to be the most cost effective for the Air Force.

AN ALTERNATIVE APPROACH

The objective of this project was to investigate alternative designs for the DP, with reduction in costs as a key factor. A final design implemented in custom LSI could prove to be a very expensive solution, not only in the developmental stages, but also in subsequent procurement, as second sourcing would be unlikely. In addition, a complex and unique machine could easily produce a software nightmare, such that the Air Force could find it quite difficult if not virtually impossible to develop DP software in-house. The responsibility would then revert to the contractor with the costs associated with a sole source supplier. The most obvious alternative to this situation is to consider the utilization of existing devices. The proliferation of MOS microprocessors in the commercial market has resulted in many low cost devices and a large amount of debugged software. There is little doubt that with a sufficient number of these devices contained within the weapon any desired function could be performed. The real question is whether or not this approach is cost effective in the long run. The intent here is to estimate the configuration of microprocessors which would be required to satisfy the missile functions.

One way in which to approach this problem is to utilize the system specifications that have been developed during the course of the current DGWT contract. (1) These figures would then be used to partition the system into modules in which microprocessing is to be performed. Due to the many tasks assigned to the DP and the limited time available for the project, only a portion of the overall system could be considered. Figure 3 indicates a functional division of the DP. From this figure, an arbitrary division was made such that only the flight control and avionics portions of the overall system would be examined. The guidance subsystems were simultaneously analyzed by an independent study. (2)

THE FLIGHT CONTROL SUBSYSTEM

The current DGWT program authorized not only the DP study but also the development of a programmable digital autopilot (PDAP). This device is a digital emulation of the analog autopilot destined for the GBU-15 glide bomb. After its feasibility was demonstrated, PDAP was transitioned into the GBU-15 System Program Office where it was renamed the weapon control unit (WCU). While the DP is responsible for all operations performed during the missile mission, its flight control responsibilities are very similar to those of PDAP. Thus, in order to analyze the requirements for the DP autopilot, it is sufficient to utilize the PDAP. A clear advantage in doing so is that the latter system is well defined and PDAP software is available. (3)

An initial examination of the PDAP program revealed that a simple instruction tally would tend to overspecify the computational capability needed for flight control. The GBU-15/PDAP/WCU encompasses three types of airframes and several varieties of midcourse and terminal guidance methods. (4) To obtain a measure of the necessary throughput, a particular module need only be selected, since alternative configurations demand only a larger program memory, not operating speed. For the purposes of this study, the configuration chosen was the planar wing weapon (PWW), aircraft data link midcourse guidance, and lock-on after launch (LOAL) electro-optical (EO) terminal guidance.

Figure 4 depicts the typical stand-off missile mission for the GBU-15. The trajectory is divided up into at least 4 stages as shown. During each stage, the autopilot must produce outputs to control the three airframe axes, i.e., pitch, yaw, and roll. The control mode employed during each trajectory stage is not in general the same for each axis, which further complicates the autopilot function. Table 1 lists the required control modes per axis and trajectory stage.

Table 1

Autopilot Flight Control System Modes

	Trajectory Stage	Pitch	Yaw	Roll
1.	Delay after launch	Rate damping	Rate damping + yaw heading	Rate damping
2.	Altitude hold	Altitude hold*	Yaw heading*	*
3.	Glide	Angle of attack hold*	Yaw heading*	*
4.	Transition	Seeker look angle hold*	EO proportional navigation*	*
5.	Terminal	EO proportional navigation*		*

*Includes rate damping

Several possibilities exist for the processor architecture and technology necessary to perform the functions in Table 1. The essential parameter is speed. Using the autopilot stability values derived by the DP contractor, rate damping calculations must be carried out at 400 Hz and steering calculations at 50 Hz for each of the three axes. If an estimate of the instructions for each calculation can be determined, then the minimum throughput rate is then known. As the PDAP software was available, the required instruction sequence for each axis could be estimated. These values are given in Table 2.

Table 2

PDAP Instruction Mix Per Axis

Calculation	Airframe Axis Pitch	Yaw	Roll
Rate Damping (400 Hz)			
Short instructions	250	250	125
16 bit multiplies	15	15	9
Steering (50 Hz)			
Short instructions	300	300	---
16 bit multiplies	18	18	---

The numbers in Table 2 do not include A/D conversion of analog signals, but do include D/A conversion for actuator signals. Thus some additional time must be allocated to A/D conversion as well. In any case, a rough estimate of autopilot processor throughput can now be made for each axis. The assumption used here is that 1 multiply is equivalent to 5 short instructions timewise.

Pitch Axis: $\simeq$ 150,000 ops/sec (150 KOPS)

Yaw Axis: $\simeq$ 150 KOPS

Roll Axis: $\simeq$ 68 KOPS

Assuming 16 channels of analog input, the PDAP instruction execution sequence amounts to approximately 275 short instructions at 400 Hz, which is an additional 110 KOPS. In fact, PDAP performs even more calculations, most of which are concerned with identifying airframe configurations and current trajectory stage (at 50 Hz). Even so, the above estimates are roughly indicative of minimum throughput.

PDAP is designed to be implemented with a single fast processor which executes all functions sequentially (Figure 5). Thus, at a minimum, it must operate at a throughput rate of nearly 500 KOPS. This has been accomplished in the WCU development program by utilizing bipolar 2 bit slices (Intel 3000 series chips). Although NMOS devices would be more desirable from a

cost and power standpoint, current devices have perhaps a 200 KOPS upper limit for a 16 bit machine and therefore cannot imitate the autopilot function in a single processor. On the other hand, it does appear that three such devices, i.e., one per each airframe axis, could perform the necessary computations in parallel (Figure 6). Before proceeding in this direction, however, it is instructive to consider an alternative configuring of the existing autopilot function.

The concept of modularity in a guided weapon implies that the system is physically partitioned in a functional manner. That is, a single module might contain all hardware (and software?) pertinent to a particular task, such as midcourse guidance, flight control, etc. With a sufficiently fast central processor for the entire missile system, all analog data is digitized at each sensor location and sequentially transmitted along a common weapon bus to the processing unit. If commercial (particularly NMOS or CMOS) processors are to be considered, the central processor configuration must be abandoned, since the MOS throughput rate is well below the required minimum. To achieve the required processing rate with slow processors, multiple processors must execute programs in parallel. These devices could be centrally located or distributed throughout the weapon, insofar as the computations are concerned. However, the speed of a centrally located unit would be again dependent upon sequentially-received data, which would substantially limit the throughput rate. Speed considerations presume that multiple slow processors receive parallel data, so that the preferred configuration would be microprocessors distributed among the various weapon modules, with little or no data communication between modules (only commands).

FLIGHT CONTROL RECONFIGURATION

Figure 7 illustrates the control system for the pitch axis during the glide portion of the PWW trajectory, in which the angle-of-attack is controlled. PDAP duplicates this function digitally, using the analog sensor signals as inputs and producing the analog fin actuator commands. It is clear, however, that this function incorporates both guidance and flight control computations. If guidance and flight control are to reside within separate modules, then the diagram in Figure 7 must be divided in some way. Assuming that the sensors do (or could) reside outside the flight control module, then it would seem reasonable to perform the raw signal processing such as filtering and limiting at the sensor. The flight control function would then apply the appropriate gains, perhaps an integration, and then summate the signals to produce the fin commands.

Figure 8 shows the glide mode pitch axis control system redrawn as described above. It is now apparent that the flight control system responsibility is substantially reduced (although the guidance modules now are required to perform some additional processing). Using the PDAP instruction set, the throughput required for the simplified autopilot was again estimated (Table 3). Note that both 400 Hz and 50 Hz channels are still required.

Table 3

Simplified Autopilot Instruction Requirements

Trajectory Stage	Instructions/Sec	Multiplies/Sec
Pitch Axis		
Altitude hold	39,000	1,700
Glide	19,500	850
Transition	19,500	850
Terminal	35,000	1,700
Yaw Axis		
Midcourse	35,000	1,700
Terminal	20,500	850
Roll Axis	53,600	3,200

From Table 3, the maximum processor load occurs during the terminal flight phase in which the airframe is following the seeker. Again assuming 4 short instructions per multiply, the throughput rate for each axis can be determined.

Pitch Axis: $35{,}000 + 1700(4) \simeq 42$ KOPS

Yaw Axis: $35{,}000 + 1700(4) \simeq 42$ KOPS

Roll Axis: $53{,}600 + 3200(4) \simeq 66$ KOPS

If the autopilot functions were to be performed sequentially, then the total processor capability required would be approximately 150 KOPS. Since the newest MOS processors operate up to 200 KOPS, it would appear that a commercial device could perform the simplified flight control function, as far as throughput is concerned.

From the simplified autopilot functions which were examined, the input data rates can also be estimated. Considering all of the possible control modes, a total of ten inputs to the flight control module are required, carrying both 50 Hz and 400 Hz data. A typical loading would consist of six 50 Hz signals and three 400 Hz signals. Assuming the data (or commands) are entering sequentially via a multiplexed bus, this represents a 16 bit word being received at a 1500 Hz rate. On a serial bus this amounts to a bit rate on the order of 24K bits/sec. No other activity on this bus would be necessary, as separate command bus would likely be used to designate trajectory stages, etc.

Avionics Subsystem

The weapon digital processor will be required to handle all communications between the weapon modules and the aircraft. These responsibilities are composed primarily of initialization procedures and the stores portion of the stores management system (SMS). If the avionics processor is charged with the task of performing the Kalman filtering for transfer alignment, then this probably represents the most critical initialization throughput requirements. However, these specifications have not yet been fully developed, so that initialization task estimates cannot be made at present. Likewise, the data are incomplete for the SMS, e.g., the functional interface which defines the software modules has yet to be established. Thus, no processor specifications for aircraft interface were developed for this report.

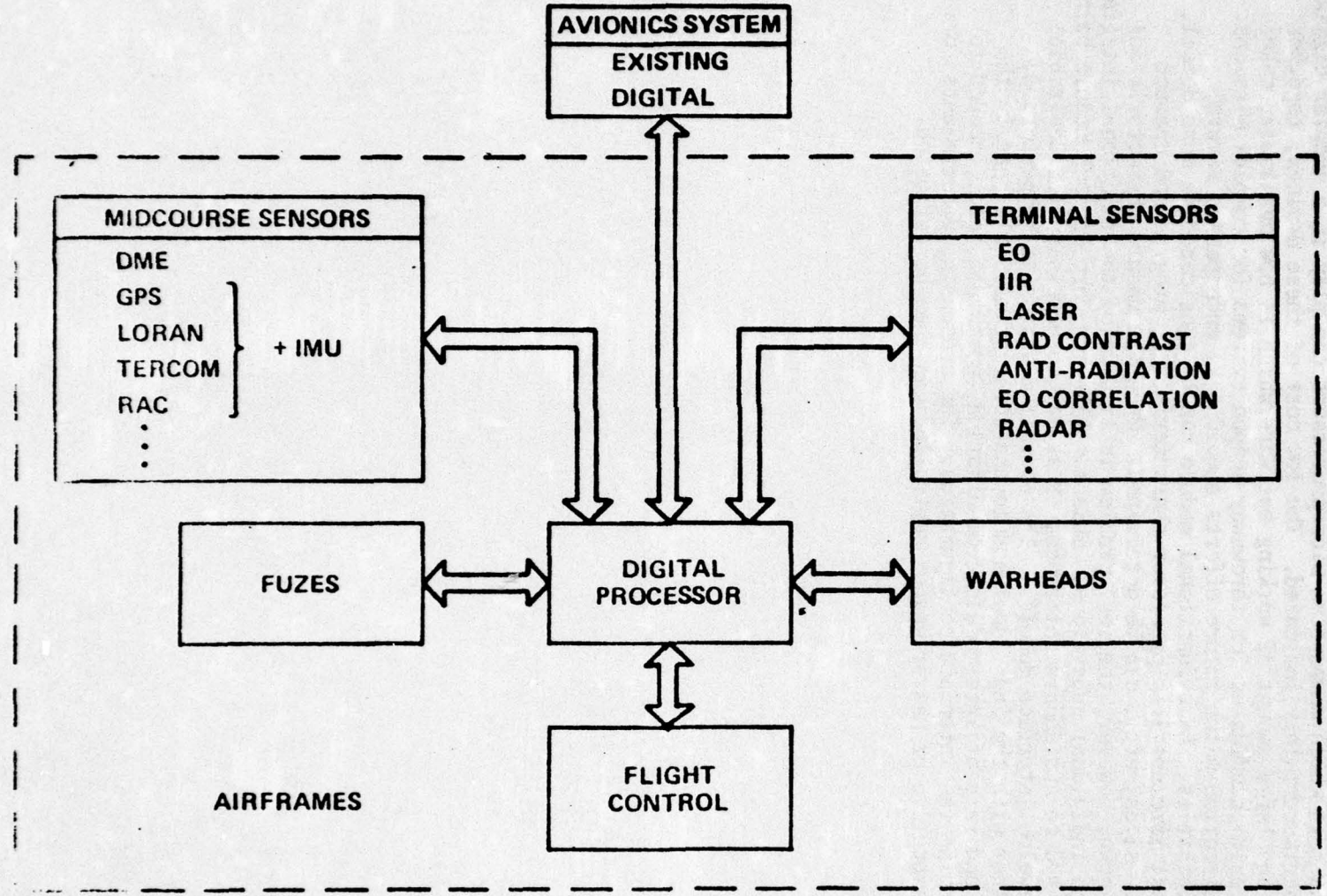
Even though no general comments concerning interfacing can be made, some specific information is available for the GBU-15/WCU Avionics interface. These data indicate that the processor loading is quite low. For the PAVE TACK mission, the aircraft sends 44 bit words to the GBU-15 at a 2Hz rate, which represents a negligible time loading on the WCU. Since SMS and all initialization procedures occur prior to weapon release, it is likely that in general the required processor throughput for the avionics interface will be low.

Conclusions and Recommendations

The objective of this study was in part to examine the feasibility of employing low cost, commercially available microprocessors for the modular guided weapon autopilot function. It was shown that the PDAP could be implemented with three MOS devices, one for each of the three airframe axes. However, in a truly modular weapon, the functions performed by PDAP do not have to be carried out within a single module, so that the autopilot can be partitioned such that its responsibilities can be met more effectively. Transducer signal processing, such as amplification, digitization and filtering are more efficiently performed at or near the sensors themselves, which would most likely not be located within the flight control module. If these basic processing tasks are thus removed from the autopilot, then the latter need only be concerned with simple tasks such as summation, integration, gain multiplication and limiting. Applying this concept to the WCU demonstrated that a single MOS machine would suffice for the flight control module. An additional benefit is the reduction in the number of signal paths necessary to input data to the flight control module, since the digital inputs can be time multiplexed on a common data bus.

It would appear for the present time that interfacing the weapon with the aircraft requires only a low processor throughput capability. Due to this fact, efforts in this area should be delayed until the overall weapon processor design is firmed up, as there may be sufficient room for these tasks within that design without requiring a separate processor for avionics interfacing alone.

From the results of the flight control analysis, further examination of the role which commercial microprocessors can play in a modular digital weapon is certainly indicated. The low cost of these devices, together with the large amount of working software which is now available, makes them prime candidates for throwaway weapon systems for complex missions. The direction which future efforts should take encompasses several possibilities. Each functional module can be considered in more detail, so that more specific processor characteristics, program and operand memory sizes, etc., can be determined. Once the module characteristics are known, however, the real problem is to develop the functional integration of the individual subsystems. This may take the form of each module being designed to a standard interface, or it may be necessary (or desirable) to develop interface modules. The overall missions to be performed, together with the individual module characteristics, will specify the type and rate of intermodule communication, bus width, etc., needed to determine the interface configuration. The processing requirements for the executive or master weapon controller can then be estimated.


AVIONICS SYSTEM
EXISTING
DIGITAL
MIDCOURSE SENSORS
DME
GPS
LORAN
TERCOM
RAC
+ IMU
TERMINAL SENSORS
EO
IIR
LASER
RAD CONTRAST
ANTI-RADIATION
EO CORRELATION
RADAR
FUZES
DIGITAL PROCESSOR
WARHEADS
FLIGHT CONTROL
AIRFRAMES

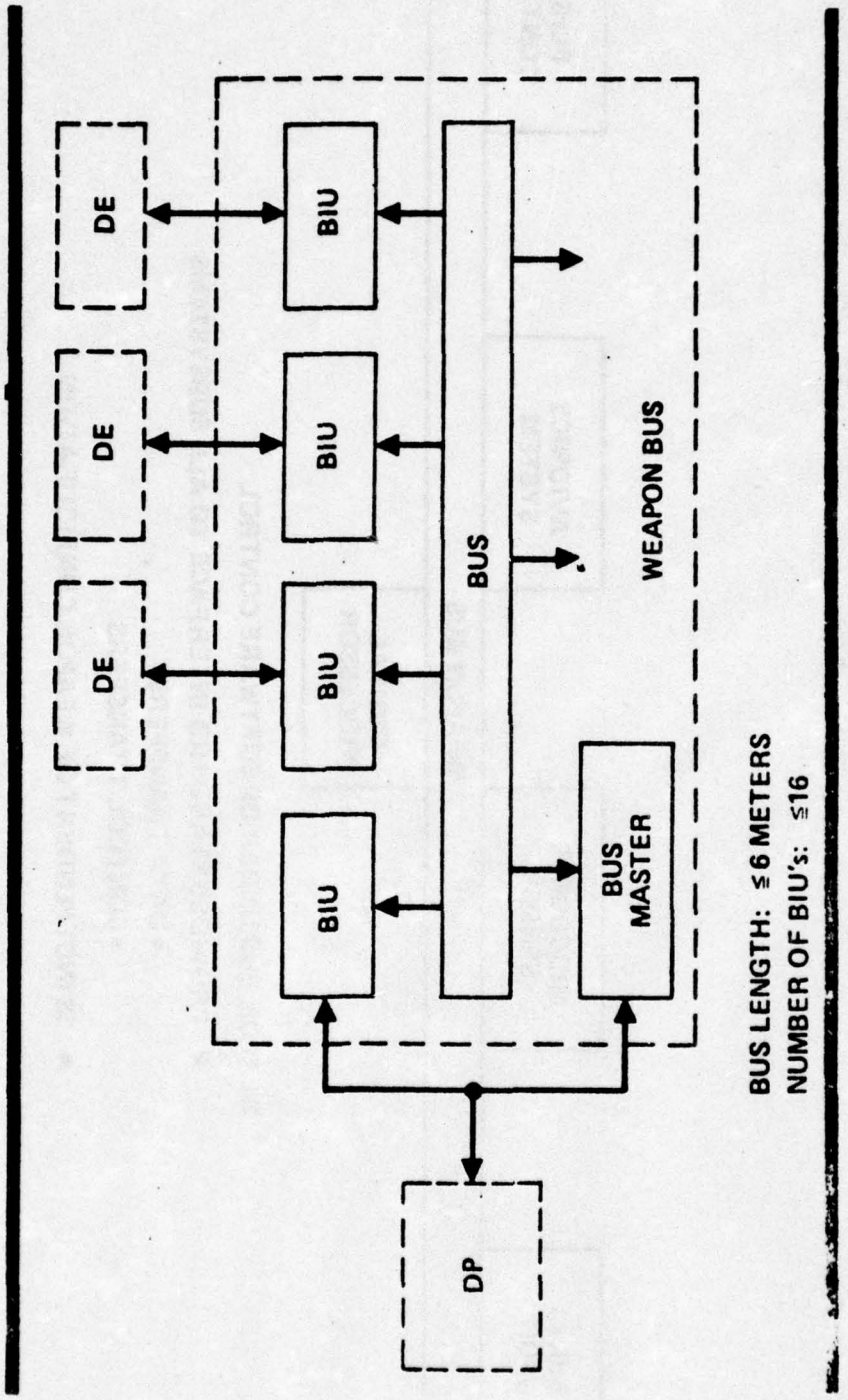
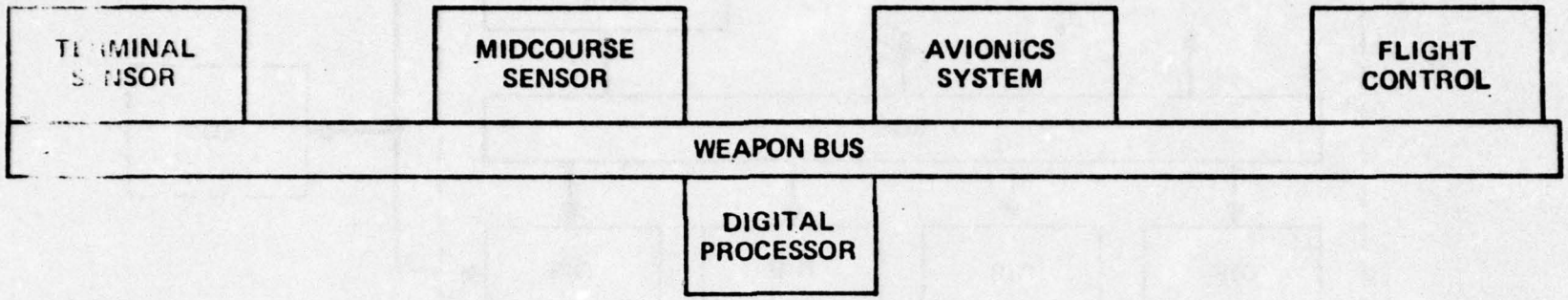


Figure 2. Weapon Bus Configuration and Interface



WEAPON BUS UNDER DP SOFTWARE CONTROL

- PROVIDES STANDARD INTERFACE TO ALL SUBSYSTEMS
  - DATA TRANSFERS
  - CONTROL TRANSFERS
- IS INDEPENDENT OF WEAPON CONFIGURATION

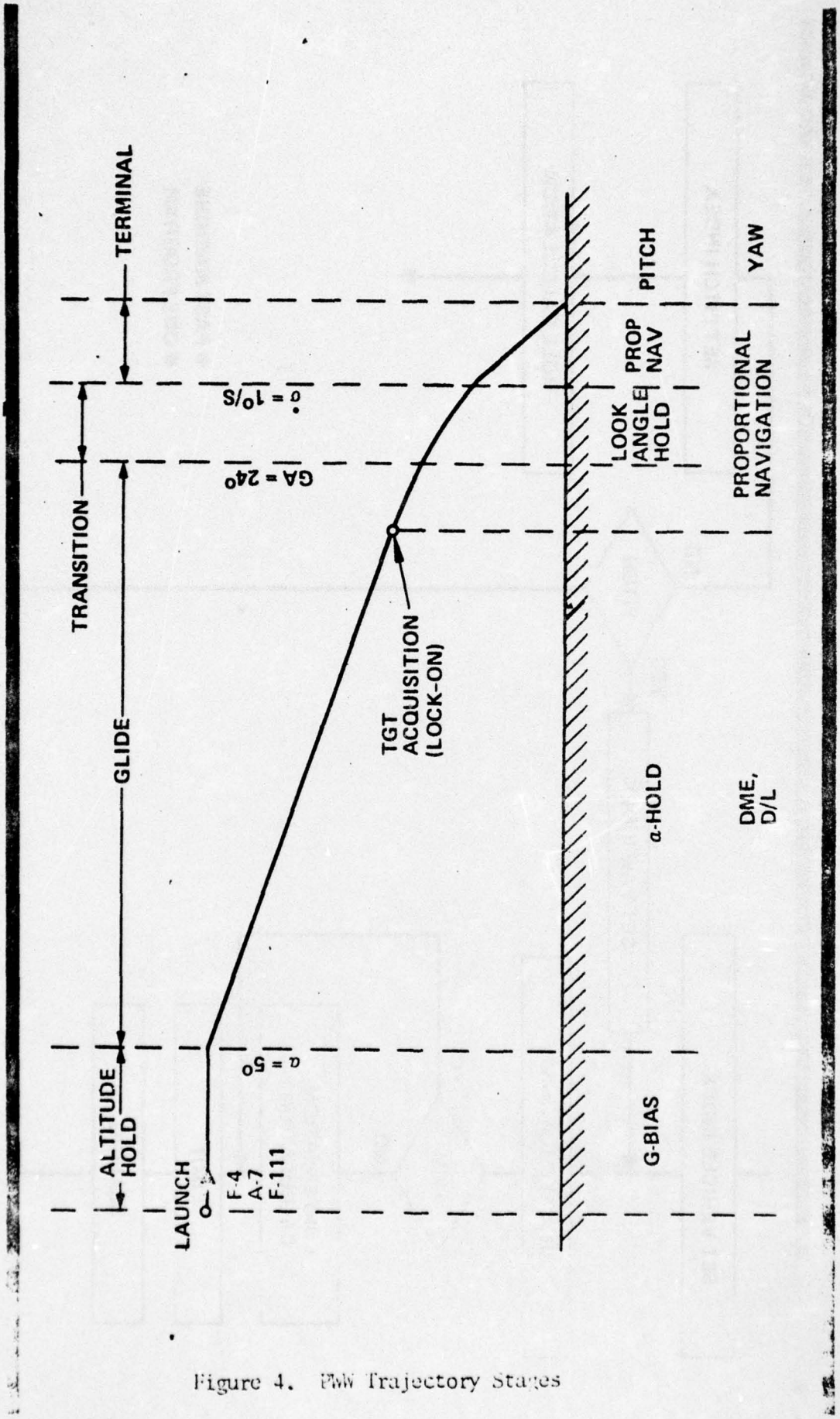
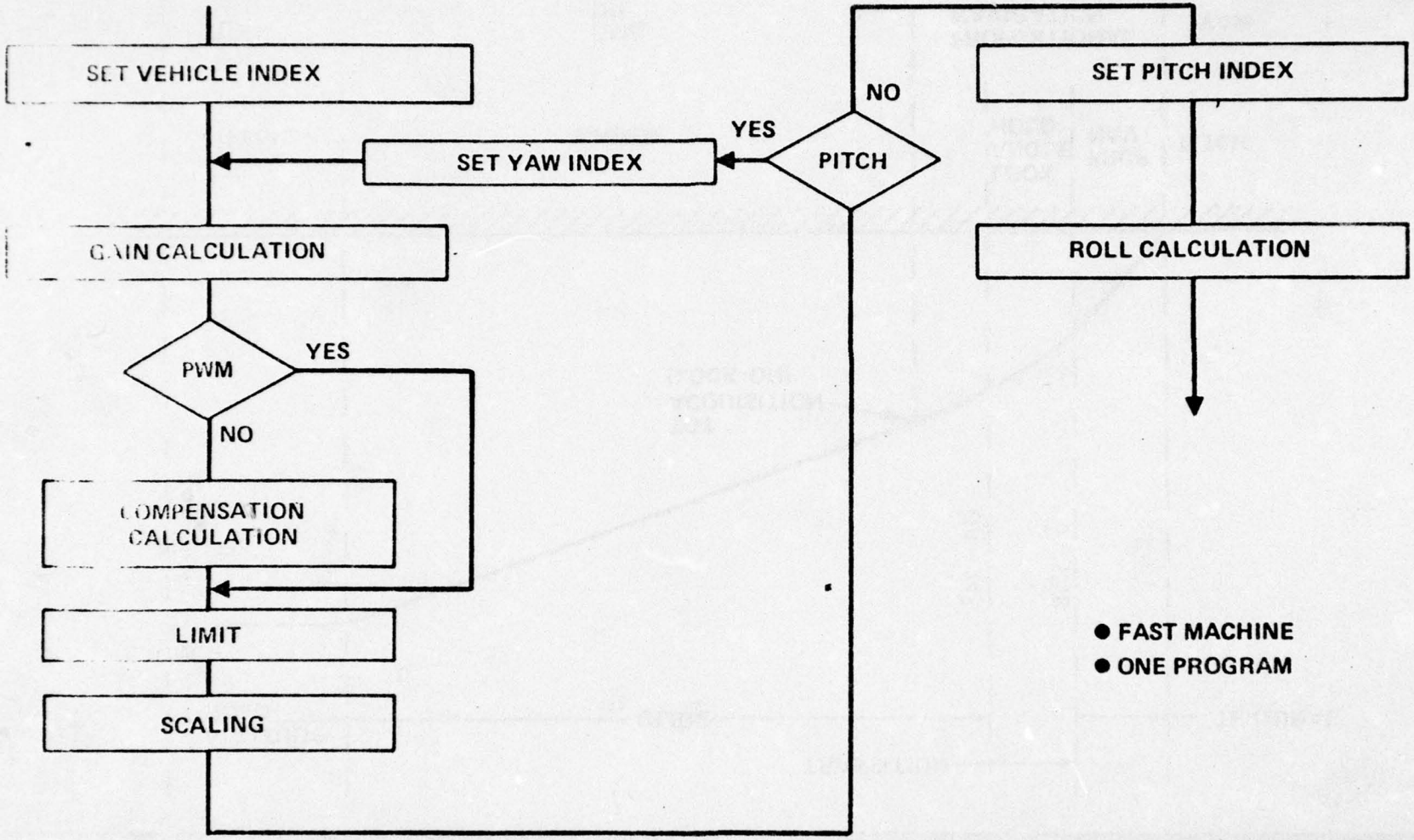
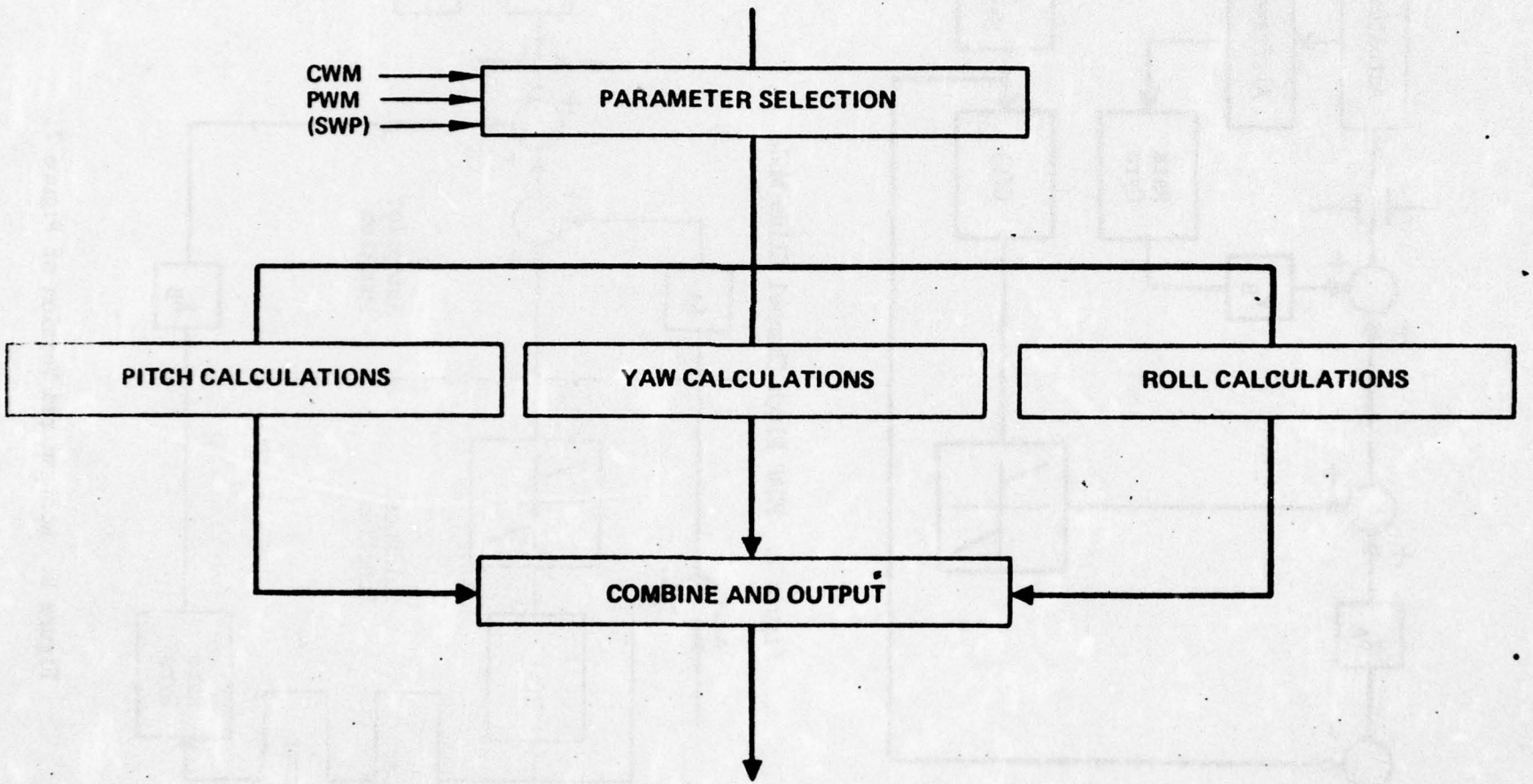


Figure 4. PWW Trajectory Stages


SET VEHICLE INDEX
GAIN CALCULATION
PWM
YES
NO
COMPENSATION CALCULATION
LIMIT
SCALING
SET YAW INDEX
YES
PITCH
NO
SET PITCH INDEX
ROLL CALCULATION
● FAST MACHINE
● ONE PROGRAM


CWM
PWM
(SWP)
PARAMETER SELECTION
PITCH CALCULATIONS
YAW CALCULATIONS
ROLL CALCULATIONS
COMBINE AND OUTPUT

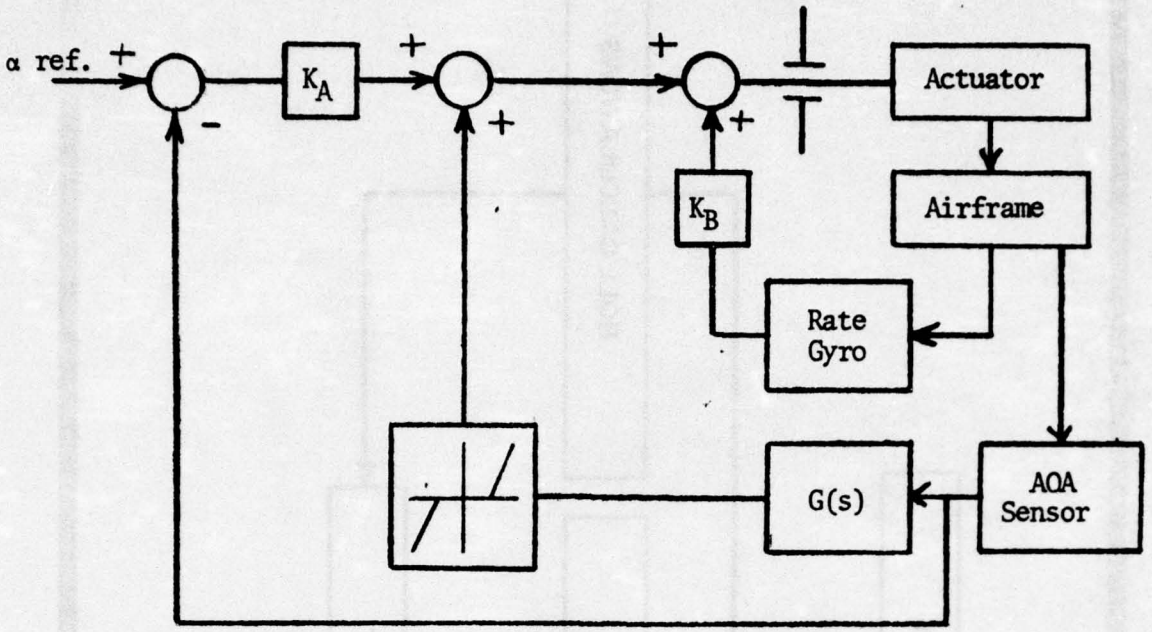


Figure 7. PDAP Pitch Channel Glide Mode

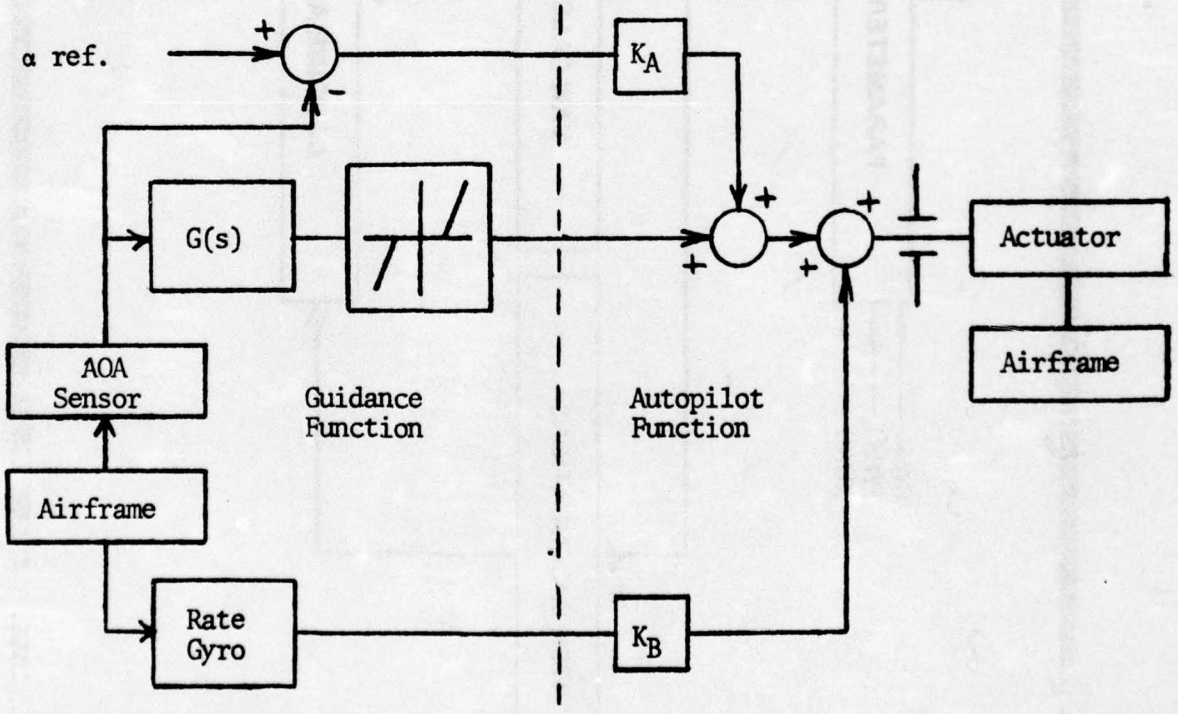


Figure 8. Reorganized Version of Figure 7.

REFERENCES

1. Digital Guided Weapons Technology Program Design Review Summary Reports

No. 1	DGWT 0120-1	25 Nov 74
No. 2	DGWT 0120-2	20 Jan 75
No. 3	DGWT 0120-3	3 Jun 75
No. 4	DGWT 0120-4	26 Aug 75
No. 4a	DGWT 0120-4a	6 Oct 75
No. 5	DGWT 0120-5	25 May 76

Hughes Aircraft Company
Missile Systems Group
Canoga Park, California

2. Sensor and Navigation System Processing Requirements for Digital Guided Missiles

R. A. Higgins — USAF/ASEE Summer Program
Final Report — 13 Aug 76

3. Digital Guided Weapons Technology Program PDAP Software Development Report

Report No. DGWT 0160-1 — 7 Jul 75

Hughes Aircraft Company
Missile Systems Division
Canoga Park, California

4. GBU-15 Weapon Control Unit

Baseline Design Review — 6 Jan 76

Hughes Aircraft Company
Missile Systems Division
Canoga Park, California

1976 USAF-ASEE SUMMER FACULTY RESEARCH PROGRAM

sponsored by
THE AIR FORCE OFFICE OF SCIENTIFIC RESEARCH

conducted by
AUBURN UNIVERSITY AND OHIO STATE UNIVERSITY

PARTICIPANT'S FINAL REPORT

SENSOR AND NAVIGATION SYSTEM PROCESSING REQUIREMENTS FOR DIGITAL GUIDED MISSILES

Prepared by:	Robert A. Higgins, Ph D
Academic Rank:	Professor
Department and University:	Department of Electrical Engineering South Dakota State University
Assignment:	
(Air Force Base)	Eglin Air Force Base
(Laboratory)	Air Force Armament Laboratory
(Division)	Guided Weapons Division
(Branch)	Air-To-Surface Midcourse Guidance
USAF Research Colleague:	Major Robert L. Haney
Date:	August 13, 1976
Contract No.:	F44620-75-C-0031

SENSOR AND NAVIGATION SYSTEM PROCESSING REQUIREMENTS FOR DIGITAL GUIDED MISSILES

by
Robert A. Higgins, Ph D

ABSTRACT

A study of the sensors and navigation systems used in the digital guided weapons program was conducted to determine their digital processing requirements. The project develops a basis for alternative designs for digital control of guided weapons. Worst case processing loads are identified. Due to favorable price trends and the availability of software, commercial microprocessors are expected to offer significant advantages in a distributed processor configuration for guided weapons. Disadvantages in the use of microprocessors include their reduced speed, sub-optimum architecture, and limited instruction sets.

ACKNOWLEDGMENT

The author greatly appreciates the support afforded him by the Air Force Office of Scientific Research, and is grateful to Mr J. Fred O'Brien, Auburn University, and the American Society for Engineering Education for the administration of this project.

The author also wishes to extend special thanks for technical assistance to Major Bob Haney, Major Larry Sokolowski, Capt James Beaumont, and Lt George Beasley of the Air-To-Surface Midcourse Guidance Branch of the Air Force Armament Laboratory.

NOMENCLATURE

A	amplitude in volts
D	distance in meters
E	electric field intensity in volts/meter
$\underline{Q}$	quaternion matrix $[q_1 \quad q_2 \quad q_3 \quad q_4]^T$
R	range in meters
t	time in seconds
v	velocity of propagation in meters/second
(x,y,z)	coordinates of a point in three-dimensional space
$\Delta\phi$	phase angle in radians or cycles
λ	wavelength in meters
ω	frequency in radians/second
$(\theta_o, \phi_o, \psi_o)$	pitch, roll, yaw angles in radians

ACRONYMS

ALSS	Advanced Location Strike System
ARS	Anti-Radiation Seeker
CIGTF	Central Inertial Guidance Test Facility
DGWT	Digital Guided Weapons Technology
DL	Data Link
DME	Distance Measuring Equipment
DP	Digital Processor
EO	Electro Optical
FCEU	Flight Control Electronics Unit
GPS	Global Positioning System
IIR	Imaging Infra Red

IMU	Inertial Measurement Unit
JTIDS	Joint Tactical Information Distribution System
KOPS	Kilo Operations Per Second
LASER	Light Amplification by Stimulated Emission of Radiation
LCIGS	Low Cost Inertial Guidance System
LOBL	Lock On Before Launch
LORAN	Low Frequency Radio Navigation
LWRM	Light Weight Radar Missile
MCG	Millimeter Contrast Guidance
MGGB	Modular Guided Glide Bomb
MOPS	Mega Operations Per Second
RAC	Radiometric Area Correlator
RACG	Radiometric Area Correlation Guidance
SAR	Synthetic Aperture Radar
SINS	Strapdown Inertial Navigation System
TDMA	Time Division Multiple Access
TERCOM	TERrain COntour Matching

INTRODUCTION

A trend has been developing in the military services towards the digitization of weapons systems due to a number of factors, including:

1. Reduced size, weight, and power requirements of digital electronics as compared to analog devices.

2. Reduced life cycle cost of digitized weapons.

3. Increased reliability of digital techniques.

4. Enhanced design and application flexibility of digital devices.

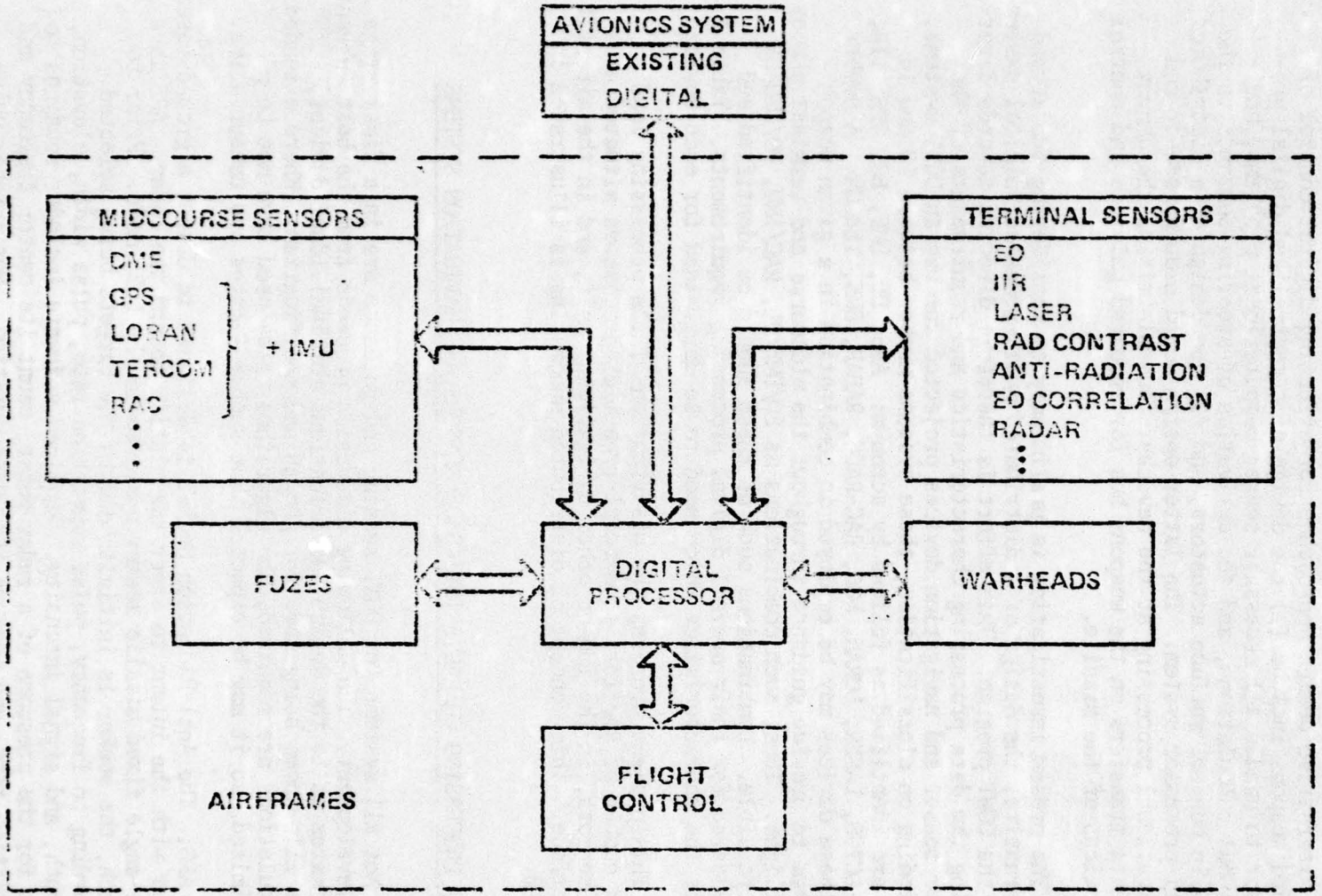
5. Improved accuracy and performance of digital systems through error checking and self-test procedures.

One approach to the digitization of weapons systems is the custom-designed digital processor to perform sensing, computational, control, and aircraft interfacing tasks for a guided weapon.[1] There may be, however, alternatives to the custom-designed digital processor which are more cost-effective, and contractor-independent.

OBJECTIVES

The primary objective in undertaking this study is to develop a basis for alternative design approaches for implementing digital control of guided weapons. It has been suggested that the use of commercially-available military-specification components, in particular, microprocessors, bears investigation for the digital guided weapons technology (DGWT) program. One important advantage resulting through this option is that design costs are significantly reduced through the definition of basic computer architecture by the microprocessor selection. A second advantage is that much of the software, assembly language routine, as well as higher-order language, has already been developed for commercial microprocessors. This software can be applied to the missile control problem at lower cost than software which must be newly developed for special-purpose, custom-designed digital processors.

The basic elements of the digital weapon system are indicated in Fig 1. In this characterization of DGWT, major elements are seen to be the midcourse and terminal sensors, flight control and aircraft avionic systems. A parallel, concurrent study[2] deals with digital flight control and avionics for DGWT.


AVIONICS SYSTEM
EXISTING
DIGITAL
MIDCOURSE SENSORS
DME
GPS
LORAN
TERCOM
RAC
+ IMU
TERMINAL SENSORS
EO
IIR
LASER
RAD CONTRAST
ANTI-RADIATION
EO CORRELATION
RADAR
FUZES
DIGITAL PROCESSOR
WARHEADS
FLIGHT CONTROL
AIRFRAMES

Alternative design approaches for effecting digital control of guided weapons include (1) the design of a centralized digital processor to handle all necessary seeker computational problems, navigational calculations, and the derivation of steering commands to the missile control surface actuators, and (2) the design of a distributed multi-processor system. The latter design would provide sensor and navigational processing at the devices, thus minimizing the amount of data transfers on the weapons bus for required guidance and control functions of the missile.

The present investigation is preliminary to considering the second alternative, the design of a distributed multi-processor digital system for the DGWT program. This effort is therefore directed towards determining the data processing characteristics and requirements of the major sensor and navigation devices projected for use in DGWT systems. Depending on classification, these systems number between 12 and 16 and are identified as follows by acronym: ARS, DL, DME, EO, GPS, IIR, IMU-LCIGS, LASER, LORAN, MCG, RAC-RACG, RADAR, SMS, TERCOM. A number of these devices may be employed in combination in a given weapon system to provide guidance throughout the midcourse and terminal phases of flight. Thus, such combinations as EO/DME/DL, RAC/IMU, EO/IMU/DL are possible. Combinations such as these should be identified and considered for their overall digital processing requirements. Table 1 lists the characteristics which need to be determined for each device.

This project proposes the distribution of the processing load to a number of smaller, commercial-type microprocessors situated at the sensors, in the IMU or other navigational unit, and in the aircraft interface. This concept of distributed processing is illustrated in Fig 2.

DATA PROCESSING CHARACTERISTICS OF SENSORS AND NAVIGATION SYSTEMS

Not all systems for DGWT sensing and guidance are in a final stage of development. The following discussion proceeds from the best current estimates as to the design specifications for individual devices, with some allowances being made for growth and modification. Where extended calculations are required, the algorithms to be used have not been optimized, so it may be expected that such estimates are conservative.

ARS. The Anti-Radiation Seeker is designed to detect a ground-based radar with the intent to steer the missile toward the radar. ARS is a wide-angle fixed missile seeker operated in the LOBL mode. Prior to launch, the seeker is initialized with the targets being selected according to frequency, pulse repetition rate, pulse width, elevation, azimuth, and signal intensity. Required software includes routines to test for the presence of a radar pulse, count its center frequency and repetition rate, and measure its pulse duration. For a radar pulse repetition rate of 100 pps, the estimated processing rate is 60 KOPS. Program and operand memory for ARS is estimated at 140 words.

Table 1

DATA PROCESSING CHARACTERISTICS OF SENSOR AND NAVIGATION DEVICES

- COMPLETE INPUT/OUTPUT DESCRIPTION OF THE DEVICE
  - ANALOG OR DIGITAL
  - SIGNAL LEVELS AND DYNAMIC RANGE
  - BANDWIDTH
  - DATA RATE
  - WORD LENGTH/PRECISION
  - DESIGNATIONS OF INPUT/OUTPUT CHANNELS
- OPERATIONAL MODES/MISSIONS OF DEVICE
- SYSTEM CONFIGURATIONS

EXS:		
	EO/DME/DL	IIR/GPS/DL
	IIR/DME/DL	*MCG/GPS
	EO/IMU/DL	*RAC
	*GPS	EO/GPS/DL
	IIR/RAC/DL	*IMU

* ALL WEATHER SYSTEM

- ALGORITHM REQUIREMENTS OF DEVICE
- PROCESSING LOAD OF DEVICE IN OPERATIONS PER SECOND
- MEMORY REQUIREMENTS OF DEVICE

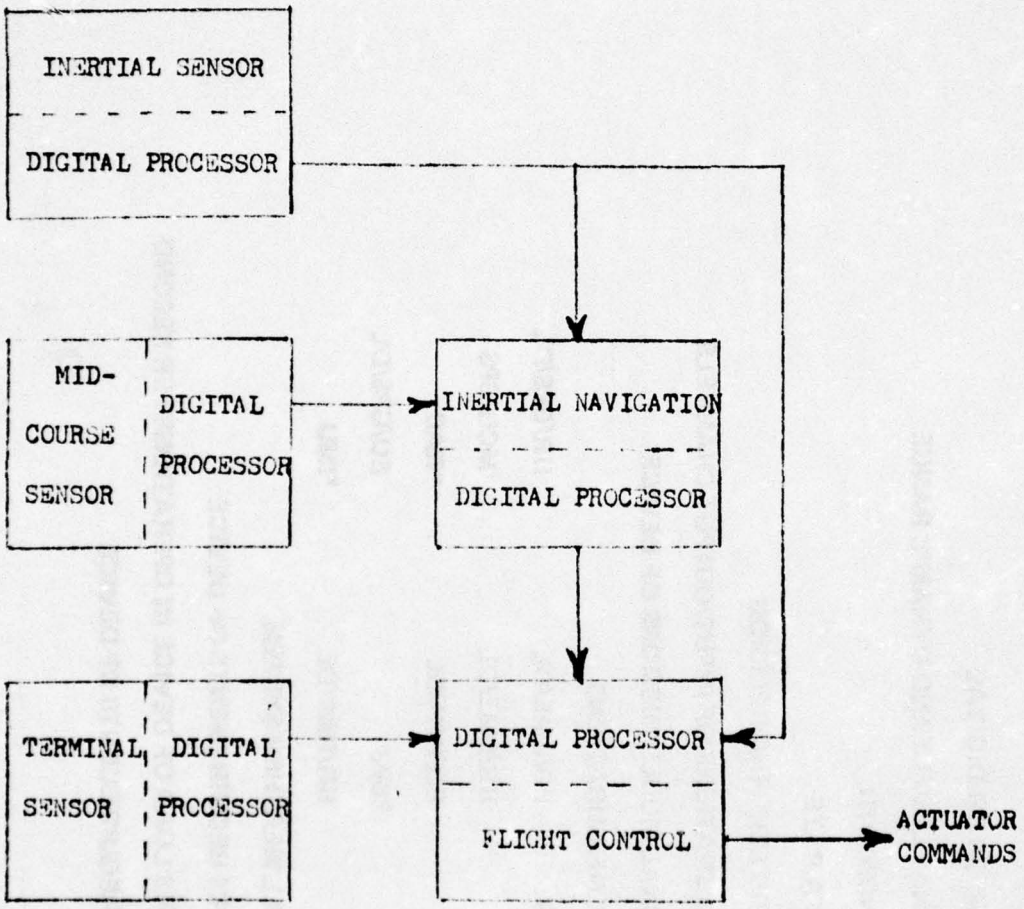


Fig. 2. Distributed Processing for Guided Weapons

DL. The Data Link is designed with the following requirements:

1. Ensure accurate commands to weapon with the lowest possible probability of command error.

2. Maintain control of weapon with the highest probability of reception of command signals.

3. Prevent jamming of command signals.

4. Prevent assumption of weapon control by an adversary.

5. Prevent adversary from knowing that command transmissions are occurring.

DME. Distance Measuring Equipment is based on the physical principle that an electromagnetic wave propagated through an anisotropic, homogeneous medium experiences a phase shift proportional to distance traveled, and inversely proportional to wave length of the energy.[4]

For an electromagnetic wave propagated from point a, with an electric field intensity,

$$E_a(t) = A \sin \omega t \qquad (1)$$

the electric field strength at point b, separated D meters from point a is

$$E_b(t) = A' \sin (\omega t - \omega t_1). \qquad (2)$$

where: $t_1 = D/\upsilon_p$ seconds

and $$E_b(t) = A' \sin (\omega t - \omega D/v_p). \qquad (3)$$

The phase lag between point a and point b is, thus,

$$\Delta\phi = \omega D/v_p \text{ radians} \qquad (4)$$

or $$\Delta\phi = D/\lambda \text{ cycles.} \qquad (5)$$

This phase difference between the functions $E_a(t)$ and $E_b(t)$ is a direct measure of the distance between points a and b, provided that f and v_p are constant. DME uses the relationship of eq. (5) between the distance traveled and the phase.

In one DME method, a signal of known frequency and phase is transmitted as the modulation on a light beam carrier from the source to a target. The total distance traveled is measured by comparing the phase of the received modulated signal with that of the transmitted signal. The range to the target is one-half of the transmission path length. Fixed phase shifts are easily calibrated out of the measurement.

Thus the range to the target is

$$R = \frac{\Delta\phi\lambda}{2} \text{ meters} \tag{6}$$

One practical realization of DME uses three noncollinear stations for range-only measurements on any number of targets to provide time-space-position information. No pointing antenna is required in such a system, now practicable with the availability of high speed digital computers.

The method involves the simultaneous solution of three distance equations, defining spheres of radii R_i, i = 1, 2, 3, equal to the measured ranges from three known points to the unknown point (x,y,z). The three intersecting spheres define two points separated by the plane of observation. If the known points defining this plane are contained on the earth's surface, only one point is of concern, i.e., the point above the plane of observation.

Letting the observation points have coordinates $(0,0,0)_1$ and $(e,0,0)_2$ and $(g,h,0)_3$, where 1, 2, and 3 are the station numbers and $e,h \neq 0$,

$$\begin{aligned} R_1^2 &= x^2 + y^2 + z^2 \\ R_2^2 &= (x-e)^2 + y^2 + z^2 \\ R_3^2 &= (x-g)^2 + (y-h)^2 + z^2 \end{aligned} \tag{7}$$

The resultant solutions for (x,y,z) are

$$\begin{aligned} x &= \frac{1}{2e}\left(R_1^2 - R_2^2 + e^2\right) \\ y &= \frac{1}{2h}\left(R_2^2 - R_3^2 + 2x(e-g) + h^2 + g^2 - e^2\right) \\ z &= \left(R_1^2 - x^2 - y^2\right)^{1/2} \end{aligned} \tag{8}$$

The processing load for DME with eqs. (8) is approximately 8 KOPS and the memory requirement is 320 words.

EO. Electro Optical seeker, or video seeker, makes use of a gimbaled, visual spectrum photo-electric detector mounted in the nose section of the guided missile. EO can be used in a manual track mode wherein the photometric data is transmitted over the missile data link to the controlling aircraft to provide the pilot with missile steering information.[5,6]

Alternatively, the EO correlation mode makes use of a stored image of the target area obtained on some previous flight. If the present "live" scene as detected by the EO seeker is sufficiently similar to the stored image, and is properly centered with respect to it, then a maximum amount of light (or a minimum if the reference

is a negative) will be transmitted. If the transparency is moved in its own plane with respect to the "live" image through coordinates (u,v) the transmitted light will decrease (increase for a negative). A "bell-shaped" function of the relative displacement can be observed, and this function is, in fact, the cross-correlation of the sensed image, S(x,y), with the reference transparency, R(x,y),except that integration limits are necessarily finite.[7,8]

The cross-correlation function, H(u,v) is given by

$$H(u,v) = K \int_{ac}^{bd} \int S(x,y)R(x-u, y-v)\, dx\, dy. \qquad (9)$$

The stored image can be recorded from almost any point in air space above the ground target. The imagery, however, must be altered by restructuring, rectification, enlargement, cropping and filtering to provide the image needed by the EO correlator. Filtering can be done by a photo-optical process, or by use of digital filtering. Digital techniques, in general, for all processing requirements, appear to have shorter turn-around time. Extensive discussion of the necessary computations can be found in the literature.[9,10] It is estimated that for a stored map of 32 x 32 elements, and an average instruction time of 5 μsec, one correlation can be completed every 30 seconds. Higher speed processing is possible through a multiprocessor design, or with faster random logic elements. Memory requirements are estimated at 2.6K words.

GPS. Global Positioning System is a universal global navigation system employing an array of 24 satellites at an altitude of 11,000 nmi. in 12 hour circular orbits. The satellites broadcast pseudorandom code and ephemerides in the L band to users for positional determination and updates. The GPS receiver (in a mobile unit) measures the pseudo-range and pseudo-range rate from the user to 4 satellites simultaneously.[11]

One principal application of GPS is to update inertial guidance measurements. The rate at which these corrections occur is dependent upon the IGS and may range from an update every 10 to 100 seconds. There are seven signals from GPS, including three position and three velocity signals, and one time signal. The maximum transfer rate for 32-bit precision and 10 second update, therefore, is approximately 23 baud.[12]

Normally, GPS will function as an aid to an IMU or LCIGS, and may be integrated with the guidance unit. Two general processing tasks are apparent with this design:

1. Receiver processing to intercept satellite signals and compute the missile coordinates.

2. Guidance processing to perform Kalman filter algorithms for enhancing accuracy of IMU or LCIGS, do alignment and calibration of IMU, and transfer loop-aiding data to the missile control circuits.

At this point, the overall design for GPS has not been determined so that it is not certain to what extent guidance processing is to be performed within GPS, itself. In addition, the final design for GPS will be dependent upon the design of LCIGS, not yet completed.[12]

The processing rate to perform all GPS and IMU calculations is estimated at 300 KOPS, assuming that both hardware floating point arithmetic and hardware double-precision multiply and divide are provided in the processor.

Although algorithms for the guidance calculations have not been optimized, it is possible to estimate the memory requirements. A conservative memory estimate to accomplish both receiver and guidance processing is a total of 20K words, of which 3K PROM is for subroutines, 8K RAM is for Kalman filter, 5K PROM is for inertial navigation, and 4K PROM is for the executive routine.

IIR. Imaging Infrared Tracker uses an opto-mechanical scanner and an array of infrared detectors to obtain image information. After summing the detector outputs to enhance the signal to noise ratio, the information is converted to a standard video format. The signal is digitized and used to produce a tracking error signal in the same manner as the electro-optical seeker. The processing rate and memory storage requirements are 1.3 MOPS and 2K words.

IMU-LCIGS. The Inertial Measurement Unit, or alternatively, Low-Cost Inertial Guidance System, is intended to operate with one or more aids for low-rate error correction, such as GPS, RAC, EO, IIR, or LORAN.[1] Whether the IMU is low-cost or not, depends upon the choice of gyro to be used. The cost of the inertial sensors is 60% to 85% of total IMU recurring cost. The Air Force production cost goal for LCIGS is $10K with long term cost goal of approximately $5K per unit, contrasted to upwards of $50K per unit for a high quality SINS. Figure 3 indicates one possible mode of operation, known as the LCIGS update mode.

In this system it is intended for GPS to serve as an update source to LCIGS every 10 to 30 seconds. The data, itself, consists of velocity along each geodetic axis, and position in geodetic coordinates. If necessary, coordinate transformation may be employed. The data is transfered asynchronously, word serial, at 16 bits per word.[13,14]

During midcourse guidance phase of a missile flight, it is possible for the GPS receiver/processor to lose its synchronism with satellite

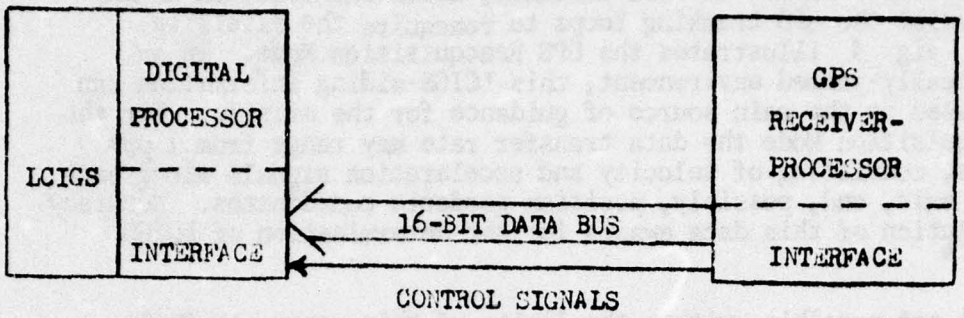


Fig. 3. LCIGS Update Mode

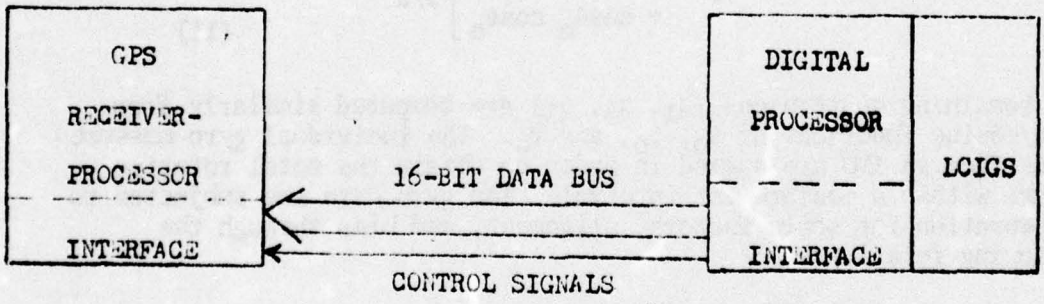


Fig. 4. GPS Reacquisition Mode

signals. Due to the complexity of the GPS signal, and the internal tracking loops in GPS, external aids may be essential for reacquisition of signal synchronism. In this instance, LCIGS can function as an aid to assist the GPS tracking loops to reacquire the satellite signals. Fig 4 illustrates the GPS Reacquisition Mode. In an electronically-jammed environment, this LCIGS-aiding information can also be used as the main source of guidance for the missile. For the GPS Reacquisition Mode the data transfer rate may range from 1 pps to 10 pps, consisting of velocity and acceleration signals along each geodetic axis, and, possibly, position geodetic coordinates. Accuracy and resolution of this data awaits further determination of LCIGS designs.[15]

It is not possible, within the limits of this paper, to fully discuss inertial guidance calculations. IMU sensor aiding and sensor processing are themselves extensive subjects, and much work remains to be done in the optimization of IMU algorithms. Undoubtedly these are fruitful areas for future research, particularly if one is to consider the various LCIGS alternatives.

A brief introduction to the computations necessary for IMU initialization is provided herein as an indication of some of the DP requirements.

It is necessary to initialize the IMU in order to establish the attitude of the missile with respect to a horizontal reference frame. A set of four Eulerian parameters, known as quaternions, is computed from the pitch, roll, and yaw angles of the missile, as follows:[16]

$$\underline{Q} = \underline{f}(\theta_o, \phi_o, \Psi_o) , \tag{10}$$

wherein

$$q_4 = 0.5x \left[1-\sin\Psi_o \sin\theta_o \sin\phi_o + \cos\Psi_o (\cos\theta_o+\cos\phi_o) + \cos\theta_o \cos\phi_o\right]^{1/2} \tag{11}$$

The remaining quaternions (q_1, q_2, q_3) are computed similarly from sine/cosine functions of θ_o, ϕ_o, and Ψ_o. The individual gyro measurements from an IMU are summed in order to obtain the total rotation amount within a measurement interval. The gyro data are subjected to compensation for scale factors, alignment, and bias through the following relationship:

$$\underline{\Delta\theta} \cong \underline{g}(\underline{d}, \underline{\Psi})\ \underline{\Delta\theta}' + \underline{\Delta t}\underline{\Delta\omega} , \tag{12}$$

where $\underline{g}(\underline{d}, \underline{\Psi})$ is the matrix of gyro scale factors and alignments, and $\underline{\Delta\omega}$ is the gyro bias matrix.

The quaternions must be periodically updated according to

$$\underline{Q} = \left[\underline{I} + h(\underline{\phi})\ \underline{Q}\right] \tag{13}$$

A transformation algorithm is used to convert rotations in navigational coordinates to equivalent rotations in the body coordinates, as follows:

$$\underline{\delta\theta}_B = \left[A\right]^T \underline{\delta\theta}_{Nav} \tag{14}$$

where $\left[A\right]$ is the direction cosine matrix in which, e.g.,

$$\begin{aligned} a_{11} &= q_1^2 + q_4^2 - q_2^2 - q_3^2 \\ a_{12} &= 2(q_1q_2 + q_3q_4) \\ a_{13} &= 2(q_1q_3 - q_2q_4) \\ &\vdots \\ a_{33} &= -q_1^2 - q_2^2 + q_3^2 + q_4^2 \end{aligned} \tag{15}$$

Estimates have been made for the computational effort to implement all of the IMU equations. The overall memory requirement is approximately 3K of 16-bit memory, and the average computational rate is 240 KOPS.[17]

LASER. The LASER tracker uses an independent pulsed laser as a source of illumination for a target. Energy reflected by the target is received by an optical system and impinges upon a four-quadrant detector. Error signals for two axes are derived from the four simultaneous pulse amplitudes, as follows:

$$\begin{aligned} \text{Axis 1 Error} &= \frac{(A + B) - (C + D)}{A + B + C + D} \\ \text{Axis 2 Error} &= \frac{(A + C) - (B + D)}{A + B + C + D} \end{aligned} \tag{16}$$

The LASER memory requirement is approximately 50 words, and the processing rate is 3 KOPS.

LORAN. LOw Frequency RAdio Navigation is intended for application as a corrective sensor for IMU or LCIGS. LORAN employs a master radio transmitter in 100 KHz frequency range and one or more slave radio transmitters with synchronous transmissions. The difference in arrival time of two signals (master and slave) fixes the observer's position along a hyperbolic locus of constant time difference. The coordinates of the observer are given by [1].

$$\frac{(x - c)}{A^2} - \frac{y^2}{C^2 - A^2} = 1 \tag{17}$$

where: x and y are the coordinates of the observer with respect to the master station,

$$A = \frac{R_1 - R_2}{2} ,$$

$$C = \frac{R_1 + R_2}{2} , \qquad (18)$$

and R_1, R_2 are the master-observer and slave-observer distances, respectively.

If one uses an additional slave station, or another relative time dimension, the observer's location is determined as a unique point in two-dimensional space. A third slave station will locate the observer uniquely in three-dimensional space.

For the master and two-slave station configuration, the processing rate has been estimated at 10 KOPS, and the required memory is 250 words, 16 bits.

MCG. Millimeter Contrast Guidance employs energy in the 35 GHz range, both actively and passively, for the detection and tracking of discrete targets. Several semi-heuristic algorithms are employed in the detection mode. The system does not make use of a stored image of the target area.[1]

Initially, the MCG system is in an active (RADAR) mode, employing narrow beam, conical scan to distinguish objects in the active area which are above a threshold level which, itself, is adaptive so as to adjust for changes in background clutter.

In some circumstances, clutter can give a high output which could be mistaken for a target. A second algorithm makes use of time-spatial processing to discriminate on spatial characteristics of an object, i.e., if amplitudes are exceeded for more than a specified interval of time or distance, the return is classified as no target.

A third algorithm makes use of changes in return signal modulation characteristics occurring for a target. With the presence of a target smaller than the conical scan area, the return will be modulated at the conical scan frequency. Background clutter will normally not provide a scan-rate modulated return signal.

Once a target is detected, the MCG system goes into a tracking mode. The system remains in the active tracking mode up to a distance of 1000 feet from the target. At this distance the target normally provides a high contrast with the background and the system goes into a passive tracking mode.

It is expected that these algorithms can be stored in 50 words of 16 bit memory, and that the processing rate is 6 KOPS.

RAC-RACG. Radiometric Area Correlator and Radiometric Area Correlation Guidance utilize passive sensing of imagery in the 35 GHz band to provide position fixes through correlation with prestored reference maps. The technique provides all-weather fix-taking which may be used as an aid to IMU and LCIGS.

Two major problems exist in RAC and RACG. A fairly large memory must be provided to store reference maps, and a relatively high speed computational capability is required to do the image and map correlations. Several algorithms have been developed to perform the correlation task [1,8,9,10,]. The correlation algorithm,

$$C(k,1) = \frac{(\underline{R}_{k,1}\ \underline{S})^2}{\left\|R_{k,1}\right\|^2 \left\|S\right\|^2}, \qquad (19)$$

where $\underline{R}_{k,1}$ is a 32^2 array within a 64^2 reference array, with $R_{k,1}$ the common element of the arrays, and

$\underline{S}$ is the sensed array, indicates a match where $C_{k,1}$ is a maximum.

The sequential similarity detection algorithm, given by

$$d(k,1) = \frac{1}{IJ} \sum_{i=0}^{I-1} \sum_{j=0}^{J-1} \left| (R_{k+1,\ 1+J} - S_{ij} - \frac{1}{IJ} (\hat{R}_{k,1} - \hat{S}) \right|, \qquad (20)$$

$$\text{where } \hat{R}_{k,1} = \sum_{i=0}^{J-1} \sum_{j=0}^{J-1} R_{k+i,\ i+j},$$

$$\text{and } \hat{S} = \sum_{i=0}^{I-1} \sum_{j-0}^{J-1} S_{ij}$$

and $I = J = 32$, indicates a match where $d(k,1)$ is a minimum. Implementing either algorithms (19) or (20) on a processor having 5 μsec

add time [20], it is estimated that one correlation for a complete map of 32^2 elements can be completed in approximately 26 seconds. Optimization and the use of a higher speed processor, or a multiprocessor, could reduce this correlation time by a factor of ten or more.

RACG, the RAC-aided SINS, provides for greater accuracy with all-weather, stand-off capability. RACG must provide additional functions in the navigation subsystem, including alignment, horizontal navigation, Kalman filtering, and SINS transformation. These functions are estimated to require approximately 25% more processing time for a total time of 31 seconds per correlation fix. The memory requirement has been estimated at 8K words, 16-bits per word. The processing rate is 30 KOPS for this correlation time. With a higher speed processor, the processing rate is estimated at 420 KOPS, resulting in a correlation time of 2.6 seconds[1].

RADAR. The Radio Detection and Ranging sensor system is provided with magnetic-tape-stored synthetic aperture radar imagery, pre-recorded in the 70 to 95 GHZ range. The radar-equipped missile navigates on its own by taking sequential position fixes from correlations of its own radar image with the stored SAR imagery. At lock-on, the radar tracks the contrast point, using angle information from the seeker gimbals to direct the missile to the target.

Correlation algorithms which have been considered for the radar sensor include product correlation coefficient (PCC) and mean absolute difference (MAD)[21]. The reference scene is compared point-by-point to the "live" scene, and the best match selected at the extremum of the coefficient. Results for the two algorithms have been nearly equivalent for a large number of independent elements in the correlated scene and a moderate signal-to-noise ratio, but insufficient experience has been gained to make a clear choice between the two algorithms.

Estimates for the computational load with the PCC coefficient indicate that 65 KOPS would provide a two-dimensional correlation for a 32^2 element map. Memory requirement has been determined as 9K words, 16-bits per word. The MAD coefficient computational load is estimated at 15 KOPS with a 5K word, 16-bit memory requirement.

TERCOM. The TERrain COntour Matching sensor is a multi-mode device which correlates "live" terrain information derived from a barometric altimeter, from a radar, or from a passive radiometer, with stored terrain profiles to establish position. The system is an all-weather sensor, and visibility or time of day have only slight effect on its operation. Prior knowledge of the terrain over which an alignment is to occur can be obtained from sources such as topographic maps or stereo photographs.[22]

Assuming that algorithms comparable to those used for radar correlations are applicable, the processing requirements would be similar to those for radar, or about 65 KOPS and 9K, 16-bit memory.

CONCLUSIONS AND RECOMMENDATIONS

Processing requirements have been estimated for the several sensor and navigational subsystems in DGWT in terms of computational rate and memory size. A portion of these results is summarized in Table 2. It should be noted that most of the algorithms and associated coding have not been optimized. Further reduction in processor load may be possible when several systems are used in combination in a given weapon, such as EO/DME/DL, RAC/IMU, and RAC/LCIGS. One of the problems in making estimates of processing load is that many systems still are under development. Allowances have been made where possible to provide for anticipated system growth.

Table 2
Digital Processing Requirements
(estimated)

Sensor of Navigation System	Memory-16-bit Kilo-words	Processing Rate Kilo-Opers/second
ARS	.07	60
DME	.16	8
EO	2.60	2000
GPS	40.00	300
IIR	2.00	1300
IMU	3.00	240
LASER	.05	3
LORAN	.25	10
MCG	.05	6
RACG	8.00	420
RADAR	9.00	65
TERCOM	9.00	65

The objective in this study of digital processing requirements for guided weapons has been to provide a basis for designs, such as a multi-processor or distributed processor, to be implemented if possible with commercial microprocessors.

Factors which favor the use of microprocessors include: Much software has already been developed, including utility programs, higher-level language, cross-assemblers, interpreters, and compilers. Both hardware and software development aids are offered for microprocessor systems. Cost trends are favorably downward for microprocessors, and the presence of competition will aid in obtaining better service.

Alternatively, penalties or disadvantages may result with the use of commercial microprocessors: Processing speed may be reduced until faster LSI technology becomes available. This problem can be overcome to some degree with the use of parallel, multi-processor designs.

Complex executive software routines may be required to do the control and bus interfacing operations for a distributed processor system. The architecture of a commercial microprocessor may not be optimum for the missile application. Certain basic operations, e.g., storing of machine states on interrupts, may be realized through execution of software, but the result is that control will be slower, and additional memory will be needed to store routines. High speed multiply, divide, and floating point arithmetic are not normally available with microprocessors. This added hardware or software will increase cost.

Several important project proposals already being undertaken by the Air Force would employ the distributed processor concept. Efforts such as GPS, LCIGS, and RACG are significant portions of the overall DGWT program. Extension of the consideration of distributed processing for other sensors appears advisable. Otherwise, the concurrent realization of a centralized digital processor and distributed processing for some sensors may result in over design of the weapon control system.

Further study, including cost analyses, is indicated to fully explore the potential use of microprocessors in digital weapons. The system integration problem, including design of appropriate interfacing and executive software, should be thoroughly examined for the distributed processor design. The worst case seeker and navigation system combinations should be examined for optimization of processing and memory loads. Actual design should be carried out for several of the most difficult systems, such as EO, IIR, IMU/LCIGS, to assess problems, feasibility, and costs of distributed processing for the DGWT program.

REFERENCES

1. "Digital Guided Weapons Technology" Report Nos. DGWT 0120-1, 0120-2, 0120-3, 0120-4, 0120-4A, 0120-5, Hughes Aircraft Co., Canoga PK CA, Jan 1975 - May 1976.

2. "Configuration Specification for A Digital Guided Weapon Flight Control Module", Participant's Final Report, 1976 USAF-ASEE Summer Faculty Research Program, by Charles Caldwell, August 1976.

3. "Alternate Advanced Data Link Study for MGGB" (SECRET), North American Rockwell Report NR 7LH-332, Dec 1971.

4. "Vector Method for Trilateration", TR 73-116, Armament Development and Test Center, Eglin Air Force Base, Fla., Dec 1973.

5. "Modular Weapon System Aerodynamic Configuration and Component Definition Study", Technical Report AFATL-TR-72-202, Aeronutronic Division, Philco-Ford Corp., October 1972.

6. "Aerodynamic Configuration and Component Definition Study", Vol 4 Guidance and Control, Report No. SD 25172R, Hughes Aircraft Co., Canoga Pk CA, October 1972.

7. "Feasibility Test Model EO Miss-Distance System", By E.R. Marcusen and M.L. Shechet, et al, RTD-ATL-TR-66-100, AFATL, AFSC, Eglin Air Force Base, Fla., October 1966.

8. "Reference Imagery for the Scene Matching Area Correlator" (U) by K.L. Hoffman, W.D. West, E.P. Matthews. Journal of Defense Research 1972, pp 421-445.

9. "A Fundamental Approach to Map-Matching Area Correlators", (U) RM-5308-PR, by H.H. Bailey, Rand Corp, Santa Monica CA, 1967.

10. "Reference Imagery for Correlation Guidance", NR71H-335, North American Rockwell Corp., Columbus OH, October 1971.

11. "A Position Fixing Algorithm for the Low-Cost GPS Receiver", by Noe and Myers, IEEE Transactions on Aerospace and Electronic Systems, March 1976, pp 295-7.

12. Personal discussion, Mr Dave Gardner, DLMM/AFATL, 12 Jul 76.

13. "Low Cost Inertial Guidance System", Teledyne Systems Company, North Ridge CA, Dec 75.

14. "Tactical Inertial Performance Requirements Analysis (TIPRA)", Honeywell Inc., Minneapolis MN, March 1976.

15. "Tactical Missile Midcourse Guidance", Honeywell Inc, Report F5541 (CONFIDENTIAL), Feb 1975.

16. "Inertial Navigation Systems", by Charles Broxmeyer, McGraw Hill Book Co., Inc., NY, 1964.

17. "Inertial Navigation Systems Analysis", by Kenneth R. Britting, Wiley Interscience, NY, 1971.

18. "Aided Inertial Guidance for Air-to-Surface Missiles In Flight Alignment", (CONFIDENTIAL), Report TR-145. The Analytic Sciences Corp., Reading, MA, January 1969.

19. "Radiometric Missile Guidance" (UNCLASSIFIED), Report SJ 242-7821-4, by Conners and Wilt. Sperry-Rand Corp., Clearwater, Fla., January 1975.

20. "16-Bit Processor Performs Like Minicomputer", by A. Lofthus and D. Ogden, Electronics, May 27, 1976, pp 99-105.

21. "Millimeter Radar Guidance Study", (SECRET), Technical Report AFAL-TR-73-238, Boeing Aerospace Company, Seattle, WN, Aug 1973.

22. "Terrain Correlation Analysis of Mocrowave Radiometry Image Data for Precision Re-Entry Vehicle Guidance Applications", (SECRET) by Moore, Hawthorne, Hooper and Seybold, Naval Weapons Center, China Lake CA, November 1975.

23. "Terminal Sensor Overland Flight Test Program" (SECRET), by Gilpin and Stobart. TR-SAMSO-TR-71-280 Vol. V. LTV Electrosystems, Inc., Dallas TX, 1971.

24. "Optical Area Correlator Study" (U) Weapons Division, ADTC, AFSC, Eglin Air Force Base, Fla., March 1975.

25. "Critical Item Development Specification For the Digital Processor", Code Ident 82577, DLMM/AFATL, Eglin Air Force Base, Fla., May 1976.

26. "Research and Technology Plan, FY 77-81, RCS-DLX-(A)-7402, Part II-Research Programs, Air Force Armament Laboratory, Eglin Air Force Base, Fla., October 1975, pp 17-20, 35-36.

27. "Proposal for Modular Digital Guided Weapons System", Vol I, Technical, Hughes Aircraft Co., Canoga Pk CA, June 1974.

28. "Analysis and Preliminary Design of JTIDS Integration into the F-4E Aircraft", International Telephone and Telegraph Corp., Nutley NJ, September 1975.

1976 USAF-ASEE SUMMER FACULTY RESEARCH PROGRAM
sponsored by
THE AIR FORCE OFFICE SCIENTIFIC RESEARCH
conducted by
AUBURN UNIVERSITY AND OHIO STATE UNIVERSITY

PARTICIPANT'S FINAL REPORT

INTERPRETATION OF LASER VELOCIMETER MEASUREMENTS IN TRANSONIC TURBULENT BOUNDARY LAYERS

Prepared by:	William G. Tiederman, Jr., P.E., PhD.
Academic Rank:	Professor
Department and University:	School of Mechanical and Aerospace Engineering Oklahoma State University
Assignment:	
(Air Force Base) (Laboratory) (Division) (Branch)	Arnold AFS Arnold Engineering Development Center Propulsion Wind Tunnel 4T Projects
ARO Research Colleague:	C. F. Lo, PhD.
Date:	August 20, 1976
Contract No.:	F44620-75-C-0031

INTERPRETATION OF LASER VELOCIMETER MEASUREMENTS IN TRANSONIC TURBULENT BOUNDARY LAYERS

by
William G. Tiederman, Jr.

ABSTRACT

The basic purpose of this research program was to identify methods and procedures for interpreting fluid velocities from the particle velocities measured by a laser velocimeter. Insofar as was possible, these methods were applied to LV data from the 1T wind tunnel at the Arnold Engineering Development Center in an effort to determine particle requirements and application limits for the present system and procedures in turbulent, transonic boundary layers and in regions of separated flow. The specific areas of the investigation include: (1) calculations to determine the potential magnitude of sampling bias errors upon the statistical estimates of the mean and fluctuating velocities; (2) estimates of particle sizes required for accurate measurements of root-mean-square fluctuation velocities and turbulent energy spectra; and (3) evaluation of the influence of the wall upon measurements of the velocity component normal to the wall.

The results from the sampling bias analysis show that potentially large errors (on the order of 100 ft/sec) can be made in mean velocity estimates by neglecting this effect in separated flows. Statistical estimates with weighting functions based upon simultaneous two-component measurements are very different from but as reasonable as unweighted estimates. Experiments in a known flow field with both controlled and uncontrolled particle seed need to be conducted to eliminate this ambiguity from the data analysis of naturally (uncontrolled) seeded flows.

Particle lag analyses show that much smaller particles are required for accurate measurement of the high frequency part of the turbulent energy spectra than for accurate measurement of the root-mean-square fluctuation velocities. In the 1T boundary layer, only signals from particles with diameters smaller than 0.5 micron can be used for energy spectra. One micron diameter particles are adequate for root-mean-square measurements while signals from particles with diameters two microns and larger should be eliminated from the data ensemble. There may also be problems resulting from particle migration due to lift and from damping due to the wall for distances within 0.1 inches of the wall. These difficulties would affect only statistical estimates involving the normal velocity component.

Considerations of particle dynamics such as those used here should be used to design LV experiments and to interpret the accuracy of LV measurements. It should be emphasized that the difficulties discussed in this report are generally restricted to small regions in the flow field where there are strong accelerations and large velocity fluctuations. While these effects place some limitations upon the application of laser velocimeters, they do not destroy the great potential of this instrument.

ACKNOWLEDGMENT

The support provided by the Air Force Office of Scientific Research, Air Force Systems Command, for this summer research program is gratefully acknowledged. The administrative assistance of Mr. J. Fred O'Brien, Jr. and his office at Auburn University and Dr. M. L. Laster at the Arnold Engineering Development Center is greatly appreciated.

The administrative and technical support provided by personnel of ARO, Inc. has been invaluable. I'm grateful for many fruitful discussions with a broad spectrum of the people associated with the laser velocimeter development at AEDC. I'm particularly grateful for the assistance provided by Dr. C. F. Lo and Mr. M. C. Altstatt.

NOMENCLATURE

a	particle radius
F_D	drag force on a particle
F_L	lift force on a particle
$f(\omega)$	normalized one-dimensional, fluid energy spectrum function
$f_p(\omega)$	normalized one-dimensional, particle energy spectrum function
f_u	break frequency in energy spectra
$g(\omega)$	function defined by Eq. (18)
i	index of summations
K	factor that accounts for deviations from Stokes' law drag
m	mass of the particle
m'	equivalent mass of the fluid, defined by Eq. (11)
N	number of velocity realizations
P	pressure
P_t	stagnation pressure
t	time
U	fluid velocity
$\overline{U}$	estimate of the time-average-fluid velocity component tangent to the surface
U_e	free-stream velocity
U_i	individual realization of the velocity component tangent to the surface
U_p	particle velocity
u	fluctuation fluid velocity component tangent to the surface
u'	root-mean-square fluctuation velocity component of the fluid tangent to the surface
u_p	fluctuation particle velocity component tangent to the surface
$\overline{V}$	estimate of the time-average-fluid velocity component normal to the surface

V_i	individual realization of the velocity component normal to the surface
v	fluctuation fluid velocity component normal to the surface
v'	root-mean-square fluctuation velocity of the fluid normal to the surface
v_p'	root-mean-square fluctuation velocity of the particle normal to the surface
x	coordinate tangent to the surface
x_t	horizontal space coordinate with respect to the wind tunnel
y	coordinate normal to the surface
y_t	vertical space coordinate with respect to the wind tunnel
α	defined by Eq. (14)
β	defined by Eq. (15)
μ	fluid viscosity
ρ	fluid density
ρ_p	particle density
τ	dummy variable of integration
ω	frequency
ω_i	weighting function

INTRODUCTION

In recent years the development of the laser velocimeter (LV) has proceeded at a rapid rate. At this time, the optical and electronic systems for obtaining, verifying and processing a signal are highly developed and a user has a substantial base of instrumentation expertise available to him. Consequently the LV effort at the Arnold Engineering Development Center (AEDC) has become one of applying this instrumentation technology to the test facilities. As one of the initial steps, several experiments were conducted in the 1T Aerodynamic Wind Tunnel with a two-component, dual-scatter, Bragg-cell type system with back-scatter collection (Ref. 1). Computational schemes have been developed to analyze the data from these experiments (Ref. 2) and the analysis has yielded both answers and questions. Many of the concerns center around the fact that a LV system measures the velocity of small particles entrained in the flow and, hence, one must deduce information about the fluid velocity from the particle velocities that are detected and measured by the system. This study is based upon the hypothesis that the LV system accurately determined the particle velocities in these experiments. Then, by concentrating upon the transonic turbulent boundary layer data from the 1T bump test, this study addresses questions of interpreting fluid velocities from the measured particle velocities.

The basic mode of LV operation used at AEDC and in most large wind tunnel applications is called the individual realization or counting mode (Ref. 3). This mode of operation is the natural result of a dilute concentration of particles in the fluid which is the typical situation when an airflow is "unseeded." In this case, an output signal occurs only when a particle that is sufficiently large to be detected passes through the measurement volume. Consequently the signal is discontinuous and the occurrence of an output signal is dependent upon the arrival of a particle. However, since the measurement volume or probe volume is designed to be small compared to the scales of the fluctuating fluid motion, the output signal is essentially a measurement of the instantaneous particle velocity. The nature of this output signal as a function of time is illustrated by the solid dots in Figure 1. Since the signal is discontinuous, statistical techniques must be used to estimate the desired quantities such as the time average fluid velocity. However, as also illustrated in Figure 1, the larger particles will not always be traveling at the fluid velocity.

Consequently there are two primary and generally separate aspects in the interpretation of fluid velocities from an ensemble of particle velocities. One is simply a question of particle dynamics or particle tracking. Namely, will the particles in the flow accurately follow the fluid accelerations and thereby yield accurate estimates of the instantaneous, local, fluid velocity? The second aspect is a question of whether the particle velocities measured by the LV system yield an unbiased or a biased sampling of the turbulent (fluctuating) fluid velocity. If the sampling is random and unbiased, then a regular statistical analysis of the data will yield good estimates of the mean and root-mean-square particle velocities. If the sampling is biased because some velocities are detected more frequently than others, then a suitable weighting factor(s) must be deduced and used in the statistical analysis. Both of these factors become more important in regions where the fluid fluctuations are large, such as in the region very near the wall in a turbulent boundary layer or in a region of separated flow.

The first section of the report will address the question of biased sampling. Data from both an unseparated and a separated boundary layer from the 1T bump test will be analyzed to determine the magnitude of the potential error introduced by this effect. The second section of the report will discuss particle dynamics. The discussion will center upon particle tracking in a turbulent boundary layer. Using existing analyses and typical conditions from the 1T tunnel, the ability of the naturally occurring particles to follow the fluid flow will be estimated. Comments will be made about the assumptions and information required to perform these estimates. It will be seen that the unknown and uncontrolled distribution of the particles sizes in the "natural" seed used in these experiments is a serious complication in interpreting some of the measurements.

In both sections of the report, it will be shown that there are flow conditions and regions within the transonic turbulent boundary layer for which an accurate and unequivocal estimate of the fluid velocities can be made from the LV measurements. On the other hand, there are also regions, particularly regions of separated flow, where both biased sampling and particle dynamics are critical to the interpretation of the data. Regions of separated flow are important in many applications and the LV system is the only available anemometer which can yield reasonable information about the flow field in these regions. Both pitot tubes and hot-wire anemometers are incapable of accurately measuring the reverse flow. Consequently recommendations will be made for additional experiments and procedures that will eliminate the uncertainties about the appropriate weighting factors for the statistical analysis of the data and about the adequacy of the seedparticles for following the flow.

OBJECTIVES

The basic purpose of this report is to identify the methods and procedures necessary for an accurate deduction of fluid velocities from the particle velocities measured by a laser velocimeter. Insofar as possible, these procedures were applied to the LV data from the 1T wind tunnel in an effort to define present limits of application and to identify research and development as well as operational procedures necessary to extend these present limits.

The specific objectives were to determine the effect of particle lag, particle migration, and biased sampling upon estimates of the mean velocity and the root-mean-square velocity in the nonseparated boundary layers and in the separated (reverse flow) regions of the 1T bump test.

BIASED SAMPLING

Throughout this section of the report, it will be assumed that the particles are accurately following the flow and that they are, on the average, homogeneously distributed in the fluid. With this homogeneous distribution of particles, the probability for having a particle in the probe volume is proportional to the flow rate through the probe volume. If there is an equal probability that each particle of a given size will be detected and yield a validated velocity realization, then more particles will be detected when the fluid velocity is higher than the time-average fluid velocity than when the fluid velocity is lower than the time-average velocity. This phenomenon is called biased sampling and it can lead to substantial errors in the statistical estimates of the mean velocity when the velocity fluctuations are large (Ref. 4). In Reference 4 weighting factors based upon the instantaneous velocity vector were proposed as a means for yielding corrected statistical estimates of the mean velocity. Experimental verification of these concepts has recently been provided by a series of redundant measurements in a turbulent channel flow of water with carefully controlled 5 to 10 μm seed particles (Ref. 5).

However, there is one theory that suggests that biased sampling will be either totally or partially eliminated by another compensating phenomenon. The compensating effect is based on the argument that slower particles yield a higher signal to noise ratio signal than faster particles and hence there is greater probability for detecting slow particles than fast particles (Ref. 6). This did not occur in the experiments conducted in Reference 5. However, since this effect is a strong function of the magnitude of the LV signal and the threshold settings used by the operator of the velocimeter, it cannot yet be discounted in the naturally seeded flows of the 1T bump test. In the 1T tests, one would expect a broader size distribution of particles and hence a broader range of signal amplitudes than were obtained in the channel flow of Reference 5.

Barnett and Bentley (Ref. 7) have also suggested that biased sampling is a function of the rate of arrival of the particles. There has not yet been unequivocal experimental evidence to either confirm or disprove their analysis which shows that there is no biasing when the particles are separated by times that are large compared to the time scale of the turbulent fluctuations.

Consequently, at the present time, it is largely a matter of opinion and judgment about whether or not a biasing correction should be applied to the 1T bump test data. In this report, data for a nonseparated and a separated boundary layer will be reduced using biasing corrections. These "corrected" estimates will be compared to regular statistical estimates to demonstrate the magnitude of the uncertainty that exists due to the biased-sampling issue.

The two positions within the flow field of the two-dimensional bump that will be analyzed are shown in Figure 2. At the station x_t = 14.5 inches, the boundary layer was not separated. However, as shown by the free-stream velocity profile and the pressure ratio profile in Figure 2, the second station, station x_t = 23.88 inches, was downstream of a shock, and in this case, the boundary layer was separated.

For each of these stations, the two-component velocity data were reduced by the following set of equations. Estimates of the mean velocity component parallel to the bump surface are given by

$$\overline{U} = \sum_{i=1}^{N} \omega_i U_i \Big/ \sum_{i=1}^{N} \omega_i \tag{1}$$

while

$$\overline{V} = \sum_{i=1}^{N} \omega_i V_i \Big/ \sum_{i=1}^{N} \omega_i \tag{2}$$

yields estimates of the mean velocity component normal to the bump surface. Similarly, the mean-square-fluctuation velocities are calculated from

$$(u')^2 = \overline{u^2} = \sum_{i=1}^{N} \omega_i (U_i - \overline{U})^2 \Big/ \sum_{i=1}^{N} \omega_i \tag{3}$$

and

$$(v')^2 = \overline{v^2} = \sum_{i=1}^{N} \omega_i (V_i - \overline{V})^2 \Big/ \sum_{i=1}^{N} \omega_i \tag{4}$$

while the correlation or Reynolds stress is given by

$$\overline{uv} = \sum_{i=1}^{N} \omega_i (U_i - \overline{U})(V_i - \overline{V}) \Big/ \sum_{i=1}^{N} \omega_i \tag{5}$$

By setting the weighting function

$$\omega_i = 1 \tag{6}$$

Equations 1 through 5 yield a standard statistical analysis of random, unbiased, independent data. When

$$\omega_i = 1 / (U_i^2)^{1/2} \tag{7}$$

the equations yield the one-dimensional biasing correction proposed in Reference 4. Since the exact, theoretical correction is proportional to the inverse of the magnitude of the velocity vector, a better estimate of the theoretical weighting factor, which can be calculated from these two-component measurements (Refs. 1 and 2), is given by

$$\omega_i = 1 / (U_i^2 + V_i^2)^{1/2} \tag{8}$$

As shown in Table I and Table II, the one-dimensional (Eq. 7) and the two-component (Eq. 8) weighting functions yield essentially identical estimates for the mean velocity components and the root-mean-square velocities in the nonseparated boundary layer. This is because $U_i >> V_i$ for all of the velocity realizations. There are differences between the unweighted ($\omega_i = 1$) and the weighted estimates but these are not particularly large differences. The weighted and unweighted estimates of the mean velocity components are compared in Figure 3. Lines have been sketched through the data points solely for visual purposes. Notice that the differences decrease as y_t increases. Estimates of the root-mean-square turbulence were not plotted for this station; however, as one can see by inspection from Table II, the differences between the weighted and unweighted estimates of u' and v' are not statistically significant.

TABLE I

COMPARISON OF MEAN VELOCITY ESTIMATES
GIVEN BY VARIOUS WEIGHTING FUNCTIONS
IN A NONSEPARATED BOUNDARY LAYER, STATION x_t = 14.5

y_t (inches)	N	$\bar{U}$ (ft/sec) with ω_i given by Eq. (6)	Eq. (7)	Eq. (8)	$\bar{V}$ (ft/sec) with ω_i given by Eq. (6)	Eq. (7)	Eq. (8)
.02	287	364	351	351	-17	-14	-14
.06	767	426	412	412	-25	-20	-20
.10	807	447	433	433	-26	-21	-21
.20	863	513	500	500	-39	-33	-33
0.30	858	571	560	560	-54	-49	-49
0.40	864	623	615	615	-59	-56	-56
0.50	818	666	660	660	-69	-66	-66
0.60	840	695	692	692	-74	-72	-72
0.70	833	713	711	711	-78	-77	-77
0.80	834	725	724	724	-90	-89	-89

TABLE II

COMPARISON OF ROOT-MEAN-SQUARE TURBULENCE VELOCITY ESTIMATES
GIVEN BY VARIOUS WEIGHTING FUNCTIONS IN A
NONSEPARATED BOUNDARY LAYER, STATION x_t = 14.5

y_t (inches)	N	u'(ft/sec) with ω_i given by Eq. (6)	Eq. (7)	Eq. (8)	v'(ft/sec) with ω_i given by Eq. (6)	Eq. (7)	Eq. (8)
.02	287	68	66	65	30	29	29
.06	767	76	77	77	43	43	43
.10	807	79	79	79	47	47	47
.20	863	76	80	79	51	52	52
.30	858	73	76	76	48	49	49
.40	864	64	68	68	44	45	45
.50	818	57	61	61	40	41	41
.60	840	42	44	44	33	33	33
.70	833	34	35	35	31	31	31
.80	834	26	27	27	27	27	27

The situation is dramatically different in the separated boundary layer at station x_t = 23.88 inches. The three estimates of $\bar{U}$, $\bar{V}$, and u' are shown respectively on Figures 4, 5, and 6. For all of the y_t-locations greater than 0.5 inches, there was no reverse flow and the three estimates in all three cases converge rapidly as y_t increases. However, for y_t less than 0.5 inches, there is some reverse flow and there are significant differences between the weighted and unweighted estimates as well as significant differences between the one-dimensional and two-component weighting. Notice that in all three figures, the unweighted estimates and the two-component weighted estimates yield smooth and very reasonable appearing profiles. From this inspection of the reduced data, there is no criteria that can be applied to accept or reject either the unweighted or the two-component weighted estimates of $\bar{U}$, $\bar{V}$, and u'.

The scatter in the one-dimensional weighted estimates suggests that there is a severe problem with the one-dimensional weighting when there is backflow and there is. The problem is that it is possible for

$$(U_i^2)^{1/2} << (U_i^2+V_i^2)^{1/2}$$

Since the probe volume is small compared to the scales of fluid motion, there is essentially no probability that a particle can enter the probe volume, come to rest, and then leave the probe volume. That is, the probability for measuring a zero velocity vector is zero. However, there is a good probability for measuring a zero or a near zero streamwise velocity component because particles can pass through the probe volume at angles that are at 90° to the streamwise direction. This concept has been verified by using the computer to identify all of the simultaneous data sets where either $(U_i^2)^{1/2} < 10$ or $(U_i^2 + V_i^2)^{1/2} < 50$. The number of these velocity measurements that had magnitudes below various limits are summarized in Table III for all of the positions with reverse flow. The point is that the one-dimensional weighting factor has a singularity when U_i is near zero and this situation does occur when there is reverse flow. In fact, the one-dimensional weighting factor was not allowed to exceed one for the estimates shown in Figures, 4, 5, and 6. Conversely, the two-component weighting function did not display this singularity. The minimum value detected for $(U_i^2 + V_i^2)^{1/2}$ was 6.8 ft/sec. This is contrasted to minimum a value for $(U_i^2)^{1/2}$ of 0.2 ft/sec. It is interesting to note that for the realization that yielded a minimum value for $(U_i^2)^{1/2}$, $(U_i^2 + V_i^2)^{1/2} > 50$ ft/sec. Consequently, it is possible and practical to use a two-component weighting function when there is reverse flow. Moreover, since there are significant differences between the unweighted and two-component estimates for $\bar{U}$, $\bar{V}$, and u', research should be conducted to eliminate the ambiguity about whether or not the measurements need a bias sampling correction.

TABLE III

NUMBER OF VELOCITY MEASUREMENTS WITH MAGNITUDES NEAR ZERO, STATION x_t = 23.88

y_t (inches)	Total Number of Simultaneous Data	Number Where $(U_i^2)^{1/2}$ Less Than			Number Where $(U_i^2 + V_i^2)^{1/2}$ < 10 ft/sec
		10 ft/sec	5 ft/sec	2 ft/sec	
0.02	168	5	3	1	3
0.05	472	6	5	4	0
0.10	347	6	4	2	0
0.15	525	13	8	4	0
0.20	445	8	4	1	0
0.25	374	11	7	4	0
0.30	471	4	1	1	0
0.35	660	1	0	0	0
0.40	712	3	3	2	0
0.45	715	1	1	1	0

PARTICLE DYNAMICS

The analysis for particle motion in a laminar flow field begins with an equation that is similar to the following (Ref. 8).

$$m\frac{dU_p}{dt} = 6\pi\mu a K(U-U_p) - \frac{m'}{\rho}\frac{dP}{dx} - \frac{m'}{2}\left[\frac{dU_p}{dt} - \frac{dU}{dt}\right] - 6a^2(\pi\mu\rho)^{1/2}\int_{t_0}^{t}\frac{d(U_p-U)}{d\tau}\frac{d\tau}{(t-\tau)^{1/2}} \quad (9)$$

Here

$$m = 4/3\ \pi a^3\rho_p \quad , \quad m' = 4/3\ \pi a^3\rho \quad (10)\ \&\ (11)$$

and K is a factor that accounts for deviations from Stokes' law drag.

It is instructive to carefully inspect Eq. (9) from the position of a LV operator who has information about the particle velocities rather than information about the flow field. We will do this inspection for the simplest form of Eq. (9) that is of interest. When the particle density is much greater than the fluid density, as it is for particles in an air flow, the second and third terms on the right-hand side of the equation are small and can be neglected (Refs. 9 and 10). When the particles are sufficiently small, the fourth term is also negligible. The resulting equation, which has been used (e.g., Refs. 11 and 12) for studying particle lag in regions of

strong acceleration in laminar flow, may be rewritten as

$$\frac{dU_p}{dt} = \frac{q}{2}\frac{\mu}{a^2}\frac{K}{\rho_p}\left[U - U_p\right] \tag{12}$$

Therefore, even when K = 1, one must measure the particle velocity, the particle acceleration, the particle size, and the particle density before one can use Eq. (12) to solve for the fluid velocity. The LV system yields the particle velocity and there is currently under development at AEDC additional instrumentation that will potentially yield particle size, in the range of interest, from the LV signal. (The particle size measurement is based upon the visibility function concept, Reference 13.) With the current LV systems, the particle acceleration must be deduced from spatial distributions of the particle velocity. In naturally seeded flows, variations in particle size and particle density will yield dispersions in the particle velocity at each point in the flow. Therefore, the particle velocity would have to be measured for the same particle at two closely spaced points in the flow before the acceleration of the particle could be accurately estimated. The complexity of two velocity measurements, at least one particle size measurement plus a particle density estimate for each particle, makes this approach for deducing fluid velocity impractical.

Instead, the approach which has been used with success (Ref. 5) and which could be substantially improved with simultaneous particle size measurement is the following. Using conservative estimates about the flow field and particle density, one can use a particle motion analysis to determine the size of particles that will follow prescribed (conservatively estimated) fluid accelerations with an acceptable accuracy. Then, either the particles that are too large must be physically eliminated from the seed, or the particle size measurement must be used to reject signals from particles that are too large to follow the fluid accelerations and fluctuations. Of course, there will be regions where all of the particles that are detectable with the LV system will not follow the flow, such as near a strong shock wave. However, outside of these regions that could be conservatively defined by analysis, the LV signals from the particle sizes determined to be acceptable from the analysis would yield accurate estimates of the local fluid velocity. Rejection of signals from particles that are too large or elimination of these large particles from the seed population will be required before accurate fluid measurements will be obtained near any region of strong acceleration, large fluctuations, or severe streamline curvature.

This latter approach is the technique that must be used in all turbulent flows because the random nature of the flow field and particle motions make the first approach even more impractical. Particle motion in turbulent flows is discussed in References 8-10 and 14-17. The basic approach in all seven references is similar, however, Berman (Ref. 8) provides the best description of the assumptions and the application of the analysis to a turbulent flow field. As discussed by Berman, two additional terms must be added to Eq. (9) before it will describe the motion of a particle in a fluctuating velocity field. However, by neglecting any possible influence of walls and by neglecting terms that are small for the particles and flows of interest in LV applications, the differential equation that is used to model the particle motion in turbulent flows is normally some variation of

$$\frac{dU_p}{dt} = \beta\frac{dU}{dt} + \alpha\beta K\left(U - U_p\right) + \beta\left(\frac{3\alpha}{\pi}\right)^{1/2}\int_{-\infty}^{t}\frac{d\left(U - U_p\right)}{d\tau}\frac{d\tau}{(t-\tau)^{1/2}} \tag{13}$$

where $$\alpha = \frac{3\mu}{\rho a^2} \tag{14}$$

and $$\beta = 3\rho/(2\rho_p + \rho) \tag{15}$$

Solutions for fluctuations about the mean motion are sought and the fluid velocity is given by $U = u \sin \omega t$ (Eq. 16). That is, the problem is posed in terms of motion relative to the time-average motion of the fluid.

A basic assumption required in the derivation of Eq. (13) is that the particle path line and the fluid streamline correspond. As discussed by Soo (Ref. 9) this is not true. However, if a distinction is made between the particle path line and the fluid streamline, the problem is intractable (Refs. 8, 9, and 14). One analysis (Ref. 16) uses an ad hoc method for relaxing this assumption and this will be discussed later. The important point is that Eq. (13) and the analysis for turbulent fluctuations represent the particle motion from a Lagrangian point of view.

The basic concern for LV operation is that a turbulent flow consists of a broad range of fluid fluctuations and the question is whether or not the particles will adequately follow the higher frequency fluctuations. The question is somewhat more subtle than it first appears. If one is interested in deducing the mean-square-fluid fluctuation velocity, then it is related to the mean-square-particle fluctuation velocity by

$$\overline{u_p^2} = \overline{u^2} \int_0^\infty g(\omega) f(\omega) \, d\omega \tag{17}$$

Here, $g(\omega) = u_p^2(\omega)/u^2(\omega)$ (Eq. 18) is obtained from the solution of Eq. (13). The function $f(\omega)$ is a normalized, one-dimensional energy spectra of the fluid fluctuations. Since the analysis for the particle motion is basically a Lagrangian formulation, the most accurate energy spectrum to use with this analysis would be a Lagrangian spectrum. However, Lagrangian spectra have not been measured and therefore Eulerian spectra must be used. These Eulerian spectra probably provide a conservative estimate of the relative fluid fluctuations seen by the particle.

It is also important to note that the Eulerian one-dimensional energy spectra decrease at a very rapid rate as ω increases. As an approximation, Berman (Ref. 8) described $f(\omega)$ as a constant for frequencies below f_u, and for frequencies greater than f_u, he assumed that $f(\omega) \sim \omega^{-2}$ (Eq. 19). Although Berman proposed this approximation for turbulent jets, it is also a reasonable approximation for boundary layers.

It will be assumed that Klebanoff's measurements of one-dimensional energy spectra in a subsonic boundary layer (see Ref. 14, p. 652) are representative of the fluctuations in the 1T boundary layer. Using these spectra, one concludes that f_u is about 2½kHz when the local velocity is 300 m/s and that Berman's analysis and results for particle motion in a jet (Ref. 8) are applicable. These results indicate that for 1 μm diameter particles there will be a negligible difference between $\overline{u_p^2}$ and $\overline{u^2}$. However, there will be a significant difference (on the order of 10 to 20 percent) for 2 μm diameter particles.

The situation is considerably different for LV measurements of the energy spectra itself. In this case, the energy spectrum function for the particles is given by (see Ref. 9)

$$f_p(\omega) = \left(\overline{u^2}/\overline{u_p^2}\right) g(\omega) f(\omega) \tag{20}$$

Thus, $f_p(\omega) = f(\omega)$ only when $g(\omega) = 1$. As shown in Reference 16, particles with diameters less than 0.5 μm are required to meet this requirement for frequencies on the order of 20kHz. Measurements at these frequencies would be required to yield a reasonable definition of $f(\omega)$ in the 1T boundary layers.

While some of the other analyses use different spectra and different relationships for the viscous drag, the conclusions are basically the same. In Reference 16, an ad hoc attempt is made to account for the differences between the particle path line and the fluid streamline. The results from this part of Reference 16 do yield different results. However, these results are unrealistic for low frequency fluctuations.

Common to all current analyses of particle motion in turbulent flows is the assumption that the particles are small compared to the size of the smallest eddy of turbulent motion. The major consequence of this assumption is that it allows one to neglect lift forces on the particle due to rotation of the particle relative to the fluid. The additional assumption implicit to this reasoning is that within an eddy the velocity gradients are small. These assumptions require closer inspection for the region very near the wall where the eddies are severely stretched in the streamwise direction. Therefore, estimates of the ratio between the lift and drag forces on a spherical particles have been made by assuming that the particle rotation is equal to one-half of the fluid velocity gradient. The maximum velocity gradient was estimated to be 5×10^5 $(\text{sec})^{-1}$ (about twice the value for the gradient of the time-average velocity at the wall). Representative fluid properties were estimated by using measured stagnation conditions and by assuming that the flow was isentropic. In particular

$$\rho = 0.07 \ \text{lb}_m/\text{ft}^3 \tag{21}$$

and

$$\mu = 1.3 \times 10^{-5} \ \text{lb}_m/(\text{sec ft})$$

A complicating feature of this analysis is that there are two significantly different theoretical results for the lift force when a particle is in the Stokes flow regime. The analysis of Rubinow and Keller (Ref. 18) gives

$$\frac{|F_L|}{|F_D|} = \frac{\frac{1}{2}\frac{dU}{dy} a^2 \rho}{6\mu} \tag{22}$$

However, the analysis of Saffman (Ref. 19) yields

$$|F_L|/|F_D| = (81.2/6\pi)\left(\tfrac{1}{2}\frac{dU}{dy}\frac{a^2\rho}{\mu}\right)^{1/2} \tag{23}$$

The data of Jeffrey and Pearson (Ref. 20) tend to support Rubinow and Keller's result but the experiments were not totally conclusive. Equation (22) yields ratios of lift to drag that vary from 6×10^{-5} for 1 μm diameter particles to 1.5×10^{-3} for 5 μm particles. However, Eq. (23) gives ratios of lift to drag that vary from 8.2×10^{-2} for 1 μm diameter particles to 0.16 for 2 μm particles and to 0.4 for 5 μm particles. Therefore, if Saffman's analysis is correct, there will be significant lift forces on particles larger than 2 μm in the high velocity gradient near the wall ($y_t < 0.1$ inches). This would bias the measurements of the velocity component normal to the wall in this region. However, this effect will be confined to a thin region near the wall because the fluid velocity gradient decreases rapidly as y_t increases.

16

Of all the analyses of particle motion in turbulent flows, only the one due to Soo and Tien (Ref. 21) considers the effect of the wall upon the particle motion. Since this analysis is based upon the inviscid, potential flow, solution of the fluid motion induced by a particle moving near a wall, it is most appropriately used to estimate the effect of the wall upon the velocity component of the particle normal to the wall. Their solution for the ratio of the normal components of the mean-square fluctuation fluid velocity is a function of the fluid viscosity and density, particle size and density, distance of the particle from the wall, mean-square-fluctuation fluid velocity normal to the wall and the Lagrangian microscale of the fluid motion. With the exception of the Lagrangian microscale, all of the variables can be either specified or estimated with reasonable accuracy. The difficulty with estimating the Lagrangian microscale is discussed in Reference 14 (pp 416-427). Following various suggestions in Reference 14, three different estimates of the microscale were made. These include: 1) Setting the microscale equal to the distance of the particle from the wall (minimum distance used was 0.001 ft); 2) Assuming that the Lagrangian integral scale is equal to the measured boundary layer thickness; and 3) Using one-dimensional energy spectra from an incompressible flat plate boundary (Ref. 14, p 652) to estimate the Eulerian integral scale (Ref. 14, p 65). The Lagrangian and Eulerian integral scales are then assumed to be equal. The last two approaches require a relationship between the Lagrangian microscale and the Lagrangian integral scale. This was obtained from the analytical approximation for the Lagrangian power spectrum function used by Soo and Tien (Ref. 21). The conclusions based upon predictions for 1 μm diameter sand particles in the 1T boundary layers depend somewhat upon the method used to estimate the Lagrangian microscale. Using methods 2) and 3) above, one predicts that the wall will not affect the particle motion and that $v_p' = v'$. However, using method 1), one predicts that there will be a significant effect upon measurements within distances on the order of 0.001 ft. from the wall. For distances greater than 0.01 ft., method 1) also predicts that $v_p' = v'$.

Consequently, these considerations of particle lift and interaction with the wall yield the conclusion that there is no special difficulty with particle tracking caused by the wall in the 1T bump tests until the probe volume is less than 0.1 inches from the surface. It should be emphasized that these concerns for particle tracking within 0.1 inches from the wall are based on conservative engineering estimates and that they are restricted to measurement of statistical quantities involving the velocity component normal to the wall.

This analysis of particle tracking has not considered situations where the streamline curvature is large. Additional consideration needs to be given to this problem.

CONCLUSIONS AND RECOMMENDATIONS

The analysis of biased sampling showed that there are differences between using weighted estimates derived to correct for biased sampling and unweighted estimates for the mean and root-mean-square fluctuation velocity components. The differences are relatively small for the unseparated boundary layer; however, the differences become quite large in the separated region. Moreover, close inspection of the two-component weighting function showed that it does not have the singularity displayed by the one-dimensional weighting function when the histogram includes both negative and positive

velocities. Therefore, it appears to be practical to use the simultaneous two-component measurements to calculate weighted estimates of the velocity functions in any situation. Definitive experiments are now needed to determine whether two-component weighted estimates or unweighted estimates should be used in the wind tunnel flows. The experiments should determine whether or not biased sampling is a function of particle arrival rate and whether or not the higher probability for detecting slow particles compensates for biased sampling in naturally seeded flows. Until these experiments are conducted, there will be a small ambiguity in the estimates within the unseparated boundary layer and a large ambiguity in the estimates of the velocity statistics within separated regions of flow. It should be emphasized that the LV offers a unique opportunity for making measurements within separated regions.

Inspection of the equations for particle motion indicates that it is impractical to measure enough information about each particle to deduce fluid velocity from a particle distribution in which some particles do not adequately follow the fluid accelerations and fluctuations. Therefore, it is recommended that either (1) the seed should be controlled so that the large majority of the particles adequately follow the flow, or (2) a particle size measurement should be used to reject signals from the particles that are too large. An analysis of the particle motion in a prescribed (conservatively estimated) flow field can yield estimates of the required particle sizes.

The analysis for particle motion in turbulent flows indicated that accurate measurements of the root-mean-square fluctuation velocities can be made in the 1T boundary layers when the scattering particles are less than or equal to 1 μm in diameter. Signals from particles 2 μm in diameter and larger should be eliminated or rejected from the data ensemble. Particles smaller than 0.5 μm are required for an accurate determination of the energy spectra.

The analysis also showed that there may be a problem with particle migration due to lift forces and a problem due to the damping effect of the wall itself for positions within 0.1 inches of the wall. These two problems could affect all of the velocity statistics involving the velocity component normal to the wall. Statistical estimates involving the velocity component tangent to the wall should not be affected. Due to the rather large uncertainties involved in the analysis, it is recommended that experiments with controlled seed be conducted to verify the assumptions in these analyses.

Considerations of particle dynamics such as those used here should be used to design LV experiments and to interpret the accuracy of LV measurements. It should be emphasized that the difficulties discussed in this report are generally restricted to small regions in the flow field where there are strong accelerations and large velocity fluctuations. While these effects place some limitations upon the application of laser velocimeters, they do not destroy the great potential of this instrument.

14

REFERENCES

1. Cline, V. A. and Lo, C. F., "Application of the Dual-Scatter Laser Velocimeter in Transonic Flow Research." Proceedings of the AGARD Symposium on Application of Non-intrusive Instrumentation in Fluid Flow Research, Saint-Louis France, May 1976.

2. Lo, C. F. and Heltsley, F. L., "Interpretation of Laser Velocimeter Measurements in a Transonic Flow Field." Twenty-second ISA Aerospace Instrumentation Symposium, May 1976.

3. Donohue, G. L., McLaughlin, D. K., and Tiederman, W. G., "Turbulence Measurements with a Laser Anemometer Measuring Individual Realizations." Physics of Fluids, Vol. 15, No. 12, December 1972, pp 1920-1926.

4. McLaughlin, D. K. and Tiederman, W. G., "Biasing Correction for Individual Realization Laser Anemometer Measurements in Turbulent Flows." Physics of Fluids, Vol. 16, No. 12, December 1973, pp 2082-2088.

5. Quigley, M. S., "Experimental Evaluation of Sampling Bias in Individual Realization Laser Anemometry." M.S. Thesis, School of Mechanical and Aerospace Engineering, Oklahoma State University, 1975.

6. Durst, F. and Whitelaw, J. H., "Theoretical Considerations of Significance to the Design of Optical Anemometers." ASME Paper No. 72-HT-7, Presented at ASME Heat Transfer Conference, August 1972.

7. Barnett, D. O. and Bentley, H. T., III, "Statistical Bias of Individual Realization Laser Velocimeters." Proceedings of the Second International Workshop on Laser Velocimetry, Purdue University, West Lafayette, Indiana, March 1974.

8. Berman, N. S., "Particle-Fluid Interaction Corrections for Flow Measurements with a Laser Doppler Flowmeter." NASA-CR-124254 (N73-23379), 1969.

9. Soo, S. L., Fluid Dynamics of Multiphase Systems, Blaisdell Publishing Company, Waltham, Massachusetts, 1967, pp 15-51.

10. Hjelmfelt, A. T. and Mockros, L. F., "Motion of Discrete Particles in a Turbulent Fluid." Applied Science Research, Vol. 16, 1966, pp 149-161.

11. Asher, J. A., Scott, P. F., and Wang, J. C., "Parameters Affecting Laser Velocimeter Turbulence Spectra Measurements." AEDC-TR-74-54, October 1974

12. Hsieh, T., "Analysis of Velocity Measurements about a Hemisphere-Cylinder Using a Laser Velocimeter." Submitted for Publication in the AIAA Journal, 1976.

13. Farmer, W. M., "The Interferometric Observations of Dynamic Particle Size, Velocity and Number Density." Ph.D. Dissertation, University of Tennessee, March 1973.

14. Hinze, J. O., Turbulence, Second Edition, McGraw-Hill Book Company, New York 1975, pp 460-471.

15. Maxwell, B. R. and Seasholtz, R. G., "Velocity Lag of Solid Particles in Oscillating Gases and in Gases Passing Through Normal Shock Waves." NASA TN D-7490, March 1974.

16. Khosla, P. K. and Lederman, S., "Motion of a Spherical Particle in a Turbulent Flow." PIBAL Report No. 73-22 (AD 779541) Polytechnic Institute of New York, November 1973.

17. Berman, N. S., "Fluid Particle Considerations in the Laser Doppler Velocimeter." Workshop on the Theory and Application of Laser Doppler Anemometers, Oklahoma State University, June 1973.

18. Rubinow, S. I. and Keller, J. B., "The Transverse Force on a Spinning Sphere Moving in a Viscous Fluid." Journal of Fluid Mechanics, Vol. 11, 1961, p 447.

19. Saffman, P. G., "The Lift on a Small Sphere in a Slow Shear Flow." Journal of Fluid Mechanics, Vol. 22, 1965, p 385.

20. Jeffrey, R. C. and Pearson, J. R. A., "Particle Motion in Laminar Vertical Tube Flow." Journal of Fluid Mechanics, Vol. 22, 1965, p 721.

21. Soo, S. L. and Tien, C. L., "Effect of the Wall on Two-Phase Turbulent Motion." Journal of Applied Mechanics, Vol. 27, Series E, March 1960, pp 5-15.

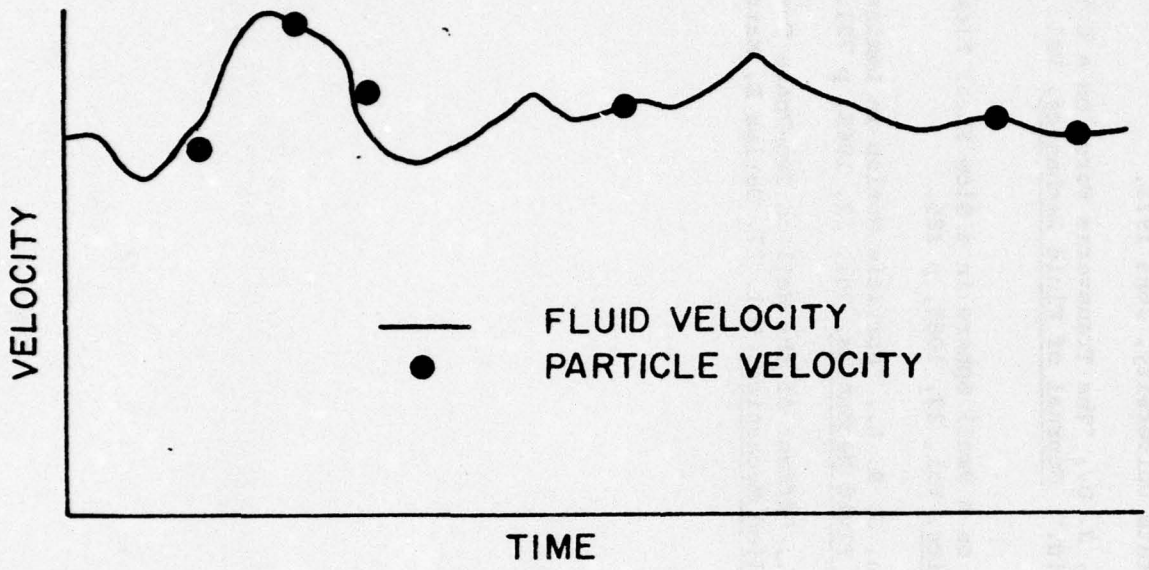


FIGURE 1. SCHEMATIC COMPARING FLUID VELOCITIES AND PARTICLE VELOCITIES

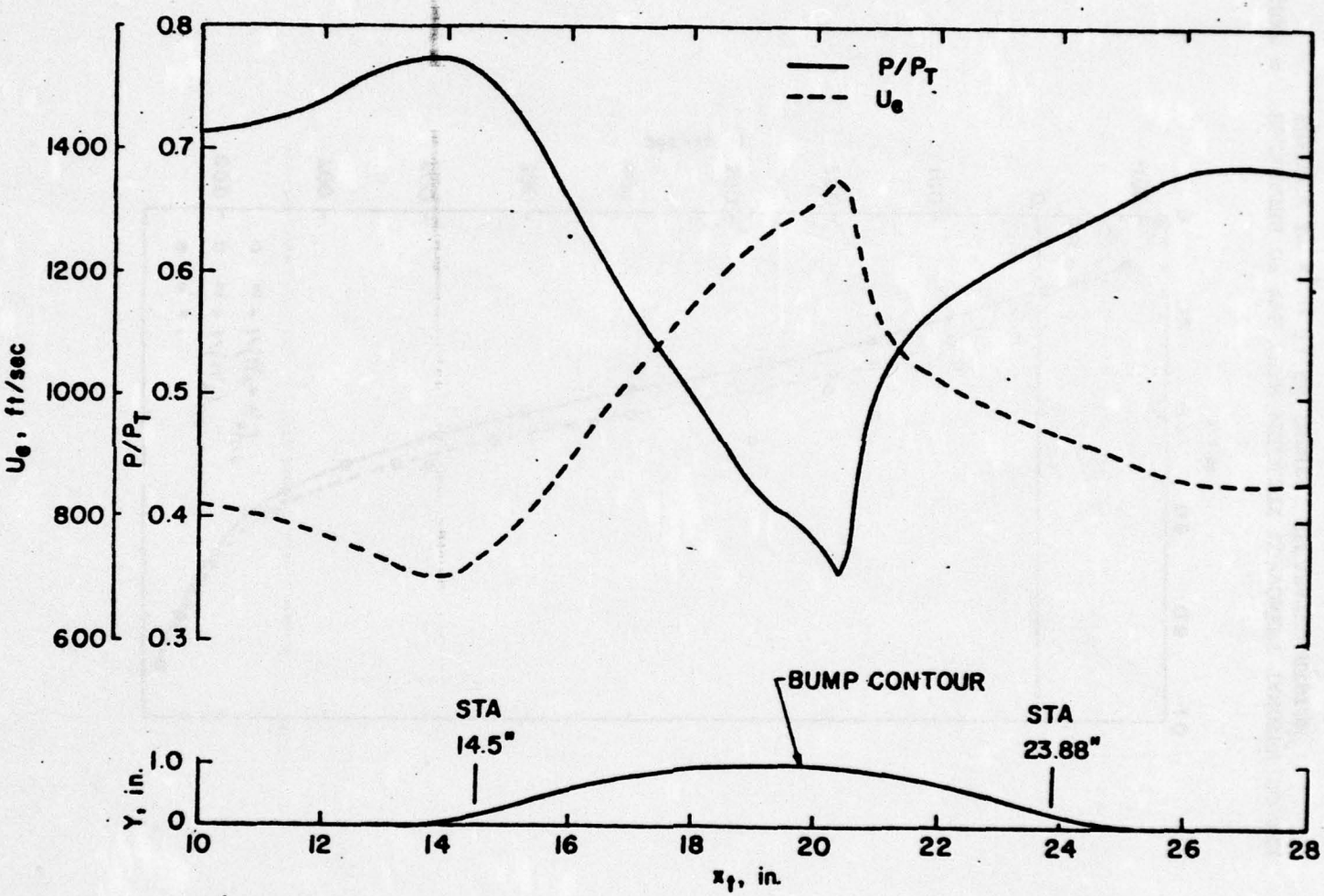


FIGURE 2. MEASUREMENT STATIONS, BUMP CONTOUR, AND FREE-STREAM PROFILES OF VELOCITY AND PRESSURE RATIO FOR THE 1T BUMP TESTS

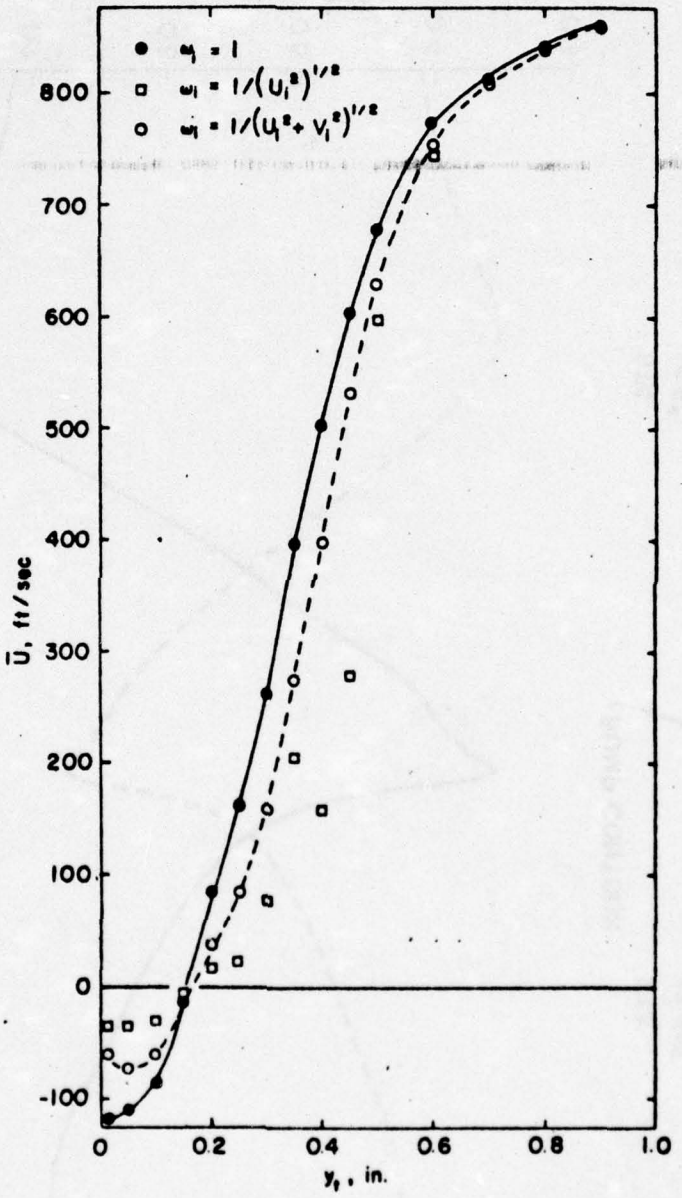


FIGURE 4. ESTIMATES OF THE MEAN VELOCITY COMPONENT TANGENT TO THE SURFACE AT x_t = 23.88 INCHES, SEPARATED REGION

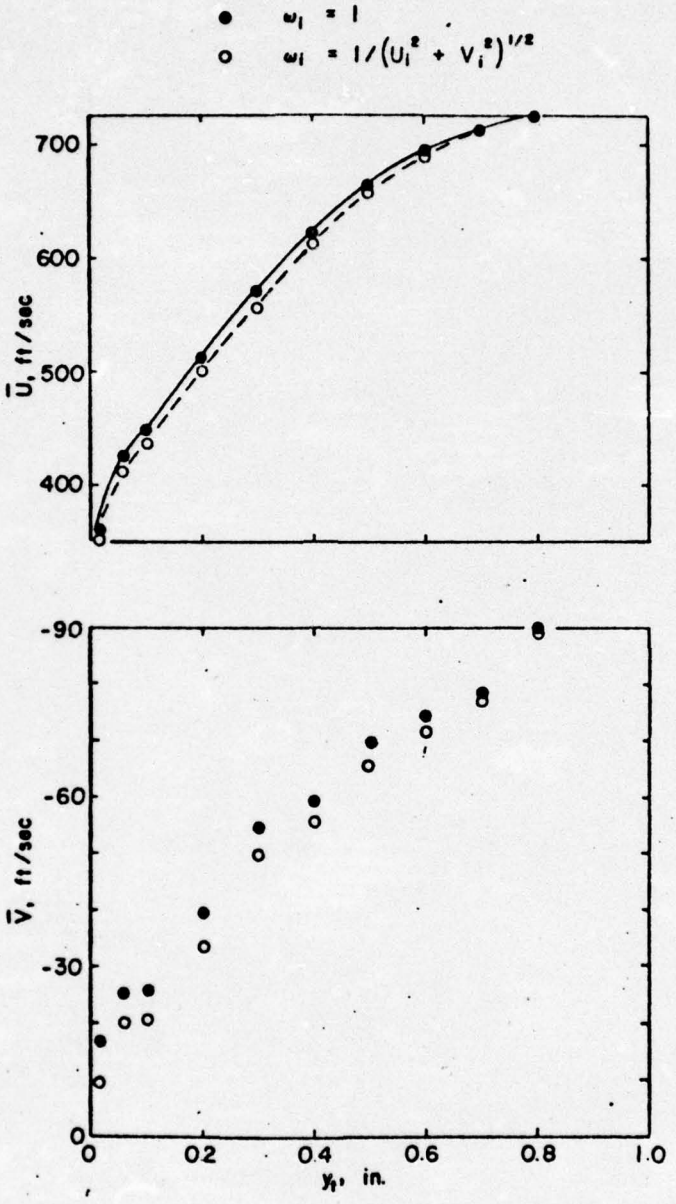


FIGURE 3. ESTIMATES OF THE MEAN VELOCITY PROFILES AT x_t = 14.5 INCHES, NONSEPARATED BOUNDARY LAYER

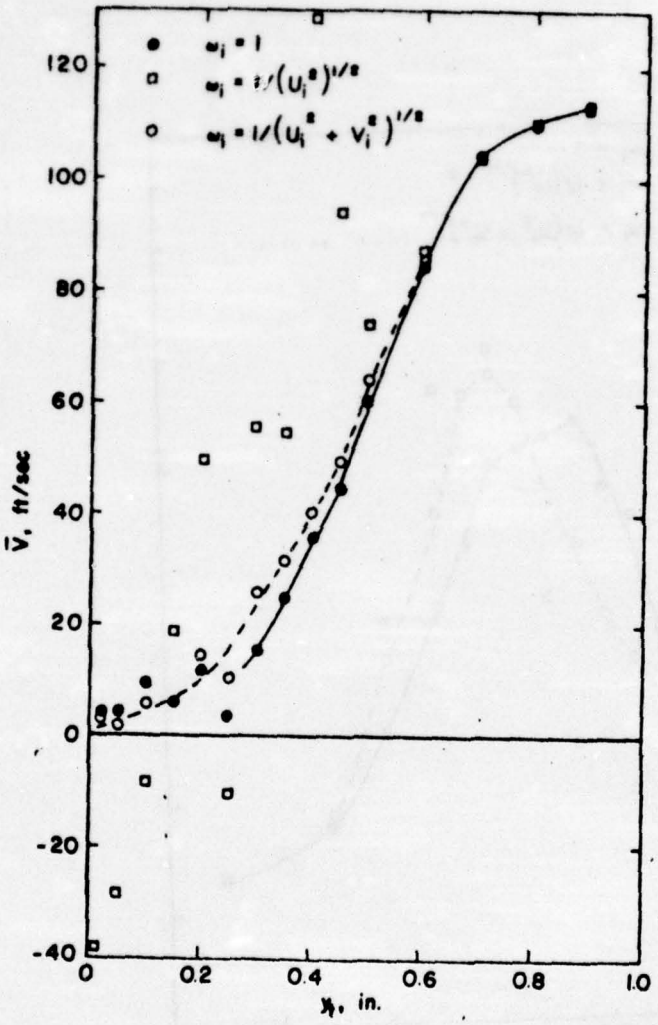


FIGURE 5. ESTIMATES OF THE MEAN VELOCITY COMPONENT NORMAL TO THE SURFACE AT x_t = 23.88 INCHES, SEPARATED REGION

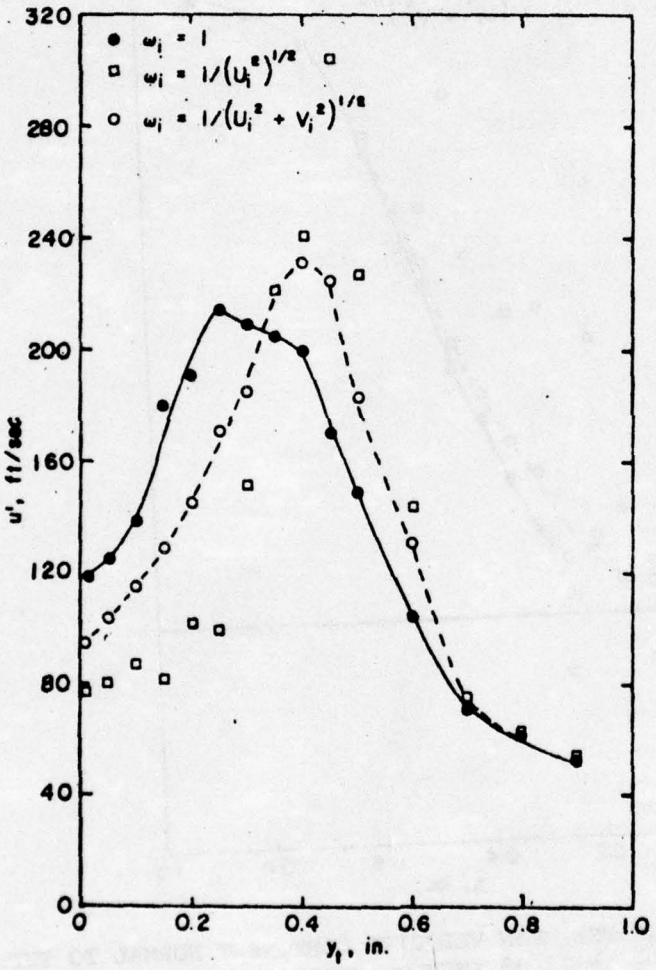


FIGURE 6. ESTIMATES OF THE ROOT-MEAN-SQUARE FLUCTUATION VELOCITY COMPONENT TANGENT TO THE SURFACE AT x_t = 23.88 INCHES, SEPARATED REGION

1976 USAF-ASEE SUMMER FACULTY RESEARCH PROGRAM
sponsored by
THE AIR FORCE OFFICE OF SCIENTIFIC RESEARCH
conducted by
AUBURN UNIVERSITY AND THE OHIO STATE UNIVERSITY

PARTICIPANT'S FINAL REPORT

METHODS TO QUANTIFY CONSTITUENTS IN BINARY COMPONENT CRYODEPOSITS

Prepared by:	Kent F. Palmer, Ph.D.
Academic Rank:	Assistant Professor
Department and University:	Department of Physics and Astronomy University of Kentucky
Assignment:	
(Air Force Base) (Laboratory)	Arnold Air Force Station Arnold Engineering Development Center
(Directorate) (Division)	Technology Research and Development
USAF Research Colleague:	Herman E. Scott, Ph.D.
Date:	August 13, 1976
Contract No.:	F44620-75-C-0031

METHODS TO QUANTIFY CONSTITUENTS

IN BINARY COMPONENT CRYODEPOSITS

by
Kent F. Palmer

ABSTRACT

Determination of the molecular composition of cryodeposits is a technical requirement of many research areas of interest to the Air Force, including investigations of the degradation of sensor optics performance and plume contamination studies. The first step towards establishing an analysis technique for multicomponent cryodeposits is the development of a method for finding the concentration of molecular species in a two-component cryodeposit.

In this study, several methods are examined for finding the concentrations of the infrared active molecular species in binary component cryodeposits. The methods depend on known accurate values of the real and imaginary refractive indices throughout the infrared spectrum. These indices must be obtained from the cryodeposit being analyzed and from cryodeposits used as standards for the various molecular species involved. A preliminary examination of the methods, using existing data, indicates that methods which incorporate the measured strengths of absorption bands would be the most reliable in determining species concentration.

The techniques for obtaining accurate values of the indices of cryodeposits are discussed. The importance of more optical data, both infrared and Raman, is stressed, and recommendations concerning future experiments are given.

ACKNOWLEDGEMENT

The author is sincerely grateful to the Air Force Systems Command for their enthusiastic support of this program for summer research, and to ASEE and Auburn University for their sponsorship. It is a pleasure to acknowledge the superb administrative abilities of Mr. Fred O'Brien and Dr. Lynn Laster.

The author is especially indebted to Dr. Herman Scott for his guidance and advice, and for his considerable efforts in obtaining the resources the author needed.

The help and kindnesses extended to the author by employees of ARO, Inc. is deeply appreciated. In particular, Dr. A. M. Smith, Dr. Jeff Roux, Mr. Bob Wood, Mr. Bill Kirby, Mr. Lee Hornbuckle, and Mr. George Lewis should be singled out for their assistance. Finally, the author thanks Ms. Janet Burks for her typing of this report.

INTRODUCTION

When gas molecules come into contact with a cryogenic surface, those molecular species which normally exist in the liquid or solid state at the temperature of the surface and at that ambient pressure will condense in the same manner that water frost forms on a cold window. Condensing rocket exhaust products and residual atmospheric gases can form solid films on cryosurfaces cooled to temperatures like those of liquid nitrogen (77K) or gaseous helium (20K). These solid films are termed cryodeposits and may affect the performance of onboard spacecraft equipment. If cryodeposits form on cooled surfaces of infrared (IR) sensors, the interference and absorptive properties of the cryodeposits can seriously degrade the sensitivity of the sensor (Ref 1).

The optical properties of cryodeposits depend on the species and concentration of the molecules contained in the film. The expectation that measurement of the optical properties of a cryodeposit will provide the information needed to identify the molecular species in the film and their concentration is the impetus for this work. For example, a cryosurface may be placed at a point in an environmental test chamber where analysis of the composition of the gases present is desired. Samples of interest include exhaust products, outgassing products, chamber contaminants, and atmospheric species. If an IR beam is reflected from or transmitted through the cryosurface and an adhering cryodeposit, the IR optical properties of the cryodeposit can be measured. Provided a scheme for decoding the optical spectra is developed, the molecular species present can be identified and their concentrations be found.

A typical cryodeposit is on the order of one or several micrometers in thickness, and composed of several constituents. The first step towards developing an in situ diagnostic tool for multicomponent cryodeposits is to devise an analysis method for two-component cryodeposits. Such a method is the primary goal of the present work.

OBJECTIVES

The objectives of this effort are:

1. To develop an in situ diagnostic method, using IR techniques, for identifying constituents in cryodeposits formed from mixtures of two gaseous components. The molecular species to be studied are the dominant atmospheric gases N_2 and O_2, and those found in rocket exhausts, such as CO_2, H_2O, NH_3, CO, CH_4 and HCl.

2. To recommend check-out procedures for determining the validity of the diagnostic method for two-component cryodeposits.

3. To determine the criteria for extending the diagnostic method to analysis of multicomponent cryodeposits.

THEORY

The optical properties of any material are conveniently summarized by its complex index of refraction $\hat{n}(\nu)$, defined as

$$\hat{n}(\nu) = n(\nu) + i\,k(\nu) \qquad (1)$$

for each value of the wavenumber ν, the reciprocal of the wavelength of incident radiation. The circumflex indicates a complex quantity. In equation (1) the real or refractive index n is the ratio of the speed of light in vacuo to the speed of light in the material, and the imaginary index k is the absorption index or the extinction coefficient. Note that k does not include attenuation of radiation by scattering. The "plus" sign in euqation (1) indicates the author's choice of the time dependence of incident radiation to be exp (-iwt), w being the radian frequency.

IR active molecular species have characteristic vibrational modes which are easily excited by absorption of IR radiation having the corresponding characteristic wavenumber (Ref 3). CO_2, H_2O, NH_3, CO, CH_4 and HCl are IR active species and in the solid phase have widely separated absorption bands (Ref 1 and 2). Characteristic vibrational bands observed in the n and k spectra of a cryodeposit can be used to ascertain the presence of an IR active species in the film. The problem of overlapping vibrational absorptions of different species is not serious for cryodeposits composed of a mixture of any two of the above molecules. The presence of IR inactive species like N_2 and O_2 must be determined from other methods such as Raman techniques.

To determine the concentration of a given molecular species in a cryodeposit, the following assumptions have been tentatively adopted. For a cryodeposit formed by a homogeneous mixture of molecular constituents, the total observed n and k is a linear sum of contributions from each constituent; furthermore, each constituent's contribution is proportional to its molar concentration. Physically these assumptions are equivalent to neglecting any change in the intermolecular forces among the molecules in the cryodeposit when the concentrations of the molecular species are altered. These assumptions have been applied to aqueous solutions of some inorganic compounds (Ref 4). They are probably not valid for the low concentrations of a species (less than one part per thousand) in a solid matrix of a host molecule (Ref 5). The hypotheses must also be modified for constituents of a cryodeposit which react chemically.

If n_i and k_i are the contributions of the ith molecular constituent to the n and k values of a cryodeposit composed of N species, the first assumption is stated mathematically as

$$k(\nu) = \sum_{i=1}^{N} k_i(\nu) \qquad (2)$$

and

$$n(\nu) = \sum_{i=1}^{N} n_i(\nu) \qquad (3)$$

at every wavenumber ν. If n_{si} and k_{si} are the known indices of species i at a known "standard" molar concentration c_{si} (mole/unit volume), the second assumption can be written

$$k_i(\nu) = \left(\frac{c_i}{c_{si}}\right) k_{si}(\nu) \tag{4}$$

and

$$n_i(\nu) = \left(\frac{c_i}{c_{si}}\right) n_{si}(\nu) \tag{5}$$

where c_i is the molar concentration of species i in the cryodeposit. Combining equations (2) and (3) with (4) and (5) gives

$$k(\nu) = \sum_{i=1}^{N} \left(\frac{c_i}{c_{si}}\right) k_{si}(\nu) \tag{6}$$

and

$$n(\nu) = \sum_{i=1}^{N} \left(\frac{c_i}{c_{si}}\right) n_{si}(\nu) \tag{7}$$

for the indices of the cryodeposit.

The average density, ρ, of a cryodeposit with a volume, V, is

$$\rho = \sum_{i=1}^{N} \frac{m_i}{V} \tag{8}$$

where m_i is the mass of molecular species i contained in volume, V. The mass of species i per unit volume can also be written as $c_i W_i$ where W_i is the molecular weight. Equation (8) is then

$$\rho = \sum_{i=1}^{N} c_i W_i \quad . \tag{9}$$

A direct consequence of the above assumptions is the calculation of vibrational band strengths for IR active molecular species. If S_{ij} represents the band strength of vibrational band j of molecular species i, then

$$S_{ij} = c_i^{-1} \int_{Band\,j} k_i(\nu)\, d\nu \tag{10}$$

where the integration ranges over band j (Ref 4). In particular, for the standard spectra of species i

$$S_{ij} = c_{si}^{-1} \int_{Band\,j} k_{si}(\nu)\, d\nu \,. \tag{11}$$

Equating equations (10) and (11) yields

$$\frac{c_i}{c_{si}} = \frac{\int_{Band\,j} k_i(\nu)\, d\nu}{\int_{Band\,j} k_{si}(\nu)\, d\nu} \,. \tag{12}$$

Equation (12) represents less stringent constraints than the original assumptions. The requirement that the intermolecular forces not change, as species concentrations are changed, is relaxed to allow changes in the k (and n) spectrum of the cryodeposit provided the band strengths are not affected.

Equations (6), (7), and (12) must be checked empirically to ascertain their validity. If the checks are negative, these equations must be replaced by others based on different assumptions such as those concerning the molar refractivity (Ref 6). A preliminary test of equations (6), (7), and (12) is presented later in the report.

METHODS OF ANALYSIS

In this section several methods for the determination of the concentration of molecular species in a cryodeposit are outlined. The procedures are based on equations (6), (7), and (12) and their underlying assumptions.

As mentioned earlier, the identification of IR active molecular species in a cryodeposit can be found from characteristic vibrational bands in the IR k-spectrum of the cryodeposit. The optical identification of IR inactive species must be done by Raman techniques. The presence of IR inactive species, however, can be inferred from the IR data alone. For instance, if after the IR species concentrations are determined, the sum in equation (9) is calculated to be less than the observed density of the cryodeposit, the missing contribution to the density may be attributed to IR inactive species.

In equations (6), (7), and (12) the molar concentrations relative to the standard molar concentrations are determined for each molecular species in a cryodeposit. The absolute molar concentrations can be determined if the standard molar concentration is known. The following methods of determining concentrations are proposed.

METHOD 1

If k of the cryodeposit is measured at l_k different wavenumbers, the l_k relations in equation (6) can be solved in a linear least squares procedure to find the relative concentrations c_i/c_{si}, provided that l_k is greater than, or equal to, the number of (IR active) species contributing to the IR absorption. The method would be applicable to the absorption regions, and would not account for IR inactive species. Equation (9) can be used as a check of the analysis if an accurate density of the cryodeposit is known.

METHOD 2

Method 2 is a least squares determination analogous to Method 1, but here l_n values of n are used in equation (7). The method is sensitive to IR inactive species as well as the IR active. Again, equation (9) can be used to check the results.

METHOD 3

Method 3 is the simultaneous use of both Methods 1 and 2, with the advantage of having both n and k in the calculation. The concentrations of both IR active and IR inactive species could be found if the sum of l_k and l_n equals at least the total number of species in the cryodeposit.

METHOD 4

Method 4 utilizes equation (12) for each vibrational band identified with species in the k spectrum of the cryodeposit. If more than one band can be used, an average value of the relative molar concentration can be found. Of course, only the concentrations of IR active species can be determined.

The number of data points that can be used in Methods 1, 2, and 3 would normally be vastly larger than the number of useful vibrational bands needed in Method 4. However, Methods 1 - 3 are wavenumber-by-wavenumber comparisons of the unknown n and k spectra with those of the standard cryodeposits. Thus, these methods are especially sensitive to differences in the compared spectra such as shifts in the vibrational band positions or their intensities, which could be caused by differences in the intermolecular forces (Ref 5) or by spectrometer calibration errors. The wavenumber integrals of k used in Method 4 are less sensitive to these types of differences, but only concentrations of IR active species can be determined from equation (12).

DETERMINATION OF THE REFRACTIVE INDICES

Accurate values of the complex refractive index $\hat{n}$ are needed to find species concentrations with the proposed methods. The indices of the sample cryodeposit, and those of the standard cryodeposits, must be precisely determined throughout the IR and visible regions. Much of the effort this summer was devoted to evaluating the accuracy of existing n and k spectra.

In previous AEDC studies (Ref 1 and 2) the lamellar model of cryodeposits was used to interpret IR spectra. In this model the cryodeposit is an isotropic homogeneous film of uniform thickness and formed on a highly specular substrate (Fig 1). The real index of the film and its thickness can be found, in regions of no absorption, by the two-angle interference method developed by Templemeyer (Ref 7). The thickness of the cryodeposit is necessary for determining its indices. In the future, simultaneous measurement of the mass deposition using a quartz crystal microbalance (QCM) will permit the density of the cryodeposit to be calculated. The density is needed to determine absolute molar concentrations of the standard cryodeposits and to check equation (9). At a given wavenumber the complex index $\hat{n}(\nu)$ of a lamellar cryodeposit is fixed, and its reflectance or transmittance varies only with thickness. When reflectance or transmittance are measured at two or more thickness values, the indices $n(\nu)$ and $k(\nu)$ of the cryodeposit can be found by a least squares fit to an appropriate model.

The model for the normal reflectance of a lamellar cryodeposit, relative to a bare mirror substrate, is presented in the work of Arnold et al. (Ref 1). The author analyzed a portion of the NH_3/N_2 cryodeposit spectra contained in Ref 1 using his own least squares computer program. The computed spectra are shown in Figures 2 and 3, and discussed in the next section. The relative computational errors, using six thicknesses, ranged from 1 to 5% for the n values, and from 2 to 15% for the k values. In general, the errors in n are larger in the absorption region, and the errors in k are larger in regions of little absorption and at the peaks of very strong absorption regions.

Pipes et al. (Ref 2) give a model for the normal transmittance of a thin lamellar film deposited on a thick transparent substrate (See Fig 1). The model was integrated into the author's nonlinear least squares computer program to fit transmission data, at a given wavenumber, as a function of cryodeposit thickness. This program incorporates the maximum neighborhood algorithm of Marquardt (Ref 8). The algorithm provides converged values of the indices about 30 to 60 times faster than the program utilized in Ref 2; however, differences in resulting index values are negligible in almost all cases. The program fitted transmission data for sixteen thicknesses of an 80°K NH_3 cryodeposit. In general the range of the relative computational errors was from less than 1% to 10% for the n values, and from 1% to 30% for the k values. For k values less than 10^{-4} the relative error was greater than 100% in most instances. The relative errors varied over the spectrum in the same manner as those computed from reflectance data. It is evident that the more thicknesses involved in the fit the more precise are the converged indices values.

In the above methods of finding the real and imaginary parts of the complex index of refraction, the real index n is assumed to be independent of the imaginary index k. Using causality arguments, n and k are related through the Kramers-Kronig (KK) dispersion relations (Ref 1 and 9),

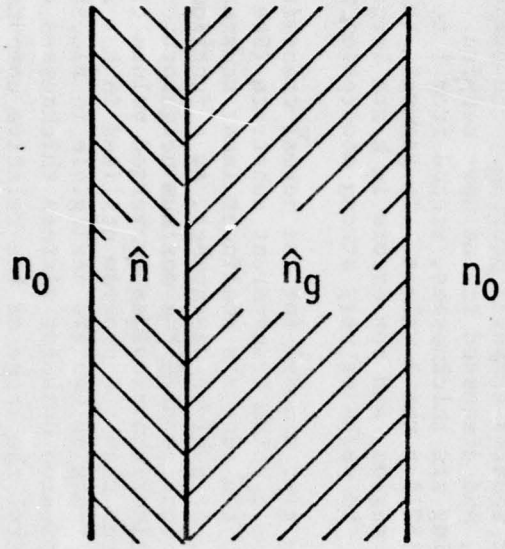


Fig. 1 Thin lamellar film of index $\hat{n}$, on a substrate of index $\hat{n}_g$, surrounded by a nonabsorbing medium of index n_o.

$$n(\nu) = n_\infty + \frac{2}{\pi} P \int_0^\infty \frac{\nu' k(\nu')}{\nu'^2 - \nu^2} d\nu', \tag{13}$$

and

$$k(\nu) = \frac{2\nu}{\pi} P \int_0^\infty \frac{n(\nu')}{\nu^2 - \nu'^2} d\nu' . \tag{14}$$

P indicates the Cauchy principal value of the integral, and n_∞ is the contribution to n (ν) from wavenumbers in the visible and ultraviolet regions. In principle it is possible to derive the n (ν) spectrum from the k (ν) spectrum, and vice-versa. In cryodeposit studies the KK relations have been used as a check of the converged n (ν) or k (ν) values fitted to the models presented above (Ref 1 and 2). Ahrenkiel (Ref 10 and 11) has modified the KK relations to form the subtractive Kramers-Kronig (SKK) relations. If ν_0 denotes a wavenumber at which the real index is known, then upon subtraction of n (ν_0), given in equation 13, from the corresponding expression for n (ν), the SKK equation for n (ν) is found to be

$$n(\nu) = n(\nu_0) + \frac{2}{\pi} P \int_0^\infty \frac{(\nu^2 - \nu_0^2)\, \nu' k(\nu')}{(\nu'^2 - \nu^2)(\nu'^2 - \nu_0^2)} d\nu'. \tag{15}$$

The principal advantage of the SKK relations is less sensitivity to contributions to the integral from outside the observed wavenumber range. When applied to the experimental k-spectrum for 80°K NH_3 cryodeposits, equation (15) obtained n values that were in equal or better agreement with the observed values of n than obtained by equation (13) (See Fig 45a of Ref 2).

To compare values of the complex refractive indices obtained for cryodeposits having identical composition but differing in their densities, Lorentz-Lorenz adjustments must be made to the indices (Ref 6 and 12). Relations derived from Ref 12 were used to adjust the real and imaginary indices of solid NH_3 at 195°K (Ref 11) to the indices values expected at 20°K. The density of NH_3 at 195°K is given by Manzheli and Tolkachev (Ref 13) and at 20°K by Roux (Ref 14). The results are shown in Figures 2 and 3 and compared to the n and k spectra of NH_3 cryodeposits observed at 20°K (Ref 2). These spectra are very similar in shape and intensity, but the 1050 cm^{-1} absorption band is slightly shifted in position. This may be due, in part, to calibration errors or changes in the solid phase (Ref 2).

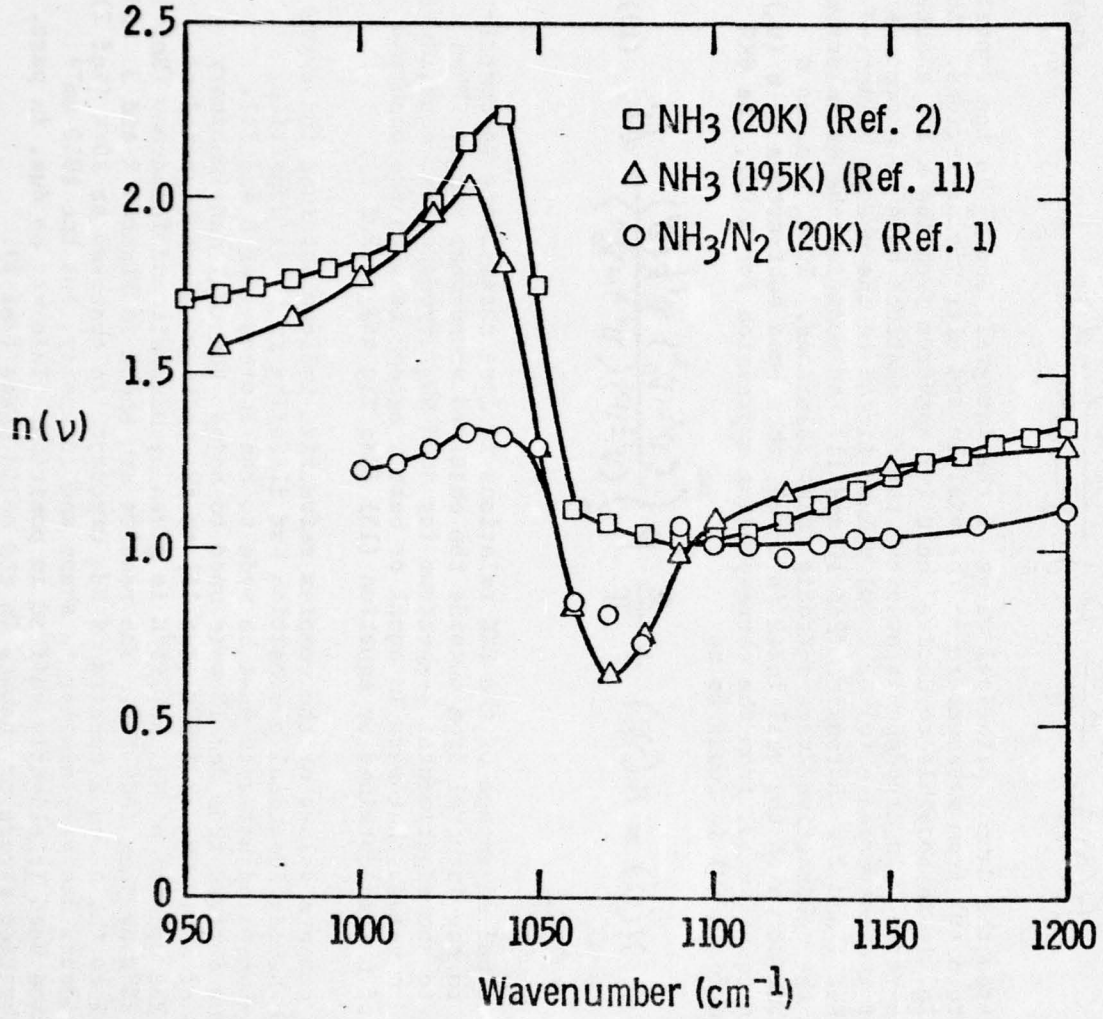


Fig. 2 The refractive index of solid NH_3 and NH_3/N_2. The 195K data are corrected to the density at 20K.

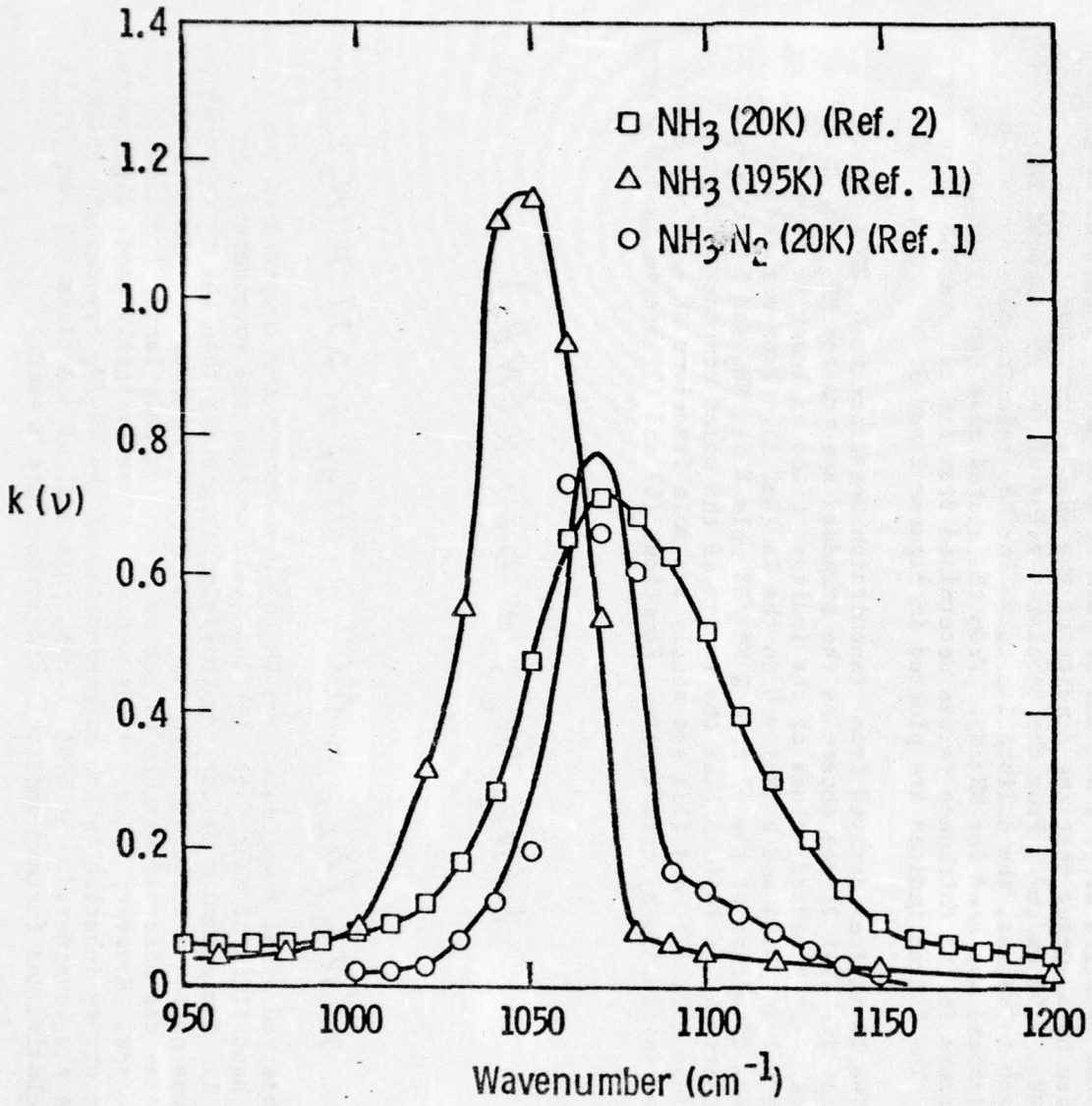


Fig. 3 The absorption index of solid NH_3 and NH_3/N_2. The 195K data are corrected to the density at 20K.

A PRELIMINARY TEST

An empirical test of equations (6), (7), and (12), for binary cryodeposits, can be made using the IR complex refractive index derived from two-component cryodeposits of known composition. Unfortunately nearly all existing data (Ref 1 and 2) is for single component cryodeposits. To fill this gap preparations have been made at AEDC to obtain data on binary mixtures. The measurements will begin in the near future but too late to be used for checking out the methods proposed in this report.

Limited reflectance data for 67 mole % NH_3/33 mole % N_2 cryodeposits at 20°K are available (Ref 1), and approximate n and k values were obtained by estimating the cryodeposit thickness. This was done by noting that the densities of films of pure NH_3 and of pure N_2 were nearly identical at 20°K, and then by assuming that the density of the NH_3/N_2 cryodeposit was that of pure NH_3, 0.94 gm/cm^3. From the tabulated value of the mass deposition given for each thickness, the calibration curve for NH_3 relating mass deposition to thickness was used for NH_3/N_2. From the stated mass deposition errors, the errors in the thickness values determined from the calibration curve are ±10%. The fitted indices are plotted in Figures 2 and 3.

The IR indices derived from transmission measurements of 20°K pure NH_3 cryodeposits (Ref 2) was chosen as the standard spectra for NH_3, an IR active species. The standard values of the indices of the IR inactive species N_2 are n (N_2) = 1.24 ±0.04 and k (N_2) = 0 in the IR (Ref 1). From our assumption that the densities of the 67 mole % NH_3/33 mole % N_2, NH_3 and N_2 cryodeposits are identical, it follows that the ratios of the molar concentrations in equations (6), (7), and (12) are simply the mole fractions of each molecular species in the NH_3/N_2 cryodeposit. Equations (6) and (7) become in the present case,

$$k(NH_3/N_2) = 0.67\, k(NH_3) \tag{16}$$

and

$$n(NH_3/N_2) = 0.67\, n(NH_3) + 0.33\, n(N_2). \tag{17}$$

The observed n and k values of the NH_3/N_2 cryodeposit are compared to the right hand sides of equations (16) and (17), at selected wavenumbers, in Table 1. The summed n values are consistently greater than the corresponding n values of the mixture by about 15%. The summed k values are consistently less than the observed mixture values by a considerably larger fraction in most cases. However, the agreement among n values is fairly good, especially if the errors inherent in the determination of the NH_3/N_2 cryodeposit thicknesses are considered. At best though, this test of equations (6) and (7) is inconclusive and further empirical comparisons are needed.

TABLE 1

TEST OF EQUATIONS 16 AND 17

ν(cm-1)	.67 k(NH_3)	k (NH_3/N_2)	.67 n(NH_3) + .33 n(N_2)	n(NH_3/N_2)
1000	0.0054	0.0071	1.62	1.22
1050	.0320	.1946	1.58	1.29
1100	.0342	.1383	1.11	1.01
1150	.0066	.0175	1.22	1.04
1200	.0033	.0041	1.31	1.11
1250	.0031	.0037	1.35	1.15
1300	.0031	.0040	1.37	1.19
1350	.0033	.0057	1.38	1.22
1400	.0034	.0080	1.39	1.24
1450	.0035	.0095	1.39	1.22
1500	.0036	.0119	1.40	1.23
1550	.0039	.0145	1.41	1.23
1600	.0048	.0208	1.44	1.23
1650	.0049	.0321	1.36	1.18
1700	.0019	.0058	1.38	1.24

Equation (12) was tested by measuring the areas under appropriate k curves in the region of an absorption band. The areas of the absorption at 1050 cm^{-1} were measured with a planimeter from the k curves of NH_3/N_2 and 20°K N_2 in Figure 3. After "background", due in part to Debye effects (Ref 15), was removed, the ratio of the areas was found to be 0.65, which is very close to the desired value of 0.67. Even when the 195°K NH_3 spectra, corrected to 20°K, is chosen as the standard, the resulting ratio is 0.71. These favorable results indicate that Method 4, based on equation (12), is a more sensitive method of determining IR species concentrations than any procedure based on equation (6) or (7).

This positive result means that further effort to quantify constituents in multicomponent cryodeposits is justified. Whether or not the present case is a real verification of equation (12) or merely fortuitous can only be answered by more data on binary cryodeposits.

CONCLUSIONS AND RECOMMENDATIONS

The IR active species in a cryodeposit, composed of a mixture of two molecular species in the proportions expected in rocket exhausts, can be identified by the characteristic vibrational bands in the IR k-spectrum of the cryodeposit. Raman data is necessary for determining the identity and concentration of IR inactive species in a binary cryodeposit. Moreover, identification of IR active species in cryodeposits of more than two components is also straightforward because of the wide gaps between absorption bands for most of the species involved in plume studies (Ref 1 and 2).

The results of this preliminary study indicate that the most reliable methods of establishing the concentrations of IR active species in a cryodeposit will be those based on strengths of characteristic absorption bands in the IR k-spectrum of the deposit. The analysis of IR spectra for multicomponent

cryodeposits should be analogous to the analysis for binary deposits. If the spectra are severely overlapped, determination of band strengths may be facilitated by subtracting the contributions to k for each identified species in the cryodeposit spectrum (Ref 4). The resulting spectra should be simpler to interpret.

The values of the absorption index extracted from IR transmission data of cryodeposits is extremely sensitive to the real refractive index of the substrate. In one instance the value of the real index of a germanium substrate was changed by less than 2% in two different determinations of n and k for an NH_3 cryodeposit at 1300 cm^{-1}. The resulting differences in computed values of n was less than 1%, but the k values differed by 35% (although both values were less than 10^{-2}).

From the results and conclusions given above, the following recommendations are proposed:

1. More IR and Raman data should be obtained for two-component cryodeposits of known composition to check the methods outlined here for determining IR active species concentrations. The gas mixture composition should be established by an independent chemical analysis.

2. Standard IR spectra of n and k should be established for single component cryodeposits. Separate standard spectra should be measured for each range of binary cryodeposit temperatures, because of possible changes in solid phases and densities (Ref 1 and 2).

3. The optical properties of the germanium substrate should be determined very accurately throughout the IR region.

4. A comparison of the sensitivity of data gathering techniuqes should be made to establish the thinnest and thickest films which can be analyzed. Such methods as measurement of the relative reflectance, absolute transmittance, transmittance relative to a bare substrate, and multiple attenuated total reflection should be examined.

5. Computer software should be generated to identify lines and to determine the appropriate band strengths.

6. The IR and Raman analysis should be extended to multicomponent cryodeposits if equation (12), or a modification of it, is shown to be valid for binary cryodeposits.

REFERENCES

1. Arnold, F., Sanderson, R. B., Mantz, A. W., and Thompson, S. B., "Infrared Spectral Reflectance of Plume Species on Cooled Low Scatter Mirrors." AFRPL-TR-73-52, September 1973.

2. Pipes, J. G., Roux, J. A., Smith, A. M., and Scott, H. E., "Infrared Transmission of Clean and Contaminated Cryocooled Optical Windows." AEDC-TR-76-60 (to be published).

3. Herzberg, G., Infrared and Raman Spectra of Polyatomic Molecules, D. Van Nostrand Company, Inc., Princeton, New Jersey, 1954.

4. Querry, M. R., Waring, R. C., Holland, W. E., Earls, L. M., Herrman, M. D., Nijm, W. P., and Hale, G. M., "Optical Constants in the Infrared for K_2SO_4, $NH_4H_2PO_4$, and H_2SO_4 in Water." Journal of the Optical Society of America , Vol. 64, No. 1, January 1974, pp. 39-46.

5. Hallam, H. E., Vibrational Spectroscopy of Trapped Species, John Wiley and Sons, Ltd., London, 1973.

6. Born, M., and Wolf, E., Principles of Optics, 4th Ed., Pergamon Press, Oxford, 1970, pp. 87-89.

7. Templemeyer, K. E., et al., "In Situ Measurements of Thickness and Other Properties of Carbon Dioxide Cryodeposits by Optical Techniques." AEDC-TR-67-226, December 1967.

8. Marquardt, D. W., "An Algorithm for Least-Squares Estimation of Nonlinear Parameters." Journal of the Society for Industrial and Applied Mathematics, Vol. 11, No. 2, June 1963, pp. 431-441.

9. Wooten, F., Optical Properties of Solids, Academic Press, New York, 1972.

10. Ahrenkiel, R. K., "Modified Kramers - Kronig Analysis of Optical Spectra." Journal of the Optical Society of America, Vol. 61, No. 12, December 1971, pp. 1651 - 1655.

11. Robertson, C. W., Downing, H. D., Curnutte, B., and Williams, D., "Optical Constants of Solid Ammonia in the Infrared." Journal of the Optical Society of America, Vol. 65, No. 4, April 1975, pp. 432-435.

12. Heavens, O. S., Optical Properties of Thin Solid Films, Butterworths Scientific Publications, London, 1955, pp. 179-180. Note that the denominator of r in Eq. 6(13) should be $\hat{n}^2 + 2$.

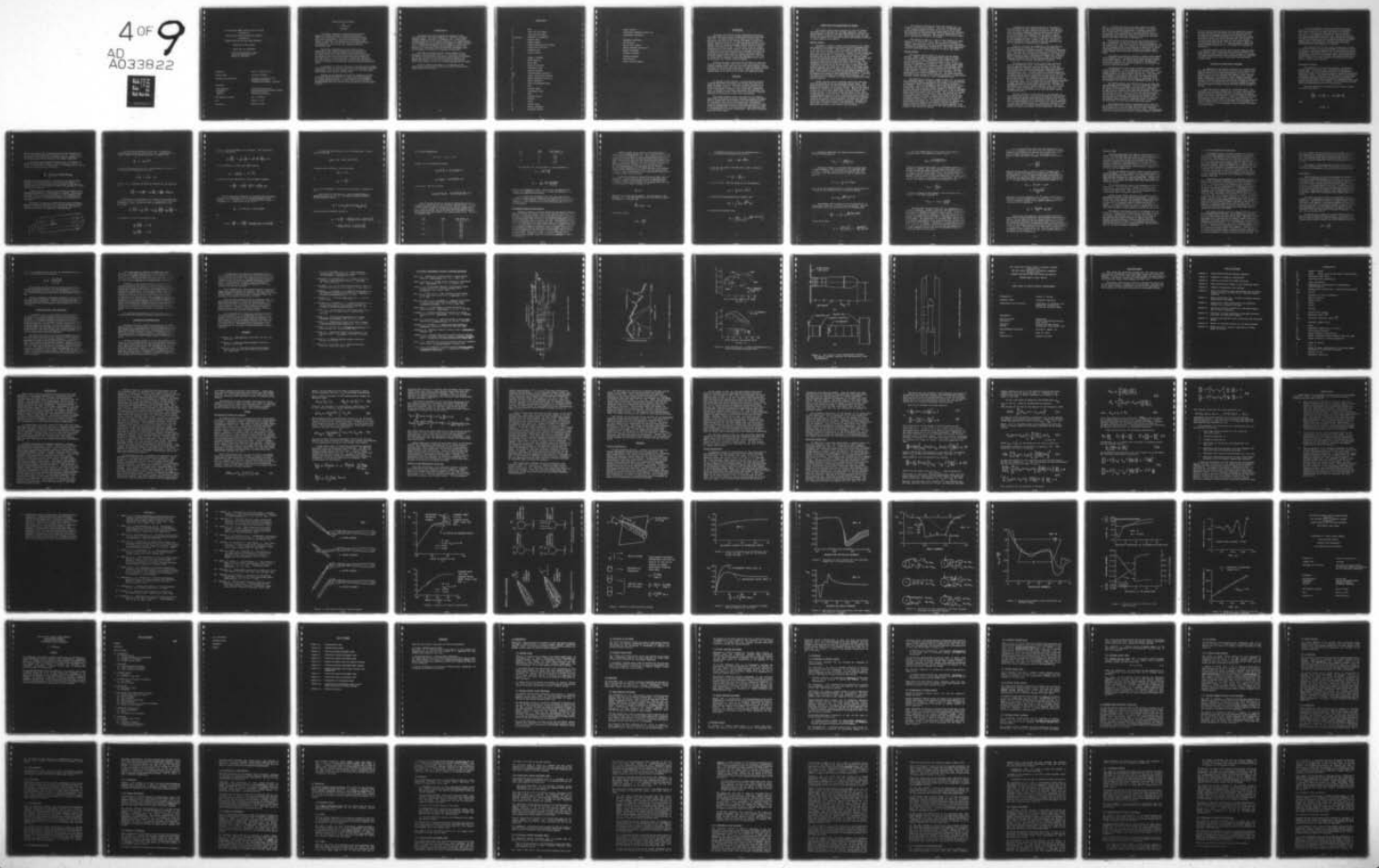
13. Manzhelii, V. G., and Tolkachev, A. M., Soviet Physics. Solid State, Vol. 5, 1964, p. 2506.

14. Roux, J. A., (private communication).

15. Kittel, C., Elementary Solid State Physics, John Wiley and Sons, Inc., New York, 1962.

AD-A033 822 AUBURN UNIV ALA SCHOOL OF ENGINEERING F/G 14/2
1976 USAF-ASEE SUMMER FACULTY RESEARCH PROGRAM.(U)
SEP 76 J F O'BRIEN F44620-75-C-0031
UNCLASSIFIED AFOSR-TR-76-1419 NL

4 OF 9
AD A033822



1976 USAF-ASEE SUMMER FACULTY RESEARCH PROGRAM

SPONSORED BY

THE AIR FORCE OFFICE OF SCIENTIFIC RESEARCH

CONDUCTED BY

AUBURN UNIVERSITY AND OHIO STATE UNIVERSITY

PARTICIPANT'S FINAL REPORT

ENGINE TEST CELL ACOUSTICS:

A Preliminary Analysis of Noise Sources and Experimental and Analytical Techniques

Prepared by:	Grant T. Patterson, Ph.D.
Academic Rank:	Assistant Professor
Department and University:	Department of Mechanical and Aerospace Engineering University of Tennessee, Knoxville
Assignment:	
(Air Force Base)	Arnold Air Force Station
(Laboratory)	Arnold Engineering Development Center
(Division)	Engine Test Facility
(Branch)	Technology Applications
USAF Research Colleague:	Glen R. Lazalier
Date:	August 13, 1976
Contract No.:	F44620-75-C-0031

ENGINE TEST CELL ACOUSTICS

by
G. T. Patterson

ABSTRACT

Preliminary information, analysis and ground work in support of a program designed to determine the acoustic field in the engine test cells at Arnold Engineering Development Center are presented. The direct connect mode of engine testing is considered. An examination of the possible noise sources is made. The noise sources found to be most significant are combustion noise, jet noise and jet/exhaust diffuser interaction noise.

The acoustic environment in the test cells is very complex due to the irregular geometry and close proximity of the reflecting and scattering surfaces to the sound sources. The entire enclosure is in the acoustic near field of the sources. An analysis by use of wave equation techniques is performed for the normal modes of a simplified model. A method for calculating the sound pressure level is presented using free field experimental data and a knowledge of experimentally determined acoustic energy decay rates.

An evaluation of analysis techniques for acoustic field-structural interactions reveals no mechanism which would allow structural vibratory amplification to the point of creating a source of sound which would significantly affect the cell acoustic field.

Several areas of experimental studies are proposed to include an acoustic survey, determination of energy decay rates (reverberation times) and model studies. It is concluded for considerations of complicating factors on cell acoustic analysis that an attempt to estimate engine free field acoustic signature from test cell data would be futile.

ACKNOWLEDGEMENTS

The author would like to express his gratitude to the Air Force Office of Scientific Research for supporting the summer research program. The author is indebted to Mr. J. Fred O'Brien of Auburn University for his careful attention to the administration of this program and for his helpful encouragement and active participation in identifying a meaningful area for research. Thanks also to Dr. M. L. Laster of the Research and Development Division of the Directorate of Technology at Arnold Engineering Development Center for his support and attention to operation of the program.

The author is thankful for the technical support of the personnel of the Engine Test Facility. In particular the author is grateful for the assistance and support given by Mr. Glen Lazalier who was the coordinator of the overall acoustics program in the Engine Test Facility. It was also a pleasure to work with the staff of the Propulsion Section of the Technology Applications Branch.

A word of thanks is expressed to Dr. James Maus of the University of Tennessee Space Institute for several helpful discussions related to this project.

NOMENCLATURE

A	Area
a	Outer test cell radius
b	Inner test cell radius
C_1, C_2, C_3, C_4	Constants of integration
c	Speed of sound
D	Nozzle diameter
E	Acoustic energy per unit volume
E_∞	Steady state value of E
f	Frequency (H_z)
g_w	Green's function
i	
I	Acoustic intensity
J	Bessel function
k	Wave number
L	Length of test cell
n	Designation index
P	Acoustic pressure
P_{rms}	Root-mean-square value of P
Q_o	General sound source function
R	Radial dependent portion of ϕ
r	Radius coordinate
r_2	Radius of microphone array
S	Area
St	Strouhal number
T_r	Reverberation time
t	Time
U	Average velocity
u	Velocity
V	Volume
W	Acoustic power
x	General coordinate
x_s	Microphone spacing

Y	Bessel function
Z	Longitudinal dependent portion of ϕ
z	Longitudinal coordinate
α	Absorption coefficient
Φ	Wave function
ϕ	Spatial wave function
Θ	Angular dependent portion of ϕ
θ	Angular coordinate
ω	Frequency (rad/sec)
∇^2	Laplacian operator
δ	Delta function
∞	Denotes ambient property

INTRODUCTION

The Engine Test Facility at Arnold Engineering Development Center has encountered acoustic problems associated with the engine test cells. Of primary concern is the impact on engine tests, in particular, the effect of the acoustic environment on engine performance and engine structure. A cause for concern has been a few specific cases of failure of test cell hardware and engine structural elements which are unexplained through analysis of known vibration sources or aerodynamic forces. This has led to brief and cursory investigations of the acoustic field in the test cells to determine if there is sufficient energy available in this form which could be transmitted to structural components and by exciting or reinforcing structural vibration modes result in hardware structural failure. The sound pressure levels which have been measured are on the order of 150 db with low frequency discrete spectrum peaks giving rise to the possibility that standing waves are present.

Although the primary concern has been the impact on structural integrity of high acoustic levels there is also the possibility that discrete frequency sound waves may couple with engine peculiar pressure variations at the nozzle exit plane and thus cause unacceptable pressure variations at various points in the engine. These may arise from standing waves in the test cell or the test cell exhauster ducting.

OBJECTIVES

In response to these concerns, a program has been initiated to define the acoustic environment in the engine test cells and to assess the impact of such an environment on engine performance and engine structural integrity. This will require analysis of noise sources contributing to acoustic levels in the cells, transmission paths, instrumentation techniques, experimental and analytical techniques of assessing acoustic field levels and a review of technology applicable to structure and acoustic field interactions.

This report documents efforts associated with four specific tasks aimed at providing preliminary information, analysis and ground work for accomplishing the objective of the above-mentioned program. This involves 1) noise source identification and classification, 2) identification and evaluation of experimental and analytical techniques for determination of acoustic field characteristics, 3) survey of technology applicable to structure-acoustic field interaction and 4) recommendations for further investigation. Each task is documented separately in this report.

IDENTIFICATION AND CLASSIFICATION OF SOURCES

The acoustic sources which contribute the test cell acoustic environment can be separated into two broad categories. These are sources interior to the test cell and those exterior to the test cell. Figure 1 shows a schematic of a typical direct connect test cell and the defined regions for interior and exterior noise sources in addition to typical specific noise sources.

Exterior Sources

The extent to which an exterior source affects the cell environment depends on the strength of the source and its transmission path to the interior of the cell. There are a number of exterior sources in the test cell area which are of significant strength such as flow noise, valve noise, machinery noise, etc. However, the only transmission path which would result in a non-negligible attenuation is that which propagates into the cell from upstream through the inlet air supply duct and from downstream through the exhaust duct. The upstream sources consist of noise associated with compressors, expansion turbines, temperature conditioning equipment and various flow devices. The transmission path from any particular source in the air supply plant is difficult to define due to the various ways in which air can be routed to the test cell supply duct. The number of 90° bends, valves and flow measuring devices for any particular path would offer sufficient acoustic impedence to preclude any significant transmission of noise. For instance a 90° bend will provide approximately four to six db reduction for frequencies above approximately 200 HZ (1). Including the effect of turning vanes will increase the attenuation. The compressor plant is, therefore, to a large extent acoustically isolated from the test cell.

Another important source of upstream noise is the shock wave structure downstream of the flow measurement venturi throat. This source arises primarily from the non-steady character of the shock position and attachment on the venturi surface. This type of noise is difficult to classify as to spectrum and level. However, the venturi is used only in the direct connect mode in tests of turbojet and turbofan engines. In the direct connect mode there is not a direct transmission path to the test cell. The wave motion in the inlet duct is approximately parallel to the duct wall, and the mating flange and labyrinth seal to which the wave is normally incident is of thickness sufficient to provide a large attenuation. The only other path is through the engine which also has large attenuation. Although this noise source is directly incident on the engine face, it is not a significant contributor to the interior test cell noise.

The sources of noise from the downstream exhauster duct are primarily the exhausters themselves. The T-cells transmission path to the exhausters consists of seven tee sections and two 90° bends plus two cooler sections consisting of water spray and heat exchangers. The attenuation for frequencies above 200 HZ is greater than 36 db due to the bends and tees alone. The exhauster noise would not appear to be a major source of noise to the T-cells.

The transmission path to J-1 and J-2 cells consists of a spray cooler, one "T" and two 90° turns. There is little attenuation of exhauster noise along this path with the exception of the water spray section. The attenuation of the water spray needs further investigation to determine its attenuation characteristics. The J-cells exhausters could be a significant source of noise to J-1 and J-2 test cells.

Interior Sources

The acoustic sources interior to the test cell are engine peculiar. These include the well-established sources of aircraft jet engine noise, namely, turbomachinery noise, combustion noise, jet noise and engine casing radiation as shown in Fig. 2 for a typical turbofan engine. The remaining source of noise is associated with the jet plume/diffuser interaction. First consider engine casing radiation. Since most of the ordered pressure waves propagate axially in a typical jet engine, the angle of incidence of these waves with respect to their containment ducting is practically zero. According to the traditional method of transmission loss calculation (2), this would result in an infinite transmission loss. The casing vibrational excitation is then a result of flow surface interactions, internal engine mechanical sources and discrete, local turbomachinery noise.

The casing may be excited in a number of modes if it is idealized as a cylindrical section. An important mode occurs at the ring frequency which has a wavelength corresponding to the cylinder cross-section circumference. Below this frequency a helical wave may propagate along the cylinder. Above the ring frequency the cylinder begins to react locally like a flat plate with critical frequency of vibration corresponding where the speed of propagation of a bending wave in the cylinder wall equals the speed of sound in the fluid media. The structure of a typical engine tends to reduce the influence of these modes and they may not be an allowed mode in actuality. Engine casing radiation has not been considered a significant source of engine noise for the size and type of engines developed to date. This has been borne out by limited experimental investigation (3). It should be pointed out, however, that future engines with larger thrust-to-weight ratios may, because of reduced structural thickness, have significant casing radiation. This radiation could also become larger due to new noise sources such as may be produced in duct burning fan engines.

Turbomachinery noise consists primarily of the discrete tones produced by the fan, compressor and turbine. Although this is a major source of engine noise, particularly fan and compressor noise, the primary transmission path for these sources (out the front of the engine) is interrupted when the engine is tested in a direct connect mode. Obviously, if the engine is tested in the free jet mode then the cell will be exposed to the full level of the turbomachinery noise. However, this study is primarily aimed at the direct connect mode and the fan and compressor noise will be considered to be appropriately attenuated.

There can, of course, be propagation of fan noise down the fan duct and out the nozzle exit. The turbine-generated noise will also propagate out through the nozzle. These may be contributors to the cell noise level although the degree of contribution should be small. The tones are scattered by the turbulence in the engine flow passages and are reduced in amplitude and broadened over a frequency band in a phenomena known as "haystacking." These tones are high frequency, generally above 2000 Hz, and therefore are not likely to reinforce any cell peculiar characteristic vibrations.

The primary contributors to cell noise levels will be the jet noise and combustion noise. The combustion noise will as a rule be a smaller contributor than will jet noise. It has only been recently that combustion noise has been definitively separated from jet noise and also has been specifically identified in the core engine noise (4,5). For most turbojet or turbofan engines the combustion noise peak is in the vicinity of 500 Hz and is spread over a frequency band of several hundred hertz as shown in Fig. 2. For high thrust conditions the combustion noise peaks several db below the jet noise level. For low thrust settings the combustion noise may be the highest level. This is because the jet noise increases according to nozzle exit velocity to the eighth power whereas combustor noise increases according to a fourth power variation (5). The effect of afterburning is to further increase combustion noise. In this case, jet noise is also increased due to an increase in velocity. The combustion noise may be dominant for all exit velocities, however, as indicated in Ref. 6.

For most conditions of high noise level, jet noise will be the dominant noise source. Jet noise arises from the turbulent shear layer between the ambient medium and the jet potential core and the fully developed turbulent region downstream of the core tip. Although there is some disagreement as to the source of the noise (whether due to a fine scale random turbulence or a large scale coherent or orderly turbulent structure) the overall characteristic of jet noise as it depends on certain jet parameters is well established. The acoustic

power of a circular jet varies as the eighth power of velocity, the square of nozzle exit diameter and the square of the density. For many flows a Strouhal-type scaling is followed according to $fD/U = \text{const}$ where f is frequency, D is nozzle diameter and U is jet velocity. For supersonic flows where there may be noise production from shock bottles the variation of sound power level with velocity will obey a 12th power relationship (7).

The variation of acoustic power per unit distance along the jet is of importance to test cell acoustic field contributions. For a subsonic jet, from theory (8) and as verified experimentally (9), the acoustic power output of a subsonic jet is constant along the jet axis to a distance of five nozzle diameters at which point it starts to decrease and beyond eight nozzle diameters the acoustic power varies inversely with the distance from the exit raised to the 6th power.

For supersonic nozzles the variation of acoustic power depends on the supersonic length (distance from the nozzle exit to the point of unity Mach number). The acoustic power output increases linearly with distance along the jet, reaches a maximum at the supersonic length and subsequently decreases in proportion to the distance from the exit to the minus six power.

The distribution of the sources according to frequency content is also of importance. For both subsonic and supersonic flows the highest frequency sources are located close to the nozzle exit. Lower frequency sources are located farther from the exit. This is due to the frequency of sound emitted from a turbulent shear layer being proportional to the turbulent length scale. An indication of the source frequency distribution can be gained by examination of Fig. 3 for supersonic flow with data from two independent sources (9, 10).

The diffuser/exhaust duct interaction with the jet plume has both advantages and disadvantages. It has the advantage of altering the jet by confining its boundary to the duct walls. This alters the spread of the turbulent shear layers and most likely breaks up some of the low frequency noise generating mechanisms. In addition the diffuser duct acts to shield the test cell from the jet noise sources within the duct. The magnitude of this shielding effect is difficult due to uncertainty associated with the sources in the duct and the amount of propagation upstream and into the test cell. The shielding effect should be a significant factor in reducing the contribution of noise from the jet plume shear layers.

The disadvantageous effect of the diffuser duct is that it may interact with the jet to produce additional noise sources which may be strong sources of noise other than the source mechanisms associated with the noise from turbulent shear layers. The impingement of the jet on the duct wall produces a flow-solid surface interaction.

This gives rise to dipole radiation from the surface due to surface pressure fluctuations. This source is a more efficient producer of sound than the quadrapole source of the turbulent layer. If the engine nozzle/diffuser configuration is such that the diffuser inlet lip is close to the edge of the shear layer (not actually in the shear layer) there may be produced a noise source known as jet-orifice interaction noise. This has been shown for model test to produce noise below 500 HZ (9). Other experimental results and several plausible explanations for the phenomena are discussed in Reference 11.

The jet/diffuser interaction may also excite resonance modes in the diffuser. This could couple with pressure variations at the nozzle exit to produce a significant pressure variation at the engine exit plane adversely affecting engine performance and also presenting a rather strong acoustic input to susceptible engine mechanical vibration modes.

ANALYTICAL AND EXPERIMENTAL TECHNIQUES

An examination of the physical environment of a typical engine test cell will reveal a more complex influence on the acoustics than might be gained from the simple representation shown in Fig. 1. In addition to inlet ducting, engine, engine support, thrust stand and exhaust ducting the cell environment includes cable trays, blowout ports, viewing ports, instrumentation ports, catwalks, radiation shields, lights and various other test peculiar hardware and supporting structure. The first impression from an acoustic standpoint is that the cell will in no way lend itself to analytical methods of analysis. There are a number of reasons for this and these will be discussed as follows.

The cells could be classified as "acoustically dirty." The irregularity of scattering surfaces plus the various obstructions and scattering objects seriously complicates a solution to the point of defying solution by traditional acoustic ray techniques or analysis by means of the acoustic wave equation. However, an analysis of acoustic standing waves can be performed by use of a simplified model. The many reflecting surfaces offer an advantage in that they should provide a rather diffuse field in the test cell which has the advantage of lending itself to the use of reverberant field techniques for analysis of acoustic levels.

The close proximity of reflecting surfaces to the engine noise source coupled with the characteristically low frequency of these sources results in the entire cell being in the acoustic near field. In the acoustic near field the acoustic particle velocity is out of phase with the pressure. This results in real and imaginary components of the wave. Most analyses are associated with the far field where the wave is composed of the real or radiant component only. The analysis of a radiant and reactive field is complex and would be particularly so considering the numerous scattering objects and surfaces of the test cell.

Not associated with the cell itself, but definitely a source of difficulty, would be an accurate knowledge of the acoustic sources in the cells. Although the magnitude of the contribution and general description of the characteristics of the noise sources from engines can be given, the detail as to location, level, spectrum and radiation characteristics cannot be provided with the necessary definition required. (Indeed if this were possible it would solve only a small portion of the analysis problems.)

Wave Equation Analysis

This approach is based upon wave acoustics. This analysis has been used to analyze the three dimensional wave motion in a bounded space. It has been applied to problems of architectural acoustics in simple enclosures of rectangular, cylindrical or spherical characteristic shape. The approach has been to treat the enclosure as containing a number of resonance modes of vibration or normal modes. Wave analysis techniques are used to determine the normal modes and thus how the energy of free vibration is distributed in these normal modes or standing waves of the enclosure. The wave equation has also found other applications such as jet noise analysis.

The three dimensional wave equation may be written in terms of velocity potential as

$$\frac{\partial^2 \Phi}{\partial t^2} - c^2 \nabla^2 \Phi = -Q_0 \, \delta(x - x_0) \qquad (1)$$

where

$$\text{grad}\, \Phi = u$$

The left hand side of Eq. (1) governs the propagation characteristics of the source term on the right hand side of Eq. (1). If the source distribution and properties (i.e., monopole, dipole, quadrapole, etc.) are known, solutions may be obtained for the radiant sound field.

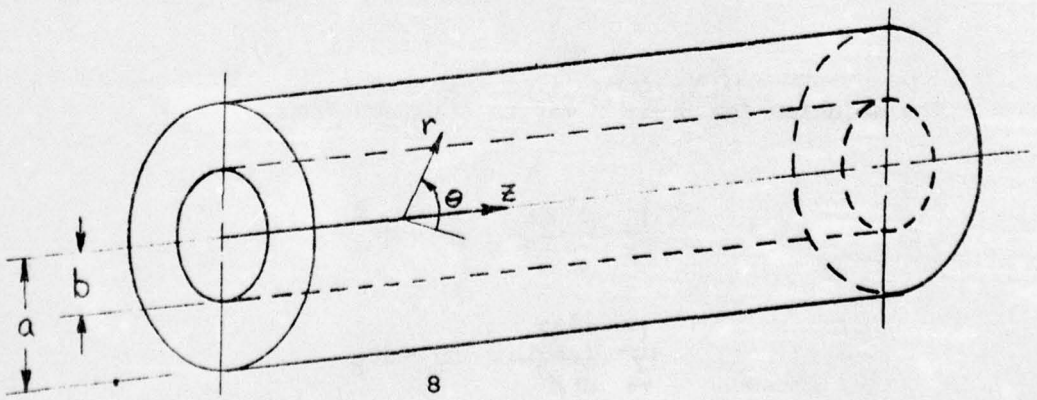
One method commonly used for solution of Eq. (1) involves the use of Green's function techniques. Green's function is the solution of Eq. (1) for Q_o equal to a unit impulse. If a solution can be obtained at each x_o, then the general solution is

$$\Phi = \int_V Q_o \, g_w(x - x_o) \, dx_1 \, dx_2 \, dx_3 \qquad (2)$$

where g_w is the Green's function. Solutions of this type have been obtained for various simplified geometries and source terms. A solution by wave equation analysis is not plausible for the test cell enclosure due to the complications of geometry and uncertainty of source location and properties.

Although a general solution is not plausible a solution for the standing wave frequencies in the enclosure is possible. The procedure for obtaining this solution is described in various mathematics texts on solution of partial differential equations. The solution for the test cell type model is not generally available and thus will be outlined here.

The model to be used will consider the test cell to be approximated by the annular space between two concentric cylinders of a given length L and closed at both ends by reflecting walls. The model is shown below along with the appropriate coordinate system.



The solution is obtained by casting Eq. 1 in cylindrical coordinates and setting the source term to zero. Assuming that the temporal portion of the velocity potential is harmonic, then

$$\Phi = \phi e^{i\omega t} \tag{3}$$

where ϕ is the spatial portion of Φ. Substituting Eq. (3) into Eq. (1) and performing the differentiation yields

$$\nabla^2 \phi + k^2 \Phi = 0 \tag{4}$$

where $k = \omega/c$. Performing the Laplacian operation, Eq. (4) is expanded to

$$\frac{\partial^2 \phi}{\partial r^2} + \frac{1}{r}\frac{\partial \phi}{\partial r} + \frac{1}{r^2}\frac{\partial^2 \phi}{\partial \theta^2} + \frac{\partial^2 \phi}{\partial z^2} + k^2 \phi = 0 \tag{5}$$

Assume that ϕ can be expressed as a product of three independent solutions, namely, R a function of r only, Θ a function of θ only and Z a function of z only. Substituting such an expression for ϕ into Eq. 5 gives

$$\frac{1}{R}\frac{\partial^2 R}{\partial r^2} + \frac{1}{Rr}\frac{\partial R}{\partial r} + \frac{1}{r^2}\frac{1}{\Theta}\frac{\partial^2 \Theta}{\partial \theta^2} + \frac{1}{Z}\frac{\partial^2 Z}{\partial z^2} = -k \tag{6}$$

The solution for Θ and Z may be obtained from

$$\frac{1}{\Theta}\frac{\partial^2 \Theta}{\partial \theta^2} = -k_\theta^2 \tag{7}$$

$$\frac{1}{Z}\frac{\partial^2 Z}{\partial z^2} = -k_z^2 \tag{8}$$

since R, Θ and Z are assumed to be independent. Then the solution for R is obtained from

$$\frac{1}{R}\frac{\partial^2 R}{\partial r^2} + \frac{1}{Rr}\frac{\partial R}{\partial r} + \left(k^2 - k_z^2 - \frac{k_\theta^2}{r^2}\right) = 0 \tag{9}$$

Let k_r be defined as a radial wave number given by

$$k_r^2 = \left(\frac{\omega_r}{c}\right)^2 = k^2 - k_z^2 \tag{10}$$

Equation (9) is then identified as a form of Bessel's equation.

$$r^2\frac{\partial^2 R}{\partial r^2} + \frac{1}{r}\frac{\partial R}{\partial r} + \left(k_r^2 r^2 - k_\theta^2\right)R = 0 \tag{11}$$

For the model being considered, the Θ solution will be neglected since the source distribution will be considered uniform in the θ direction at $r = b$ and there will be no forcing function to support a ϕ dependence on θ . The solution of Eq. (8) is

$$Z_1 = C_1 \cos k_z z + C_2 \sin k_z z \tag{12}$$

and

$$u_z = -\frac{\partial \phi}{\partial z} = -R\frac{\partial Z_1}{\partial z} = R k_z \left(C_1 \sin k_z z - C_2 \cos k_z z\right) \tag{13}$$

The particle velocity must be zero at both end walls. Boundary conditions are then

$$u_z = 0 \quad \text{at} \quad z = 0 \text{ and } z = L \tag{14}$$

To satisfy these conditions C_2 must be zero and

$$k_z L = n\pi$$

or

$$\omega_z = \frac{n\pi c}{L} \tag{15}$$

where ω_z is the frequency of standing waves along the z or longitudinal axis.

The solution for the lateral or r directed standing wave is obtained by solution of Eq. (11). The general solution of Bessel's equation applicable here is

$$R = C_3 J_{0k_\theta}(k_r r) + C_4 Y_{0k_\theta}(k_r r) \tag{16}$$

Now the solution for particle velocity is

$$u_r = -Z_1 \frac{\partial R}{\partial r} = -Z_1 \left[C_3 \frac{\partial}{\partial r} J_0(k_r r) + C_4 \frac{\partial}{\partial r} Y_0(k_r r) \right]$$

$$= Z_1 \left[C_3 J_1(k_r r) + C_4 Y_1(k_r r) \right] \tag{17}$$

The boundary conditions are

$$u_r = 0 \; ; \quad r = a, \; r = b$$

Equation (17) at the boundaries becomes

$$C_3 J_1(k_r b) + C_4 Y_1(k_r b) = 0 \tag{18}$$

$$C_3 J_1(k_r a) + C_4 Y_1(k_r a) = 0 \tag{19}$$

Combining Eqs. (18) and (19) gives

$$J_1(k_r b)\, Y_1(k_r a) - J_1(k_r a)\, Y_1(k_r b) = 0 \tag{20}$$

The radial wave numbers are obtained by determining the value of k_r which will satisfy Eq. (20) for specified values of a and b. To obtain a compact solution, consider solutions to Eq. (20) for various values of b/a. A computer program was written employing canned routines for the Bessel functions and Eq. (20) was solved by use of the IBM 370 computer for the first three wave numbers k_r for various values of b/a. The results are presented below.

b/a	mode	Wave number, k_r
	1	6.3
1/2	2	12.6
	3	18.8
	1	4.9
1/3	2	9.5
	3	14.2
	1	4.4
1/4	2	8.5
	3	12.6
	1	4.2

b/a	mode	Wave number, k_r
1/5	2	8.0
	3	11.9
	1	4.1
1/6	2	7.7
	3	11.4

Recalling Eq. (10), the wave number k can be expressed as

$$k = \sqrt{k_r^2 + k_z^2}$$

or

$$f = \frac{c}{2\pi} \sqrt{k_r^2 + \left(\frac{n\pi c}{L}\right)^2} \qquad (21)$$

Where f is the frequency in hertz. Equation (21) thus expresses the characteristic frequencies of the test cell model corresponding to the allowed normal modes of the vibration.

In the actual cell environment there will more than likely be a variation of the functional dependence shown here for the lateral waves. However, the values obtained for the standing waves in the longitudinal direction, Eq. (15), should yield accurate values applicable to the test cell environment.

Reverberation Times and Known Sources

Although a solution of the wave equation for the specific characteristics of the test cell acoustic field at each position in the cell is not practical, a technique combining experimental data on acoustic energy decay in terms of reverberation times in various frequency bands coupled with an energy balance and a model of the cell reflection characteristics may prove useful in determining the cell sound power level. The reverberation time is the time required for the sound pressure level in the enclosure to decay to a level 60 db below the initial steady state level. Reverberation time is an acoustical property of enclosures and is the traditional criterion for the design of rooms and auditoriums based on audience judgements of the acoustic quality of existing rooms and auditoriums. What is desired in this analysis is the rate of decay of acoustic energy in various frequency bands. Reverberation time will be used to express this rate since much of the acoustic theory of enclosures is expressed in terms of this parameter.

Consider a model for the reverberation characteristics of an enclosure proposed by Eyring (12). The buildup or decay of sound in an enclosure is considered to be a step wise process as reflected waves from the source begin to reach the observation point during energy buildup or cease to reach the observation point during energy decay. If an emitter begins to emit sound of power level W at time equal zero the direct radiation from the source will be observed at the observation point followed by a reflected wave of power $W(1-\alpha)$ and subsequently by waves of power $W(1-\alpha)^2$, $W(1-\alpha)^3$ ---- $W(1-\alpha)^n$ where n identifies the nth reflection and α is the average surface acoustic absorption coefficient. Thus the energy buildup in the enclosure can be modeled as a buildup of source (direct waves) and source images (reflected waves).

Consider the increase in energy density at a time t over an interval Δt. The time interval Δt cannot be an arbitrary value. It must be the time interval between arrival of reflected waves. The energy incident on all surfaces of an enclosure with total area S in an interval of time Δt is given by (13)

$$\frac{Ec}{4} S\Delta t$$

where E is the acoustic energy density. The total energy in the enclosure is EV. The time required for the total energy to undergo one reflection is obtained from

$$\frac{Ec}{4} S\Delta t = EV \tag{22}$$

and solving Δt gives

$$\Delta t = \frac{4V}{Sc} \tag{23}$$

Considering the reflection past the observation point in the time interval Δt the change in the energy is

$$V\Delta E = W(1-\alpha)^n \Delta t$$

However, over the interval from time zero to time t, there are n reflections and

$$n = \frac{t}{\Delta t} = \frac{S_c}{4V} t \tag{24}$$

by use of Eq. (23). The total energy may now be expressed as

$$VE = \sum_n W(1-\alpha)^n \Delta t \tag{25}$$

and if this sum is approximated as an integral, then

$$VE = \int_0^t W(1-\alpha)^{\frac{S_c}{4V} t} dt \tag{26}$$

Performing the integration gives

$$E = \frac{4W}{S_c \ln(1-\alpha)} \left[1 - e^{\frac{S_c}{4V} t \ln(1-\alpha)}\right] \tag{27}$$

As t approaches a large value, the energy density approaches an equilibrium value given by

$$E_\infty = -\frac{4W}{Sc\ln(1-\alpha)} \tag{28}$$

The decay of sound in an enclosure when the source ceases to radiate behaves in the reverse manner to the mechanism which describes the buildup. We can deduce then from Eq. (25) that the energy at any time after the source ceases to radiate (time zero) is

$$E = E_\infty - \sum_n W(1-\alpha)^n \Delta t \tag{29}$$

Again if the sum is approximated by an integral, and the integration is performed, the expression for the energy decay becomes

$$E = E_\infty e^{\frac{Sc}{4V} t \ln(1-\alpha)} \tag{30}$$

Reverberation time is defined as the time required for the energy level to fall to a value 10^6 times less than E_∞. Thus, the reverberation time T_r may be obtained from the following ratio

$$\frac{E_\infty}{E} = 10^6 = e^{-\frac{Sc}{4V}\left[\ln(1-\alpha)\right] T_r} \tag{31}$$

Solving for T_r gives

$$T_r = -\frac{4V\ln 10^6}{Sc\ln(1-\alpha)} = -\frac{55.26\,V}{Sc\ln(1-\alpha)} \tag{32}$$

The steady-state energy level of an enclosure in the presence of a source of power W is expressed in terms of T_r as

$$E_\infty = \frac{0.07238\, W\, T_r}{V} \tag{33}$$

Relating the acoustic energy density to a measurable parameter presents somewhat of a problem. The acoustic pressure and velocity in the cell has both reactive and radiant components due to the close proximity of any point in the cell to the sound sources. The energy density will not be a simple function of the acoustic pressure as for plane radiant waves. However, a technique which has been used effectively (14) is to assume that the local field is a superposition of plane waves. The relationship between energy density and root-mean-square pressure is then

$$E_\infty = \frac{P_{rms}^2}{\rho c} \tag{34}$$

The local rms pressure is then related to test cell source power, reverberation time and medium properties by

$$P_{rms} = .269\, c \sqrt{\frac{W\, T_r}{\rho V}} \tag{35}$$

The power level for most sources will vary considerably as a function of frequency. Therefore, the power level should be specified as a function of frequency or frequency band rms level. If the reverberation time as a function of frequency is known, then the pressure as a function of frequency may be determined. The determination of reverberation times will be described under the experimental section later in this report. The specification of the source power level will have to be made from measurements of the acoustic field of a typical engine close to the engine sources. A suggested set of measuring stations is shown in Fig. 4. If possible, the partition should be placed as shown to simulate the barrier effect of the inlet duct and labyrinth seal in shielding compressor and fan noise from the measurement location as would be the case in the test cell.

Once the sound pressure levels have been obtained, the power levels may be determined. The method will be to relate the acoustic pressure to the intensity and integrate the intensity over a proper area to determine the power level. For either plane waves or spherical waves, the acoustic intensity is related to the pressure by

$$I_n = \frac{|P_n|^2}{2\rho c} \tag{36}$$

where the I_n and p_n refer to values for the nth frequency band. Now consider that the sound pressure level measured at a microphone, say microphone No. 1, is the sound pressure level which exists over the surface of a cylinder of radius r_2 and height x_s whose axis coincides with the engine axis and is centered axially on microphone No. 1. The power radiated through this cylindrical segment is then

$$W_{n_1} = \int I_n dA = I_n A$$

$$= \frac{\pi r_2 x_s |P_n|^2}{\rho c} \tag{37}$$

where Wn_1 is the power radiated in the nth frequency band through the cylindrical surface corresponding to microphone No. 1. If the power for each cylindrical surface is then summed an expression for the total power will be obtained as

$$W_n = \frac{\pi r_2 x_s}{\rho c} \Sigma |P_n|^2 \tag{38}$$

Equation (34) would appear to neglect radiation from the jet exhaust and to perhaps underestimate the sound power from forward engine sources. The jet exhaust enters the exhaust ducting at the nozzle exit and as mentioned previously, the duct shields some of the jet noise. The microphone position and the integration surface of the cylinder being centered on the exhaust plane should account for some of the underestimation of the jet noise. Modifications to the power level in various bands may be necessary based on experimental data. Once the power level has been determined, the rms pressure in the cell for the engine operating may be estimated by use of Equation 35.

Acoustic Survey

One of the first steps to be taken in characterizing the cell acoustic field experimentally is to perform a sound pressure level survey in the cell under specified engine operating conditions which are suspected to produce the most severe acoustic environment. Condenser microphones and appropriate electronics are used quite widely in aeroacoustic noise measurements. A 1/2 inch or 1/4 inch microphone should prove satisfactory for use in test cell measurements as they have good response and are omnidirectional to approximately 5000 and 10,000 Hz, respectively.

The cell environment could pose a problem to proper operation of the microphone. The cell temperature is not allowed under normal operating conditions to exceed 200°F. This should not affect microphone operating parameters or structural properties. However, care should be taken to assure that other components such as preamplifier, cable, etc. can withstand the thermal environment particularly the radiation component.

The microphone will be placed in the secondary flow field of the test cell. Air flow over the microphone can result in flow noise which is picked up by the microphone and is a troublesome source of extraneous noise. This noise can be eliminated by use of a wind screen, which is available commercially.

Perhaps the most severe environment which adversely affects microphone measurement is the vibration environment. In order to obtain good acoustic response, the microphone diaphragm mass should be low. Due to this low mass, the microphone is also subject to excitation due to mechanical vibration transmitted through its support. A 1g rms acceleration will result in an equivalent sound pressure for a typical 1/4 inch microphone of between 85 and 90 db. Steps should be taken to assure vibration isolation for the microphone.

The purpose of the acoustic survey is to determine the level of sound in the cell and its characteristics with respect to position in the cell. Characteristics to be noted are sound pressure level and frequency and how these vary as a function of cell position. This should produce useful information to support analytical estimates and should provide a continuing data base upon which empirical estimates can be made. It is suggested that the survey be performed as shown in Fig. 5, employing either stationary microphone or traversing microphone measurements.

Reverberation Characteristics Measurement

Reverberation time as mentioned previously is a parameter of an enclosure which indicates the rate of change of the acoustic energy in the enclosure due to wall absorption and acoustic wave interference. More specifically it is the time required for the acoustic energy level to drop to 60 db less than the steady-state level when the sound source suddenly ceases to radiate. The concept was first formulated using the assumptions of a diffuse field and geometric acoustics. Useful information can be obtained when these assumptions are violated if the reverberation characteristics are determined as a function of frequency or frequency band. The information thus gained is useful for estimations of steady-state acoustic levels and also for the determination of the frequencies for which additional absorption must be provided to increase the acoustic decay rate.

Reverberation time measurements are performed by use of a sound source which is capable of driving the enclosure to a steady-state level of 30 to 40 db above the background for all frequencies of interest. For the test cell this frequency range is between 50 and 10,000 Hz. This is accomplished in a number of ways depending on the desired frequency excitation, i.e., loudspeakers, pistol discharge. For the determineation of test cell acoustics, it is suggested that a loudspeaker having good response over the 50 to 10,000 Hz range (two speakers may be required) be driven by a random signal such that a white noise is produced in the cell. Microphones installed in the cell at various locations will monitor the acoustic levels. When the signal to the loudspeaker is shut off the acoustic decay as measured by the microphones is recorded. This recorded signal can then be filtered to observe the decay in various frequency bands and to determine reverberation times for these bands. In determining reverberation times, it will be necessary to establish a linear decay rate which best describes the actual decay rate and extrapolate this to the -60 db level.

The problem naturally arises as to where in the cell to locate the loudspeakers and microphones. The loudspeaker is a localized source of sound whereas the noise sources from an engine are distributed along the engine casing and along the jet plume. The solution would then appear to be a distribution of speakers. However, this would complicate the speaker installation and possibly in itself affect the reverberation characteristics. It is suggested that a single speaker be used at various locations in the cell. A suggested method is shown in Fig. 4. The engine is replaced by sections of straight duct of the same diameter as the mean engine casing diameter. A section of duct is removed and a speaker section is inserted as shown. The opening of the duct opposite the speaker is sealed off and the bulkhead lined with acoustic material to prevent radiation from the duct walls. The

sound will radiate into the cell through the circumferential slot and thus approximate a circumferential distribution of sound sources. This speaker set up can be used at step wise cross-sections of the duct. Reverberation times may be averaged over the various locations or source localized reverberation times may be determined for use in Eq. (35).

The position of the microphones should be in the vicinity of the engine location as this is the critical point in the field. The actual position will depend on the results of the acoustic survey.

Model Studies

Model studies can be used to good advantage to determine the effect of jet plume/exhaust diffuser interaction. It has been noted that under certain test conditions the jet can excite resonance modes of the exhaust duct. It can also produce interaction noise with inserts and various diffuser inlet configurations designed to prevent recirculation of exhaust gases into the cell. In addition, there is the problem as mentioned earlier of determining the shielding effect of the diffuser on the noise produced by jet-induced turbulence inside the diffuser. Experimental studies of model configurations can be used to gain insight into the parameters which control these interactions.

The ability to scale the results of experimental studies is necessary if the experimental results are to have more than qualitative significance. The scaling of the data is straight forward if dynamic similarity can be achieved. The procedure requires only that scale model data at the point of interest be analyzed in constant-percentage frequency bands (15). The sound-pressure-level estimate for the full-scale configuration will be the same as for the model, with the frequency for the full scale given by dividing the frequency of the model test by the scale factor.

In most tests it is difficult to match both Mach number and Reynolds number to obtain absolute similarity. It has been found that for circular subsonic and ideally expanded supersonic jets the frequency spectra obeys a Strouhal type scaling mentioned previously:

$$St = \frac{fD}{U} \tag{39}$$

The scaling of power levels of jet noise was first deduced from the work by Lighthill[8] and can be written as

$$W \propto \frac{\rho^2 U^8 D^2}{\rho_\infty c_\infty} \qquad (40)$$

This relation has been shown to be good for subsonic flows and for shock free supersonic flows. The area of supersonic jet noise producing mechanisms is an active topic of discussion in the literature and no conclusive scaling law can be given for non-ideally expanded supersonic jets.

The noise produced by jet/diffuser interaction is not all due to noise from free jet turbulence. Some noise will be produced due to flow and solid surface interaction. In this case a dipole type source term arises and the power can be expected to scale according to a U^6 type relationship.

STRUCTURE-ACOUSTIC FIELD INTERACTION

A considerable amount of time associated with this project was devoted to a literature search to assess the state-of-the-art concerning the interaction of acoustic fields with structural panels and shells. The ultimate objective was to determine if acoustic energy input to a panel at a frequency different from the vibrational resonance frequency of the panel could reinforce the resonance vibration by feeding energy into this mode. If this were possible for a number of frequencies then a very high amplitude resonance mode could be excited in the structure. The result of the survey is that no support can be found for the existence of a mechanism which could accomplish this in typical aircraft engine structural components.

The possible existence of the reinforcing mechanism would, of necessity, require the existence of a number of frequency components of a sound field close to the resonance frequency. It would then be appropriate to assume a Gaussian distribution of the sound field at least in the vicinity of the resonance frequency. Analysis of random noise interaction with structure is a fairly well developed discipline due to its importance in the analysis of acoustic fatigue of aircraft structure. The analysis follows a statistical approach (16) of considering the response of a large number of normal modes and casting the response in terms of the response spectral density. This is then related by means of transfer functions for vibration of each mode to the pressure spectral density of the sound field.

Each normal mode of a structure is modeled as a simple resonator. Now a simple resonator has very small admittance to all excitation frequencies except those in the vicinity of the model frequency. The badwidth associated with large admittance is fairly small typically a few hertz. The wide spread use of this model and its verification by experimental results has proven its integrity.

Therefore, if the resonance condition can only be excited by sound frequencies very close to its natural frequency, the question arises as to the possibility of coupling various modes together either through the structure or the acoustic medium to reinforce a particular resonance mode. If the acoustic medium is air, then coupling is ruled out due to the low density of air. Coupling through the structure is a definite possibility. This involves the response of the mode due to co-spectrum response (co-spectrum is the real part of cross-spectra). This response has been analyzed by Davis (17). His results show that the co-spectrum response for typical aircraft structures (damping ratio of .01) is less than 30 percent of total response for frequencies outside a range within five percent of the mode frequency with contribution by no frequencies greater than 50 percent. It is pointed out that these are maximum possible values. This should not result in significant mode amplification.

An unreferenced bibliography concerning the interaction of acoustic fields with structure is presented following the References.

CONCLUSIONS AND RECOMMENDATIONS

The engine test cells at AEDC were designed with no thought given to acoustics. The cells with the required supporting structure, test hardware and instrumentation have many reflecting and scattering objects and surfaces which results in a complex acoustic field and hampering of acoustic analysis. Analysis is further complicated by the close proximity of reflecting surfaces to low frequency noise sources resulting in the entire enclosure being in the acoustic near field.

The many scattering surfaces in the test cell enclosure should result in a fairly diffuse acoustic field and thus should be amenable to an analysis taking advantage of these characteristics. The reverberation times used with known sources take advantage of this and the method should give useful results. It is recommended that priority be given to obtaining the energy decay data or reverberation times as these data would be useful in determining the frequency range over which acoustic damping may be necessary in addition to supplying the data necessary for the analysis mentioned above.

An evaluation of noise sources and transmission paths leads to the conclusion that the exterior noise sources do not significantly contribute to the test cell acoustic level with the possible exception of J-1 and J-2 cells. The dominant interior sources are combustion noise, jet noise, and possibly jet/diffuser interaction noise. It is recommended that model studies be performed to evaluate the effect of the jet/diffuser geometry on the noise emitted to the test cell enclosure.

It is recommended that first priority be given to an acoustic survey under a severe engine test condition. This will supply much needed information concerning the severity of the acoustic environment, the distribution of sound with respect to frequency content and the variation of sound pressure level within the cell.

State-of-the-art analysis of acoustic field/structural interaction primarily consists of statistical energy methods. This is particularly applicable to the test cell enclosure assuming a diffuse acoustic field. Structural response is modeled as many simple resonators. There is no support found for a coupling mechanism between modes which would unduly amplify a particular mode and result in high amplitude radiation source.

Due to the complexities associated with the test cell from an acoustic standpoint, it is inconceivable that data could be obtained which would allow one to determine the engine acoustic emission characteristics in a normal operating environment. The data necessary for this determination should be taken from free field tests with the engine operating on either a test stand or in an anechoic room. The anechoic room is preferable as test scheduling would not be subject to perturbations due to climatic conditions.

REFERENCES

1. Beranek, L. L., Noise Reduction, McGraw-Hill, New York, 1960, pp 453-454.

2. Veranek, L. L., Noise and Vibration Control, McGraw-Hill, New York, 1971, p 330.

3. Kazin, S. B., et. al, "Core Engine Noise Control Progran," Federal Aviation Administration Report No. FAA-RD-74-125. August 1974.

4. Mathews, D. C. and Rekos, N. F., Jr., "Direct Combustion Generated Noise in Turbopropulsion Systems - Prediction and Measurement," AIAA Paper No. 76-579.

5. Motsinger, R. E. and Emmerling, J. J., "Review of Theory and Methods for Combustion Noise Prediction," AIAA Paper No. 75-541, March 1975.

6. Abdelhamid, D. T., et. al, "Noise Characteristics of Combustion Augmented High Speed Jets," AIAA Paper No. 73-189, January 1973.

7. Nagamatsu, H. T. and Sheer, R. E., "Subsonic and Supersonic Jets and Supersonic Suppressor Characteristics," in Progress in Aeronautics and Astronautics, Vol. 37, 1975.

8. Lighthill, M. J., "Jet Noise" AIAA Journal, Vol. 1, July 1963, pp 1507-1517.

9. MacGregor, G. R. and Simcox, C. D., "Location of Acoustic Sources in Jet Flows by Means of "Wall Isolation Technique" in Progress in Aeronautics and Astronautics, Vol. 37, 1975.

10. Potter, R. C. "An Investigation to Locate the Acoustic Sources in a High Speed Jet Exhaust Stream." NASA CR 101105, June 1969.

11. Potter, R. C. "Jet-Orifice Interaction Noise," in Basic Aerodynamic Noise Research, NASA SP-207, July 1969.

12. Eyring, C. F., "Reverberation Time in 'Dead' Rooms," Journal of the Acoustical Society of America, Vol. 1, p 217, 1930.

13. Kinsler, L. E. and Frey, A. R., Fundamentals of Acoustics, John Wiley and Sons, Inc., New York, 1962, p 421.

14. Harper, W. L., "Experimental Study of Noise Produced by Jet-Flap Type Nozzles," M.S. Thesis University of Tennessee, 1971.

15. Baranek, L. L., Noise and Vibration Control, McGraw-Hill, New York, 1971, p 534.

16. Smith, P. W., Jr. and Lyon, R. H., "Sound and Structural Vibration," NASA CR-160, March 1965.

UNREFERENCED BIBLIOGRAPHY ON ACOUSTIC-STRUCTURE INTERACTION

Kana, D. D., "Response of a Cylindrical Shell to Random Acoustic Excitation," AIAA Journal, Vol. 9, No. 3, March 1971.

Hwang, C. and Pi, W. S., "Random Acoustic Response of a Cylindrical Shell," AIAA Journal, Vol. 7, No. 12, December 1969.

Cottis, M. G., "On the Dynamic Response of an Orthotropic Finite Cylindrical Shell to an Arbitrary Pressure Field," J. Sound Vib., Vol. 7, No. 1, 1968.

Fahy, F. J. and Wee, R. B. S., "Some Experiments with Stiffened Plates Under Acoustic Excitation," J. Sound Vib., Vol. 7, No. 3, 1968.

Bhat, B. R., Rao, B. V. A. and Wagner, H., "Response of Structures to Random Acoustic Excitation-An Experimental Study," J. Spacraft and Rockets, Vol. 11, No. 4, April 1974.

Nemat-Nasser, S., "On the Response of Shallow Thin Shells to Random Excitations," AIAA Journal, Vol. 6, No. 7, July 1968.

Elisakoff, I., "Turbulent Flow-Excited Vibrations of a Shallow Cylindrical Shell," AIAA Journal, Vol. 13, No. 9, September 1975.

Lyon, R. H. and Maidanik, G., "Power Flow Between Linearly-Coupled Oscillators," J. Acout. Soc. Am., Vol. 34, No. 5, May 1962.

Richards, E. J. and Mead, D. J., Noise and Acoustic Fatigue in Aeronautics, John Wiley and Sons, Ltd., New York, 1968.

Clarkson, B. L., "Structural Aspects of Acoustic Loads," AGARDograph 65, September 1960.

Clarkson, B. L., "Scaling of Near Field Pressure Correlation Patterns Around a Jet Exhaust" Acoustical Fatigue in Aerospace Structures (Ed. W. J. Trapp and D. M. Forney). Syracuse Univ. Press, 1965.

Geers, T. L., "Excitation of an Elastic Cylindrical Shell by a Transient Acoustic Wave," J. Applied Mechanics, September 1969.

Powell, Alan, "An Introduction to Acoustic Fatigue" Acoustical Fatigue in Aerospace Structures (Ed. W. J. Trapp and D. M. Forney) Syracuse Univ. Press, 1965.

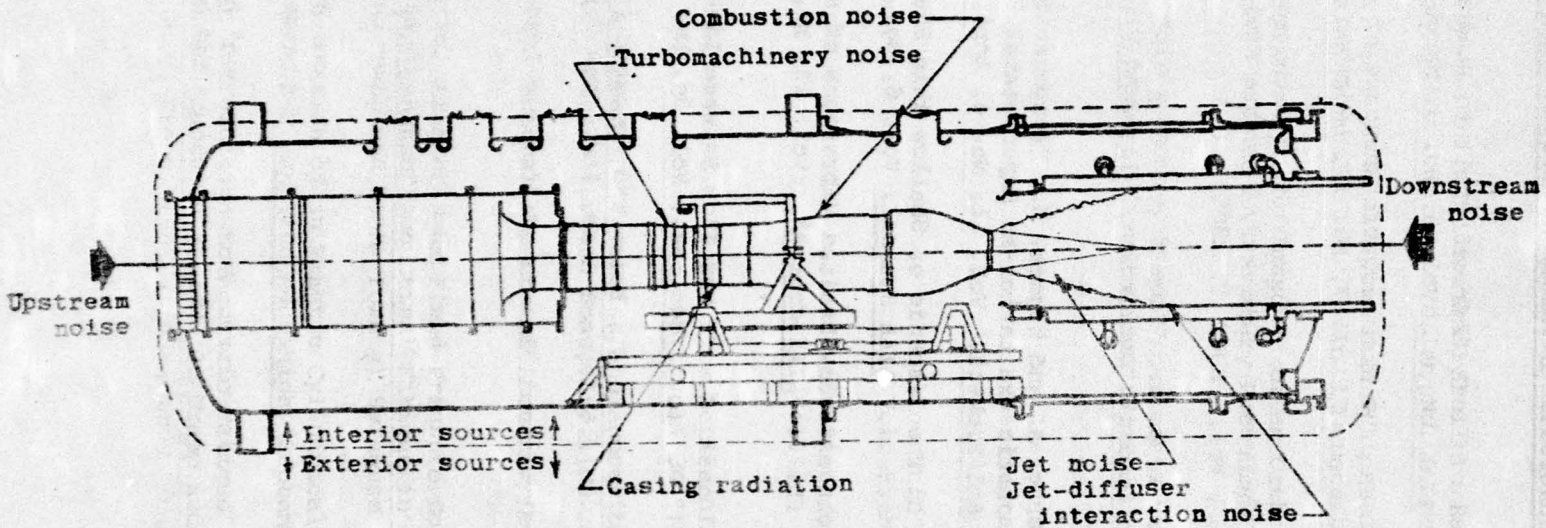


Figure 1. Test Cell Noise Sources

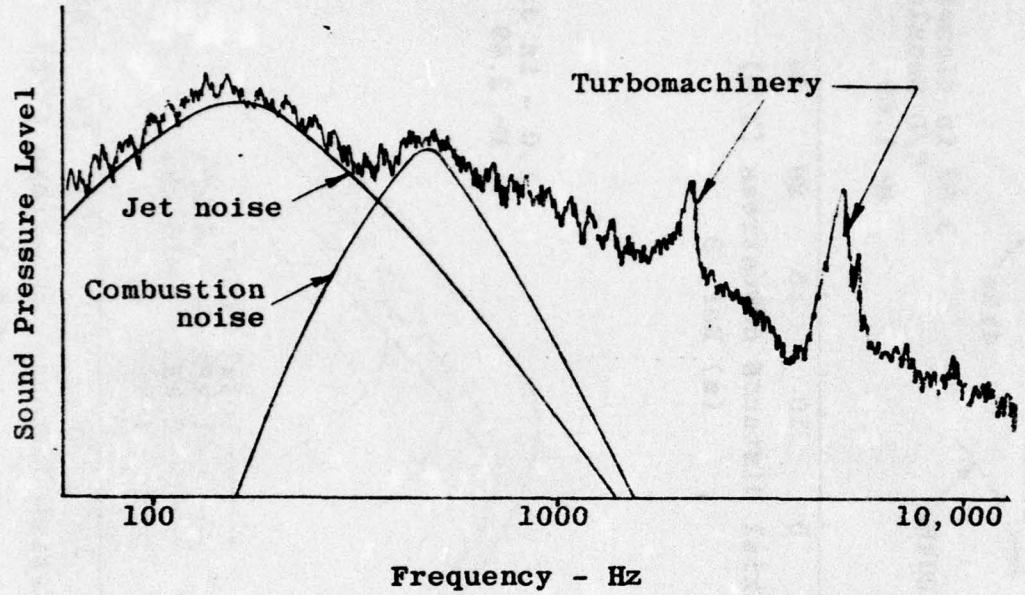
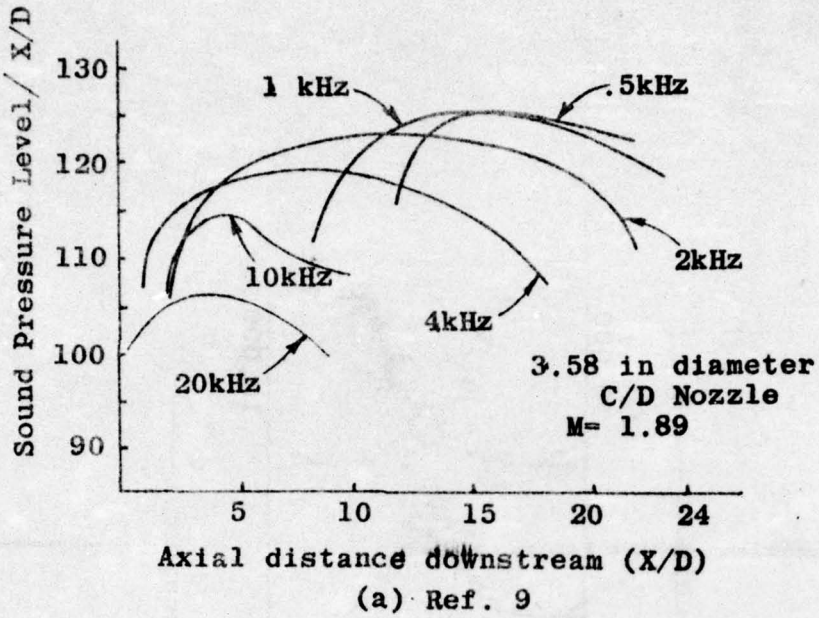
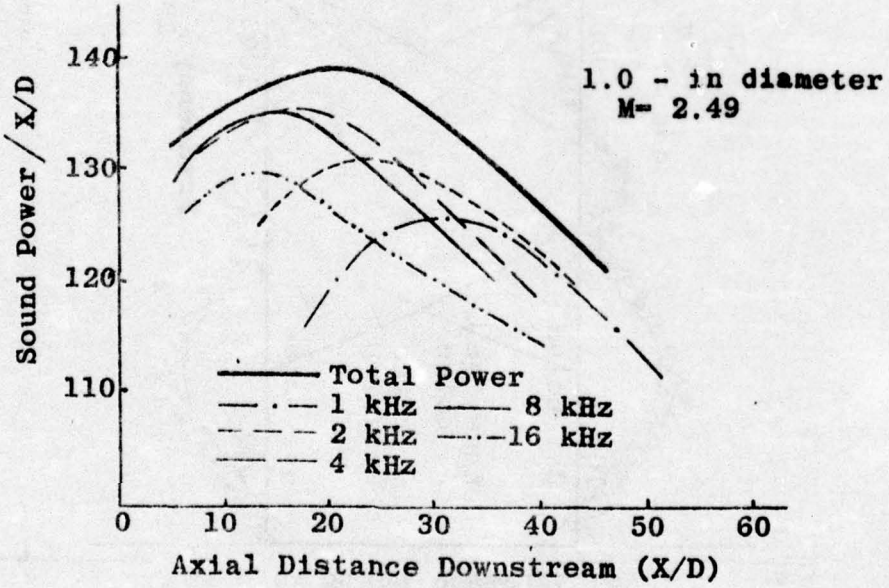


Figure 2. Typical Jet Engine Noise Spectra



(a) Ref. 9



(b) Ref. 10

Figure 3. Axial Distribution of Source Frequencies in an Ideally Expanded Supersonic Jet.

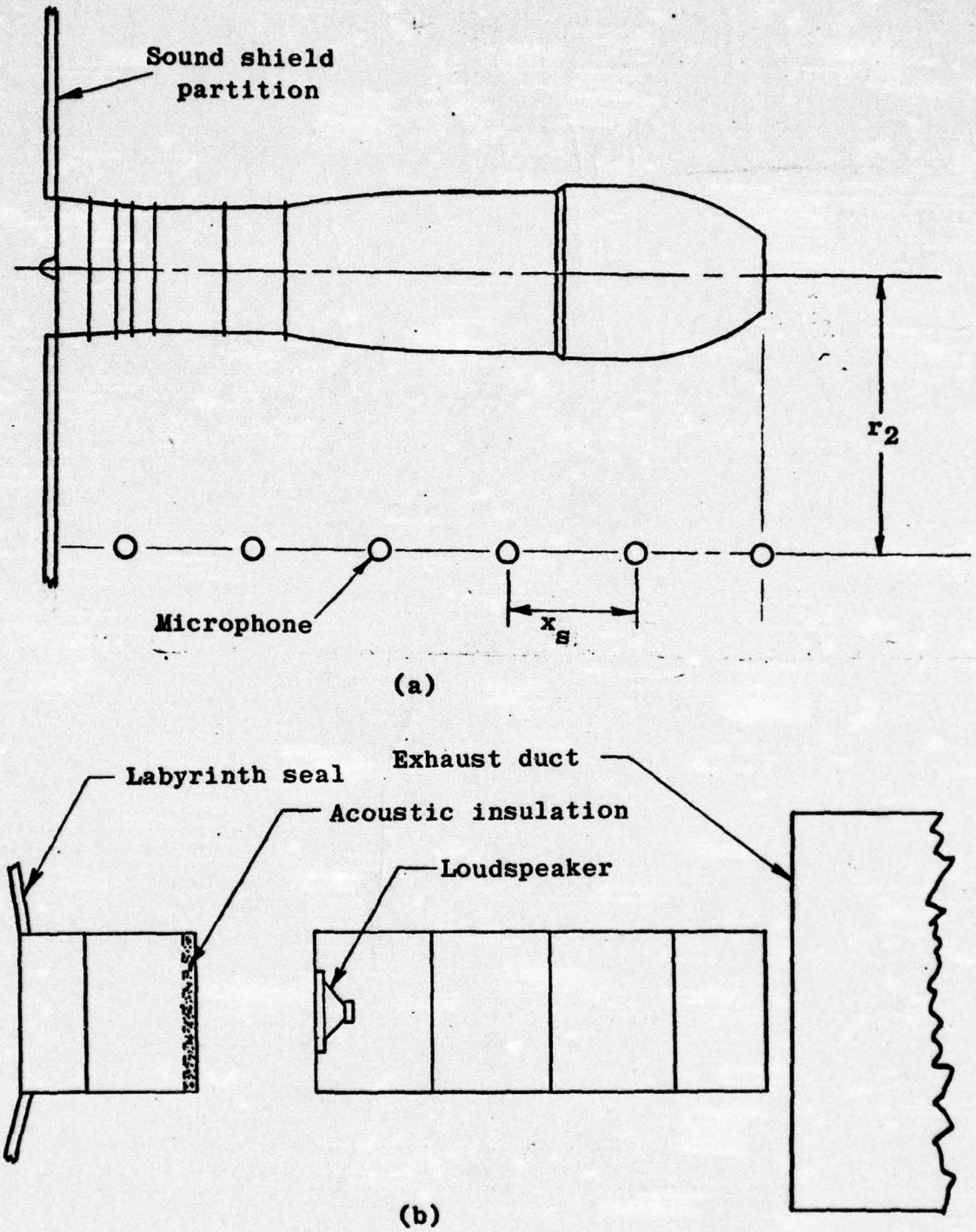


Figure 4. (a) Acoustic field measurement stations
(b) Typical speaker location for reverberation time measurements.

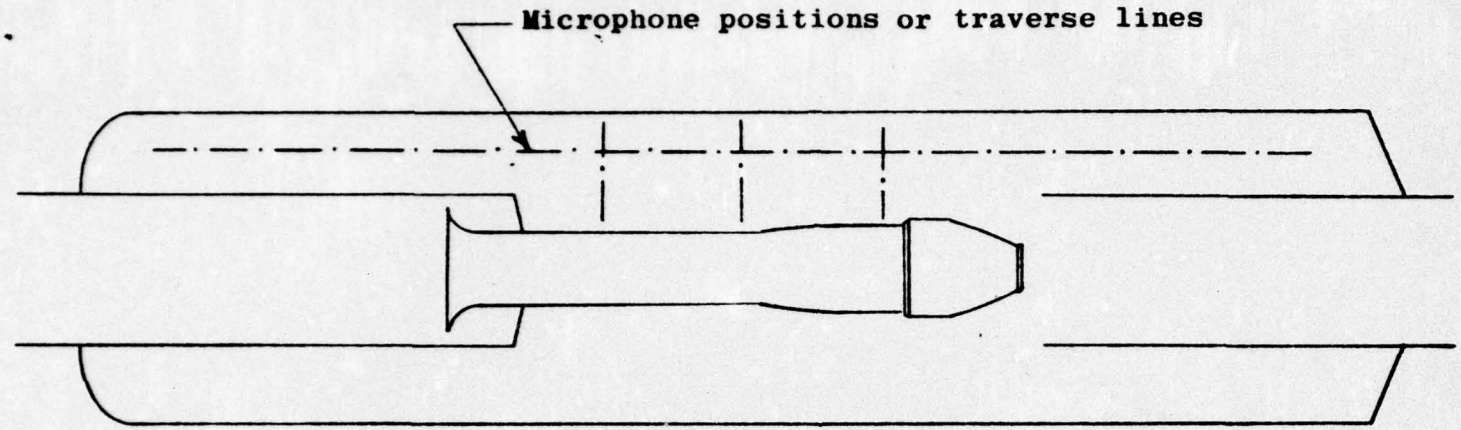


Figure 5. Acoustic Survey Microphone Positions

12-36

1976 USAF-ASEE SUMMER FACULTY RESEARCH PROGRAM
sponsored by
THE AIR FORCE OFFICE OF SCIENTIFIC RESEARCH
conducted by
AUBURN UNIVERSITY AND OHIO STATE UNIVERSITY

PARTICIPANT'S FINAL REPORT

HIGH ANGLE OF ATTACK SUPPORT INTERFERENCE

Prepared by:	Robert C. Nelson
Academic Rank:	Assistant Professor
Department and University:	Department of Aerospace and Mechanical Engineering University of Notre Dame

Assignment:

Air Force Base Laboratory	Arnold AFS Arnold Engineering Development Center
Division Branch	Propulsion Wind Tunnel Aerodynamic Wind Tunnel (4T)
ARO Research Colleague:	William B. Baker, Jr.
Date:	July 23, 1976
Contract No.:	F44620-75-C-0031

ACKNOWLEDGMENT

This study was performed between May 17th and July 23rd, 1976 and was sponsored by the Air Force Office of Scientific Research as part of the 1976 USAF-ASEE Summer Faculty Research Program. The author gratefully acknowledges the cooperation and technical support from members of ARO, Inc.

The author particularly wishes to express his gratitude to his ARO research colleague Mr. William Baker (PWT/4T) and to Dr. Marion Laster (AEDC/DYR) the Air Force Coordinator of this program at the Arnold Engineering Development Center.

LIST OF FIGURES

Figure 1. High Angle-of-Attack Support Systems

Figure 2. Examples of Support Interference

Figure 3. Sketch of Missile with Body Vortices

Figure 4. Wake Patterns as Viewed in the Crossflow Plane

Figure 5. Sketch of Impulsive Flow Analogy

Figure 6. Ratio of Crossflow Drag Coefficient for a Finite Length Cylinder to that for an Infinite Length Cylinder

Figure 7. Drag Coefficient for a Circular Cylinder Started Impulsively from Rest

Figure 8. Variation of Drag Coefficient with Reynolds Number for a Circular Cylinder

Figure 9. Variation of Drag Coefficient with Mach Number for Circular Cylinders

Figure 10. Variation of Drag Coefficient and Wake Patterns with Mach and Reynolds Numbers

Figure 11. Relationship Between Drag Coefficient and Strouhal Number

Figure 12. Effect of Splitter Plates on the Wake Pressure

Figure 13. Range Data for a Missile Launched at 90 deg Angle of Attack

NOMENCLATURE

a	Speed of sound
A_b	Cross-sectional area at the base of the missile
A_r	Reference area $\pi d^2/4$
C_{d_c}	Crossflow drag coefficient
C_D	Drag coefficient
C_j	Differential corrections for aerodynamic characteristics
C_N	Normal-force coefficient $\sim$ normal force/$1/2\rho V_\infty A$)
$C_{N_{\delta^2}}$	$\partial C_N/\partial \delta^2$
f	Frequency of vortex shedding
m	Mass of missile
N	Normal force
P_j	$\partial X/\partial C_j$
P_j'	$\partial X'/\partial C_j$
P_j''	$\partial X''/\partial C_j$
r	Missile body radius
R_e	Reynolds number $\frac{V_\infty d}{r}$
R_{e_c}	Crossflow Reynolds number $\frac{V_c d}{\nu}$
S	Strouhal number fd/V_∞
t	Time
V_c	Crossflow velocity $V_c = V_\infty \sin \alpha$
V_∞	Free-stream velocity
X	Axial distance along missile
X_m	Moment reference center measure from the nose
X_{sep}	Axial location of vortex separation
α	Angle of attack
δ	$\pi/2 - \alpha$
η	Ratio of drag coefficients of a finite length cylinder to an infinite cylinder
ρ	Density of air
ν	Kinematic viscosity

INTRODUCTION

Many modern tactical aircraft and missiles have been designed with increased emphasis on achieving more maneuverability. The demand for increased maneuverability requires some of these vehicles to fly at extreme angles of attack. Our knowledge of the aerodynamic stability and control characteristics of slender bodies at low angles of attack is relatively well understood. Unfortunately our understanding of the basic aerodynamic phenomena in the high angle-of-attack regime is still quite limited. The ability of any aerospace vehicle to perform its mission is heavily dependent upon the effectiveness of its control system, which in turn is dependent upon the aerodynamic forces and moments acting on the vehicle. Therefore in order to design a flight control system for a high angle-of-attack vehicle which uses either aerodynamic control surfaces, thrust vector control, or a combination of both, we must increase our understanding of high angle-of-attack aerodynamics.

In recent years the Army, Navy, Air Force and NASA have sponsored research programs to develop a systematic aerodynamic data base for highly maneuverable missile configurations. To date, aerodynamic force and moment data have been obtained over a wide Mach number range (0.4→3.0) and angles of attack from 0→180 deg. The data base also includes the influence of systematic variations of tail planform, nose shape, missile fineness ratio, etc. Much of this evolving data base has been obtained by the Arnold Engineering Development Center.

In order to perform aerodynamic testing of missile configurations for angles of attack ranging from 0→180 deg, various support combinations (e.g., aft sting, strut, or nose sting) are usually required. Figure 1 shows some of the various support combinations that might be used in the high angle-of-attack region. Support interference in general is quite small for most of the test conditions. That is the mismatch in measured force coefficients at overlapping angles of attack for the aft sting, strut and nose sting supports is usually quite small. However, in the subsonic and transonic Mach number ranges, noticeable differences in the force and moment coefficients have been observed when going from one support system to another. Some examples of support interference are shown in Fig. 2. In part a of this figure, there is excellent data matching for sting and strut supported measurements up until angles near 70 deg. The sting data are found to be very sensitive to Reynolds number, whereas, the strut data exhibits no Reynolds number effect. On the other hand in part b, a noticeable mismatch in the normal force occurs at an angle of attack of 45 deg. In this test, an aft sting is used from 0→45 deg and a strut support from 40→90 deg. This figure is representative of the type of interference that has been noted in the high angle-of-attack region.

Before attempting to describe how the support system can interfere with the measured force coefficient, it is necessary to describe the flow field about a slender body at large angles of attack. The flow around a slender body configuration can be characterized by a number of different flow regimes. Figure 3 is a sketch of a slender missile at angle of attack. As the angle of attack of the missile increases, the cross-flow boundary layer separates due to the adverse pressure gradient on the leeward side. The fluid from the separated boundary layer then rolls up into two symmetric, concentrated vortices in the wake behind the body. As the angle of attack exceeds approximately 25 deg, the symmetric vortex wake becomes asymmetric. The occurrence of this asymmetry in the flow field can give rise to large side forces and yawing moments for symmetric flight conditions (angle of sideslip equals zero). In Fig. 4, the flow around a missile at some fixed axial location is illustrated for various angles of attack. As the figure illustrates, the wake is composed of two symmetric vortices in the low angle-of-attack range. The starting position of the body vortices moves toward the nose as the angle of attack is increased. Increasing the angle of attack to a range between 25→50 deg, the vortex pattern becomes asymmetrical but steady. Also, the appearance of more than two body vortices is possible in this range. Further increases in angle of attack to the 50→70 deg range result in an unsteady asymmetric pattern. This unsteady pattern resembles the classic Von Karman Vortex Street. Finally, in the range of 70→90 deg, the wake becomes turbulent. The patterns shown in Fig. 4 depend upon the crossflow Mach number, crossflow Reynolds number, and nose geometry and therefore only represent a qualitative description of the flow field. More will be said with regard to the influence of crossflow, Mach number, and Reynolds number on the flow field in a later section of this report. Upon examining Figs. 3 and 4, it is not at all surprising that support interference occurs for high angle-of-attack testing.

As mentioned earlier, the support interference is most noticeable at subsonic and transonic Mach numbers. This brings us to an important point. Since missiles are designed for supersonic flight, then why worry about the support interference since it is not generally a problem at supersonic speeds. To answer this question, one must review current trends in missile design within the Department of Defense. In so doing, one would find a number of missile concepts which employ an "Air Slew Maneuver." The air slew maneuver can be used to achieve very rapid and at times, very large heading changes. Basically, these missiles employ thrust vector control to rapidly rotate the missile to face the desired target. The gross heading changes occur shortly after launch and therefore the missile will be maneuvering

at subsonic speeds during the slew maneuver. Since such high angle-of-attack maneuvers will occur near the launch aircraft, it is therefore important that wind tunnel data used for designing such vehicles be free of support interference.

The objective of this ten-week investigation was to examine the various support systems and attempt to identify potential sources of flow field interference. In addition, an assessment of the flow field interference on AEDC's angle-of-attack force and moment data was performed.

THEORY

Aerodynamic Prediction Methods

At present there are no theoretical flow field models suitable for examining support interference at large angles of attack. Therefore several semi-empirical methods were examined to determine if they might be used to study support interference (Ref. 3-8). The various methods considered assume that the force and moment acting on the body to consist of an inviscid and a viscous contribution. The methods differ in how they account for the viscous contribution. However, in general they all employ what is commonly referred to as the impulsive flow analogy or unsteady crossflow analogy. This analogy is based upon the premise that the flow at different axial locations on a slender body can be approximated by the flow about a two-dimensional cylinder impulsively started from rest. Figure 5 shows a sketch illustrating the impulsive flow analogy. Imagine a plane fixed to the fluid and also perpendicular to the body axis. As the body pierces this plane, the flow that would be seen in the moving plane would look like the flow field developing around a two-dimensional cylinder which was impulsively started from rest.

Allen and Perkins (Ref. 3) were the first to propose using the viscous crossflow concept to predict the static longitudinal characteristics of slender bodies at large angles of attack. Basically, they assumed that the increment in normal force could be related to the drag force on a cylinder at the appropriate crossflow Mach and Reynolds numbers. That is, the normal force per unit length could be computed from the following equation

$$dN = 2 r C_{d_c} (\rho V_c^2/2)\, dx \qquad (1)$$

where r is the radius of the body at position X, and V_c is the crossflow velocity. C_{d_c} is the drag coefficient for a circular cylinder at the crossflow Mach number and Reynolds number

$$M_c = V_c / a \qquad R_{e_c} = 2rV_c / \nu \quad (2)$$

Finally, the increment in normal-force coefficient, due to the viscous effects, can be expressed as follows:

$$\Delta C_N = \frac{2\eta \sin^2\alpha}{A_r} \int_0^\ell r C_{d_c} dx \quad (3)$$

The crossflow drag proportionality factor, η, is the ratio of the crossflow drag coefficient for a cylinder of finite length to that for an infinite cylinder. Figure 6 is a plot of η versus the length to diameter ratio of a circular cylinder. The increment in pitching-moment coefficient can be obtained from the following equation:

$$\Delta C_m = \frac{2\eta \sin^2\alpha}{A_r d} \int_0^\ell r(x_m - x) C_{d_c} dx \quad (4)$$

The normal-force and pitching-moment coefficients for the vehicle are then determined by adding the viscous contribution to the coefficients obtained from slender body theory.

Later Kelly (Ref. 4) modified the preceding approach to account for a transient drag coefficient. He used the drag data obtained by Schwabe (Ref. 10) for circular cylinders started impulsively from rest. Figure 7 shows Schwabe's experimental results. To use the impulsive drag coefficient one must relate the parameter Vt/r (nondimensional distance traveled by the infinite cylinder in crossflow) to the axial station on the missile. The relationship is shown below:

$$\frac{V_c t}{r} = \frac{V \sin\alpha}{r} \; t = \frac{V \sin\alpha}{r} \; \frac{x - x_{sep}}{V \cos\alpha} \quad (5)$$

$$\frac{V_c t}{r} = \frac{x - x_{sep}}{r} \tan\alpha$$

Although Kelly was able to obtain good agreement with experimental data, his results seem somewhat fortuitous when one examines the data presented by Sarpkaya (Ref. 11) for an impulsively started cylinder. Sarpkaya's data have been accepted as truly representing the transient drag coefficient and are included in Fig. 7.

The methods discussed in the preceding paragraphs have been used successfully to predict the static longitudinal aerodynamic coefficient for angles of attack up to 30 deg. However, Jorgensen (Ref. 9) was the first one to extend Allen and Perkins method to the high angle-of-attack region. Jorgensen's formulas are listed below:

$$C_N = \frac{A_b}{A_r} \sin\alpha \cos\frac{\alpha}{2} + \eta C_{d_c} \frac{A_p}{A_r} \sin^2\alpha \qquad (6)$$

$$C_m = \left[\frac{V - A_b(\ell - X_m)}{A_r X}\right] \sin 2\alpha \cos\frac{\alpha}{2} + \eta C_{d_c} \frac{A_p}{A_r}\left(\frac{X_m - X_c}{X}\right) \sin^2\alpha$$

The first term in the above equations is the familiar slender body result and the second term is the viscous crossflow contribution. Also it should be noted that Jorgensen's technique does not use the impulsive drag coefficient. That is, the technique uses the appropriate steady two-dimensional drag coefficient.

Since Jorgensen's equations have been shown to accurately predict the aerodynamic characteristics at large angles of attack, they were therefore selected to study the support interference. These equations are strongly dependent upon the crossflow drag coefficient. Thus, if one can show the effect of the strut or sting on the local drag coefficient then Jorgensen's equations could be used to assess the interference in the measured coefficients. However, before proceeding with this analysis it would be appropriate to review the state of knowledge with regard to the drag coefficient of an infinite circular cylinder.

Review of Two-Dimensional Drag Data

The drag coefficient of an infinite circular cylinder is a function of both Reynolds and Mach numbers. Figure 8 shows the influence of Reynolds number on the drag coefficient for free-stream Mach numbers less than the critical Mach number (i.e., the free-stream Mach number at which flow around the cylinder just becomes sonic). In the Reynolds

number range between 10^5 to 5×10^5 the drag coefficient changes significantly. In this Reynolds number range, the flow around the cylinder also changes from laminar boundary layer separation to a turbulent boundary layer separation. In the Reynolds number range from 2×10^5 to 4×10^5 the laminar boundary layer has undergone turbulent transition. The wake is narrow and disorganized with no apparent vortex street. However, as the Reynolds number is increased beyond 4×10^5 the drag coefficient increases up to a value of 0.7. The flow in this region is characterized by the re-establishment of the turbulent vortex street as shown in Fig. 8 (Ref. 12, 13).

Figure 9 shows the influence of Mach number on the drag coefficient. Note that when the Reynolds number is in the critical Reynolds number range the drag coefficient changes significantly for Mach numbers less than 0.44. Additional insight into the flow patterns around circular cylinders in the critical Mach number range are highlighted in the paper by Naumann et al (Ref. 16). Figure 10 shows the essential features of the drag coefficient as a function of Mach number. The three curves correspond to cylinders of different diameters. For the curved marked by the Roman numeral I the critical Mach number occurs at a subcritical Reynolds number. Local shock waves develop which prevent the separation point from moving farther downstream even when the boundary layer becomes turbulent. Thus, when the critical Reynolds number is reached the flow pattern remains essentially unchanged. On the other hand, the curve marked by Roman numeral II, the critical Mach number, occurs at super critical Reynolds number. Now in this case the boundary layer is turbulent at the point of separation. Once again shock waves develop on the cylinder and because of the pressure rise across the shock the separation point is fixed at a smaller azimuth angle. As a result, the wake is wider and again a vortex street is formed. The local shock waves occurring on the cylinder were found to alternate from side to side at the same frequency as the shedding of the vortices. Included in Fig. 10 is a series of sketches illustrating the variation of flow patterns that may exist around a circular cylinder at different Mach and Reynolds numbers.

The relationship between the drag coefficient and Strouhal number as a function of Reynolds number is presented in Fig. 11. The quantity 0.22/S has been used in place of the usual 1/S. Note that the curves fall almost on top of one another. This curve clearly establishes the dependence of the drag coefficient on the vortex shedding characteristics.

The drag and lift acting on a circular cylinder can be shown to be related to the vortex-induced low pressure region in the wake. Thus, the drag and lift might be reduced if the vortex action could be inhibited. Various experiments have been performed to investigate the influence of vortex inhibitors (Ref. 12, 17, 18). These investigations showed that a splitter plate placed parallel with the cylinder axis and the free stream could obstruct the vortex formation and also eliminates the extreme reduction in pressure in the wake. The splitter plate may reduce the drag coefficient by as much as 30%. However, the splitter plate was found only to be effective in the subcritical Reynolds number region. In the supercritical regime Roshko (Ref. 12) could not detect any effect on the drag coefficient.

The length of the splitter plate as well as its downstream location in the wake are shown in Fig. 12. The first curve shows the effect on the local pressure coefficient of a splitter plate almost five diameters in length. The plate is very effective in eliminating the extreme reduction of pressure in the wake. The second curve shows the influence of spacing a short splitter plate at various downstream locations in the wake. As the figure illustrates, the splitter plate is effective in reducing the base pressure coefficient C_p for distances up to 3.8 diameters. From this point on, the splitter plate is ineffective. Roshko (Ref. 12) contends that the alternate vortex shedding can re-establish itself between the aft end of the cylinder and the splitter plate.

ANALYSIS

Strut Interference

In the preceding section, a method for predicting the static aerodynamic characteristics was presented. The forces and moments were shown to be related to the crossflow drag coefficient of an infinite cylinder having a Mach number and Reynolds number identical to the crossflow Mach and Reynolds numbers of the missile. Furthermore, a brief discussion of the drag coefficient of an infinite cylinder and its wake characteristics as a function of Reynolds number and Mach number was presented. The drag and flow patterns were found to be extremely complicated. Since the normal force and pitching moment are related to the crossflow drag coefficient, then this offers a procedure for qualitatively evaluating the potential interference effects caused by either a sting or strut support. If one can show the influence of the strut or sting on the local crossflow drag coefficient, then the interference may be assessed by means of the aerodynamic prediction methods.

As was shown in Fig. 12, the drag coefficient of an infinite cylinder can be modified by placing a splitter plate in the cylinder's wake. Now if we consider the strut support shown in Fig. 1, as well as the crossflow analogy, then the strut would appear as a splitter plate moving away from the body as we move axially along the missile. Thus, the crossflow drag coefficient in the vicinity of the strut should be modified by the presence of the strut support. In Fig. 2b, a 10% difference in measured normal-force coefficient was observed in going from the sting to strut support system. The data presented in this figure were obtained at a Reynolds number of 3×10^6. Now Roshko found the splitter plate to be ineffective at such a large Reynolds number for experiments performed below the critical Mach number. However, Nauman et al (Ref. 16) found the flow around a cylinder above the critical Mach and Reynolds numbers to be similar to the flow pattern associated with subcritical Reynolds and Mach number flow. Since the flow patterns are similar, we will assume that the strut acts like a splitter plate and will modify the drag coefficient accordingly. The difference in prediction of the normal-force coefficient for the modified and unaltered crossflow drag coefficient is 11% at an angle of attack of 45 deg. This of course agrees favorably with the observed difference.

For the data shown in Fig. 2a, the crossflow Reynolds number is in the critical range and therefore the wake may appear more like that shown in Fig. 10 for condition D. That is, the wake is transitioning from a completely turbulent flow to a turbulent vortex street. In this region, the strut should have little influence on the wake or force or moment coefficients.

Sting Interference

A potential source of interference in the sting data is the possibility of the interaction of the sting and model wake vortices. For the sting, data shown in Fig. 2a, the Reynolds number was varied from 2×10^5 to 4×10^5 whereas the sting Reynolds number varied from 10^5 to 2×10^5. From Fig. 11 which shows the similarity of the drag coefficient to the inverse of the Strouhal number, one can see that both the drag coefficient and Strouhal number vary significantly in the Reynolds number range at which the model was tested. In this Reynolds number range, the crossflow drag coefficient would be decreasing and, therefore, the normal-force coefficient would decrease with increasing Reynolds number. This is opposite to the trend exhibited by the data. On the other hand, if the curve shown in Fig. 11 were shifted to the left, that is the transition region has occurred at a lower Reynolds number, the crossflow drag coefficient would be

increasing with Reynolds number. Such an effect has been demonstrated in experiments conducted with two-dimensional cylinders having various degrees of surface roughness. The influence of increased roughness is to lower the transition Reynolds number. The model used in this experiment had No. 180 grit applied along the windward side and, therefore, could account for the increase in normal-force coefficient with Reynolds number. Unfortunately, the same argument should hold for the strut data. But as Fig. 2a indicates, the strut data are not influenced by changes in Reynolds number.

An alternate explanation of the anomaly in the sting data is the possibility of an interaction of the sting wake with that of the model. If the presence of the sting vortices cause the model wake to widen it would be possible to obtain the trend exhibited by the data. However, no information on such an effect could be found in the literature to substantiate such an argument. The influence of model-sting wake interaction could be assessed by a simple experiment. The test would consist of obtaining high angle-of-attack data for a slender body for several sting diameters. The diameter of the sting should be varied up to the model diameter. If the anomaly is due to differences in vortex shedding frequency or wake width, it should be apparent in the measured force and moment coefficients for the different sting arrangements.

Ballistic Range Data

In addition to the wind tunnel data, a limited amount of data was available from tests performed at AEDC's Hyperballistic Range (G), Ref. 19. These tests were performed to obtain high angle-of-attack data which were free of support interference. A slender body of revolution was launched at 90 deg angle of attack (i.e., broadside). By balancing the center of mass at the approximate location of the aerodynamic center, the missile was trimmed to fly at approximately 90 deg angle of attack. The missile was launched at Mach numbers from 0.5 to 1.1. Figure 13 shows the results from a typical flight. The normal-force coefficient was determined from a simple formula obtained from integrating the drag equation. The difficulty in using this approach is that the normal-force coefficient in this Mach number and Reynolds number range is varying significantly, therefore this approach will yield only an average value of the normal-force coefficient. From a simple analysis of the drag equation using a variable C_N based upon experimental measurements, it was determined that the technique used for extracting C_N would be in error by as much as 20%. Therefore, it was decided that a more sophisticated data reduction procedure was warranted. The parameter identification procedure selected was based upon the technique developed by Chapman and Kirk (Ref. 20, 21).

The basis for any parameter identification procedure is to minimize the deviation between the experimentally determined motion and the calculated motion. If we can minimize this deviation we have achieved the "best fit" to the experimental data, and the coefficients used in the calculated motion are the desired aerodynamic coefficients.

Now let us consider the Drag Equation

$$m \frac{d^2x}{dt^2} = D = -\tfrac{1}{2} \rho \left(\frac{dx}{dt}\right)^2 C_D \, A \qquad (7)$$

or

$$\frac{d^2x}{dt^2} + \left(\frac{\rho A}{2m}\right) C_N \left(\frac{dx}{dt}\right)^2 = 0 \qquad (8)$$

for a missile at 90 deg angle of attack having initial conditions $X(0) = C_1$ and $X'(0) = C_2$. Recall that earlier the normal-force coefficient was shown to be proportional to the drag coefficient of an infinite cylinder. Therefore, in the above equation C_N can be expressed as function of both Reynolds number and Mach number. Since the missile oscillates in angle of attack as it flys down the range, C_N is expressed as a function of angle of attack. Rewriting equation 8 we have

$$\frac{d^2x}{dt^2} + \left(\frac{\rho A}{2m}\right)\left[C_{N_{\pi/2}}(M, R_e) - C_{N_{\delta^2}}(M, R_e)\, \delta^2\right]\left(\frac{dx}{dt}\right)^2 = 0 \qquad (9)$$

Since a functional relationship is available for the dependence of C_{d_c} on Mach and Reynolds number from Ref. 1, the above equation will be expressed as follows:

$$\frac{d^2x}{dt^2} + \frac{\rho A}{2m}\, \bar{f}(M, R_e)\left[C_{N_{\pi/2}} - C_{N_{\delta^2}}\, \delta^2\right]\left(\frac{dx}{dt}\right)^2 = 0 \qquad (10)$$

where $\bar{f}$ is the ratio of $C_{d_c}\big|_t / C_{d_c}\big|_{t=0}$. Now it should be noted that we could have included additional terms into the above equation to account for the Mach number and Reynolds number variation. For example, $C_N + C_{N_M} M + C_{N_{M^2}} M^2$, etc. However, the data are quite limited so it was decided that the best approach would be to include the Reynolds and Mach

number effects by means of the function $\bar{f}$ which was formulated from the drag curves of Ref. 1. Therefore, the coefficients that we obtain represent the values at the start of the data.

We are interested in obtaining the coefficient $C_{N_{\pi/2}}$ $C_{N_{\delta^2}}$, C_1 and C_2. This is accomplished by finding the minimum of the Sum of the Squares of the Residuals (SSR)

$$SSR \quad \sum_{i=1}^{n} \left(X_{exp}(t_i) - X_{cal}(t_i) \right)^2 \qquad (11)$$

In order to find the minimum of Equation (11) we can employ the method of differential corrections. Assume for the time being that approximate values of the $C_{N_{\pi/2}}$, $C_{N_{\delta^2}}$, etc, are known. If X is expanded about the approximate solution by means of Taylor series the following equation can be established.

$$X_{cal}(t_i) = X_{cal}(t_i)\Big|_0 + \sum_{j=1}^{4} \left(\frac{\partial X}{\partial C_j} \right)_i \Delta C_j \qquad (12)$$

$$i = 1, 2, \ldots n$$

where $X_{cal}(t_i)\big|_0$ is the value of X at time t_i which is obtained by numerical integration of Equation (10). Substituting (12) into (11) yields,

$$SSR \quad \sum \left[X_{exp}(t_i) - X_{cal}(t_i)\Big|_0 - \sum_{j=1}^{4} \left(\frac{\partial X}{\partial C_j} \right)_i \Delta C_j \right]^2 \qquad (13)$$

To find the minimum of this equation we take the derivative of SSR with respect to C_k (the corrections to the coefficients) and set the derivative equal to zero.

$$\frac{\partial SSR}{\partial \Delta C_k} = \sum_{i=1}^{n} 2 \left[X_{exp}(t_i) - X_{cal}(t_i)\Big|_0 - \sum_{j=1}^{4} \left(\frac{\partial X}{\partial C_j} \right)_i \Delta C_j \right] \frac{\partial X}{\partial C_k} = 0 \qquad (14)$$

$$\therefore \sum \left[X_{exp}(t_i) - X_{cal}(t_i)\Big|_0 - \sum_{1}^{4} \left(\frac{\partial X}{\partial C_j} \right)_i \Delta C_j \right] \frac{\partial X}{\partial C_k} = 0$$

This equation can be rewritten as follows:

$$A_{jk} = \sum_{i=1}^{n} \left(\frac{\partial x}{\partial C_j}\right)_i \left(\frac{\partial x}{\partial C_k}\right)_i \tag{15}$$

$$B_j = \sum_{i=1}^{n} \left[X_{exp}(t_i) - X_{cal}(t_i)\Big|_0\right] \left(\frac{\partial x}{\partial C_j}\right)_i$$

where $$A_{jk}\,\Delta C_k = B_j \tag{16}$$

If we could evaluate the derivative ($\partial x/\partial C_j$) then it would be a simple matter to obtain the corrections ΔC_k. Unfortunately these derivatives are not easily evaluated. Chapman and Kirk obtained the necessary derivatives by means of parametric differentiation. The procedure will be illustrated by applying the method to the preceding equations.

First we must define the following nomenclature.

$$P_j = \frac{\partial x}{\partial C_j} \qquad P_j' = \frac{\partial P}{\partial t} = \frac{\partial x'}{\partial C_j} \qquad P_j'' = \frac{\partial^2 P_j}{\partial t^2} = \frac{\partial x''}{\partial C_j} \tag{17}$$

Furthermore, it is assumed that the order of differentiation can be reversed that is

$$\frac{\partial}{\partial C_j}\left(\frac{\partial x}{\partial t}\right) = \frac{\partial}{\partial t}\left(\frac{\partial x}{\partial C_j}\right) \tag{18}$$

If we differentiate Equation (10) with respect to C_j we obtain the following differential equations.

$$\frac{d^2P_1}{dt^2} + 2\bar{f}\left[C_{N\pi/2} + C_{N\delta^2}\,\delta^2\right]\left(\frac{dx}{dt}\right)\frac{dP_1}{dt} = -\bar{f}\left(\frac{dx}{dt}\right)^2 \tag{19}$$

$$\frac{d^2P_2}{dt^2} + 2\bar{f}\left[C_{N\pi/2} + C_{N\delta^2}\,\delta^2\right]\left(\frac{dx}{dt}\right)\frac{dP_2}{dt} = -\bar{f}\,\delta^2\,\frac{dx}{dt}$$

$$\frac{d^2P_3}{dt^2} + 2\bar{f}\left[C_{N_{\pi/2}} + C_{N_{\delta^2}}\delta^2\right]\frac{dx}{dt}\frac{dP_3}{dt} = 0$$

$$\frac{d^2P_4}{dt^2} + 2\bar{f}\left[C_{N_{\pi/2}} + C_{N_{\delta^2}}\delta^2\right]\frac{dx}{dt}\frac{dP_4}{dt} = 0 \qquad (19)$$

The initial conditions for these equations are

$$P_1 = P_2 = P_4 = 0\,,\ P_3 = 1\,,\quad P_1' = P_2' = P_3' = 0\,,\quad P_4' = 1$$

Integration of these equations will yield the desired derivatives $\partial X/\partial C_j$. The derivatives $(dx/dt)i$ are obtained from integration of Equation (10). δ is obtained from the experimental measurements as is $\bar{f}$.

The procedure for determining the coefficients can now be outlined as follows:

1. Make some initial guesses on the values of the coefficients.
2. Integrate Equation 10.
3. Integrate Equation 19.
4. Use $\partial X/\partial C_j$ to obtain ΔC_j from Equations (15) and (16).
5. Calculate SSR from Equation (13) and compare with some previously determined tolerance.
6. Determine new values of coefficients $C_j = C_j + \Delta C_j$
7. With new coefficients return to step 2 and repeat process until SSR remains essentially constant.

A thorough evaluation of this approach was not possible due to the time limitations of the Summer Faculty Research Program, however, preliminary results appear to be quite encouraging. A computed trajectory is included in Fig. 13. The value of the normal-force coefficient was found to be approximately 15% higher than the normal-force coefficient reported in Ref. 19. The approach developed in this section could be used to obtain more accurate estimates of the aerodynamic coefficients than the approach used in Ref. 19. However, if more trajectory data were available, AEDC's nonlinear parameter identification techniques should be used.

CONCLUSIONS

Based upon this preliminary investigation of high angle-of-attack support interference, the following tentative conclusions have been reached:

1. The influence of the strut support on the aerodynamic characteristics of a slender body at large angles of attack may act in a manner similar to that of a splitter plate located downstream of an infinite cylinder in crossflow. Basically, the splitter plate controls the vortex formation in the wake of the cylinder. At subcritical Reynolds number the splitter plate has been shown experimentally to reduce the two-dimensional drag coefficient by 30%. Although the influence of the splitter plate has been studied only in flows below the critical Mach number ($M < 0.44$) one might expect a similar result for flows at Reynolds and Mach numbers greater than the critical values, because the high speed wake flows around a two-dimensional cylinder resemble the low speed subcritical Reynolds number flow where the splitter plate is effective.

2. A potential source of sting interference is the interaction of the model and sting wake. It is recommended that additional high angle-of-attack data be obtained on a slender body of revolution for several sting diameters. By varying the sting diameter, the influence of the width and shedding frequency of the sting on the model aerodynamic coefficients could be assessed.

3. The use of grit (i.e., surface roughness) on wind tunnel models in order to obtain a better simulation of the flow characteristics of the full-scale vehicle should be examined. In reviewing the experimental measurements made on slender bodies at large angles of attack, one finds a variety of grit patterns being used. The patterns include a ring of grit around the nose, rays or lines of grit running along the length of the model, no grit, and grit over the entire model. The effect produced by these patterns will be strongly dependent upon angle of attack. It is recommended that AEDC in cooperation with the other wind tunnel facilities conducting high angle of attack research study the influence of grit patterns, with the objective of establishing guide lines or standards for grit application.

4. Preliminary tests by AEDC using the Hyperballistic Range (G) to investigate high angle-of-attack aerodynamic characteristics could be developed into a unique capability. The major limitation at present is the lack of a sufficient number of data stations. This is due to the fact that only a small portion of the available range is used when the projectile is launched at transonic Mach numbers. If additional trajectory data could be obtained, then the nonlinear aerodynamic parameter identification routines available at AEDC could be employed to determine the aerodynamic characteristics of slender bodies at large angles of attack. Until more data can be acquired, a method similar to the one developed in this report could be used.

REFERENCES

1. Baker, W. B. "Static Aerodynamic Characteristics of a Series of Generalized Slender Bodies with and without Fins at Mach Numbers from 0.6 to 3.0 and Angles of Attack from 0 to 180 deg." AEDC-TR-75-124, Vol. 1 and 2, May 1976.

2. Baker, D. C. and Reichenau, D. E. A. "Aerodynamic Characteristics of an MX Missile at Free-Stream Mach Numbers from 0.3 to 1.3 and Angles of Attack up to 180 deg." AEDC-TR-75-34, April 1975.

3. Allen, H. J. and Perkins, E. W. "A Study of the Effects of Viscosity on Flow Over Slender Inclined Bodies of Revolution." NACA TR 1048, 1951.

4. Kelly, H. R. "Estimation of Normal-Force, Drag, and Pitching-Moment Coefficients for Blunt-Based Bodies of Revolution at Large Angles of Attack." Journal of Aeronautical Sciences, Vol. 21, pp 549, 1954.

5. Fidler, J. E. and Bateman, M. C. "Aerodynamic Methodology (Isolated Fins and Bodies) Army Missile Command Report OR 12,399, March 1973.

6. Thomson, K. D. "The Estimation of Viscous Normal Force, Pitching Moment, Side Force and Yawing Moment on Bodies of Revolution at Incidence up to 90°," Australian Department of Supply, Weapons Research Establishment, Report 782, October 1972.

7. Baker, W. B. "An Aerodynamic Coefficient Prediction Technique for Slender Bodies with Low Aspect Ratio Fins at Transonic Mach Numbers and Angles of Attack to 180 Degrees." Ph.D Dissertation University of Tennessee (To be Published).

8. Jorgensen, L. H. "Prediction of Static Aerodynamic Characteristics for Space-Shuttle-Like and Other Bodies at Angles of Attack from 0° to 180°." NASA TN D-6996, 1973.

9. Goldstein, S. "Modern Development in Fluid Dynamics." Oxford, The Claredon Press, Vol. 2, 1938.

10. Schwabe, M. "Pressure Distribution in Nonuniform Two-Dimensional Flow." NACA TM No. 1039, 1943.

11. Sarpkaya, T. "Separated Flow about Lifting Bodies and Impulsive Flow about Cylinders." AIAA Journal, Vol. 4, No. 3, March 1966.

12. Roshko, A. "Experiments on the Flow Past a Circular Cylinder at Very High Reynolds Numbers." Journal of Fluid Mechanics, Vol. 10, Part 3, 1961.

13. Lienhard, J. "Synopsis of Lift, Drag, and Vortex Frequency Data for Rigid Circular Cylinders." Bulletin 300, College of Engineering-Research Division, Washington State University, 1966.

14. Finck, R. D., et al. "USAF Stability and Control DATCOM." Flight Control Division, Air Force Flight Dynamics Laboratory, Wright-Patterson AFB, Ohio, Revised January 1974.

15. Fidler, J. and Bateman, M. C. "Aerodynamic Methodology (Isolated Fins and Bodies)." United States Army Missile Command Report OR-12,399, March 1973.

16. Naumann, A., Morsbach, M., and Kramer, C. "The Conditions of Separation and Vortex Formation Past Cylinders." AGARD Conference Proceeding, Separated Flows, AGARD CP No. 4, May 1966.

17. Gove, A., Shair, F., Petersen, R., and Acrivos, A. "An Experimental Investigation of the Steady Separated Flow Past a Circular Cylinder." Journal of Fluid Mechanics, Vol. 19, Part 1, 1964.

18. Apelt, C., West, G., and Szewczyk, A. "The Effects of Wake Splitter Plates on Bluff-Body Flow in the Range $10^4 < R < 5 \times 10^4$." Journal of Fluid Mechanics, Vol. 61, 1973.

19. Lawrence, W. "AFFDL/AEDC High Alpha Aerodynamics Test." Data Report Project V41G-35A, April and May 1975.

20. Chapman, G. and Kirk, D. "A Method for Extracting Aerodynamic Coefficients from Free-Flight Data." AIAA Journal, Vol. 8, No. 1, 1970.

21. Chapman, G. "Aerodynamic Parameter Identification Ballistic Range Tests." Proceedings of the 1972 Army Numerical Analysis Conference, Edgewood Arsenal, Edgewood, Maryland, April 1972.

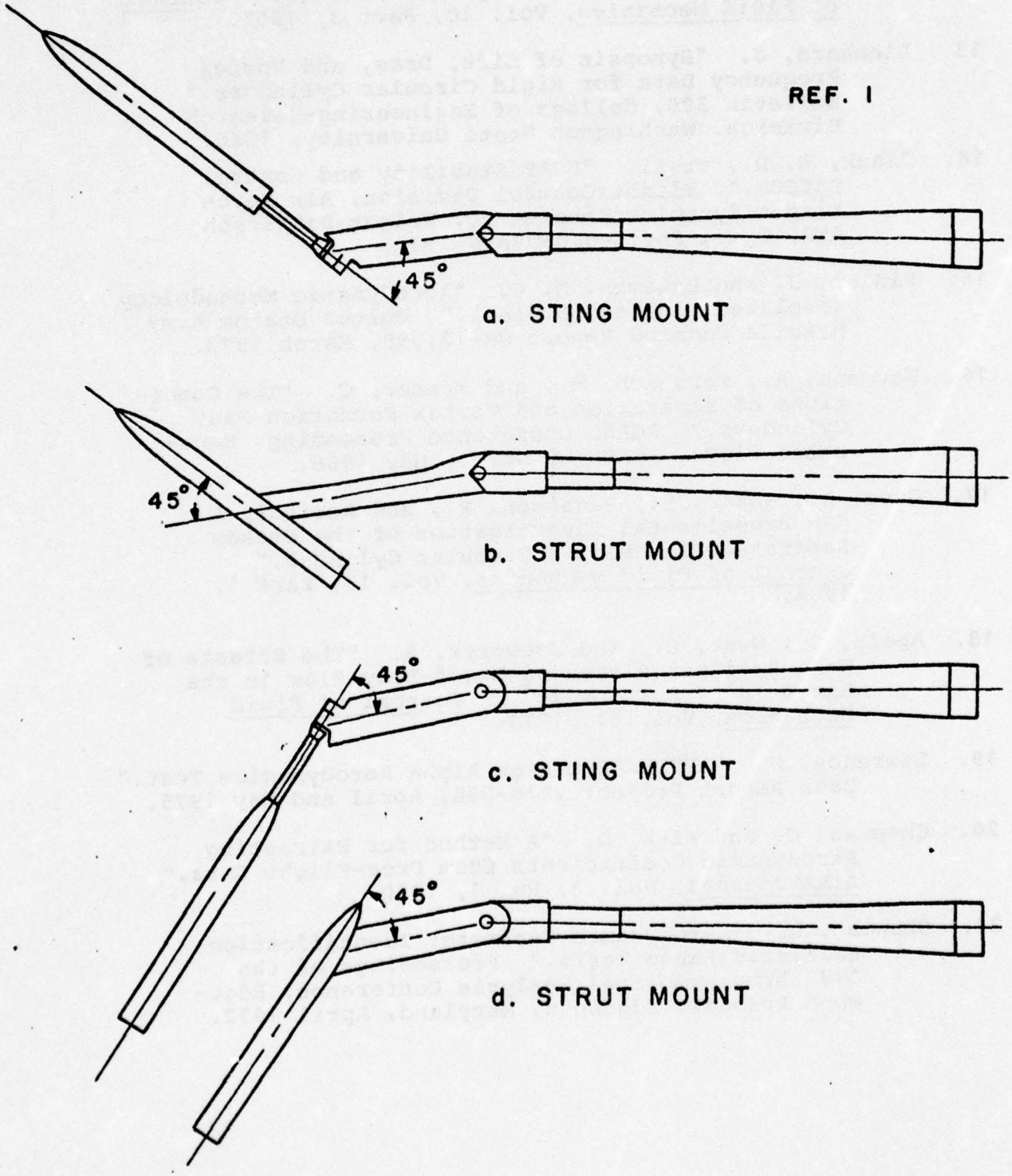
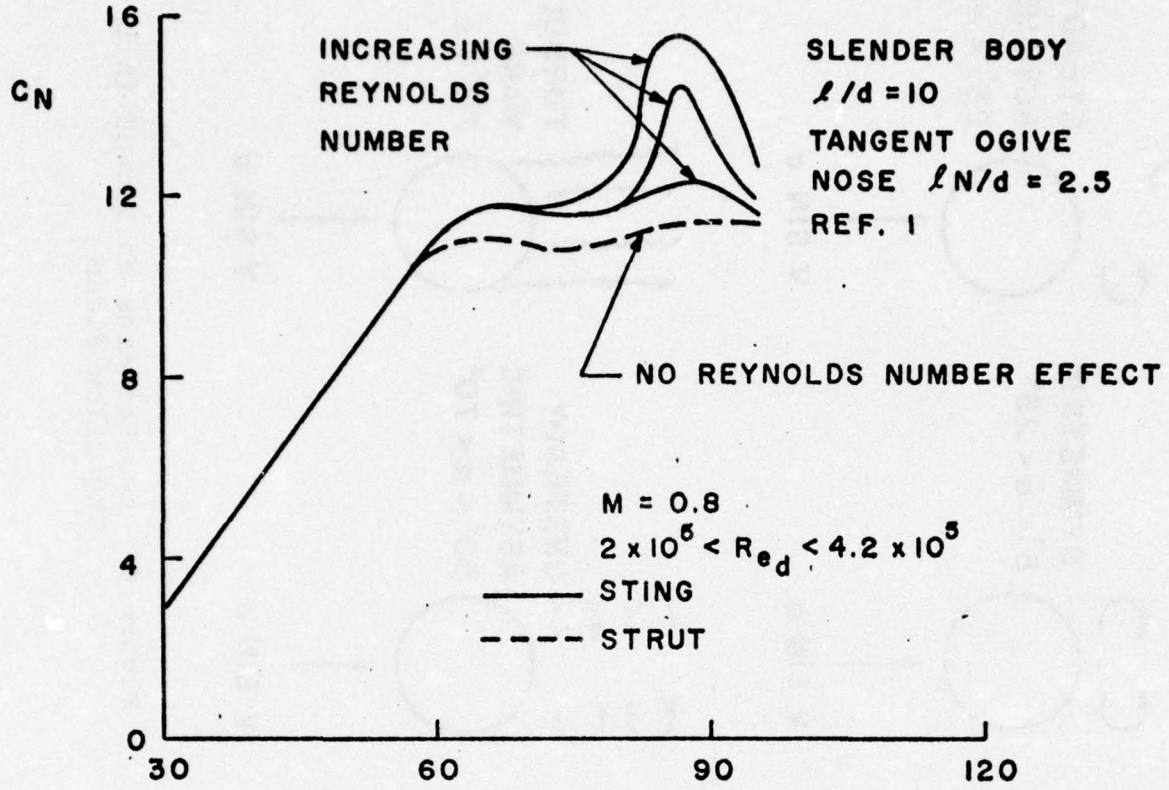


Figure 1 High Angle-of-Attack Support System



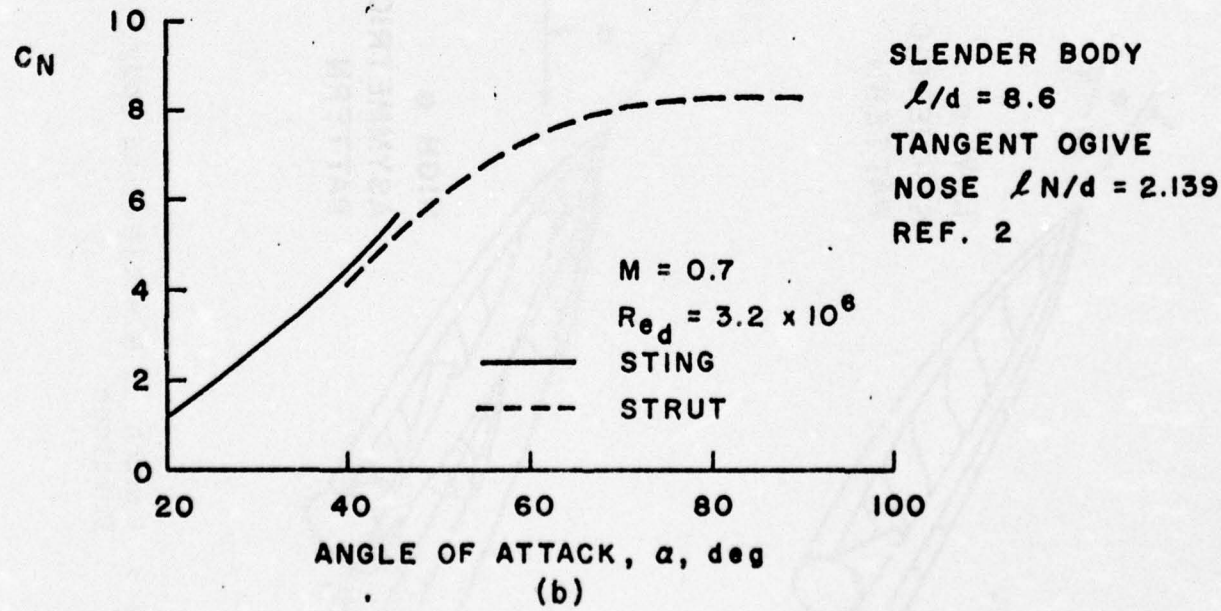


Figure 2 Examples of Support Interference

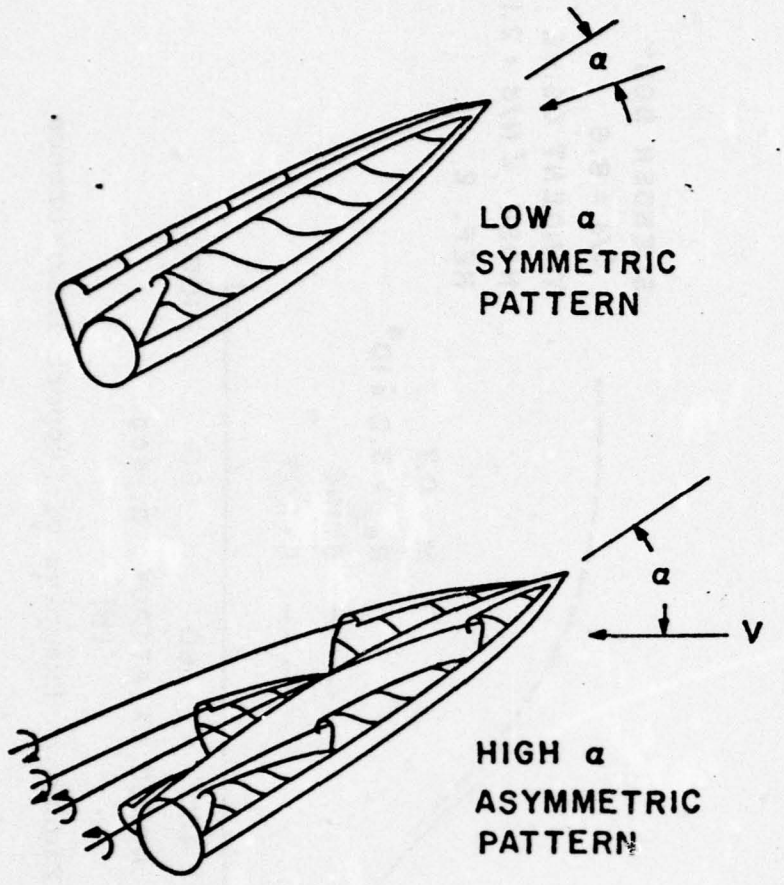


Figure 3 Sketch of Missile with Body Vortices

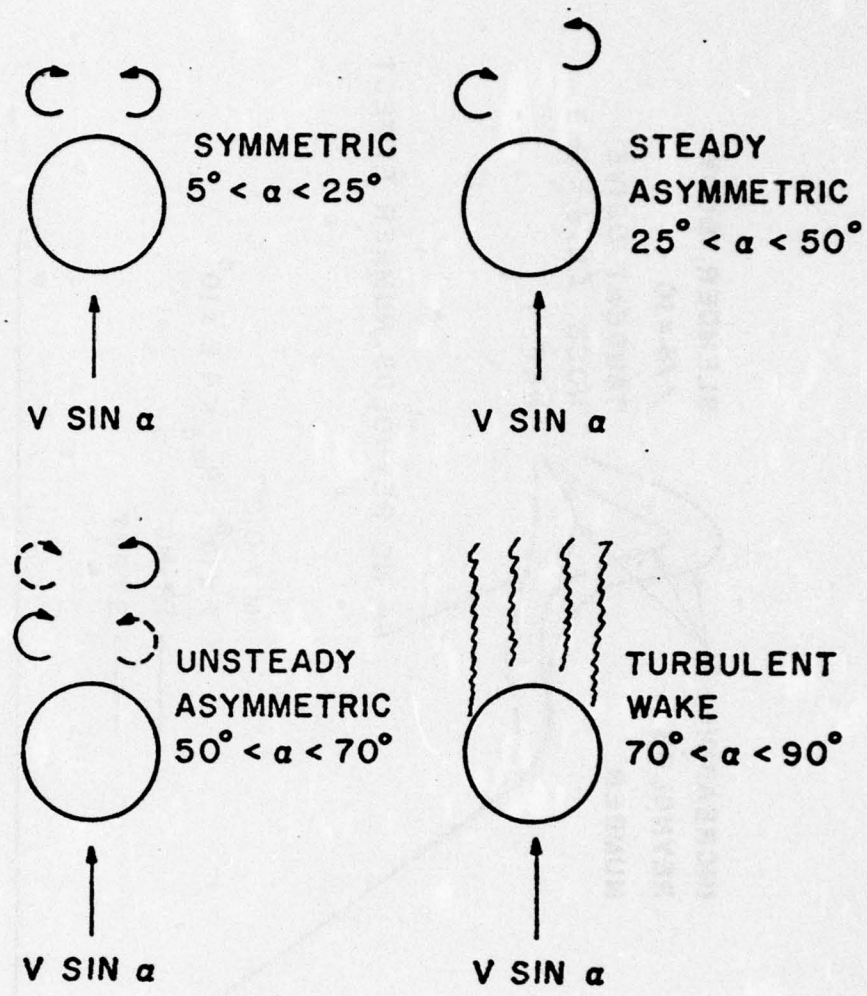
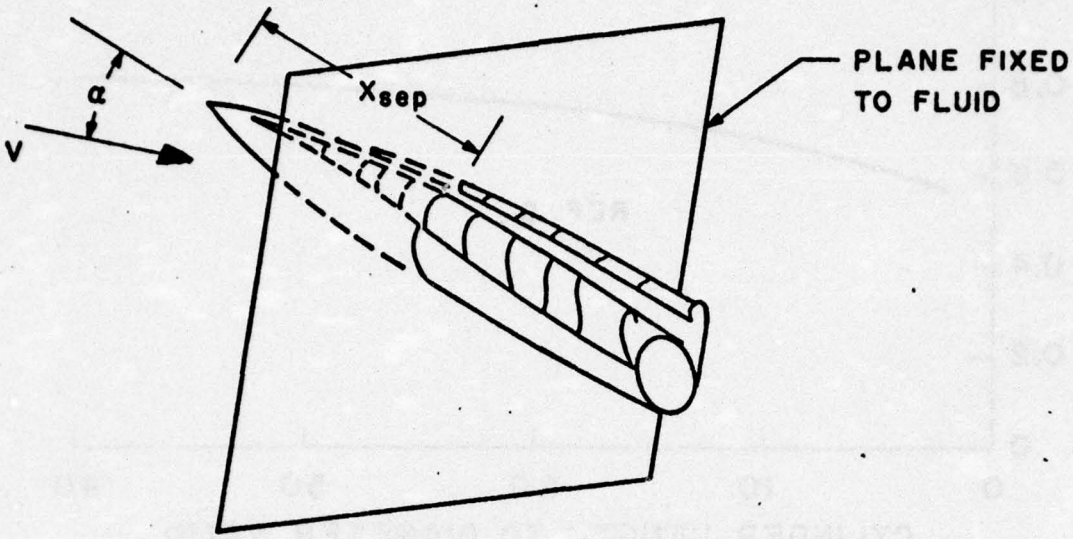
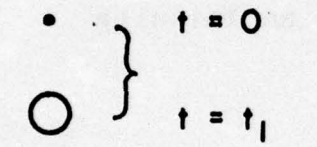


Figure 4 Wake Patterns as Viewed in the Crossflow Plane





NOSE STATIONS



BEGINNING OF SEPARATION





VORTICES MOVE OFF THE BODY

RELATIONSHIP BETWEEN CROSSFLOW PLANE ON THE MISSILE TO THAT OF AN INFINITE CYLINDER IMPULSIVELY STARTED FROM REST

$$\Delta t = \frac{X - X_{sep}}{V \cos \alpha}$$

$$\frac{Vt}{R} = \frac{V \sin \alpha}{R} \quad \frac{X - X_{sep}}{V \cos \alpha}$$

$$\frac{Vt}{R} = \frac{X - X_{sep}}{R} \tan \alpha$$

Figure 5 Sketch of Impulsive Flow Analogy

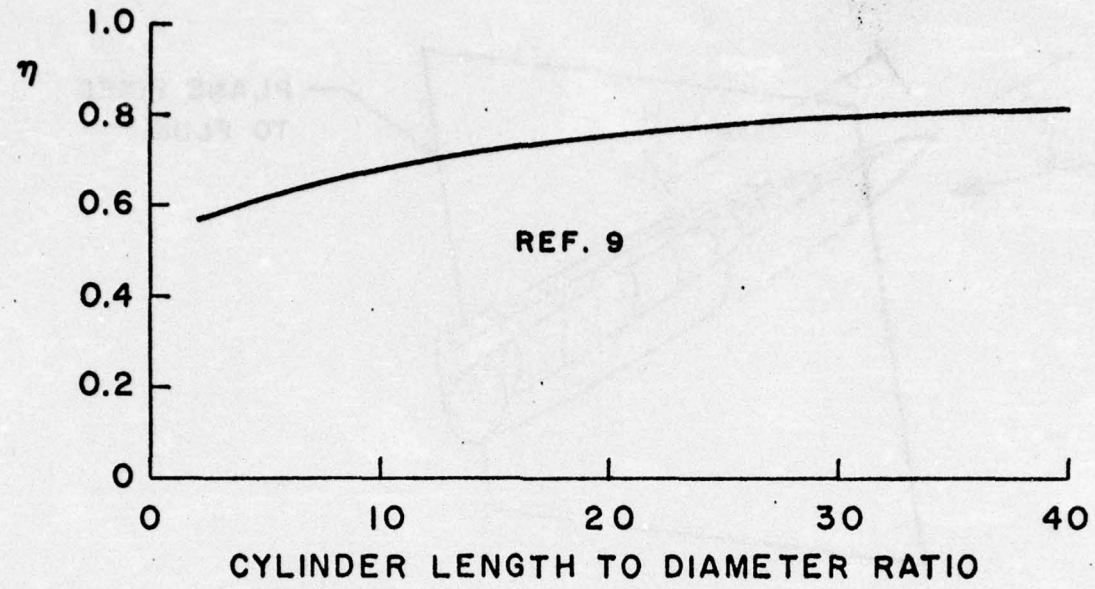


Figure 6 Ratio of Crossflow Drag Coefficient for a Finite Cylinder to that for an Infinite Length Cylinder

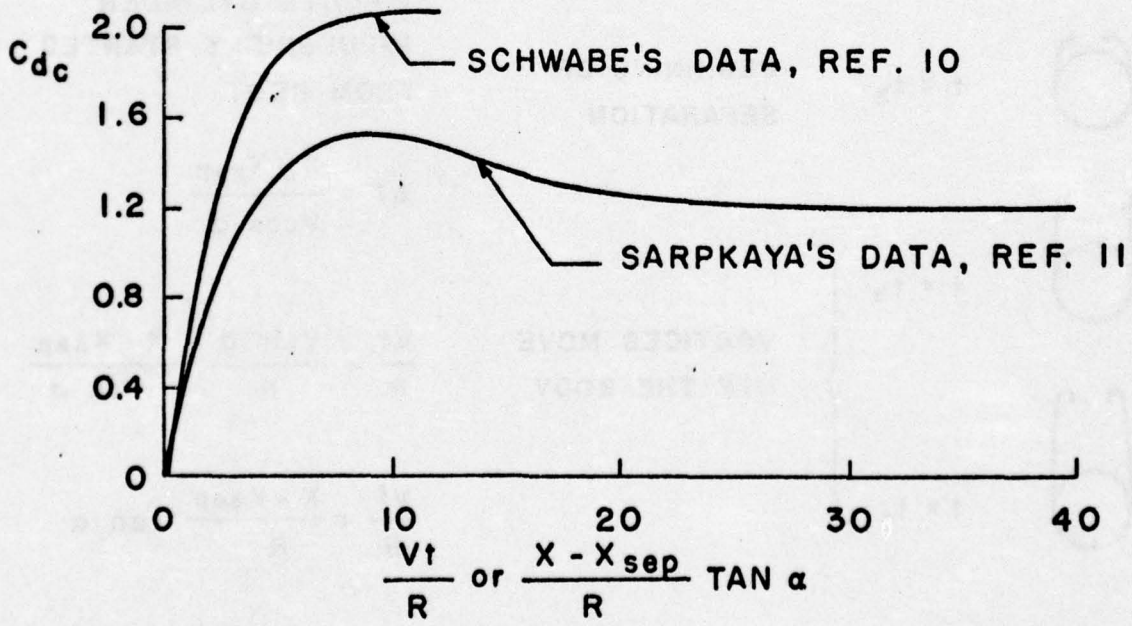


Figure 7 Drag Coefficient for a Circular Cylinder Started Impulsively from Rest

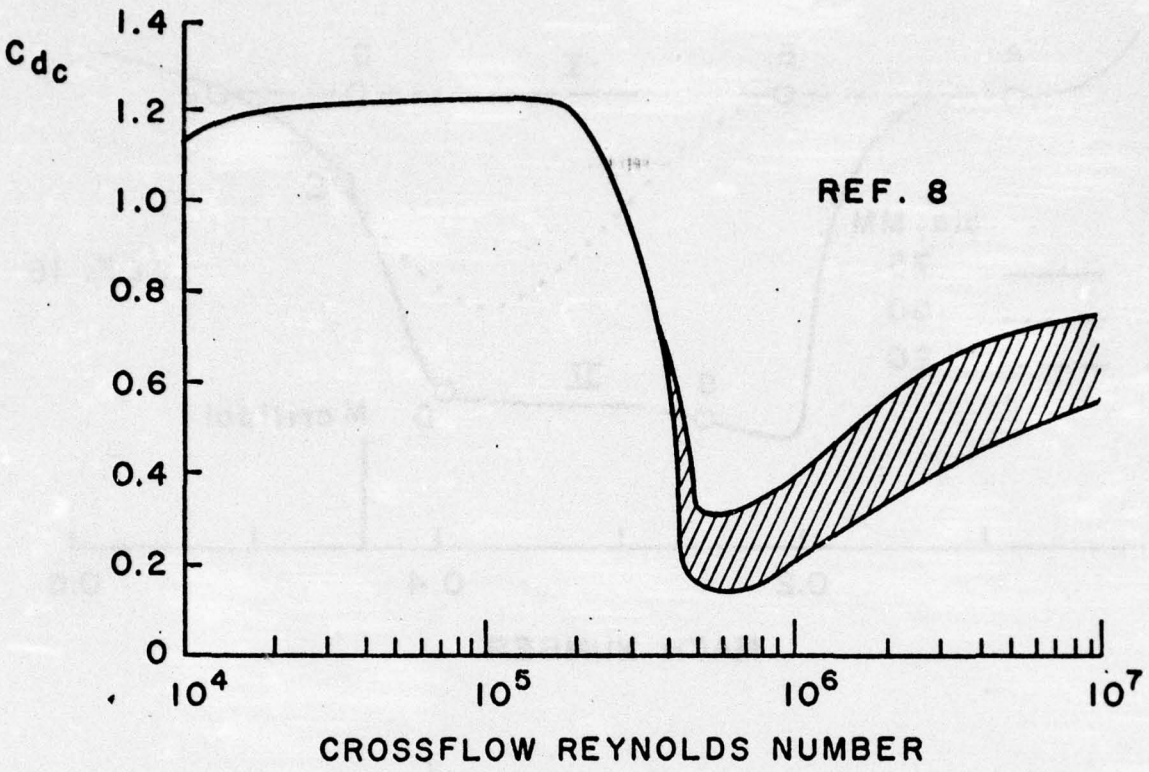


Figure 8 Variation of Drag Coefficient with Reynolds Number for a Circular Cylinder

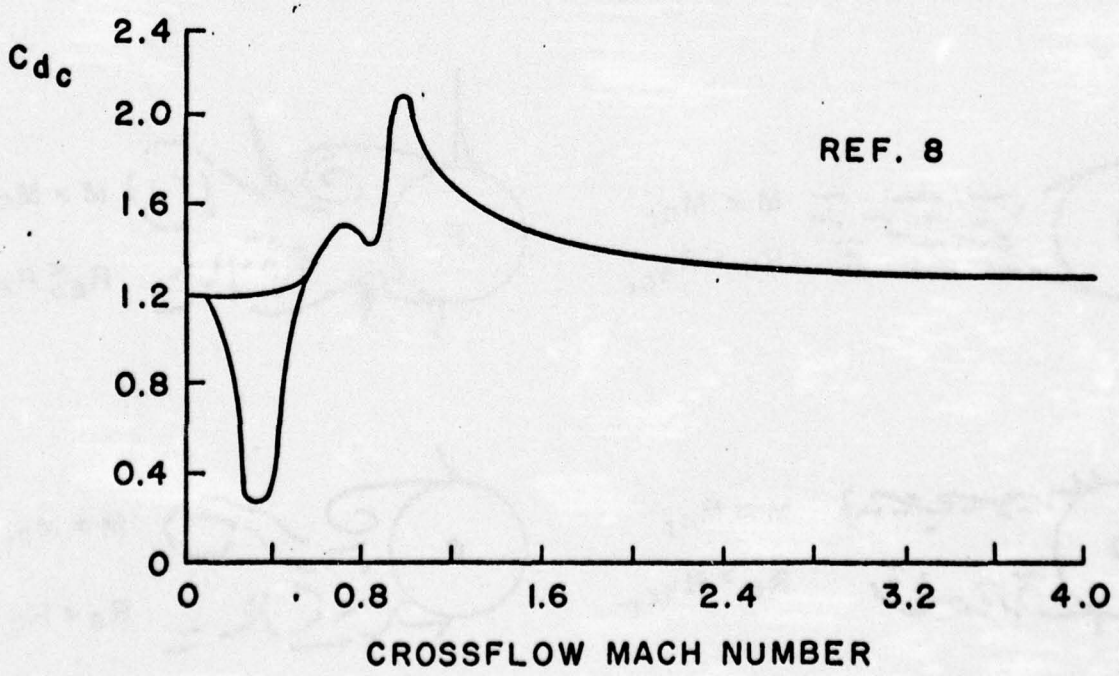
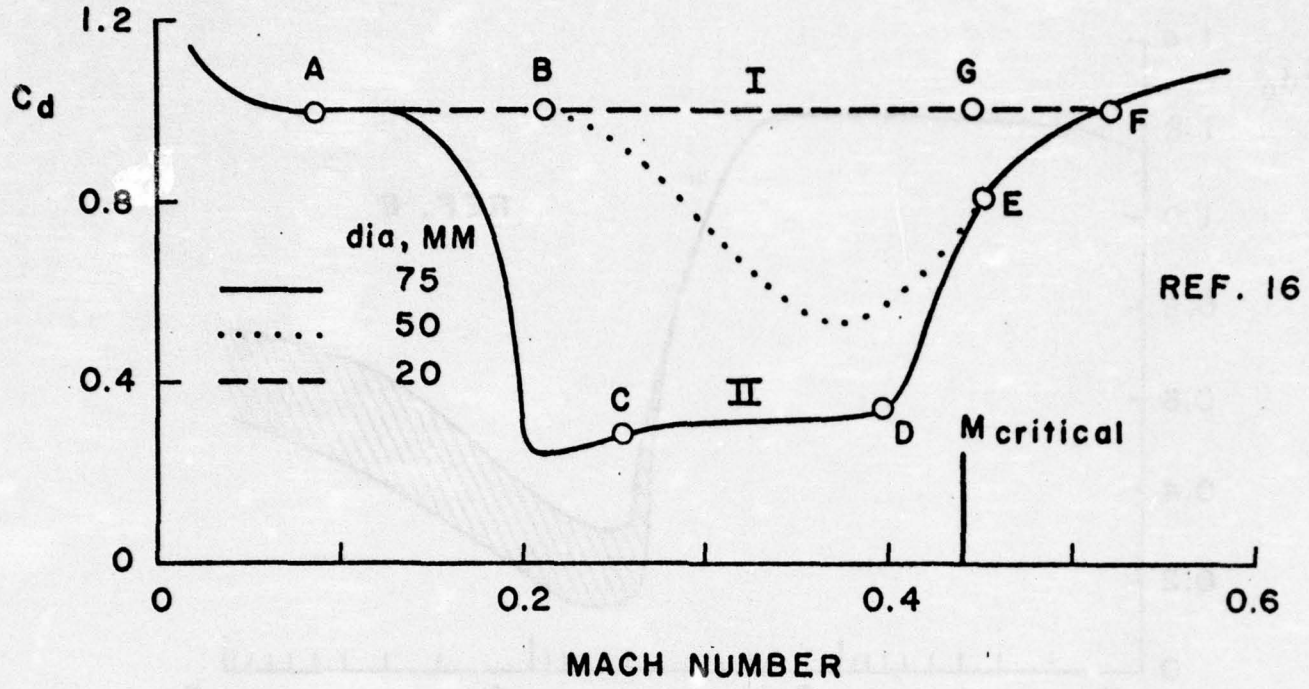


Figure 9 Variation of Drag Coefficient with Mach Number for Circular Cylinders



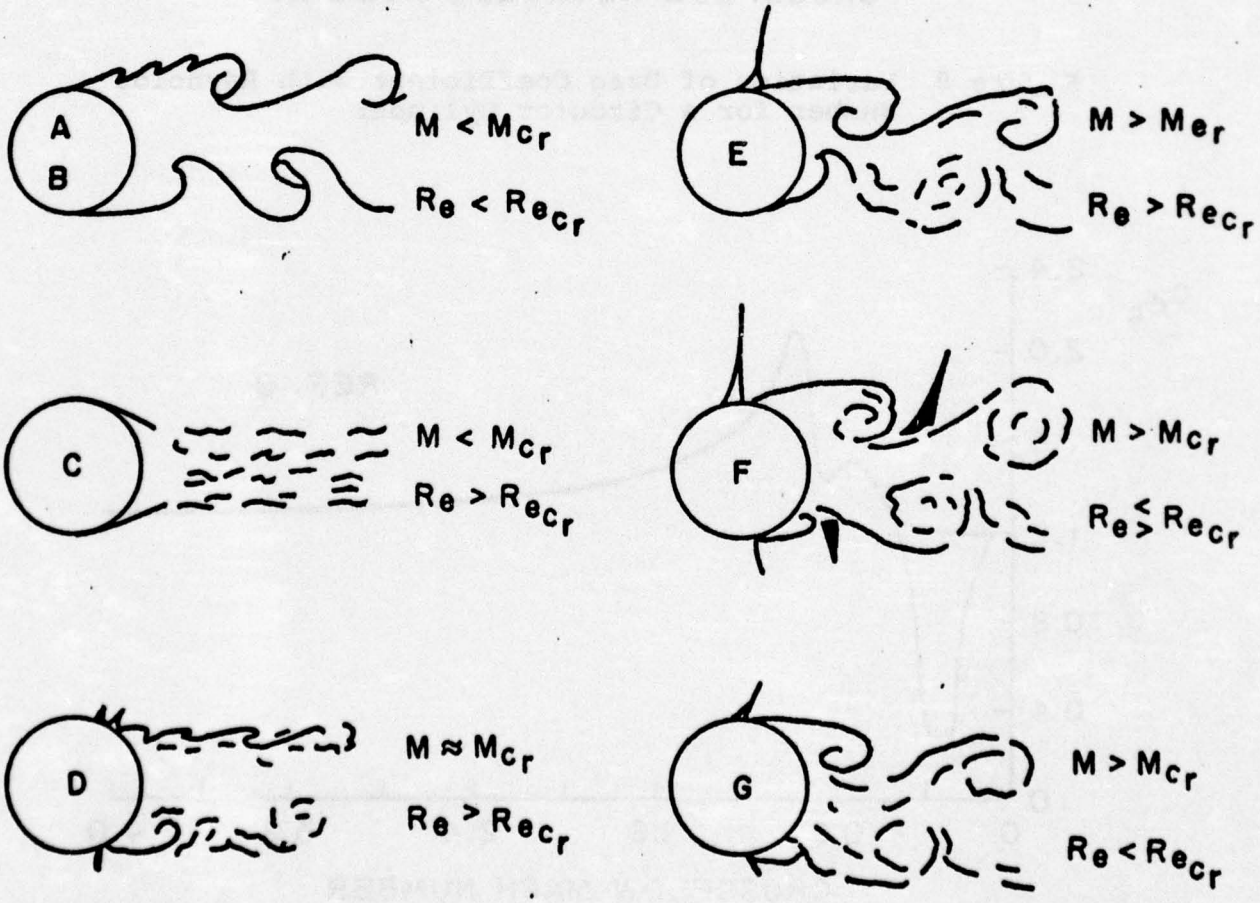


Figure 10 Variation of Drag Coefficient and Wake Patterns with Mach and Reynolds Numbers

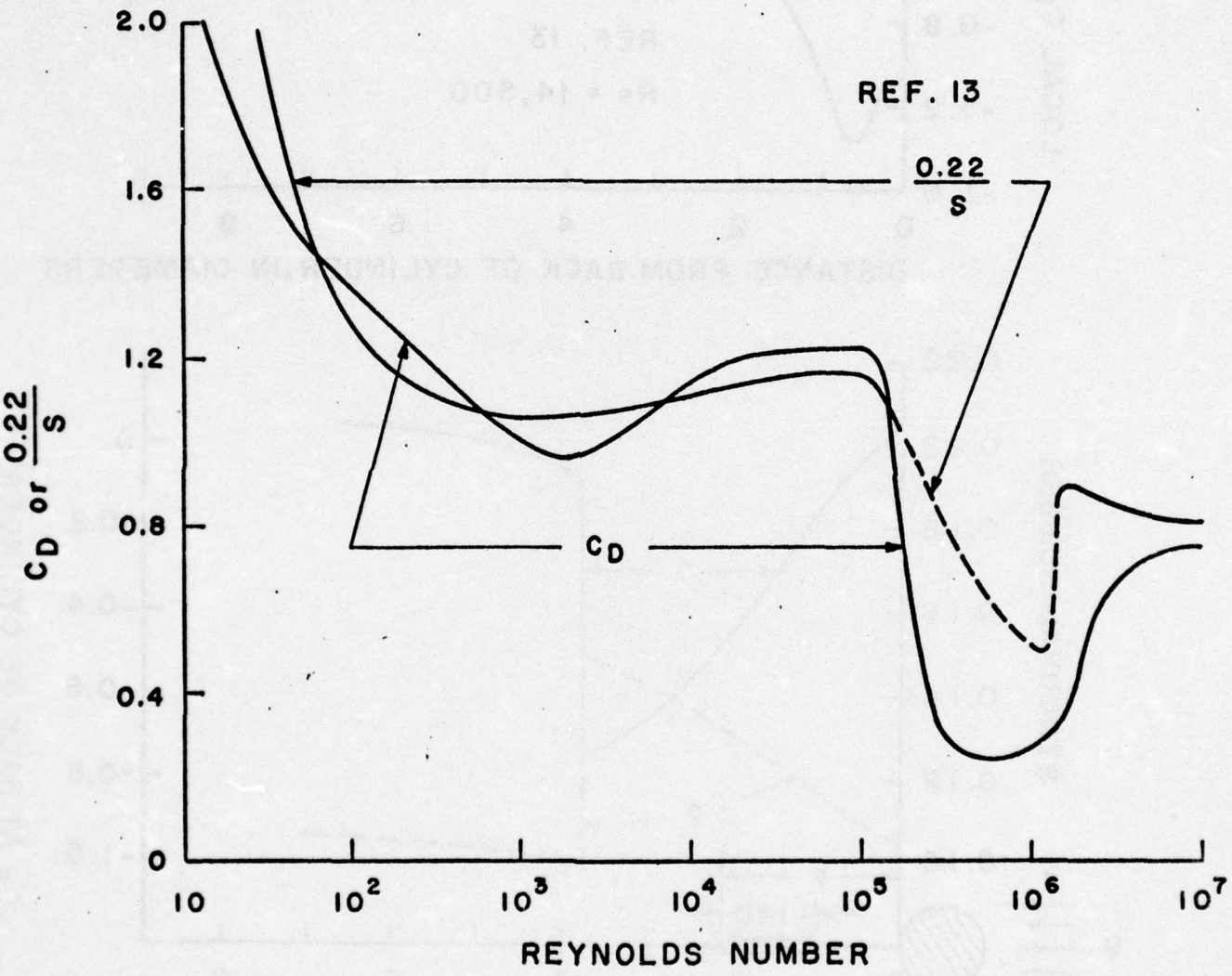


Figure 11 Relationship Between Drag Coefficient and Strouhal Number

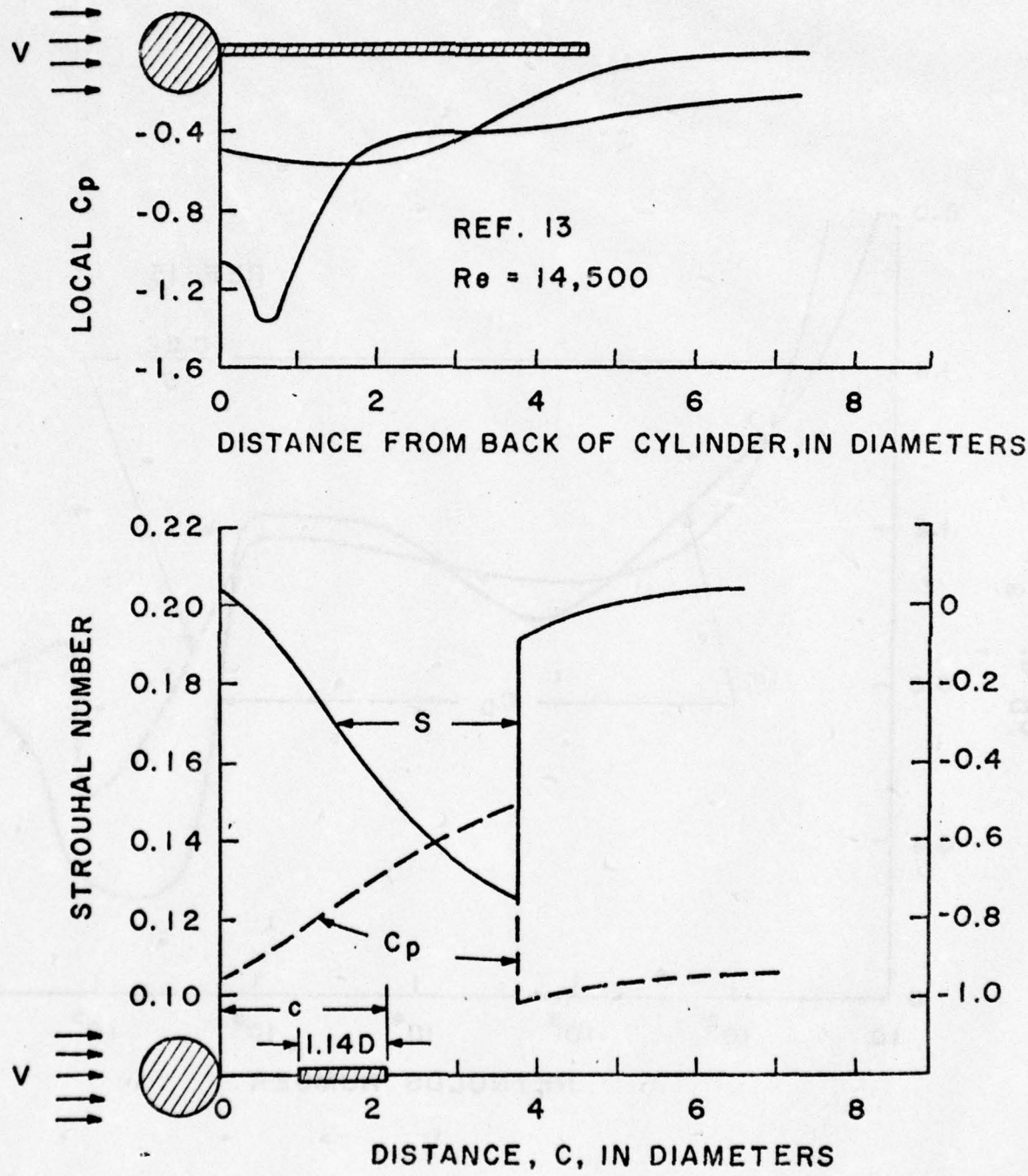
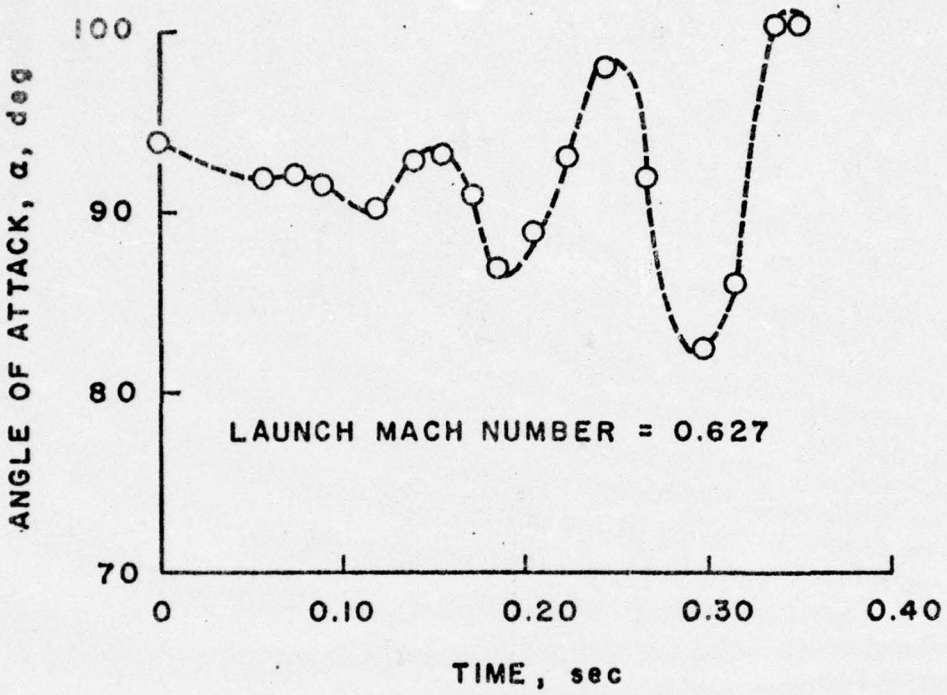


Figure 12 Effect of Splitter Plates on the Wake Pressure



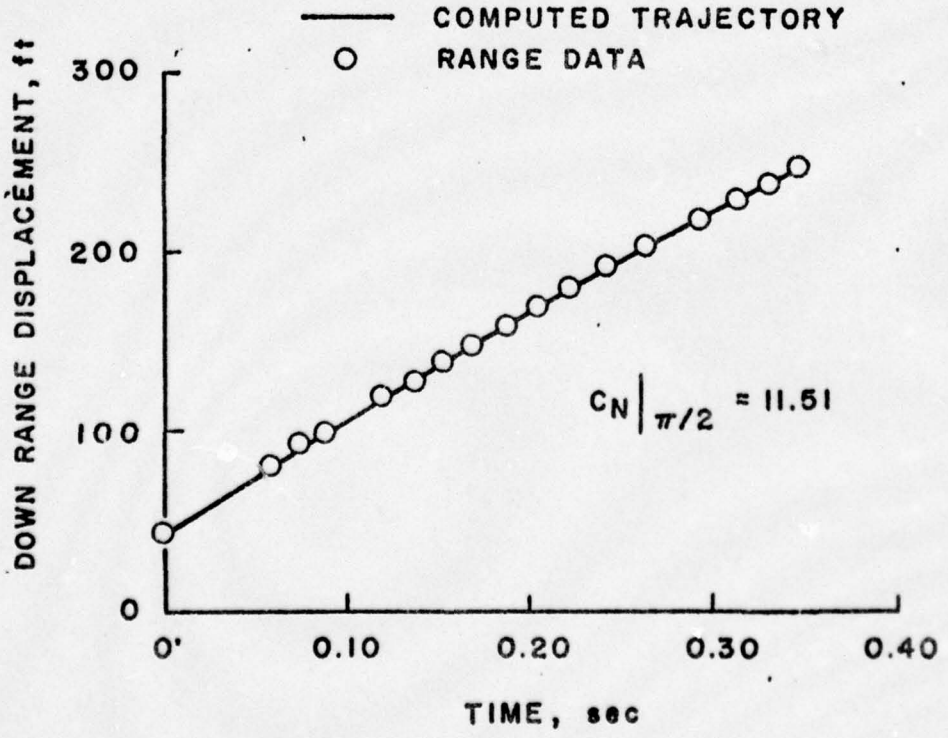


Figure 13 Range Data for a Missile Launched at 90 deg Angle of Attack

1976 USAF-ASEE SUMMER FACULTY RESEARCH PROGRAM
sponsored by
THE AIR FORCE OFFICE OF SCIENTIFIC RESEARCH
conducted by
AUBURN UNIVERSITY AND OHIO STATE UNIVERSITY

PARTICIPANT'S FINAL REPORT

DEVELOPMENT OF A NESTED VIRTUAL MACHINE, DATA-STRUCTURE ORIENTED SOFTWARE DESIGN METHODOLOGY AND PROCEDURE FOR ITS EVALUATION

Prepared by:	Melvyn M. Drossman, Ph.D.
Academic Rank:	Professor
Department and University:	Departments of Computer Science and Electrical Engineering Technology New York Institute of Technology
Assignment:	
(Air Force Base) (Laboratory) (Division) (Branch)	Griffiss AFB Rome Air Development Center Information Sciences Information Processing
USAF Research Colleague:	Rocco F. Iuorno
Date:	August 11, 1976
Contract No.:	F44620-75-C-0031

DEVELOPMENT OF A NESTED VIRTUAL MACHINE, DATA-STRUCTURE ORIENTED SOFTWARE DESIGN METHODOLOGY AND PROCEDURE FOR ITS EVALUATION

by
M. M. Drossman

ABSTRACT

The complexity of present-day computer programs makes it very difficult to achieve reliability in their performance. This has motivated a substantial amount of research into the design of quality software. A methodology for the design of software is proposed which is based on two key concepts which have emerged from this research. A procedure for evaluating this methodology is presented. A software quality model is developed and validated as part of this procedure.

The proposed methodology provides an approach to the critical, early stages of software design. This phase of the design, the conception of the functional structuring of the program, is left to the ingenuity of the designer in the majority of other design methods. It utilizes a graphical portrayal of successive refinements of the data structures to define a sequence of nested virtual machine programs which are structured to match the data. This methodology is shown to satisfy many of the general criteria and guidelines associated with the design of quality software.

TABLE OF CONTENTS

Page

ABSTRACT

OBJECTIVES

LIST OF FIGURES

1.0 INTRODUCTION
- 1.1 Software Design
- 1.2 Proposed Software Design Methodology
- 1.3 Evaluation of Methodology
- 1.4 Software Quality Model

2.0 BACKGROUND
- 2.1 Early Computing Environment
- 2.2 Present Computing Environment
- 2.3 Future Computing Environment

3.0 SOFTWARE QUALITY
- 3.1 Background
- 3.2 Software Quality Model

4.0 SOFTWARE DESIGN METHODOLOGY DESCRIPTION
- 4.1 Key Concepts
- 4.2 Major Attributes

5.0 METHODOLOGY
- 5.1 Development Charts
- 5.2 Procedures

6.0 RELATIONSHIP WITH OTHER REPORTED RESEARCH
- 6.1 Program Design Languages (PDL's)
- 6.2 Design Procedures
- 6.3 Data Structures
- 6.4 Requirements Specifications
- 6.5 Data Abstraction
- 6.6 Design Specifications for Program Validation
- 6.7 Design of Program Families

7.0 MANAGEMENT CONSIDERATIONS
- 7.1 Initial Development
- 7.2 Control
- 7.3 Dissemination of Information

8.0 EVALUATION
- 8.1 Software Design Courses
- 8.2 Projects
- 8.3 Comparison of Results
- 8.4 Calibration and Validation of Software Quality Models

9.0 CONCLUSIONS

ACKNOWLEDGEMENTS

REFERENCES

FIGURES

5

LIST OF FIGURES

Figure 3.1. Characteristics Tree

Figure 3.2. Software Quality Model

Figure 5.1. Top-level program development chart

Figure 5.2. Second-level program development chart

Figure 5.3. Third-level program development chart

Figure 5.4. Program development chart for unusual situation

Figure 5.5. Third-level program development chart overlays

Figure 5.6. Program development chart levels, overlays, and segmentation

Figure 5.7. Fourth-level program development chart

Figure 5.8. Fifth-level program development chart

Figure 5.9. Introduction of intermediate nodes

Figure 5.10. Introduction of intermediate nodes in gross salary computation for payroll example

Figure 5.11. Functional grouping

6

OBJECTIVES

There are three specific objectives to be met by this project.

1. Provide a software quality model.
This model is to serve the needs of this project. It is to reflect work already done in this area and is not intended as a substitute for more extensive work planned on this topic.

2. Develop essentials of a software design methodology.
This methodology should be sufficiently structured so that it can be taught and should permit the design of uniformly high-quality software. This project should develop the methodology sufficiently to permit an evaluation of its feasibility.

3. Describe procedures for evaluating the software design methodology and validating the software quality model.

1.0 INTRODUCTION

Present-day computer programs are designed to solve very complex problems. This makes it very difficult to produce reliable software. Substantial research effort in this area has produced various theories, concepts, and methods directed toward the design of quality software.

1.1 Software Design

There is, as a result of the newness of the software design field, no established body of theory. Consequently, much of the research has produced general concepts and philosophies rather than specific methods(5). Some efforts to codify these concepts have been oversimplistic and have distorted their essential significance. The "goto controversy" (1) is a good example of this state of affairs.

A few recent efforts have been directed to the incorporation of these newly evolved theories of design into well conceived methods of software design. The major concern behind many of these efforts is the production of software which can be proven to be correct. Virtually all of these techniques provide a mechanism for specifying the behavior of the design once the basic conception of the design has been formulated.

In summary, most of the research in the design of computer software has either produced general theories and philosophies or has produced methods for precise specification of already conceived designs.

1.2 Proposed Software Design Methodology

The proposed software design methodology (SDM) provides a structured approach to the early stages of software design during which the essential program structure is established. This phase of design is critical to the ultimate software quality (28).

The methodology is based on a synergistic combination of concepts. The two key concepts incorporated in it are the concept of nested virtual machines (5, 30) and the concept of matching the program structure to the data structure (15,28). The design is achieved by a sequence of stepwise refinements (24) of the data structures, starting with the highest "level of abstraction" (as described by Burns(3), not by Constantine(28)), or least detailed representation of the data structure, and ending with the most detailed representation. The data structures are represented by directed graphs similar to those used by Earley (9) but with modifications and extensions.

The proposed methodology is intended to fill the void between general theories and guidelines for the software design process on the one hand, and the detailed specification of the already conceived design on the other hand.

1.3 Evaluation of the Method

The method is evaluated by having two groups of teams design software, one using the proposed methodology and the other not using it. The effectiveness for the methodology is determined by comparing the resulting software products.

1.4 Software Quality Model

The criteria for software quality are not well defined at the present time. Considerable research is being conducted to define these criteria and to determine the relationships among them.

A provisional software quality model is presented for the evaluation of the software products developed in the course of this project. This model will be based, to a large extent, on reported research results in the area of software quality factors.

2.0 BACKGROUND

The phenomenal rate of progress in digital computation has strained our ability to effectively utilize this tool. Recent developments have required major reversals in our approach to software development. Current achievements suggest continuing changes in the software environment.

2.1 Early Computing Environment

The introduction of the stored program concept by John Von Neumann marked a major event in the history of computation. It provided the computer with the ability to modify its own program; the key element needed for adaptive behavior. This capability, primarily used for address modification in handling arrays of data, also provided major headaches for software designers. Debugging a changing program was simply too much of a problem. The solution to the problem came in the form of architectural changes in the computer hardware, the introduction of index registers and indirect addressing, which obviated the need for the program to modify itself.

With this problem taken care of, programming digital computers was not a terribly difficult task. The limited memory capacity and relatively slow speeds of early machines restricted the complexity of problems to which they could be applied, so that tedium, rather than intellectual challenge, was the major problem for the programmer.

The hallmark of the expert programmer was the ability to squeeze a large program into the limited memory or the ability to shave a few milliseconds from the execution time by the use of clever tricks.

The creation of high level languages did much to relieve the tedium of programming while also making it more difficult for the master programmer to exercise his craft. Instead, analysts turned their attention to solving more complex problems.

2.2 Present Computing Environment

Improvements in computer hardware have provided great increases in computer speed and tremendously increased memory capacities. Architectural advances provide better efficiency so that the computer can now handle problems whose complexity is vastly greater than the problems which strained the capabilities of the machines of two decades ago.

It is this complexity which is the programmer's challenge. The mathematician has developed algorithms for solving the problem but they are complex and the programs required for their implementation are complex. The old program design paradigm, based on the use of clever tricks to gain efficiency, results in an incomprehensible, unreliable software product (1).

The essential message of structured programming (1) and structured design (28) is to simplify program structure. The situation is similar to that which existed when programmers stopped writing programs which modified themselves; they had to give up a measure of flexibility in order to gain simplicity. The difference is that there wasn't as long a period of time to establish the practice of writing programs that were self-modifying as there has been for designing programs whose major quality criteria are efficiency of storage utilization and minimal execution time.

2.3 Future Computing Environment

Current work in microprocessors and microprogramming points toward widespread use of multiprocessors and distributed computing systems of various sorts, as well as an increased flexibility in computer architecture and instruction sets. Ongoing work in the technology of memory devices suggests more widespread use of firmware in place of software for certain applications and increased system memory capacities. The imminence of these developments requires that software design methods be evaluated in terms of their suitability for such environments.

3.0 SOFTWARE QUALITY

The objective of software design methods is to design high quality software. Many people use the term "software quality" and generally have

10

relatively similar characteristics in mind, but there are no precise definitions for it nor is there agreement as to which components are most important. Boehm, et al in a TRW study (2) conclude that the criteria for software quality depend on the needs and priorities of the prospective user of the software. Despite this, it is essential to agree upon some set of definitions and criteria if there is to be meaningful communication and work in this area.

3.1 Background

3.1.1 Components of Software Quality

There is general agreement that the following are components of software quality:

(1) Reliability - In terms of software, reliability is generally associated with correctness. Robustness, or the ability to function appropriately in a bad environment, e.g. when receiving incorrect data, is sometimes included in reliability. The following definition is from a TRW study on software quality by Boehm, et al:

> "Software possesses the characteristic reliability to the extent that it can be expected to perform its intended function satisfactorily."

(2) Testability - It is important that the reliability of a program can be ascertained before it is put to use. There are two approaches to this task: verification and testing.

Verification uses formal or informal methods to prove or demonstrate that a program accurately implements its specifications. The major problem with verification, apart from developing a verification method, is that the specifications themselves may not be appropriate.

Testing procedures may be divided into two categories. Exhaustive testing requires that all possibilities be exercised. This is almost always an impossible task. The other testing procedure involves selective exercise of the program. One such technique (22) requires exercising each branch of the flow chart and each path emanating from a decision statement. Whatever the specifics of the method may be, it is clear that the structural complexity of the program will affect the ease of testing the program.

The following definition of testability is from the TRW study on software quality by Boehm, et al:

> "A software product possesses the characteristic testability to the extent that it facilitates the establishment of acceptance criteria and supports evaluation of its performance."

(3) Maintainability - A software product is not a static object. It must be changed due to changes in its application, changes of the

operating system and computer hardware configuration which determine its environment, and the correction of bugs which are discovered in it during its use. Maintainability is a measure of the ease with which this can be accomplished. The following definition of maintainability is taken from the TRW report by Boehm, et al:

> "A software product possesses the characteristic maintainability to the extent that it facilitates updating to satisfy new requirements."

(4) Portability - Great amounts of money are spent to modify large volumes of software which have been designed to run on one system so that they will run on another system. Even software written in so-called universal, high-level languages often cannot be transferred directly from one system to another. Portability is a measure of the ease with which such a transfer can be made.

The following definition of portability is from the same report by Boehm, et al:

> "A software product possesses the characteristic portability to the extent that it can be operated easily and well on computer configurations other than its current one."

These are not the only software quality components which have been recognized but are the ones of interest in this report because of the specific applications which motivate this work.

3.1.2 Measurement of Software Quality

Methods for measuring software quality fall into two categories: dynamic and static.

Dynamic measurement requires running the program and/or performing the activity associated with the component of quality being measured, e.g. running the program on various systems in order to measure its portability. The components of quality can be measured directly by dynamic measurement.

Static measurement is performed by examining the program code, or some other product of the software production process, which reflects the software design and implementation. Static measurement does not permit direct measurement of the quality components; instead, certain software characteristics are measured from which information about the quality components must be inferred. Advantages of static measurement are that it is generally simpler and more economical. The chief advantage, however, is that knowledge of the software characteristics that result in high quality serves as guidelines for the design of quality software.

12

3.1.3 Software Characteristics

Boehm, et al in the TRW report on software quality investigate the software quality components and related software characteristics. They define a set of software characteristics which are related to each other by the characteristics tree shown in Fig. 3.1. The software characteristics include the software quality components, which are located in the various upper and intermediate levels, and the software characteristics which are directly measurable by static methods. The measurable characteristics are located on the lowest level of the tree and are referred to as primitive characteristics. The characteristics on each level are selected so as to be independent of each other. The branches of the tree show the relationships between the various characteristics. Associated with each primitive characteristic is a metric which defines a measurement scale for the characteristic.

3.2 Software Quality Model

For the purposes of this study a somewhat simpler software quality model, the three level structure of Fig. 3.2, is adequate. Each level consists of elements which are qualitatively different from the elements on the other levels.

3.2.1 Software Quality Factors

The lowest level software characteristics correspond to the primitive characteristics of the Boehm report. In this study they are called software quality factors (SQF's) because they affect the software quality but are not components of it. These are the software characteristics which are directly measurable by static methods.

Associated with each software quality factor is a metric which defines a scale of measurement for the factor. The numerical value of a metric, derived from measurements made on a software product, is a measure of the extent to which the software procuct possesses the associated quality factor. Selection of a set of software quality factors should include as wide a range of factors as feasible so that no relevant information is omitted; it is not necessary that these factors be independent. The set of factors will, in practice, be limited by the problems of measuring them.

3.2.2 Software Quality Parameters

The intermediate characteristics are the components of software quality. In this study they are called software quality parameters (SQP's) because their values determine the overall quality of a software product.

The software quality parameters are directly measurable but dynamic methods must be used. They can be determined by static measurement

only if the relationships between them and the values of the software quality factors are known. Part of this project involves determining these relationships using a regression analysis technique.

The selection of software quality parameters depends on the application and requirements of the software user. The ones shown in Fig. 3.2 are typical.

3.2.3 Software Quality Index

The software quality index (SQI) is a measure of overall software quality. A linear combination of the software quality parameters provides a simple and usable formulation:

$$SQI = \sum_i a_i \, SQP_i \qquad (3.1)$$

where the summation is over all software quality parameters and a_i is the weighting factor associated with the ith software quality parameter.

The values of the weighting factors represent the subjective judgements of the software users as to the relative importance associated with each software quality parameter. The set of weighting factors is not fixed, but must change to reflect the varying quality criteria associated with different applications, environments, and users. This formulation for the software quality index permits selection of a universal set of software quality parameters which includes all possible parameters. The weighting factors of those software quality parameters which are not of interest for a given application are assigned values of zero, effectively eliminating those parameters.

4.0 SOFTWARE DESIGN METHODOLOGY DESCRIPTION

The proposed software design methodology (SDM) provides an approach to the earliest phases of software design, the conceptualization of the program structure required to solve the given problem. Some sources refer to this as the requirements phase (10) and consider design to start with the programming process. Whatever it is called, there is no question that this earliest phase has profound impact on the structure of the resulting program; if it is done poorly there is no hope of obtaining quality software. This part of the design process had been considered by many to be outside the realm of design methodology, to depend solely on the ingenuity and experience of the designer. The proposed methodology does not provide an automatic process for generating optimal designs but it does provide a structured approach to this activity.

14

4.1 Key Concepts

The methodology is based primarily on the synergistic union of two results of research in software design: the concept of nested virtual machines and the concept of matching program structure to data structure.

4.1.1. Nested Virtual Machines

The concept of nested virtual machines was first introduced by Dijkstra, who referred to it by the term "system hierarchy", in connection with the design of the @THE' operating system (7). The concept was also used by Liskov in the design of the Venus operating system (18) and is described by Denning (5).

A program is written using a set of high-level instructions or functions which are defined to facilitate writing of the program. These instructions are not, in general, executable on any machine nor are they part of an existing programming language. They are called virtual instructions and are only executable on a virtual machine. The next step is to write a program which simulates this virtual machine. This program is written using somewhat simpler instructions which are also virtual instructions executing on a second virtual machine. This process is repeated iteratively until a set of instructions are used which execute on the machine being used or are included in an established language for this machine. The hierarchy of virtual machines is the set of nested virtual machines. The highest level is the one on which the high-level, virtual, program instructions are executed; the lowest is the physical machine, possibly together with a language compiler.

4.1.2 Matching Program Structure to Data Structure

The idea of designing a program to match the data structure for a system is presented by Jackson (15) while Constantine suggests this as one of the guidelines of structured design (28). The concept of matching program structure to data structure is due to Jackson while the graphical technique used in the development process is related to work on data structures by Earley (9). Earley's technique is modified and extended for the purposes of this methodology.

The program is designed by means of a sequence of step-wise refinements of the data structures. Associated with each refinement of the data structure is a set of program operations which corresponds to one level of the nested virtual machines. The top-most level corresponds to the initial and least refined presentation of the data structures while the lowest level corresponds to the final, most refined presentation of the data structures.

15

4.2 Major Attributes

The concepts embodied in the software design methodology impose certain limitations on the methodology and also provide it with characteristics that generate software which satisfies certain quality criteria. These attributes of the methodology are discussed in the following paragraphs.

4.2.1 Reliability

The reliability of software produced using the proposed methodology is enhanced indirectly by enhancement of another software quality parameter, code reusability. Code reusability refers to the suitability of using the same code in numerous programs. This factor increases reliability because the greater the usage of a block of code, the more likely it is that bugs will be detected and corrected. The same factor also increases design efficiency because blocks of code that have already been written can be used in new programs.

The nested virtual machine concept results in modularization of programs into virtual instructions. The designer, since he is considering the design of language instructions (as opposed to a function for a single application), is prone to generalize the functions he defines so they have broad usefulness. The highest level instructions are most specific while the lowest level instructions are broadest in their application. Intermediate instructions can be defined and grouped so as to form languages which support different application areas. In military applications, for example, there might be one intermediate level language for command and control, another for procurement purposes, and another for general accounting applications. This attribute satisfies the criteria called for by Dowson (8) with respect to reusable code, specifically that programs consist of relatively independent, identifiable, functionally oriented modules which can be isolated. These same considerations suit the proposed methodology to the design of program families as discussed by Parnas (23).

4.2.2 Testability

Modularization into virtual instructions, in addition to providing code reusability, also results in enhanced testability. In dividing programs into virtual instructions, which are then further subdivided, the program is separated into small units which can be isolated, specified very precisely, and coded. The functional isolation and compactness of each unit lends itself to writing precise requirements specifications using a language designed for this purpose (10), to writing the design specifications using an appropriate language (4, 14, 21, 25), the use of sophisticated mathematical approaches to insure correct interfaces (12), and to the use of verification methods(17, 21, 26). This use of various techniques in conjunction with the proposed SDM illustrates their complementary nature. SDM is

not a substitute for these methods, but a methodology to be used at an earlier stage of design for guidance in areas not addressed by these methods.

4.2.3 Maintainability

The modularization into relatively isolated instructions enhances maintainability because changes which must be made can be isolated to a few distinct routines which need not affect other routines.

4.2.4 Portability

Portability is enhanced because only the implementation of the lowest level virtual language need be changed when the software is moved to a new system. All the higher level languages remain the same. This same feature permits various kinds of implementations. For example, it may be reasonable to directly implement an intermediate level language on a microprogrammable computer. Thus, the nested virtual machine concept offers great flexibility in terms of varying implementations. This will be well suited for use with future machines utilizing firmware and/or hardware modules to implement some of the functions currently being performed by software.

4.2.5 Top-Down Design

There is widespread agreement that certain design and programming approaches tend to result in high-quality software. In a study of software certification, Keirstead(16) lists a number of these, including the top-down approach. The top-down approach implies that the designer considers the overall problem, designs the main program which serves primarily to invoke subroutines to perform the program functions, and then performs the detailed design of these subroutines. This is in contrast to the bottom-up approach in which the individual functions are programmed first. Their integration into a single program commences when the individual subroutines have been completed and tested.

The proposed software design methodology is clearly a top-down approach starting, as it does, with the overview of the entire problem and gradually reaching greater refinements of all its parts. Use of a pure top-down approach is generally not optimal. As Gill (1) points out, a combination of top-down and bottom-up techniques, with greater emphasis on the top-down approach is generally best. The bottom-up technique is used iteratively with the top-down approach to globally optimize the design achieved using the sequence of stepwise refinements of the data structures.

4.2.6 Functional Decomposition

Functional decomposition is another approach that Keirstead cites as being associated with the production of high-quality software. Liskov and Zille's data abstractions (19, 20) and Parnas' information hiding modules (1) are similar concepts. The idea is that all operations related to an object (such as a data file) are handled by one routine so that any changes in the object impact only on the one routine. Sometimes the operations on the object are performed by a few routines instead of a single one but the essentials of the concept remain the same. The proposed design methodology procedures tend to result in such a functional decomposition.

4.2.7 Teachability

Dijkstra (1,6) comments on the need to be able to teach programming methodologies in as explicit a manner as possible. The proposed software design methodology is sufficiently structured so that it can be taught and students can use it to direct their design activities.

4.2.8 Language Independence

Flow-charting is a classical approach to program design. People have found a number of faults in this approach. One of these faults is the language dependency of flow charts; the level of detail of the flow chart is generally quite different for an assembly language program than that for a high-level language. There may even be differences in the flow chart which depend on the choice of high-level language.

The proposed software design methodology, since it is based on data flow and function, rather than implementation is not subject to this problem. If anything, it can be criticized for not providing sufficient information about the program functionality which determines the implementation. The graphical technique used in this methodology, like HIPO charts (13, 14), is dependent on notes for detailed functional information. The notes are keyed to labels contained in the graphs. This approach provides the advantage of permitting the use of an appropriate narrative form for these notes; it might be a mathematical formalism or simply English language that is used.

4.2.9 Sequence of Operations

Another shortcoming of flow charts is the fact that a flow chart shows the program as a sequence of operations. Sometimes it is necessary that operations be done in the sequence shown; at other times, however, the sequence is arbitrary. Careful analysis of the flow chart is required to determine which case holds in a particular instance. As a consequence of this, flow charts are not well suited to multiprocessor computer systems.

The proposed methodology eliminates this problem because the graphical

technique used depicts data flow rather than a time sequence of operations. The only sequences implied by this technique are those inherent in defining the value of a datum before it is used. Thus, the method is ideally suited for multiprocessor configurations.

4.2.10 Dependence on Data Structure

The major contribution of this method is that it provides a procedure for arriving at a design for a program structure. Clearly, there must be some input to guide the designer. This input is the set of data structures for the application.

Frequently, this information is given, either explicitly or implicitly, by the problem statement or the environment in which the system is to operate. When this is the case, the designer should have little difficulty in applying the method. Furthermore, different designers should arrive at substantially similar results, thus increasing the uniformity of software production.

The method does not insure the same level of uniformity when the data structures are not given. In that case, the designer must establish the data structure, which will then determine a program structure. Even in this case the method is useful because it provides a sequence of steps which leads the designer to develop the data structures in a reasonable way using a top-down approach. Moreover, it is hypothesized that the data structures developed by different designers for a given problem would tend to be more similar to each other than would be their functional approaches to the problem solution.

4.2.11 Levels of Availability

This is a new concept introduced to permit the designer to handle the physical implementations of the data which the software is designed to process. A number of techniques, such as data abstraction and information hiding modules, have been proposed to avoid the detailed software design considerations associated with the physical implementation of a system, especially those related to data storage, until the latter stages of implementation. The intent of these techniques is to convert the physical data format into a logical format using one module. The remainder of the program need not be concerned with the physical details but can treat the data as logical elements.

This approach is very fine as far as it goes but it doesn't address the very real problem of handling the physical forms of the data; problems of timing, accessing, etc. The concept of levels of availability is an attempt to solve this difficulty. It proposes that a class of storage devices, with their associated media, be modelled by an abstract model, called a "level of availability", which will be characterized by access modes and times, data block sizes, etc. The more readily the data is available for program processing, the higher the level of availability; the highest level is one and lower levels

are assigned successively higher numbers. Thus, main memory is generally level 1. For a particular system, magnetic disks might be level 2, magnetic tapes might be level 3, punched card I/O would be level 4, and line printer level 5. The assignments of levels would be different for different systems and even for different applications on the same system. The level assignments reflect a combination of both the physical characteristics of the device and the logical function it is serving in the system.

5.0 Methodology

The proposed software design methodology (SDM) consists of nine procedures. Much of the design is accomplished using a sequence of directed graphs called program development charts, or simply charts or graphs when it is clear that it is actually the development charts that are being referred to. The key to the method is that the functional decomposition and design of the program is "driven" by the data structures which the program is to process.

5.1 Development Charts

The program development chart (PDC) is a directed graph in which the nodes represent data elements and the edges represent program operations and data flow.

5.1.1 Nodes

The data elements represented by the nodes may correspond to any level of data aggregate from the set of all input or output data files down to the value of a single scalar variable. The nodes are labelled with an identifier for the data element.

Two types of nodes are used in the graphs. A circle represents a logical data element which can be directly processed by the computer or central processing unit. A small square represents a physical data element which is input to or output from the computer. It cannot be directly processed by the central processing unit. Where appropriate, the level of availability of these nodes may be indicated by placing the appropriate number inside the square.

5.1.2 Edges

Edges of the graph are represented by lines with arrowheads. These represent program operations, including input and output, and data flow. The program development charts display data structures as well as data flow. Solid lines are used to show data flow and the

combination of data through program operations. Broken lines are used to show components of a larger data structure. Thus, the broken lines correspond to the edges used by Earley (9) in describing data structures. The process of selecting a portion of a data structure can be considered as a simple program operation so that the broken "selector" edge is a special case of the solid edge. The operation indicated by the broken edge is referred to as a selection process.

5.2 Procedures

The software design methodology is best described by means of a simple illustration. The example used is a simple payroll application. The program is to provide two output files:

(1) REPORT(Rpt)- contains the name, social security number, gross pay, federal withholding tax, FICA withholding, and net pay for the payroll period for each employee plus appropriate heading and trailer information.

(2) NEW MASTER FILE(NMF)- contains social security number, name, address, telephone number, birth date, hourly wage, year-to-date gross pay, year-to-date federal withholding tax, year-to-date FICA withholding, and year-to-date net pay plus appropriate header and trailer information.

The input to the program consists of two files:

(1) TRANSACTIONS(Trns)- contains social security number, date, and number of hours worked for pay period for each person who worked during pay period. This file also contains a header card with the date and payroll file identification.

(2) OLD MASTER FILE(OMF)- contains same information as new master file prior to update.

The designer is to complete specification of the data files and is to design the program to implement the system. The transaction input file is a punched card file, the report file is output on a line printer, and the master files are on magnetic tape.

The software design methodology consists of nine phases, called procedures, which are described below.

5.2.1 Initial Program Development Chart

The software design methodology starts with the drawing of the initial program development chart. This graph is almost universal. In most cases it takes the form shown in Figure 5.1 which simply indicates that a program is to be designed which transforms input data into output data. The graph also indicates that the input and output are in some physical format but it does not indicate anything about the form,

21

the format of the data, or any other details.

The particular graph of Figure 5.1 together with some trivial variations of it (possibly a graph with no input) account for the vast majority of all software systems. Thus, even the novice designer would have little difficulty with this procedure.

5.2.2 Second Level Program Development Chart

The second level program development chart is a refinement of the first level program development chart. It is obtained from the first level chart using the following rule.

> Each of the data elements in the top-level (initial) program development chart is subdivided into components which are both functionally and physically distinct.

The objective of this rule is to identify the major functional files which the program is to process. The requirement that they be physically distinct enables even the novice designer to make the required distinctions. The added requirement that the data elements also be functionally distinct is intended to avoid separating multi-volume files into separate data elements.

The second-level program development chart for the payroll example is shown in Figure 5.2. It shows the components of the original data elements connected to the original data elements by broken lines, indicating a selection process. It also indicates the flow of data between the input and output components by solid lines. The drawing of these solid lines represents functional analysis in that the designer must determine which output depends on which input.

There is little room for variation in the second-level graph. For the payroll example, any designer with a correct understanding of the problem would have to arrive at a graph equivalent to the one of Figure 5.2.

The components of the original data elements are shown as squares to indicate thay are distinct physical quantities. Beyond this, however, there is no more information concerning the data elements.

5.2.3 Third-Level Program Development Chart

The third-level program development chart is obtained from the second-level chart by means of the following rule:

> Each of the data elements in the second-level program development chart is subdivided into its major functional components using data format as a guide.

This chart is the point at which the designer generally has to start

making design decisions concerning the broad structure of the data files. An often used pattern is header-body-trailer. One non-functional guideline the designer may use in determining whether two parts of a file are distinct major functional entities is whether the data formats could be the same. In general, there is no way in which the header information could be put in the same format as a transaction record. Note that this guideline does not require that the formats be set but merely that possible formats be considered.

The third-level chart need not show the initial data elements, i.e. the "Input" and "Output" elements of the top-level chart, because the relationship between these and their major components is shown in the second-level chart. It is only necessary to show the relationship between the components of the second-level chart and the newly introduced components in the third-level chart.

The third-level program development chart for the payroll example is shown in Figure 5.3. There are four general points that should be noted:

(1) The graph illustrates the normal data flow. Unusual conditions may result in a rather different graph. For example, in the payroll example, the file identification on the transaction header card is compared with the file identification in the old master file header record. If they don't agree, the program is aborted with an appropriate error message to the report. This may be shown by a bastardized chart such as that of Figure 5.4 or it may be omitted from the program development charts, noted, and incorporated at a later stage in the program design. In general, if the unusual condition is not difficult to detect and/or handle, it is best omitted from consideration in the program development charts although a note should be made so that it will not be overlooked entirely. These approaches are applicable to any level program development chart.

(2) In creating the program development charts, the designer must envision the solid lines as representing data flow. An attempt to consider these lines as program functions at this point confuses the process because it defeats the purpose of the method which is to separate the designer's concerns and problems. The program function interpretation is implemented in a subsequent procedure of the methodology.

(3) The designer does have to consider the functional aspects of the program at this time in order to construct the solid lines which depict the data flow. In Figure 5.3, for example, there is an edge from RBD (report body) to NBD (new master file body). This reflects the decision by the designer to use some of the results computed for the report in the new master file rather than recomputing the results from the original input data.

In some designs this third-level program development chart becomes quite complex and is more easily depicted by a set of

23

overlays as shown in Figure 5.5. The overlays are partial charts which can best be thought of as a set of overlay transparencies, which when superimposed produce the complete program development chart. (For convenience in actual practice, the various parts of the chart are not always drawn to provide actual physical registration as would be required for a real set of transparency overlays.) This overlay concept can be applied to any level program development chart. The only rule that should be followed in producing a set of overlay program development charts is the following:

> For every node shown on an overlay development chart, either all of its inputs or none of its inputs should be shown. Since there is, in general, nothing to be gained by showing the inputs more than once, the inputs to each node will generally be shown on one, and only one, of a set of overlay program development charts.

The reason for this rule is based on the program function interpretation of the charts. It essentially insures that all inputs to a function are shown on one overlay which facilitates the assignment of program functionality. The only other guidance for the preparation of the overlays is that, since their purpose is to provide a clear presentation, an excessive number of crossing lines on a single overlay should be avoided. If showing an element on an overlay does not enhance the clarity of the overall set of overlays it should be omitted. Each element, must of course, be shown on at least one overlay.

(4) The newly introduced data components in the third-level program development chart are logical elements since they form groups of components, each (group) of which corresponds to a single physical element. From this point on, until the designer returns to the task of refining the handling of physical data (Section 5.2.9), all data is in logical form.

5.2.4 Refinement of Data Structures

This procedure consists of step-wise refinements of the data structures by reductions of these structures into simpler components. Examples of this are reduction of an n-dimensional array into a set of (n-1)-dimensional arrays and the division of a record into its component fields. This process is repeated iteratively until each data element has been reduced to simplest possible form or to a form which can be appropriately processed by an already existing function. This process generally requires a sequence of program development charts. In addition to separating these charts into sets of overlays, they can also be segmented as parts of a single chart which has been cut up to into smaller size sheets. The paths used for cutting should not be arbitrary but should follow paths which are least disruptive to the clarity of the presentation of the charts. This is generally achieved by cutting along paths which are straight lines and which cross a

minimal number of edges. It is often useful to duplicate certain portions of the chart which are near the boundaries to facilitate understanding of the charts. The resulting segmented charts are very much like a map which is presented on multiple pages. A representation of possible levels, overlay sets, and segmented charts is shown in Figure 5.6. This structuring of a sequence of program development charts is similar to the organization of HIPO Charts (13).

Generally, only the lowest level data elements of a program development chart are shown on the next lower-level chart. This results in a simpler chart and does not eliminate any information which would not be redundant. If a higher-level data element enters directly into the data flow depicted on a given chart, it is treated as an exception to this principle and shown for the sake of clarity.

Figure 5.7 shows the fourth-level program development chart for the payroll example divided into three segments. Part (a) of the figure indicates that both the transaction header(THD) and old master file header (OHD) consist of two elements: the identifications (TID and OID) and dates (TDT and ODT). Both identifications should be the same in which case their value becomes the report header identification (RID) and new master file header identification (NID). If the identification in the transaction file is not the same as that in the old master file, the program is aborted after printing an error message. The transaction file date is checked to insure that it follows the old master file date; if it does it becomes the report date (RDT) and the new master file date (NDT). If the dates are not sequenced properly an appropriate message is printed and the program is aborted. This same figure also indicates that the report identification (RID) and date (RDT) are transferred directly to the new master file. This is different from Figure 5.5 which shows the input to the new master file header (NHD) from transaction header (THD) and old master file header (OHD). The discrepancy is due to the designer's realization that the method in Figure 5.7 is simpler. Figure 5.5 should be changed during the subsequent global optimization procedure to reflect this.

Part (b) of Figure 5.7 depicts the processing of a single transaction to produce a line of the report and a record in the new master file. The two edges labelled SEL both represent the operation of selecting a single record from a one-dimensional array of records while both edges labelled INC represent the operation of incorporating a record into a one dimensional array.

The two edges labelled CMP1.1 and CMP1.2 represent the operations required to compute an output line (LN) for the report while the two edges labelled SMRY1.1 and SMRY1.2 represent the operation required to generate the corresponding summary record for the new master file (NRD). In addition to this normal situation, the functions CMP1 and SMRY1 must handle missing transactions due to absence and missing master file records due to new employees who have not, by error, been entered onto the master file. The detailed representation of the required processing would appear in more detailed program development

charts; the fourth-level chart remains as shown in Figure 5.7(b).

Part (c) of Figure 5.7 depicts the data flow required to generate the report trailer (RTR). It indicates that the report trailer consists of three values: the number of absent employees (ABS), the number of new employees not yet entered into the master file (NEW), and the error (ERR), if any, in the old master file trailer tally as compared with the actual number of records in the file.

There is no fourth-level program development chart segment for the new master file trailer because the third-level chart shows it in simplest form. The new master file trailer consists of a tally which is equal to the number of records written into it and, in addition, it contains the old master file tally.

All the data elements in Figure 5.7, except those in part (b) are atomic data elements, i.e. data elements which cannot be reduced any further while still maintaining their identities. Therefore only part (b) can be refined into a fifth-level program development chart.

The fifth-level chart is shown in Figure 5.8. The only discrepancy between it and the preceding graphs is that FICA is computed differently. Whereas the earlier graphs imply that new year-to-date FICA (NYFC) is computed by adding the current FICA to old year-to-date FICA (OYFC), this graph depicts computation of NYFC from FICA followed by computation of current FICA by subtraction of OYFC from NYFC. This discrepancy is the result of a change in the designer's computational plan; the earlier charts should be changed accordingly during the subsequent optimization process.

The data element EDT (employee date) in the transaction body (TBD) record appears to serve no function. It is checked against report date (RDT) (Figure 5.7) and if the dates don't match the transaction is treated an if it were absent except the report message that is printed is different. This does not show up in Figure 5.8 because it is an unusual situation rather than the normal one.

All the data elements in Figure 5.8 are atomic elements; therefore this fifth-level program development chart completes this procedure. The first four procedures result in a top-down design. They serve to separate and isolate the designer's concerns. Consideration of the data flow has directed the designer's attention to particular small segments of the functional design of the program. The payroll example is a very simple one. Although it seems almost self evident that the procedures would be effective for a more complex system as well, its effectiveness for a complex system should be tested. The design for an experimental study is described in a subsequent part of this report.

5.2.5 Introduction of Intermediate Nodes

This procedure introduces additional nodes based on consideration of the program algorithms. At this point the broad functional

decomposition of the program has been achieved; this procedure provides a detailed functional decomposition. There are two rules which are used in this procedure.

> Intermediate nodes are added to define the sequence of mathematical and logical operations.

An example of the application of this rule is shown in Figure 5.9(a). The second rule is:

> Intermediate nodes are added to eliminate redundant computations.

The application of this rule is illustrated in Figure 5.9(b); it corresponds to factoring out common expressions. The two rules are not independent. The second rule may be treated as a special case of the first rule but the consideration of isolating common elements may alter the way in which the nodes are grouped. This process will, in general, result in the creation of additional levels of program development charts. Figure 5.10 illustrates the application of this procedure to part of the payroll problem. Part (a) shows the original graph while part (b) corresponds to a refined chart in which the overtime hours (OVT) are multiplied by a factor and added to regular hours (REG) to give effective hours (EHR) which is multiplied by the rate (ORT) to give the gross salary (GR).

5.2.6 Global Optimization

An iterative approach involving a combination of top-down and bottom-up design is used to globally optimize the sequence of program development charts. In the payroll example there were certain discrepancies between higher and lower level charts resulting from changes the designer decided to make as the program was considered in more detail at the lower levels. These discrepancies are resolved at this point by making the appropriate changes in the higher-level charts. This is an application of the bottom-up approach. The designer, before going onto the next procedure, reviews the complete set of charts looking for areas where the design can be improved and makes the necessary modifications. Care must be taken to insure consistency between all levels when making changes.

One of the considerations the designer should have in mind is the possibility of modifying certain data flows so that the same function can be used in different places. This consideration is used in subsequent phases as well.

The descriptions of the various procedures in this report, of necessity, must be presented in some sequence. While the sequence of description follows the usual sequence of application to the extent that a sequence of application exists, the application of these procedures involves iterative combinations in which the various procedures are intermixed. In other words, a procedure is not initiated and completed before the next procedure is initiated;

rather, procedure A is applied but not finished, then procedure B, then C, back to B, then C, then possibly A, and so on.

5.2.7 Functional Grouping

The edges in the program development charts reflect data flow rather than functional considerations, although the data flow is obviously influenced by the functional behavior of a program. As a result of this, it is not possible, in general, to associate a program function with an edge. Instead, each node except the source nodes, i.e. those with no edges entering them, has associated with it a program function which produces the data element represented by the node. All the edges entering a node are combined to define the function. This is the reason for requiring that all input edges to a node be shown in a single overlay.

The designer can identify the functional decomposition of the program using the notation illustrated in Figure 5.11 which represents three functions: F1, F2, and F3. In this illustration, each function has two edges associated with it which are indicated by labelling each with the function name concatenated with a period concatenated with an integer which uniquely identifies the edge. The integers start with 1 and continue in order for each function.

In this procedure, as in the previous one, the designer should look for common elements or functions which can be modified so that they are the same.

5.2.8 Identification of Virtual Instructions

The functions that were identified in the previous procedure are formulated as virtual instructions. If a set of virtual instructions already exist these should be reviewed to determine whether they can be used to implement any of the functions.

The designer should formulate the specifications for each virtual instruction very precisely using an appropriate design language and/or system (12, 14, 17, 20, 21, 25, 27). The specification technique should provide for subsequent comprehensive testing and/or validation of the implementation of the virtual instructions (26) as well as providing the specifications that define the behavior of the instruction.

The virtual instructions should be formulated as generally as possible without giving up too much in the way of efficiency. The following guidelines should be utilized in this procedure:

(1) It may be possible to define a single virtual instruction that implements a number of functions by providing parameters in it to tailor it to the individual requirements. This should not be carried to extremes which detract excessively from efficiency.

(2) Virtual instructions are part of a virtual language that will, hopefully, be utilized for other software systems in addition to the present one. Therefore, the instructions should be designed so as to be generally useful.

An example of the type of thinking which might enter into this process can be given in terms of a functional requirement to add two ten-element, one-dimensional arrays together. The designer, cognizant of the above guidelines, may decide to generalize the routine to add two one-dimensional arrays together with the number of elements being provided as a parameter rather than fixing it at ten elements. The designer may also consider further generalization to a routine which adds arrays of any number of dimensions but would likely reject this because it would seriously detract from the efficiency.

The exercise of careful judgement in this procedure can have a significant effect on future projects. This implies that the amount of effort devoted to such considerations should be determined by the expected number of additional software designs which may utilize the virtual instructions which are being designed. There is nothing to prevent substitution of a virtual instruction by a more general one at a later time if that becomes desirable. These considerations are directly relevant to work by Parnas on the design of software families (23) and indicate the usefulness of this method in that area.

This process is performed for each level of program development chart. Each level utilizes the virtual instructions of the lower level or levels to define its virtual instructions. Robinson (25) and Robinson, et al (27) present a formal methodology for specifying this decomposition. Hamilton and Zeldin (12) provide techniques which insure proper interfacing of modules and well-structured implementations.

5.2.9 Refinement of Physical Data Structures

The previously described procedures serve to refine the data structures and program. The major emphasis in those procedures is on the logical aspects of the data structures. The physical features of the data structures are intentionally given as little attention as possible in those procedures.

The intent of this procedure is to refine the physical data structures without getting involved with the specific implementation details of a particular hardware configuration. This is accomplished by using the levels of availability abstraction discussed in section 4.2.11. The objective is to store data economically and to have it available for the program to process when it is required.

There are three relatively distinct aspects of this procedure.

(1) Development of an abstract model

It is necessary to decide what aspects of the devices are important and should be incorporated in the abstract models. It is also necessary to determine how precise the model must be; the more precisely it must represent the devices, the narrower the class of devices which a single model may represent. In the extreme, each model will represent all aspects of one device and the entire concept loses its value. At the other extreme, the model may be useless because it provides insufficient information.

This aspect of the procedure is a one-time problem. A single set of models for an installation should be adequate for most applications. This concept is essentially an extension of Liskov and Zille's concept of data abstractions into the physical, rather than logical, domain. It can also be viewed as an extension of Parnas' information hiding concept into the physical domain. Additional study is required in this area to select the device parameters that should be used in the models and to determine the groups that comprise the various levels of availability.

(2) Timeliness of Data availability

Timing of I/O activities becomes a somewhat critical problem in many systems because of the slowness of I/O devices. In general, it is desirable to initiate an I/O activity as early as possible so that the data will be available, or the buffer will be clear, when it is needed. The structure of the program, e.g. looping, often limits the extent to which this can be done. If the data handling operations delay the program execution despite early I/O initiation, the only recourse is to use a faster I/O storage device. This may result in data being transferred from one peripheral to another before entering main memory or after exiting from memory.

(3) Efficiency of Peripheral Utilization

Although transfer between peripherals may increase the efficiency of operation of the central processing unit it does involve the use of two peripherals instead of one, thereby making a peripheral that would otherwise be available for other purposes, unavailable.

It is the designer's task to reach a balance between these conflicting requirements based on the application, its priority, and the hardware system and operating system on which the program is being executed. Imminent changes in hardware and architectural design can be expected to have considerable impact on this problem.

The program development charts provide a method for representing the transfer of data between peripheral devices. The concept of levels of availability permits the designer to start work before the detailed specifications for I/O devices are known. As the software system is refined it is possible to obtain better estimates of execution time from the program development charts. If already implemented virtual instructions are used, it is possible to use measured execution times for them to arrive at accurate timing estimates with relative ease.

AD-A033 822 AUBURN UNIV ALA SCHOOL OF ENGINEERING F/G 14/2
1976 USAF-ASEE SUMMER FACULTY RESEARCH PROGRAM.(U)
SEP 76 J F O'BRIEN F44620-75-C-0031
UNCLASSIFIED AFOSR-TR-76-1419 NL

5 OF 9
AD A033822



These timing estimates can be combined with more specific information concerning the speed associated with a level of availability, or a specific device if it has been specified, to check adequate functioning and/or to indicate areas for design revision.

This procedure completes the proposed software designing methodology. To summarize, the proposed methodology starts with the specification of requirements stage and ends prior to implementation using a programming language. It is complemented by use of a program design language, and possibly a requirements specification language. The function of the methodology is the structuring and modularization of a proposed software system; this is accomplished by a sequence of step-wise refinements of the data structures.

6.0 Relationship With Other Reported Research

In this section, the proposed software design methodology (SDM) and the program development chart (PDC) are compared with other methods, approaches, and concepts. A number of researchers have developed methods and/or languages for specification of program designs. These efforts are motivated by various concerns including the desire to verify software implementations against specifications, to check the internal consistency of specifications, to impose certain structural constraints on implementations, or to facilitate precise and unambiguous communication between people working on a project. The proposed software design methodology is compared with a sampling of such methods.

6.1 Program Design Languages (PDL's)

Efforts in this area are characterized by those of Caine and Gordon (4), IBM's PDL (14), and mcGee and Pizzarello's (Honeywell) Rational Programming Technique. The primary, but not sole, purpose of these languages is to foster unambigious communication, principally between the designer and the programmer.

These languages do not provide the designer with an approach to the design process as does SDM nor do they provide a graphic representation of the developing design. They complement SDM by providing a vehicle with which to express the design in a precise standardized form.

6.2 Design Procedures

These techniques, like SDM, are intended for the early design stages. There are substantial variations among these methods so a few of the better known works are discussed individually.

31

6.2.1 IBM'S HIPO Charting

There are three types of HIPO charts: a visual table of contents, overview diagrams, and detail diagrams (13). The visual table of contents presents a hierarchical modularization of the software system design but it does not, nor is it intended to, aid the designer in achieving this modularization, i.e. its function is more one of documentation rather than design. The overview and detail diagrams are in some ways similar to the PDC's of the proposed methodology in that they permit stepwise refinements of the program structure and also use notes keyed to the graphic charts. Unlike the PDC's which use nodes and edges, the HIPO charts use nested boxes to show data elements and program components. HIPO charts are uniformly structured with input on the left, program in the middle, and output on the right.

From a purely mechanical point of view, HIPO charts are more difficult to draw because of various types of stylized arrows, etc. Although templates are available and this is not of major theoretical import, it does seem that this task would interfere with the designer's concentration on the essential task of system design.

The more important distinction between HIPO charting and SDM is that the only guidance given to the designer using HIPO charts is the input-program-output paradigm whereas SDM provides a structured design approach. HIPO charts are an effective means of presenting and documenting a software design.

6.2.2 Presser and Rector's Systematic Step-wise Refinements

Presser and Rector's approach (24) is covered in a paper which presents a case study in disciplined design. it is not presented as a developed general methodology so comparison is somewhat unfair. It is included here because there are some similarities between their approach and SDM. Their approach uses a sequence of graphical representations with increasing refinement. Program elements are indicated by ovals and data elements by rectangles. The hierarchy of program modules is shown by a tree structure of the program modules and the data is shown as input and output to and from the program modules. In comparison with SDM, the approach does not provide guidance as to how to achieve the modularization. It is not as well structured nor does it seem as comprehensive.

6.2.3 Contantine's Structured Design

Constantine's methodology, as presented in the paper "Structured Design" (28) provides extensive coverage of the design process. A very thorough analysis of program structures is presented along with numerous guidelines. Much of the paper is devoted to these guidelines and the reasons behind them. This part of the work does not have the structure required of a "method"; it is more a discussion of principles and concepts.

The latter part of the paper is devoted to the presentation of a design methodology which utilizes structure charts to provide a graphic design vehicle. The design is centered around a tree type development of the structure chart from which the program is developed. The starting points and direction of movement (in the design process) are essentially opposite for this method and SDM.

Constantine's method requires that the designer identify the major input and output streams, locate the points of "highest abstraction" for these streams (i.e. the point farthest removed from the physical form, or alternatively, the point where the data is most highly processed but still identifiable as input or output), connect the input and output at these points by a program module and then work out from these points toward the physical forms providing modules which transform between the existing abstract form and the less abstract form which ultimately terminates when the actual physical form is reached.

SDM starts at the physical forms and works in toward the more abstract forms. The advantage in using SDM is that the designer does not have to make the leap to the point of highest abstraction at the very beginning. It is questionable whether designers other than very talented and experienced experts can do that.

The guidelines and principles given by Constantine are excellent criteria for judging the effectiveness of a design methodology. An evaluation of SDM in terms of these criteria follows:

(1) Coupling between modules should be low.

The implementation of a program by a series of levels of virtual instructions insures very low coupling.

(2) Interface complexity should be simple.

The interface between virtual instructions is straightforward. Each instruction invokes a sequence of lower level instructions. This is the kind of interface that Hamilton and Zeldin (12) build in to their methodology in order to insure proper interfacing. The only type of global interface would be through a block which associates data attributes with variables names, as is done in PL/1 with the DECLARE statement or in COBOL with the data division.

(3) Connections between modules should be normal (reference to module by name), not pathological (reference to element inside module).

The virtual instructions which comprise the program do not have provision for pathological references. Arguments must come from a common area or a formal parameter list; there is no way to branch into the middle of a routine.

(4) Type of communication is best held to minimum control coupling (subroutine calls) and passing of "element of control" (e.g. flag).

The typical communication in programs designed using SDM is by subroutine, or function call. SDM does, by requiring the designer to attempt to combine sets of functions into single virtual instructions which can be tailored for a given application by means of parameters, encourage the use of control arguments (arguments that determine the behavior of a function). This type of communication is generally, according to Constantine, better avoided. The pros and cons of such usage would have to be considered carefully since it does inhance the software efficiency.

(5) Cohesiveness of a module should be as high as possible.

Modules in a program designed using SDM are defined by virtue of producing a single data element as output. This essentially guarantees functional binding, which is the highest form of binding.

(6) Modules should be predictable (should provide identical outputs each time they are called with the same inputs).

It is in the nature of instructions that the outputs are well defined functions of the inputs. Modules in a program designed using SDM are predictable since they are virtual instructions.

(7) Match program to problem.

Satisfaction of this guideline is insured since the program structure follows the data structure which is either explicitly given as part of the problem statement or is developed by the designer in response to the problem statement.

(8) Scopes of effect and control.

The scope of control of a module is that module plus all modules that are ultimately subordinate to that module. The scope of effect of a decision is the set of all modules that contain some code whose execution is based upon the outcome of the decision. The system is simpler when the scope of effect of a decision is in the scope of control containing the decision.

Satisfaction of this guideline essentially eliminates the use of control flags. This would preclude the use of modules whose sole or major function is to perform certain tests and report back to the higher level module. It is not clear that this restruction is necessarily advantageous in the context of SDM.

(9) Module size should not be too small or too large.

Defining modules as virtual instructions tends to avoid overly large modules. Modules which are too small are combined into the higher level virtual instructions which they are part of.

(10) Error and end-of-file flags should not indicate what is to be done about these conditions.

Virtual instructions would normally be defined so as to sense and report these conditions but not to indicate the response.

(11) Special initialization modules should be avoided if possible.

It is the nature of instructions that they do not have to be externally initialized. Where initialization is necessary, the designer will have to make explicit provision for it.

(12) Selection of modules should eliminate duplicate functions but not duplicate code.

The procedures used to generate common functions and the attempt to generalize functions in defining virtual instructions effectively eliminate duplicate functions. In software designed using SDM there is no duplicate code which is not a duplicate function. Change of code requires a change of the function or virtual instruction.

(13) Isolate specifications.

SDM achieves this by having each element input by a routine which performs a selection process. If a specification for the data element changes only the function which implements the selection process need by changed; the remainder of the program remains the same.

(14) Reduce parameters.

The procedure of introducing intermediate nodes reduces the number of parameters to each function. The data flow formulation of the PDC indicates which parameters are essential.

From the foregoing analysis, it is evident that the software produced by use of SDM is likely to satisfy most of the criteria for a well designed software product as given by Constantine.

6.3 Data Structures

Earley (9) has investigated data structures. His work does not cover the design of programs to transform data structures although he does discuss the transformation of data structures. He references a programming language, VERS, related to his work on data structures and proposes an ultimate system which will accept graphical representations of data structure transformations and produce appropriate programs to achieve them. At present, however, his work appears to be primarily involved with the data structures themselves.

6.4 Requirements Specifications

Teichroew is credited as the major investigator in this area and is the originator of the system described by Eiden and Moore (10). This system, which consists of a language and an analyzer (which is a

35

software product), is intended to permit the designer to specify the user's requirements with the language and to prepare various reports, including graphical representations, from this data.

This technique does not provide any assistance in the design of a software system which is the function of SDM.

6.5 Data Abstraction

The data abstraction concept of Liskov (19,20), the information hiding concept of Parnas, and the transaction analysis of Constantine are all related to a single concept which is known by other names as well. The essence of the concept is that all operations on a data object are performed by one or more modules which make it unnecessary for the remainder of the program to be concerned with the detailed formats or other physical characteristics of the data. This minimizes the impact of data specification changes on the bulk of the program.

SDM provides such an isolation of the data objects by means of the selector functions, represented by the broken lines in the PDC's.

6.6 Design Specifications for Program Validation

These are design languages which permit specification of the design in unambiguous, functionally-oriented notation. Designs may be checked for internal consistency and programs may be checked against their design specifications using manual and/or automatic tools. Liskov and Zilles (20), Robinson (25), Robinson and Levitt (26), Hamilton and Zeldin (12), and McGee and Pizzarello (21) have all done work in this general area.

The work of Hamilton and Zeldin and the work of Robinson resemble SDM in the use of a hierarchical decomposition and nested virtual machine concepts respectively. Both of these techniques, along with the others, differ from SDM in that the designer essentially starts with a relatively complete decomposition or modularization in mind. The method permits precise specification of this decomposition and imposes constraints on the design in order to avoid certain pitfalls. SDM, on the other hand, is intended to provide an approach for generating the decomposition or modularization with which these procedures start.

6.7 Design of Program Families

Parnas discusses the problems of designing program families by means of three approaches: conventional sequential development, step-wise refinement, and specification of information hiding modules (23). Of the three, the last two are shown to be useful for this problem while the first is not.

SDM is most similar to the step-wise refinement method. It would be

expected to be somewhat more effective because it has some of the characteristics of the information hiding method as well and, in addition, the explicit attempt to define generally useful virtual instructions of program families.

7.0 Management Considerations

The usefulness of SDM in environments where many programs, which fall into a few application-oriented categories, are to be produced has already been noted. The lowest-level languages support the entire range of programs because of the general nature of their instructions. The specific nature of the high-level language instructions limits their usefulness to one or a very limited number of programs. The intermediate level programs support a moderate range of programs which tend to coincide with application-oriented categories as a consequence of the similarities between programs in a given category.

Controls on the languages are necessary to provide stability so that different people working in this environment can use a language with confidence that it performs according to current documentation. This requires a management system to control the languages, to determine what changes are desirable, to implement these changes, and to disseminate up-to-date information.

7.1 Initial Development

The initial problems in setting up such a system are quite different than those which exist once the languages are established. In the beginning, each programming team will have the freedom to define whatever instructions they require at whatever levels they wish.

Frequent meetings between representatives from all teams should be held with the objectives of detecting redundant instructions or instructions which are sufficiently similar so that they may be replaced by a single instruction. This committee will have the responsibility of standardizing those instructions used by more than one programming team.

The work of this group is facilitated by submission of forms, which document newly defined instructions, to an individual or group which is responsible for comparing them and detecting redundancies. These forms also provide the basis for documentation of the languages.

7.2 Control

During the initial period a sufficient range of instructions are collected so that a designer has a reasonable chance of finding, in

the lower and intermediate levels at least, instructions which permit him to implement a substantial part of his design. Once this point is reached the management techniques must change. A number of things must be done during this ongoing phase which include:

(1) Identify application-oriented categories.

(2) Group instructions into languages which are characterized by the category or categories they serve.

(3) Establish standards for virtual instructions. Some standards will apply to all languages, some to a certain level of language, others to languages for certain application-oriented categories.

(4) Establish procedures for adding to or modifying a language. Higher level languages will require more freedom to implement changes while lower level languages demand more stringent control.

7.3 Dissemination of Information

It is essential that up-to-date information on the languages be available. Techniques that have been used for standard programming languages can provide the basis for dissemination of information on the virtual languages but they must be modified to handle the more frequent changes which can be expected in this environment. Computer aided updating is essential for this application; many text editing software products are available which are suitable for this purpose. In addition to printed updates, CRT terminal access to the current information is very desirable.

Responsibility for control of the languages and dissemination of updates should be vested in some facility. The quality control facility proposed to Rome Air Development Center by the MITRE Corporation (11)) would be an appropriate facility for this function.

8.0 Evaluation

An experimental design for the evaluation of the proposed software development method is presented in this section.

8.1 Software Design Courses

Two groups of undergraduate college students enrolled in a computer science curriculum will be registered in seminar project courses. The students will primarily be in the upper junior semester and will have had similar courses in mathematics and computer programming including

computer fundamentals, BASIC, FORTRAN, assembly language, PL/1, list processing techniques, and systems software. The seminar project course is a four credit course and normally requires two semesters for its completion.

The two groups of students will be matched as well as possible in terms of scholastic performance and courses taken in computer science.

One group of students will attend a series of lecture/recitation classes covering techniques for, and approaches to, the design of quality software. The second group will attend a similar series of classes but the proposed software design methodology will be included in their course.

8.2 Projects

Upon completion of the classes, each group of students will be divided into chief programmer teams. Each team will design, implement, and test a software product designed to the same requirements. Then each team will be assigned a second project which is similar to the first project.

The teams will maintain comprehensive documentation of their designs and their activities to permit evaluation and comparison of their work and the resulting software products.

8.3 Comparison of Results

The software products and documentation of the two groups of students will be compared in order to answer the following questions:

(1) How does the software quality of the teams using the method compare with that of the teams not using the method?

(2) How does the uniformity of the quality of the teams in one class compare with that of the other class?

(3) How does the uniformity of the software produced by the teams using the method compare with that of the teams not using the method?

(4) How does the amount of reusable code differ between the two classes?

(5) How much effort was required by each class?

(6) How much effort was required by each class on each project?

(7) How comprehensive a testing job was each class able to perform?

8.4 Calibration and Validation of Software Quality Model

There are three elements which comprise the software quality model: the software quality factors together with their associated metrics, the software quality parameters, and the software quality index. These elements are related to each other and to a given software product as shown in Fig. 8.1.

The judgemental factors relating the software quality parameters to the software quality index reflect the opinions of the software users. The methods for static measurement of the software quality factors are incorporated in the definitions of the metrics. The regression coefficients which relate the software quality parameters to the software quality factors must be determined experimentally.

Calibration of the software quality model refers to the process of determining the regression coefficients. It is done by making static measurements of the software to evaluate the software quality factors and by making dynamic measurements (by testing the software) to evaluate the software quality parameters. A regression analysis is performed to determine the regression coefficients. Thayer, et al (29) discuss variations on standard regression analysis which are relevant to this application. Separate sets of coefficients will be developed for the two classes of students (those not using the proposed methodology and those that are using it) to determine whether the models are different or not. Calibration will be performed using the first project.

Validation refers to the process of checking that the software quality model is valid. This is done by comparing the predicted software quality parameters for the second project, obtained using the regression coefficients, with the corresponding measured values, obtained by dynamic measurement.

9.0 Conclusions

The proposed software design methodology presented in this paper provides the software designer with a structured approach to the critical, initial stages of software design, the functional decomposition of the software system. The methodology is based on widely accepted design concepts, principally the concept of nested virtual machines and the concept of matching the program structure to the data structure.

The methodology has not as yet been applied to the design of a substantial software product but plans to do so are complete and this project will commence shortly. It is expected that the methodology will be refined, augmented, and changed as a result of this experience.

The project for evaluating the proposed methodology involves a software

quality model which is essentially a simplified version of one developed by TRW. The model used in this work is limited to a three level tree structure for simplicity and because this seems adequate for the purposes of this project. The more extensive model is more appropriate for general purposes.

A number of the topics considered in this paper require substantially more work. The purpose of covering them in this paper is to provide an overview of the research to be conducted in this area. On the other hand, some important topics have been given very little attention for various reasons.

One very important area that has been omitted is the process of coding. This is relatively straightforward at all levels except the lowest because the instructions at each level are defined in order to implement the next higher level. The lowest level must be implemented using an existing language. Structured code should be used for this implementation. The decomposition of the program into virtual instructions which are simple elements should facilitate this work. It would be very useful to carry the design phase to a point from which structured code could be generated using a routine procedure. Continuing research in this area will address this problem.

ACKNOWLEDGEMENTS

The work reported in this paper was performed at the Rome Air Development Center while I was a participant in the 1976 USAF-ASEE Summer Faculty Research Program. I extend my thanks and commendations to Mr. J. Fred O'Brien, Jr., who did an excellent job in administering the program.

I want to express my special thanks to Mr. Rocco F. Iuorno, my research colleague at RADC, who contributed a great deal to the selection and definition of the problem and provided me with much of the material on the design of quality software.

In addition, thanks are due to the people at RADC who made my summer a very pleasant and productive one. Captain Sam Ruple and Messrs. Frank Sliwa and William Rzepka who directed me to much of the relevant literature. My gratitude also to Ms. Carmella DeProspero, Ms. Deborah Danti, and Mr. Stanley Borek for their typing of the report.

42

REFERENCES

1. D. Bates (Ed) Structured Programming, Infotech State of the Art Report, Berkshire England, 1976.

2. B. W. Boehm, J. R. Brown, H. Kaspar, M. Lipow, G. L. McLeod, and M. J. Merritt Characteristics of Software Quality TRW, Redondo Beach California, 1973.

3. D. Burns "A Bridge Between Structure and Reality" Structured Progamming 1976.

4. S. H. Caine and E. K. Gordon "PDL-A Tool for Software Design" National Computer Conference 1975.

5. P. J. Denning "A Hard Look at Structured Programming" Structured Programming 1976.

6. E. W. Dijkstra "Programming Methodologies: Their Objectives and Their Nature" Structured Programming 1976.

7. E. W. Dijkstra " The Structure of the @THE'-Multiprogramming System" Comm. of the ACM v 11, n 5, May 1968.

8. M. Dowson "The Evolution of Programs in Process-Structured Computing Systems" Structured Programming 1976.

9. J. Earley "Toward an Understanding of Data Structures" Comm. of the ACM v 14, n 10, Oct 1971.

10. H. J. Eiden and C.R. Moore User Requirements Language (URL) Users Manual Information Systems Technology Applications Office, Hanscom AFB, MA 01731, 1975.

11. R. J. Fleischer and J. E. Sullivan Concept of a Quality Control Facility Mitre Corp., Bedford Mass., 1976.

12. M. Hamilton and S. Zeldin "Higher Order Software-A Methodology for Defining Software" IEEE Trans on Software Eng v SE-2, n 1, Mar 1976.

13. IBM HIPO-A Design Aid and Documentation Technique.

14. IBM Structured Programming Series v 8.

15. M. A. Jackson "Data Structure as a Basis for Program Design" Structured Programming 1976.

16. T. E. Keirstead On the Feasibility of Software Certification Stanford Research Institute, Menlo Park California, 1975.

17. B. H. Liskov, "A Design Methodology for Reliable Software Systems" Fall Joint Computer Conference 1972.

18. B. H. Liskov "The Design of the Venus Operating System" Comm of the ACM v 15, n 3, Mar 1972.

19. B. H. Liskov and S. N. Zilles "Programming with Abstract Data Types" SIGPLAN Notices v 9, Apr 1974.

20. B. H. Liskov and S. N. Zilles "Specification Techniques for Data Abstraction" IEEE Trans on Software Eng v SE-1, n 1, Mar 1975.

21. R. C. McGee and L. Pizzarello Use of Rational Programming Techniques for the Development of Reliable Software Honeywell, Phoenix Arizona, 1976.

22. E. F. Miller Methodology for Comprehensive Software Testing General Research Corporation, Santa Barbara,CA., 1975.

23. D. L. Parnas "On the Design and Development of Program Families" IEEE Trans on Software Eng v SE-2, n 1, Mar 1976.

24. L. Presser and G. Rector " A Case Study in Disciplined Design" Structured Programming 1976.

25. L. Robinson Specification Techniques Stanford Research Institute, Menlo Park California, 1976.

26. L. Robinson and K. N. Levitt Proof Techniques for Hierarchically Structured Programs Stanford Research Institute, Menlo Park California, 1975.

27. L. Robinson, K. N. Levitt, P. G. Neumann, and A. R. Saxena A Formal Methodology for the Design of Operating System Software Stanford Research Institute, Menlo Park, California, 1975.

28. W. P. Stevens, G. J. Myers, and L. L. Constantine "Structured Design" IBM Sys J v 13, n 2, 1974.

29. T. A. Thayer, G. R. Craig, L. E. Frey, W. L. Hetrick, M. Lipow, E. C. Nelson, J. A. Yoxtheimer, and J. A. Whited Software Reliability Study TRW, Redondo Beach California, 1976.

30. M. Woodger "The Aims of Structured Programming" Structured Programming 1976.

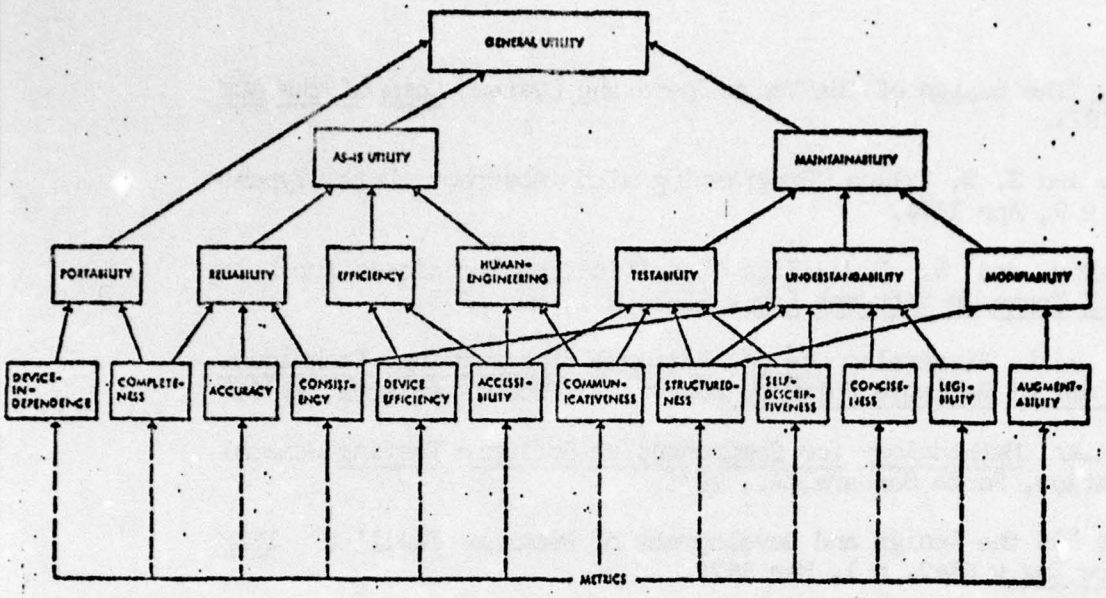


Figure 3.1 Characteristics Tree (2)

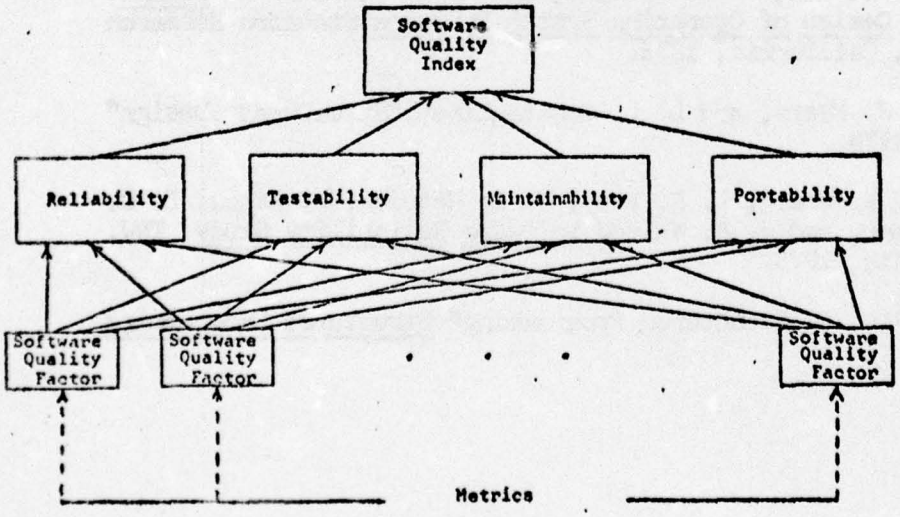


Figure 3.2 Software Quality Model

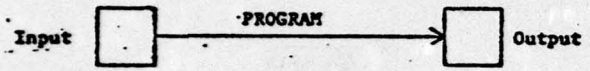


Figure 5.1 Top-level program development chart

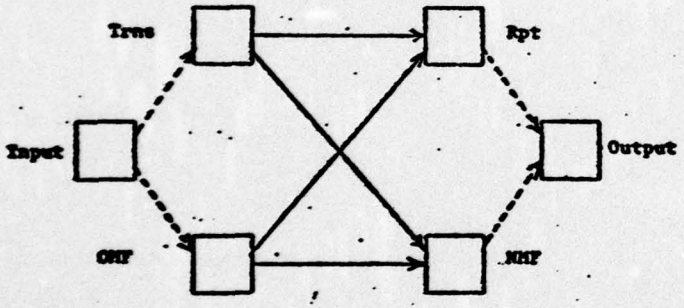


Figure 5.2 Second-level program development chart

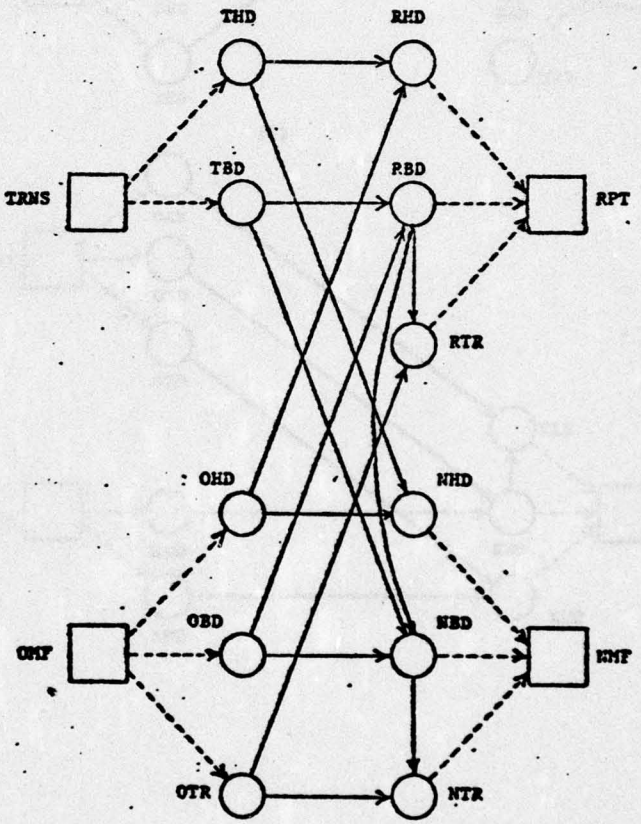


Figure 5.3 Third-level program development chart

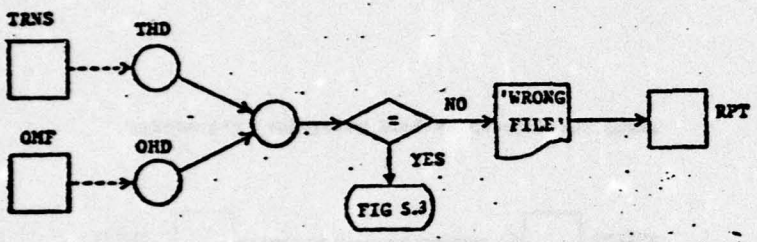
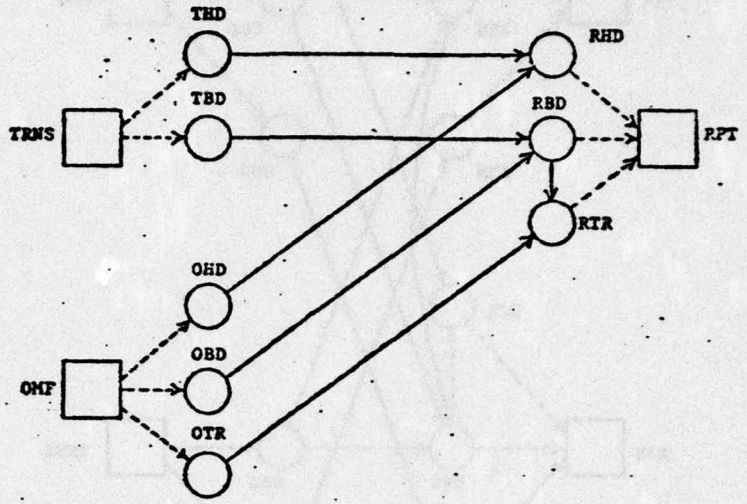


Figure 5.4 Program development chart for unusual situation



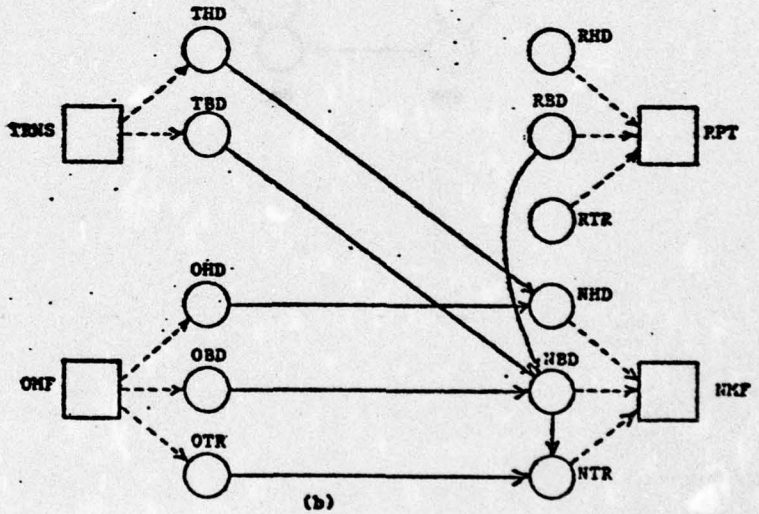


Figure 5.5 [illegible] program development chart [illegible]

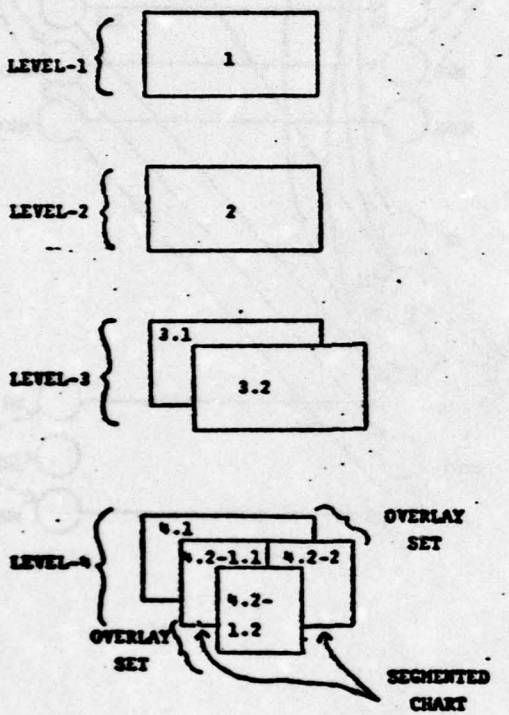


Figure 5.6 Program development chart levels, overlays, and segmentation

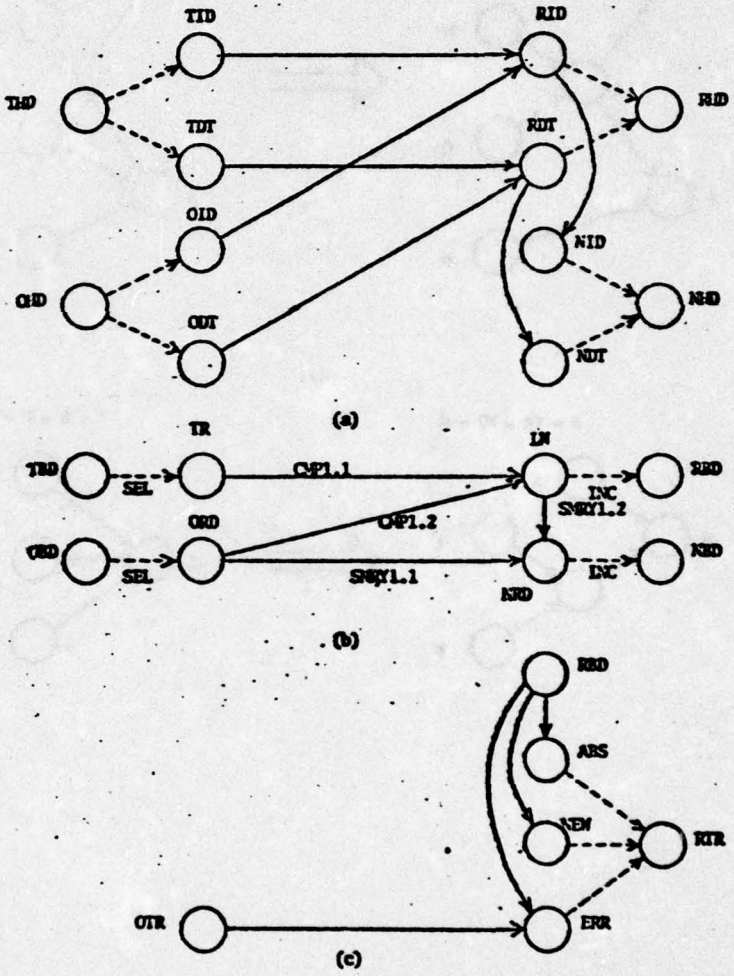


Figure 5.7 Fourth-level program development chart (segmented)

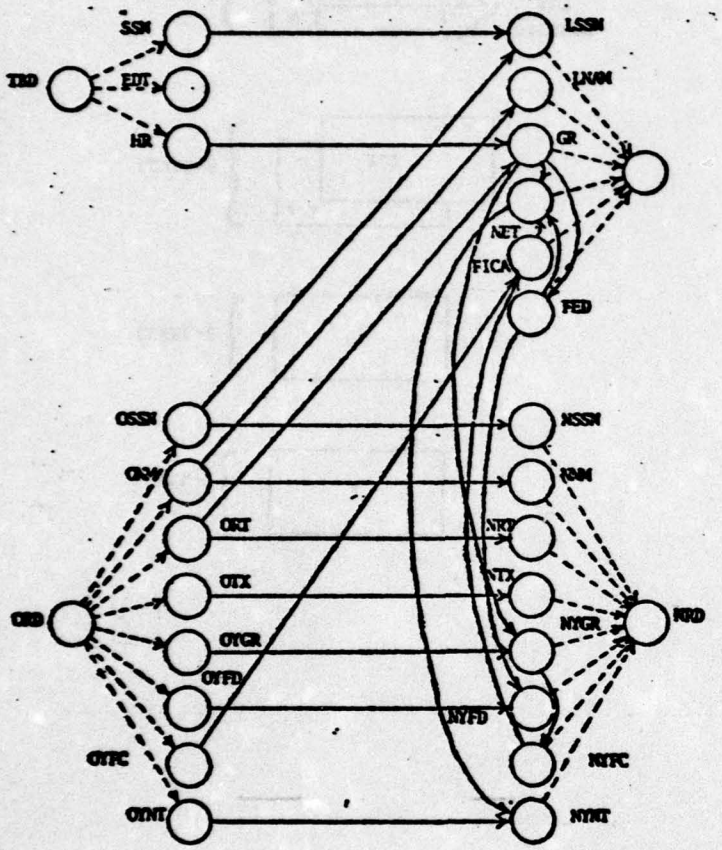


Figure 5.8 Fifth-level program development chart

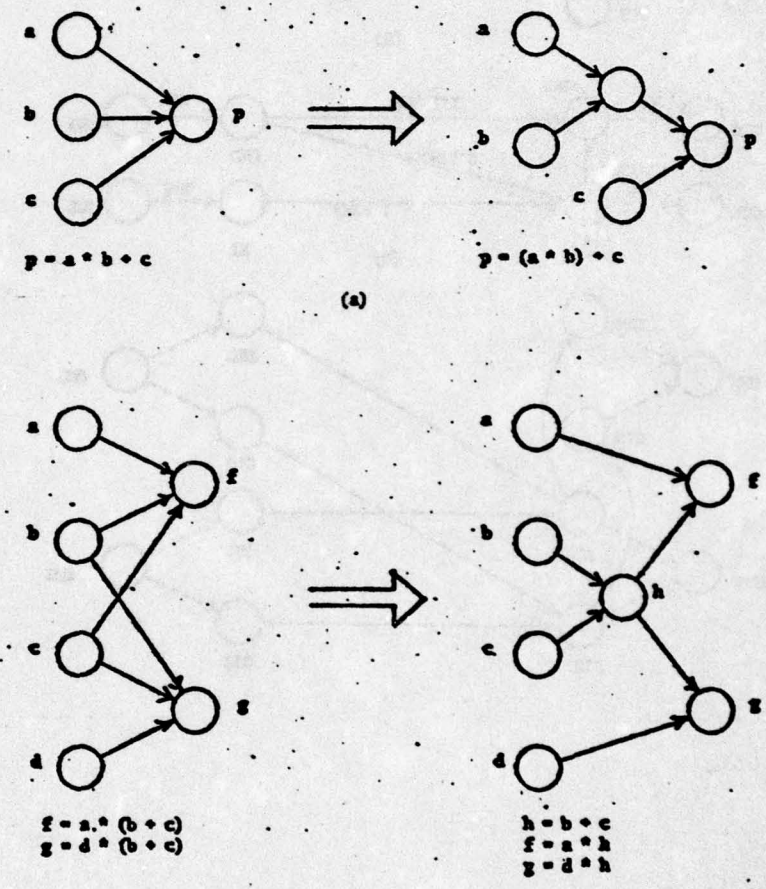


Figure 5.9 Introduction of intermediate nodes
(a) Based on algorithm;
(b) based on elimination of redundant computation

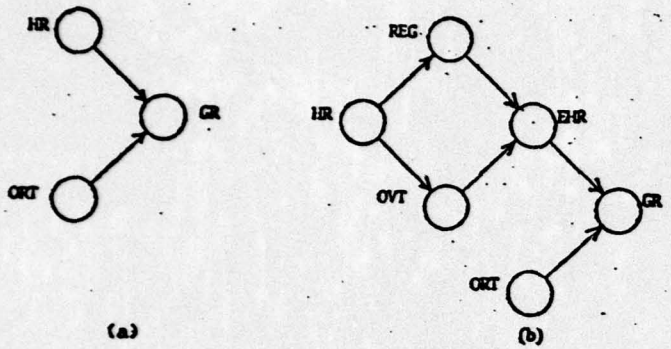


Figure 5.10 Introduction of intermediate nodes in gross salary computation for payroll example
(a) Program development chart segment before introduction of intermediate nodes; (b) refined program development chart segment obtained by introduction of intermediate nodes

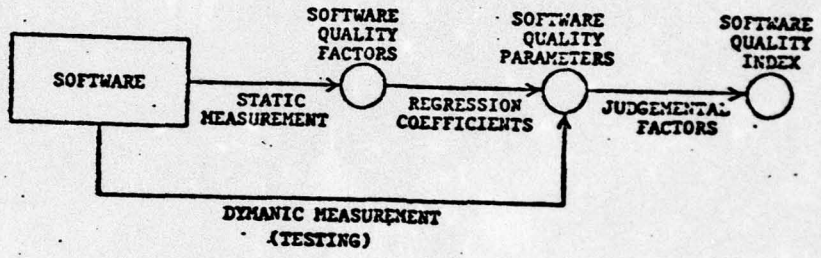


Figure 8.1 Relationships among elements of software quality model

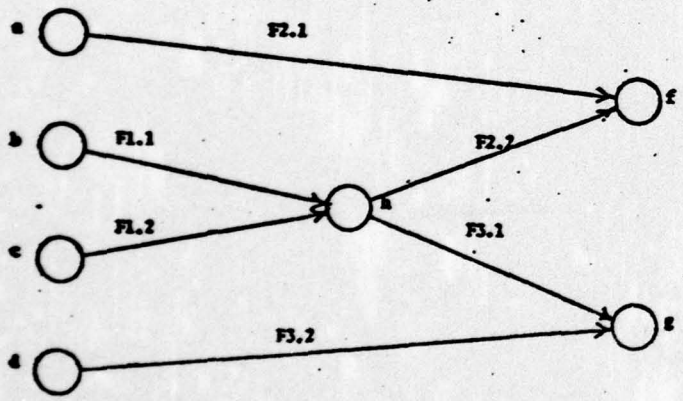


Figure 5.11 Functional grouping

1976 USAF-ASEE SUMMER FACULTY RESEARCH PROGRAM
sponsored by
THE AIR FORCE OFFICE OF SCIENTIFIC RESEARCH
conducted by
AUBURN UNIVERSITY AND OHIO STATE UNIVERSITY

PARTICIPANT'S FINAL REPORT

REAL-WORLD LIMITATIONS OF RADAR SIGNATURES FOR TARGET IDENTIFICATION

Prepared by:	Robert D. Strattan, Ph D.
Academic Rank:	Associate Professor
Department and University:	Division of Engineering Systems University of Tulsa
Assignment:	
(Air Force Base)	Griffiss AFB, NY
(Laboratory)	Rome Air Development Center
(Division)	Surveillance
(Branch)	Techniques
USAF Research Colleague:	Fred Demma
Date:	August 13, 1976
Contract No.:	F44620-75-C-0031

REAL-WORLD LIMITATIONS OF RADAR SIGNATURES FOR TARGET IDENTIFICATION

by
Robert D. Strattan

ABSTRACT

The feasibility of extracting characteristic features of aircraft targets from their radar signatures is within the state-of-art. The methods for classifying and identifying aircraft from their radar signatures have been examined. The objective has been to identify the limiting factors and propose analysis and simulation procedures for evaluating the performance in a real-world tactical environment.

Modern radar technology provides means of high resolution target description. Microwave radars using wide bandwidth, digitally coded waveforms, and coherent signal processing techniques can provide amplitude and phase signatures with resolution to a small part of an aircraft's overall dimensions. Synthetic aperture processing can provide a two-dimensional image of radar highlights.

Low frequency approaches using wavelengths in the Rayleigh and resonance regions have been proposed by researchers at Ohio State University. These methods offer several attractive feature extraction possibilities, such as natural resonance frequencies and three-dimensional images. The hardware implementation of these radars, perhaps operating at frequencies as low as 10 MHz, appears unattractive for the tactical case, however.

Pattern recognition concepts as well as radar sensor design enter into this problem. The probable approach would be to attempt a detailed classification of the target based upon its radar signature features and other measurable quantities, and then proceed to a judgmental identification: friend, foe or neutral, from the classification result and other information. The central pattern recognition problems are feature space definition and the source for training set data.

It is concluded that an imaging microwave radar appears most feasible for the tactical environment. The analysis of the performance degradation effects of the limiting factors on several design concepts using simulation techniques is recommended as the next step. Several associated research questions are raised.

TABLE OF CONTENTS

ABSTRACT

ACKNOWLEDGEMENTS

LIST OF FIGURES

LIST OF TABLES

I. OBJECTIVES

II. INTRODUCTION

III. RADAR PRINCIPLES

IV. IDENTIFICATION PRINCIPLES

V. MICROWAVE RADAR IDENTIFIERS

3 GHz Identify While Scanning Radar
18 GHz Dedicated Identification Radar

VI. OTHER RADAR IDENTIFICATION APPROACHES

VII. CONCLUSIONS AND RECOMMENDATIONS

VIII. REFERENCES

ACKNOWLEDGEMENTS

This work has been performed under the USAF-ASEE Summer Faculty Research Program sponsored by the Air Force Office of Scientific Research. The program was directed by J. Fred O'Brien, Jr., of Auburn University. The opportunity to participate in this program and the enthusiastic and helpful cooperation of the staff of Rome Air Development Center, and particularly my research colleague, Fred Demma, are gratefully appreciated.

LIST OF FIGURES

1. Coherent Radar System Block Diagram
2. Linear Systems Theory Analysis of Radar Signals
3. Probability Distributions for the Single Feature, 2 Class Example
4. General Concept of the Identification Process
5. 3 GHz Identify While Scan Radar Block Diagram
6. Image Acquisition Times Required for the 3 GHz Radar, 1 m Resolution, for a .5 km/sec (950 kts.) Target

LIST OF TABLES

1. General Requirements for the Microwave Radar Identifier
2. Design Parameters for 3 GHz Identify While Scanning Radar
3. Design Parameters for 18 GHz Dedicated Identification Radar

REAL-WORLD LIMITATIONS OF RADAR SIGNATURE FOR TARGET IDENTIFICATION

I. OBJECTIVES

The stated objective of this Summer Faculty Research Program has been:

> Investigate limitations posed by target RCS phenomena and dynamics, atmospheric effects, system degradation factors and limited observation times on the capability to identify aircraft and other targets through radar signatures and radar imaging using all weather, wideband modulation microwave radars.

This broad objective statement was narrowed to three specific objectives that were partially attainable during the ten week period. These objectives are:

1. Evaluate the applicability of classification methods discussed in the literature, with specific emphasis on the low frequency approach.

2. Identify and quantitatively describe the key elements required to simulate an identification radar with the RADSIM simulator systems.

3. Discuss aircraft radar signature and camouflage characteristics and their implication to the identification process.

The results of the efforts on the first two objectives are summarized in the body of this report. The security classification of the third objective precludes the inclusion of other than general comments.

II. INTRODUCTION

The immediate application conceived for this research would be on tactical surveillance radars, although results could have much broader applications. The mission of a tactical radar is to detect and locate the airborne targets within its surveillance zone, typically a circle of 370 km (200 nautical miles) radius. A third function is to identify the targets.

Ideally, the identification would include detailed information such as the aircraft's tail number, nation of registry, destination and mission. This is possible to achieve by communications with cooperative targets. However, in the military scenario, the uncooperative target during a battle must be contended with. Coded transponders have been used for years to provide active positive recognition of friendly targets. The transponder may fail to operate, or be

disabled intentionally to provide silent operation in an electronic warfare zone. The possibility of neutral as well as friend and foe aircraft in a zone further confuses the situation.

The question is then: Can passive identification of aircraft be realized from their radar signatures? Research on radar target classification techniques has existed for many years. Significant results have been achieved for space object identification. These developments and the feasibility of high resolution radar technology and digital data processing encourage one to answer yes to the question.

A closer look at the tactical problem brings out radar related problems other than the basic pattern recognition problem; waveform distortion due to atmospheric effects and ground reflections, clutter and ECM vulnerability are examples. Before these effects can be evaluated, a point design is needed. There are two basic approaches to the sensor design: low frequency or microwave. These approaches concentrate on different target features. Which is better?

The main goal of this work has been to explore the nature of each approach with the plan in mind of evaluating the approaches on a simulator. The task is considerable and certainly was not completed in the ten week period. However, the problem has been analyzed and hopefully restated in a more expedient and coherent manner. Many interesting areas for further research have been identified. The answers are not in hand, but the path to follow is much clearer.

The principles of radar systems theory and pattern recognition have been summarized in Section III and IV as they apply to the problem. The possibilities of a microwave radar implementation are then considered through the preliminary design of two radars in Section V. The alternatives, primarily in the form of the low frequency approach are considered in Section VI. Conclusions and recommendations for further research that will hopefully quantitatively answer some of the questions brought up here are presented in Section VII.

III. RADAR PRINCIPLES

The purpose of this section is to set down in a concise manner the basic principles and relationships needed for the analysis of coherent radar systems. The principles of pulse compression radars with coherent processors come from References 1, 2, and 3. The target scattering impulse analysis is described in Reference 4. The detailed analyses of a radar system are certainly more involved than indicated here. This is intended to identify only those primary factors controlling the performance of a radar as they effect the identification process.

The major elements of a coherent radar system are shown in the block diagram of Figure 1. The methods of linear systems theory will be used in the discussion and analysis of the radar signal flow. The modulator and coherent source generate a waveform (e_t) that is broadcast through space by the

transmitter and antenna. The target scatters a portion (e_s) of the incident signal (e_i) back to the antenna and receiver. The tracking matched filter and coherent detector process the received waveform (e_r) to produce a range-time intensity and phase (RTI, Ø) profile. If the resolution is sufficient, detailed information about the location of the target's scattering centers is revealed.

A two-dimensional image of the target may be formed if the target's aspect angle (θ) changes. The RTI, Ø profiles are retained in memory over an integration time that assures sufficient target rotation. A Fourier transform with respect to aspect angle (or integration time) yields a cross range image of the radar highlights of the target.

The radiated signals are delayed in time and diminished by the inverse range law of propagation. The antenna has specific polarization properties which determine the incident (p_i) and scattered (p_s) polarizations of interest. The incident wave is scattered in all directions, but only that backscattered to the receiver is of interest here. The magnitude of the backscattered signal is usually expressed as the radar cross section (σ). σ is a strong function of many parameters; e.g., frequency, polarizations and aspect angle as well as the size, shape and material composition of the target. More useful information is contained in the impulse response of the scatterer, however.

The implementation of a high resolution matched filter and coherent processing implies that the target is tracked in range and doppler shift. The range tracking requires selecting a short range window for high resolution processing. The doppler shift resulting from the target's radial velocity must be offset in the receiver. Relative motion between the radar and target, and time varying scattering mechanisms are non-linear effects not accommodated by linear system theory. They do provide useful auxiliary inputs to the identification process, however.

The nature of the radar signals encountered in the application of linear systems theory is shown in Figure 2. The problem is essentially one of designing a waveform that will reveal the target's unique characteristics while suppressing interference from other targets. The target may be thought of as a filter in a transmission channel and may be described in terms of either its frequency or time domain properties.

The transmitted waveform may be described as a staggered repetition rate phase encoded pulse burst. Each pulse of duration, T_b, is made up of subpulses of duration, T_a. The subpulse phase (or frequency) is modulated according to an optimumly selected code. The pulse to pulse interval is also varied according to an optimumly selected code with an average interval of T_c. The total duration of the waveform is T_d. The frequency domain spectrum will have a bandwidth of $B \approx 1/T_a$ centered at the carrier frequency f_c.

The receiver is described in terms of its matched filter ambiguity function $\psi(\tau,\nu)$, where τ is time delay and ν is doppler shift. The ambiguity function ψ describes the time and doppler resolution, sidelobes and ambiguity characteristics of the optimum processing scheme for the transmitted waveform. The time-frequency autocorrelation of the transmitted waveform

$$\chi(\tau, \nu) = \int_{-\infty}^{+\infty} e_t(t) e_t^*(t + \tau)\, e^{-j2\pi\nu t}\, dt$$

is related to the ambiguity function by

$$\psi(\tau, \nu) = \left| \chi(\tau, \nu) \right|^2$$

A characteristic "bed of spikes" ambiguity function is shown on the τ, ν plane in Figure 2. A large value of ψ implies a strong output response while a low value implies strong rejection of a target's response at those coordinates. The origin is considered to be located at the desired target's range and velocity coordinates by the tracking functions of the filter.

The response to a motionless point target, i.e., impulse response is an impulse, is $e_o = \chi(\tau,o)$. Therefore, the range time (τ) resolving capability is the width of the peak in the τ direction, a value given approximately by $\Delta\tau_r \approx 1/B$. The ability to resolve targets of differing velocity but at the same range is given by the ν axis peak width $\Delta\nu_r \approx 1/T_D$. The τ, ν variables are related to range and radial velocity by

$$\tau = \frac{2y}{c} \qquad \nu = \frac{2\dot{y}}{\lambda} = \frac{2f_c\dot{y}}{c} \qquad c \approx 3 \times 10^8 \text{ m/sec.}$$

The widths of the central peak of ψ and the sidelobe level surrounding it are of the utmost importance in determining the ability to resolve scattering centers on a target. However, a surveillance radar must also have the ability to reject other targets and clutter over a wide range of τ and ν. The range ambiguity peaks at $\tau = \pm nT_D$ resulting from repeating the waveform and doppler ambiguity peaks at $\nu = \pm n/T_c$ resulting from the pulse repetition rate are also of concern. The range ambiguity at $\tau = \pm nT_c$ has been suppressed by staggering the repetition rate with T_c being the average interval. The code length required for the PRF staggering is $N_r = T_d/T_c$. The separation between pulses must be sufficient to prevent overlapping. This condition is met for $4T_d \geq N_r^{5/2} T_b$. The maximum unambiguous range of the radar is determined by the burst length, $R_{max} = \frac{cT_d}{2}$, and the first doppler ambiguity should be sufficiently removed to correspond to double the velocity of the fastest target to eliminate foldover, or

$$\frac{1}{T_c} \geq \frac{4f\dot{y}_{max}}{c}$$

The elementary form of the radar range equation, neglecting losses, is

$$P_r = \frac{P_T G^2 \lambda^2 \sigma}{(4\pi)^3 R^4}$$

where P_r is the received power, P_T is the transmitter power, $\lambda = c/f_c$ is the wavelength, σ is the radar cross section of the target, R is the range, and $G \approx 4.1 \times 10^4/\theta_B \phi_B$ is the antenna gain with θ_B and ϕ_B the azimuth and elevation beamwidth in degrees. The detected signal to noise ratio for an integrating pulse compression radar is given by

$$\frac{S}{N} = \frac{P_r N_r N_p}{kTB}$$

where $N_r = T_d/T_c$ is the number of integrated pulses in the waveform, $N_p = T_b/T_a$ is the pulse compression ratio, kT is Boltzman's constant times the noise temperature ($kT \approx 4 \times 10^{-21} W/Hz$), and $B \approx 1/T_a$ is the bandwidth.

The scattering properties of the target may be described by its frequency domain scattering length function G(w) or its time domain impulse response g(t). They are a Fourier transform pair according to linear system theory. The radar cross section is related by $\sigma = |G(w)|^2$. These functions are related to $F_I(t - n/c)$ and F(w) of Reference 4 by the constant $\sqrt{\pi}c$. Geometrical optics specular scattering characteristic of short wavelengths may be associated with the impulses of g(t) and the cyclic interference pattern of G(w) at high frequencies for multiple scattering center targets. The ringing in the g(t) and resonance peaks in G(w) are associated with creeping wave and resonance mode responses most apparent when scatterer dimensions are comparable to the wavelength. The low order moments of g(t) and the low frequency asymptotic behavior of G(w) are related to Rayleigh scattering, primarily controlled by target volume at wavelengths much larger than the target dimensions. These functions are shown for a simple two sphere target in Figure 2. The high frequency approximation of g(t) is simply the impulses corresponding to the geometrical optics or other concentrated short wavelength dominant scattering centers.

The output of the matched filter is a modulated carrier or intermediate frequency sinusoid that must be synchronously detected to retain phase as well as amplitude information. This information is usually output in terms of the in-phase and quadrature signals defined by

$$e_o = e_I(\tau) \cos 2\pi f_c t + e_Q(\tau) \sin 2\pi f_c t$$

The variation of e_I and e_Q with range time τ locates the scattering centers in the y or slant range direction. If the target is rotated slightly, the phase of the scattering centers will change. If the range time intensity and phase (RTI, Q) profiles of e_I and e_Q are retained for equally spaced intervals over a rotation angle of $\Delta\theta_m$ and a Fourier transform taken across the angular variable, that variable is transformed to cross range distance (x). As discussed in References 5, 6 and 7, the cross range resolution is $\Delta x_r \approx \lambda/2\Delta\theta_m$ and the number of profiles integrated should be at least equal to the ratio of the maximum cross range dimension of the target to Δx_r. The transforms should be performed at slant range intervals no larger than the range resolution $\Delta y_r \approx c/2B$. The angular interval needed for the cross range scale factor may be determined approximately from flight path tracking data.

The accurate processing of this synthetic aperture image requires phase coherence among all of the RTI, Ø profiles. This would normally require continuous tracking over the full integration time, an excessively long period for a scanning surveillance radar. Although no confirmation of validity has been uncovered, it seems reasonable that an intense and stable scattering center could be selected as a reference rotation center and scan to scan RTI, Ø profiles referenced to this point as the zero phase coordinate for all scans. This method would also compensate for range tracking errors and jitter.

IV. IDENTIFICATION PRINCIPLES

The identification process is essentially the classification problem from pattern recognition theory: given the values of the feature coordinates of an unknown, assign it to the class it most closely resembles. There are many procedural approaches to this classification process, and the results are dependent upon selection of feature coordinates and their relationship to the discrimination among classes. A simple classification problem is presented as an example in order to explain some basic terminology and concepts. The characteristics of the aircraft identification by radar are discussed in some detail. Only the most elemental aspects are discussed here; the detailed investigation of the problem is beyond the scope of this project.

Bayes decision theory is a fundamental statistical approach to the classification problem, (Reference 8). The Bayes approach yields the lowest possible error rate but requires the a priori knowledge of the probability distributions. The nearest neighbor method (References 8 and 9) requires no knowledge of the probabilities, but may have an error rate as great as twice the Bayes error rate. The ease of implementation of the nearest neighbor approach may compensate for the reduced accuracy. These methods are illustrated in the following example.

Consider a two class, single feature problem with the probability distributions shown in Figure 3. The spread of the x values about the central value of a class could be due to noise or fluctuations caused by physical phenomena or measurement imperfections. The problem is: given a value of x, determine

the class, w_1 or w_2. There is no question that $0 < x < 1$ corresponds to w_1 and $2 < x < 3$ corresponds to w_2, but a non-deterministic decision must be made for $1 < x < 2$, with some chance for error.

Bayes decision theory states that the lowest possible error rate occurs when

$$p(x_b|w_1)P(w_1) = p(x_b|w_2)P(w_2)$$

and

$$\text{class} = w_1 \text{ if } x < x_b$$

$$= w_2 \text{ if } x > x_b$$

for the example $x_b = 1.667$ and the error rate is 11.11 percent. An error occurs for $x < x_b$ when the class is w_2, or $x > x_b$ when the class is w_1.

The nearest neighbor method assigns the unknown to the class having an element of its training set closest to the unknown's feature value. If $x_1 = 1$ and $x_2 = 2$ are taken as the training set, values of $x < 1.5$ are closest to x_1 and $x > 1.5$ are closest to x_2 with the result of

$$\text{class} = w_1 \text{ if } x < 1.5$$

$$= w_2 \text{ if } x > 1.5$$

The resulting error rate is 20.8 percent.

If larger training sets are considered, in this case distributed uniformly according to the assumed probabilities, the nearest neighbor results are:

3 element set: $x_1 = .707$ and 1.293 $\quad x_2 = 2.0$

$$\text{class} = w_1 \text{ if } x < 1.647$$

$$= w_2 \text{ if } x > 1.647$$

error rate = 11.13 percent

12.

9 element set: x_1 = .408, .707, .913, 1.087, 1.293 and 1.592

x_2 = 1.577, 2.0 and 2.423

class = w_1 if $x < 1.435$ or $1.585 < x < 1.796$

w_2 if $1.435 < x < 1.585$ or $x > 1.796$

error rate = 18.60 percent

This method may be extended to the Kth nearest neighbor method. The unknown is assigned to the class of the largest number of the K nearest neighbors to the unknown's feature value. This method reduces to the example above for K = 1. If the method is applied to the 9 element training set above, the results are:

K = 3 class = w_1 if $x < 1.647$

= w_2 if $x > 1.647$

error rate = 11.13 percent

K = 5 class = w_1 if $x < 1.755$

= w_2 if $x > 1.755$

error rate = 11.50 percent

This simple example demonstrates several basic principles. No method may have a lower error rate than the Bayes method, but the easily implemented nearest neighbor method's error rate does not exceed twice the Bayes rate and approaches it in some cases. The a priori probabilities required by the Bayes method are usually unknown, while the nearest neighbor training set is a very direct method of describing feature data. The error rate of the nearest neighbor method is dependent upon the training set as well as the sophistication of the decision process.

Most classification schemes are variations of these basic methods. The complexity and difficulty of implementation increases rapidly as the number of classes and dimensions of the feature vectors increase. The selection of the feature coordinates and the functions for mapping raw data to feature space become central problems to optimizing the classifier. Iterations of physical

considerations and empirical data manipulation using facilities such as the Waveform Processing System (WPS) and On-Line Pattern Analysis and Recognition System (OLPARS) at RADC (Reference 10) are usually required to develop a workable algorithm.

The selection of feature space must rely upon the physics of the sensor-target interaction. Features accentuating unique features that are readily measured are desired. Size, planform arrangement, flight envelope extremes and propulsion characteristics are favored features for aircraft at microwave frequencies. Two-dimensional images provide size and planform arrangement information. Some information may be extracted from a one-dimensional profile (RTI) at the near nose and tail aspects where two-dimensional images are difficult to obtain. Propulsion modulation data should be most available at nose and tail aspects, complimenting the two-dimensional image's broadside utility. Aspect angle, speed, altitude and other flight parameters are extractable from general tracking loop functions.

A general concept of the identification problem is shown in Figure 4. The sensor determines certain signature characteristics of the unknown, subject to corruption by natural and hostile noise and distortion sources. The classifier compares the unknown's features with those of the training sets in a reference file. The order of the classification problem is so large that some form of sequential decision tree order reduction will be necessary. First sorting by target overall dimension, then engine count, then aspect angle, etc., could quickly reduce the problem to several small manageable problems. The output of the classifier is a detailed description of the target, e.g., MIG-23C with external stores, heading 235 degrees at Mach 1.5, 2 km altitude, confidence level 95 percent. The identifier then correlates this detailed classification with other information, e.g., air order of battle, geographical origin of track, other inputs such as ELINT, optical and IR reports, and makes a judgment on the identification: friend, foe or neutral. The judgment based on the non-radar features is essential as one aircraft type with indistinguishable radar features could conceivably belong to all three identification classes with the proliferation of international arms sales. However, the radar measured features will be one of the essential identification inputs.

The source of the training sets for the classifier's reference file is a matter for careful attention. There are four basic sources:

1. Measurements on actual aircraft by a reference facility.
2. Measurements on scale models by a reference facility.
3. Calculated features using a math model.
4. Measurements acquired and assimilated on actual classified targets by the sensor system while in operation.

Sources 1 and 2 are probably most feasible for initial operation while source 4 could be used to continually update and adaptatively sharpen performance during

routine surveillance duty. The complexity of the optics region scattering from targets as large and complex as aircraft, particularly when forward and aft aspect scattering is dominated by cavity and sensor reflections not tractable to calculation, tends to discourage the use of source 3.

V. MICROWAVE RADAR IDENTIFIERS

Two general concepts of a radar identifier appear to be emerging from the technical community. One may be described as the "low frequency approach" being researched at Ohio State University and discussed in Section VI. The other is the "microwave approach" that is essentially the radar technologist's response to applying modern radar theory to the identification problem (References 11 - 16). From the pattern recognition viewpoint, it concentrates on the target's fine structure at the expense of gross feature characteristics. However, from the hardware implementation and multiple function tactical operation viewpoint, it represents an extention of current practice rather than the radical departure required by the alternate.

An example is used to illustrate some of the design considerations of a microwave identifier. A set of general specifications are assumed and two alternate designs are presented. Both designs seem to be feasible and within current state-of-art. Obviously, a much more detailed analysis would be needed to optimize the many tradeoffs and evaluate performance. Much of this analysis could be done by simulation on RADSIM, WPS and OLPARS (References 10 and 17). Some microwave scattering properties of aircraft are discussed.

The assumed general radar system specifications are listed in Table 1. The basic requirements are that the radar perform the traditional tactical surveillance radar functions of detection and location as well as the added function of identification. The ability to form a two-dimensional image of the target is taken as the primary identification requirement. The implications of these requirements and other characteristics of the system will be discussed as the designs are developed. The radar principles outlined in Section III are the basis for calculating the design parameter values.

3 GHz IDENTIFY WHILE SCANNING RADAR

The first design assumes that 360 degrees surveillance of a 370 km radius area must be performed by the radar while the identification is occurring. The design parameters are listed in Table 2. The microwave frequency of 3 GHz was selected arbitrarily.

The waveform length is set by R_{max} and the average rate of the staggered pulse interval is set by the maximum target velocity. The stagger interval code length is 100 units, limiting the pulse width to 0.1 usec to prevent overlapping of pulses. The range resolution sets the subpulse width, resulting in a 15-unit pulse compression code length and a bandwidth of 150 MHz.

As the antenna beam scans past the target, several hits per waveform interval are desired. The scan to scan interval needs to be properly spaced to acquire

the 100 RTI, Ø profiles over a reasonable period of time and target rotation angle. The beam must be narrow enough to give good location information and suppress clutter and jamming interference. A possible rotating antenna design would have four parabolic reflectors arranged on a square with four narrow 2 degree beams at 90 degrees azimuth intervals. At 33 rpm rotation rate, each target would be scanned 2.2 times per second, requiring 45 seconds to acquire the 100 RTI, Ø profiles necessary for an image. Each beam would dwell on the target for 10 msec, producing four hits per beam with subsequent averaging to improve the quality of the resulting RTI, Ø profiles. The doppler resolution of one waveform period is 400 Hz, corresponding to 20 m/sec (40 kts). The velocity resolution could be reduced by a factor of four by integrating over the full beam dwell time of 10 msec.

Neglecting losses, but assuming no integrating gain for the multiple hits per beam, the integration over the 100 pulses with a pulse compression ratio of 15 requires a peak transmitted power of 25 MW and an average power of 100 kW per beam.

The block diagram of the radar is shown in Figure 5. Separate transmitters and receivers are provided for each of the four antenna beams. A separate tracking matched filter is provided for each target assigned to the identifier. All receivers would feed the detection and target location track functions of the radar. The image processing, classifying and identifying functions are software and would probably be in a multiprocessing mode.

The pulse interval staggering code and intrapulse phase codes modulate the coherent 3 GHz source. The pulse train is radiated, reflected, and fed to the receiver through the rotating antenna. Detection and tracking data are acquired and displayed in conventional manners. The range and azimuth coordinates of a target to be identified are assigned to a tracking memory. This memory also determines and remembers the doppler offset required for the target. The target's modulation spectral data is filtered out for separate analysis and classification.

The main airframe doppler line is processed by the matched filter to produce the in phase and quadrature high resolution range-time (RTI, Ø) profiles of the target. An interval of 100 m (.67 usec) of RTI, Ø data with a resolution of 1 m (6.7 nsec) is recorded in memory after averaging over the four hits of that beam scan. Another beam scans the target 450 msec later and another RTI, Ø profile is recorded. After 45 seconds, 100 profiles have been recorded.

An intense and stable peak in the RTI, Ø profiles is identified and used as a phase reference point to establish a scan to scan coherence for the phase of the RTI, Ø profiles. This becomes a separate pattern recognition and processing problem, but appears feasible.

A Fast Fourier Transform (FFT) processor then transforms the aspect angle (sequential profiles number) coordinate into cross range dimension along each slant range cell. If the target's aspect angle changed 2.9 degrees at a constant rate, a cross range resolution of 1 m results.

The two-dimensional image, along with other data extracted from the radar signals such as aspect angle, target modulation features, flight profile data, etc., are fed to the classifier. The classifier proceeds through a logical sequence of narrowing the range of possible classes. Length and width, engine count, rotary or fixed wing, speed and other readily determined features could reduce the dimension of the problem considerably.

The most detailed classification would then be made on the basis of matching images at the predetermined aspect angle. The classifier then passes its detailed classification to the identifier. The identifier assimilates the classification with all other pertinent information and makes a judgment on the identity: friend, foe or neutral. The identifier would probably require human involvement to handle the judgment factors, but all other functions could be automatic and in real time.

The imaging process requires an aspect angle change to develop cross range images. Figure 6 shows the contours of constant required acquisition time for 1 m resolution if the target is traveling at .5 km/sec (950 kts). The target is assumed to fly a straight path at a fixed offset range. The time is least about broadside and at close range. There is little aspect change near nose and tail aspects for an overflight. The image acquisition times will be large, and cross range resolution poor at near nose and tail aspects for long ranges. These cases should produce the best quality propulsion modulation data, complimenting the poor quality image data. Images will be of their best quality about broadside where propulsion modulation is not available.

18 GHz DEDICATED IDENTIFICATION RADAR

The image acquisition time can be reduced by decreasing the wavelength for a given resolution. Therefore, a higher frequency radar could be advantageous. Table 3 presents the design parameters for an 18 GHz identifying radar. This radar is not required to perform standard surveillance functions, but would be collocated with the surveillance radar. An electronically steerable phased array antenna is sequentially switched to up to 10 targets within a sector, but track is maintained on each target.

The waveform length is 2.5 msec to provide the full 370 km maximum range. The pulse repetition rate should be 240 kHz to assure the full unambiguous velocity range; however, a pulse stagger code of 600 units would be needed, requiring a pulse width of only 1.1 nsec to prevent pulse overlapping. Rather than operate with such a large bandwidth, an option for a 6.7 nsec pulse and a 120 kHz average PRF is selected. The doppler ambiguity at ±1 km/sec (2000 kts) should not be an excessive problem for a tracking radar. The short pulse does not require subpulse modulation.

The beam dwells on the target for at least 10 msec each scan cycle to assure four hits. The scan cycles could vary according to conditions; but on a 10 target sequence, 10 RTI, Ø profiles would be acquired per second on each target. An image could then be formed in 10 seconds. The required acquisition times of Figure 6 are divided by six for the 18 GHz case. Classification and identification proceed as before. A velocity resolution of 3 m/sec is achieved from one waveform period, or .75 m/sec (1.5 kts) for a full beam dwell period.

These radars are certainly more complex than existing tactical radars. However, they appear to be within current state-of-art and could offer improved surveillance performance and ECCM capability in addition to providing the identification function. The designs are not necessarily optimized. In depth analysis of performance factors and operational requirements would be needed to firm up a recommended design. They do provide a basis for comparison of two approaches. One would be to increase the complexity of a scanning surveillance radar to add the identification capability. The other approach is to provide dedicated auxiliary tracking radars to provide the identification function. Either approach could be viable; the selection would require a detailed systems analysis. Another alternative, which would probably take the form of an auxiliary radar, is discussed in Section VI.

The microwave region scattering properties of aircraft targets need to be discussed in terms of classification features. A great deal of effort has been expended on the analysis of scattering (References 4, 5, 18 - 23). Much understanding of the scattering mechanisms has resulted, but the ability to reliably predict the radar cross section (RCS) of an aircraft at microwave frequencies is still an elusive art (Krueger and Mentzer, Reference 5). Experimental methods prevail for determining and disecting the short wavelength RCS of aircraft. Most of the comments that follow are based upon recollections of 15 years of experience in RCS signature analysis and reduction research. Only generalities can be stated, as specifics become classified. Reference 23 presents detailed discussion of many of these topics.

The microwave scattering from aircraft is aspect dependent. A region within ±30 degrees of the roll plane, the plane perpendicular to the direction of flight, is usually dominated by specular reflections from the fuselage, wing and empennage surfaces. These are relatively easily and accurately calculated from geometrical optics theory. However, the remainder of the aspect sphere is dominated by combinations of scatterers that are not easily modeled.

Returns from the engine inlet cavities, nose radar compartment, cockpit and other sensor bays usually dominate forward aspects. Exhaust nozzle cavities generally dominate tail aspects. Each of these scatterers presents peculiar scattering situations. The incident energy enters the inlet ducts, experiences multiple reflections, scattering by the rotating engine compressor or fan blades, more reflections and reradiation. The nose radar compartment, visible through the radar transparent radome, is a difuse arrangement of scattering objects, sometimes dominated by a large scanning antenna capable of reflecting very intense signals. Other breaks in the streamlined conducting skin, such as the cockpit, armament or sensor bays, protruding sensors, cooling air ducts, etc., become scattering centers. General planform silhouette features, such as wing leading and trailing edges, fuselage or nacelle edges or empennage surfaces will not contribute significantly to the reflections unless they are viewed at a direction perpendicular to an edge or surface.

Scattering from control surface discontinuities, surface undulations and other minor scattering centers exist but are usually at too low a level to be of significance in a first order classification problem.

Although the dominant scatterers are difficult to theoretically analyze, they are distinctive features of an aircraft. The locations of engines, cockpit and sensor bays could be more revealing than a silhouette. It could permit sub-classification within a type of aircraft. The sensor bay distribution of a reconnaissance version should be distinctive from that of an attack version of the same aircraft type. There are also some possibilities that methods of scene analysis could extract these differences without cell by cell matching to reference images.

The ability to suppress and camouflage these scattering centers is an obvious countermeasure. Techniques for effecting this countermeasure are discussed in Reference 23.

A conceptual sketch of a radar image is shown in Figure 5. The two engine ducts, nose radar compartment, and cockpit are assumed to be the dominant scatterers. Minor reflections from the starboard wing leading edge, stabilizer, and fuselage-wing join could also exist at this aspect angle. The major feature of the image would be the relative intensity and spacing of the engine, nose and cockpit spots, along with some length, wingspan and wing sweep information. The aspect angle would be known approximately from the ground track vector.

While microwave radar signature of aircraft are very difficult to calculate from the mathematical model approach, the estimating of the general features of a two-dimensional radar image is conceivable. After gaining some experience, an analyst should be able to identify the location and image qualities of an aircraft from only a few pages of drawings and specifications. The alternative is to measure the high resolution signature of the aircraft and extract the features to be used in the classifier. Reasonable success with the extraction of features such as number of peaks (target complexity), target length, peak RCS and polarization sensitivity from short pulse backscatter range measurements of space objects is reported in Reference 16. The more traditional approach of aircraft signature math modeling (Reference 18) has been extended to the high resolution case and even to imaging in Reference 16. The major deficiency of this work is the difficulty of modeling the non-specular scattering centers. Additional research directed toward the scene analysis and prediction of two-dimensional radar images of aircraft could prove productive both in the classifier design and training set generation problems. Experimental validation would be an essential phase of this research.

TABLE 1. General Requirements for the Microwave Radar Identifier

Maximum Unambiguous Range	370 km (200 n. mile)
Maximum Unambiguous Velocity	±1 km/sec (±2000 kts)
Range Resolution	1 m (3 ft.)
Velocity Resolution	5 m/sec (10 kts.)
Image Size and Resolution	100 x 100 m with 1 x 1 m res.
Sensitivity	13 dB S/N vs. 0.1 m^2 @ max. R

TABLE 2. Design Parameters for 3 GHz Identify While Scanning Radar

Waveform length (T_d)	2.5 msec (400 Hz)
Pulse repetition interval, average (T_c)	25 usec (40 kHz)
Pulse repetition code length (N_r)	100
Pulse Width (T_b)	.1 usec
Subpulse width (T_a)	6.7 nsec
Bandwidth (B)	150 MHz
Pulse compression code length (N_p)	15
Antenna	Four 2° az. by 6° el. parabolic reflectors at 90° az. intervals (3.5m square) rotating at 33 rpm. 35 dB gain.
Dwell time per beam	10 msec
Scan Rate	2.2 scans/sec
Transmitter power (per beam)	Peak: 25 MW Average: 100 kW

TABLE 3. Design Parameters for 18 GHz Dedicated Identification Radar

Waveform length (T_d)	2.5 msec (400 Hz)
Pulse repetition interval, average (T_c)	8.3 usec (120 kHz)
Pulse repetition code length (N_r)	300
Pulse width (T_b)	6.7 usec
Subpulse width (T_a)	6.7 usec
Bandwidth (B)	150 MHz
Pulse compression code length	1
Antenna	1° pencil beam electronically scanned within 30° sector, sector mechanically scanned 10 targets assigned per antenna.
Dwell time per scan	10 msec
Scan rate	10 scans/sec
Transmitter power	Peak: 32 MW Average: 26 kW

VI. OTHER RADAR IDENTIFICATION APPROACHES

Most of the open literature on radar target identification concentrates on the low frequency approach. This approach has evolved from research at Ohio State and has been applied to the identification problem in three distinct feature extraction modes. The approaches have been demonstrated in laboratory environments with small class ranges. The major disadvantage of the approach is in hardware implementation of a system suitable for tactical operation. This approach is summarized and some other related topics are discussed in this section.

The basis for much of the low frequency theory is the impulse response or time domain concept of scattering documented in Reference 4. The frequency domain emphasis is on the upper Rayleigh and lower resonance regions where the wavelength ranges from about four times to 1/2 of the characteristic target dimension. The scattering is strongly dependent upon target features such as volume, shape and aspect ratios at these frequencies.

Ksienski, Lin and White present a straightforward approach to target identification from low frequency scattering information in Reference 24. The magnitude and phase of the reflected signal at harmonically related frequencies (f_1, $2f_1$,

$3f_1$, --- nf_1) define the feature space used. Linear discriminants could be found for simple shapes, but a more robust classification algorithm was needed for aircraft. A nearest neighbor method with a priori aspect angle interval information was shown to be effective for a four class aircraft classification using feature vectors of 4 to 16 components. Although classification was achieved in low noise cases with as few as two frequencies, reliable classification for larger class ranges and noisy environments would require more frequencies and multiple polarization modes. Frequencies as low as 10 MHz would be required for aircraft targets. An advantage of the low frequency approach is that training set feature may be calculated from mathematical models (Reference 22) rather than measured data.

A time domain imaging approach has been developed by Young (References 25 - 27). The ramp response, whose second derivative is the impulse response, has been shown to have a strong similarity to the area profile of a target. The area profile is the physical cross sectional area of target in a plane perpendicular to the direction of incidence as a function of range, or range-time, in the incidence direction. Physical optics predict the exact correlation between the area profile and ramp response for the illuminated portion of the target. It has been experimentally observed that the relation extends into the shadow region with reasonable accuracy.

The knowledge of the ramp response defines an approximate area profile in the corresponding direction. If the ramp response is determined for several directions, a synthetic three-dimensional image of the target's shape can be deduced from intersections of the area profile functions. Good results have been obtained for simple symmetrical shapes.

Since ramps are not propagated and their responses cannot be directly measured, the ramp response must be synthesized. Let G(w) be the complex scattering length of a target for a sinusoidal carrier at angular frequency w. A Fourier series synthesis of the response to any waveform a(t) is given through convolution as

$$f(t) = \sum_{n=1}^{N} A_n G(nw_o) e^{jnw_o t}$$

where A_n are the Fourier coefficient of a(t):

$$a(t) = \sum_{n=-N}^{N} A_n e^{jnw_o t}$$

N should be as large as possible and $w_o < \frac{2\pi}{T}$ where T is the maximum duration of f(t). For an impulse, $A_n = 1$ for all n; for a step function, $A_n = 1/jnw_o$; and for a ramp function $A_n = 1/(jnw_o)^2$. The impulse response of a sphere has

effectively decayed in a time comparable to the propagation time of 15 diameters, or $w_0 < C/5D$ or $\lambda_0 > 10\pi D$. The sharpness of the pulses and square corners of the synthesized waveform increase with increasing N.

The Ohio State approach has been to synthesize the ramp response for a target from measurements of the complex scattering lengths at harmonically related frequencies. Ten terms are usually used beginning with $\lambda_0 \approx 3D$, or $w_0 \approx 2\pi C/3D$. A ten-frequency phase and magnitude radar measurement system has been developed for laboratory use.

Three levels of feature extraction are possible from the synthesized ramp response. The integral of the ramp response is related to the Rayleigh scattering coefficient which is related to volume. As discussed earlier, the ramp response waveform is related to the area profile function. Thirdly, multiple area profiles may be used to synthesize a three-dimensional image.

Another method of discrimination from ramp response data has been reported by Moffatt and Mains (References 28 and 29). The pole locations on the complex frequency plane is a frequently used concept to describe the natural frequencies of a lumped parameter filter. The response of a scatterer is not unlike that of a filter, and it also may be characterized by its natural frequencies. The natural frequencies of a scatterer are considered to be independent of excitation direction or polarization. Obviously, the response is dependent on the excitation direction and polarization. This dependence may be related to the zeros of the pole-zero transfer function representation.

A linear difference equation is used as a predictor operating on the ramp response waveform. The predictor uses a set of natural frequencies and several previous values of the measured ramp response waveform to predict the future values of the waveform. If the correct natural frequencies were used, the predicted and measured waveforms will correlate well.

A classification algorithm can be developed to assign the target to the class whose predicted waveform correlates best with the measured waveform. The ramp response must be synthesized from harmonic frequency scattering measurements as discussed before. The aspect angle independence of the natural frequencies and their compactness in feature space are major advantages of this approach. This method has proven useful in extracting ground targets from clutter and has been demonstrated for a two-class aircraft problem. It has been suggested that aircraft discrimination could be performed with 120 and 180 MHz pulse radars using 20 MHz amplitude modulation, giving the 6 through 10 th harmonics of a 20 MHz fundamental.

An alternate identification method based upon estimating the natural resonances of a target has been proposed by Berni (Reference 30). The concept is based upon the hypothesis of Marin (Reference 31) that the transient response of a target can be expressed as an infinite summation of simple pole responses. A random modulation code would be imposed on the radar pulses. The impulsive responses, corresponding to specular geometrical optics returns, would be stripped from the scattered waveform. The remaining "late returns" response contains the natural resonance information. The natural resonance

pole locations are extracted through a matrix analysis eigenvector procedure. The pole locations are the features used for classification. The implementation of this method is not well defined, but it could have applications to microwave radar.

The classification of targets by polarization properties has been discussed by Copeland (Reference 32). Apparently the concept has not been exploited since its publication over 15 years ago. The possibility of extracting useful feature information from polarization properties of a target could be implemented with little additional radar hardware. The characteristic patterns produced by a rotating linearly polarized radar antenna would be the basis of feature extraction, along with the fact that the polarization properties of any target can be represented by an equivalent sphere and linear target.

The concept of inverse scattering is an interesting conjecture. Lewis (Reference 33) has shown very concisely and elegantly that if backscattering exactly obeyed the laws of physical optics, which it does not, that a compact transform relationship exists between the physical shape of a conducting convex body and the scattered fields. He is able to limit the quantity of scattering data required for a transformation into the shape domain. The futility of this approach has been discovered by Tabbara (References 34 and 35) in working with a sphere. The concept is powerful, but the limited domain of accuracy of the physical optics approximation emasculates its utility. The ramp response imaging methods of Young result in an approximation to inverse scattering in a related manner that has proven useful.

While these approaches have certainly made a valuable contribution to radar target identification research and have utility for many applications, they do have some serious limitations for the tactical aircraft identification application. The upper Rayleigh - lower resonance region extracts feature related to size and general shape. Classification between broad classes may be effected with these features, but the accuracy needed to discriminate between aircraft within a broad class may be difficult to obtain. Concave shape details such as engine ducts and sensor bays are suppressed in the low frequency scattering. Propulsion modulation data for all except propellor driven and rotary wing aircraft will be suppressed. The hardware implementation of a transportable tactical radar presents some major problems. An antenna capable of 360 degrees coverage with adequate angular resolution, ECCM capability and low altitude long range performance could be a major design problem. The dispersion of atmospheric propagation effects over the wide percentage bandwidth required may seriously degrade the accuracy of the essential phase measurements. It is questionable if the identification radar could also perform the traditional detection and location functions.

The low frequency approach has some definite advantages, however. The compactness of feature space, particularly with the natural resonance methods, limits the classifier to a manageable size. The feasibility of constructing the training set from mathematical models is also attractive. Radar cross section reduction countermeasures are ineffective in this part of the spectrum.

24

Perhaps an analogy is the best way to summarize the differences between the low frequency and microwave approaches to the aircraft identification problem. Assume you were given a set of coins and asked to classify and identify the nationality of each. You have two choices of approach:

1. You are blindfolded but may hold the coins in your fingers and feel their size, shape, and surface texture.

2. The coins are placed across a dark room and you may only view them at one aspect through a low-power telescope with a directional collocated light source. The size is not as easily gaged, but the possibility of reading some of the fine detail markings exists.

Neither situation is optimum; you would like the advantages of both. Coin-operated vending machines work on the first principle. Store clerks and bank tellers work on the second principle. The coin collector uses both. The first approach is analogous to the low frequency method, and the latter corresponds to the high frequency approach. Which is better?

VII. CONCLUSIONS AND RECOMMENDATIONS

The feasibility of performing classification and identification of aircraft in a tactical environment appears good. The problem is non-trivial and 100 percent accuracy in all situations should not be expected. The advantages of even an imperfect system should be of great benefit to the information flow of a command operation and should be sufficient motivation for its implementation.

There are two basic approaches to the radar sensor problem. One is the "low frequency" approach and has been researched in some depth at Ohio State University. A 10 frequency laboratory radar has been used to demonstrate classification of aircraft for up to a four class problem. There are serious questions about the feasibility of a tactically operational radar, however.

The second approach uses microwave radar with high resolution waveforms and signal processing to extract target details. Radars capable of this function are more sophisticated than current tactical radars, but well within the state-of-the-art. Special purpose radar installations have demonstrated the feasibility of the approach.

There are two major pattern recognition problems in the aircraft identification process. One is the selection of the best feature space and methods of mapping easily acquired data into that space. The other is the acquisition of reference or training data that defines the numerous classes of targets. The low frequency versus microwave sensor decisions have major impact on these problems.

The microwave approach appears better for the near term implementation of a tactical aircraft identifier. A radar to perform this function could be

designed today. There are some major questions that need further research, and the design task would require the application of the most modern simulation, design and analysis methods.

An approach to the design can be recommended. The detailed plan will be more complex and considers many other systems management factors, but the technical plan could follow this course of action:

1. Establish several preliminary design approaches working from general systems performance specification. Section V is an abbreviated example.

2. Evaluate and optimize these designs using simulation methods such as WPS, OLPARS and RADSIM. Gather and use experimental data whenever feasible.

3. Select the best approach and proceed into design and prototype evaluation and test.

Along with these rather straightforward radar design tasks, a parallel but closely coupled pattern recognition design must be developed.

Several smaller research-oriented problems have been suggested during this study. They are:

1. Could a learning mode be feasible in a classifier, where the operational radar would observe identified targets and store their processed features in its reference file?

2. What effect does the modulation spectrum of time varying target effects, such as propulsion component movement, rotary wings, scanning antennas, aerodynamic undulations of the airframe and control surface motion have on the coherent signal processing and two-dimensional image quality?

3. Can scan to scan phase coherence of RTI, Ø profiles be approximated by identifying and referencing phase to a stable and intense scattering center?

4. Can a practical and accurate method of image estimation and scene analysis be developed for the microwave signature characteristics of aircraft?

REFERENCES

1. Nathanson, Fred E., Radar Design Principles, McGraw-Hill Book Company, 1969.

2. Skolnik, Merrill I., Introduction to Radar Systems, McGraw-Hill Book Company, 1962.

3. Skolnik, Merrill I., Radar Handbook, McGraw-Hill Book Company, 1970.

4. Kennaugh, E. M. and Moffatt, D. L., "Transient and Impulse Response Approximations," Proceedings of the IEEE, Vol. 53, No. 8, pp. 893-901, August, 1965.

5. Proceedings of National Conference on Electromagnetic Scattering, University of Illinois at Chicago Circle, June 15-18, 1976, Communications Lab Report 76-1.

6. "Monostatic Tracking Radar Imaging Theory for Rotating Point Target Models with Various Bandwidth and Coherence Conditions," Syracuse University Research Corporation TN 75-139, June, 1975.

7. Rafael, Murray L., "Aircraft Identification by Radar Imaging Feasibility Study (U)," Syracuse University Research Corporation TR 74-223, September, 1974. (Confidential)

8. Duda, Richard O. and Hart, Peter E., Pattern Classification and Scene Analysis, John Wiley and Sons, Inc., 1973.

9. Cover, T. M. and Hart, P.E., "Nearest Neighbor Pattern Classification," IEEE Transactions on Information Theory, Vol. IT-13, No. 1, pp. 21-27, January, 1967.

10. Faust, John C., Webb, Haywood E. and Gerhardt, Lester A., "The RADC Interactive Laboratory for Design of Pattern Recognition Systems and Their Application," 1975 Conference on Computer Graphics, Pattern Recognition and Data Structure, 15 May, 1975, Beverly Hills, California. Reprints available from authors.

11. Stanley, T. P. and Nahin, P. J., "A Review of Technology Applicable to the Identification of Non-Cooperative Aircraft (U)," Institute of Defense Analyses Paper P-1130, September, 1975. (Secret)

12. "AWARE Measurement Program (U)," Westinghouse Defense and Electronics Systems Center, 8 August, 1975. (Secret)

13. Petts, George E., Orentas, Alfred A., Bonanno, Ernest J. and Reed, W., "S-Band Study, Final Report (U)," Westinghouse Defense and Electronics System Center, AFAL-TR-75-84, October, 1975. (Secret).

14. Kimbal, D. S., "Advanced Surveillance Radar Techniques (U)," Westinghouse Defense and Electronics Systems Center, RADC-TR-73-1, AD 524-952, 19 December, 1972. (Secret)

15. Orentas, A. A. and Bonanno, E. J., "Aircraft Signature Evaluation Study (U)", Westinghouse Defense and Electronics Systems Center, AD 525-268, 26 March 1973. (Secret)

16. Cisco, D. O., Cable, G. P. and Gruver, G. W., "Radar Signature Investigation Vol. I - Measurements Report, Vol. II - Target Classification," General Dynamics Convair Aerospace Division, RADC-TR-70-257 Vol. I and II, November, 1970.

17. Hancock, R. J., "Generalized Multimode Radar System Simulation Model, 3 Volumes," General Dynamics - Convair/Fort Worth, RADC-TR-73-273, Vol. I, II and III, August, 1973.

18. Crispen, J. W. and Siegel, K. M., Methods of Radar Cross Section Analysis, Academic Press, 1968.

19. Ruck, George T., et. al., Radar Cross Section Handbook, Vol. I and II, Plenun Press, 1970.

20. Bowman, J. J., Senior, T. B. A. and Uslenghi, P. L. E., "Electromagnetic and Acoustic Scattering by Simple Shapes," North-Holland Publishing Company and Wiley Interscience, 1969.

21. Bennett, C. L. and Hieronymics, R. M., "Intergal Equation Solution," Speny Research Center, RADC-TR-76-59, March, 1976.

22. Lin, Yar T. and Richmond, Jack H., "EM Modeling of Aircraft at Low Frequencies," IEEE Transactions on Antennas and Propagation, Vol. AP-23, No. 1, pp. 53-56, January, 1975.

23. Proceedings of 1975 Radar Camouflage Symposium (U), Wright-Patterson Air Force Base, Ohio, 1-3 October, 1975, AFAL-TR-75-100, December, 1975. (Secret)

24. Ksienski, Aharon A., Lin, You-Tang and White, Lee James, "Low-Frequency Approach to Target Identification," Proceedings of IEEE, Vol. 63, No. 12, pp. 1651-1660, December, 1975.

25. Young, Jonathan D., "Radar Imaging from Ramp Response Signatures," IEEE Transactions on Antennas and Propagation, Vol AP-24, No. 3, pp. 276-282, May, 1976.

26. Shubert, K. A., Young, J. D. and Moffatt, D. L., "Target Imaging from Multiple Frequency Radar Data," Ohio State University Electro Science Lab, RADC-TR-76-45, February, 1976.

27. Yound, J. D. and Ko, W. L., "Measurement and Analysis of Spectral Signatures," Ohio State University, RADC-TR-73-304, November, 1973 and RADC-TR-71-114, June 1971.

28. Moffatt, David L. and Mains, Richard K., "Detection and Discrimination of Radar Targets," IEEE Transactions on Antennas and Propagation, Vol. AP-23, No. 3, pp. 358-367, May 1975.

29. Tesche, Fredrick M., "On the Analysis of Scattering and Antenna Problems Using the Singularity Expansion Technique, " IEEE Transactions on Antennas and Propagation, Vol. AP-21, No. 1, pp. 53-62, January, 1973.

30. Berni, Albert J., "Target Identification by Natural Resonance Estimation," IEEE Transactions on Aerospace and Electronic Systems, Vol. AES-11, No. 2, pp. 147-154, March, 1975.

31. Marin, Lennart, "Natural-Mode Representation of Transient Scattering from Rotationally Symmetric Bodies," IEEE Transactions on Antennas and Propagation, Vol. AP-22, No. 2, pp. 266-274, March, 1974.

32. Copeland, J. R., "Radar Target Classification by Polarization Properties," Proceedings of the IRE, Vol. 48, No. 7, pp. 1290-1296, July, 1960.

33. Lewis, Robert M., "Physical Optics Inverse Diffraction," IEEE Transactions on Antennas and Propagation, Vol. AP-17, No. 3, pp. 308-314, May, 1969.

34. Tabbara, Walid, "On an Inverse Scattering Method," IEEE Transactions on Antennas and Propagation, Vol. AP-21, No. 2, pp. 245-247, March, 1973.

35. Tabbara, W., "On the Feeasibility of an Inverse Scattering Method," IEEE Transactions on Antennas and Propagation, Vol. AP-23, No. 3, pp. 446-448, May, 1975.

COHERENT RADAR SYSTEM BLOCK DIAGRAM

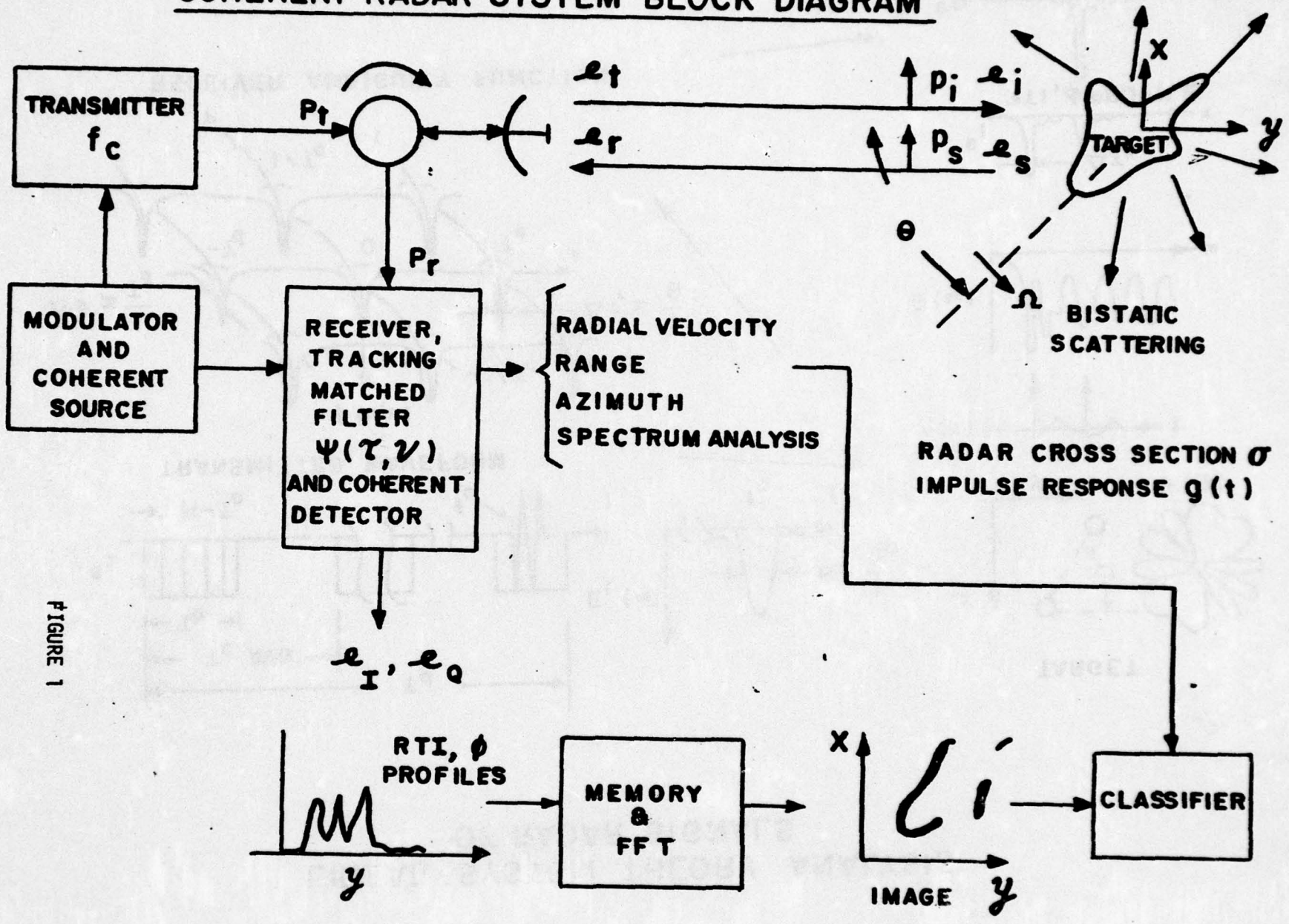


FIGURE 1

LINEAR SYSTEM THEORY ANALYSIS OF RADAR SIGNALS

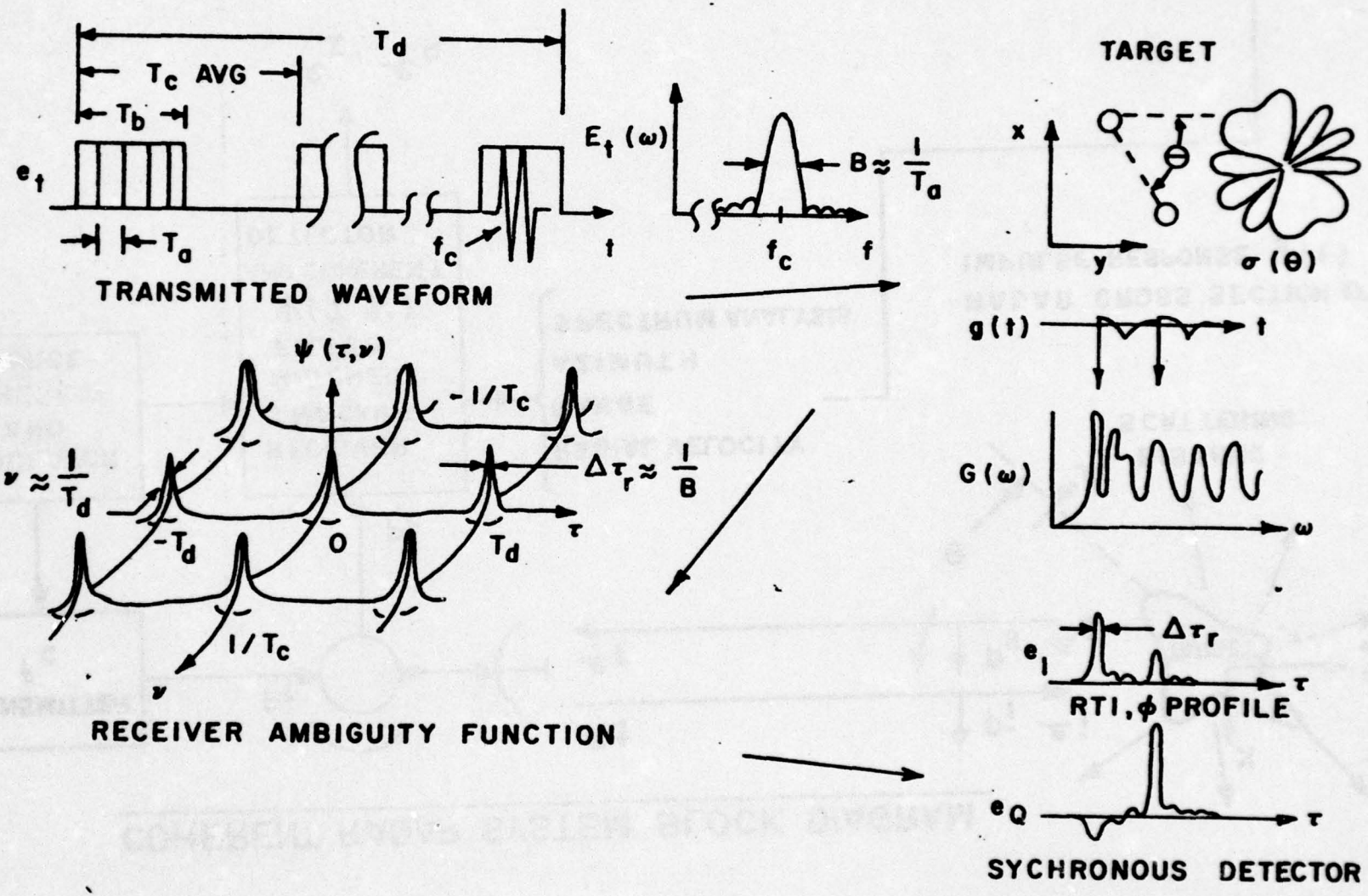


FIGURE 2

PROBABILITY DISTRIBUTIONS FOR THE SINGLE FEATURE, 2 CLASS EXAMPLE

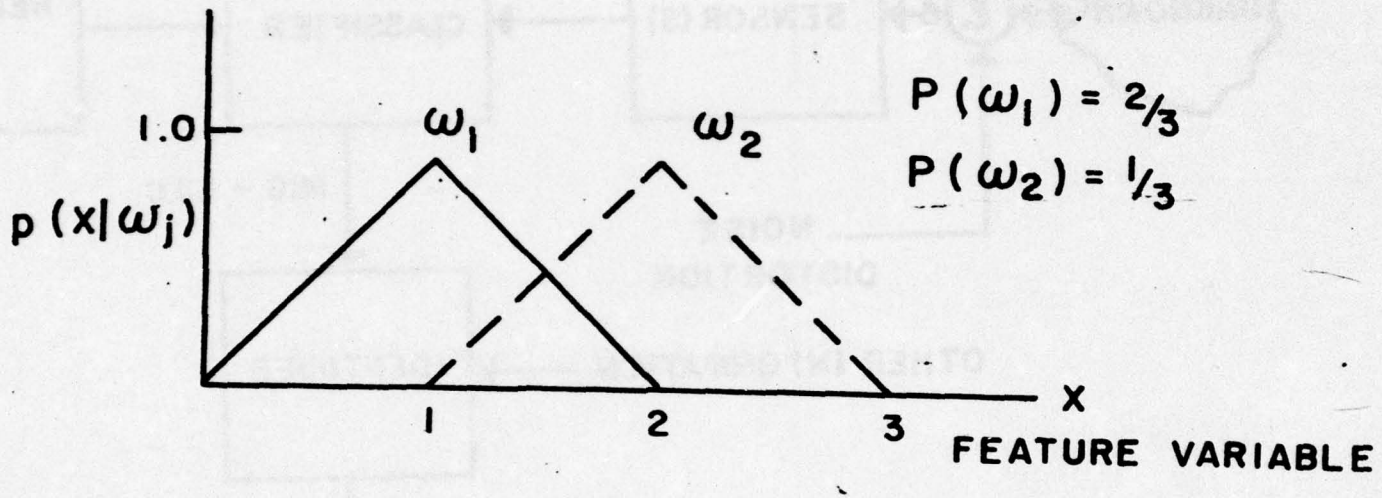


FIGURE 3

GENERAL CONCEPT OF THE IDENTIFICATION PROCESS

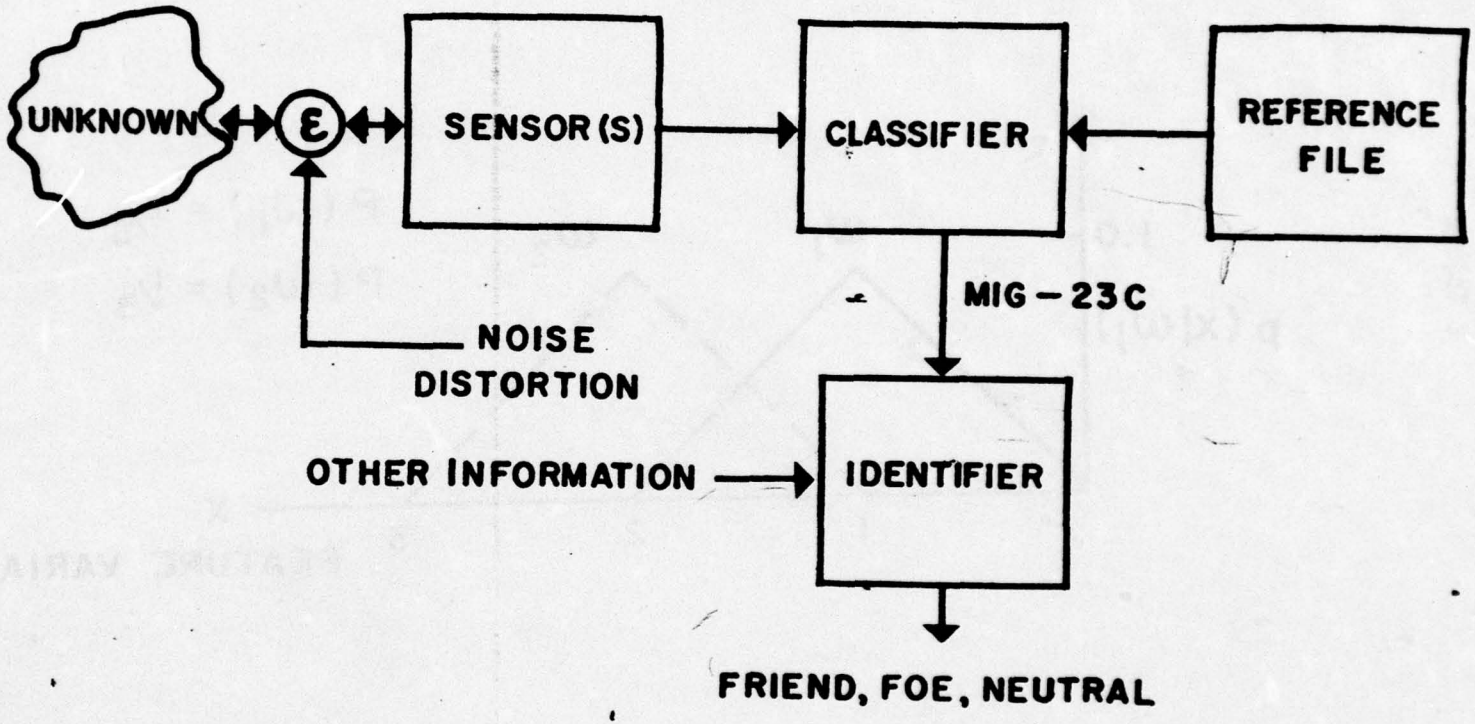


FIGURE 4

3 GHz IDENTIFY WHILE SCAN RADAR BLOCK DIAGRAM

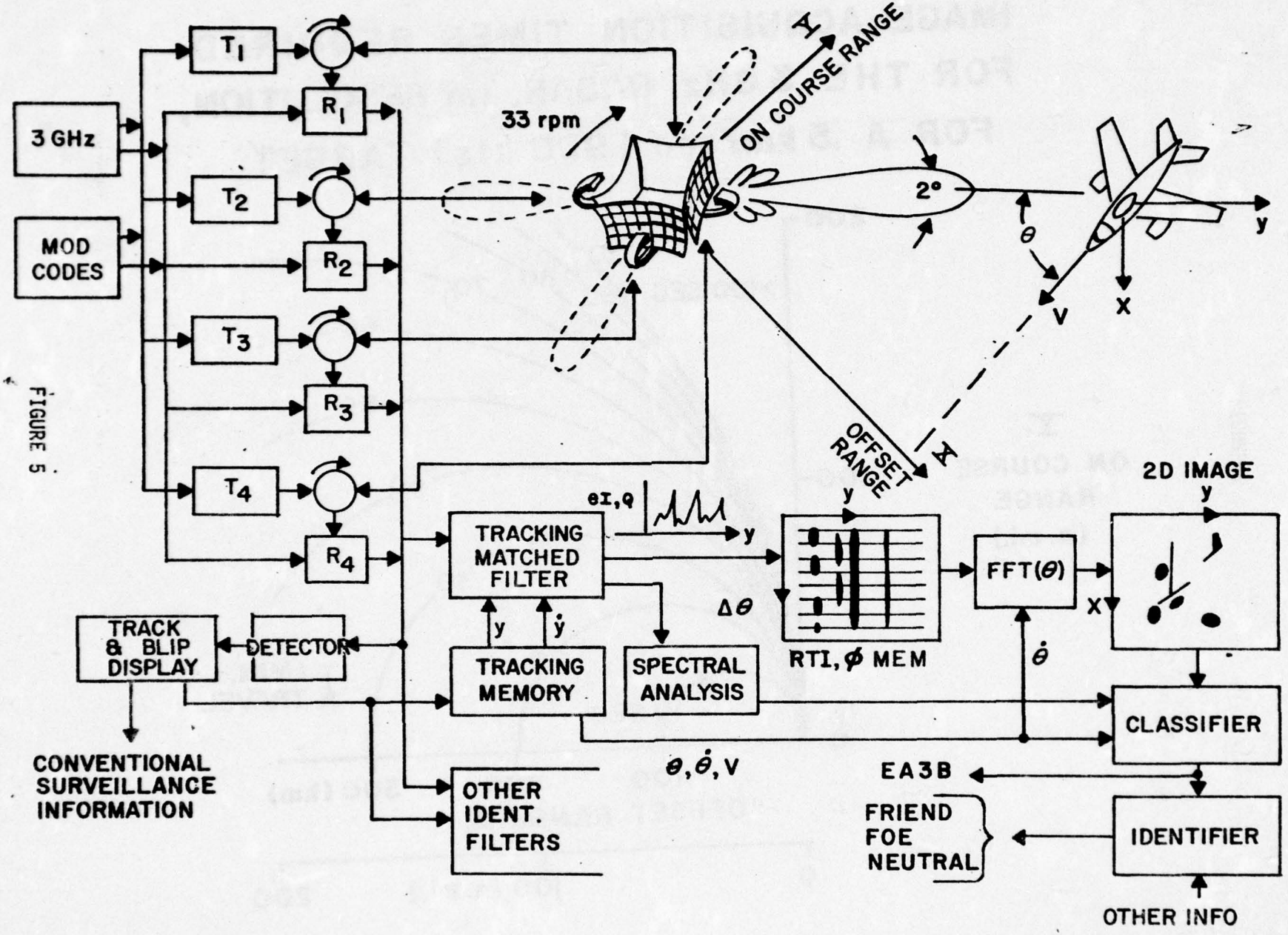


FIGURE 5

IMAGE ACQUISITION TIMES REQUIRED FOR THE 3 GHz RADAR, 1m RESOLUTION, FOR A .5 km/sec (950 kts) TARGET

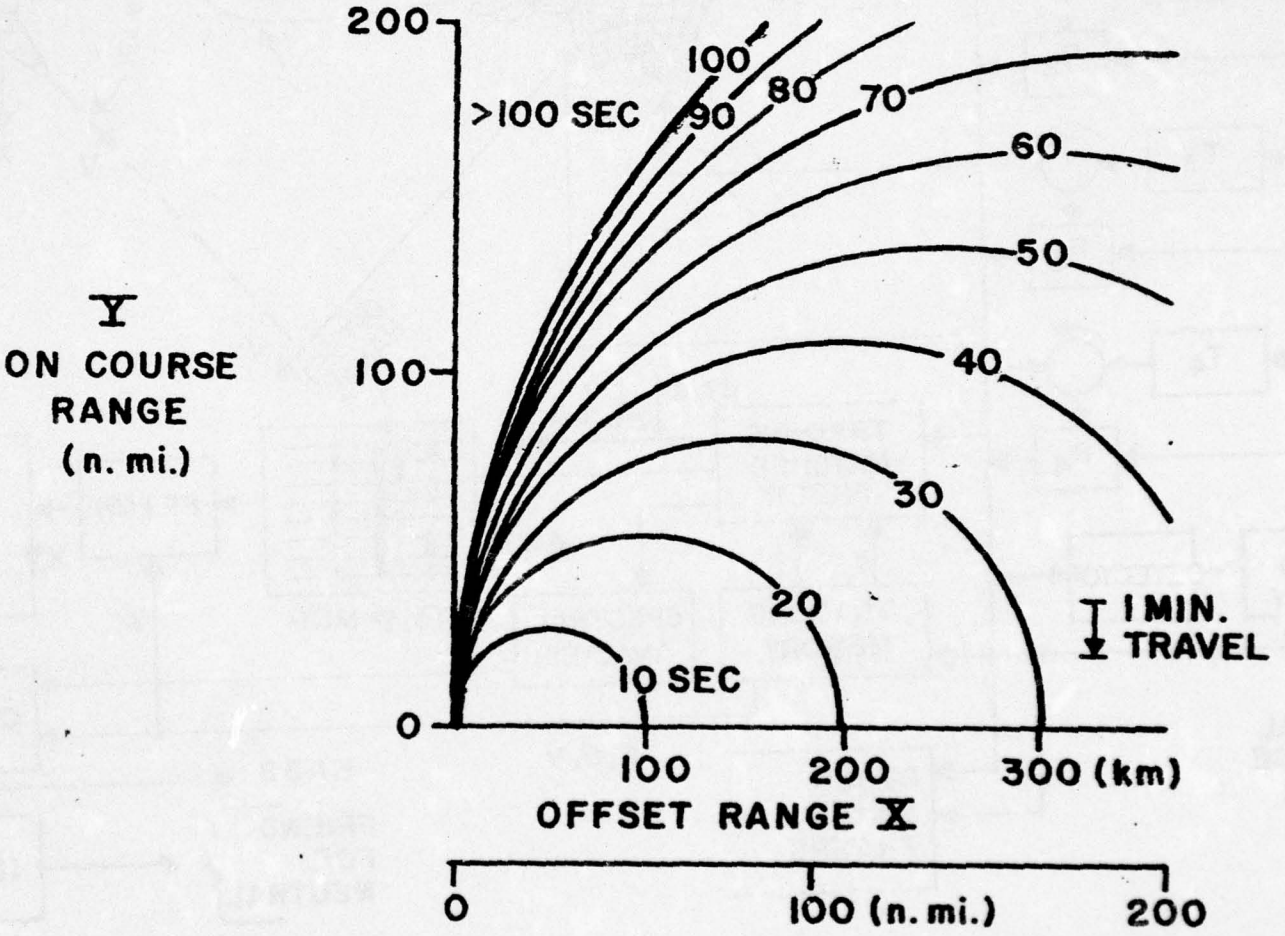


FIGURE 6

1976 USAF-ASEE SUMMER FACULTY RESEARCH PROGRAM
sponsored by
THE AIR FORCE OFFICE SCIENTIFIC RESEARCH
conducted by

AUBURN UNIVERSITY AND OHIO STATE UNIVERSITY

PARTICIPANT'S FINAL REPORT

CONFIDENCE LEVELS FOR LIFE CYCLE COST ANALYSIS

Prepared by:	Henry A. Wiebe Ph.D
Academic Rank:	Associate Professor
Department and University:	Department of Engineering Management University of Missouri-Rolla

Assignment:

(Air Force Base)	Griffiss AFB NY
(Laboratory)	Rome Air Development Center
(Division)	Reliability & Compatibility Division
(Branch)	Reliability Branch

USAF Research Colleague:	Jerome Klion
Date:	13 August 1976
Contract No.:	F44620-75-C-0031

CONFIDENCE INTERVALS FOR LIFE CYCLE COST ANALYSIS

by

H. A. WIEBE

ABSTRACT

The Department of Defense has increasingly been faced with the problem of restricted budgets and increasing costs of hardware acquisition and ownership. This situation has dictated an increased emphasis on cost control efforts to insure that maximum value is received for every dollar expended. One of the major techniques used to achieve cost effectiveness in its hardware acquisition programs is the use of Life Cycle Cost (LCC) procedures. These procedures call for estimates to be made of the total cost to the Government of acquisition and ownership of a system over its full life. LCC estimates must first be made during the early part of a system's life cycle and as a result are often based on very little firm data.

A review of existing LCC models and the role they played in the systems acquisition process was undertaken during this ten week study. The impact of uncertainty on model output and the decision-making process was qualitatively analyzed. This study recommends that the uncertainty associated with the input data used for making LCC projections be reflected in the overall LCC estimate by using a Monte Carlo simulation model. Desirable characteristics of a Monte Carlo simulation model for use in LCC analyses has been outlined. Further, it is recommended that the output of this simulation model be in the form of a probability distribution describing LCC and that confidence intervals be established to quantify the uncertainty associated with the estimate.

TABLE OF CONTENTS

1. OBJECTIVE

2. INTRODUCTION

   2.1 General Background

   2.2 Role of LCC in Systems Acquisition and Development

3. TYPES OF EXISTING LCC MODELS

4. BENEFITS OF A STANDARD MODEL FRAMEWORK

5. UNCERTAINTY IN LIFE CYCLE COST ANALYSES

   5.1 Problems Created by Uncertainty

   5.2 Approaches to Handling Uncertainty

   5.3 A Simulation Approach to Life Cycle Cost Analyses

6. CONCLUSIONS AND RECOMMENDATIONS

7. REFERENCES

1. OBJECTIVE

The objective of this ten week study was to initiate the development of a probabilistic life cycle cost model that would permit confidence intervals to be established around an estimate of life cycle cost.

2. INTRODUCTION

2.1 General Background.

The Department of Defense has increasingly been faced with the problem of restricted budgets and escalating costs of hardware acquisition and ownership. This situation has dictated a greater emphasis on cost control efforts to insure that maximum value is received for every dollar expended. One of the major techniques used to achieve cost effectiveness in its hardware acquisition programs is the use of Life Cycle Cost (LCC) procedures. The Department of Defense Directive Number 5000.28, 23 May 75, and Air Force Regulation 800-11, 3 August 73, establish policy and guidance in the area and have provided the impetus for inclusion of LCC provisions in recent hardware acquisition contracts.

The LCC of a system is defined as the total cost to the Government of acquisition and ownership of that system over its full life. It includes the cost of research and development, production, operation, support, and where applicable, disposal. The general magnitude and time-phasing of these costs for Air Force systems are shown in Figure 1 below. The total time span often exceeds a ten year period. Use life is usually taken as 10 years alone. When R&D and production time are added, the time period will exceed 10 years.

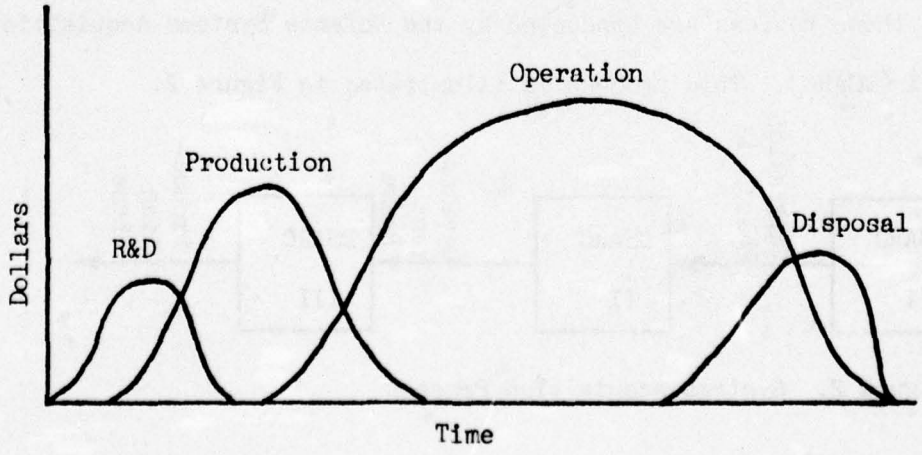


Figure 1. Time Distribution of Life Cycle Costs

There is a great need to achieve visibility of costs in all the above categories during early design stages of a project, yet problems exist to prevent the easy attainment of this goal. These problems are created by the interrelationships that exist among the various design and operational characteristics of the equipment, the time span of the projects, the variety of controlling and using government agencies, and the funding mechanisms used to generate money for the development, acquisition and support of various systems. The use of LCC procedures is seen as a way of overcoming some of these problems by providing a means of estimating and quantifying the total cost incurred by a system in its lifetime. A clearer view of the contributions made by LCC analysis can be obtained by briefly examining the systems development and acquisition process with respect to the role played by LCC.

2.2 Role of LCC in Systems Acquisitions and Development.

There are four generally recognized phases in the equipment development and acquisition process. These are the conceptual, validation, development, and production phases. Comprehensive reviews take place after each of the first three phases at which time previous work is examined along with projections of future alternatives. A decision is made at the end of each review as to whether or not to proceed to the next phase. At the systems level these reviews are conducted by the Defense Systems Acquisition Review Council (DSARC). This process is illustrated in Figure 2.

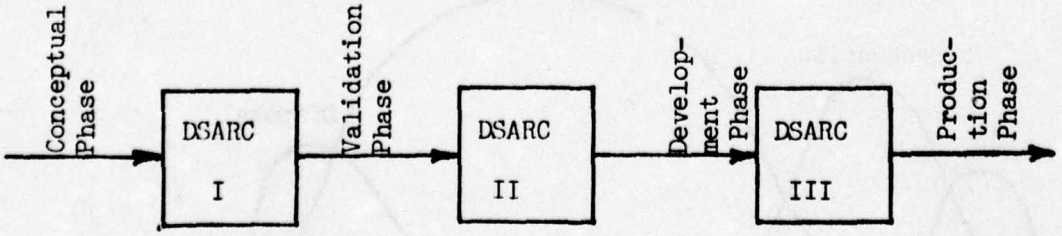


Figure 2. Systems Acquisition Process

During the conceptual, validation, and development phases of an equipment's life cycle, decisions impacting various equipment design parameters (such as reliability and maintainability) are constantly being made. These decisions often have an impact on cost that carries into the operational phase of the equipment. The magnitude of this impact becomes apparent when one considers the fact that over 50% of the total life cycle cost is frequently due to operation and support costs alone (see Figure 1). Further, it has been pointed out (1) that about 70% of the decisions which influence or dictate these ownership costs are made in the very early stages of the equipment's life cycle. In view of this, it is only logical that one of the criteria used in making design decisions should be the design's impact on life cycle costs.

The validity of LCC as a decision-making criteria has been recognized and it is for this reason that DOD Directive 5000.28 states that an initial Design to Cost goal shall be established before program initiation (DSARC Milestone I) or at the earliest possible date thereafter, but in no case later than entry into full-scale development (DSARC Milestone II in Figure 2). Establishment of this design to cost goal requires that a LCC analysis be conducted in order to insure that adequate consideration is given to future operating and support costs during design formulation.

Early use of LCC analyses is also recommended by the Joint AFSC/AFLC Commanders' Working Group on Life Cycle Cost (4). They say that a LCC analysis should be made during the conceptual phase. The Group states that the analysis should be quantitative where possible but, as a minimum, at least contain the qualitative life cycle cost implications of identified alternatives. In addition, it is recommended that this information be broken out to the

third work breakdown structure level (i.e., airframe, propulsion system, avionics) if feasible. It is felt by the Group that such an analysis is necessary to properly evaluate the financial impact of potential design trade-offs.

To meet this need, a large number of LCC models have been developed since the early 1960's by contractors and government personnel in all branches of the service. As of 1968, the Army had developed at least 27 automated cost models [1] and a more recent study by Rand[2] summarizes 46 models applicable to Air Force cost analysis situations. The Rand study indicates that its sample of 46 models represents only one-third to one-half of the available models. Most of these are models that have been developed to help analyze specific acquisitions, but some are more general and are intended for broader application.

3. TYPES OF EXISTING LCC MODELS

As indicated by the earlier referenced Rand and Army surveys, there are many LCC models available. These models take many forms and serve a variety of purposes. Some of the surveyed models are not true LCC models in the sense that they fail to cover the entire life cycle of an equipment item. Others cover only a portion of the costs associated with an equipment item. Terminology also changes greatly from model to model along with the data inputs required. These differences often create difficulty in the selection of the proper model to use for analysis purposes.

The Joint AFSC/AFLC Commanders' Working Group on Life Cycle Cost has attempted to clarify the situation by classifying existing LCC models based primarily on the type of use for which each model was initially designed. These classifications are:

1. Accounting Models
2. Economic Analysis Models
3. Cost Estimating Relationship Models
4. Reliability Improvement Cost Models
5. Level of Repair Analysis Models
6. Maintenance Manpower Planning Models
7. Inventory Management Models
8. Warranty Models

This classification scheme is somewhat arbitrary and, at times, the categories overlap. However, they do provide a framework that can be used to help describe existing modeling work that has been done in the life cycle cost area. Each of the above categories is briefly discussed below.

Accounting models are perhaps the most common type of model to be found. They typically sum costs in different categories such as spares, maintenance, etc., to arrive at a grand total life cycle cost. Some models accumulate costs at the general systems level while others accumulate costs for individual "First Line Units." Typical examples would be the "Logistics Support Cost Model" (7) and the "Cost Analysis Cost Estimating Model" (8).

Economic analysis models compare program life cycle costs in terms of the present value or future value of the dollars involved. They are typically applied to situations where one must decide whether or not to spend funds in early years to achieve savings in later years. An example of such a model is one called"Research into the Economics of Design and User Cost Effects" (9).

Cost estimating relationship models express cost as a function of system parameters such as weight, utilization, or reliability. Statistical

regression is used to fit cost data from existing or similar systems to descriptive data associated with the equipment under study. These types of models have been used extensively in estimating acquisition costs but have seen only limited use in estimating total life cycle costs or operating and support costs. An example of such a model is the work done by General Electric Co. for RADC (10) to provide a basis for estimating costs of reliability design programs.

Reliability improvement cost models are specifically designed to address the relationship between equipment reliability and cost. These models are useful in helping to determine how much money should be budgeted to attain given levels of equipment reliability and can also help determine the level of reliability that will minimize life cycle costs. An example (in addition to the one by General Electric (10) cited immediately above) is described in Models and Methodology for Life Cycle Cost and Test and Evaluation Analyses (11).

Level of repair analysis models help determine the proper level of repair to be used on equipment under development to minimize life cycle costs. Level of repair models seek an answer to the question of whether it is less costly to (a) discard at failure, (b) repair at the base or, (c) repair at the depot. Some models address this question from a single item, single indenture point of view while other take a more comprehensive approach and address it from a multi-indenture or a systems viewpoint. An example of a single item, single indenture model is the "Optimum Repair Level Analysis Model" used by AFLC & AFSC (12).

Maintenance manpower planning models are used to evaluate the impact of various equipment designs and/or maintenance policies on the cost of

manpower to maintain the equipment. An example of such a model would be the "Logistics Composite Model" (13) developed by Rand Corporation.

Inventory management models are designed to help determine optimum stock levels for spare parts. Once this optimum stock level is determined, it can be used to help minimize total life cycle costs. There are many inventory models in existence. An example of a comprehensive multi-echelon model is the "Multi-Echelon Technique for Recoverable Item Control" (14) developed by Rand Corporation.

Warranty models are designed to assist in determining the benefits to be achieved from reliability warranties on specific hardware items. They attempt to answer questions such as what is the optimal warranty time period. A fairly recent model is described in Use of Warranties for Defense Avionic Procurement (15).

4. BENEFITS OF A STANDARD MODEL FRAMEWORK

Of significance is the fact that none of the models developed have received sufficient exposure or use to become established as a standard tool for life cycle cost estimation. In addition, even with the aid of model descriptions and classification schemes such as the one just given above, it is not possible to simply select a model for use in a particular application. Careful screening is still necessary to insure that the capabilities of the selected model match the analysis requirements at hand. This is not an especially easy task. The situation would be greatly improved if a standard model framework were adopted by all LCC analysts.

The benefits to be derived from a standard model framework are many. First, the problem of variations in terminology would be alleviated. Currently, every new model considerd for potential use must be studied to determine just what is meant by various phrases describing the different cost categories. Second, the tremendous variety of data sources now needed to satisfy the data input requirements of the various models would be reduced. Model users would know what to expect in terms of data requirements and could, therefore, be better prepared to meet these requirements. Third, a standard model framework would permit the use of standardized output format. This should greatly enhance understanding of model results because of the increased familiarity gained through repeated exposure. Finally, continued use should also lead to better understanding of the relationships existing between the various cost categories and better understanding of how the model treats different costs. This will allow the technique to be refined and usefulness to be improved with better documentation.

5. UNCERTAINTY IN LIFE CYCLE COST ANALYSES

5.1 Problems Created by Uncertainty.

All problems will not be solved by DOD requiring that LCC analyses be conducted during the early part of an equipment's life cycle as is now dictated by DOD Instruction 5000.28. Nor will all problems be solved by the adoption of a standard LCC model framework (should that fortunate event ever occur or be dictated by DOD). The fact remains that very little firm information is available when the first estimate of life cycle costs must be produced. Uncertainties are often great enough to cause a reversal of a decision with the exact decision depending on which values within the range of the uncertainty are used as representing future costs. This means that any estimate or cost projection stands a large chance of being wrong.

The benefit derived from achieving cost visibility is greatly diminished if projections are frequently wrong and the costs portrayed are not representative of reality. As a result, methods must be used to account for the uncertainty involved and in this manner develop more credible projections of LCC.

5.2 Approaches to Handling Uncertainty.

Complete certainty can be obtained only from a historical perspective and this is too late to assist in the planning of the project at hand. However, various approaches to handling uncertainty are available and have been used at one time or another. Four of these approaches are briefly discussed below.

Safety Margins: Perhaps one of the oldest techniques for protecting oneself against uncertainty is to provide a margin of safety in the estimates of critical parameters. Quite often, the worst possible value

of a parameter is used to represent the projected outcome. While this procedure can be used to establish an upper bound on possible costs, it can work to the disadvantage of a program by eliminating certain courses of action as too expensive when, in fact, they may be too expensive only if the worst possible set of circumstances occur.

Expected Values: Basing decisions on an expected outcome may well be one of the most common decision-making procedures in use today. The advantage of this approach is that it requires only a single estimate representing what the analyst feels will actually happen. Also, if the decision is made many times, the expected return will be realized. The disadvantage is that the degree of uncertainty that may affect the final decision is not reflected and it may not be possible to make the decision many times.

Sensitivity Analysis: Sensitivity analysis is another fairly common way of treating uncertainty. Use of this approach calls for one value, such as reliability, to be varied over its range while other values are held constant. This makes it possible to determine the degree of sensitivity that a LCC estimate has to various input parameters. The technique works best when uncertainty exists about only a few parameters and when the parameters are independent (i.e., the effect on costs of the various parameters is separable). However, when uncertainty exists in a large number of input variables, the number of possible combinations of values becomes very large and may prohibit one from analyzing all possibilities. Also, the likelihood of some combinations occuring will be much less than the likelihood of other combinations. Straightforward sensitivity analysis will not reflect these changing probabilities and a

LCC resulting from extreme values of all input parameters will appear just as likely as one resulting from the use of average input values.

Monte Carlo Simulation: Monte Carlo simulation provides yet another way of accounting for the uncertainties in input parameters of a LCC analysis. Such an approach requires that information concerning input variables be available to the LCC analysis model in the form of probability distributions. This means that either the raw input data must consist of probability distributions or else the model itself must convert deterministic input data into a probability distribution.

Likewise, the model output consists of a distribution of life cycle costs. From this output distribution it is possible to determine both the expected life cycle cost and the uncertainty associated with the estimate.

There are several advantages of a Monte Carlo simulation approach to LCC analysis over the more traditional sensitivity analysis approach. First, and perhaps most importantly, it provides information concerning the probability of occurrence of specific life cycle costs. LCC values arising from a sensitivity analysis are simply point estimates of a life cycle cost and nothing is formally given about the likelihood of any particular value occurring. Common sense tells us that the occurrence of extreme values in two or more parameters simultaneously is not as likely as the simultaneous occurrence of more moderate values. However, this difference in probability is not quantified during a normal sensitivity analysis where it can be when the analysis is conducted by Monte Carlo simulation.

Second, it relieves the analyst of the responsibility of deciding what combinations of parameter values to use in calculating a life cycle

cost. Deciding which combinations of values warrant investigation and then making the proper calculations can be a burdensome task when there are a large number of input parameters.

It is for the above reasons that a Monte Carlo approach to LCC analysis is recommended in this report and is discussed further on the following pages.

5.3 A Simulation Approach to Life Cycle Cost Analyses.

There are several major considerations that should shape the development of any simulation model being designed for use in conducting a LCC analysis. First, it must be as accurate as possible. Next, it should be simple to operate and last, the output should be structured so that it is easy to understand. It is only by following these guidelines during model development that proper visibility can be given to the costs incurred by an equipment item over its life.

Model Accuracy: Model accuracy is largely a function of three things. These are:

(1) Validity of the input data.

(2) Completeness of the cost categories.

(3) Treatment of the costs within the model.

Validity of the input data is in many respects an intangible that is difficult to quantify. It is dependent both on the ability of the analyst to extract and formulate the data as well as on the availability of data sources. As a result, the validity of input data can vary greatly from application to application. To accommodate this situation, data input requirements for a model should be as limited as possible while still enabling the model to meet its output objectives. This point is pursued further in the discussion on model completeness immediately below.

Insuring that the cost categories of a model are adequately complete requires a great deal of attention. The model must contain a sufficient number of categories to be complete and also provide sufficient detail for control and decision-making purposes when evaluating design trade-offs. At the same time, the number of categories must be restricted in order to retain simplicity. The exact structure of the cost categories should represent a balance between accuracy and simplicity. The ultimate model structure is therefore somewhat dependent on the use to be made of the model results.

The use of CERs introduces a unique problem when insuring that the cost categories of a model afford complete coverage. CERs are not always straightforward and the original cost data upon which the relationships are based may not be readily available for analysis and verification. This means that the use of CERs should be restricted to those that are thoroughly documented or that can be verified in some manner.

Treatment of costs within the model may consist of simply summing up costs in different categories. The main caution to be observed on this point during model development is to make sure that all relevant costs are included and that none are included more than once. This is particularly true if CERs are used to estimate cost. As stated earlier, the model builder must know in detail what costs are covered by a specific CER. One should also be willing to judge whether or not the history represented by the old data points used to structure the CER will repeat itself in the application being analyzed.

One other topic that needs to be considered when discussing the treatment of costs within the model is the Monte Carlo sampling procedure. A Monte Carlo Procedure operates by taking samples of possible values of input variables and combining them as dictated by the logic internal to the model to produce a final result. The input variables on most models are independent which means that any value of one variable can be selected and combined with any value of another variable. This is not always the case when dealing with a cost model and requires special attention to insure that the model yields accurate results.

The problem of dealing with dependent input variables (i.e., dependent cost categories) can be solved in two ways. The first is to combine all costs into more highly aggregated groupings which are no longer dependent. This is not desirable if the model is to be used to evaluate design trade-offs because the necessary cost detail will be lost.

The second method involves modifying the normal sampling procedure used by a Monte Carlo model. The cost categories must first be ranked in a priority or precedence order. This order can change from sample to sample, but must remain constant during a single sampling operation. The model will then obtain sample values of all input variables in the order dictated by the priority listing. The first value obtained will be selected from the entire range permitted of that variable. However, from that point on each subsequent variable will be checked to determine if a dependence exists between it and the variable previously selected. If a dependency does exist, the potential range of the second variable will be restricted to reflect the dependency relationship. The type of restriction imposed is dynamic and will vary from sample to sample during the simulation run. Model complexity will be greatly reduced if the priority list can be structured so that each variable will have to be checked for dependency only against the one preceding it on the list.

Simplicity of Operation: Simplicity of model operation goes a long way toward establishing its eventual usefulness. A model that is too complex to operate will not be used enthusiastically and as a result, may fall into disuse. As far as an analyst is concerned, simplicity of operation is determined by the requirements imposed on structuring the input data. Care must be exercised in this regard when dealing with Monte Carlo simulation models. Traditional thinking says that better results will be obtained when more precisely structured input data are used. With Monte Carlo models this often means that input data must be structured in the form of a histogram or probability distribution. This is a severe requirement and one that can only be carried out with difficulty for typical life cycle cost data.

An alternative to this approach is to structure the model so that it fits a known probability distribution around some type of point estimate (or possibly around a point estimate along with an indication of the distribution variance). It is something close to this latter approach that is recommended here in order to achieve the required simplicity in structuring the input data.

It is felt that a limited choice on the exact form of the distribution to be used can be left to the analyst without introducing undue complications. The recommended forms are either the uniform (i.e., rectangular) or the triangular distribution. Either of these can be easily specified by indicating the mean and a range around the mean. This type of estimate eliminates the need to formulate a probability statement to describe every piece of input data. Data items known with complete certainty would be input as a single point with no range associated with them. The rectangular distribution would be used when it is felt that no information whatsoever is available about the magnitude of the estimated or future cost with respect to its estimated range. The triangular distribution lends itself

to the situation where sufficient information is available so that one is at least able to say that the occurrence of a cost near the extreme end of the estimated range is less likely to occur than a value near the estimated expected value. It is logical that as the life cycle progresses through the conceptual, validation & development stages, the ability to refine cost estimates will increase. This should result in a general narrowing of the input cost ranges as well as a shift from rectangular distributions to triangular distributions. In addition, the emergence of primary cost drivers, possibly as the result of sensitivity analyses, will occur and emphasis can be placed on refining these estimates to a higher degree than the less important cost estimates.

Model Output Structure: As indicated earlier, the prime consideration in structuring the output is to make it easy to understand and thus give visibility to the costs (and the associated uncertainty) incurred by an equipment item over its life.

A basic item of output required from the Monte Carlo analysis is a probability distribution describing the life cycle cost of an item. This could appear in tabular form or as shown graphically in Figure 3 below.

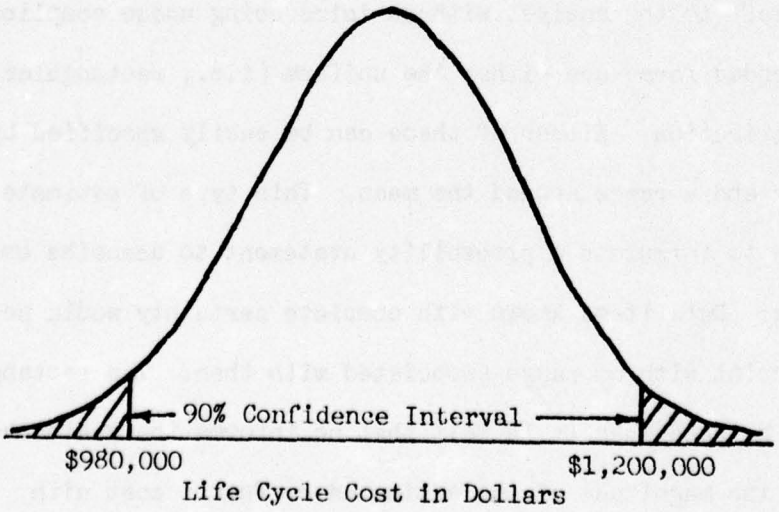


Figure 3. Distribution of Life Cycle Cost

Once this is obtained, it is a relatively easy matter to give the degree of confidence associated with any particular interval estimate of life cycle cost. The example in Figure 3 shows that there is a 90% chance that the total life cycle cost of some hypothetical system will be between $1,200,000 and $980,000. A program manager is now in a much better position to make decisions concerning program funding with uncertainties concerning cost exposed for consideration.

It may be desirable to structure the probability distribution of life cycle cost in terms of a cumulative probability distribution. This information would then indicate the probability of a life cycle cost having a specific value or less. It could be shown graphically as in Figure 4 below.

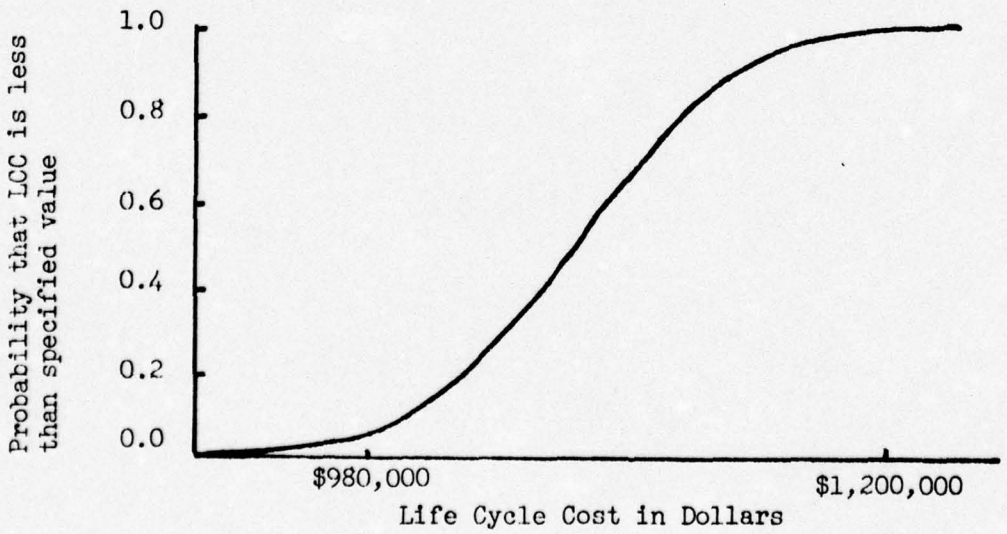


Figure 4. Cumulative Distribution of Life Cycle Cost

In addition, it is felt that an option should be available where life cycle costs would be broken down into annual amounts. This would provide a cost profile that would further aid decision-making by giving visibility to the continuing as well as the peak year funding necessary to carry out a project. The penalty paid for the use of this option would be an increased requirement for data inputs. Cost data would either have to be input on a year-by-year basis or else an arbitrary allocation scheme would have to be exercised by the model to accomplish a year-by-year assignment of cost.

An option could also be provided so that costs could be shown either with or without the impact of inflation and the application of a 10% discount factor.

6. CONCLUSIONS AND RECOMMENDATIONS

This study has resulted in the following conclusions and recommendations:

1. A life cycle cost analysis should be a significant part of the decision-making process associated with systems acquisitions.

2. Uncertainty in life cycle cost estimates needs to be quantified by establishing confidence intervals around the expected life cycle cost.

3. A Monte Carlo simulation model should be formulated and used to quantify the uncertainty associated with life cycle cost estimates.

4. Care must be exercised during the development of a Monte Carlo simulation model to insure that it is accurate, simple to operate and has output that is easy to understand. Guidelines for achieving this are contained in Section 5.3 of this report and briefly require the following:

a. Development of the capability within the model to conduct a sensitivity analysis so that a determination can be made of whether or not possible variation in certain input variables can be ignored in structuring model input.

b. Determination of the impact of using different probability distributions for describing input variables.

c. Structuring the model to handle a possible dependency among input variables during the Monte Carlo sampling procedures.

7. REFERENCES

1. Getting "Real" Data for Life Cycle Costing, M. R. Fiorello, Rand Corporation, p-5345, January 1975.

2. A Survey of Army Automated Cost Models, Paul Curd and Ogden Allsbrook, Office of the Comptroller of the Army, AD-829321L, 1968.

3. Using Logistics Models in System Design and Early Support Planning, R. M. Paulson, R. B. Waina, and L. H. Zacks, Rand Corporation, R-550-PR, February 1971.

4. Life Cycle Cost Analysis Guide, Joint AFSC/AFLC Commanders' Working Group on Life Cycle Cost, WPAFB OH, November 1975.

5. Estimating Life Cycle Costs: A Case Study of the A-7D, Marco Fiorello, Rand Corporation, R-1518-PR, February 1975.

6. DOD Life Cycle Costing Guide for System Acquisitions (Interim), DOD Life Cycle Costing Steering Group, Pentagon, Wash DC, LCC-3, January 1973.

7. Logistics Support Cost Model Users' Handbook AFLC/AQMLE, June 1975.

8. Cost Analysis---USAF Cost Analysis and Planning Factors, AFR-173-10, Volume 1 (U), 6 February 1975.

9. The REDUCE Model: Description, ASD/XR-72-34, Caywood-Schiller Division, A. T. Kearney, Inc., July 1972.

10. Reliability Acquisition Cost Study, RADC-TR-73-334, General Electric Company, November 1973.

11. Models and Methodology for Life Cycle Cost and Test and Evaluation Analyses, OAS-TR-73-6, Office of the Assistant for Study Support, AFSC.

12. Optimum Repair Level Analysis (ORLA), AFLCM/AFSCM 800-4, 25 June 1971.

13. The Logistics Composite Model: An Overall View, Rand Corporation, RM-5544-PR, May 1968.

14. METRIC: A Multi-Echelon Technique for Recoverable Item Control, Rand Corporation, RM-5078-PR, November 1966.

15. Use of Warranties for Defense Avionic Procurement, RADC-TR-73-249, ARINC Research Corp., June 1973.

1976 USAF-ASEE SUMMER FACULTY RESEARCH PROGRAM
sponsored by
THE AIR FORCE OFFICE OF SCIENTIFIC RESEARCH
conducted by
AUBURN UNIVERSITY AND OHIO STATE UNIVERSITY

PARTICIPANT'S FINAL REPORT

COMPUTER AIDED DESIGN OF SPECIAL MONOPOLE AND DIPOLE ANTENNAS

Prepared by: Shreedhar G. Lele, Ph. D.

Academic Rank: Associate Professor

Department and University: Department of Electrical Engineering
Tennessee Technological University
Cookeville, Tennessee 38501

Assignment:

Hanscom AFB
Deputy for Electronic Technology
Electromagnetic Sciences Division
Antenna and Radar Techniques Branch

USAF Research Colleague: Charles J. Drane, Ph. D.

Date: August 6, 1976

Contract No.: F44620-75-C-0031

COMPUTER-AIDED DESIGN OF SPECIAL MONOPOLE AND DIPOLE ANTENNAS

by

Shreedhar G. Lele

ABSTRACT

This report describes a study of two kinds of antenna structures, viz., an umbrella-type, top-loaded monopole, and a two-dipole end-fire antenna array on a transmission line. An antenna modeling program (AMP) was used in a computer analysis of both of these antennas. Calculations were made to study the variation of input impedance of the monopole antenna with umbrella strut length and the various parameters defining the ground system. The end-fire antenna array gain was calculated for different interdipole distances along a transmission line which was terminated in its characteristic impedance in one case and an open circuit in the other.

Both studies have produced interesting results. The radial wire ground system is found to simulate quite nicely an infinitely conducting earth. The antenna strut length affects both the resistive and reactive components of the antenna terminal impedance. There exists an optimum combination of length and number of radial ground wires. The two-dipole antenna array shows gain variations in the end-fire direction for various inter-dipole distances on the transmission line. The maxima and minima of gain for array on an open-ended transmission line appear to be closely related to resonances of the system consisting of the two dipoles and the transmission line between them.

ACKNOWLEDGEMENTS

The author expresses his gratitude to the Air Force Office of Scientific Research for support of this summer research project. A deep appreciation is due to ASEE and Auburn University and, in particular, Mr. Fred O'Brien, Jr., for excellent administration of this program.

The author appreciates very much the efforts of Mr. C.J. Sletten, retired director and Dr. Allan Schell, the present director of the Electromagnetic Sciences Division in providing facilities to conduct the research work. It has been a great pleasure to work closely with Dr. Charles J. Drane on these ongoing projects of interest to U.S. Air Force.

I. INTRODUCTION

This report describes some of the properties of each of two kinds of wire antennas: one an umbrella-type, top-loaded monopole antenna and the other a two-dipole antenna array, the dipoles being situated on a two-wire transmission line. Both problems are of special interest to the U.S. Air Force and are a part of the on-going research activity in the Antenna and Radar Techniques Branch of the Electromagnetic Sciences Division. The umbrella-type monopole antennas are used for VLF and LF communications purposes and are usually tower antennas. However, the one described in this report is suspended from a balloon and the central monopole and umbrella struts are wire conductors. Some data are available on the performance characteristics of the tower-type umbrella monopole, whereas, to the author's knowledge no such data are available for the suspended-type umbrella monopole. The problems of feeding the antennas (dipoles) in an antenna array with proper voltages in correct phase could be avoided if the dipoles are located on a transmission line, and distances between the dipoles are arranged so as to yield a large end-fire gain for the array. The array gain could be further optimized by perturbing the lengths of the individual dipoles.

II. OBJECTIVES

Use AMP, the antenna modeling program:

1. to calculate the input impedance of an umbrella-type, top-loaded monopole antenna for various antenna parameters, e.g., umbrella strut length and radialground wire systems, and to discuss the results.

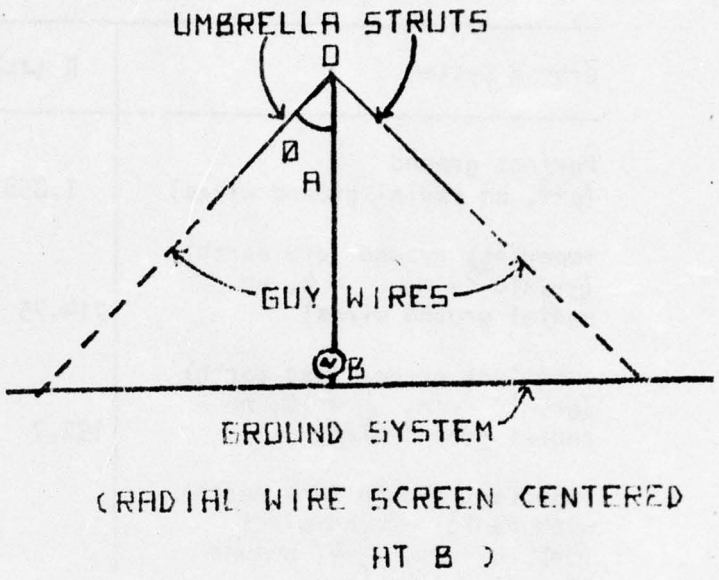
2. To calculate the gain of the two-dipole array in the end-fire direction for different interdipole distances on a transmission line, and to discuss the significance of the results towards maximizing the array gain in the end-fire direction.

III. ANTENNA MODELING PROGRAM (AMP)

The computer analysis presented here uses AMP (Antenna Modeling Program) prepared by M.B. Associates of California under the joint sponsorship of the U.S. Army, Navy and Air Force. Preliminary experience with the AMP program indicated that the accuracy of computations is critically dependent on the lengths and number of segments into which the given antenna wires are subdivided for analysis. It was also found that accuracy is high when the segments of all wires are of almost equal length. These considerations dictated the size and number of elements into which a given antenna wire was divided for analysis. This choice was further confirmed by a close check between the input impedance of a given dipole calculated from AMP and other experimental and theoretical values provided for the same antenna. A similar check was made for the umbrella top-loaded antenna using the experimental data of Gangi, et al[1] for such an antenna.

IV. UMBRELLA TOP-LOADED ANTENNA

The umbrella top-loaded antenna is sketched on the right. These antennas are electrically short, i.e., the central monopole is less than $\lambda/8$ in length. The extensions of the umbrella struts are used as guy wires. An insulating spacer electrically separates the antenna struts from the guy wires. The vertical monopole is above a ground system which consists of a perfect ground or more commonly, an imperfect ground with several radial conducting wires buried in the ground. The antenna is suspended at the point O from a balloon. The parameters of the antenna held constant in the following computer analysis were



Height of the monopole, H = 513 ft

Number of umbrella struts = 3

Angle between the struts and the monopole, $\theta_A = 49^\circ$

Radius of the monopole, strut wires, and ground radials = 0.01844 ft

Other parameters were varied one at a time and their effects on the antenna terminal impedance ($Z_A = R + jX$) are studied. Table I shows the effect of different ground parameters on the antenna impedance.

In the absence of any radial ground screen the antenna input impedance changes drastically with the type of earth. In the case of wet earth it is much lower than that for dry earth. When a radial wire ground screen is put on top of dry or wet earth it is noteworthy that the reactive component of the input impedance is the same as that for the case of a perfectly conducting earth. The resistive component, however, is lower for the ground screen case than that for the perfect earth. Maley and King[2] have also reported negative values of ΔR where,

ΔR = R (radial ground wire system) - R (perfect ground system).

Table 1. Effect of Ground System on Antenna Input Impedance (strut length 385.73 ft, frequency = 100 Khz)

Ground System	R (Ω)	X (Ω)
Perfect ground ($\sigma=\infty$, no radial ground wires)	1.858	-556.21
Imperfect ground (dry earth) ($\sigma=5\times10^{-5}$ v/m, $\epsilon_r = 4$, no radial ground wires)	714.75	-2076.0
Imperfect ground (wet earth) ($\sigma=5\times10^{-3}$ v/m, $\epsilon_r = 10$, no radial ground wires	152.7	-716.06
Imperfect ground (dry earth) with radial ground wires ($\sigma=5\times10^{-5}$ v/m, $\epsilon_r=4$, number of radial wires = 6 length of each radial wire = 596 ft	1.4064	-556.15
Imperfect ground (wet earth) with radial ground wires as above but $\sigma = 5\times10^{-3}$ v/m and $\epsilon_r = 4$	1.5718	-556.11

The effect of strut length on the antenna input impedance is shown in Table 2 for the cases of perfect ground and radial wire systems on dry earth.

Table 2. Variation of Antenna Input Impedance with Strut Length

Strut Length (ft)	Perfect Ground R	Perfect Ground X	Dry earth with radial ground wire system (radial wire length=596 ft, frequency=100 KHz) R	Dry earth with radial ground wire system (radial wire length=596 ft, frequency=100 KHz) X
300	1.9814	-693.94	1.67	-693.9
385.7	1.858	-556.21	1.4064	-556.15
515	1.555	-399.75	1.48	-399.84
600	1.333	-322.5	2.35	-323.1
700	1.0615	-248.35	4.78	-250.66

As indicated earlier, the reactive part of the input impedance is almost the same for perfect as well as radial ground system at each strut length and decreases monotonically with increasing strut length. But, it is interesting to note that for perfect ground, R decreases monotonically with increasing strut length while for the imperfect earth-radial wire ground system it assumes a minimum value somewhere in the range of strut lengths given in the table. Further, ΔR changes its sign also in the same range of strut values.

The dependence of input impedance on the length and number of radial wires is shown in Tables 3 and 4 respectively.

Table 3. Variation of Input Impedance with Radial Wire Length (dry earth, six radial ground wires, strut length=300 ft, frequency=100 KHz)

Radial Length (Meters)	Impedance	
	R (Ω)	X (Ω)
1	-0.9926	-687.10
5	0.7852	-691.27
10	1.3123	-692.67
25	1.6625	-693.86
40	1.6728	-693.93
50	1.67	-693.91
181.6	1.67	-693.9

The data for radial lengths of 1 and 5 m and perhaps for 10 m do not seem reliable when compared with similar results from other sources. These lengths are a very small fraction of a wavelength and computational error is quite likely. Besides this fact, it can be seen that the antenna impedance changes little with the length of ground radial wires above a certain length which is about 40 m in this case.

The effect of number of radial ground wires on the antenna input impedance is shown in the following table.

Table 4. Variation of Input Impedance with Number of Radial Wires (radial wire length = 596 ft, strut length = 515 ft, dry earth)

Number of Radial Wires	Impedance	
	R (Ω)	X (Ω)
6	1.4803	-399.84
12	1.5751	-399.77
24	1.5793	-399.75
48	1.57	-399.75

It can be seen from Table 4 that the input impedance for such an antenna varies very little with the number of radial wires if it is above a certain minimum which is near twelve in this case.

The variation of antenna input resistance with frequency is shown in Fig. 1. It is found that R varies approximately as f^2, which is the usual case with electrically short antenna. The antenna reactance as a function of frequency is shown in Fig. 2.

V. DIPOLE ARRAY ON A TRANSMISSION LINE

Radiation characteristics of antenna arrays depend on spacings between the individual antennas and the amplitude and phase of the voltages fed to each of them. However, it is not always easy to satisfy the feed requirements. One possible solution to this problem is to place the individual antennas (here dipoles) on a lossless transmission line and then to adjust the inter-dipole spacing and individual dipole lengths to optimize a certain radiation characteristic, e.g., gain in the end-fire or broadside direction.

In the present work only a two-dipole array of half-wave dipoles is considered and the end-fire gain of the array is calculated for various interdipole spacings on the transmission line. The line was terminated in its characteristic impedance in one case and it was open-circuited in the other. The variation of the end-fire array gain is shown as a function of inter-dipole separation in Figs. 3 and 4 for the above two cases, respectively.

In both cases the distance between successive gain maxima or minima is about 0.5λ. The array gain with open-ended transmission line is several dB higher than that for the array on a transmission line terminated in its characteristic impedance. Further, for the case of open-ended termination, the dipole array gain maxima decrease in value with increasing inter-dipole distance. The reverse is approximately true for the other case.

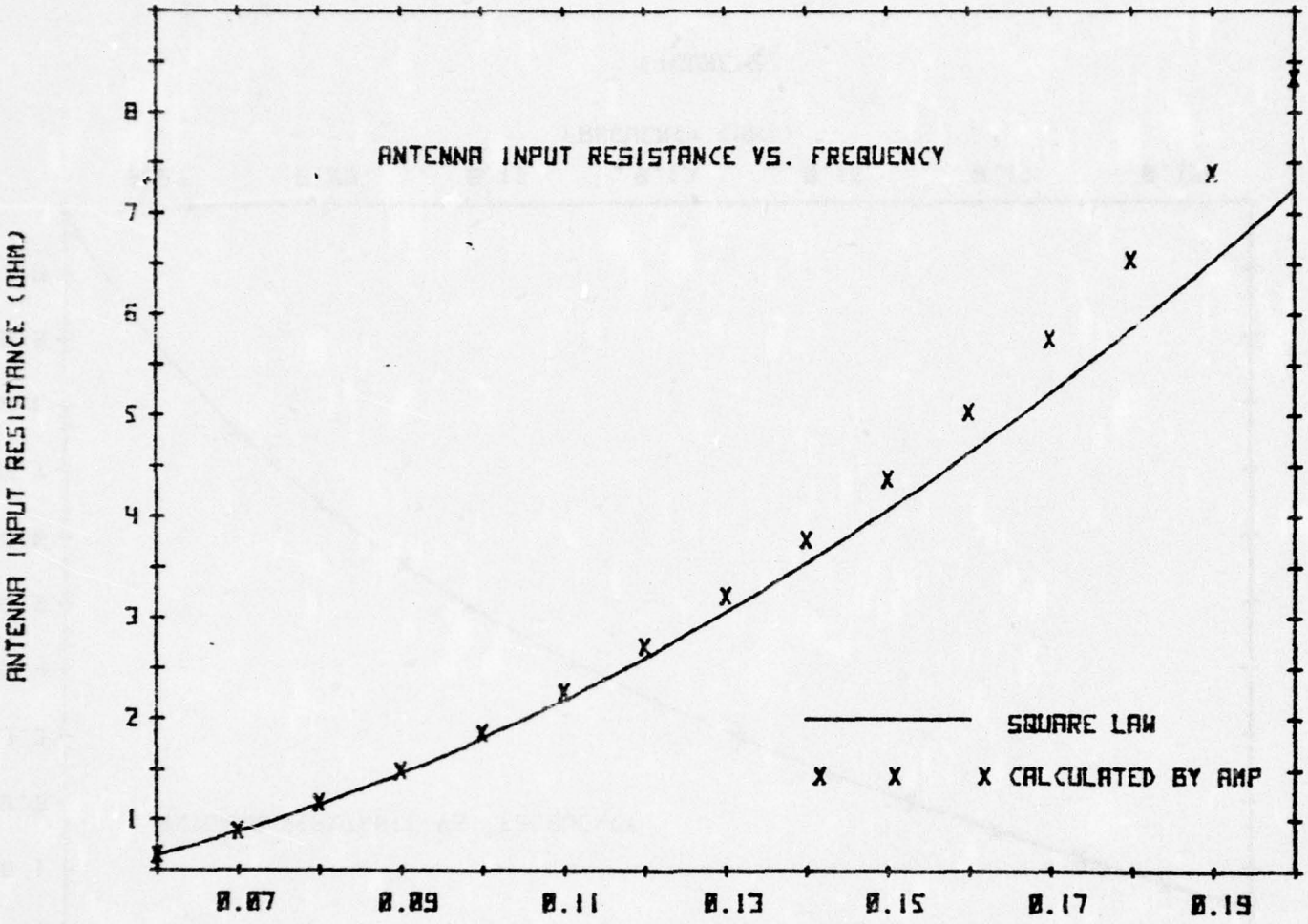

ANTENNA INPUT RESISTANCE VS. FREQUENCY
ANTENNA INPUT RESISTANCE (OHM)
8
7
6
5
4
3
2
1
0.07
0.09
0.11
0.13
0.15
0.17
0.19
FREQUENCY (MHZ)
SQUARE LAW
X X X CALCULATED BY AMP

FIGURE 1

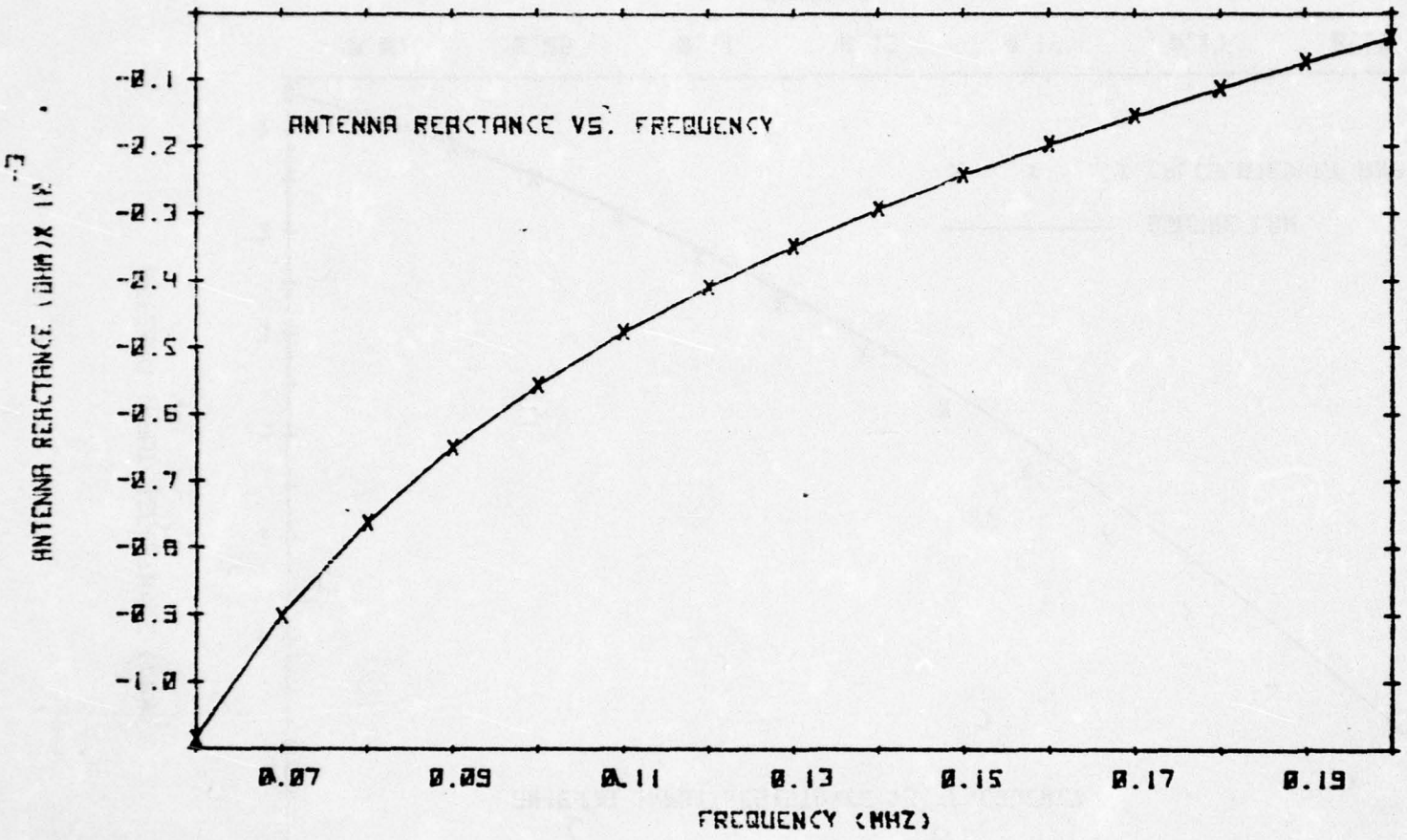

ANTENNA REACTANCE VS. FREQUENCY
ANTENNA REACTANCE (OHM)X 10
-0.1
-0.2
-0.3
-0.4
-0.5
-0.6
-0.7
-0.8
-0.9
-1.0
0.07
0.09
0.11
0.13
0.15
0.17
0.19
FREQUENCY (MHZ)

FIGURE 2

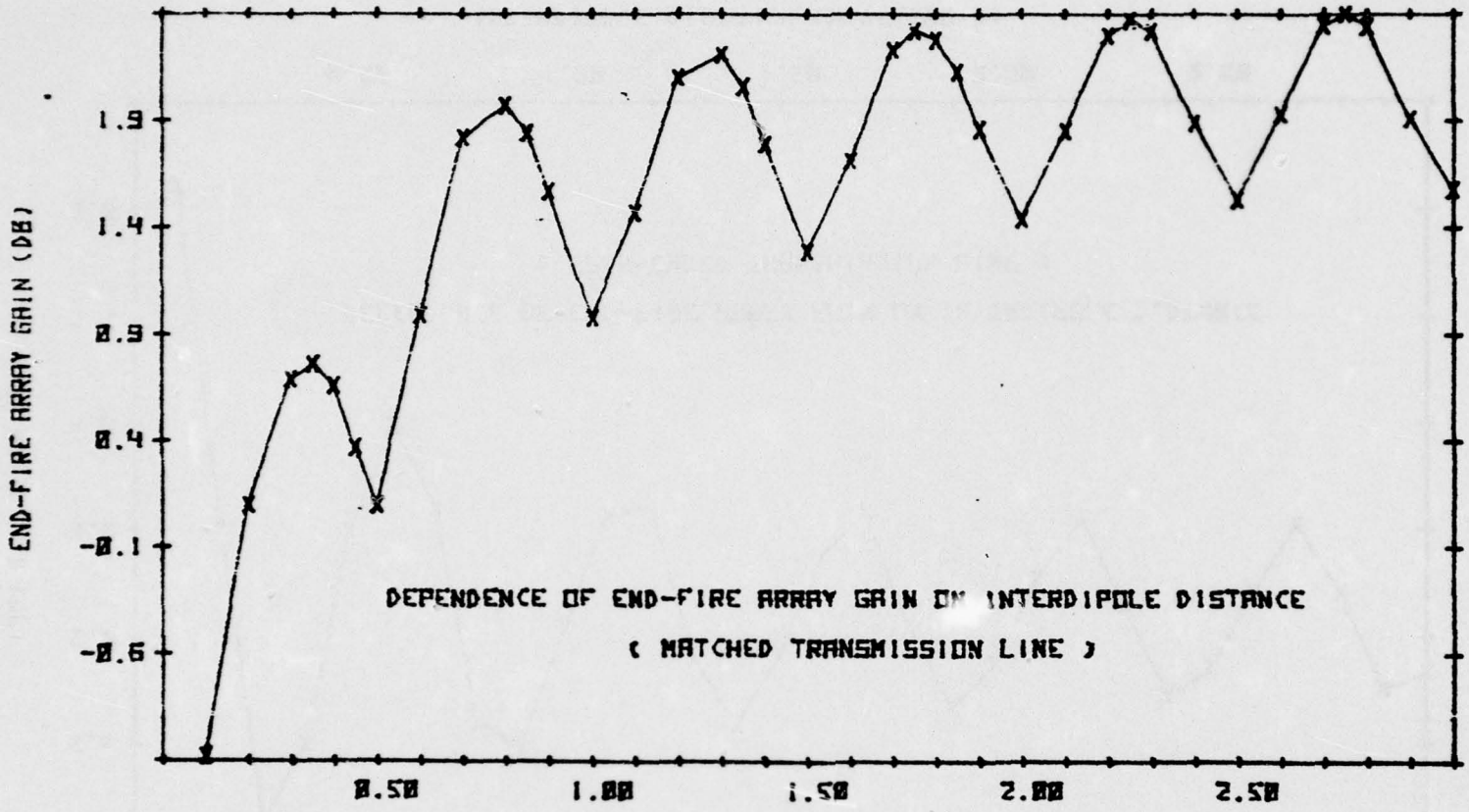

END-FIRE ARRAY GAIN (DB)
1.9
1.4
0.9
0.4
-0.1
-0.6
0.50
1.00
1.50
2.00
2.50
INTERDIPOLE DISTANCE (WAVELENGTH)
DEPENDENCE OF END-FIRE ARRAY GAIN ON INTERDIPOLE DISTANCE
(MATCHED TRANSMISSION LINE)

FIGURE 3

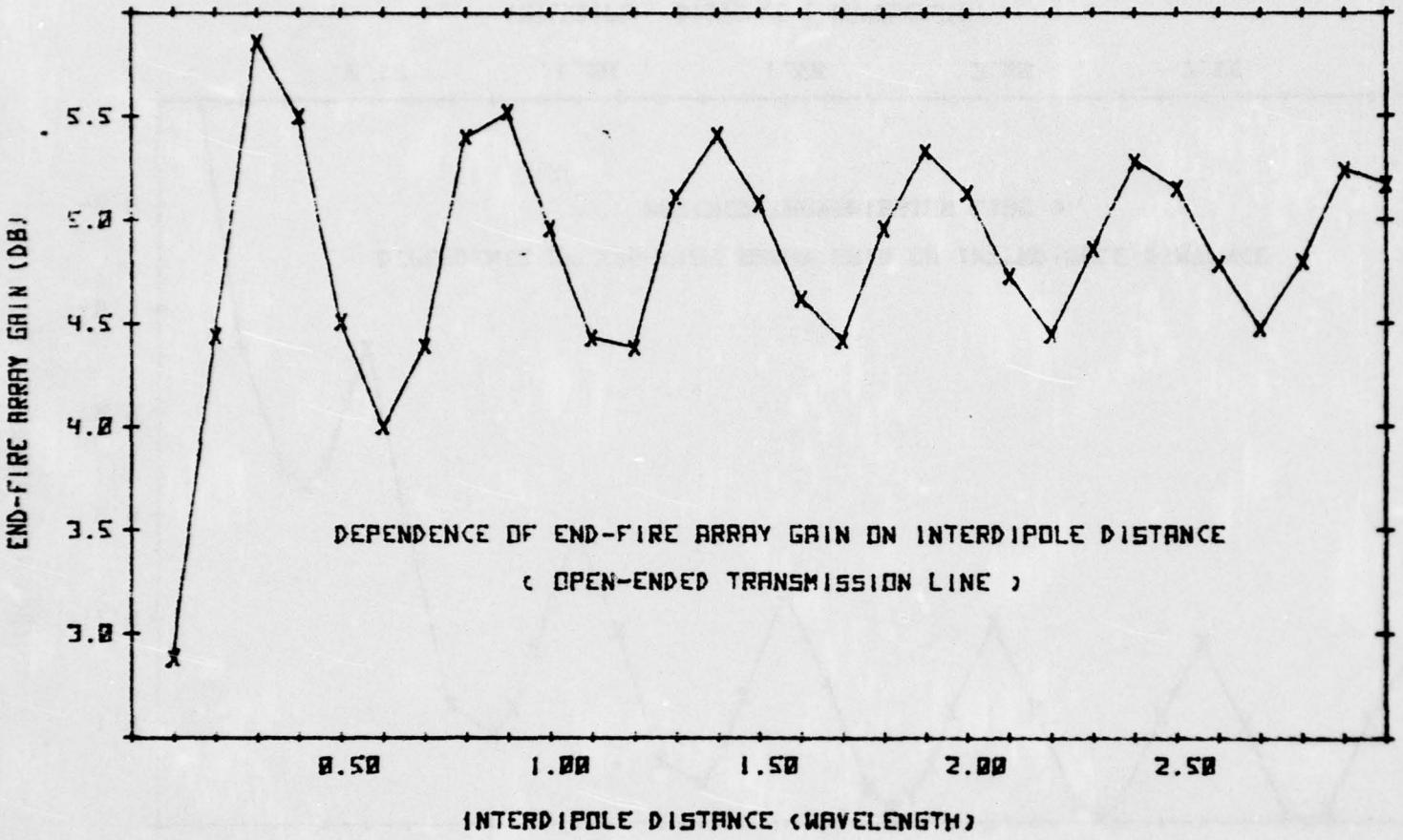

END-FIRE ARRAY GAIN (DB)
5.5
5.0
4.5
4.0
3.5
3.0
DEPENDENCE OF END-FIRE ARRAY GAIN ON INTERDIPOLE DISTANCE
(OPEN-ENDED TRANSMISSION LINE)
0.50
1.00
1.50
2.00
2.50
INTERDIPOLE DISTANCE (WAVELENGTH)

FIGURE 4

VI. CONCLUSIONS AND RECOMMENDATIONS

The input impedance of an umbrella-type, top-loaded monopole antenna is found to be a function of, among other things, the electrical properties of the earth, the radial wire ground system and the umbrella strut lengths. Higher earth conductivity results in a drastically lower value of antenna impedance. The antenna reactance for a perfectly conducting earth and an imperfect earth with radial ground-wire system is almost the same. It is observed that with certain strut lengths the antenna resistance is even lower for the latter case. It is found that above a certain minimum number and length of radial ground wires the antenna resistance is essentially constant. Further, the antenna reactance is found to be capacitative, and the antenna resistance varies approximately as the square of the frequency.

Preliminary data on the gain of an end-fire, two-dipole array situated on a transmission line indicates a higher gain when the transmission line is open-circuited than when it is matched. In both cases the gain maxima and minima are about a half-wavelength apart. Further, the gain maxima and minima of the array on an open-ended transmission line appear to be closely related to the resonant and anti-resonant conditions of the system consisting of the two dipoles and the length of transmission line between the dipoles. The situation with the other case is not quite as clearly understood. More work is needed to verify these preliminary findings.

It is felt that additional work on both these problems, viz., the umbrella type, top-loaded monopole and the dipole array on a transmission line is justified. The input impedance of an umbrella-type antenna could be further studied in terms of the angle between each of the umbrella struts and the vertical height of the monopole, number and length of struts, radius of the monopole, struts and radial ground wires and the earth conditions. It is recommended that radiation efficiency be calculated for each of these cases and be maximized.

The gain calculations for the two-dipole end-fire array situated on a transmission line should be continued for various terminations. These data are expected to provide a clue to the gain mechanism of such arrays. The work should then be extended to arrays of more than two dipoles. All this work should lead to the optimum design of an end-fire array consisting of several identical dipoles situated on a properly terminated transmission line. This design could be improved further by independently perturbing the individual lengths of these dipoles. Finally, some effort should be directed toward solving the above optimization problem analytically.

REFERENCES

1. Gangi, A.F., Sensiper S., and Dunn, G.R., "The Characteristics of Electrically Short, Umbrella Top-Loaded Antennas," IEEE Trans. on Antennas and Propagation, Vol AP-13, pp 864-871, November 1965.

2. Maley, S.W. and King, R.J., "Impedance of a Monopole Antenna with a Radial-Wire Ground System on An Imperfectly Conducting Half-Space," Part I, Journal of Research (NBS), Vol 66D, pp 175-180 (1962), 68D, pp 157-163 (1964), 68D, pp 297-301 (1964).

3. Wait, J.R. and Pope, W.A., "The Characteristics of a Vertical Antenna with a Radial Conductor Ground System," App. Sci. Res., B4, pp 177-195, 1954.

1976 USAF-ASEE SUMMER FACULTY RESEARCH PROGRAM
sponsored by
THE AIR FORCE OFFICE SCIENTIFIC RESEARCH
conducted by
AUBURN UNIVERSITY AND OHIO STATE UNIVERSITY

PARTICIPANT'S FINAL REPORT

SATELLITE BASED
REMOTE PROBING OF ATMOSPHERIC VISIBILITY:
A BIBLIOGRAPHY OF RELEVANT LITERATURE

Prepared by:	George C. Sherman, Ph.D.
Academic Rank:	Assistant Professor
Department and University:	The Institute of Optics University of Rochester
Assignment:	
(Air Force Base)	Hanscom AFB
(Laboratory)	AF Geophysics Laboratory
(Division)	Optical Physics
(Branch)	Atmospheric Optics
USAF Research Colleague:	Eric P. Shettle
Date:	September 3, 1976
Contract No.:	F44620-75-C-0031

Extra

SATELLITE BASED REMOTE PROBING OF ATMOSPHERIC VISIBILITY:

A BIBLIOGRAPHY OF RELEVANT LITERATURE

by

George C. Sherman

ABSTRACT

Since tactical military operations are affected strongly by the visibility conditions of the atmosphere in the theater of operations, it would be useful to have the means for determining the slant range visibility under various geometries in remote areas by utilizing data obtained from satellite measurements. At present, there is no known method for obtaining the desired information using satellite based measurements, nor is there any published literature that deals with the subject directly. There is, however, a small body of literature that deals with the determination of the properties of particulates suspended in the atmosphere. Such literature is pertinent to the problem at hand since the properties of the aerosol particles present in the atmosphere are the primary determinants of atmospheric visibility for fixed directions of viewing and illumination.

The present report is a bibliography of literature relevant to the problem of attempting to determine slant path atmospheric visibility and contrast reduction from satellite measurements. Of the literature uncovered that deals with remote sensing of the atmospheric aerosol from satellites, the bibliography includes all journal papers, all reports not adequately covered by journal papers or later reports, and all oral papers presented at meetings published in proceedings when they are not superseded by other publications. Literature dealing with ground or aircraft based remote sensing of aerosols is included provided the method used has potential for being applied with a satellite platform. The bibliography also includes several primary sources in the form of books, review papers, pedagodgial summaries, and bibliographies that treat fundamental subjects of interest including visibility, atmospheric aerosols, remote sensing, and models of the optical properties of the atmosphere.

INTRODUCTION

Tactical operations are affected strongly by the visibility conditions of the atmosphere in the theater of operations. Not only is the ability of the military personnel to see important, but of equal importance is the influence that the atmospheric aerosol has on the performance of electro-optical military systems by reducing light transmission and optical contrast. Advanced knowledge of the optical properties of the atmospheric aerosol present in the theater of operations would help dictate the optimum electro-optical systems to be used and would be a valuable tool for the forecasting of the probable success of planned missions. Techniques that apply satellite measurements would permit determination of the desired information over a wide range of areas and over hostile territory.

OBJECTIVE

The object of the present study is to search the atmospheric-optics and remote-sensing literature to identify the available literature dealing with remote sensing techniques that may be applicable to the probing of atmospheric visibility from a satellite. Of particular interest are methods for determining the contrast reduction to be expected along slant paths from aircraft in the lower atmosphere.

CONCLUSIONS

The results of the literature search are presented in the bibliography. No papers dealing directly with the problem of remote sensing of visibility from a satellite platform were found. There is, however, a small body of literature concerned with satellite-based probing of the properties of particulates suspended in the atmosphere. That literature is pertinent to the problem at hand since the properties of the aerosol particles present in the atmosphere are the primary determinants of atmospheric visibility for fixed directions of viewing and illumination. Of that body of literature uncovered, the bibliography includes all journal papers, all reports not adequately covered by journal papers or later reports, and all oral papers presented at meetings published in proceedings when they are not superseded by other publications. Reference to the interim reports and oral papers can be found in the primary references given in the bibliography. Literature dealing with ground or aircraft based remote sensing of aerosols is included provided the method used has potential for being applied with a satellite platform.

In order to make the connection between the aerosol probing papers presented in this bibliography and the visibility problem of interest, references are included that tell how the atmospheric visibility and contrast reduction are determined from a knowledge of the properties of the aerosol particles present in the atmosphere. The reports which present the atmospheric models required for the relevant calculations are included also. Finally, for the convenience of the user, the bibliography includes some basic references in the form of books, review articles, pedagogical papers, and bibliographies that provide a ready access to the fundamentals and the current state of the art of the pertinent fields of visibility, atmospheric aerosols, and remote probing of the atmosphere.

AD-A033 822 AUBURN UNIV ALA SCHOOL OF ENGINEERING F/G 14/2
1976 USAF-ASEE SUMMER FACULTY RESEARCH PROGRAM.(U)
SEP 76 J F O'BRIEN F44620-75-C-0031
UNCLASSIFIED AFOSR-TR-76-1419 NL

6 OF 9
AD A033822



ACKNOWLEDGEMENT

The USAF-ASEE Sponsored Summer Faculty Research Program has been an especially rewarding experience for me. I appreciate the financial support provided by the Air Force Systems Command and the administrative support provided by Mr. Fred O'Brien of Auburn University and Mr. Henry Novak of AFGL.

I have enjoyed working with the Atmospheric Optics Branch of the Optical Physics Division of AFGL and wish to thank the members of the group there for their support. Numerous technical discussions with Mr. Eric Shettle and Dr. Robert Fenn were especially helpful to me.

An important part of my research consisted of searching the scientific literature. I wish to express my appreciation to Mr. Randall Bergmann of the AFGL Research Library for working closely with me on that task.

BIBLIOGRAPHY

Barrett, E. W., and O. Ben-Dov, 1967: Application of the lidar to air pollution measurements. J. Appl. Meteorology 6, 500-515.

Bullrich, K., 1964: Scattered radiation in the atmosphere and the natural aerosol. In: H. E. Landsberg and J. van Mieghem (eds.), Advances in Geophysics, Vol. 10 (Academic Press, New York), pp 99-260.

Collis, R. T. H., P. B. Russell, E. E. Uthe, and W. Viezee, 1973: Lidar observations of atmospheric particulate content. Proc. of the UCLA International Conf. on Radiation and Remote Probing of the Atmosphere, 28-30 Aug. 1973, Dept. of Meteorology, UCLA, Los Angeles, CA, J. G. Kuriyan (ed.), pp. 367-394.

Collis, R. T. H., W. Viezee, E. E. Uthe, and J. Oblanas, 1970: Visibility measurement for aircraft landing operations. Stanford Research Institute, Menlo Park, CA, Report No. AFCRL-70-0598, Sept., 148 p., (AD-716-483).

Coulson, K. L., and R. S. Fraser, 1975: Radiation in the atmosphere. Reviews of Geophysics and Space Physics 13, 732-836.

Cunnold, D. M., C. R. Gray, and D. C. Merritt, 1973: Stratospheric aerosol layer detection. J. Geophys. Res. 78, 920-931.

Curcio, J. A. and G. L. Knestrick, 1958: Correlation of atmospheric transmission with backscattering. J. Opt. Soc. Am. 48, 686-689.

Curran, R. J., and W. L. Barnes, 1976: Active probing of the atmosphere to infer skylight effects. Goddard Space Flight Center, Greenbelt, MD. Preprint X-941-76-34, 31p.

Deirmendjian, D., 1964: Scattering and polarization properties of water clouds and hazes in the visible and infrared. Appl. Opt. 3, 187-196.

Deirmendjian, D., 1969: Electromagnetic Scattering on Spherical Polydispersions. (American Elsevier Publishing Co., Inc., New York).

Derr, V. E. (ed.), 1972: Remote sensing of the troposphere. National Oceanic and Atmospheric Administration, Environmental Research Laboratories, Wave Propagation Laboratory, Boulder, Colorado, 15 Aug, (For sale by U.S. Govt. Printing Office).

Derr, V. E., M. J. Post, R. L. Schwiesow, R. F. Calfee, and G. T. McNice, 1974: A Theoretical analysis of the information content of lidar atmospheric returns. National Oceanic and Atmospheric Administration, Boulder, CO. Report No. NOAA-TR-ERL296-WPL29, (Nov.), 284 p., (COM-75-10393/7st).

Duntley, S. Q., A. R. Boileau, and R. W. Preisendorfer, 1957: Image transmission by the troposphere I, J. Opt. Soc. Am. 47, 499-506.

Duntley, S. Q., J. I. Gordon, J. H. Taylor, C. T. White, A. R. Boileau, J. E. Tyler, R. W. Austin and J. L. Harris, 1964: Visibility. Appl. Opt., 3, 550-598.

Edgerton, C. F., 1974: Visibility at sea: an annotated bibliography. Report, Visibility Laboratory, University of Calif., San Diego, CA, Naval Weapons Center Contract No. N000123-74-C-0251 (AD 786-758).

Elterman, L., 1968: UV, visible, and IR attenuation for altitudes to 50 km, 1968. AFGL, Hanscom AFB, MA, Report No. AFCRL-68-0153, April, 49 p.

Elterman, L., 1970a: Vertical-attenuation model with eight surface meteorological ranges 2 to 13 kilometers. AFGL, Hanscom AFB, MA, Report No. AFCRL-70-0200, Mar., 58 p.

Elterman, L., 1970b: Relationships between vertical attenuation and surface meteorological range. Appl. Opt. 9, 1804-1810.

Evans, W. E., E. J. Wiegman, W. Viezee, and M. G. H. Ligda, 1966: Performance specifications for a meteorological satellite lidar. Report, Stanford Research Institute, Menlo Park, CA, NASA Contract NASr-49(22), [N6629977].

Fenn, R. W., 1966: Correlation between atmospheric backscattering and meteorological visual range. Appl. Opt. 5, 293-295.

Fenn, R. W., and K. Agazarian, 1972: Atmospheric haze models for contrast transmittance calculations. Electro-optical systems design conf., 12-14 Sept. 1972, New York Industrial and Scientific Conference Management, Inc.

Fernald, F. G., B. M. Herman, and J. A. Reagan, 1972: Determination of aerosol height distribution by lidar. J. Appl. Meteorology 11, 482-488.

Fesenkov, V. G., 1967: Sounding of optical properties of the Earth's atmosphere by means of artificial satellites. Astronomicheskii Zhurnal, Moscow, 44, 3-11. Transl. into English in Soviet Astronomy AJ, 11, 1-7 (1967).

Fraser, R. S., 1964: Computed intensity and polarization of light scattered outwards from the earth and an overlying aerosol. J. Opt. Soc. Am. 54, 157-168.

Fraser, R. S., 1974: Measurement of atmospheric particles from satellites. Proc. of a Technical Conf. on the Observation and Measurement of Atmospheric Pollution, 30 July - 4 August 1973, Helsinki. World Meteorological Organization - No. 368, Special Environmental Report No. 3, pp. 443-454.

Fraser, R. S., 1976: Satellite measurement of mass of Sahara dust in the atmosphere. Appl. Opt. (in press).

Fymat, A. L., 1974: Microstructure, composition and dynamical evolution of scattering particulates determined from optical data. Proc. of the International Colloquium on Drops and Bubbles, Vol. II, 28-30 Aug. 1974, Pasadena, CA, Calif. Institute of Technology and Jet Propulsion Lab., pp 572-591.

Fymat, A. L., 1975a: Remote monitoring of environmental particulate pollution: A problem in inversion of first-kind integral equations. Appl. Math. and Computation 1, 131-185.

Fymat, A. L., 1975b: Remote probing of atmospheric particulates from radiation extinction experiments: a review of methods. Conf. on Optical Propagation in the Atmosphere, 27-31 Oct. 1975, Lyngby, Denmark. Electromagnetic Wave Propagation Panel of the Advisory Group for Aerospace Research and Development, North Atlantic Treaty Organization, pp. 12-1 to 12-30.

Fymat, A. L., 1976a: Inverse atmospheric radiative transfer problems: A nonlinear minimization search method of solution. Phys. Earth Planet. Inter. 12 (in press).

Fymat, A. L., 1976b: Methodology for optical remote sensing of clouds and aerosols. Symposium on Radiation in the Atmosphere, 19-28 Aug. 1976, Garmisch-Partenkirchen, FR Germany, International Association of Meteorology and Atmospheric Physics, Radiation Commission and Commission on Atmospheric Chemistry and Global Pollution.

Gray, C. R., H. L. Malchow, D. C. Merritt, R. E. Var, 1971: Aerosol monitoring by satellite horizon scan. First Joint Conference on Sensing of Environmental Pollutants, 8-10 Nov. 1971, Palo Alto, CA sponsored by Am. Chem. Soc., AIAA, EPA, IEEE, Instrument Soc. Am., NASA, and NOAA (available from AIAA Library, 750 3rd Ave., New York, N.Y. 10017), pp. 231-238.

Gray, C. R., H. L. Malchow, D. C. Merritt, R. E. Var, and C. K. Whitney, 1973: Aerosol physical properties from satellite horizon inversion. Mass. Inst. of Technology, Dept. of Meteorology and the Charles S. Draper Laboratory, Inc., Cambridge, MA, NASA Contract NAS1-11092. Report No. NASA CR-112311. (73N27330).

Griggs, M., 1973: Determination of aerosol content in the atmosphere. Symposium on significant results obtained from the Earth Resources Technology Satellite-1, Vol. I, 5-9 Mar. 1973, New Carrollton, MD held by Goddard Space Flight Center. NASA SP-327, pp. 1105-1113.

Griggs, M., 1973b: Determination of aerosol content in the atmosphere from ERTS-1 data. Science Applications, Inc., LaJolla, CA. National Aeronautics and Space Administration Contract No. NAS5-21860. Report No. CR-137441, Oct., 55 p.

Griggs, M., 1975a: A study on the determination of the atmospheric aerosol content using ERTS data. Science Applications, Inc., LaJolla, CA. Final report on contract NOAA-4-35365, Report No. SAI-75-566-LJ, April, 18 p.

Griggs, M., 1975b: Measurements of atmospheric aerosol optical thickness over water using ERTS-1 data. APCA Journal 25, 622-626.

Grossman, J. J., H. G. Gross, and H. A. Hyatt, 1973: Study of laser remote sensing techniques from space platforms. Tenth annual meeting of the Am. Astronautical Society, 19-21 June 1973, Dallas, TX (73A38591).

Harris, F. S., Jr., 1971: A bibliography on atmospheric particulates. In: I. H. Blifford, Jr. (ed.) Particulate Models: Their Validity and Application. A work shop held 21 Aug. 1970 at National Center for Atmospheric Research, Boulder, Colorado. Report No. NCAR-TN/PROC-68 (Aug.), pp. 256-294.

Hall, F. F., Jr., 1974: Laser systems for monitoring the environment. In: Laser Applications (Academic Press, Inc.).

Harris, F. S., Jr., 1975: Laser applications to atmospheric sciences - a bibliography. Old Dominion University, Norfolk, VA. NASA contract NGR47-003-068. Report No. NASA CR-2536, June, 134 p.

Harris, F. S., Jr., 1976: Atmospheric aerosols: A literature summary of their physical characteristics and chemical composition. Old Dominion University, Norfolk, VA, Report No. NASA CR-2626, Jan.

Herman, B. M., M. King, and J. A. Reagan, 1976: The use of inversion techniques for lidar and radiometric aerosol studies. Symposium on Radiation in the Atmosphere, 19-28 Aug. 1976, Garmisch-Partenkirchen, FRG, International Association of Meteorology and Atmospheric Physics, Radiation Commission and Commission on Atmospheric Chemistry and Global Pollution.

Hodkinson, J. R., 1966: The optical measurement of aerosols. In: C. N. Davies (ed.) Aerosol Science (Academic Press, New York) Chap. X, pp. 287-357.

Jacobowitz, H., and K. L. Coulson, 1972: The effects of aerosols on the outgoing terrestrial radiation. Conf. on Atmospheric Radiation, 7-9 Aug. 1972, Fort Collins, Colorado. Amer. Meteorological Society, pp. 24-28.

Jacobowitz, H., and K. L. Coulson, 1973: Effects of aerosols on the determination of the temperature of the Earth's surface from radiance measurements at 11.2μm. Report, National Oceanic and Atmospheric Administration, Report No. NOAA-TR-NESS 66, Sept., 18 p.

Jacobowitz, H., W. L. Smith, and A. J. Drummond, 1971: Satellite measurements of aerosol backscattered radiation from the Nimbus F ERB experiment. Conf. on Air Pollution Meteorology, 5-9 April, 1971, Raleigh, N.C. American Meteorological Society.

Jacobowitz, H., W. L. Smith, and A. J. Drummond, 1972: Satellite measurements of aerosol backscattered radiation from the Nimbus F Earth radiation budget experiment. Report, National Oceanic and Atmospheric Administration, Report No. NOAA TR NESS 60, Aug., 9 p. (COM-72-51031).

Kattawar, G. W., and G. N. Plass, 1968: Influence of particle size distribution on reflected and transmitted light from clouds. Appl. Opt. 7, 869-878.

Koepke, P. and H. Quenzel, 1976: On the feasibility to determine the atmospheric turbidity from a geostationary satellite. Symposium on Radiation in the Atmosphere, 19-28 Aug., 1976, Garmisch-Partenkirchen, FRG, International Association of Meteorology and Atmospheric Physics, Radiation Commission and Commission on Atmospheric Chemistry and Global Pollution.

Kostko, O. K., 1976: Use of laser radar in atmospheric investigations (review). Sov. J. Quant. Electron. 5, 1161-1177.

Kuriyan, J. G., 1973: Particulate sizes from polarization measurements. Proc. of the UCLA International Conf. on Radiation and Remote Probing of the Atmosphere, 28-30 Aug. 1973, Los Angeles, CA, Dept. of Meteorology, UCLA. J. G. Kuriyan (ed.), pp. 337-366.

Kuriyan, J. G., 1975: Remote measurement of aerosol particle characteristics and their significance to meteorology. Opt. Engineering 14, 332-338.

Kuriyan, J. G., D. H. Phillips, and R. C. Willson, 1974: Determination of optical parameters of atmospheric particulates from ground-based polarimeter measurements. Quart. J. R. Met. Soc., 100, 665-677.

Ludwig, C. B., M. Griggs, W. Malkmus, and E. R. Bartle, 1973: Air pollution measurements from satellites. General Dynamics, Corp., San Diego, CA National Aeronautics and Space Administration Contract NAS1-10466, Report No. NASA CR-2324, Nov., 222p.

Malila, W. A., and R. F. Nalepka, 1973: Atmospheric Effects in ERTS-1 data, and advanced information extraction techniques. Symposium on significant results obtained from the Earth Resources Technology Satellite-1, Vol. I, 5-9 Mar. 1973, New Carrollton, MD held by Goddard Space Flight Center, NASA SP-327, pp. 1097-1104.

Marchuk, G. I., and G. A. Mikhailov, 1973: Solution of the radiative transfer theory problems by the Monte Carlo Method. Proc. of the UCLA Conf. on Radiation and Remote Probing of the Atmosphere, 28-30 Aug. 1973, Los Angeles, CA, Dept. of Meteorology, UCLA. J. G. Kuriyan (ed.), pp. 58-73.

McClatchey, R. A., R. W. Fenn, J. E. A. Selby, F. E. Volz, J. S. Garing, 1972: Optical properties of the atmosphere, (Third Edition). AFGL, Hanscom AFB, MA, Report No. AFCRL-72-0497, 24 Aug., 108 p.

McClintock, M., T. A. Hariharan, and A. McLellan IV, 1970: Studies on techniques for satellite surveillance of global atmospheric pollution. Space Science and Engineering Center, University of Wisconsin, Madison. National Air Pollution Control Administration Contract CPA 22-69-101, Sept., 88 p.

McClintock, M., A. McLellan, and L. A. Sromovsky, 1971: Satellite measurement of spectral turbidity and albedo, and their rates of change. Space Science and Engineering Center, Univ. of Wisconsin, Madison. Environmental Protection Agency Contract 68-02-0002. Report No. UWI-SSEC-GAP-71-003.

McClintock, M., A. McLellan, and L. Turner, 1972: Research on the optical state of the atmosphere. Space Science and Engineering Center, University of Wisconsin, Madison. Environmental Protection Agency Contract EPA-68-02-0337. Report No. EPA-R3-72-027, Nov., 60 p. (PB-220-394/1).

Middleton, W. E. K., 1952: Vision Through the Atmosphere (University of Toronto Press, Toronto).

National Aeronautics and Space Administration, 1971: Particles in the atmosphere, Sec. IV of Remote Measurement of Pollution, the report of a working group sponsored by NASA and administered by Langley Research Center. Convened at Norfolk, VA, 16-20 Aug. 1971.

Neuman, J., W. Low, A. Cohen, and F. Goldwater, 1971: Application of laser techniques to investigation of clouds and particles in the atmosphere. Final Report, Dept. of Meteorology, Hebrew University, Jerusalem, Israel. Contrib-71-12NOAA-72091644. (COM-72-11427).

Newell, R. E., and C. R. Gray, 1972: Meteorological and ecological monitoring of the stratosphere and mesosphere. Report, Mass. Institute of Technology, Cambridge, MA, NASA Contract NAS1-9884, Report No. NASA CR-2094, 165 p.

Plech, K. R., and J. R. Schott, 1974: Atmospheric corrections for satellite water quality studies. Meeting on Scanners and Imagery Systems for Earth Observation, 19-20 Aug. 1974, San Diego, CA, Society of Photo-Optical Instrumentation Engineers. pp. 84-89.

Plass, G. N., and G. W. Kattawar, 1968: Calculations of reflected and transmitted radiance for Earth's atmosphere. Appl. Opt. 7, 1129-1135.

Plass, G. N., and G. W. Kattawar, 1970: Polarization of the radiation reflected and transmitted by the Earth's atmosphere. Appl. Opt. 9, 1122-1130.

Plass, G. N., and G. W. Kattawar, 1972: Effect of aerosol variation on radiance in the Earth's atmosphere-ocean system. Appl. Opt. 11, 1598-1604.

Potter, J. F., and M. A. Mendlowitz, 1975: On the determination of haze levels from Landsat data. Proc. of the Tenth International Symposium on Remote Sensing of the Environment (Vol. II), 6-10 Oct. 1975, Ann Arbor, Michigan. Environmental Research Institute of Mich., pp. 695-703.

Reagan, J. A. and B. M. Herman, 1971: Three optical methods for remotely measuring aerosol size distributions. First Joint Conf. on Sensing of Environmental Pollutants, 8-10 Nov. 1971, Palo Alto, CA, pp. 59-68, (72A10528).

Rogers, E. H., 1972: Study to demonstrate the feasibility of and determine the optimum method of remote haze monitoring by satellite. Progress Report, Aerospace Corp., El Segundo, CA, Report No. NASA CR-128093 (72N31360).

Rogers, R. H., and K. Peacock, 1973: A technique for correcting ERTS data for solar and atmospheric effects. Symposium on Significant Results Obtained from the Earth Resources Technology Satellite-1, Vol. I, 5-9 Mar. 1973, New Carrollton, MD held by Goddard Space Flight Center. NASA SP-327, pp. 1115-1122.

Rozenberg, G. V., 1968: Optical investigations of atmospheric aerosol. Soviet Uspekhi 11, 353-380.

Ruger, J. F., 1975: Using lidar for measuring visibility. Conf. on Optical Propagation in the Atmosphere, 27-31 Oct. 1975, Lyngby, Denmark. Electromagnetic Wave Propagation Panel of the Advisory Group for Aerospace Research and Development, North Atlantic Treaty Organization. pp. 44-1 to 44-8.

Schappert, G. T., 1971: Techniques for Measuring Visibility. Appl. Opt. 10, 2325-2328.

Sekera, Z., 1967: Determination of atmospheric parameters from measurements of polarization of upward radiation by satellite or space probe. Icarus 6, 348-359.

Sekera, Z., and R. E. Bradbury, 1973: Development of an experiment for visible radiation polarization measurements from a satellite. Institute of Geophysics and Planetary Physics, University of Calif., Los Angeles, CA. NASA Contract NAS1-10107, Report No. NASA CR-2297 (N74-14268/8GA).

Sekera, Z., and L. L. Stowe Jr., 1973: Effects of particulate matter on the radiance of terrestrial infrared radiation: Theory. Beitr. Phys. Atmos. 46, 101-111.

Severs, R. K., 1974: Atmospheric aerosol measurements from air or space platforms. 67th Annual Meeting of the Air Pollution Control Association, 9-13 June 1974, Denver, Colorado, Paper 74-115.

Severs, R. K., and J. C. Peng, 1975: Characterization of ambient aerosols by seven channel solar radiometry and other measurements. Proc. of the 68th Annual Meeting of the Air Pollution Control Association, 15-20 June 1975, Boston, MA, Paper 75-28.5.

Shettle, E., 1973: Calculations of the optical contrast reduction in the visible and near IR through clear and hazy atmospheres. Unpublished report of AFCRL Environmental Consultation Service, RCS No. 3-101. Available from Air Force Geophysics Laboratory (OPA), Hanscom AFB, MA 01731.

Shettle, E. P., 1976: Effects of different aerosol models on radiation transfer in scattering atmospheres. Symposium on Radiation in the Atmosphere, 19-28 Aug. 1976, Garmisch-Partenkirchen, FRG, International Association of Meteorology and Atmospheric Physics, Radiation Commission and Commission on Atmospheric Chemistry and Global Pollution.

Shettle, E. P., and R. W. Fenn, 1975: Models of the atmospheric aerosols and their optical properties. Conf. on Optical Propagation in the Atmosphere, 27-31 Oct. 1975, Lyngby, Denmark. Electromagnetic Wave Propagation Panel of the Advisory Group for Aerospace Research and Development, North Atlantic Treaty Organization, pp. 2-1 to 2-16.

Shipley, S. T., J. H. Joseph, J. T. Trauger, P. J. Guetter, E. W. Eloranta, J. E. Lawler, W. J. Wiscombe, A. P. Odell, F. L. Roesler, J. A. Weinman, 1975: The evaluation of a shuttle borne lidar experiment to measure the global distribution of aerosols and their effect on the atmospheric heat budget. Final Report, Dept. of Meteorology, Univ. of Wisconsin, Madison. NASA Grant NSG 1057, Report No. NASA-CR-146134, April, 150 p. (N76-16597).

Steffens, C., 1956: Visibility and air pollution. In P. L. Magill, F. R. Holden, C. Ackley (eds.), Air Pollution Handbook (McGraw-Hill Book Co., Inc., N.Y.), pp 6-1 to 6-43.

Stowe, L. L., Jr., 1974: Effects of particulate matter on the radiance of terrestrial infrared radiation: results. J. Atmospheric Sciences, 31, 755-767.

Stowe, L. L., Jr., and H. E. Fleming, 1976: The error in satellite retrieved temperature profiles due to the effects of atmospheric aerosol particles. Symposium on Radiation in the Atmosphere, 19-28 Aug. 1976, Garmisch-Partenkirchen, FRG, International Association of Meteorology and Atmospheric Physics, Radiation Commission and Commission on Atmospheric Chemistry and Global Pollution.

Stowe, L. L., Jr. and H. D. Giroux, 1972: Study of the effects of atmospheric turbidity on temperature soundings, radiation energetics, and polarization of terrestrial infrared radiation. University of Calif., Los Angeles, National Oceanic and Atmospheric Administration grant no. NOAA-E143-69(G). Final report, 1 Aug. 71 - 1 Aug. 72, Jul., 71 p.

Takashima, T., 1975: Polarimetric investigation of the size distribution and refractive index of the atmospheric aerosols by using remote sensing satellite measurements. J. of the Meteorological Society of Japan 53, 458-466 (76A29325).

Takashima, T., 1976: Polarimeter investigation of the atmospheric aerosols over the ocean surface at $\lambda = 0.40\mu m$ by remote sensing. Symposium on Radiation in the Atmosphere, 19-28 Aug. 1976, Garmisch-Partenkirchen, FRG, International Association of Meteorology and Atmospheric Physics, Radiation Commission and Commission on Atmospheric Chemistry and Global Pollution.

Takashima, T., and Rao, 1976: Determination of atmospheric turbidity and surface properties from photopolarimetry of the diffuse radiation at the top of the atmosphere. Symposium on Radiation in the Atmosphere, 19-28 Aug. 1976, Garmisch-Partenkirchen, FRG, International Association of Meteorology and Atmospheric Physics, Radiation Commission and Commission on Atmospheric Chemistry and Global Pollution.

Thomas, R. W., and A. C. Holland, 1976: On the use of maximum sky polarization as an index of atmospheric aerosol properties. Symposium on Radiation in the Atmosphere, 19-28 Aug. 1976, Garmisch-Partenkirchen, FRG, International Association of Meteorology and Atmospheric Physics, Radiation Commission and Commission on Atmospheric Chemistry and Global Pollution.

Turner, R. E., and M. M. Spencer, 1972: Atmospheric model for correction of spacecraft data. Proc. of the Eighth International Symposium on Remote Sensing of Environment (Vol. II), 2-6 Oct. 1972, Ann Arbor, Michigan, Environmental Research Institute of Mich., pp. 895-934.

Viezee, W., J. Oblanas, and R. T. H. Collis, 1973a: Lidar observations of slant range visibility for aircraft landing operations. Stanford Research Institute, Menlo Park, CA, Report no. AFCRL-TR-73-0146, Feb., 46 p. (AD 760-128).

Viezee, W., J. Oblanas, R. T. H. Collis, 1973b: Evaluation of the lidar technique of determining slant range visibility for aircraft landings operations. Stanford Research Institute, Menlo Park, CA, Report No. AFCRL-TR-73-0708, Nov., 138 p. (AD 776-054).

Wang, C. P., 1974: Application of lasers in atmospheric probing. Acta Astronautica 1, 105-123.

Wolf Research and Development Group, 1976: A study of techniques for the remote sensing of aerosols. Report, Applied Systems Department, EG&G/ Washington Analytical Services Center, Inc. Prepared for NASA, Wallops Flight Center, Jan., Report No. 001-76.

Yamamoto, G., and M. Tanaka, 1973: Radiative transfer of visible radiation in turbid atmospheres. Proc. of the UCLA International Conf. on Radiation and Remote Probing of the Atmosphere, 28-30 Aug. 1973, Los Angeles, CA, Dept. of Meteorology, UCLA. J. G. Kuriyan (ed.), pp. 74-134.

Zuev, V. E., G. M. Krekov, and I. E. Naats, 1974: Determination of aerosol parameters of the atmosphere by laser sounding from space. Acta Astronautica 1, 93-103 (74A33306).

1976 USAF-ASEE SUMMER FACULTY RESEARCH PROGRAM
sponsored by
THE AIR FORCE OFFICE OF SCIENTIFIC RESEARCH
conducted by
AUBURN UNIVERSITY AND OHIO STATE UNIVERSITY

PARTICIPANT'S FINAL REPORT

ANALYSIS OF SPECTROSCOPIC DATA FOR TRACE GASES IN THE EARTH'S ATMOSPHERE

Prepared by:	Louise Gray Young, Ph.D.
Academic Rank:	Research Scientist
Department and University:	Physics Department Texas A & M University

Assignment:

(Air Force Base)	Hanscom Field AFB
(Laboratory)	Air Force Geophysics Laboratory
(Division)	Optical Physics
(Branch)	Infrared Physics
USAF Research Colleague:	Robert A. Mc Clatchey, Ph.D.
Date:	August 13, 1976
Contract No.:	F44620-75-C-0031

ANALYSIS OF SPECTROSCOPIC DATA FOR TRACE GASES IN THE EARTH'S ATMOSPHERE

by
Louise Gray Young

ABSTRACT

Two computer programs are described. Each is designed to obtain more accurate spectroscopic constants from a least-squares fit to laboratory measurements of the frequencies for a large number of lines in the infrared region of the spectrum. One program is for the ammonia molecule, the other for the nitric oxide molecule. Different physical proces contribute to the energy states from which the lines arise. The two computer programs were developed in parallel and ten weeks proved to be too short a time for the work to be completed.

ACKNOWLEDGMENT

The author is grateful to the Air Force Systems Command for support of this summer research. Appreciation is due to Col. Bernard S. Morgan, Commander AFGL, and to Dr. John Howard, Chief Scientist, for allowing me to participate in this productive summer program. The Optical Physics Laboratory, and the Infrared Physics branch, in particular, provided a pleasant and helpful work environment. It has been a pleasure and an educational experience to work with Drs. S. A. Clough, L. Rothman, and Robert McClatchey.

INTRODUCTION

The research performed at AFGL covers a broad spectrum of topics in the environmental sciences. In the Optical Physics Laboratory, analyses are conducted to determine and understand the optical and infrared properties of the atmosphere. These properties determine how well the atmosphere transmits radiant energy, and also how much energy the atmosphere radiates, both under natural and perturbed conditions. Any optical or infrared detection, or surveillance , reconnaissance or weapons system that operates in or above the atmosphere must either look through the atmosphere or against a background of the atmosphere or sky. As a result, the optical properties of the atmosphere must be known, in order to see how they will enhance or limit the operation of these systems.

A major area of investigation by the Optical Physics Laboratory involves the atmospheric attenuation or transmission of radiation by the atmosphere, including laser beams. Atmospheric molecules absorb optical and infrared radiation selectively at discrete wavelengths.

The Infrared Physics branch program concentrates on the infrared region of the spectrum, and it includes research on the mechanisms of absorption, transmission and emission of infrared radiation in the aerospace environment. Among other things, it includes the atmospheric attenuation of infrared radiation from natural sources, natural or man-made disturbances, or targets such as missile plumes. The measurement and study of atmospheric transmission or emission also provides a method for remotely sensing atmospheric composition including the effect of the addition of contaminents, for example, from high altitude missile or jet engine exhausts. This can also be used to sense meteorological conditions such as temperature and humidity.

The results of these efforts are computer codes which allow the prediction of infrared absorption, emission and transmission for any situation. Two basic models for the infrared radiation properties of the atmosphere have been developed. The first model is of low resolution (20 cm^{-1} spectral resolution). The second model is potentially superior to the first model. It uses absorption profiles of individual molecular absorption lines. This model should yield more accurate low resolution results when the data are appropriately averaged onve wavelength. It is the only approach capable of computing very high resolution spectra for the transmittance of laser beams through the atmosphere. In order to answer the question of what laser frequencies are attenuated least by the atmosphere, it is necessary to compile the fundamental spectroscopic data (including line-intensities, frequencies, and half-widths) of all molecules responsible for absorption in the spectral region of interest.

The best set of absorption band constants for the atmospheric absorbing molecules have to be determined and then the required spectroscopic data can be generated from these constants. Data are already

available for CO_2, H_2O, O_3, N_2O, CO, CH_4, and O_2. Extensive computer programs have been developed which make use of the vast collection of spectroscopic data. These have been used to predict the transmission of laser beams. In addition, transmission codes have been extensively applied to the design and improvement of remote atmospheric sensing devices on the Air Force meteorological satellites. Another application of this data base has been its use to understand the signature of a hot gas (for example, the exhaust plume of an aircraft) as viewed through a colder atmosphere.

The AFCRL Atmospheric Absorption Line Parameters Compilation is currently being improved. This involves both the revision of existing data and the addition of new material. The new material which is being incorporated in the data base, includes weak absorption features of the major atmospheric absorbing gases, as well as absorption parameters for thrace atmospheric and pollutant gases. Some of the trace gases which have been incorporated in the data compilation include SO_2 and NO_2. Preliminary data are also available for the molecules NO and NH_3. For these latter two trace gas molecules, the data were not of sufficiently high quality that they could be used to accurately predict laser beam transmission through these gases.

This report documents the efforts made to obtain better spectroscopic data for the two molecules, NO and NH_3.

THE AMMONIA MOLECULE

The NH_3 molecule has a symmetrical pyramidal structure with the N atom at the top. Of the four fundamental modes of vibration, the strongest band which occurs in an atmospheric window region of the spectrum, is ν_2. This is a totally symmetric fundamental, and a notable feature is the fact it is double. This doubling is due to the situation that there are two equilibrium positions for the N atom at the two sides of the plane formed by the three H atoms. It is termed "inversiondoubling." All vibrational levels are split into two sublevels, a lower positive and an upper negative level; the splitting being largest for those levels in which the height of the pyramid changes most during the vibration. In the infrared, the selection rule is $+ \leftrightarrow -$, hence each band has two components whose separation is the sum of the splittings of the upper and lower levels. The same selection rule holds, of course, for the pure rotation spectrum and therefore every line of the rotational spectrum is double; the line splittings again being the sum of the splittings of the upper and the lower states. But here the splitting is the same in the upper and lower states and so the line splitting is just double the splitting in the vibrational ground state. The same splitting of the ground state is also observed in the pure inversion spectrum; i.e., for transitions from the lower to the upper rotational sub-level.

Costain suggested that the line positions in the pure inversion spectrum should be fit by a formula of the type

$$E(J,K) = \nu_0 \exp\left(bJ(J+1) + (b-c)K^2 + d_J J^2(J+1)^2 + d_{JK} K^2 J(J+1) + d_K K^4 + h_J J^3(J+1)^3 + h_{JJK} J^2(J+1)^2 K^2 + h_{JKK} J(J+1)K^4 + h_K K^6 + \ldots \right). \quad (1)$$

That is, a power series in terms of the quantum numbers, analogous to the usual power series for energy levels in the pure rotational spectrum, except that the "energy" appears in the exponent. This formulation follows from the snalysis of a general double potential well, done by Dennison and Ullenbeck. A fit of equation (1) to the inversion spectrum of ammonia, as reported recently by Poynter and Kakhar, does not reproduce their observations well. The standard error associated with the fit using an equation of the form of equation (1) with 10 free parameters is 0.49 MHz; a 21 parameter fit gives a standard error of 0.034 MHz. In an attempt to obtain a better fit to the measurements of Poynter and Kakhar, we have used a Padé approximation; that is, a formula of the type

$$E(J,K) = \frac{\nu_0 + A(J(J+1) - K^2) + B(J^2(J+1)^2 - K^4) + C(J^3(J+1)^3 - K^6) + \ldots}{1 + \alpha(J(J+1) - K^2) + \beta(J^2(J+1)^2 - K^4) + \delta(J^3(J+1)^3 - K^6) + \ldots} \quad (2)$$

This gives a standard error of 0.21 MHz for an 11 parameter fit; with 19 free parameters, equation (2) gives an error of 0.0075MHz. We have obtained a considerably more accurate fit than that found by Poynter and Kakhar, using 10 parameters. Having obtained accurate constants for the contribution to the total energy due to the inversion spectrum, we proceeded to analyse the pure rotational spectrum. Again the contribution of the rotational energy to the total energy was represented by an equation of the form of equation (2). The Padé approximation was again more successful in describing the energy levels than the conventional expression. We used Dowling's data for the rotational line frequencies. When we attempted to fit the data of Garing, Nielsen and Rao for the ν_2 band (with 33 parameters), it turned out that we were still off from the measured frequencies of lines for high J,K quantum numbers. We are unable to obtain any better accuracy than the conventional formulae yield. That is to say, we are off by 1.35 cm^{-1} at (15,15). We suspect that this is due to the fact that the data of Dowling have systematic errors and that our parameters derived from that spectrum are inaccurate as a result. The next step in our treatment of the NH_3 molecule is to use the perpendicular bands to find ground state constants. Since it is known that ν_4 perturbs $2\nu_2$, we suspect that the ν_2 band may have some special difficulties associated with it's analysis. For this reason we plan to analyse some other infrared bands of ammonia before returning to the problem of the ν_2 band.

THE NITRIC OXIDE MOLECULE

The spectrum of the NO molecule is interesting because the electronic ground state is $^2\Pi$, instead of the more customary Σ ground state. The usual method of analyzing the NO spectrum is to consider it as belonging to Hund's case (a) and then doing a perturbation expansion. The frequency measurements made by Keck for the P and R branches of the fundamental sub-bands at 5 microns have been fit by an expression of the form,

$$\omega - \omega_o = am + bm^2 + cm^3 + dm^4 + em^5 + fm^6 + \ldots \quad (3)$$

where the index m = -J" for the P branch and m = J" + 1 for the R branch; The coefficients a, b, c, etc are the usual combinations of the rotational constants B_v, D_v, H_v, etc. Because there are two sub-bands, the constants found from a least-squares fit to Keck's data are really effective constants and not the true constants for the NO molecule. Keck's frequency measurements only gave the average frequency for the lamda doublets. However the lamda doubling was computed for these branches of the fundamentals and was submitted for inclusion in the AFGL Data Tape. These bands are the strongest features in the 5 micron region. It was felt that better constants could be obtained by fitting all 3 branches of the fundamentals (Q was ignored before) and of the satellite bands. In adition, it seemed reasonable to also include Dowlings measurements of the pure rotation spectrum and the microwave data.

For the NO molecule, we have the quantum numbers L = 1 (and it's projection $\Lambda = 0, \pm 1$) and S = 1/2 (with it's projection $\Sigma = \pm 1/2$) and $\Omega = \Lambda + \Sigma$. With these quantum numbers, six Hund's case (a) states can be formed with the designation $^{2S+1}|\Lambda|_{\Omega}$: $^2\Pi_{1/2}$, $^2\Pi_{-1/2}$, $^2\Pi_{3/2}$, $^2\Pi_{-3/2}$, $^2\Sigma_{1/2}$, and $^2\Sigma_{-1/2}$. The interactions of these six states form a 6x6 matrix. This matrix can be factored by chosing as a basis functions, symmetric and antisymmetric conbinations of the 6 pure case (a) wave functions. The factorization breaks the Hamiltonian matrix into two 3x3 blocks of opposite parity, as shown below.

$$\begin{array}{c} \Sigma^s_{1/2}\ \ \Pi^s_{1/2}\ \ \Pi^s_{3/2}\ \ \Sigma^a_{1/2}\ \ \Pi^a_{1/2}\ \ \Pi^a_{3/2} \\ \begin{bmatrix} \chi^s & \mu^s & \eta & 0 & 0 & 0 \\ \mu^s & \beta & \epsilon & 0 & 0 & 0 \\ \eta & \epsilon & \gamma & 0 & 0 & 0 \\ 0 & 0 & 0 & \chi^a & \mu^a & \eta \\ 0 & 0 & 0 & \mu^a & \beta & \epsilon \\ 0 & 0 & 0 & \eta & \epsilon & \gamma \end{bmatrix} \end{array} = H_{rot} + A(\vec{L}\cdot\vec{S}) \qquad (4)$$

Here $\chi^s = \alpha + \delta$, $\chi^a = \alpha - \delta$, $\mu^s = \theta + \zeta$, $\mu^a = \theta - \zeta$,

$\theta = \langle\pi|A\ L_y + 2B\ L_y|\Sigma\rangle = (a + 2b)$,

$\zeta = 2\langle\pi|B\ L_y|\Sigma\rangle (J + 1/2) = 2b(J + 1/2)$

$\alpha = B_\Sigma (J + 1/2)^2 + E_\Sigma - E_\pi$

$\delta = B_\Sigma (J + 1/2)$

$\beta = G_v - (1/2)A_v + (B_v - A_J)(J + 1/2)^2 - D_v(J + 1/2)^4 + H_v(J + 1/2)^6$

$\gamma = G_v + (1/2)A_v - 2(B_v + 2D_v) + (B_v + 4D_v + A_J)(J + 1/2)^2$

$\quad - D_v(J + 1/2)^4 + H_v(J + 1/2)^6$

$\epsilon = (B_v + 2D_v - 2D_v(J + 1/2)^2)(\ (J - 1/2)(J + 3/2)\ )^{1/2}$

Equation (4) reduces to two 3x3 matrices for the energy, which are readily diagonalized numerically to obtain the energy eigenvalues for each value of the rotational quantum number, J. Differences between the energy levels of appropriate symmetry yield the frequencies of the allowed rotational lines, including Λ-doubling, for the NO molecule. Conversely, a least squares fit to measured frequencies can give the "best" values for the constants G_v, B_v, D_v, H_v, A_v, A_J, $\underline{a}$ and $\underline{b}$, if B_Σ and $E_\Sigma - E_\pi$ are assumed to be known. This procedure has been applied to the microwave lines and to the pure rotation spectrum in an attempt to determine inproved constants for the ground state. We had hoped to use these ground state values in fitting the fundamental and satellite bands, where the upper state constants would be found. However, combination differences based on Keck's measurement of the fundamentals showed that Dowling's far infrared data, for the pure rotation band, have systematic errors in the measurements. As a result, we decided to fit all the data to simultaneously determine both the $v = 0$ and the $v = 1$ state constants.

The computer program which calculates line frequencies and lamda doublings for the lines is working. What remains to be done is to do the least squares fit to the data.

REFERENCES

J. M. Dowling, "The rotation-inversion spectrum of Ammonia," J. Mol. Spectry, 27, 527-538 (1968)

J. S. Garing, H. H. Nielsen and K. N. Rao, "The low frequency vibration-rotation bands of the Ammonia molecule," J. Mol. Spectry, 3, 496-527 (1959)

R. T, Hall and J. M. Dowling, "Pure rotational spectrum of Nitric Oxide," J. Chem. Phys, 45, 1899-1903 (1966)

D. B. Keck, "High-resolution absorption, Zeeman, and Magnetic rotation spectra of the fundamental and satellite bands of Nitric Oxide in the near infrared," Ph.D. Thesis, Michigan State Univ.,1967

1976 USAF-ASEE SUMMER FACULTY RESEARCH PROGRAM
sponsored by
THE AIR FORCE OFFICE OF SCIENTIFIC RESEARCH
conducted by
AUBURN UNIVERSITY AND OHIO STATE UNIVERSITY

PARTICIPANT'S FINAL REPORT

POTENTIAL TECHNOLOGY BREAKTHROUGHS IN NEXT GENERATION RADARS

Prepared by:	John D. Spragins, Ph D.
Academic Rank:	Associate Professor
Department and University	Department of Electrical and Computer Engineering Oregon State University
Assignment:	
(Air Force Base) (Laboratory) (Division) (Branch)	Hanscom AFB Deputy for Development Plans
USAF Research Colleague:	Donald B. Brick, Ph.D.,P.E.
Date:	August 27, 1976
Contract No.:	F44620-75-C-0031

POTENTIAL TECHNOLOGY BREAKTHROUGHS IN NEXT GENERATION RADARS

by
John Spragins

ABSTRACT

Three major trends influencing the development of new radars are use of sophisticated data processing techniques (especially digital techniques), interconnection of different radars to form radar networks, and reduction of the requirements for on-site manning of radar systems. Some important implications of these trends are examined.

In addition to giving improved estimates of conventional radar parameters such as range, azimuth and elevation in the presence of clutter or other disturbances, the newer processing techniques automatically make other parameters such as target radial velocities, return signal strengths, the spatial distribution of returns from a target, the location of unusual concentrations of clutter or other disturbances, etc. readily available. Use of the velocity information for tracking is shown to potentially give substantial improvements in tracking accuracy. Possible improvements from utilizing some of the other parameters are also discussed.

Next, some of the problems in and implications of radar netting are discussed. Communications problems (in collecting data from different radars and disseminating it to users) and data processing problems, and tradeoffs between communications and data processing, are discussed. A few tentative conclusions defining recommended radar network architecture are given.

The final area examined is that of minimally attended or unattended radars. Brief reformulations of some of the standard reliability/availability calculations are given, and problems which must be solved to meet the reliability requirements of such systems are discussed.

INTRODUCTION

The Air Force is about to embark on the development of a new generation of ground and/or air-based surveillance radars. Further, major changes in the manner in which tactical radars are utilized and new types of equipment for use in tactical situations are being developed. Three major trends influencing the development of both types of radars are use of sophisticated data processing techniques (especially digital techniques), interconnection of different radars to form radar networks, and reduction of the requirements for on-site manning of radar systems. Some important implications of these trends and problems which must be solved to fully realize their potential benefits are examined.

Three distinct, though interrelated, topics are covered in the material below. In each case, the discussion is a summary of an initial survey of a topic which merits considerable additional study and could lead to significant breakthroughs in radar system performance. (This possibility is the motivation for the title of the report.)

The first portion of the report discusses making use of some extra parameters which can very easily be obtained with some of the sophisticated radar data processing techniques which are currently being developed. Parameters either in the standard outputs or readily obtainable from Lincoln Lab's MTD processing are discussed, since this is one of the better examples of the type of processing techniques currently being developed. (Similar parameters should be obtainable with other techniques such as those being developed by Westinghouse, Bendix, Texas Instruments, etc., but relatively little documentation on these alternative techniques is available.) In addition to giving improved estimates of the conventional parameters such as range, azimuth and elevation (despite the presence of clutter or other disturbances), such processing techniques automatically make other parameters such as target velocities, return signal strengths, the spatial distribution of returns from a target, the location of unusual concentrations of clutter or other disturbances, etc. readily available.

A brief analysis of potential improvements in tracking accuracy which can be obtained by utilizing target velocity as an additional parameter for tracking algorithms is given. (This analysis is due to R. J. Kulpinski of MITRE Corp., Bedford, Mass.). The analysis indicates that very substantial improvements in tracking accuracy, as measured by the size of ellipses of range/azimuth ambiguity, can be obtained if velocity information is used. Some potential uses for other parameters are then discussed. Several of the parameters appear to be especially useful in an ECM environment.

The second topic examined is that of radar netting. Netting

of tactical radars is emphasized, since the problems encountered are more severe than those encountered with netting of fixed surveillance radars. Some of the major problems which need to be solved if radar netting is to realize its potential include finding techniques for insuring adequate compatibility among the outputs of different types of radars, merging information from different radars (of widely varying types) which may have overlapping coverage, incorporating other information such as intelligence information or meteorological data into situation displays, appropriate dissemination of information to users, providing for survivability of the surveillance and communication networks, etc. A large part of the hope for finding reasonable solutions to these and similar problems arises from the development of sophisticated radar data processing techniques such as those discussed in the first section, but sophisticated techniques for communication of information and for processing other types of data are also needed.

Present applications of radar netting tend to be extremely crude in comparison with the types of networks which appear to be technologically feasible. Hence, it is difficult to make many definitive statements about preferred network architectures. Nevertheless, persuasive arguments for some desirable features can be given, and these arguments appear to lead to some conclusions for recommended architectures. Some arguments of this type are given. A few major design tradeoffs are then enumerated and briefly examined.

The final topics treated concern minimally attended or unattended radars. Two major classes of minimally attended or unattended radars are those intended for surveillance and those to be used in tactical situations (these two classes correspond to the two classes of radar networks discussed above). In surveillance situations development of such radars is primarily motivated by personnel costs, which tend to be the largest single costs in the life cycles of most radars. In tactical situations minimally attended or unattended radars are more likely to be small expendable radars placed very near the FEBA or in other exposed situations. In either case, such radars are becoming more feasible because of the trends toward sophisticated data processing at the site and radar netting discussed earlier.

The major problems related to minimally attended or unattended radars discussed here are concerned with the reliability/availability of such radars. Reliability and availability are normally more severe for surveillance radars than for tactical radars in these categories since the tactical radars are more likely to be considered to be expendable. Hence this discussion focuses on surveillance radars.

Reliability theory is plagued by a multitude of conflicting definitions for the same or very similar terms. The picture is

further complicated by the fact that different groups are responsible for different portions of the factors determining reliability. The major factors causing confusion are explained. Some modifications to the usual techniques for analyzing reliability and availability are then developed for application to such systems, and some possible techniques for achieving the reliability/availability goals are discussed.

USE OF EXTRA PARAMETERS

Historically most radars have been described as 2-D radars or 3-D radars, with the distinction between the two types depending on whether they provide just range and azimuth for targets or range, azimuth and elevation. Although other parameters such as doppler shifts are often obtained, these have normally been used only for internal processing (most commonly to separate moving targets from stationary targets). The only real output parameters have been the two or three location parameters listed. Until fairly recently technology limitations tended to limit the availability of additional parameters, but the newer technologies now coming into widespread use make it simple to extract additional parameters. Nevertheless, tradition seems to be prevailing, so that these additional parameters are not really utilized. As an example, the only real parameters allowed to be transmitted from radar sites to the ROCC, if JSS formats are used are range, azimuth and elevation [1]. (A few additional parameters, such as actual IFF replies in the beacon formats, time in storage before the message was transmitted and the extent of the azimuth angle over which a search message is received are provided, but these are not the types of parameters of real interest for this discussion.) The tracking algorithms used in the ROCC only utilize the range, azimuth and elevation data [1].

Typical Parameters Available

A good example of the type of new technologies now coming in is Lincoln Lab's MTD processor. Each target report from the MTD processor (now implemented on a 2-D radar) consists of two 32-bit words, a PAZ word and a VRS word [2]. The PAZ word gives the pulse repetition frequency and azimuth for the report, and the VRS word gives velocity, range and signal strength. (Up to 38 VRS words per PAZ word are allowed, corresponding to 38 detections, at different ranges, for the same azimuth.) These two words contain the standard range and azimuth parameters plus three additional ones (prf, velocity and strength). In addition, a great deal of other information is readily obtainable. A disc memory holds 368, 640 clutter words, one for each range-azimuth resolution cell (768 range resolution cells and 480 azimuth resolution cells - the latter are normally termed coherent processing intervals, CPIs, in MTD). This clutter map contains an average value of the ground clutter (obtained from the output of the MTD zero velocity filters), obtained from previous scans.

Eight times this many, or 2,949,120, different range-azimuth-velocity thresholds are independently adjusted, with 8 different velocities examined for each range-azimuth pair. With the digital processing techniques used in MTD, any of these values could be read out if this is desired. Other quantities utilized in computing these values could easily be obtained, or the results of performing some computations with any of the listed parameters (so long as the capacity of the MTD processor is not exceeded), can be other outputs. Hence, a tremendous variety of output parameters can be obtained with MTD.

Other radar processing techniques similar to MTD are being developed by a number of different companies; companies mentioned to the author in various conversations have included Westinghouse, Hughes, Bendix, Litton, Texas Instruments and Univac. Other operational radar systems, such as E3-A, use digital-processing techniques of a slightly different nature. Hence, it is not at all unrealistic to expect a large percentage of the radar systems developed in the future to provide the type of parameters discussed here.

Example of Parameter Use--Velocity Information

As an example of potential gains through use of additional parameters, the use of velocity information in tracking is discussed. The results given here are due to R. J. Kulpinski of MITRE who has given the author a copy of the equations he utilized. The results of the analysis (though not the derivations) are included in [3].

The technique Kulpinski used to define a tracking algorithm was a Taylor-series expansion approach to finding a least-sum-squared-error solution. A good recent exposition of the technique (also called Gauss or Gauss-Newton interpolation) is given by Foy [4], but this is a classical technique which has been utilized for many years. It is relatively simple to use, and can readily incorporate multiple measurements and mixed-mode measurements. On the other hand, it requires an initial guess at a solution and iterative improvements to it, with no guarantee of convergence. (Experience indicates, though, that the initial solution guess can be quite far off without preventing good convergence, so it will normally converge.) Although this approach to tracking could prove to be completely adequate (with failure to converge initially taken care of by altering the initial guess), other techniques should be investigated. The analysis given here should be considered to be a first cut at comparing tracking algorithms which do and do not utilize velocity information.

The tracking algorithm assumes a constant velocity flight path which is described by the target speed (S), the time of

closest approach to the radar site (t_c), the target bearing at closest approach (Θ_c), and the target range at closest approach (R_c). These four parameters completely describe the constant velocity flight path. In order to estimate these parameters, a sequence of measurements, at known times (t_i), of bearing angles (Θ_i), range (R_i), and (if velocity information is used) range rate ($\dot{R}_i$) are obtained. Relationships between the parameters describing the flight path and the measurements are readily obtained with the aid of Figure 1. From this figure it is easy to see that:

$$\Theta_i = \Theta_c + \tan^{-1}\left[\frac{S}{R_c}(t_i - t_c)\right] \qquad (1a)$$

$$R_i = \left[R_c^2 + S^2 (t_i - t_c)^2\right]^{1/2} \qquad (1b)$$

$$\dot{R}_i = \frac{S^2 (t_i - t_c)}{\left[R_c^2 + S^2 (t_i - t_c)^2\right]^{1/2}} \qquad (1c)$$

Note that if values for Θ_c, S, R_c and t_c are assumed, this is equivalent to assuming values for Θ_i, R_i and $\dot{R}_i$ also since these latter three quantities can be computed from the assumed values by simple geometric arguments. Assumed values of terms in the following arguments will be denoted by the letter a in parentheses, e.g. Θ_c (a) is the assumed value for Θ_c. The Taylor-series approach to estimating the track involves expanding both sides of equations (1) in Taylor-series about the assumed values, keeping only terms below second order. Thus the form of the expansion for (1a) is

$$\Theta_i - \Theta_i(a) \approx \frac{\partial \Theta_i}{\partial \Theta_c}(\Theta_c - \Theta_c(a)) + \frac{\partial \Theta_i}{\partial S}(S - S(a)) + \frac{\partial \Theta_i}{\partial R_c}(R_c - R_c(a)) + \frac{\partial \Theta_i}{\partial t_c}(t_c - t_c(a)) \qquad (2)$$

with similar expansions for R_i and $\dot{R}_i$.
After the indicated differentiations are performed, the following matrix equation is found

$$\underline{z}_i \approx J_i(a)\,\delta + e_i \qquad (3)$$

with

$$\underline{z}_i = \begin{bmatrix} \Theta_i - \Theta_i(a) \\ R_i - R_i(a) \\ \dot{R}_i - \dot{R}_i(a) \end{bmatrix} \qquad (4a)$$

$$J_i = \begin{bmatrix} 1 & \frac{u_i}{S(1+u_i^2)} & - \frac{u_i}{R_c(1+u_i^2)} & \frac{-S}{R_c(1+u_i^2)} \\ 0 & u_i\,(t_i - t_c) & \frac{R_c}{R_i} & -Su_i \\ 0 & u_i R_c \frac{(R_i^2+R_i^2)}{R_i^3} & - \frac{R_c^2 Su_i}{R_i^3} & - S^2 \left(R_i^2 - \frac{R_c^2 S^2 u_i^2}{R_i^3}\right) \end{bmatrix} \qquad (4b)$$

with $J_i(a)$ in equation (3) indicating assumed values for the terms are used and

$$u_i = \frac{S}{R_c}\,(t_i - t_c) \qquad (4c)$$

Also

$$\delta = \begin{bmatrix} \Theta_c - \Theta_c(a) \\ S - S(a) \\ R_c - R_c(a) \\ t_c - t_c(a) \end{bmatrix} \qquad (4d)$$

and e_i represents the matrix of measurement errors, which are assumed to be normally distributed with zero mean and covariance matrix

$$\Lambda_1 = \begin{bmatrix} \sigma_\Theta^2 & 0 & 0 \\ 0 & \sigma_R^2 & 0 \\ 0 & 0 & \sigma_{\dot{R}}^2 \end{bmatrix} \qquad (5)$$

As equation (5) indicates, the measurement errors are assumed to be mutually independent and equal for all i (hence no subscript i).

If n sets of measurements are obtained (at least two must be obtained to estimate the track since there are four track parameters and only three measurements), the equivalent formulas are

$$Z_{(n)} \approx J_{(n)}(a)\,\delta_{(n)} + e_{(n)} \qquad (6)$$

with

$$Z_{(n)} = \begin{bmatrix} Z_1 \\ Z_2 \\ \vdots \\ Z_n \end{bmatrix} \qquad (7a)$$

a 3n x 1 matrix with each Z_i of the form in equation (4a). Similarly

$$\underline{J}_{(n)} = \begin{bmatrix} J_1 \\ J_2 \\ \cdot \\ \cdot \\ \cdot \\ J_n \end{bmatrix} \tag{7b}$$

is a 3n x 4 matrix,

$$\underline{\delta}_{(n)} = \begin{bmatrix} \delta \\ \delta \\ \cdot \\ \cdot \\ \cdot \\ \delta \end{bmatrix} \tag{7c}$$

consists of n copies of the matrix in equation (4d) and

$$\underline{e}_{(n)} = \begin{bmatrix} e_1 \\ e_2 \\ \cdot \\ \cdot \\ \cdot \\ e_n \end{bmatrix} \tag{7d}$$

Further, the error covariance matrix can be written in the form

$$\underline{\Lambda}_{(n)} = \begin{bmatrix} \Lambda_1 & 0 & \cdots & 0 \\ 0 & \Lambda_1 & \cdots & 0 \\ \cdots & \cdots & \cdots & \cdots \\ 0 & 0 & \cdots & \Lambda_1 \end{bmatrix} \tag{8}$$

with n copies of the matrix in equation (5) along the main diagonal and zeros elsewhere.

The Taylor-series approach to finding the least-sum-squared-error estimates of the track parameters is to start with the assumed values of the track parameters

$$P_1 = \begin{bmatrix} \theta_c\ (a) \\ S\ (a) \\ R_c\ (a) \\ \\ t_c\ (a) \end{bmatrix} \qquad (9)$$

This assumed solution point is replaced by a new estimated solution given by

$$P_1' = P_1 + (J^T \Lambda^{-1} J)^{-1} J^T \Lambda^{-1} Z \qquad (10)$$

The entire calculation is then repeated with P_1' replacing P_1. This procedure iterates until the change in solutions generated becomes essentially zero, indicating convergence. The errors in the final solution obtained have covariance matrix

$$\Lambda_o = (J^T \Lambda^{-1} J)^{-1} \qquad (11)$$

As was stated earlier, convergence is not assured with this approach, but it is unusual to have convergence fail to occur. Further, additional attempts to find a solution can be made by simply varying the initial assumed values, with a high probability of success on each trial.

A completely analogous solution for least-sum-squared-error tracking without the use of velocity information can be found by simply deleting the third rows of the matrices in equations (4a), (4b) and (5) (and deleting the final column in the last matrix). The analysis will not be repeated here.

Typical Improvements from Using Velocity

Kulpinski studied the improvements in tracking accuracy obtainable through incorporating velocity measurements under the target tracking conditions in Table 1(3).

TABLE 1

Target Tracking Conditions

Assumed Flight Path	Constant Velocity
Tracking Algorithm	Algorithm Described
Number of Scans of Measurement	Four Scans
Performance Computed for	Predicted Track in Fifth Scan
Std. Dev. Bearing Measurement	0.2 degrees
Std. Dev. Range Accuracy	300 ft and 3000 ft.
Std. Dev. Doppler Accuracy	No doppler and 5 fps
Scan Rate	6 rpm
Target Range	25 nm and 50 nm
Target Aspect Angle	0 to 90 degrees

Some of the results of Kulpinski's comparisons are given in Figures 2 - 6 (reproduced from [3]). Figures 2 and 3 illustrate how the sizes of error ellipses for target location shrink when velocity information is utilized. Figure 4 plots location error (as defined in the figure) versus target aspect angle, and Figures 5 and 6 give standard deviations for estimates of track heading and speed. In each case, use of velocity information gives substantial improvements in accuracy. Though these calculations were made for one specific tracking algorithm, it is reasonable to expect similar improvements when other algorithms are modified to utilize velocity information.

The primary criticism of Kulpinski's results that should be made is that they are based on an overly idealized model of the type of input data a tracker may normally have. MTD is a handy example of this, with examples of the type of input data available to the tracker accessible by the author [5]. Typical track reports for MTD are often obtained from 20 or so threshold crossings (occasionally as many as 40 or more crossings). (As was stated earlier, almost 3,000,000 different range-azimuth-velocity cells are thresholded separately.) A single target can cause threshold crossings in cells corresponding to two to four ranges, as many as seven azimuths, and as many as six or seven velocities. (Multiplying the numbers quoted indicates as many as 200 threshold crossings could occur, but not all of the possibilities actually result in threshold crossings.) At present, use of the velocity information in tracking algorithms (defining tracks by adjacencies in range-azimuth-velocity space) has been largely rejected since factors such as propeller modulation (which can give doppler components at velocities coming from propeller rotation which are considerably larger than the components from overall aircraft motion) has resulted in multiple tracks being initiated for one target when velocity information is used to determine adjacencies.

Despite the weaknesses just noted, an analysis such as Kulpinski's analysis given above is valuable in pointing out the possibility of major improvements in tracking accuracy if additional data is used. Finding reasonably optimum tracking algorithms which utilize the other parameters available is an important unsolved problem.

Other Applications of Additional Parameters

Numerous other ways in which the additional radar parameters now readily obtainable can be used are easily visualized. Careful examination of the manner in which such information might best be utilized could be the subject of considerable useful research. Only a few tentative suggestions will be given here.

No real applications of the return signal strength information

provided by radar processors such as MTD has been discussed so far. One application of strength information by MTD has been in determining weighting factors for target returns in order to accurately locate the targets in azimuth [5]. Although the MTD radar has an azimuth resolution of .75° (480 coherent processing intervals per antenna revolution), and individual target reports may span as many as 5 to 7 CPIs, the rms azimuth error for the MTD radar is currently around .15° [5]. Similar use of the strength for defining weighting factors can improve the accuracy of various other estimates, such as range or relative velocity. Some caution in the application of such weighting factors based on signal strength should be used because of the extreme variability of reflections from a complex target.

A quick and not very systematic examination of a limited amount of MTD track data (given to the author by Dr. R. M. O'Donnell of Lincoln Laboratory) indicates some definite patterns in aircraft tracks which should make it possible to improve tracking algorithms if such information were utilized. The target reports corresponding to a typical track tend to display a reasonably smooth transition between doppler velocities (for the dominant doppler components) as the target moves along a track. As the target approaches a tangential track several things happen: the dominant doppler velocity components approach zero frequency shift (since the radial velocity approaches zero), the strength of the return signal tends to increase markedly (since the planes being tracked are normally being observed broadside), and the number of different range-azimuth-velocity cells for which threshold crossings are observed tends to increase considerably. (The latter factor is probably a secondary effect of the increased strengths of returns from a broadside target; since the total signal return strength is far greater, threshold crossings begin sooner, (when a shoulder of the main beam is illuminating the target) and end later, and other minor return signal components may also exceed thresholds.)

The sample of track reports leading to the above comments was too limited for much weight to be given to the track report patterns discussed. Further, some of the difficulties previously mentioned, such as strong propeller modulation components in the returned waveforms, do not appear to be important in the limited set of data analyzed. Nevertheless, the tendency for successive track reports to form predictable patterns appeared to be strong enough to merit further study.

The extra parameters provided by radar processors such as MTD should be especially useful in an ECM environment. As a general principle, making it possible to use more information in the received waveform should help to combat ECM, assuming this information is used in the correct manner. (Basing a

tracking algorithm strongly on parameters which are easily corrupted by the enemy is hardly optimum, whether these parameters are currently utilized or not.) Proper processing of information-bearing signals (e.g. by matched filters) makes it possible to extract the information despite an adverse signal-to-noise ratio, though, and the same general principle holds here. If two devices utilize all the information they are given in an optimum manner, but one is given more information than the other (all the information given to the latter plus additional information), the device given more information cannot perform worse than the device given less information. The key assumption in this reasoning is that both devices make optimum use of the information they are given; finding optimum ways of operating in an ECM environment may be so difficult that the arguments just given become meaningless.

One category of ECM techniques especially susceptible to the type of techniques suggested above (the use of pattern recognition techniques in tracking) is the deception types of ECM. Techniques such as sensing a radar signal and reradiating a subtly altered copy of the signal (to deceive the radar as to target range or azimuth, etc.) could become far more difficult if the detailed time sequence in return signals from an actual target had to be mimiced. Some advantage in a jamming environment might be gained, also, but this is more speculative (depending on the extent to which the effective signal-to-noise ratio might be increased).

Generating strobes to locate jammers would be greatly simplified through use of some of the types of extra information provided by MTD or similar techniques. All the information needed to generate such strobes is contained in the descriptions of ground and weather clutter within MTD. Mr. C. E. Muehe of Lincoln has indicated to the author that generating such strobes would be a trivial modification of MTD. If the variations in jammer signals were examined, it might even be possible to distinguish between the signals from different jammers sufficiently to eliminate ambiguities in strobe crossing patterns for multiple jammers. Thus, if jammer location is attempted by plotting intersections of strobes as reported by two different radars, n jammers would result in $n(n+1)$ crossings with no identification of jammers being used. If, however, the 2n lines plotted could be labeled so that 2 were known to correspond to jammer number 1, another 2 to jammer number 2, etc., all n jammers could be uniquely located.

Numerous other potential uses for extra radar parameters can be visualized, but those suggested should illustrate the potential advantages from use of extra parameters and sophisticated data processing.

A large number of influential people are very critical of the idea of transmitting track data, rather than radar video data, in a tactical environment. They state that in a tactical situation a highly skilled radar operator can extract information from a radar display, despite the presence of jamming, chaff, etc. far more reliably than this can be done automatically. Though this may be true, the communications requirements for transmitting radar video between large numbers of sites are so formidable as to make this approach impractical. The author strongly suspects, moreover, that all the extra data these operators utilize is included among the extra parameters available from radars such as the MTD radars, and that with appropriate effort techniques for extracting this data can be developed. Further, he would suggest that any team attempting to develop such techniques include one or more of these fabled highly skilled operators.

RADAR NETTING

As more sophisticated radar data processing techniques come in, it will become feasible to more fully exploit the potential of radar netting. Only limited applications of radar netting have been made so far, but numerous other applications have been proposed. A truly effective radar net could greatly expand the effectiveness of the radars tied into the net. Advantages of radar netting are well known, but some of the major ones are briefly summarized here.

The basic defining feature of radar netting is coordination of the use of various geographically dispersed radars. This includes both appropriate merging of the reports of different radars which provide multiple coverage of the same area and exchange of information about targets in geographical areas covered by different radars. The net results is greatly improved and coordinated coverage of the entire area spanned by the total radar net. Currently there tends to be relatively little coordination between different radars; often there is no exchange of data between radars covering the same area (e.g. between Army missile system radars and Air Force surveillance radars), or when data is exchanged it amounts to little more than verbal (telephone conversation or similar communication) transmission of track data to hand over coverage from one area to another.

If the capability for exchanging information among radar sites is available, other advantages besides improved radar coverage are readily obtained. It becomes much easier to provide integrated command, control, surveillance and weapon systems which cover wide geographical areas. This can, for example, provide the capability of continuously controlling aircraft as they transit over the entire area spanned by the radar network., Numerous advantages for operating in an ECM

environment could also be mentioned, since the different radars will have many new ways of cooperating to foil ECM techniques. A few of these are discussed below.

Two major categories of netted radars that have been discussed are netted tactical radars and netted surveillance radars to operate in a peacetime environment (with a few limited capabilities for operating in a tactical situation often provided.) The problems involved in netting of tactical radars are, as a whole, much more severe than those involved in netting peacetime surveillance radars. This report concentrates on the more severe problem case of netted tactical radars; the problems involved in netted peacetime surveillance are largely a subset of those in netted tactical radars.

Basic Assumptions

Before any conclusions regarding recommended netted radar configurations can be made, the basic assumptions leading to these conclusions need to be stated. Some basic assumptions made here are as follows:

1. A wide variety of radars may be utilized in the network. Although the radars used will not necessarily be current radars (in fact the fact that this report is concerned with next generation radars indicates most of the radars used will not be current models), a brief listing of a few of the types of radars that would be utilized if such a net were implemented now will illustrate the variety of types of radars to be expected later. The types that would currently be included would include Air Force surveillance radars such as TPS-43Es and numerous other types, Army missile system radars such as SAM D and HAWK radars, various Navy radars, airborne radars such as the E-3A radar, air traffic control radars used within various national boundaries, etc. Other radars besides the airborne ones can be expected to have some degree of mobility. If the network is to survive the very likely rapid ground advance by an enemy (with strong numerical manpower and armament superiority) during initial stages of combat, it would seem to be imperative that a great deal of reliance be placed on mobile radars.

In addition to their being of varied types, the radars to be utilized in a network are likely to differ in many, if not all, of their basic parameters. Thus, there will be a variety of pulse widths and pulse repetition frequencies used (including low prf, medium-prf and high-prf classes of radars, or even cw radars with no real prfs defined); both 2-D and 3-D surveillance radars (plus other types such as those designed primarily for tracking) will be used, as will varied-range radars (possibly even including OTH radars). Also, antenna rotation times will differ substantially (if complete 360° rotation even occurs);

antenna beamwidths and gains, and numerous other parameters will differ.

2. Despite the differences in radar systems just discussed, the general types of sophisticated radar data processing techniques discussed earlier (in the material on utilization of extra radar parameters) will be generally available. Either this data processing capability will be designed into the radar initially, or the radar will be modified to include it, or at the very minimum the radar output data will be fed into systems to interface with the rest of the net and these interface systems will have the type of processing capabilities discussed. If this assumption is not true, there seems to be little hope of utilizing the radar in the network in anything other than a superficial manner.

3. The communications facilities used to link together radars in the network will be of fairly narrow bandwidth (e.g. voice-grade or similar facilities). Although reasonable transmission rates on such facilities are going up, so that speeds on the order of 9600 bits/sec. or higher are entirely reasonable to assume within the time framework considered here, transmission of raw radar video information is impractical to consider over more than a small fraction of the network. (It may be reasonable to transmit radar video to data processing systems interfacing with the network, if no real data processing capability exists at the radar. It is not at all certain that this should be done, however; normally such processing should be at the radar site. Arguments for this are developed later.)

4. Adequate dissemination of radar data to various command and control centers, weapon systems, etc. is as important as adequate collection and evaluation of the radar data. To the extent possible, the information disseminated should be merged with information from other sources, such as IFF/SIF data, meteorological data, intelligence data, etc.

The same trends leading toward more sophisticated radar data processing at the radar site make it reasonable to assume the users have their own data processing capabilities also.

5. A prime goal in designing a tactical radar network is system survivability. Destruction of major parts of the network should not disable the remaining parts.

6. Growth capability and flexibility of the network are also prime concerns. Removing elements from the network or adding new elements (possibly new types of elements) should have minimum impact on the rest of the network.

Many other desirable features for the network could be listed, but the assumptions listed seem to be the most fundamental

ones defining system requirements.

Implications for Architecture

The basic assumptions listed above lead to some tentative conclusions about the type of radar network architecture that should be implemented. Some conclusions of this type and arguments for their validity are given here. It should be emphasized, however, that these are only tentative conclusions at the moment. Though the author feels the arguments given here do indeed lend to the conclusions stated, additional information such as modification of the system requirements, demonstration that the approach suggested is infeasible, etc. could easily change the conclusions.

The requirements that the radar network be able to utilize a wide variety of radars while providing flexibility and growth potential (including the potential to handle new types of radar as they are developed) imply that standardized network interfaces must be developed. Without such interfaces, it may be possible to handle a variety of radar types by treating each case separately and developing interfaces for each, but this tends to greatly complicate the system and make expansion or modification difficult. Hence, the information transmitted over the main communication links utilized should be standardized formats, with a limited set of such standardized formats defined.

The exact locations of the standardized interfaces is a bit more difficult to specify, and some flexibility in location may be provided. Normally it would seem most logical to put such an interface at the radar itself, but on occasion it may be logical to perform the interface functions slightly further into the network. The latter location might be the only feasible location when attaching older radars (developed before the interface standards); for such radars it might be best to interpose additional interface elements between the radars and the network. If necessary the interface elements could be some distance away from the radars (assuming adequate data transmission facilities were available).

The type of standardized data to be transmitted on the communications network also needs to be specified. A variety of types of messages will probably be transmitted, including messages involved with system maintenance, various command and control messages, etc., but this report will concentrate on messages containing radar surveillance data. Formats for the other types of messages must also be established, with reasonable flexibility maintained, when a detailed architecture is developed.

The requirement that the network use fairly low bandwidth data transmission facilities places strict constraints on the types of radar data that may be transmitted between locations.

Transmission of unedited radar video is obviously ruled out. Transmitting large amounts of clutter data is also ruled out, as the analysis given below indicates. The two most legitimate types of radar reports to consider for transmission appear to be target reports and track reports. (One other possibility is transmitting information obtained by applying data compaction techniques to radar video, but this possibility has not been examined carefully during the course of this study.) It does not appear that either track reports or target reports has a clear-cut advantage.

The chief advantage of transmitting track reports is that these reports more concisely summarize all the most relevant information about targets than do a series of target reports. It is relatively simple to utilize all the information about targets which is available at the radar site to generate track reports, since only the algorithms used at that site are affected by whether such extra parameters as relative velocity or return signal strength are utilized or not; such parameters do not need to be transmitted to other locations. Also, current technology trends indicate that adequate data processing capability for generating tracks at the radar sites will soon be easy to provide; doing this job at the sites may more fully utilize the data processing capability that will probably be there anyway. At the very least, correlation of target reports with IFF/SIF data at radar sites seems to be indicated.

On the other hand, better overall tracks might be generated when the tracking is done at central sites. This is especially likely to be true when the targets being tracked are in areas covered by multiple radars since a central site is more likely to have reports from all relevant radars. (On the other hand, a central site might be able to edit track-reports from other sites to include the extra reports just as easily as it could construct tracks by merging target reports.) Further, utilization of additional relevant information, such as intelligence information, in tracking is more likely to be feasible at central sites. If target reports are the reports generated at the radar sites, some editing or condensation of them before transmission is likely to be needed, however. The necessity for this is pointed out by a simple calculation. Assuming 100 target observations per scan (a reasonable number) are generated, and 100 bits per target report (the JSS format for beacon reports reinforced by reports from 3-D radars requires 104 bits per report), then an average 833 bits/sec. are generated with one report per target and a scan rate of 5 scans per minute. With multiple reports per target (recall that the last section indicated 20 different reports per target was common with MTD, the different reports distinguished by slight variations in range, azimuth or doppler frequency), or with the number of clutter reports common with many current radars, the communications capacity of the lines is

likely to be exceeded with moderate numbers of targets being observed.

Although the arguments given in favor of or against the use of track reports or target reports are both incomplete and inconclusive, the author's current bias is toward the use of track reports, with provision for further editing of these reports at another site with more information. A limited indication of the quality of the track reports would aid in the editing, at a minimum this quality report might be a record of the number of times this target was detected on the past n scans (with n at least equal to the number of successive detection failures required to be observed before the track is dropped).

Some major architectural questions that need to be settled are the general type of network topology (manner in which the network elements are interconnected) and the general classes of network control algorithms that should be used. These are interacting questions which are strongly influenced by the types of data processing and communications facilities available and by the system goals. The network survivability goal mentioned earlier is one of the most dominant goals in this connection.

Survivability of the network would appear to dictate that the devices attached to the network operate as autonomously as possible so that as much as possible of the network might continue to operate if other portions were destroyed. Further, a high degree of connectivity of the communication circuits, in order to allow communication to take place despite destruction of major parts of the system, would appear to be indicated. If it were not for the resultant cost and complexity problems, a completely interconnected network of completely autonomous devices might appear to be ideal from a survivability viewpoint.

When practical questions such as cost and complexity are considered, a completely interconnected network of completely autonomous devices is easily seen to be unrealistic. Complete interconnection of N devices requires N (N-1)/2 different communications channels, a number which is only realistic for N small. (Complete interconnection of a small number of centers at the highest level of a hierarchical system might be advisable though; this would be analogous to the manner in which AT and T has completely interconnected the approximately half dozen switching offices at the highest level of their nationwide DDD (direct distance dialing) network.) The closest approach to use of completely autonomous devices in a data processing/communications network at present may well be the ARPA computer network (which is doubly connected, with at least two independent paths between any pair of nodes). The IMPs (interface message processors) in the ARPA network, which handle communications between nodes, operate almost completely autonomously; each IMP maintains

its own routing tables indicating its current estimates of the best routings to other nodes or IMPs, and updates these tables periodically with information received from the other nodes. There are major practical problems in achieving this degree of autonomy in a tactical radar network, however. There are likely to be too many nodes, and too much variability in the configuration of the network, for each node to realistically maintain routing tables for communication with all other nodes; adding or subtracting nodes would have to result in redoing the routing tables at all other nodes. Further, it is hardly realistic to expect all nodes in a tactical radar network to contain communication processors approaching the sophistication of ARPA's IMPs.

A realistic form for the communications network in a tactical radar network would be a hierarchical network, with the form of the hierarchy similar to the current FACP-CRP-CRC-TACC (forward air control post - control reporting post-control reporting center-tactical air control center) pyramid. For survivability, each level should be multiply connected, with multiple connections to other adjacent levels. The degree of multiple connectivity which should be used will often depend on what can physically be provided, e.g. with line-of-sight microwave communications, alternate paths can only be provided to the extent that alternative nodes are within line-of-sight distances or other relay facilities, such as airborne relay systems, can be provided. The important factor, though, is that no single node need be cognizant of the complete set of paths available to all other nodes.

In addition to the technical simplifications introduced by a hierarchical network, it could simplify political problems such as those likely in a tactical radar network interfacing Air Force, Army, Navy and civilian radars. Each political unit could be given considerable control over the interactions within its jurisdiction, with well-defined interfaces to other jurisdictions. (Although this fact is not well known, the areas served by local switching offices in the U. S. telephone system tend to be in areas with the same political jurisdiction, with well-defined interfaces to switching offices in other political jurisdictions, as this simplifies the process of getting construction permits, etc. for the systems.)

The number of levels for the hierarchy and the precise manner in which they should be defined and interact need to be worked out. The four levels in the FACP-CRP-CRC-TACC pyramid seem reasonable, but other numbers should be considered. Although the definitions of higher levels of the hierarchy should be based on geography (e.g. a tactical region of operations), a combination of geography and political considerations will probably be better at lower levels (e.g. Army SAM-D radars, E3-A radars, or civilian radars in a given area). Each level would be responsible for appropriately summarizing the information available at that level,

plus transmitting information to and from other levels.

One of the primary assumptions given earlier was that appropriate dissemination of surveillance data to users was one of the most important functions of the radar network. Speed of dissemination would be greater, and communications requirements would be less, if the reports to users originated as close to the original data sources as possible, i.e. at low levels in the hierarchy. On the other hand, with the type of hierarchy sketched, these low levels are likely to have a much less complete picture of the total situation than higher levels which have additional inputs (possibly including others from the same geographical area). This implies that reports to users should originate as far up in the hierarchy as is necessary to give complete information (possibly including information from non-radar sources such as intelligence information). Whenever response time and availability of communications facilities permit, originating reports at a high level is recommended. Two main exceptions might be noted. If quick notification of some event (such as a SAM launching) is extremely critical, such a report should be able to be originated at the first point where the event is noted. Also, the tactical situation could result in isolation of some lower levels from the rest of the network. They might still provide useful information if they are provided with the capability to originate reports (based on all the data they have available) to users who are connected to them.

A variety of communications control algorithms for the network need to be investigated. Both centralized and decentralized control are worth consideration, the former because of its simplicity and greater potential efficiency and the latter because of its apparent advantages in survivability. Types of switching algorithms which merit investigations include circuit switching, message switching, packet switching and various types of multiplexing or concentration schemes. These and similar questions merit considerable additional study before decisions are made.

Tradeoffs in Assembling Composite Picture

One area where new techniques will need to be developed is in combining reports from different radars to form a composite overall picture. Passing control of aircraft from one radar system to another is common practice in long-range radar flight control systems, but this does not mean the techniques for passing control are sophisticated or that any real composite radar reports are generated. The only description the author has found so far of an operational system where reports from asynchronously scanning radars are really merged is in [6], which describes a radar detection and tracking system developed by NRL which merges reports from two different shipborne radars (of two different types) to generate tracks. This paper and some of its references are worth studying in conjunction with developing techniques, but there are fundamental

differences between the situation discussed here and that discussed by Cantrell, et al, in [6]. One of the most significant differences is that their radars were very nearly contiguous to one another (located on the same ship), while much greater geographical separation is likely with radars in the type of radar network visualized here. Another significant difference is that it was much simpler for Cantrell, et al to provide common timing data to both radars; they simply fed the same clock to both.

Provision of common timing to all radars in a computer network is obviously necessary if the reports from the radars are to be merged successfully, since the differences in times of observation of a target must be known. Similarly, the relative locations of radars must be known. These are most likely to be problems with mobile radars where the radar location may change with time. A variety of techniques for handling the radar location and timing problems are available (problems of this type are common), and no attempt at describing them or comparing them will be made here.

If adequate information to determine relative timing and, if necessary, relative position for two radars is available, but the two radars are not synchronized, a plot of error ellipses for successive scans of one target bing tracked might look something like the plot in Figure 7 (reproduced from reference [3]). Note that the difference in geographical locations of the two radar sites results in distinctly different orientations of the error ellipses, a factor which would not be present with two radars located close together such as those described in [6]. Intuitively it seems that a tracking algorithm which utilized information from both radars in an optimum manner would be characterized by error ellipses with each axis close to the minimum of the values which would be obtained by measurements from site A or from site B. The author has not seen any real study of tracking algorithms for this case, though.

Three modes of radar target data netting have been listed by Allen, et al in an initial study of tactical surveillance architecture [7]. They have called these modes sequential netting, interleaved netting and simultaneous netting. Sequential netting, which they expect to be the normal mode of operation, implies that at any one time one sensor has primary responsibility for generating the target track and reporting it. Other sensors, which may observe the same track, do not report it unless their track is of higher quality than the primary sensor's track. (Obvious problems with this approach include computation of an adequate quality index for tracks, making this quality index and the corresponding track available to each sensor that might see the target, and having each sensor correlate its data with the received data adequately enough to determine whether it should report the

target also or not.) Interleaved netting corresponds to the general situation in Figure 7 with two or more radars reporting non-simultaneous observations of a target and the reports merged for tracking. They assume this mode will be primarily used for tracking rapidly maneuvering targets where the observations from one radar may not be frequent enough to maintain tracking. The third mode of simultaneous netting implies simultaneous observations by multiple sensors and is analogous to multilateration. With the wide variety of radars likely to be used in a tactical radar network, simultaneous netting will probably not be achievable in many cases, although it may be feasible for a given pair of radars if at least one has a phased array antenna. Allen, et al feel this mode is most likely to be used in ECCM for accurate jamming strobe triangulation and tracking.

The primary reason why Allen, et al have indicated a preference for sequential netting as a normal mode of operation is that it minimizes communication requirements by minimizing the number of track reports communicated. For their postulated network structure and communication facilities this is a valid reason for preferring sequential netting. The author feels, though, that in a hierarchical radar network of the type suggested here, interleaved netting should be feasible and is definitely the preferred mode of operation. (Simultaneous netting would not be feasible because of the wide variety of radars used.) Defining and using an adequate quality index for tracks, reporting the tracks with associated quality indices to all appropriate sensor sites, and having each site correlate its target tracks with tracks communicated to it and decide whether it should send in its own report or not, are far more complex than simply requiring each site to transmit all its target reports or tracks (whichever is the chosen parameter to use) to the next higher stage in the hierarchy. This higher stage could then make its own decision on whether it should use the data or not. Further, with reasonable assumptions on data traffic volume, there appear to be no real problems in providing adequate communications rates to handle the necessary traffic.

A rough indication of the one-way communications rates that might be needed to send all relevant information to the next stage in the hierarchy can be obtained by assuming 100 bits per report (track or target) and an average of 5 scans per minute. This implies an average transmission rate of 8.3 bits per second multiplied by the average number of reports per scan. With 100 reports per scan (a heavy traffic level if these are really good quality reports so that almost all are reports on actual distinct targets), 833 bits per second would be the average data transmission rate from a radar to its next reporting level. Most communication facilities proposed could handle higher rates. If, in turn, this level transmitted edited versions of the reports it received to a higher level, the average transmission rates necessary on this next higher level link should not exceed 4800 bits/sec. for data

from as many as six radars being summarized for transmission over this link. (This assumes some slight condensation of information results from editing at this level.) Transmission rates on links at still higher levels might be somewhat above those currently available on analog voice-grade transmission facilities, but they should be readily obtainable. Provision for such higher rates at these levels in the network does not appear unreasonable. One possibility for types of links used might be HF links for lower levels and tropo links for higher levels in the network.

The transmission rates that should be provided for communication in the reverse direction (i.e. from locations where surveillance data has been summarized to users of this data) will depend strongly upon the nature of these links and the types of summaries felt necessary to be exchanged over these links. It may or may not be necessary to transmit such summaries to sensor sites (so the data Allen, et al, assumed these sites would have may or may not be there). It is more important to get the data out to locations which would be responsible for sending it to users. Selective dissemination of information, of the general nature of that purportedly to be provided by JTIDS [8], appears advisable. Whether JTIDS would be able to provide adequate informaation rates for this dissemination of information is a question that has not been investigated.

A major type of tradeoff in netting that needs to be investigated is the tradeoff between processing data at a site and communication of the data to another site for processing. An example of an unresolved question of this type is the question addressed above of whether target reports or track reports should be communicated from radar sites to other sites at higher levels of the network hierarchy proposed here. The previous discussion of this question left the answer unresolved, with arguments in favor of and against each approach given. The precise form of the recommended radar network and its imposed loads have not been pinned down precisely enough to make it possible to make precise recommendations on how much processing to do where. A few general statements can be made, however.

Current technology trends, especially LSI and the rapid development of microprocessors, are making it advisable to do more and more processing at radar sites. Any processing that is heavily dependent upon use of local information (e.g. creation and use of a clutter map or of weather data such as MTD uses) should normally be done at the site. There may be exceptions, but usually the reduced data transmission requirements resulting from not having to transmit the site dependent data and being able to transmit only processed data (normally condensed from unprocessed data) will outweigh any other factors. On the other hand, it is very likely that processing dependent upon information from a central data bank should be done at the central location. There

are more exceptions to this case than to the previous one, but either transmitting individual files of information to the radar sites for processing or maintaining multiple copies of the data bank cause problems. The latter is especially troublesome, with detecting and reconciling any possible differences between the data banks some of the major problems.

A common tradeoff is one between increased data processing time and increased communications time. Usually (but not always) any data processor at a remote radar site could be expected to be less powerful than the data processor that might be located at a central site serving a number of remote sites. (The microprocessor speeds currently available and projected to become available soon are so great that it might appear that it is easy for the processor at a remote site to be faster than that at the central site. It is not at all unusual to have a fast microprocessor poorly matched to a job, due to a mismatched instruction set or other reasons, so that it is a much slower on that job than a larger processor, with considerably slower cycle time, that is better matched to the job. Since microprocessors tend to be very specialized, this situation is common.) If the relative speeds are as stated, the data processing location giving the better response time will depend on the relative magnitudes of the changes in data processing time versus data transmission time as the processing location is changed. The author has seen reasonable cases favoring each location. Further, the result of the tradeoff can vary with load. If there are a fairly large number of remote locations per central location, even if the processors at the remote sites are so slow that processing at the central site gave faster response times at light loads, the multiple slow processors might still be able to handle larger total loads than the single fast processor. Hence, response times with processing at remote locations might still be reasonable when the central processor would be saturated if the processing were done there.

The preceding comments assumed that a particular data processing job could be done at either one or the other of two locations. Often the tradeoff is more complex, with possibilities of doing more or less of the job at each location and transmitting more or less information back and forth. The same analysis procedure would hold in the more complex cases, with relative changes in data processing and data transmission compared.

From a reliability viewpoint it is normally best to minimize the number of different devices used in accomplishing a job. This could imply processing is better done at the radar site, though this is not always true. Thus, if the job is not really finished until data is available at the central site, and equipment is fixed, it may (to a first approximation at least) make little difference whether processing is done at the radar site followed by transmission to the central site or transmission to the central

site is followed by processing there. A precise study of reliability would depend on so many unspecified parameters that little more can be said now.

Cost is another factor that could favor either approach. Relying heavily on processing at each of N remote sites could conceivably require N applications of equipment that might be needed only once for processing at the central site. The picture is seldom so clear-cut, though, since the equipments that would be utilized in the two cases will differ, e. g. the single processor at the central site would probably be more powerful than one of the remote site processors. Also, with current trends in technology, there is very likely to be some type of data processor at each remote site; as an extreme case doing the processing there might be essentially free if there were enough excess processing capability available. Further, changes in communication costs also need to be considered.

UNATTENDED AND MINIMALLY ATTENDED RADARS

The largest single increments in the total life-cycle costs of most fixed surveillance radars are normally the costs of manning and maintaining the radars. This fact and the greater potential for automated operation afforded by the new technologies discussed in the previous sections have led to considerable recent emphasis on the development of unattended or minimally attended radars. These types of radars could soon give lower life-cycle costs while maintaining performance levels similar to or better than those of current attended radars.

Two factors which may limit the gains in life-cycle costs to be obtained with unattended or minimally attended radars are the impacts of higher initial acquisition costs (especially for unattended radars) and the effects of current Air Force standards on support for personnel at a site (for minimally attended radars). Although the reliability requirements for unattended radars are probably technically feasible in today's era when electronic equipment and other types of equipment are regularly designed for extremely long-term space flight missions, the reliability requirements are extremely severe. The degree of redundancy required for such systems, the requirements for derating of components to prolong their life, the careful testing and burn-in of components necessary, and the many other special factors that must be considered in designing for extremely high reliability may make the initial acquisition costs of such systems prohibitive in most situations. Hence, the next logical alternative suggested is minimally attended radars. If minimally attended radars are defined to be radars with minimal on-site operations and maintenance crews, though, the life-cycle-cost savings due to decreasing the number of personnel attending the radar site may be much less than most persons would anticipate. This results from the current Air Force standards on support for the crew attending the radar.

The support personnel (including chaplains, medical personnel, cooks and other mess hall personnel, etc.) normally greatly outnumber the radar operations and maintenance personnel, so a major reduction in radar operation and maintenance personnel would have a small reduction in the number of personnel required at the site [9].

The constraints just mentioned indicate that the best approach to minimize radar life-cycle costs might be through an alternative approach with the radars not normally attended, but maintenance personnel available to be flown in from other sites whenever repairs are necessary. This would tend to greatly increase the MTTR (mean time to repair the equipment) but the true total costs for maintaining the radars would be greatly reduced. An alternative to this approach could be contractor maintenance, assuming the contractor does not have support standards for his personnel similar to the Air Force's. (Simply paying the maintenance personnel high salaries to compensate them for long periods of isolation is cheaper than eliminating the isolation through elaborate support.)

Since the technologies discussed in the previous sections of this report can be used to provide automated operation of radars, with transmission of surveillance data to remote sites, the central problem in developing unattended/minimally attended radars is providing adequate reliability. (An illuminating description of the motivation for unattended/minimally attended radars, with examples of applications, is given in [10].) Hence this section of the report focuses on reliability requirements. Fixed surveillance radars are emphasized instead of tactical radars since the reliability requirements for the former tend to be more severe. (The latter type may often be viewed as expendable, with satisfactory operation during a mission of limited duration the primary requirement.) Tactical radars definitely have reliability problems also, but it should be feasible to remedy these by techniques such as replacing critical components, eliminating critical adjustments, reducing the stress on components, establishing a satisfactory margin of performance, and automating the status-monitoring and target-reporting functions. An excellent discussion of such techniques is given in [11].

The next subsection is a brief discussion of some of the major concepts of reliability theory, with emphasis on trying to clarify some of the more confusing aspects. This is followed by two brief theoretical analyses which give reinterpretations of some reliability formulas applicable to unattended/minimally attended radars. The final subsection then discusses some special factors that can greatly impact the reliabilities of such radars, but are very difficult to handle with current techniques.

Comments on Reliability Theory

A brief study of reliability theory, as it is currently applied for predicting the reliability of equipment of various types, can be thoroughly confusing to a novice who is conscientious enough to try to carefully examine the formulas being presented. A major reason for this confusion is the multitude of conflicting definitions used for very similar terms. (A friend of the author's, who works on reliability prediction for one of the country's largest corporations, has collected hundreds of different definitions for similar reliability theory terms.) The differences in definitions commonly result in slightly different formulas for what, at first glance, would appear to be the same thing.

Two factors contributing to the proliferation of definitions and formulas are the difficulty in precisely defining terms and the division of responsibility for reliability among different organizations which normally prevails.

Two examples of terms which are difficult to define are the fundamental terms "failure" and "repair". The definitions of these terms become especially difficult in systems with built-in redundancy to allow them to survive outages. A failure of such systems may, or may not, be said to have occurred if one of the redundant modules goes down; if a failure is considered to have occurred, its duration may only last until a spare module is switched in (with various degrees of preparing the spare module to take on the load leading to more definitions), or the failure may be defined to last until the spare module is repaired. Degraded function operation resulting from partial failure of equipment may or may not be considered to result in system failure. The differing viewpoints of different organizations involved in system reliability also come into play; thus a maintenance organization will not normally consider a failure to have occurred (according to any records it keeps) until it is notified, but a user organization may consider it down as soon as they notice the failure (which could be some time after it really occurred). Short self-clearing outages would not normally be considered to be failures by the maintenance organization if they were not reported to it. Another situation that may or may not be considered to be a failure is when the maintenance organization makes a "no trouble found" maintenance call; i.e. they didn't find anything wrong and the system was working when they left. Periodic scheduled preventive maintenance is another source of ambiguities as it may or may not be considered to represent a failure or outage.

Repair times are especially difficult to define precisely. Some possible components that may or may not be included in repair times quoted are the time period between failure and call of a repairman, the further time delay before the repairman shows up

(including travel time and other delays), the time required to diagnose the failure, the time required to obtain any necessary parts (which may or may not require ordering parts which are not in a local spare parts supply), the time required to remove the old parts and install the new ones (or perform any other actual repair actions), and the time required to check out the equipment and verify it is in operating condition. Other time intervals that might be considered will be added in special circumstances.

A lack of understanding of the effects of the unavoidable divisions of responsibility for reliability among design, manufacturing and maintenance organizations can, and often does, lead to unreasonable reliability specifications. An interesting example of the evolution of radar reliability specifications and achieved reliabilities over a period of several years is given in [12]; a curve plotted there shows specified mean times between failures (MTBFs) increased rapidly with time while the achieved MTBFs remained essentially constant. (The orginal reference for this curve was some work at Lincoln Laboratory cited in the reference; the cited reference is quoted here rather than the original reference since the original reference is classified.) Another consequence of lack of understanding of the division of responsibility is that specifications for reliabiity sometimes, if interpreted strictly, impose requirements on those persons making the specifications that they are not likely to be able to meet. In the author's opinion a good example of this is the current mean time to repair specification given by the Alaskan Air Command for the SEEK/IGLOO proposal [13]. The current specification for mean time for repair (MTTR) is 1/2 hour, which the Alaskan Air Command has indicated should be interpreted as an operational MTTR. This implies that the total time the radar is down for any reason should not average more than 1/2 hour. Major portions of this total down time (see the time components listed above) will be the responsibility of the Alaskan Air Command, especially if Air Force maintenance is the adopted policy. To further point up the stringency of this MTTR requirement, it might be noted that in order to counter the effects of a single ten hour repair time (not at all unusual, especially if parts ever have to brought in from remote locations) a total of 38 repair times averaging 1/4 hour (or some equivalent combination) are needed; to counteract a single 5-day repair (the maximum time period when weather conditions are expected to make it impossible for a repairman to go from a nearby living quarters site to the radar site) a total of 478 repair times averaging 1/4 hour are needed.

In general it is unreasonable to expect knowledgeable contractors to be bound to reliability specifications which are largely beyond their control. Unless the same contractor who designs and builds the equipment is responsible for its maintenance (including all required logistics support, etc.), the most the

contractor can do is achieve a certain MTBF (assuming the terms are defined adequately) and provide facilities for quick "hands-on" diagnosis and repair of the equipment. (This can, and sometimes does, lead to specification of the actual hands-on portions of the repair times.) Such repair time components as the time before a repairman is called, travel time for the repairmen, times to obtain spare parts, etc. are largely beyond his control. A complete and realistic technique for specifying reliability would involve specifying the required reliability performance for each group involved in achieving the desired reliability.

Although each of the definitions of reliability terms in current use makes good sense in the context for which it was intended, and the multitude of definitions is primarily due to conscientious attempts at rigorously defining some very slippery concepts, another factor tends to make many of the fine distinctions meaningless from a practical viewpoint. This factor is the standard lack of information about precise values of many of the parameters needed for accurate reliability calculations. Fine distinctions between different definitions of such terms as time to failure or repair time become meaningless if the parameters themselves are only known to within a factor of two or three, or even an order of magnitude. Yet parameters dominating the reliability calculations are often known no more accurately than this. Two examples where important values are especially unlikely to be known are the rates at which dependent failures of two or more different components occur and the rates at which software failures occur. Dependent failure modes and software failure modes are even less well understood than most other failure modes at present, but dependent failures are very likely to dominate the total system failure rates for highly redundant systems while software failures usually dominate the failure rates for data processing systems with fairly complex software. In general, the most difficult single step in reliability prediction is usually obtaining reasonable values for the parameters needed by the reliability prediction model used.

A final comment on standard reliability theory techniques is that the statistical models upon which they are based are no more than useful approximations, and there is convincing evidence that some of the standard assumptions are not strictly true. The most widely applied reliability theory techniques are based on an assumption of exponential failure rates, which is widely felt to be applicable over the greatest portion of the equipment life (after an initial burn-in period during which weak components were weeded out and before the wear-out period at the end of the equipment's useful life.) A large body of evidence has been accumulated which indicates that the decreasing failure rate characterizing the initial burn-in period is really characteristic of the total useful life of the equipment [14-16]. The accumulated data indicates that the decreasing failure rate persists throughout the useful life of the equipment with only nominal corrective action taken [14,15]. In real life, however, the following quotation from [16] is more applicable, "All of the mathematical folklore

of Reliability works with the assumption of constant failure rate, but all of the management effort in today's Reliability arena is to make sure that failure rate is a controllable variable." If a conscientious reliability improvement program is maintained throughout the useful life of the equipment, there seems to be little doubt that reliability can be consistently improved throughout most of the equipment's lifetime, and some of the data referenced seems to indicate some limited improvement can be expected even without a very conscientious reliability improvement program.

The implications of the cited results for the unattended/minimally attended radar program are that demonstrating adequate reliability in qualification tests may require a much longer burn-in test period for the equipment than the conventional assumptions would indicate, and that failure to achieve the desired reliability goals during the initial time period after the first radars are installed does not necessarily mean the goals won't be attained by the same equipment at a later date.

Reinterpretation of Some Theoretical Results

A limited amount of theoretical analysis directly related to the reliability of unattended/minimally attended radars has been published. These analyses reflect a variety of definitions of the terms unattended and minimally attended. Some modifications to a few of the approaches are briefly studied in this section.

One approach to analyzing the reliability of unattended radars is to compute the mean time between failures (MTBF) needed to achieve a specified probability of operating without failure for the unattended period. (This analysis involves making the assumption of constant failure rates, or constant MTBFs. No attempt to incorporate decreasing failure rate statistics, which the previous subsection indicated were more realistic, will be made here.) With the specified approach, the following MTBF values would be considered to be needed to achieve 90% probability of satisfactory operation for the stated period. All MTBF values have been rounded to two significant digits to partially reflect the fact that such parameter values are not normally known precisely. (Even two significant digits can be misleading.)

MISSION TIME INTERVAL		REQUIRED MTBF
Months	Hours	Hours
0.5	365	3,500
1	730	6,900
3	2,190	21,000
6	4,380	42,000
12	8,760	83,000

All of the listed MTBFs, especially the ones for the more

useful mission time intervals of three months or longer, are far beyond the values obtained with current equipment. Hence, all approaches to meeting these MTBF goals involve the use of highly redundent, highly sophisticated, and very expensive, designs.

Fortunately, the completely unattended type of operation leading to the above MTBF values is more than should be really necessary in most radar situations. Essentially all current and proposed radars (aside from possible space-borne radars) are repairable. Even if they are not normally attended, repair crews can be dispatched to the sites when they go down, assuming the fact they have gone down is known. (Weather conditions, such as may be experienced in Arctic environments, or other factors, could delay dispatch of the repair crews.) Under most conditions, it is more meaningful to discuss the reliability obtainable with repair crews available, but with the repair crews not necessarily located at the radar site.

An analysis of the repair situation just described is given in [17]. This report gives the result of an analysis, using standard statistical techniques (an approach described as either use of equations of detailed balance or of birth-and-death equations) of a situation with M machines and Q repair crews, with both the failure times and repair times exponentially distributed. The results are obtained as functions of M, Q and the ratio of the mean time to repair (MTTR) to the mean time between failures (MTBF). The results given in [17] include plots of operational readiness (defined to be the probability no more than K machines are down) versus MTTR/MTBF for various values of M, Q and K. Typical plots for M = 13 (the number of radars planned for the Alaskan SEEK IGLOO program) and various values of Q are given for the case K = 0 in Figure 8 and for K = 1 in Figure 9.

If they are carefully interpreted, a reasonable analysis of the effects of using different numbers of repair crews (different values of Q) can be obtained from Figures 8 and 9 and the other material in [17]. It is easy to reach the misleading conclusion that, under the assumed conditions, increasing the number of repair crews above two provides little improvement, however. The fact that there is little difference between the plotted curves for Q = 2 and Q = 13 seems to imply this. Increasing the number of repair crews above two can substantially reduce the MTTR, and hence the ratio MTTR/MTBF used as the abscissa in the figures, so that the relevant point on the curves shifts to the left.

In order to more clearly show the impact of the number of repair crews on performance, some arbitrary assumptions will be made. It will be assumed that with 13 repair crews, one would be located at each site and the (extremely optimistic) SEEK IGLOO goal of 1/2 hour MTTR [13] can be achieved. Further, it will be assumed that with one repair crew, the MTRR (including travel time) would equal approximately two days (listed as a reasonable value for a DEW-Line type of environment in the transmittal letter for [17]). Further, in the absence of any evidence to the contrary the (wild) assumption of a linear

dependence of MTTR on Q will be made. The precise formula used will be

MTRR = 52 1/2 - 4Q (12)

(The value assumed for Q = 1 was increased from 48 to 48 1/2 to simplify the formula). Further, the MTBF will be assumed to be 1100 hours (the current SEEK IGLOO specification).

With these assumptions, values of the ratio MTTR/MTBF have been computed for various values of Q and the corresponding values of operational availability read off of Figures 8 and 9 (interpoluting between the curves for Q=2 and Q=13 where necessary). This gave the curves plotted in Figure 10, which shows that using more than two crews can substantially improve reliability.

One other factor which has sometimes been treated in a misleading manner is the possibility of unattended periods for radars which normally have on-site maintenance. The motivation for considering this is again SEEK IGLOO, since there may be periods (stated to be as long as five days) when weather conditions make it impossible to reach the radar site from nearby living quarters. In [13] this possibility is treated by assuming the reliability of the system during an unattended period is equal to its availability during this period. Reliability, however, is normally taken to be the probability a system remains operational during a period of time, while availability is normally taken to be the probability the system is operational at a randomly chosen instant of time. Even if the radar failed during an unattended period, a randomly chosen instant of time falling within the unattended period could fall within the time interval when the radar was still operating. A more accurate analysis allows for this possibility.

An approximate, but more realistic, model can be obtained by assuming that the availability during attended periods is identical to what it would be without the unattended periods existing, while the availability during unattended periods is the fraction of these unattended periods that the radar is operating. (This neglects transient effects at the end of unattended periods when the availability could be expected to be less than assumed. The duration of such transient effects will normally be too short to for them to significantly affect the results.) If an unattended period is of length δ and the radar is up for a period t_1 after the beginning of this period, then the availability during the period will be taken to be t_1/δ for $t_1 < \delta$ and 1 otherwise. The usual assumption of exponential failure times will be made so that the needed values are readily computable. If the MTBF (or mean system "up" time) is denoted by U this gives a term of the form

$$\frac{1}{\delta}\int_0^{\delta}\frac{t_1}{U}e^{-t_1/U}dt_1 + \int_{\delta}^{\infty}\frac{1}{U}e^{-t_1/U}dt_1$$

$$= \frac{U}{\delta}\left(1 - e^{-\delta/U}\right) \qquad (13)$$

as the conditional availability during the unattended period, given the system was operational at the beginning of this period. This term should be multiplied by the availability at the beginning of this period to get the corresponding unconditional availability.

If there is one unattended period of length δ in a longer period of length T (for SEEK IGLOO, as the specifications are now stated, δ would equal 5 days and T one year), the overall availability can be obtained by taking δ/T times the term just computed plus $(T-\delta)/T$ times the availability, A_0, of a fully attended system. Thus

$$A = A_0\left[\frac{T-\delta}{T} + \frac{U}{T}\left(1-e^{-\delta/U}\right)\right] \qquad (14)$$

where A_0 is the abailability of a fully attended system

$$A_0 = \frac{U}{U+D} \qquad (15)$$

with D the system MTTR (or mean "down" time).

If multiple unattended periods, of lengths δ_i, $i = 1, 2 \cdots n$, occur, an obvious extension is

$$A = A_0\left[\frac{T-\sum_{i=1}^{n}\delta_i}{T} + \frac{U}{T}\left(1-\sum_{i=1}^{n}e^{-\delta_i/U}\right)\right], \qquad (16)$$

After deriving the above results, the author discovered an alternative derivation of almost identical formulas by Levy [18]. (Levy's formulas are very slightly more complex since he averaged the availability over transient periods at the end of unattended periods, but the extra terms he obtained are insignificant in any practical situation.) Further, Levy has shown, by taking the lowest order terms in the expansion of the exponential functions (and ignoring his extra terms) that

$$A \approx A_0\left[1-\frac{1}{2UT}\sum_{i=1}^{n}\delta_i^2\right], \qquad (17)$$

so that the effect of unattended periods is proportional to the square of their length. Thus the single 5 day period postulated by SEEK IGLOO is equivalent to one 3 day period plus one 4 day period.

Although the results given here, and by Levy, provide an

improved way of handling unattended periods, a realistic approach would involve utilizing the probability distributions for the number and duration of unattended periods, with statistical averages computed with the aid of the formulas given.

General Comments on Reliability

Some special factors that should be considered in evaluating the reliability of systems such as those being considered here should be briefly mentioned.

In systems designed for extremely high reliability, with appropriate amounts of redundancy to achieve this reliability, it is common for the reliability to be primarily determined by dependent failures (where more than one failure occur at once much more frequently than an independent failure model would indicate, or where one failure tends to make other failures more likely by increasing loads on other components or some other mechanisms.). One class of systems where dependent failures have been found to be dominant, to the surprise of many persons, is that of telephone communication systems with redundant lines. The manner in which the telephone plant is installed causes a large amount of common equipment to be used by different telephone lines, so failures of two or more lines are much more common than the reliability literature tends to indicate. Other mechanisms may cause similar dependent failures for other classes of redundant communication links. A second major source of dependent failures is software systems. This is especially true if backup is provided by having a backup system which executes the same programs as the primary system so that immediate switching can occur if the primary system fails. Since software bugs often are of a type which cause failure every time a particular section of code is executed, both systems are likely to fail simultaneously if a software bug is the problem.

Predicting the reliability of highly redundant systems for which dependent failure modes may dominate the failure statistics is especially difficult since the parameters to describe the dependent failures are usually among the least accurately known reliability parameters for the whole systems. This can easily result in having much less accurate reliability estimates for systems for which reliability is a prime design goal than for systems for which reliability has been considered to be less important.

Another factor which is ignored in the majority of the reliability computations done for redundant systems found in the literature is reliability of some of the special added equipment added to secure extra reliability. Thus in triplicated systems with voting the reliability of the vote-takers is extremely important, or in other systems with switching the reliabilities

of the switches need to be considered.

CONCLUSIONS AND RECOMMENDATIONS

Three primary areas have been discussed in this report. The first major section discussed the possibility of utilizing extra radar parameters, such as velocity return signal strength, etc. (parameters which are automatically available for use with some of the more advanced radar data processing techniques) in order to improve radar performance. The second major section discussed some of the major problems and design tradeoffs associated with radar netting, and the third section discussed reliability considerations in unattended/minimally attended radars. Each of the discussions was a very preliminary nature, and each topic merits considerable additional work.

The initial section on use of extra parameters demonstrated fairly convincingly the fact that marked improvements in performance are possible if such additional parameters are used. A variety of extensions of the techniques are needed. These include more careful examination of the accuracy with which such parameters as velocity may be known, including the effects of such things as propeller modulation or range/velocity ambiguity patterns. Major improvements in the realism with which actual measurement data is modeled are needed; e.g. the measurements obtained from systems such as MTD are far more complex than the modeling assumptions. Techniques for utilizing other parameters besides velocity, such as return signal strengths as a function of time, could also be fruitful. ECCM capabilities of the techniques discussed could be powerful, but have hardly been investigated.

The most tentative ideas presented in this report have been given in the discussion of radar netting. An attempt has been made to present an approach to radar netting in which the basic form of the network follows from reasonably convincing reasoning based on the system requirements. Reasonably convincing arguments for a few basic elements of an overall network architecture have been given. In the opinion of the author, similar arguments can be extended to develop an overall architecture superior to any others he has seen. Most of the work on defining such an architecture still needs to be done, however. This is especially true for the architecture of the communications network, which may well be the most difficult portion of the system to design and implement. Numerous other difficult problems, such as tradeoffs between data processing and data communications, need to be investigated also.

The final area covered, of reliability problems in unattended/minimally attended radars, is the area where ongoing work seems to the author to be most likely to yield satisfactory results. The major concern is whether the resulting radars are going to be

cost-effective in an actual Air Force operating environment. The major emphasis of this portion of the report has been on clarifying some of the relevant reliability theory concepts. Some advances in these techniques are needed, though, especially in finding techniques for handling such things as dependent failure modes.

Although the three areas covered in the report appear at first to be disjoint, they are all important problems resulting from the same general technology trends. Each is becoming important because of the increasing use of sophisticated radar data processing techniques, primarily digital techniques, which are far more flexible than previous techniques (as exemplified by MTD's use of almost three million separately computed thresholds in range/azimuth/velocity space) and provide the capability for greater automation of the radar data processing. Such techniques are now coming in and seem almost certain to provide revolutionary improvements in the effectiveness of radar systems. In order to realize the full potential of such techniques, however, the problems outlined here (and other related problems) will have to be solved.

Lincoln Laboratory's MTD has been the primary example of new radar data processing algorithms discussed in this report. It has been utilized as an example partially because of accessibility of information on it, but primarily because it is the best example of state-of-the-art radar data processing known to the author. It is based on implementing some radar data processing algorithms that are very nearly optimum for the class of radars for which it is currently implemented, with the implementation taking better advantage of the flexibility of digital data processing than any other similar implementation known to the author (save for the systems based on MTD now being developed by various manufacturers). Use of three million separate range/azimuth/velocity cells, each with independent thresholding, and use of a fine-grained clutter map with separate clutter values for 370,000 different range/azimuth cells are both examples of techniques which are simply not feasible with older analog techniques. Similar techniques, with implementation of near optimal algorithms in a manner which takes full advantage of current processing techniques, need to be applied for other classes of radar such as long-range 3-D radars, OTH radars, airborne radars, etc. The precise algorithms used by MTD are not necessarily recommended for other classes of radars, but the philosophy of MTD is recommended. Other new techniques such as CCD techniques, optical signal processing techniques, SAW device technologies, etc. could supplant some of the digital techniques used in MTD in some future systems.

The potential breakthroughs which may result from the new innovations in radar systems now coming in are exciting. The problems to be solved in order to realize their potential are challenging though. Hopefully, this report may make some contribution toward meeting the challenges. Much future work is needed, though.

ACKNOWLEDGMENTS

The author would like to express his appreciation to the United States Air Force and the Americal Society for Engineering Education for making this program possible. He is especially grateful to his research colleague, Dr. Donald B. Brick, for his assistance prior to and during the program. Other persons, too numerous to name, at MITRE Corporation, Lincoln Laboratory, Rome Air Development Corporation as well as other ESD personnel, provided a great deal of assistance. He would also like to express his appreciation to Mrs Dimitrou Murphy for her assistance in typing the manuscript.

REFERENCES

1. "System Specification for the Region Operations Control Center Segment of the Joint Surveillance System," Specification No: ESD-RS 968H, 1 June 1976.

2. Drury, W. H., "Improved MTI Radar Signal Processor," ATC Surveillance/Communication Analysis and Planning Project Report ATC-39, 3 April 1975.

3. Waldman, A., Kulpinski, R. J., Hunt, S. N. and Cook, C. E., "On-Site Processing Requirements for Tactical Netted Surveillance," MITRE Corporation, Bedford Operations, Working Paper No. 20566, 20 January 1976.

4. Foy, W. H., "Position-Location Solutions by Taylor-Series Estimation," IEEE Transactions on Aerospace and Electronic Systems, Vol. AES-12, No. 2, pp. 187-194, March 1976.

5. Muehe, C. E. and O'Donnell, R. M., MIT Lincoln Laboratories, Lexington, Mass., Personal Communications.

6. Cantrell, B. H., Trunk, G. V., Queen, F. D., Wilson, J. D. and Alter, J. J., "Automatic Detection and Integrated Tracking System," Conference Record for IEEE International Radar Conference, Arlington, Va., Apr 21-25, 1975, pp. 391-395.

7. Allen, L. W., Cook, C. E., Davis, R. C., Daelhousen, J. A., Hunt, S. N., Kulpinski, R. J., Rubin, R., Waldman, A. and Westley, A. L., "An Evolutionary Tactical Surveillance Architecture," MITRE Corporation, Bedford Operations, Working Paper No. 20639A, 8 March 1976.

8. Workman, B. J., "An Overview of the Joint Tactical Information Distribution System (JTIDS), MITRE Corporation, Bedford Operations, Report No. MTR-3228, April 1976.

9. Paltauf, Lt. Col, R. C., Rome Air Development Center, Rome, N. Y., personal communication.

10. Blasberg, L. A., "Unattended/Minimally Attended Radar Systems-Description and Requirements," MITRE Corporation, Bedford Operations, Working Paper No. 20448, 9 Jan 1976.

11. Bridge, W. M., Talley, W. K. and Tiffany, G. B., "Tactical Radar Modification for Life-Cycle Cost Reduction," MITRE Corporation, Bedford Operations Working Paper No. 20603, 5 Apr 1976.

12. Fowler, C. A., "Some Radar Design Problems and Considerations," Conf. Record for IEEE International Radar Conference, Arlington, Va., 1975, pp. 300-305.

13. AFSC (ESD)/AAC SEEK IGLOO Study, Second Interim Report, 26 April 1976.

14. Anderson, J. E., "Correlation of Reliability Performance Mrasurements," 1970 Annual Symposium on Reliability, pp. 206-211.

15. Lyman, K. A., "A Unifying Reliability Analysis Philosophy," 1970 Annual Symposium on Reliability, pp. 221-227.

16. Codier, E. O. "Reliability Growth in Real Life," 1968 Annual Symposium on Reliability, pp. 458-469.

17. Ormsby, J. F. A., "Multiple System and Repair Crew Operational Readiness Versus MTTR and MTBF," MITRE Corporation, Bedford Operations Memo No. D55-M-277, 7 Jan 1976. Circulated with transmittal letter from J. G. Wohl to Commander, Headquarters, ESD. (MITRE Technical Information Letter 6710-10), 9 Jan 1976.

18. Levy, J. E., "System Availability," MITRE Corporation, Bedford, Mass., Memo No. D81-M-3167 (to G. A. Klein), 15 April 1976.

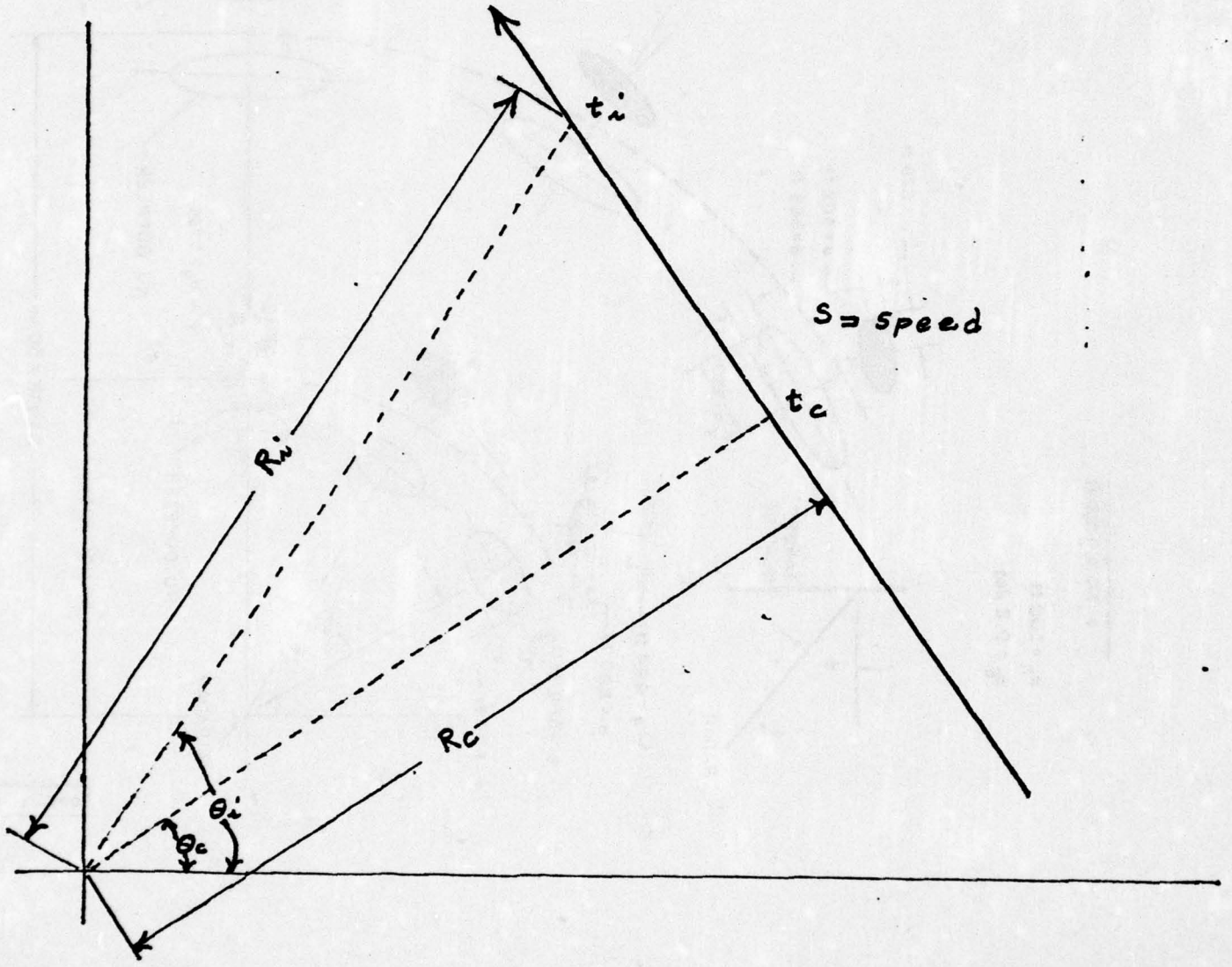


Figure 1 PARAMETERS USED IN

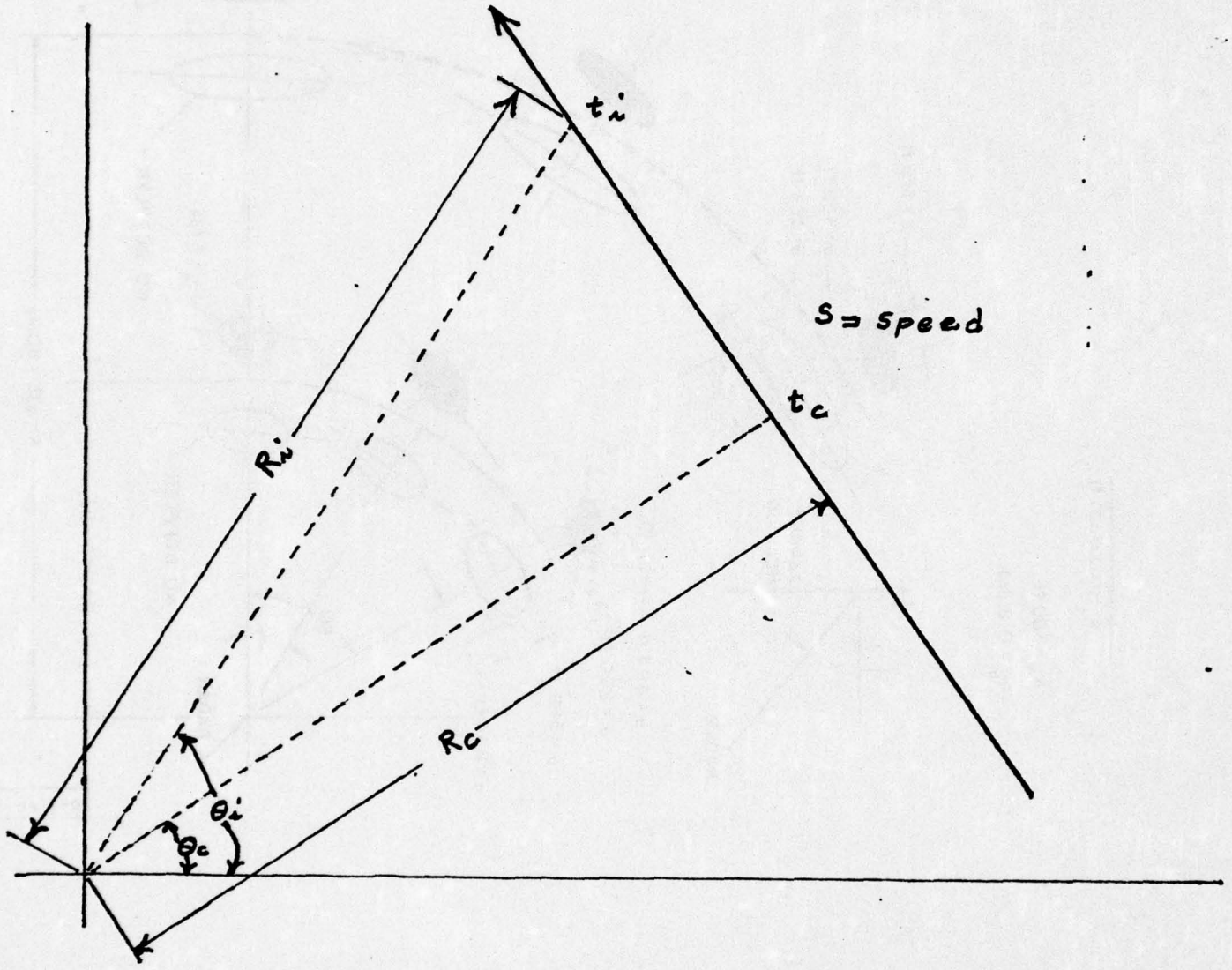


Figure 1 PARAMETERS USED IN TRACKING ALGORITHMS

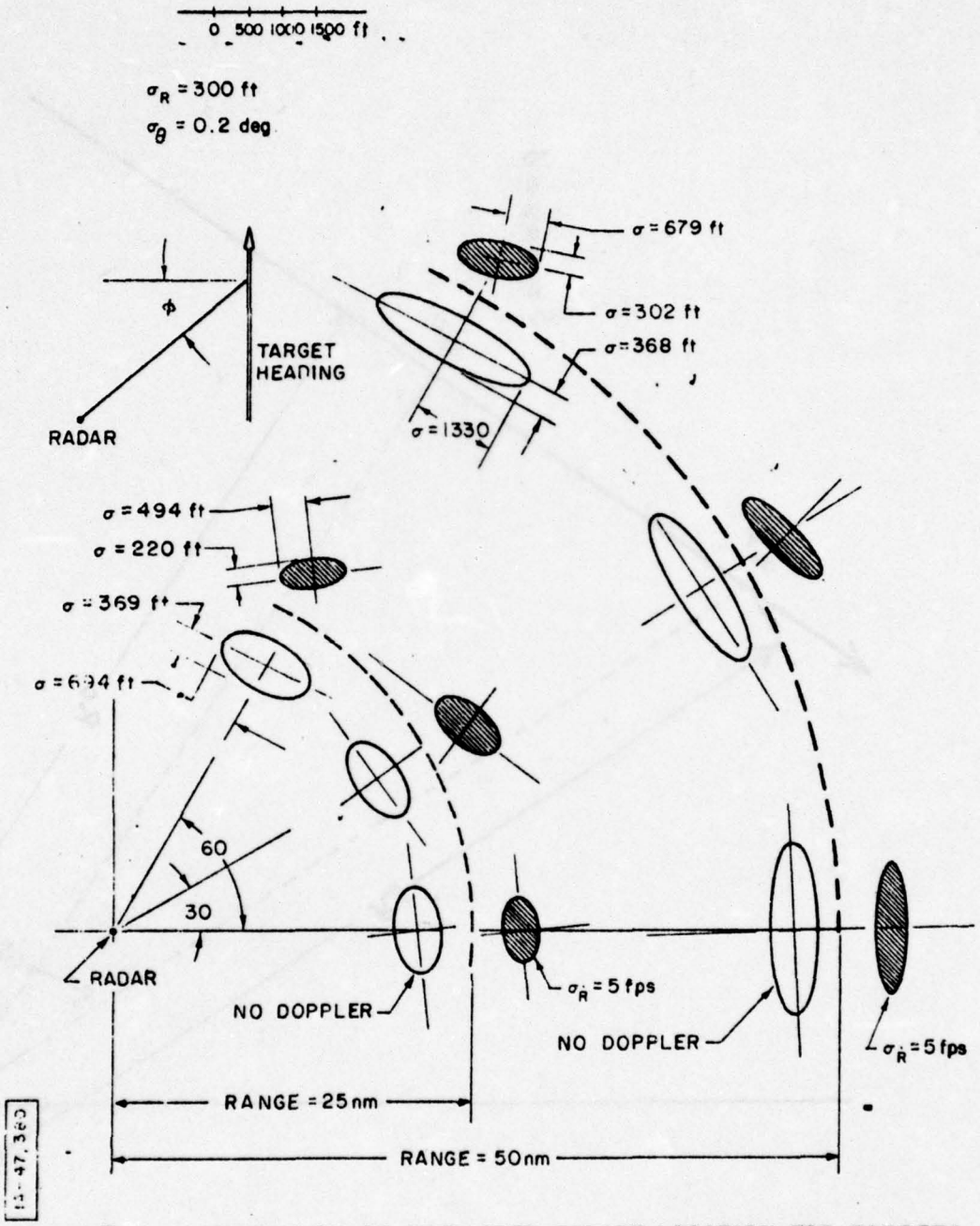


Figure 2. DISTRIBUTION OF PREDICTED TARGET LOCATION FOR TARGETS AT R = 25 nm AND 50 nm AND FOR ϕ = 0, 30 AND 60 DEGREES AND FOR RANGE MEASUREMENT UNCERTAINTY σ_R = 300 ft.

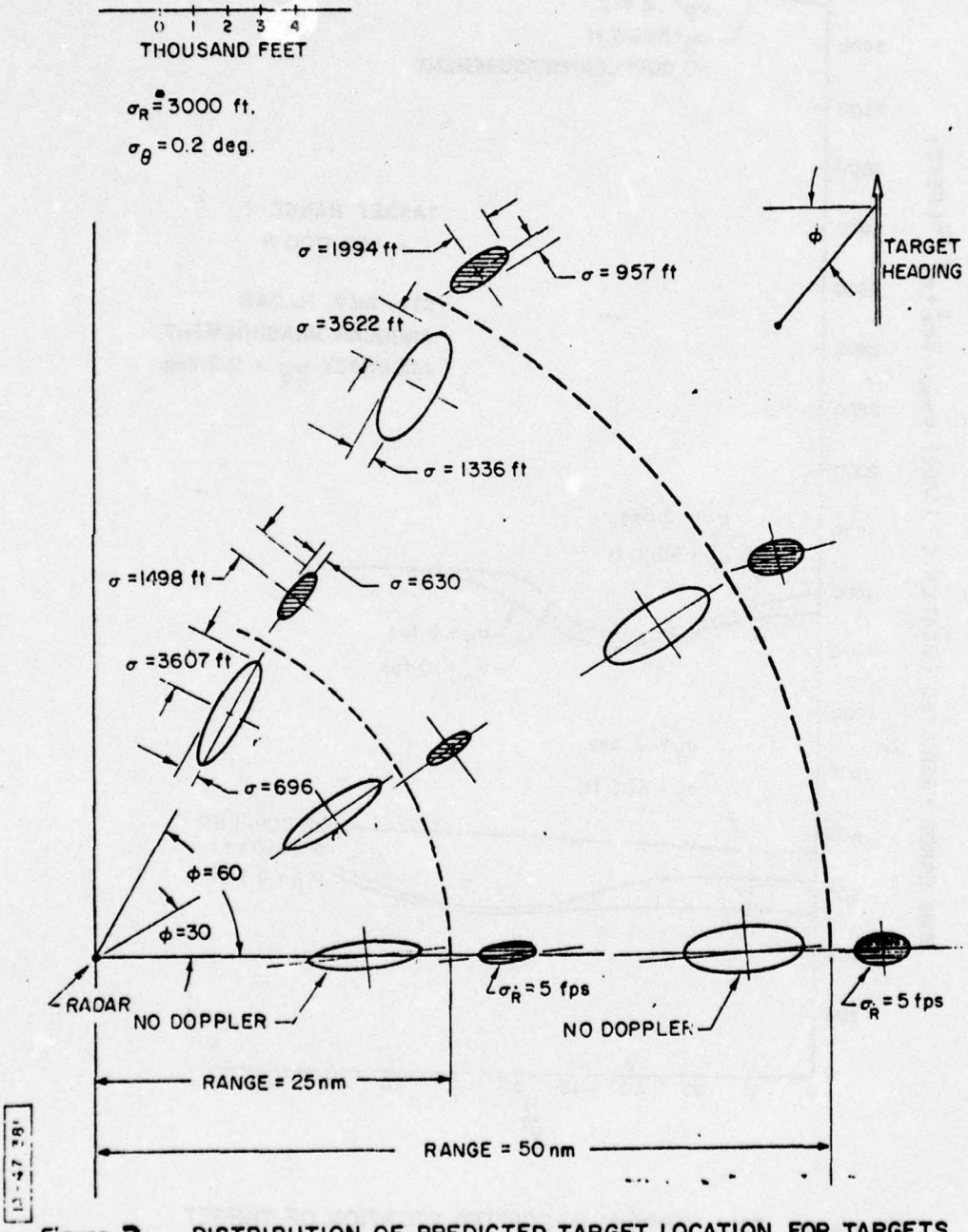
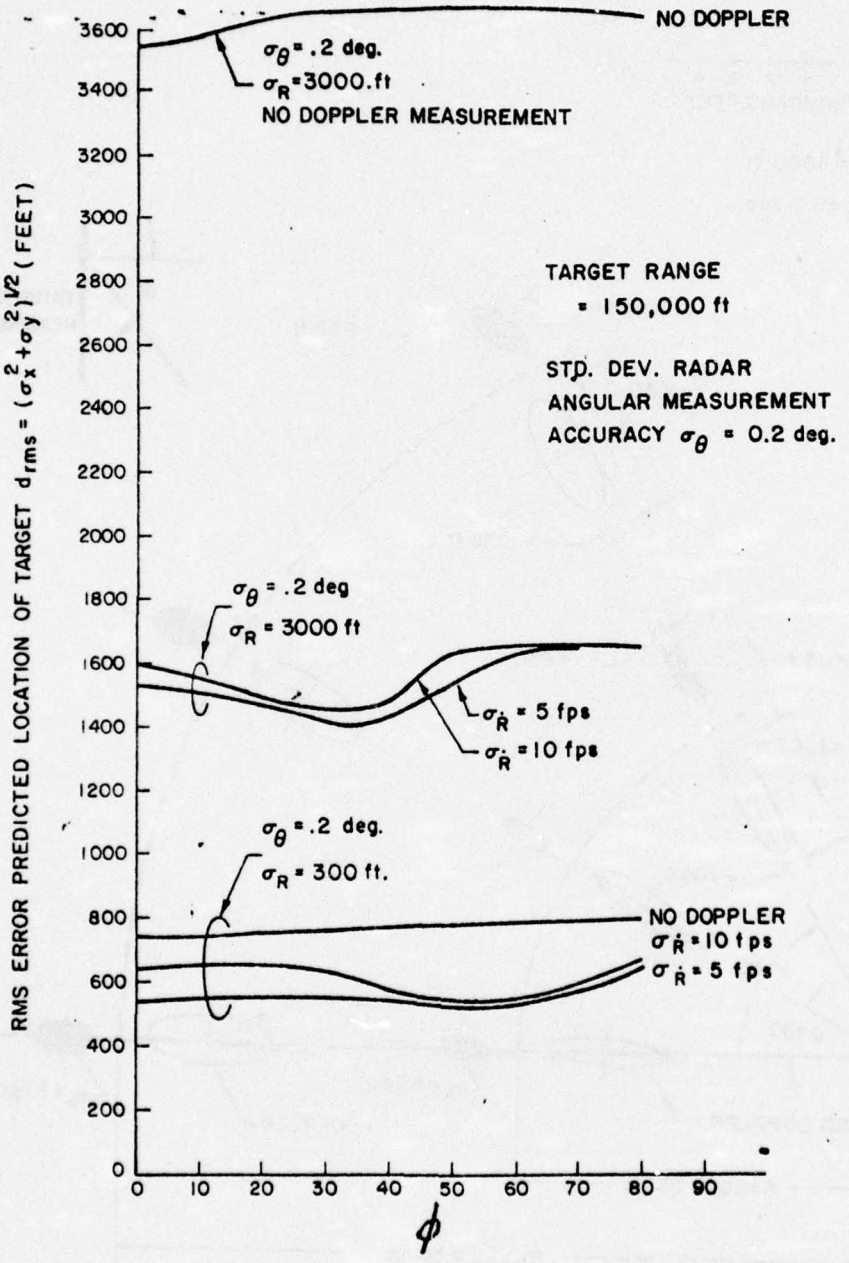


Figure 3 DISTRIBUTION OF PREDICTED TARGET LOCATION FOR TARGETS AT R = 25 nm AND 50 nm AND FOR ϕ = 0, 30 AND 60 DEGREES AND FOR RANGE MEASUREMENT UNCERTAINTY σ_R = 3000 ft.



18-47,382

Figure 4 RMS ERROR, PREDICTED LOCATION OF TARGET

IA-47,383

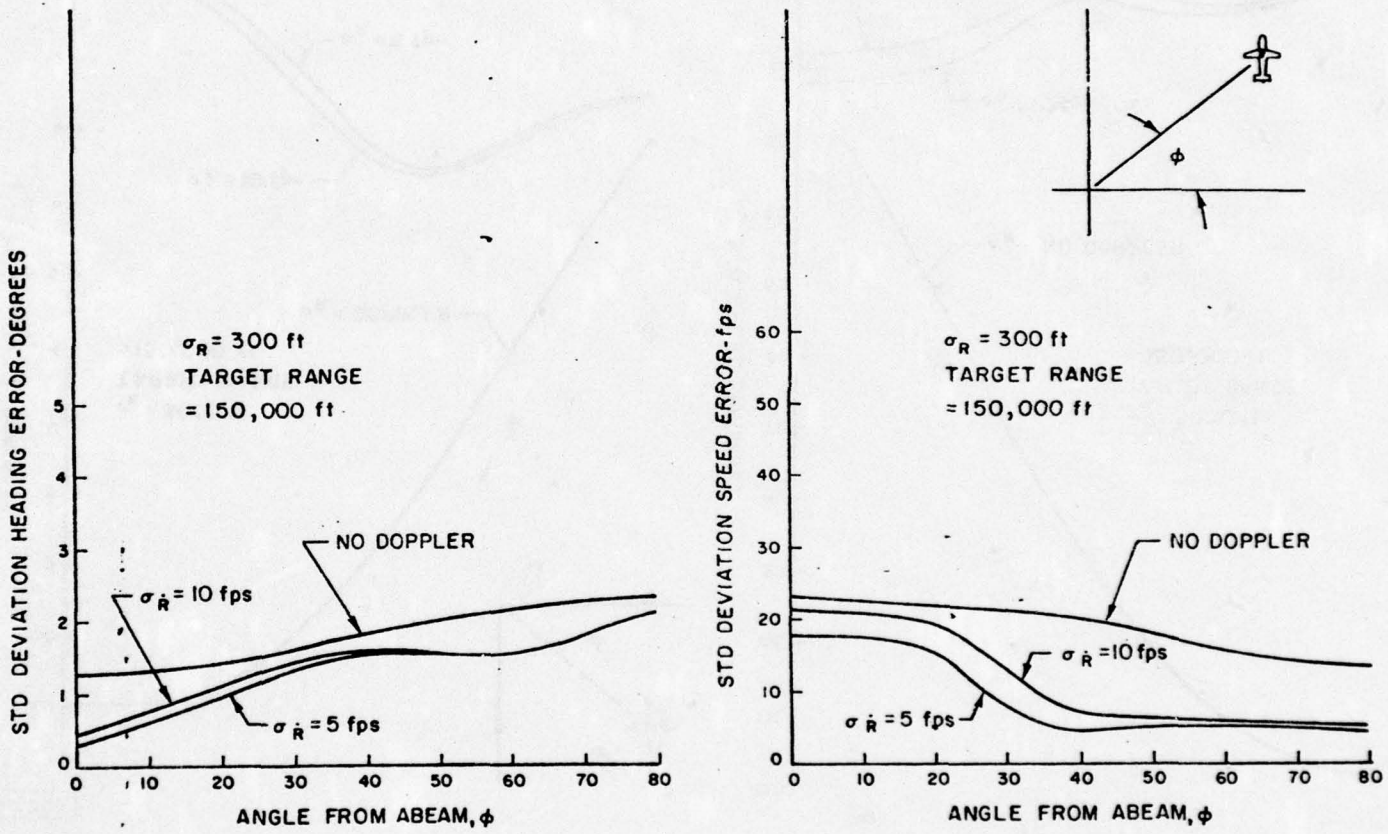


Figure 5 STANDARD DEVIATION TRACK HEADING AND SPEED ERROR FOR σ_R = 300 ft

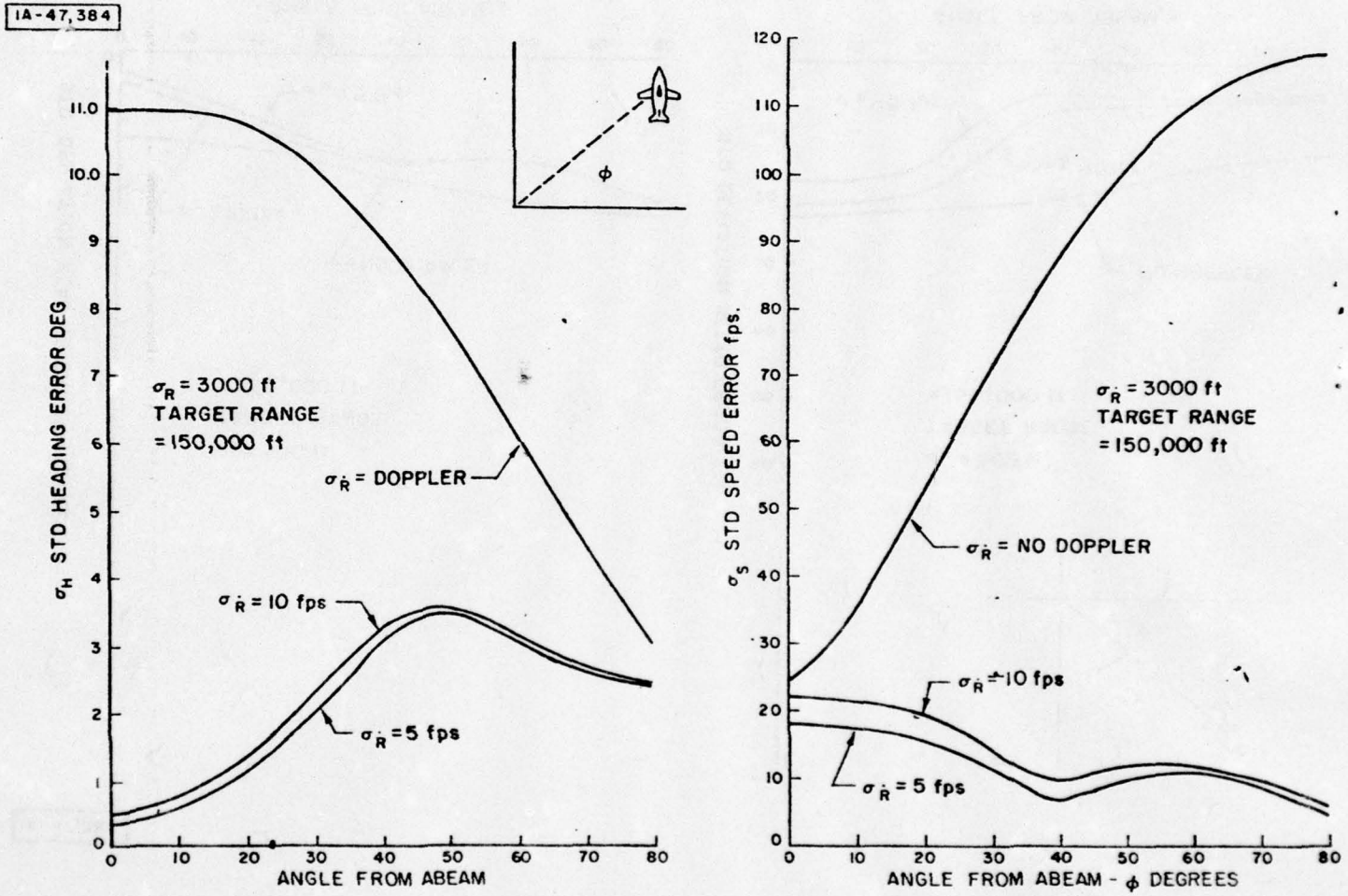
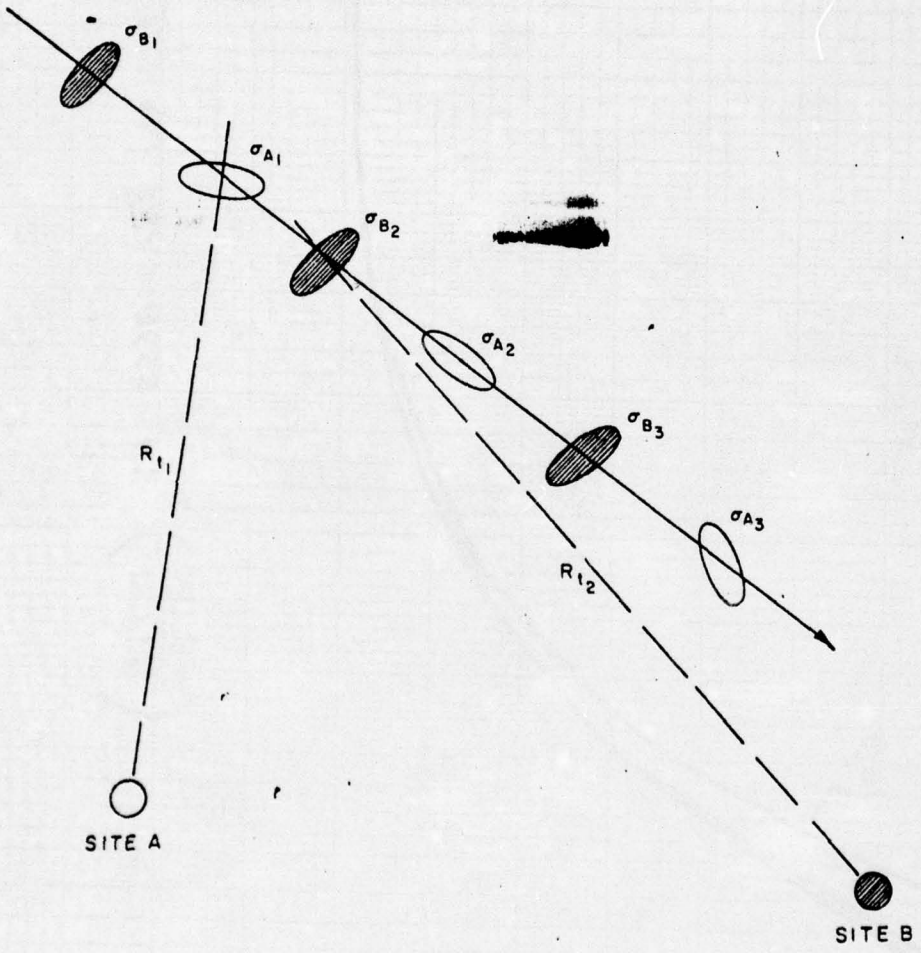
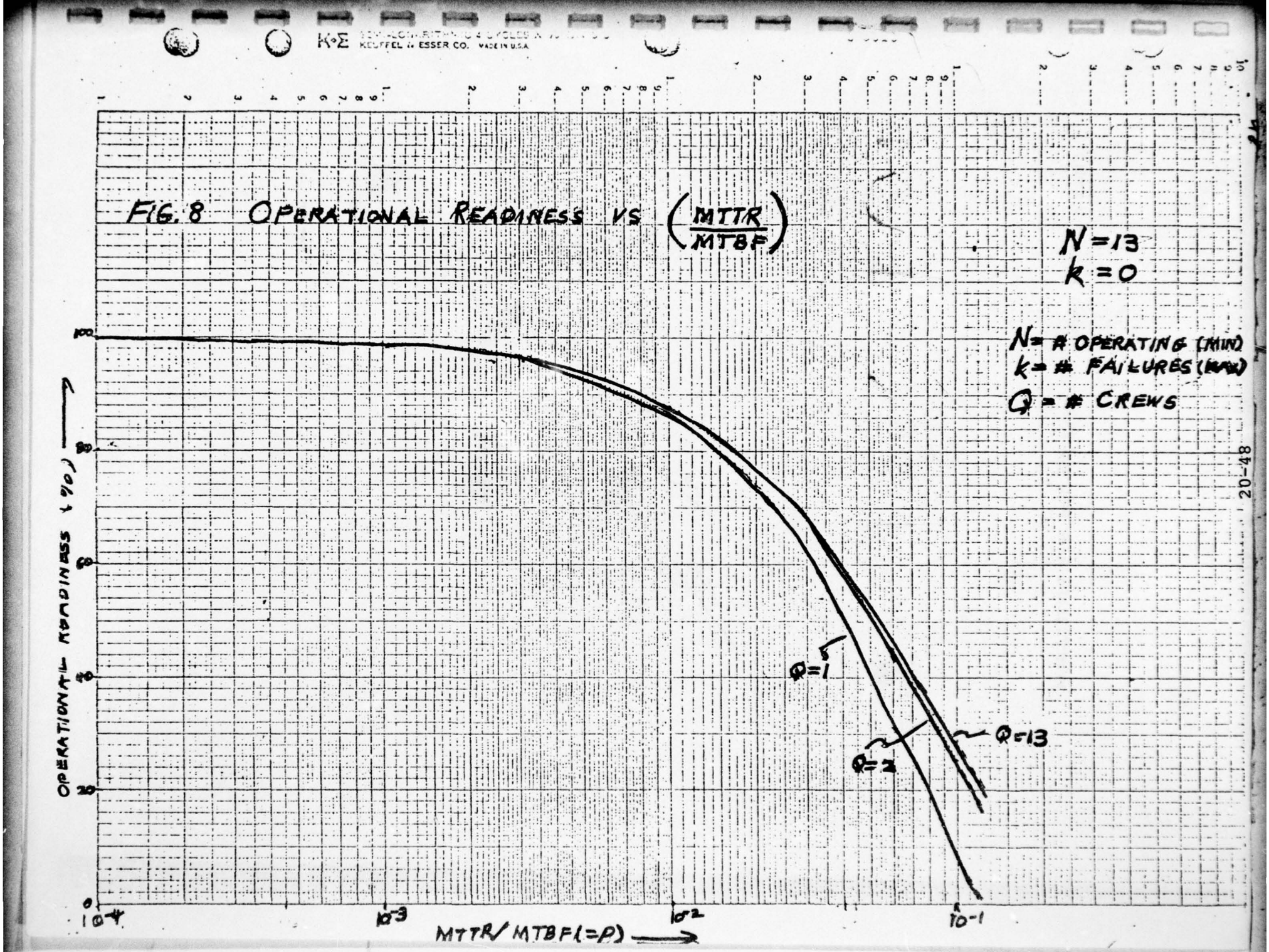


Figure 6 STANDARD DEVIATION TRACK HEADING AND SPEED ERROR FOR σ_R = 3000 ft



LA-47,376

Figure 7 RADAR ERROR ELLIPSES FOR DUAL SITE SURVEILLANCE


FIG. 8 OPERATIONAL READINESS VS (MTTR/MTBF)
N = 13
k = 0
N = # OPERATING (MIN)
k = # FAILURES (MAX)
Q = # CREWS
Q=1
Q=2
Q=13
OPERATIONAL READINESS (%)
100
80
60
40
20
0
10⁻⁴
10⁻³
10⁻²
10⁻¹
MTTR/MTBF (=ρ)
20-48

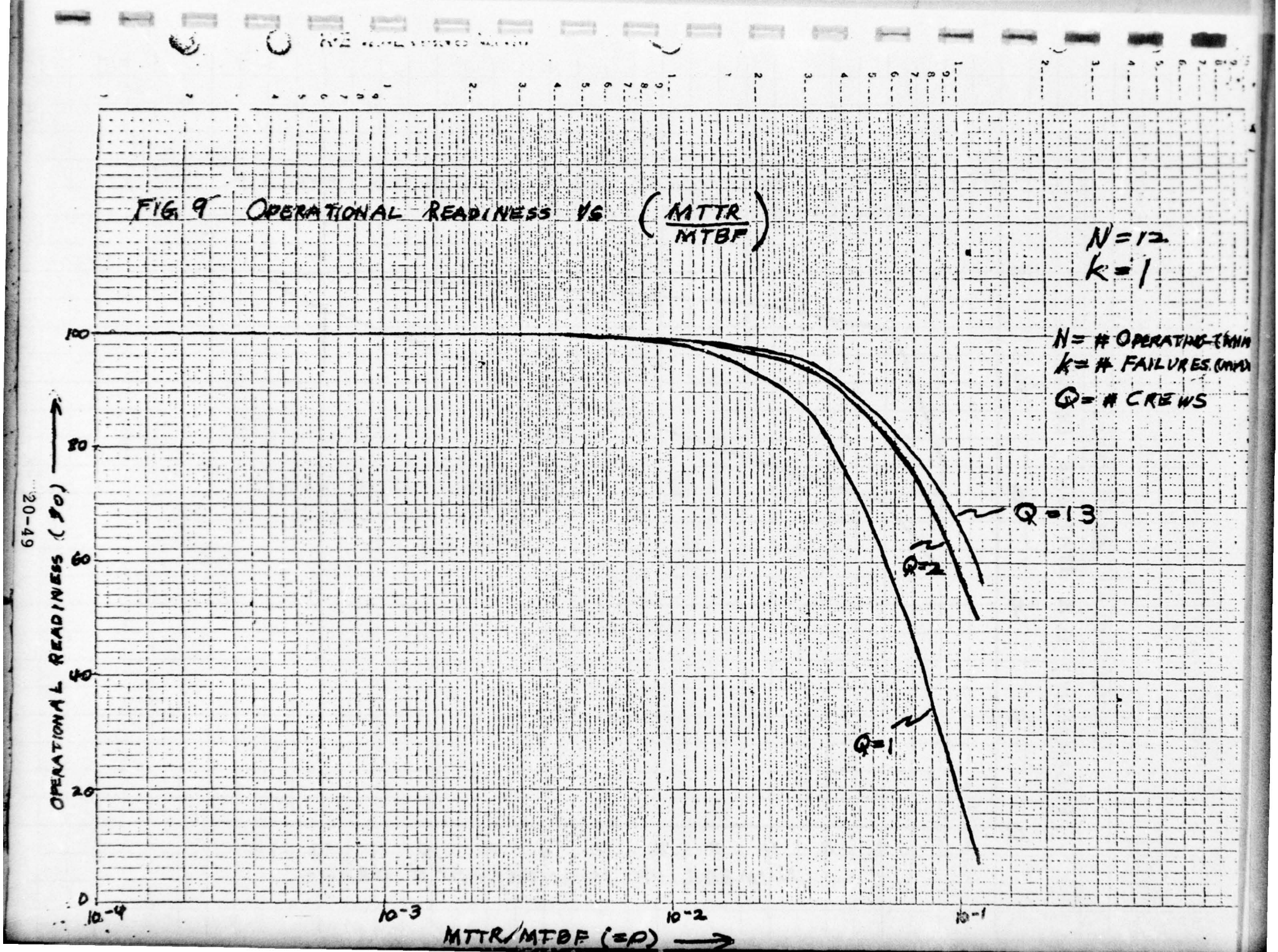
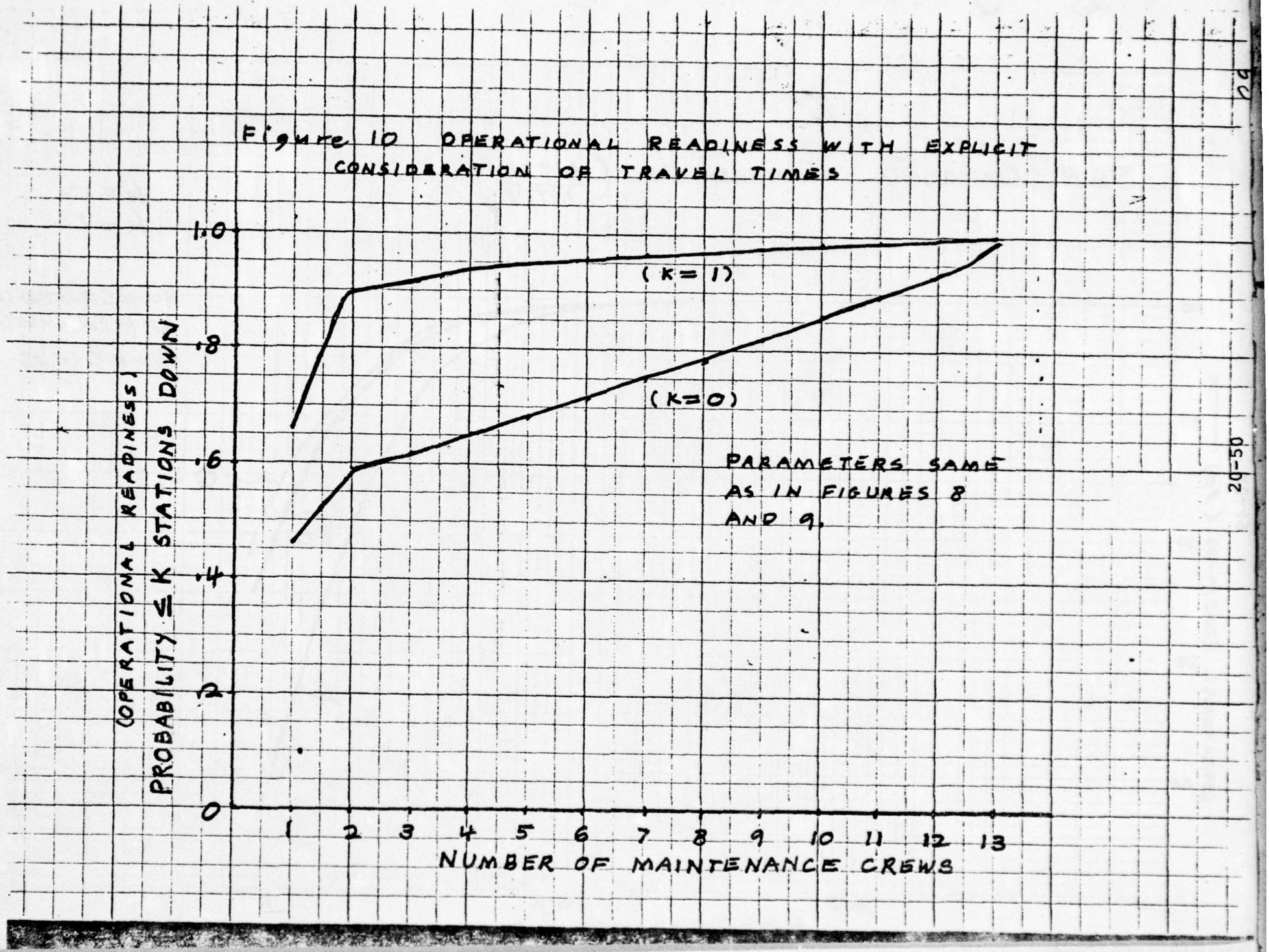

FIG 9 OPERATIONAL READINESS VS (MTTR/MTBF)
N=12
k=1
N= # OPERATING UNITS
k= # FAILURES (MAX)
Q= # CREWS
Q=3
Q=2
Q=1
100
80
60
40
20
0
OPERATIONAL READINESS (OR)
10-4
10-3
10-2
10-1
MTTR/MTBF (=ρ)

Figure 10 OPERATIONAL READINESS WITH EXPLICIT CONSIDERATION OF TRAVEL TIMES



20-50

1976

USAF-ASEE SUMMER FACULTY RESEARCH PROGRAM

sponsored by
THE AIR FORCE OFFICE SCIENTIFIC RESEARCH

conducted by
AUBURN UNIVERSITY AND OHIO STATE UNIVERSITY

PARTICIPANT'S FINAL REPORT

ANALYSIS AND SYNTHESIS OF MRAS IDENTIFICATION TECHNIQUES FOR HUMAN OPERATOR DYNAMICS

Prepared by:	Bruce K. Colburn, Ph.D.
Academic Rank:	Assistant Professor
Department and University:	Department of Electrical Engineering Texas A&M University

Assignment:

(Air Force Base)	Brooks AFB
(Laboratory)	School of Aerospace Medicine
(Division)	Biometrics
(Branch)	Medical Computing

USAF Research Colleague:	Sherwood Samn, Ph.D.
Date:	August 6, 1976
Contract No:	F44620-75-C-0031

ANALYSIS AND SYNTHESIS OF MRAS IDENTIFICATION TECHNIQUES FOR HUMAN OPERATOR DYNAMICS

by

Bruce K. Colburn

ABSTRACT

A method of developing identification algorithms referred to as the model-reference adaptive system (MRAS) approach is studied as regards its use in human operator compensatory tracking tasks. Both algorithms and analysis techniques are developed to further the available theory for identification of aircraft pilot models. In particular, on-line, non-stationary techniques are studied. Examples are included to illustrate the application of the MRAS identification approach with and without noise.

I. INTRODUCTION

The human operator (i. e. pilot) is an important instrument in the Air Force's arsenal of equipment and manpower. As ever higher performance aircraft are designed and tested, it becomes even more imperative that an accurate handle on the dynamics of the human pilot be available for analysis and evaluation. Aircraft gunnery, pilot flying in a closed loop manner, effects of stress (eye level blood pressure due to G_z, nuclear radiation, heat), are examples where accurate knowledge of human dynamics are important.

During the last decade a great volume of work has been done in the area of off-line identification of linear systems [1-10]. Generally, the most popular algorithmic technique has been the maximum likelihood technique, a gradient type approach [11-15]. Such an approach has been successfully applied to determination of human operator dynamics [16-20]. Other approaches include least squares [21], weighted least squares [22], generalized least squares [23, 24] instrument variable [25, 26], frequency domain [27], cross correlation [28, 29], stochastic approximation [30-32], Bayesian [33], Kalman Filtering [34-36], and the Kleinman optimal control model [37-39].

The basic human operator problem to be considered is the single axis compensatory tracking problem shown in Figure 1 [40]. The idea is to determine techniques and procedures for obtaining analytical models of the human in a tracking task mode. One very common approach which has received much attention in the literature is that of assuming a linear, time invariant model for the human with an added noise remnant error signal to account for differences between actual human response and the linear model response [41-42]. The model is usually of the type

$$\frac{K(\tau_1 s + 1) \quad e^{-\tau s}}{(\tau_2 s + 1)(\tau_3 s + 1)} \tag{1}$$

or simpler [43]. This simplified linear model form is shown in Figure 2. For "short" time frames K, τ_1, τ, τ_2, τ_3 may be considered as constant, but for "longer" periods there is evidence that the human varies those parameters [17, 44-46].

In attacking the problem of determining the coefficients of the model, a vast amount of literature has been written on the subject. A few of the relevant surveys include [2-4]. In recent years a new approach to identification has emerged, that of the model-reference adaptive system (MRAS) concept [47-67]. This method is a signifigant departure from traditional approaches in a number of ways, (1) a scalar metric $\lim_{t\to\infty} e(t) = 0$ or $\lim_{t\to\infty} E\{e\} = 0$ as opposed to scalar or vector summation or integral criterion (2) using Lyapunov theory it is possible to insure global stability of the parameter identification, (3) the MRAS technique is inherently an on-line sequential approach, allowing for its use in the identification of nonstationary systems, (4) unknown system parameters are treated as "gains" of a model, with the end result being the matching of model parameters to those of the system.

II. MRAS APPROACH

The basic MRAS control approach is illustrated in Figure 3. There is a common input to both the plant and model with an error vector used as an on-line measure of identification tracking accuracy. The plant dynamics are of the form

$$\dot{\underline{x}}_p(t) = A_p(t)\, \underline{x}_p(t) + B_p(t)\, \underline{u}(t) \tag{2}$$

where $\underline{x}_p$ is an n- vector of system states, $\underline{u}$ is an r- vector of plant inputs $A_p(t)$, $B_p(t)$ are n x n and n x r plant matrices, possibly time-varying. There is a corresponding model of the form

$$\dot{\underline{x}}_m(t) = A_m(t)\,\underline{x}_m(t) + B_m(t)\,\underline{u}(t) \tag{3}$$

where $\underline{x}_m$ is an n- vector, $A_m(t)$, $B_m(t)$ are n x n, n x r model matrices. For the general MRAS case, an error vector $\underline{e}$ can be defined as

$$\underline{e}(t) = \underline{x}_m(t) - \underline{x}_p(t) \tag{4}$$

Typically for the adaptive control case (the reverse of the identification approach), Equations (2)-(4) are used to define an error differential equation

$$\dot{\underline{e}}(t) = A_m(t)\underline{e}(t) + [A_m(t) - A_p(t)] + [B_m(t) - B_p(t)]\underline{u}(t) \tag{5}$$

If it is assumed that $A_p(t)$, $B_p(t)$ are of the form

$$\begin{aligned} \left[a_{ij}^{p}(t)\right] &= \left[c_{ij}^{a}(t) + K_{ij}^{a}(t)\right] \\ \left[b_{ij}^{p}(t)\right] &= \left[c_{ij}^{b}(t) + K_{ij}^{b}(t)\right] \end{aligned} \tag{6}$$

where $c_{ij}{}^{a}(t)$, $c_{ij}{}^{b}(t)$ are unknown time varying parameters and $K_{ij}{}^{a}(t)$, $K_{ij}{}^{b}(t)$ are adaptive gains yet to be determined.

It can be shown [50] that by using an appropriate Lyapunov function, expressions for the adaptive gains $K_{ij}{}^{a}(t)$, $K_{ij}{}^{b}(t)$ can be derived which only require on-line available data,

$$K_{ij}{}^{a}(t) = \alpha_{ij} \int_{t_o}^{t} \left[\sum_{k=1}^{n} e_k \, q_{ki} \, x_{pj} \right] dt$$

$$K_{ij}{}^{b}(t) = \gamma_{ij} \int_{t_o}^{t} \left[\sum_{k=1}^{n} e_{ki} \, u_j \quad dt \right] \qquad (7)$$

where α_{ij}, γ_{ij} are constants >0, and q_{ij} are elements of a p.d. symmetric constant matrix Q. If $A_p(t)$, $B_p(t)$ either constant or meets certain criteria [51, 60, 68], and $A_m(t)$, $B_m(t)$ are constant matrices, then $\lim_{t\to\infty} e(t) = 0$ and the plant states will track the model states. This concept has been explored in depth for many years, resulting in a number of adaptive control procedures. Note that in this case all plant states are assumed measurable.

The MRAS identification case is basically the reverse of the control case. This configuration is shown in Figure 4. Here it is the plant which is assumed to be unknown but fixed and the model is adjusted so that $\lim_{t\to\infty} \underline{e} = 0$ and $a_{ij}{}^{m}(t) \to a_{ij}{}^{p}(t)$ and $b_{ij}{}^{m}(t) \to b_{ij}{}^{p}(t)$. Because generally not all states are available for measurement, a considerable effort was extended to be able to identify a linear single input single output (SISO) system from only input - output data. For a special case this problem was solved in 1973 [53], although earlier papers alluded to the problem [54, 55]. Some additional work has been done since then [65, 69-71].

To understand the concepts of on-line and off-line control, refer to Figure 5. On-line means that data is processed in real time, as it occurs, and

an inherent assumption underlying this is that the computations can be computed fast enough to keep up with the data. Off-line means all of the data is recorded and stored prior to the start of the computation process. Algorithmic speed is unimportant here, but it is inherent in all off-line approaches that the system parameters being identified are constant. So called "recursive" maximum - likelihood procedures have been developed [72, 73] but they are essentially off-line methods which operate sequentially on packets of data which are subsets of an entire block of recorded data. In these subintervals it must be assumed the coefficients are constant, although for each subinterval one could assume different time-invariant models, resulting in a sequence of "frozen time" constant models.

III. IDENTIFICATION WITH MRAS

A. Analysis of Tuning Procedures for a Class of Identifiers

Consider the nth order system

$$\begin{aligned} \underline{w}(k+1) &= \Phi\ \underline{w}(k) + G\ u(k) \\ z(k) &= c^T\ \underline{w}(k) \end{aligned} \tag{8}$$

where $\underline{w}$ is an nth order state vector, u is a scalar input, and Φ, G are n x n and n x r constant matrices.

It can be shown that (8) can be put in the $(2n-1)^{th}$ order non-minimal realization form [74]

$$\begin{aligned} \underline{x}(k+1) &= \begin{bmatrix} a_1 & a^{-T} & b^{-T} \\ \overline{r} & F & o \\ o & o & F \end{bmatrix} \underline{x}(k) + \begin{bmatrix} b_1 \\ o \\ \overline{r} \end{bmatrix} u(k) \\ y(k) &= x_1(k) \end{aligned} \tag{9}$$

The unknown system parameters are given by the vector $\underline{c}^T = (a_1\ \overline{a}^T\ b_1\ \overline{b}^T)$ with $\overline{a}$, $\overline{b}$ of size(n-1)x1. The pair $(\overline{r}^T, F)$ is completely observable, F being

of size (n-1)x(n-1) with eigenvalues λ_i such that $|\lambda_i|<1 \quad i = 2, 3, \ldots, n$

$\underline{x}$ is of the form $\underline{x}^T = [x_1 \; \overline{x^1}^T, \; \overline{x^2}^T]$, $\overline{x^1}$, $\overline{x^2}$ each of size (n-1)x1. An observer is developed for parameter estimation ($\hat{}$ denotes an estimate) as follows:

$$\begin{aligned} x_1(k+1) &= \hat{a}_1(k+1)x_1(k) + \underline{\hat{a}}^T(k+1)\overline{\hat{x}^1}(k) \\ &\quad + \hat{b}_1(k+1)u(k) + \underline{\hat{b}}^T(k+1)\overline{\hat{x}^2}(k) \\ &\quad + \lambda_1[\hat{x}_1(k) - x_1(k)] \end{aligned} \tag{10}$$

$$\overline{\hat{x}^1}(k+1) = F\,\overline{\hat{x}^1}(k) + \overline{r}\,x_1(k)$$

$$\overline{\hat{x}^2}(k+1) = F\,\overline{\hat{x}^2}(k) + \overline{r}\,u(k)$$

with λ_1 a constant, $|\lambda_1|<1$. Defining a scalar identification error $e(k) = \hat{x}_1(k) - x_1(k)$, by use of Lyapunov theory a parameter identification equation can be developed. Defining a parameter vector $\underline{c}^T = [a_1, \; \overline{a}^T, \; b_1, \; \overline{b}^T]$ and $q^T = [x_1, \; \overline{\hat{x}}^{1T}, \; u, \; \underline{\hat{x}}^{2T}]$ then

$$\underline{\hat{c}}(k+1) = \underline{\hat{c}}(k) - \frac{\alpha P[c_1(k) - \lambda_1 e_1(k-1)]q(k-1)}{\lambda_{max} q^T(k-1)q(k-1)} \tag{11}$$

where $0<\alpha<2$, P is an arbitrary positive definite symmetric matrix, and λ_{max} is the largest eigenvalue of P. Use of equations (9)-(11) will insure global stability of $\underline{\hat{c}} \rightarrow \underline{c}$, independent of the initial condition. But the question arises as to how the various parameters P, λ_i, λ_{max}, α effect the error convergence rate.

One approach to this problem is the development of a linearized error characteristic equation (LECE) [75, 76], wherein free design parameters are analyzed in terms of root locus expressions. Defining

$$\underline{\phi} = \underline{\hat{c}} - \underline{c}, \tag{12}$$

and assuming $u(k) = u^o$ = constant, k "large",

$$p_{ii} = p_{jj} = p > 0 \qquad (13)$$

$$p_{ij} = 0 \quad i \neq j$$

F is a diagonal matrix with elements $\lambda_2, \lambda_3, \ldots, \lambda_n$, and $\underline{r}^T = (1, 1, \ldots, 1)$.

The state error e_1 and parameter misalignment error $\underline{\phi}$ can be written as

$$e_1(k+1) = \lambda_1 e_1(k) + \underline{b}^T \underline{e}^2(k) + \underline{\phi}^T(k+1)\, \underline{q}(k) \qquad (14)$$

$$\phi(k+1) = \phi(k) - \frac{\alpha p[e_1(k) - \lambda_1 e_1(k-1)]\, q(k-1)}{\lambda_{max} < \underline{q}(k-1), q(k-1) >} \qquad (15)$$

Under the assumptions given, $\lim_{k \to \infty} \overline{\underline{e}^2}(k) = 0$. Suppose $\lim_{j \to \infty} x_1(j) = x_1^o$ = constant, then

$$\lim_{j \to \infty} \begin{matrix} \hat{\underline{x}}^1(j) = \hat{\underline{x}}^{1^o} = \text{constant} \\ \hat{\underline{x}}^2(j) = \hat{\underline{x}}^{2^o} = \text{constant} \end{matrix} \qquad (16)$$

Suppose, due to a non-zero entry ϕ_j, a perturbation occurs in e_1, i.e.

$$\begin{aligned} e_1 &= e_1^o + \Delta e_1 \\ \underline{\phi} &= \underline{\phi}^o + \Delta\underline{\phi} \end{aligned} \qquad (17)$$

where e_1^o and $\underline{\phi}^o$ are zero. Then the error perturbation equation for e_1 is

$$\begin{aligned} e_1^o + \Delta e_1(k+1) &= \lambda_1[e_1^o + \Delta e_1(k)] + \underline{b}^T \underline{e}^2(k) \\ &+ [\underline{\phi}^o + \Delta\underline{\phi}(k+1)][\underline{q}^o + \Delta\underline{q}(k)] \end{aligned} \qquad (18)$$

and the parameter identification perturbation vector,

$$\begin{aligned} \phi^o + \Delta\underline{\phi}(k+1) &= (\underline{\phi}^o + \Delta\underline{\phi}(k)) - \alpha p[(e_1^o + \Delta e_1(k)) \\ &- \frac{\lambda_1(e_1^o + \Delta e_1(k-1))](\underline{q}^o + \Delta\underline{q}(k-1)}{\lambda_{max}[\underline{q}^o + \Delta\underline{q}(k-1)]^T[\underline{q}^o + \Delta q(k-1)]} \end{aligned} \qquad (19)$$

but $\Delta\underline{q} = \underline{o}$. From (13), $Pe_1\underline{q} = pe_1\underline{q} = pe_1\underline{q}$ and $\lambda_{max} = p$. Equation (19) becomes

$$\Delta\underline{\phi}(k+1) = \Delta\underline{\phi}(k) - \frac{\alpha[\Delta e_1(k) - \lambda_1 \Delta e_1(k-1)]\, \underline{q}^o}{< \underline{q}^o, \underline{q}^o >} \qquad (20)$$

and (18)

$$\Delta e_1(k+1) = \lambda_1\, \Delta e_1(k) + \Delta\phi^T\,(k+1)\, \underline{q}^o \qquad (21)$$

Performing z-transform operations on (20), (21), an error root locus equation for Δe_1 results

$$1 + \frac{\alpha}{z-1} = 0 \tag{22}$$

Since it has been proven independent of this linearization that the system is asymptoticaly stable, then the closed loop root in (22) is inside the unit circle, which checks with the previous constraint $o < \alpha < 2$.

Equation (22) is applicable to the special case when P is diagonal with equal entries. As for the general case, refer to (19). Performing the z-transform operation and removing the restriction in (13) yields

$$\Delta\phi_1(z) = - \frac{(1-\lambda_1 z^{-1})}{(z-1)} \left(\frac{\alpha \sum_{k=1}^{n} p_{ik}\, q_k}{\lambda_{max} < \underline{q}^o, \underline{q}^o >} \right) \Delta e_1(z) \tag{23}$$

Using (27)

$$\Delta e_1(z) \left\{ 1 + \frac{\alpha \sum_{i=1}^{n} \left[\sum_{k=1}^{n} p_{ik}\, q_k\, q_i \right]}{\lambda_{max} < \underline{q}^o, \underline{q}^o > (z-1)} \right\} = 0 \tag{24}$$

Note that (24) reduces to (22) for the special case of (13). Analysis of (24) is difficult, however, because of the individual weighting due to the p_{ij} elements.

B. Development and Analysis of Continuous Time Observers

One of the greatest hurdles to complete observer theory was the means of using only input-output data for a general n^{th} order system, completely identify the system characteristics but simultaneously insuring global asympototic stability of the observer. A solution was found in the Meyer-Kalman-Yacubovich (MKY) Lemma [77-80] which was first used in adaptive control by Parks [49] and applied by Carrol [53] and Narendra [65] to the observer problem in order to eliminate all but a single state variable from the computation

of parameter estimator equations.

Based on an observer approach proposed by Lüders and Narendra [57], a new method for linear systems identification is obtained by developing a Lyapunov function with additional terms not found in previously proposed methods. The new resulting identification rule is analogous to the Gilbert, Monopoli, and Price [52] method for adaptive control. The additional terms in the Lyapunov function leads to parameter estimator gains proportional to not only the integral factor developed by Lüders and Narendra, but also proportional and derivative terms. It is shown that the additional terms improve the identification convergence rate. The possible effects of noise, however, may limit the proposed technique in practice.

Consider the linear, time-invariant plant

$$\begin{aligned} \dot{\underline{x}}_p &= A_p \underline{x}_p + B_p \underline{u} \\ y &= C \underline{x}_p \end{aligned} \tag{25}$$

where $\underline{x}_p$ is on n^{th} order vector, u is a scalar input, C is an 1xn row vector, y is a scalar output, and $\{A_p, B_p\}$ is controllable and $\{A_p, C\}$ observable. It is known [57] that the triple $\{A_p, B_p, C\}$ may be expressed as $\{A, \underline{b}, \underline{h}\}$, where

$$A = T^{-1} A_p T, \quad \underline{b} = T^{-1}, \quad \underline{h}^T = CT \tag{26}$$

and T is a non-singular transformation. For this study, the following canonical configuration is employed

$$\dot{\underline{x}} = \begin{bmatrix} a_1 & | & \\ \hline a_2 & | & \\ \vdots & | & \\ a_n & | & \end{bmatrix} \underline{x} + \begin{bmatrix} b_1 \\ b_2 \\ \vdots \\ b_n \end{bmatrix} u \tag{27}$$

$$y = (1 \ o \ o \ldots o) \ \underline{x}$$

where A is an (n-1)x(n-1) diagonal matrix with arbitrary constant diagonal elements $-\lambda_i$, $\lambda_i > o$, $i = 2, 3, \ldots, n$ and $\underline{a}^T = (a_1, a_2, \ldots, a_n)$ and

$\underline{b}^T = (b_1, b_2, \ldots, b_n)$ the 2n unknown parameters which are to be identified.

A model is constructed

$$\dot{\hat{\underline{x}}} = \begin{bmatrix} \alpha_1 & | & \\ \alpha_2 & | & \\ \cdot & | & \\ \cdot & | & \\ \cdot & | & \\ \alpha_n & | & \end{bmatrix} \begin{bmatrix} x_1 \\ \hat{x}_2 \\ \hat{x}_3 \\ \cdot \\ \cdot \\ \cdot \\ \hat{x}_n \end{bmatrix} + \begin{bmatrix} \beta_1 \\ \beta_2 \\ \cdot \\ \cdot \\ \cdot \\ \beta_n \end{bmatrix} u + \underline{w} \qquad (28)$$

where $\dot{\hat{\underline{x}}}$ is an nth order observer vector, α_1 and β_1 are the coefficients that are adaptively adjusted, and $\underline{w}$ is an auxiliary input vector, $\underline{w}^T = (w_1, w_2, \ldots)$, where $w_1 = -\lambda_1(\hat{x}_1 - x_1)$ and $w_2, w_3, \ldots$ are to be determined.

The adaption response error is defined to be

$$\underline{e} = \hat{\underline{x}} - \underline{x} \qquad (29)$$

Since an adaptive identification scheme is inherently nonlinear, parameter convergence is important. To insure global stability independent of the initial guess of the parameters, a Lyapunov V function is employed. The basic idea is to design the identification gains in such a way that as $t \to \infty$, $\underline{e} \to o$, $\underline{\psi} \to o$, $\underline{\phi} \to o$. In addition to insuring stability, the V and $\dot{V}$ functions selected can be used to estimate the system convergence rate [81, 82]. Through an involved series of transformations it can be shown that (27) and (28) can be employed to obtain a scalar error equation

$$\begin{aligned} \dot{e}_1 = {} & \lambda_1 e_1 + x_1 \phi_1 + H \mathcal{L}^{-1} \left[(sI - \Lambda)^{-1} x_1(s) \right] \underline{\phi} \\ & + u \psi_1 + H \mathcal{L}^{-1} \left\{ (sI - \Lambda)^{-1} u(s) \right\} \underline{\psi} \\ & + H \exp[\Lambda t] \, \underline{e}(t_o) \end{aligned} \qquad (30)$$

where $H = (1, 1, \ldots, 1)$ is an (n-1) row vector, $\underline{e}(t_o)$ is the initial condition on $\underline{e}$, and $\underline{P}^T = (P_2, P_3, \ldots P_n)$, $\underline{\phi} = \underline{\alpha} - \underline{a}$ and $\underline{\psi} = \beta - b$. The design objective is to adjust $\underline{\alpha}$ and $\underline{\beta}$ such that as $t \to \infty$, $\underline{\phi} \to \underline{o}$ and $\underline{\psi} \to \underline{o}$. It has been shown [51] that forcing $\underline{e}$ to zero is not a sufficient condition for insuring that $\underline{\phi}$ and $\underline{\psi}$

tend to the origin also.

Developing a Lyapunov function as in [83], it can be shown that if adaptive gains

$$\alpha_1 = -c_j \int_{t_o}^{t} e_1 x_1 dt - f_1 e_1 x_1$$

$$\alpha_j = -c_j \int_{t_o}^{t} e_1 \mathcal{L}^{-1}\left\{\frac{x_1}{s+\lambda_j}\right\} dt - f_j\, e_1 \mathcal{L}^{-1}\left\{\frac{x_1}{s+\lambda_j}\right\} \tag{31}$$

$$\beta_1 = -d_1 \int_{t_o}^{t} e_1\, u\, dt - g_1 e_1 u \tag{32}$$

$$\beta_j = -d_j \int_{t_o}^{t} e_1 \mathcal{L}^{-1}\left\{\frac{u}{s+\lambda_j}\right\} dt - g_j\, e_1 \mathcal{L}^{-1}\left\{\frac{u}{s+\lambda_j}\right\} \tag{33}$$

$c_j, d_j, \lambda_j > o;\ f_j, g_j \geq o \quad j = 1, 2, 3, \ldots, n$

$$v_i = \mathcal{L}^{-1}\left\{\frac{x_1(s)}{s+\lambda_i}\right\} \tag{34}$$

$i = 2, 3, \ldots, n$

$$s_i = \mathcal{L}^{-1}\left\{\frac{u}{s+\lambda_i}\right\} \tag{35}$$

$$w_i = -c_i v_i^2 - d_i s_i^2 - f_i v_i \frac{d}{dt} e_i v_i - g_i s_i \frac{d}{dt} s_i e_i \tag{36}$$

$i = 2, 3, \ldots, n$

are employed and if u is sufficiently "frequency rich," then $e_1 = 0$

$\phi = \psi \triangleq 0$.

It is desired to use the LECE technique to develop a design approach for determining the selection of the c_i, d_i, λ_i coefficients and show how their selection affects the adaptive error transient response. It can be shown [83] that if $\dot{e}_i$, $\dot{\phi}_i$, $\dot{\psi}_i$ are expanded in a Taylor series under an appropriate operating condition, the resulting LECE can be expressed as

$$1 + \frac{(K_1 + K_2 s)}{s(s + \lambda_1)} = 0 \tag{37}$$

where

$$\begin{aligned} K_1 &= c_1 {x_1}_o^2 + c_2 {v_2}_o^2 + c_3 {v_3}_o^2 + \ldots + c_n {v_n}_o^2 + d_1 {u}_o^2 \\ &\quad + d_2 {s_2}_o^2 + d_3 {s_3}_o^2 + \ldots + d_n {s_n}_o^2 \\ K_2 &= f_1 {x_1}_o^2 + f_2 {v_2}_o^2 + f_3 {v_3}_o^2 + \ldots + f_n {v_n}_o^2 + g_1 {u}_o^2 \\ &\quad + g_2 {s_2}_o^2 + g_3 {s_3}_o^2 + \ldots + g_n {s_n}_o^2 \end{aligned} \tag{38}$$

For the Lüder-Narendra case, (37) becomes

$$1 + \frac{K_1}{s(s+\lambda_1)} = 0 \tag{39}$$

where K_1 is as before. This shows that the new identification technique allows for greater flexibility by providing for an additional zero compensator.

IV. EXTENSIONS TO PRACTICAL SITUATIONS

In this section the uses of the MRAS approach in practical situations such as nonstationary systems, stochastic case, multi-input multi-output are discussed. This is because in practice the human acts in a noisy, time-varying manner.

To test the time varying parameter tracking ability of the MRAS identifiers in Section III, a third order system was simulated, with the plant of the form

$$\frac{y_p}{u}(z) = \frac{a(t)\, z^2 + 1}{z^3 - .6z^2 + .11z - .006}$$

where $a(t) = 2.5 + \sin(.002t)$. Using a model of the form

$$\frac{y_m}{u}(z) = \frac{b_3 z^2 + b_2 z + b_1}{z^3 + a_3 z^2 + a_2 z + a_1}$$

The input was a control stick error signal from a human tracking problem where an $\tan^{-1}$ type waveform was being followed. The result for the time varying term is shown in Figure 6. Note that as $\alpha \to 1$, tracking response improves, which is as predicted.

To further demonstrate the importance of on-line identification for time-varying systems, the previous test case was used. The classical least squares (LS) technique was used on data from this nonstationary system. Of course the LS is an off-line method which assumes the parameters are constant. The results are tabulated in Table I. Note the terrible answers which result from the LS method.

TABLE I

COEFFICIENT TRACKING ACCURACY

Actual	See Fig. 6	1	0	-.6	.11	-.006
Least Squares	3.15	-2.62	-.16	-1.71	.96	-.21
On Line	See Fig. 6	1.02	.01	-.62	.15	-.01

As for random noise on the input and output corrupting the measured signals. First a correlated input noise was added to the previous third order example. The plant equation was of the form

$$\sum_{i=1}^{4} a_i\, y(k-i+1) = \sum_{i=1}^{3} b_1\, u(k-i+1) + c_1 \nu(k) + c_2 \nu(k-1)$$

$c_1 = c_2 = 1$, $a_1 = 1$, where $\nu(j)$ is a gaussian white noise sequence with mean zero and variance σ^2. The identification was implemented without identifying C_1 and C_2. A nonstationary set of values of σ was simulated along with a fixed control case, the results tabulated in Table II. The overall output tracking accuracy is shown in Table III, where a scalar tracking parameter $\bar{e}$ is defined to be

$$\bar{e} = \sqrt{\frac{\sum_{i=1}^{N} (y_{ai} - y_{pi})^2}{\sum_{i=1}^{N} y_{ai}^2}}$$

N = number of data points

y_a = actual output

y_p = predicted output

TABLE II

COEFFICIENT TRACKING ACCURACY

Actual	-.6	.11	-.006	0	1	0
σ = .05 * R	-.648	.118	-.004	-.005	1.075	-.134
σ = .25 * R	-.496	-.012	.006	.15	1.069	-.135
σ = 20	-.915	.303	-.021	-.245	.988	-.120

TABLE III

TIME RESPONSE TRACKING ACCURACY

Input Noise	$\bar{e}$
Deterministic	.005
σ = .05 * R	.06
σ = .25 * R	.302
σ = 20	.272

The multi-input, multi-output case can also be handled by the MRAS approach. The standard ARMA process, as shown before is also amenable to this approach. The difficulty comes in attempting to obtain exact analytical results in the presence of disturbances. Some work has been done [84 - 86] but the complexity of the Lyapunov functions employed makes results difficult. The metric employed in the noise case would be $\lim_{t \to \infty} E\{e(t)\} = 0$ or some related quantity.

Much of what has been discussed with regard to the MRAS problem applies also to SISO systems. Some work has been done on the MIMO case, however [57, 87-89]. One recurring theme in all identification approaches, MRAS or otherwise, is the necessity for the input being sufficiently "frequency rich" or "exciting". Because of this work has been done on the form of the input function [57, 90-95].

Related to the identification algorithm phase of identification theory is that of model order and structure. Generally, some sort of model structure is hypothesized and the order fit determined by Chi-square, t-test, F-statistic [21], whiteness test [36], a goodness-of-fit test C_p [96], and other techniques [97-99]. Work has also been done in the area of system structure [100-104].

One other area relating to modeling that has previously been discussed is that of the Kleinman optimal controller. This approach presumes that the human operates in some "optimal" manner. Generally some form of a quadratic error and error rate criterion is employed. Unfortunately, it is not clear that this is how the human operates [105].

V. SUMMARY AND CONCLUSIONS

Most identification techniques employed for human operator identification have involved the use of off-line algorithms, with model parameters and noise statistics assumed time-invariant. Recently, the (MRAS) concept, wherein human

operator parameters are treated as gain terms of a model, has come into use. Here parameter stability and convergence are assured as part of the identification algorithm development. It is especially useful because in practice, it can handle the time-varying, adaptive human characteristics. Limited study of MRAS stochastic identifiers suggests that it can be a viable technique with further development.

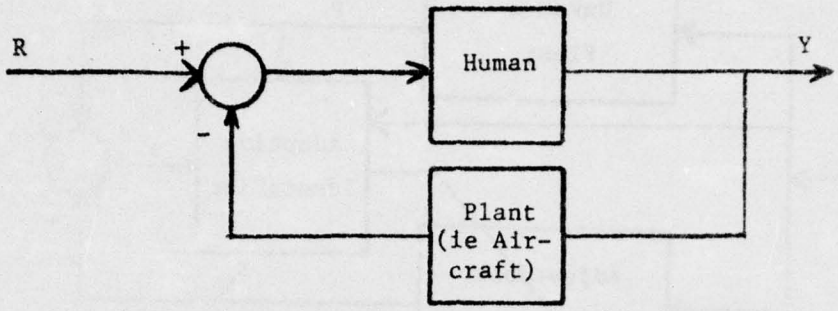


Fig. 1 Single axis compensatory tracking system

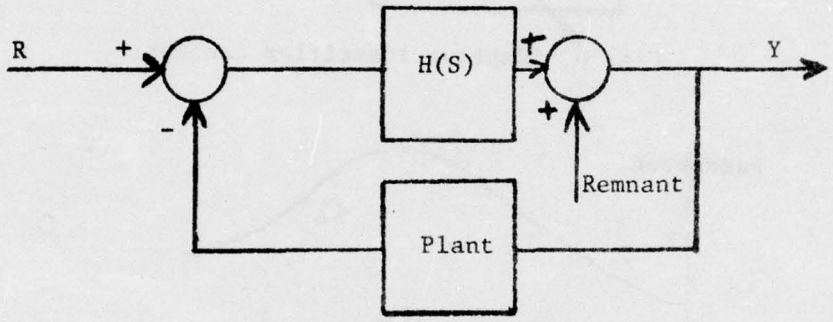


Fig. 2 Standard linear model for Fig. 1

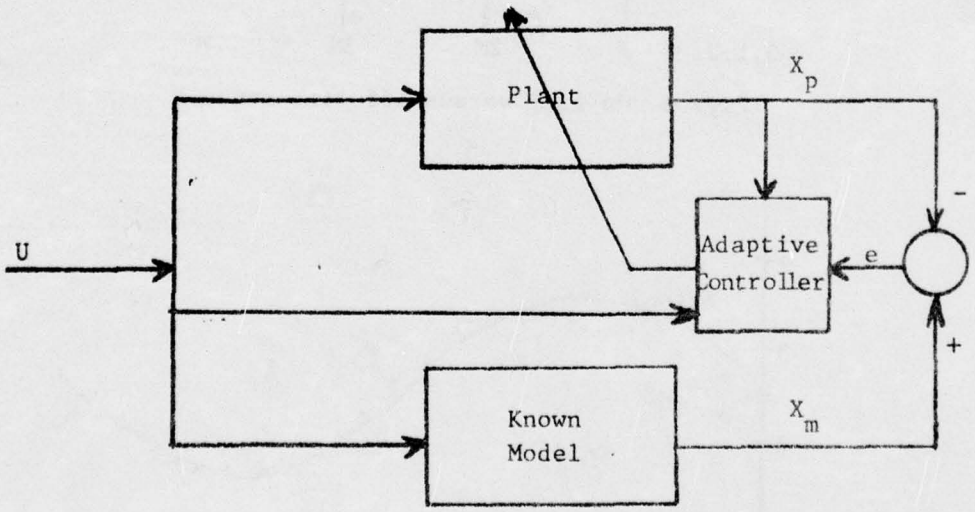


Fig. 3 MRAS control system concept

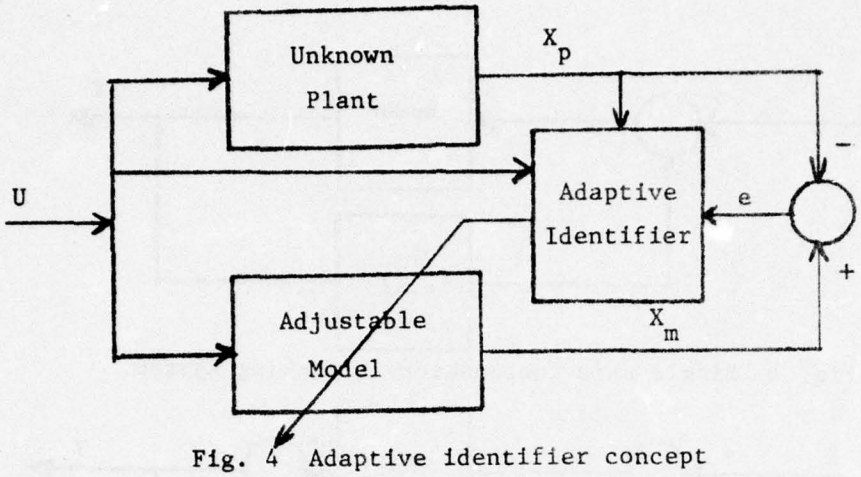


Fig. 4 Adaptive identifier concept

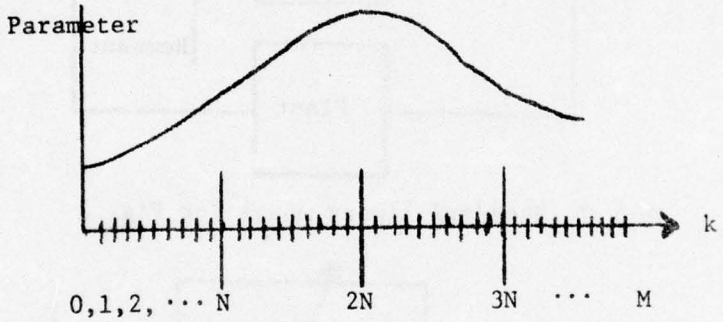


Fig. 5 On-line versus off-line concept

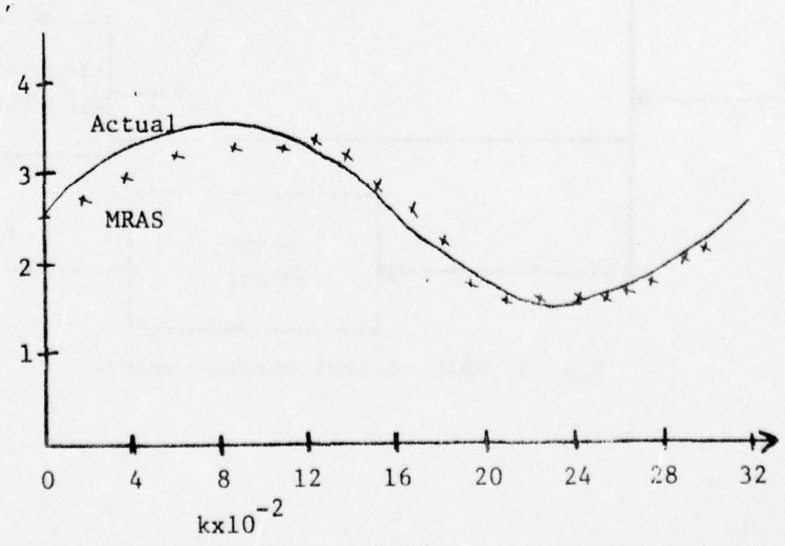


Fig. 6 Discrete On-line identification of a time-varying parameter

REFERENCES

1. Astrom, K.J., Bohlin, T., and Wensmark, S., "Automatic Construction of Linear Stochastic Dynamic Models for Stationary Industrial Processes with Random Disturbances Using Operating Records," TP 18.150, IBM Nordic Laboratory, Sweden, 1965.

2. Cuenod, M., and Sage, A.P., "Comparison of Some Methods Used for Process Identification," Automatica, Vol 4, 1968, pp. 235-269.

3. Eykhoff, P., "Process Parameter and State Estimation," Automatica, Vol 4, 1968, pp. 205-233.

4. Astrom, K.J., and Eykhoff, P., "System Identification - A Survey,", Automatica, Vol 7, 1971, pp. 123-162.

5. Rajbman, N.S., "The Application of Identification Methods In The U.S.S.R. - A Survey," Automatica, Vol 12, 1976, pp. 73-95.

6. Sage, A.P., and Melsa, J.L., System Identification, Academic Press, N.Y., 1971.

7. Eykhoff, P., System Identification: Parameter and State Estimation, John Wiley and Sons, London, 1974.

8. Gupta, N.K. and Mehra, R.K., "Computational Aspects of Maximum Likelihood Estimation and Reduction in Sensitivity Function Calculations," IEEE Trans Auto Cont, December 1974, pp. 774-783.

9. Kashyap, R.L., "Maximum Likelihood Identification of Stochastic Linear Systems," IEEE Trans on Auto Cont, February 1970, pp. 25-34.

10. Mendel, J.M., "Gradient Estimation Algorithms for Equation Error Formulations," IEEE Trans on Auto Cont, December 1974, pp. 820-824.

11. Mehra, R.K., "Identification of Stochastic Linear Dynamic Systems Using Kalman Filter Representation,"AIAA Journal, Jan. 1971, pp. 28-31.

12. Iliff, K.W., "Identification and Stochastic Control with Applications to Flight Control In Turbulence," VLLA-ENG-7340, 1973.

13. Bohlin, T., "On the Maximum Likelihood Method of Identification," IBM J of Res and Dev, January 1970, pp. 41-51.

14. Mehra, R.K., et al, "A Generalized Method for the Identification of Aircraft Stability and Control Derivatives From Flight Test Data," Proc 1972 JACC, pp. 525-534.

15. Sarris, A.H. and Eisner, M., "Parameter Estimation of ARMA Models Using A Computationally Efficient Maximum Likelihood Technique," Proceedings of the 1973 Conference on Decision and Control, pp. 640-644.

16. Norris, D.O., "Modeling of Human Operator Performance," AMRL-TR-72-121, Wright-Patterson AFB, Ohio, June 1973.

17. Phatak, A.V., et al., "Application of System Identification to Modeling the Human Controller Under Stress Conditions," IEEE Trans on Auto Cont, October 1975, pp. 657-664.

18. Phatak, A.V., "Improvements in Weapon System Effectiveness by Application of Identification Methods for Determining Human Operator Performance Decrements Under Stress Conditions," Report AMRL-TR-73-38, Wright-Patterson AFB, Ohio, June 1973.

19. Mehra, R.K. and Tyler, J.S., "Modeling the Human Operator Under Stress Conditions Using System Identification," Proc 1972 JACC, pp. 34-43.

20. Repperger, D. and Junker, A., "A Maximum Likelihood Approach for Identifying Human Operator Remnant In a Tracking Task," Proc of 1974 IEEE CDC, pp. 534-540.

21. Box, Jenkins, Time Series Analysis, Holden, Doy: San Francisco, 1970.

22. Taylor, L.W. and Iliff, K.W., "Systems Identification Using A Modified Newton-Raphson Method - A Fortran Program," NASA TN D-6734, May 1972.

23. Clarke, D.W., "Generalized Least Squares Estimates of the Parameters of a Dynamic Model," Paper 3.17, IFAC Symposium on Identification, Praque, 1967.

24. Hsia, T.C., "New Generalized Least Squares Estimation Algorithm for System Identification," Paper FP3-4, Proc 1973 IEEE CDC.

25. Young, P.C., "An Instrumental Variable Method for Real-Time Identification of a Noisy Process," Automatica, Vol 6, 1970, pp. 271-287.

26. Wong, K.Y. and Polak E., "Identification of Linear Discrete Time Systems Using the Instrumental Variable Method," IEEE Trans on Auto Cont, 1967, pp. 707-718.

27. Funahashi,H., "Identification of Discrete-Time Systems Using A Composite Sinusoidal Signal," Int. J. Control, vol. 18, no. 5, 1973, pp. 945-962.

28. Hill, J.D. and McMurtry, G., "An Application of Digital Computer to Linear Systems Identification," IEEE Trans on Auto Cont, 1964, pp. 536-538.

29. McNee, R.C., Albanese, R.A., "The Correlational Structure of Traditional Task Measures and Engineering Analogues of Performance In the Cognitive Domain," Paper C1, AGARD Conference Proceedings on Higher Mental Functioning in Operational Environments, 1975.

30. Saridis, G.N. and Stein, G., "Stochastic Approximation Algorithms for Discrete - Time System Identification," IEEE Trans on Auto Cont, 1968, pp. 515-523.

31. Mendel, Fu, Adaptive, Learning, and Pattern Recognition Systems: Theory and Applications, Academic Press: New York, 1970, Chapter 9.

32. Saridis, G.N. and Stein, G., "Stochastic Approximation Algorithms for Discrete-Time System Identification," IEEE Trans on Auto Cont, 1968, pp. 592-594.

33. Alspach, D.L., "A Bayesian Nonlinear Filtering Algorithm for Linear Systems with Unknown Time-Varying Noise Statistics," Paper TP6-4, Proc 1973 IEEE CDC.

34. Mehra, R.K., "On-Line Identification of Linear Dynamic Systems with Applications to Kalman Filtering," IEEE Trans on Auto Cont, February 1971, pp. 12-21.

35. Schiess, J. and Roland, V., "Kalman Filter Estimation of Human Pilot-Model Parameters," NASA TN D-8024, 1975.

36. Mehra, R.K., "On the Identification of Variances and Adaptive Kalman Filtering," IEEE Trans on Auto Cont, April 1970, pp. 175-184.

37. Kleinman, D.L., et al., "An Optimal Control Model of Human Response," Automatica, Vol 6, 1970, pp. 357-370.

38. Kleinman, D.L. and Perkins, T.R., "Modeling Human Performance In A Time-Varying Anti-Aircraft Tracking Loop," IEEE Trans on Auto Cont, August 1974.

39. Phatak, A.V., et al., "Identification of a Modified Optimal Control Model for the Human Operator," Automatica, Vol 12, 1976, pp. 31-41.

40. Newsom, T., et al., "Training and Performance of Rhesus Monkeys as Operators In A Compensatory Manual Control System," Perceptual and Motor Skills, Vol 42, 1976, pp. 695-705.

41. McRuer, D. and Jex, H., "A Review of Quasi-Linear Pilot Models," IEEE Trans Human Factors in Elect, September 1967, pp. 231-249.

42. McRuer, D. and Krendel, E., "Mathematical Models of Human Pilot Behavior," AGARDograph No 188, January 1974.

43. Caruthers, F. and Levenstein, H., Adaptive Control Systems, Pergamon Press: New York, 1963, pp. 203-219.

44. Albanese, R., et al., "The Human As An Adaptive Controller," Paper C6, AGARD Conference on Higher Mental Functioning in Operational Environments, October 1975.

45. Johnson, C.W., "Adaptive Servomechanisms," IRE Trans Med Elect, September 1959, pp. 134-140.

46. Higgins, T. and Holland, D.B., "The Human Being As A Link In An Automatic Control System-Part I," IRE Trans Med Elect, September 1959, pp. 125-133.

47. Osborn, P.V., Whitaker, H.P. and Keezer, A., "New Development in the Design of Adaptive Control Systems," Institute of Aerospace Sciences, Paper 61-39.

48. Shackcloth, B. and Butchart, R., "Synthesis of Model Reference Adaptive Systems By Liapunov's Second Method," Proceedings of 1965 IFAC Symposium on Adaptive Control, pp. 145-152.

49. Parks, P.C., "Liapunov Redesign of Model-Reference Adaptive Control Systems," IEEE Trans on Auto Cont, Vol AC-14, July 1966, pp. 362-367.

50. Winsor, C.A. and Roy, R.J., "Design of Model-Reference Adaptive Control Systems by Liapunov's Second Method," IEEE Trans on Auto Cont, Vol AC-13, April 1968, p. 204.

51. Porter, B. and Tatnall, M.L., "Performance Characteristics of Multi-Variable Model-Reference Adaptive Control Systems Synthesized by Liapunov's Direct Method," Internation Journal on Control, Vol 10, 1969, pp. 241-257.

52. Gilbart, J.W., Monopoli, R.V. and Price, C.F., "Improved Convergence and Increased Flexibility in the Design of Model-Reference Adaptive Control Systems," 1970 IEEE Symposium on Adaptive Processes, Decision and Control, Austin, Texas, December 1970, pp. IV.3.1-10.

53. Carroll, R.L. and Lindorff, D.P., "An Adaptive Observer for Single-Input Single-Output Linear Systems," IEEE Trans on Auto Cont, Vol AC-18, October 1973, pp. 428-435.

54. Pazdera, J.S. and Pottinger, J., "Linear System Identification Via Liapunov's Design Techniques," Proc 1969 JACC, pp. 795-801.

55. Mekel, R., "Adaptive Identification of Parameters in Models of Physiological Systems," Proc Eighth Ann Conf Manual Cont, May 1972, pp. 299-305.

56. Boland, J.S. and Colburn, B.K., "Adaptive Attitude Control of the Re-Entering Space Shuttle Vehicle," The Applications of Control Theory to Modern Weapons Systems, Naval Weapons Center, China Lake, California, May 1973, pp. 213-232.

57. Luders, G. and Narendra, K.S., "An Adaptive Observer and Identifier for a Linear System," IEEE Trans on Auto Cont, Vol AC-18, October 1973, 496-499.

58. Luders, G. and Narendra, K.S., "Liapunov Functions for Quadratic Differential Equations with Applications to Adaptive Control," IEEE Trans on Auto Cont, Vol AC-17, December 1972, pp. 798-801.

59. Luders, G. and Narendra, K.S., "A New Canonical Form for an Adaptive Observer," IEEE Trans on Auto Cont, Vol AC-19, April 1974, pp. 117-119.

60. Boland, J.S. and Sutherlin, D.W., "Model Reference Adaptive Control System Design Technique," ASME Journal of Dynamic Systems, Measurement and Control, Vol 95, December 1973, pp. 374-379.

61. Shahein, H.I.H., Ghonaimy, M.A.R., and Shen, D.W.C., "Accelerated Model-Reference Adaptation via Lyapunov and Steepest Descent Design Techniques," IEEE Trans on Auto Cont, Vol AC-17, February 1972, pp. 125-128.

62. Landau, I.D., "Model-Reference Adaptive Systems--A Survey (MRAS)--What is Possible and Why?," ASME Journal of Dynamic Systems, Measurement, and Control, June 1972, pp. 119-132.

63. Colburn, B.K. and Boland, J.S., "Extended Lyapunov Stability Criterion Using a Nonlinear Algebraic Relation With Application to Adaptive Control," AIAA Journal, Vol 14, No 5, May 1976, pp. 648-655.

64. Colburn, B.K. and Boland J.S., "Extended Lyapunov Adaptation Law for Modd-Reference Adaptive Systems," to be published in IEEE Trans on Auto Cont, December 1976.

65. Kudva, P. and Narendra, K.S., "Synthesis of an Adaptive Observer Using Lyapunov's Direct Method," Int Journal of Control, December 1973, pp. 1201-1210.

66. Narendra, K.S. and Kudva, P., "Stable Adaptive Schemes for System Identification and Control," IEEE Trans Systems, Man, and Cybernetics, November 1974, pp. 542-560.

67. Carroll, R., "New Adaptive Algorithms in Lyapunov Synthesis," IEEE Trans on Auto Cont, April 1976, pp. 246-249.

68. LaSalle and Lefschetz, Stability by Liapunov's Direct Method, Academic Press: New York, 1961.

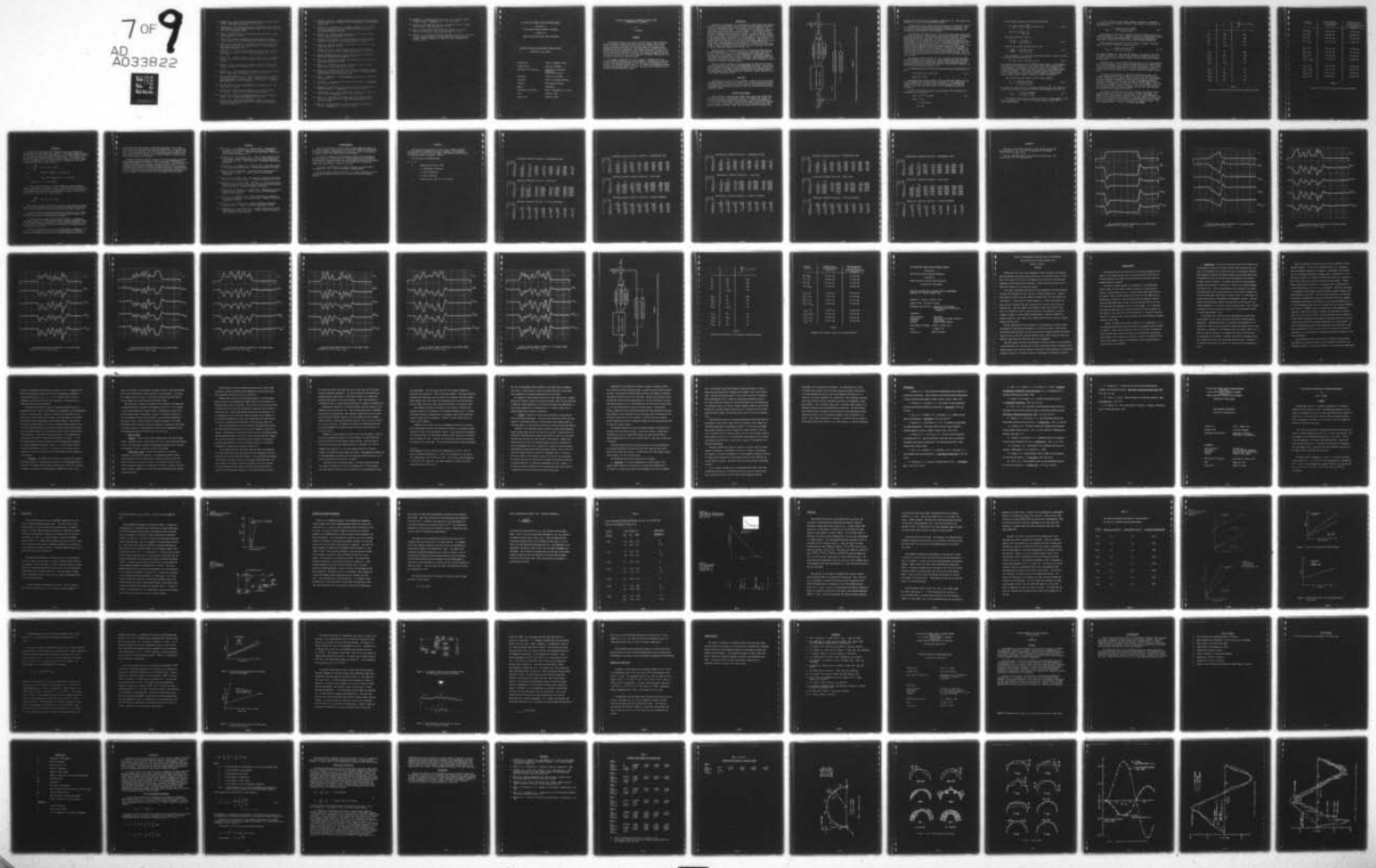
69. Carroll, R., "Application of Liapunov Model-Tracking Parameter Identification for the CH-47 Helicopter," Proc 1974 CDC, pp. 858-863.

70. Hirsch, J. and Peltie, P., "Real-Time Identification Using Adoptive Discrete Model," Proceedings of the Third IFAC Symposium on Sensitivity, Adaptivity and Optimality, pp. 290-297.

71. Landau, I.D., "Unbiased Recursive Identification Using Model Reference Adaptive Techniques," IEEE Trans on Auto Cont, April 1976, pp. 194-202.

AD-A033 822 AUBURN UNIV ALA SCHOOL OF ENGINEERING F/G 14/2
1976 USAF-ASEE SUMMER FACULTY RESEARCH PROGRAM.(U)
SEP 76 J F O'BRIEN F44620-75-C-0031
UNCLASSIFIED AFOSR-TR-76-1419 NL

7 OF 9
AD A033822



72. Kashyap, R.L., "Maximum Likelihood Identification of Stochastic Linear Systems," IEEE Trans on Auto Cont, 1970, pp. 25-34.

73. Soderstrom, T., "An On-Line Algorithm for Approximate Maximum Likelihood Identification of Linear Dynamic Systems," Report 7308, March 1973, Lund Institute of Technology, Sweden.

74. Kudva, P. and Narendra, K.S., "The Discrete Adaptive Observer," Proc of the 1974 CDC, pp. 307-312.

75. Colburn, B.K., "Design Considerations in Model Reference Adaptive Control Systems," Ph.D. Dissertation, Auburn University, December 1975.

76. Colburn, B.K. and Boland, J.S., "Analysis of Error Convergence Rate for a Discrete Model-Reference Adaptive System," to be published in IEEE Trans on Auto Cont, 1976.

77. Yakubovich, V., "Solution of Certain Matrix Inequalities Occurring in the Theory of Automatic Controls," Dokl. Akad. Nauk. USSR, Vol 143, No 1, 1962.

78. Kalman, R.E., "Lyapunov Functions for the Problem of Lure in Automatic Control," Proc of the Nat Acad of Sciences, Vol 49, March 1963, pp. 201-205.

79. Meyer, K.R., "On the Existence of Lyapunov Functions for the Problem of Lure," Journal of SIAM Control, Series A, Vol 3, No 3, 1966, pp. 373-383.

80. Monopoli, R.V., "The Kalman-Yacubovich Lemma in Adaptive Control System Design," IEEE Trans on Auto Cont, October 1973, pp. 527-529.

81. Kalman, R.E. and Bertram, J.E., "Control System Analysis and Design via the 'Second Method' of Liapunov, Part I: Continuous Time Systems," Trans ASME Journal of Basic Engineering, Vol 82, Series D, June 1960, pp. 371-393.

82. De Russo, Ray, and Close, State Variables for Engineers, Wiley: New York, 1965, pp. 519-520.

83. Colburn, B.K., "Model Reference Adaptive Linear Identifier Design and Analysis," (manuscript to be submitted for publication.)

84. Lindorff, D.P., "Effects of Incomplete Adaptation and Disturbance in Adaptive Control," Proc of the 1972 JACC, pp. 562-567.

85. Schooley, D.J., "Model-Referenced Adaptive Control of Plants with Noise and Inaccessible State Vector," Ph.D. Dissertation, University of Missouri, Rolla, 1970.

86. Colburn, B.K., et al., "Adaptive Spacecraft Altitude Control Utilizing Eigenaxis Rotations," AIAA Paper 75-158, 13th Aerospace Sciences Meeting, January 1975.

87. Passeri, D.P. and Herget, C.J., "Parameter Identification of a Class of Multiple Input/Multiple Output Linear Discrete-Time Systems," Proc of the 1972 JACC, paper 28-2.

88. Anderson, B., "Adaptive Identification of Multi-Input Multi-Output Plants," Proc of the 1974 CDC, pp. 273-281.

89. Narendra, K.S. and Kudva, P., "Identification and Adaptation Using Lyapunov's Direct Method," Proc of the 1973 CDC, pp. 521-527.

90. Mehra, R.K., "Optimal Inputs for Linear System Identification," Proc of the 1972 JACC, pp. 811-820.

91. Swanson, G., et al., "Forcing Function Selection for Identification In Human Respiratory Control," Proc of the 1973 CDC, pp. 516-520.

92. Kalaba, "Optimal Inputs for Nonlinear Process Parameter Estimation," IEEE Trans on Aeros and Elect Systems, May 1974.

93. Grewal, M., "Relationship Between Identifiability and Input Selection," Proc of the 1974 CDC, pp 526-528.

94. Mehra, R.K., "Time-Domain Synthesis of Optimal Inputs for System Identification," Proc 1974 CDC, pp. 480-487.

95. Mehra, R.K., "Optimal Input Signals for Parameter Estimation in Dynamic Systems-Survey and New Results," TR-654, Division of Engineering and Applied Physics, Harvard University, 1974.

96. Daniel, C. and Wood, F., Fitting Equations to Data, Wiley: New York, 1971, pp. 86-88.

97. Woodside, C., "Estimation of the Order of Linear Systems," Automatica, Vol 7, 1971, pp. 727-733.

98. Unbehaven, H. and Gohring, B., "Tests for Determining Model Order in Parameter Estimation," Automatica, Vol 10, 1974, pp. 233-244.

99. Van Den Boom, et al., "The Determination of the Orders of Process and Noise Dynamics," Automatica, Vol 10, 1974, pp. 245-256.

100. Tether, A., "Construction of Minimal Linear State-Variable Models from Finite Input-Output Data," IEEE Trans on Auto Cont, August 1970, pp. 427-436.

101. Root, W., "On the Structure of a Class of System Identification Problems," Automatica, Vol 7, 1971, pp. 219-231.

102. Guidoryi, R., "Canonical Structures in the Identification of Multivariable Systems," Automatica, Vol 11, 1975, pp. 361-374.

103. Clark, J., "The Consistent Selection of Parameterizations In System Identification," Proc 1976 JACC, pp. 576-580.

104. Tse, E., "Identification and Estimation of Dynamic Linear Models with Unknown Structure," Proc of the 1976 JACC, pp. 581-585.

105. Miller, R.A., "Continuous Performance Measurement of Manually Controlled Systems," Research Reports, 1975 USAF-ASEE Summer Faculty Research Program, School of Engineering, Auburn University, September 1975, pp. 6-1 to 6-10.

1976 USAF-ASEE SUMMER FACULTY RESEARCH PROGRAM

sponsored by

THE AIR FORCE OFFICE SCIENTIFIC RESEARCH

conducted by

AUBURN UNIVERSITY AND OHIO STATE UNIVERSITY

MODELING THE HUMAN BLOOD-PRESSURE CONTROL SYSTEM RESPONDING TO $+G_z$ STRESS

Prepared by:	James J. Freeman, D. Eng.
Academic Rank:	Associate Professor
Department and University:	Department of Electrical Engineering University of Detroit
Assignment:	Brooks Air Force Base
Laboratory:	School of Aerospace Medicine
Division:	Environmental Sciences
Branch:	Biodynamics
USAF Research Colleague:	Kent K. Gillingham, M. D., Ph.D.
Date:	August 6, 1976
Contract No:	F44620-75-C-0031

MODELING THE HUMAN BLOOD-PRESSURE CONTROL SYSTEM RESPONDING TO $+G_z$ STRESS

by

J. J. Freeman

ABSTRACT

A mathematical model of the closed loop human blood pressure regulation system was derived from eye-level blood pressure responses to $+G_z$ stress. Fourier transforms of input $+G_z$ profiles and output radial arterial blood pressure (sensed at eye level) were previously taken on 3 subjects during USAFSAM/VNB centrifuge experiments. The transfer functions (TF) were calculated as the Fourier transform of the eye-level blood pressure divided by the Fourier transform of the input $+G_z$ stress. The ensemble average of this data (3 subjects, 21 test runs) was used to identify the dynamic characteristics of the human blood pressure regulation system.

The ensemble averaged TF was used to generate a mathematical TF and transfer functions simulated on an analog computer. Frequency error analyses of the TFs and time error analyses of the blood pressure responses were calculated. The simulated TFs were used to: (a) predict blood pressure responses to arbitrary $+G_z$ stress inputs, (b) reveal the closed loop characteristics of the blood pressure regulation system.

INTRODUCTION

Experimental investigations on centrifuges have demonstrated that subjects exposed to $+G_z$ stress exhibit a non-linear drop in blood pressure, characteristic of an underdamped system, with a similar return to normal with the completion of the stress input. A block diagram of the physiologic parameters which characterize this system is given in Figure 1. The closed loop blood pressure regulating system functions to maintain a constant systemic arterial pressure. A decrease in blood pressure, sensed primarily by the baroreceptors in the carotid sinus and secondarily by the baroreceptors in the aorta, results in an increased neural output Ni(t) of the baroreceptors. This increased afferent neural activity $N_e(t)$ is sensed by the medullary vasomotor and cardiac centers which then increase the blood pressure by increasing heart rate, stroke volume, and peripheral arterial resistance. If the $+G_z$ stress is great enough to reduce the eye-level blood pressure to about 30 mm. Hg., blood flow to the eye ceases and black-out will follow. [1]

Previous work on correlating $+G_z$ stress to blood pressure has been done on anesthetized dogs [2 - 7] or in verifying the steady state human response [8 - 9]. The data on dogs is not readily applicable to humans due to the administration of an anesthetic and the differences in physiologic parameters. The steady state human studies are unable to predict human tolerances to non-steady state forms of $+G_z$ stress, due to the dynamic time constants and natural frequency of the blood pressure response.

The data needed to determine the human dynamic eye-level blood pressure response to $+G_z$ stress was taken on the USAFSAM/VNB centrifuge. This data was used to determine a transfer function relating input $+G_z$ stress and eye-level blood pressure. This transfer function was simulated on an analog computer, its characteristic forms representing the closed loop transfer function of the blood pressure regulating system.

OBJECTIVE

The objective of this study was to generate a model of the blood pressure regulation system in order to: a) predict, for any $+G_z$ stress input, the eye-level blood pressure and particularly the point of zero eye-level blood flow, b) generate new physiological information about the closed loop blood pressure regulation system.

MATERIALS AND METHODS

Data Collection: Three relaxed, experienced, unprotected subjects were previously tested on the USAFSAM centrifuge. Each subject had at least one ramp $+G_z$ input stress (Gradual Onset Run--GOR) (.1 G/sec with a maximum of 4.3 to 6 G_z) and four plateaus (Rapid Onset Run--ROR) (1 G/sec with a maximum of 2.5 to 4 G_z). Each subject was also tested with Simulated Aerial Combat Maneuver (SACM) $+G_z$ stress. Eight different SACM profiles were used with a

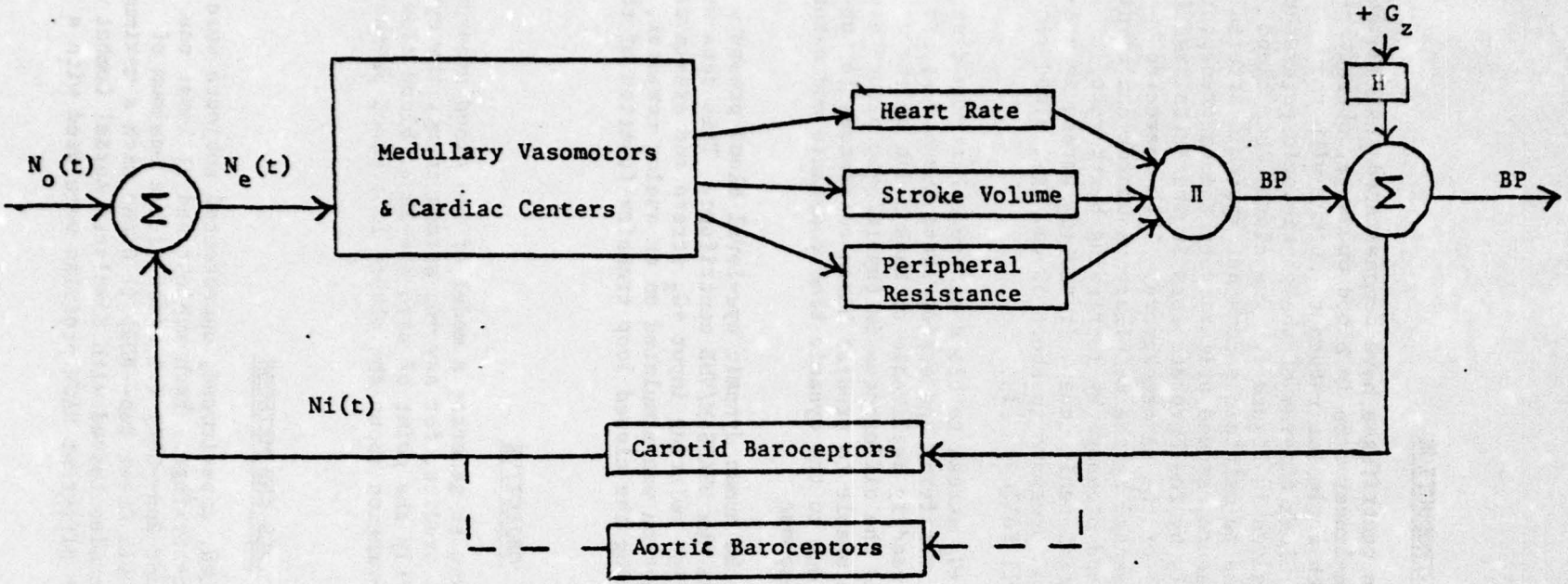


FIGURE 1

A block diagram of the physiological parameters of the blood pressure regulation system.

maximum slope of 1.8 G/sec and a maximum G magnitude of 4.5. Each subject was exposed to at least four different SACM profiles.

The eye-level arterial blood pressure was measured by inserting a cannula in the radial artery and placing the pressure transducer at eye-level. The $+G_z$ stress and blood pressure were simultaneously recorded during each run. All data was tape-recorded for later analysis.

After low-pass filtering (3 dB at 1 Hz), the eye-level blood pressure and $+G_z$ stress was put into a Hewlett-Packard 5451B Fourier Analyzer. The sampling period was 200 seconds. The interface circuitry was a 10 bit ADC with a sampling rate of 1.275 samples/sec. The data was transformed into the frequency domain and the transfer functions were generated by dividing the output blood pressure by the $+G_z$ forcing function. The ensemble average of the 21 transfer functions generated from the $+G_z$ profiles was calculated. The rectangular and polar coordinate form and the impulse response of the averaged transfer function ($\overline{TF}$) are given in Appendix A. The first 25 frequency channels (5 mHz per channel) are shown for the transfer functions. The first 50 channels (.078 sec per channel) are shown for the impulse response. Only the first 25 frequency channels were used since 99.7% of the $+G_z$ stress energy was below .125 Hz.

The averaged transfer function was used to generate the eye-level blood pressure response to the $+G_z$ profiles. Typical results are shown in Appendix B. It was assumed that a mathematical expression which duplicates the frequency profile of $\overline{TF}$ could predict the eye-level blood pressure response to an arbitrary $+G_z$ stress input with zero error.

The frequency profile of $\overline{TF}$ was previously determined to approximate the form:

$$(R + 25.5)^2 + (X - 3.5)^2 = 10^2 \qquad \text{Eq. 1}$$

where $TF = R + jX$

This geometrical transfer function (TF_m) was "keyboard" entered into the Fourier Analyzer with the results shown in Appendix A. This geometrical transfer function was then used to generate the eye-level blood pressure response to the same $+G_z$ stress inputs. Typical responses are shown in Appendix B.

The form of the impulse response corresponding to $\overline{TF}$ was examined and determined to be of the form:

$$TF(t) = K_1 e^{-at} \sin(\omega t + \phi) \qquad \text{Eq. 2}$$

where $a = .30$

$\omega = .26$ rad./sec.

$\phi = -42^\circ$

This TF impulse response can be written in the form:

$$IM = \left\{ \frac{(b - a)^2 + \omega^2}{\omega^2} \right\} e^{-at} \sin(\omega t + \phi) \qquad \text{Eq. 3}$$

where $\phi = \tan^{-1}\left\{ \frac{\omega}{b - a} \right\}$

The Laplace Transform of IM is:

$$L\{IM\} = \frac{s + b}{(s + a)^2 + \omega^2} \qquad \text{Eq. 4}$$

Therefore the transfer function has the form:

$$L\left\{ \frac{P}{G} \right\} = \frac{-(23.48s + 2.17)}{s^2 + .6s + .16} \qquad \text{Eq. 5}$$

This corresponds to the following differential equation relating $+G_z$ stress (G) and eye-level blood pressure (P).

$$\ddot{P} + .6\dot{P} + .16P = -(23.48\,\dot{G} + 2.17\,G) \qquad \text{Eq. 6}$$

This equation was simulated on an EAI-MINIAC analog computer. The parameters, P (eye-level blood pressure) and G ($+G_z$ input stress) were sampled by the Fourier Analyzer. The Fourier Transform was taken and $P(\omega)$ divided by $G(\omega)$. The resulting transfer function (25 terms) and the resulting impulse response is shown in Appendix A. This simulated transfer function (TF_a) was then used to generate the eye-level blood pressure response to the previously used $+G_z$ stress inputs. Typical responses are shown in Appendix B.

This transfer function, simulated on the analog computer:

$$TF_a = \frac{-13.56(1 + 10.77s)}{(1 + 3.75s + 6.25s^2)} \qquad \text{Eq. 7}$$

was used as the first "fit" for a regression analysis on $\overline{TF}$. The closest fit (neglecting the aberrant 18th point) using the same characteristic form, is:

$$TF_{reg.} = \frac{-16.2\,(1 + 9.68s)}{(1 + 5.04s + 6.03s^2)} \qquad \text{Eq. 8}$$

This transfer function had a standard deviation of .35 with respect to the first 17 channels of $\overline{TF}$. The first 17 channels contain at least 95% of the $+G_z$ stress power.

In order to better fit the higher frequency components, a regression analysis was done with another zero added to the function. The equation that was generated is:

$$TF_{reg.} = \frac{-19.9(1 + 4.51s + 5.34s^2)}{(1 + 2.63s + 7.33s^2)} \qquad \text{Eq. 9}$$

With respect to the first 17 channels of $\overline{TF}$ this transfer function had a standard deviation of .30. Only a regression curve for a higher order equation could yield a smaller standard deviation. Considering the physiological compartments being modeled, further analysis was considered impractical.

The regression equation form was then altered to include a time delay term. The "best fit" equation, of this form, is:

$$TF_{reg.} = \frac{-20.6(1 + 3.21s)\ e^{1.19s}}{(1 + 2.47s + 6.47s^2)} \qquad \text{Eq. 10}$$

The standard deviation, of this transfer function, with respect to the first 17 channels of $\overline{TF}$ is .28. Note that the time delay is negative (positive exponent), implying an anticipatory component of the blood pressure response to $+G_z$ stress.

The single zero, two pole transfer function ($TF_{reg.}$, Eq. 8) was simulated on the analog computer. The frequency characteristics of this transfer function and the resulting impulse response is shown in Appendix A. This transfer function was then used to generate the eye-level blood pressure response to the previously used $+G_z$ stress inputs. Typical responses are shown in Appendix B.

A frequency error analysis of the transfer functions was done. The ensemble averaged transfer function ($\overline{TF}$) was used as the standard function. As seen in Appendix A, the higher frequency components are not "well behaved." The higher frequency components were "smoothed" by changing the pertinent frequency components to the average of the next lower and higher frequency components. This generated the "smoothed transfer function ($\overline{TF}_{sm}$). The "best fit" simulated transfer function was $TF_{reg.}$. The error analysis, therefore, was done with $\overline{TF}$, $\overline{TF}_{sm}$, and $TF_{reg.}$ compared to TF_a and TF_m. This frequency error analysis data is summarized in table 1.

The transfer functions were then used to generate the eye-level blood pressure response to various $+G_z$ stress inputs (7 SACMs, GOR, ROR). The maximum absolute blood pressure deviations were noted, using $\overline{TF}$, $\overline{TF}_{sm}$, and $TF_{reg.}$ as the standard transfer functions. Also since "black out" would occur at the minimum eye-level blood pressure, the maximum absolute blood pressure deviation occurring at the point of minimum blood pressure was noted. This data is shown in table 2. These are the worst case values.

x	y	$\int_0^{.125} \lvert x - y \rvert^2 \, df$
$\overline{TF}$	$\overline{TF}_{sm}$	1462
$\overline{TF}$	TF_m	1365
$\overline{TF}$	TF_a	2077
$\overline{TF}$	TF_{reg}	162
$\overline{TF}_{sm}$	$\overline{TF}$	1462
$\overline{TF}_{sm}$	TF_m	582
$\overline{TF}_{sm}$	TF_a	766
$\overline{TF}_{sm}$	TF_{reg}	277
TF_{reg}	$\overline{TF}$	162
TF_{reg}	$\overline{TF}_{sm}$	277
TF_{reg}	TF_m	79
TF_{reg}	TF_a	191

TABLE 1

Frequency error analysis of the generated transfer functions

Transfer Functions	Maximum Blood Pressure Deviation (absolute)	Maximum Deviation at the Point of Minimum Blood Pressure (absolute)
$\overline{TF}$ & $\overline{TF}_{sm}$	4.10 mm. Hg.	2.03 mm. Hg.
$\overline{TF}$ & TF_m	6.40 mm. Hg.	3.07 mm. Hg.
$\overline{TF}$ & TF_a	12.67 mm. Hg.	3.11 mm. Hg.
$\overline{TF}$ & TF_{reg}	4.38 mm. Hg.	4.38 mm. Hg.
$\overline{TF}_{sm}$ & $\overline{TF}$	4.10 mm. Hg.	2.03 mm. Hg.
$\overline{TF}_{sm}$ & TF_m	7.10 mm. Hg.	7.04 mm. Hg.
$\overline{TF}_{sm}$ & TF_a	4.60 mm. Hg.	4.15 mm. Hg.
$\overline{TF}_{sm}$ & TF_{reg}	7.65 mm. Hg.	7.05 mm. Hg.
TF_{reg} & $\overline{TF}$	4.38 mm. Hg.	4.38 mm. Hg.
TF_{reg} & $\overline{TF}_{sm}$	7.65 mm. Hg.	7.05 mm. Hg.
TF_{reg} & TF_m	2.90 mm. Hg.	1.85 mm. Hg.
TF_{reg} & TF_a	4.30 mm. Hg.	3.22 mm. Hg.

TABLE 2

Response error analysis using all $+G_z$ stress profiles

DISCUSSION

The model of the blood pressure regulation system was derived from average (21 tests) data taken from 3 subjects. The averaged transfer function ($\overline{TF}$), between $+G_z$ stress input profiles and eye-level blood pressure outputs, was "smoothed" to reduce the number of aberrant terms. The frequency and response errors, between $\overline{TF}$ and $\overline{TF}_{sm}$ as shown in tables 1 and 2, was assumed to be the inherent error in the analysis system. Therefore a "zero error" model should meet the following criteria:

a) $$\int_0^{.125} | \overline{TF} - TF | \, df \leq 1462$$

b) $$| BP_i(\overline{TF}) - BP_i(TF) | \leq 4.10 \text{ mm. Hg.}$$

c) $$| BP_{min}(\overline{TF}) - BP_{min}(TF) | \leq 2.03 \text{ mm. Hg.}$$

where i = 1, 2, 3...256 samples

As can be seen from table 1, the first criterion is met for TF_m and TF_{reg}. The frequency error value of TF_a is 2077, however 31% of the total error is generated by the frequency components above .10 Hz. Since only 3.6% of the power of the worst case $+G_z$ stress profile is above .10 Hz, the frequency "fit" of TF_a should be acceptable since:

$$\int_0^{.10} | \overline{TF} - TF_a | \, df = 1432$$

From table 2, it can be seen that the eye-level blood pressure response generated by the simulated transfer functions does not meet the second criterion. The deviation from the criterion value is from .28 to 8.57 mm. Hg.

Since the .28 mm. Hg. deviation was generated with TF_{reg}, this transfer function most accurately predicts eye-level blood pressure. However, this error occurred at a point of minimum blood pressure.

The minimum blood pressure, being of special interest, is singularly tested by criterion "c." The simulated transfer functions generated a worst case minimum blood pressure deviation from the criterion of from 1.04 to 2.35 mm. Hg. This deviation is considered to be minimal in predicting when eye-level blood flow will cease.

The major variability occurred at the higher frequency components (.075 → .125 Hz). The simulation process required the devision of two frequency functions which generated more error at the higher frequencies than at the

lower because very small values of input and output power occur at these higher frequencies and round-off error become significant. It has also been shown that the best frequency fit to $\overline{TF}$ occurs when a TF has a negative time delay. Therefore there is a rise in blood pressure before the onset of $+G_z$. This indicates that the subjects, while relaxed, exhibited a cardiovascular change in anticipation of the stress.

Clearly the simulated transfer function of the blood pressure regulation system yields adequate information to predict eye-level blood pressure of relaxed human subjects as a function of $+G_z$ stress inputs. When this model is extended to include subject straining maneuvers and anti-G suit, it can, in conjunction with previously determined transfer functions of arterial oxygen saturation [10] and yet to be determined transfer functions of eye-level blood flow, be of general interest to those who model physiological systems and of specific interest to those who model pilot performance in aerial combat.

REFERENCES

1. Krutz, R. W., S. A. Rositano, R. E. Mancini, 1973. "Physiological Assessment of the Transcuntaneous Doppler Ultrasonic Flowmeter during $+G_z$ Acceleration." Preprints, Aerospace Medical Association, Annual Scientific Meeting, p.77.

2. Koushanpour, E., J. W. Spickler, 1975. "Effect of Mean Pressure Levels on the Dynamic Response Characteristics of the Carotid Sinus Baroceptor Process in Dog." IEEE Transactions on Biomedical Engineering, 22:502-507.

3. Levison, W. H., G. O. Barnett, W. D. Jackson, 1966. "Nonlinear Analysis of the Baroceptor Reflex System." Circulation Research, 18:673-682.

4. Spickler, J. W., P. Kedzi, 1967. "Dynamic Response Characteristics of Carotid Sinus Baroceptors." American Journal of Physiology, 212:472-476.

5. Scher, A. M., A. C. Young, 1963. "Servoanalysis of Carotid Sinus Reflex Effects on Peripheral Resistance." Circulation Research, 12:152-162.

6. Koushanpour, E., D. M. Kelov, 1972. "Partition of the Carotid Baroceptor Response in Dogs Between the Mechanical Properties of the Wall and the Receptor Elements." Circulation Research, 31:831-845.

7. Erickson, H. H., H. Sandler, H. L. Stone, 1976. "Cardiovascular Function during Sustained $+G_z$ Stress." Aviation, Space, and Environmental Medicine, 47(7):750-758.

8. Green, J. F., N. C. Miller, 1973. "A Model Describing the Response of the Circulatory System to Acceleration Stress." Annals of Biomedical Engineering, I:455-467.

9. Miller, N. C., J. F. Green, 1974. "A Model Describing Acceleration-induced Blackout." Annals of Biomedical Engineering, 2:58-68.

10. Gillingham, K. K., R. R. Burton, 1975. "Transfer Functions for Arterial Oxygen Saturation during $+G_z$ Stress." Aviation, Space, and Environmental Medicine, 46(11):1329-1335.

ACKNOWLEDGEMENT

The author is grateful to the Air Force Systems Command for support of this summer research. Appreciation is due Mr. Fred O'Brien of Auburn University and the ASEE for administration of the project. Their work created an environment suitable for concentrating on the research.

The author is indebted to the Biodynamics Branch of the Environmental Sciences Division at the USAF School of Aerospace Medicine for providing a professionally interesting problem and an environment suitable for the pursuit of its solution. Because of this, the author would like to thank Harry Hughes, Ph.D. and Sidney D. Leverett, Jr., Ph.D.

It has been a professional and personal pleasure to work with Kent K. Gillingham, M.D., Ph.D. This work has been a combined effort.

The author would also like to thank Mr. R. C. McNee for his help in the computerized regression analysis and R. R. Burton for his help with the graphics.

APPENDIX A

The frequency characteristics of the various transfer functions used are given in rectangular and polar coordinates. The frequency coordinates are given in the left column. The frequency value is equal to the column number multiplied by .005 HZ.

The "SF" code is translated below

SF A B C

A — Magnitude scale factor (10^A)

B — 4 = Rectangular coordinates

5 = Polar coordinates

0 = Time coordinates

C — Sampling period code (22 = 200 seconds)

AVERAGED TRANSFER FUNCTION - RECTANGULAR FORM

```
W 0 0 25
W 0 0 25
SF      -2       4      22
(        0)      0       0    -259     -12    -313     -52    -330    -111
(        4)   -348     -40    -421    -113    -432     -70    -498     -51
(        8)   -511     -92    -425     -27    -535     103    -541      52
(       12)   -491      11    -512     137    -414     200    -458     161
(       16)   -398     219    -391     228    -769     291    -274     101
(       20)   -354     210    -209     145    -129     304    -260      73
(       24)   -287     122       0       0
```

AVERAGED TRANSFER FUNCTION - POLAR FORM

```
W 0 0 25
W 0 0 25
SF      -2       5      22
(        0)      0       0     259  -17747     317  -17069     348  -16142
(        4)    350  -17354     435  -16496     438  -17082     501  -17418
(        8)    519  -16988     426  -17648     545   16906     544   17443
(       12)    491   17861     530   16499     460   15411     486   16059
(       16)    455   15108     453   14961     823   15921     293   15963
(       20)    412   14925     255   14511     331   11282     270   16427
(       24)    312   15687       0       0
```

AVERAGED TPANSFER FUNCTION - IMPULSE RESPONSE

```
W 0 0 50
W 0 0 50
SF      -1       0      22
(        0)  -1911   -1992   -1843   -1488    -987    -427     102     519
(        8)    777     861     797     630     422     227      86      14
(       16)      9      48     103     150     170     160     125      77
(       24)     32      -3     -19     -20     -11       3      16      26
(       32)     34      44      55      67      76      78      68      46
(       40)     13     -23     -51     -63     -54     -24      21      69
(       48)    108     128     125
```

SMOOTHED AVERAGE TRANSFER FUNCTION - RECTANGULAR FORM

```
W Ø Ø 25
W Ø Ø 25
SF      -2        4       22
(       Ø)        Ø        Ø     -518      -23     -626     -103     -659     -222
(       4)     -677     -247     -841     -226     -862     -216     -985     -216
(       8)    -1022     -183    -1016      -62    -1069      206    -1016      246
(      12)     -954      276    -1023      274     -924      400     -916      322
(      16)     -796      439     -781      457     -616      461     -616      461
(      20)     -554      430     -554      461     -462      461     -462      461
(      24)     -462      400        Ø        Ø
```

SMOOTHED AVERAGE TRANSFER FUNCTION - POLAR FORM

```
W Ø Ø 25
W Ø Ø 25
SF      -2        5       22
(       Ø)        Ø        Ø      519   -17747      634   -17069      695   -16142
(       4)      721   -16002      870   -16496      889   -16597     1008   -16767
(       8)     1038   -16988     1018   -17654     1089    16906     1045    16637
(      12)      994    16380     1059    16499     1007    15656      971    16059
(      16)      909    15108      905    14961      770    14311      770    14311
(      20)      702    14211      722    14018      653    13499      653    13499
(      24)      611    13908        Ø        Ø
```

SMOOTHED AVERAGE TRANSFER FUNCTION - IMPULSE RESPONSE

```
W Ø Ø 50
W Ø Ø 50
SF      -1        Ø       22
(       Ø)    -3682    -3937    -3740    -3111    -2155    -1038       54      949
(       8)     1534     1771     1694     1398     1004      630      359      227
(      16)      219      288      370      409      376      272      125      -22
(      24)     -126     -163     -132      -51       43      114      137      106
(      32)       33      -53     -118     -139     -106      -25       78      174
(      40)      237      250      214      145       66        2      -32      -28
(      48)        4       48       82
```

GEOMETRICAL TRANSFER FUNCTION - RECTANGULAR FORM

```
W 0 0 25
W 0 0 25
SF      -2       4      22
(       0)       0       0    -372     -26    -406     -75    -454    -116
(       4)    -506    -137    -565    -144    -622    -137    -675    -114
(       8)    -721     -80    -756     -35    -778      19    -785      76
(      12)    -778     133    -756     186    -721     232    -675     267
(      16)    -622     290    -564     297    -506     290    -454     267
(      20)    -408     232    -373     186    -351     133    -343      76
(      24)    -352      19       0       0
```

GEOMETRICAL TRANSFER FUNCTION - POLAR FORM

```
W 0 0 25
W 0 0 25
SF      -2       5      22
(       0)       0       0     373  -17601     413  -16967     468  -16576
(       4)     524  -16488     583  -16574     636  -16759     685  -17043
(       8)     725  -17369     757  -17742     778   17856     788   17442
(      12)     789   17026     779   16609     757   16209     726   15832
(      16)     686   15492     638   15220     584   15012     527   14943
(      20)     470   15034     417   15337     376   15918     352   16742
(      24)     352   17683       0       0
```

GEOMETRICAL TRANSFER FUNCTION - IMPULSE RESPONSE

```
W 0 0 50
W 0 0 50
SF      -1       0      22
(       0)   -2707   -2762   -2513   -2005   -1323    -580     112     659
(       8)    1009    1152    1118     962     749     535     360     239
(      16)     167     129     104      77      44       9     -19     -29
(      24)     -16      16      57      93     111     106      78      38
(      32)      -3     -29     -33     -14      22      59      88      97
(      40)      85      56      20     -11     -25     -19       5      38
(      48)      68      86      84
```

SIMULATED TRANSFER FUNCTION - RECTANGULAR FORM

```
W 0 0 25
W 0 0 25
SF      -2       4      22
(       0)       0       0    -341     -62    -385    -142    -432    -200
(       4)    -488    -241    -586    -263    -672    -275    -761    -229
(       8)    -832    -169    -899     -98    -932     -15    -947      79
(      12)    -949     163    -916     245    -884     319    -829     377
(      16)    -777     420    -727     452    -668     490    -625     502
(      20)    -574     503    -530     483    -480     521    -448     500
(      24)    -421     484      -1       0
```

SIMULATED TRANSFER FUNCTION - POLAR FORM

```
W 0 0 25
W 0 0 25
SF      -2       5      22
(       0)       0       0     346  -16980     410  -15974     475  -15523
(       4)     544  -15372     642  -15588     726  -15776     794  -16330
(       8)     849  -16853     904  -17378     933  -17913     950   17519
(      12)     963   17022     949   16498     940   16010     911   15550
(      16)     883   15155     857   14807     829   14366     802   14116
(      20)     763   13873     718   13755     709   13264     672   13177
(      24)     642   13094       1   17999
```

SIMULATED TRANSFER FUNCTION - IMPULSE RESPONSE

```
W 0 0 50
W 0 0 50
SF      -1       0      22
(       0)   -3220   -3483   -3303   -2693   -1755    -653     421    1290
(       8)    1835    2012    1859    1475     993     540     212      47
(      16)      35     121     234     308     304     218      78     -71
(      24)    -179    -216    -176     -76      45     146     195     179
(      32)     110      14     -74    -124    -120     -67      17      99
(      40)     152     161     124      56     -18     -72     -89     -62
(      48)      -4      67     123
```

REGRESSION TRANSFER FUNCTION - RECTANGULAR FORM

```
W 0 0 25
W 0 0 25
SF      -2       4      22
(       0)       0       0   -2044     129   -2101    -510   -2102    -758
(       4)   -2577    -748   -2915    -754   -3097    -944   -3321    -852
(       8)   -3397   -1155   -3777    -525   -3494    -105   -3477      50
(      12)   -3781      70   -3517     535   -3788     670   -4055     769
(      16)   -3729     874   -3290     996   -3206     893   -3494     754
(      20)   -3046     996   -2833     963   -2913    1083   -2658     852
(      24)   -2967    1022       0       0
```

REGRESSION TRANSFER FUNCTION - POLAR FORM

```
W 0 0 25
W 0 0 25
SF      -2       5      22
(       0)       0       0    2048   17638    2162  -16637    2234  -16018
(       4)    2683  -16383    3011  -16551    3237  -16305    3429  -16561
(       8)    3588  -16123    3813  -17209    3496  -17829    3477   17916
(      12)    3782   17891    3557   17132    3847   16995    4127   16924
(      16)    3830   16679    3438   16313    3328   16442    3575   16781
(      20)    3205   16187    2992   16121    3108   15959    2792   16220
(      24)    3138   16097       0       0
```

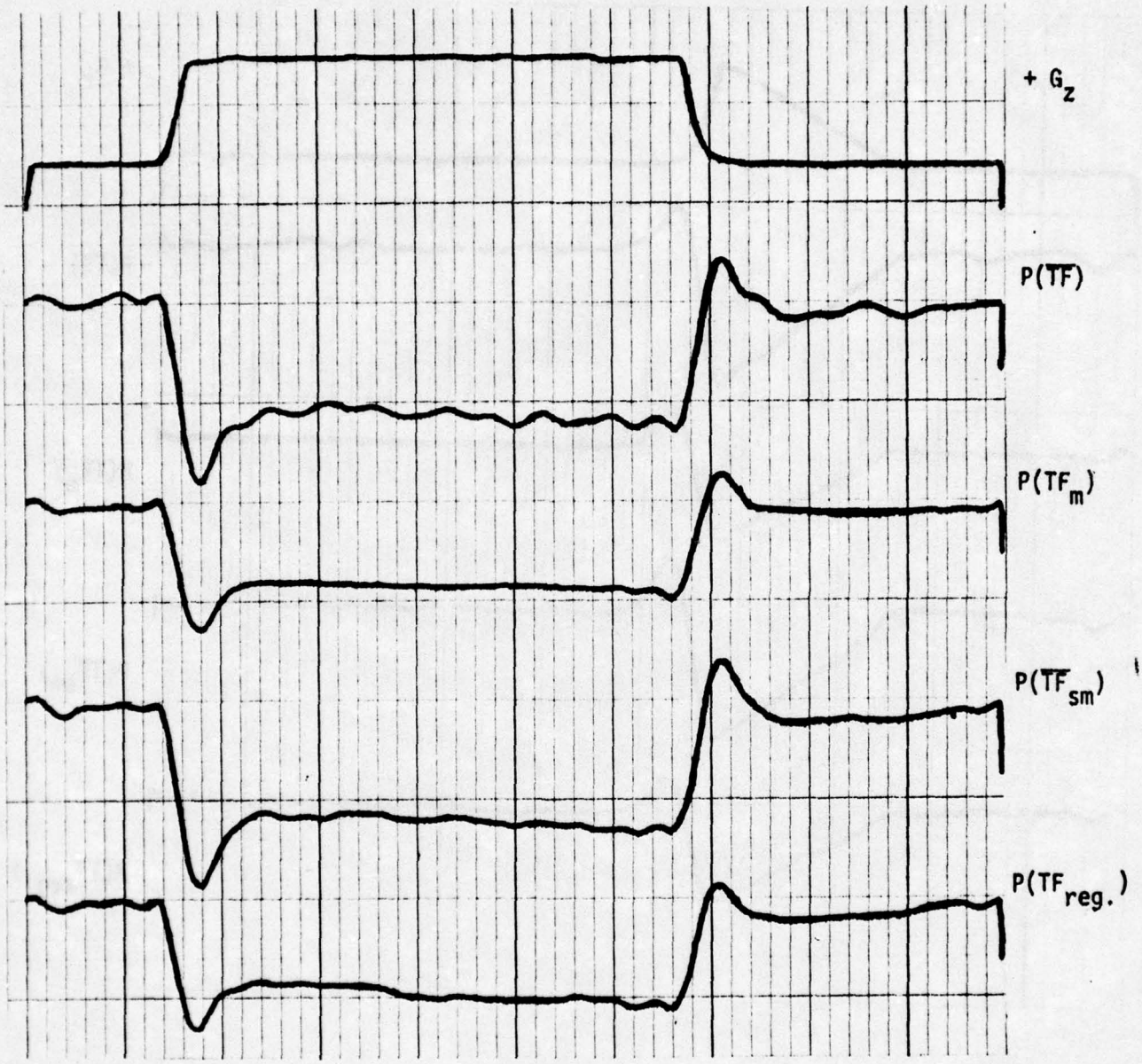
REGRESSION TRANSFER FUNCTION - IMPULSE RESPONSE

```
W 0 0 50
SF       0       0      22
(       0)   -1512   -1495   -1290    -933    -491     -45     331     580
(       8)     681     646     513     337     170      53       3      14
(      16)      64     121     158     158     121      58      -8     -57
(      24)     -75     -58     -17      34      75      92      80      45
(      32)      -3     -45     -68     -66     -40       1      42      71
(      40)      81      71      46      18      -5     -12      -5      14
(      48)      33      45      43
```

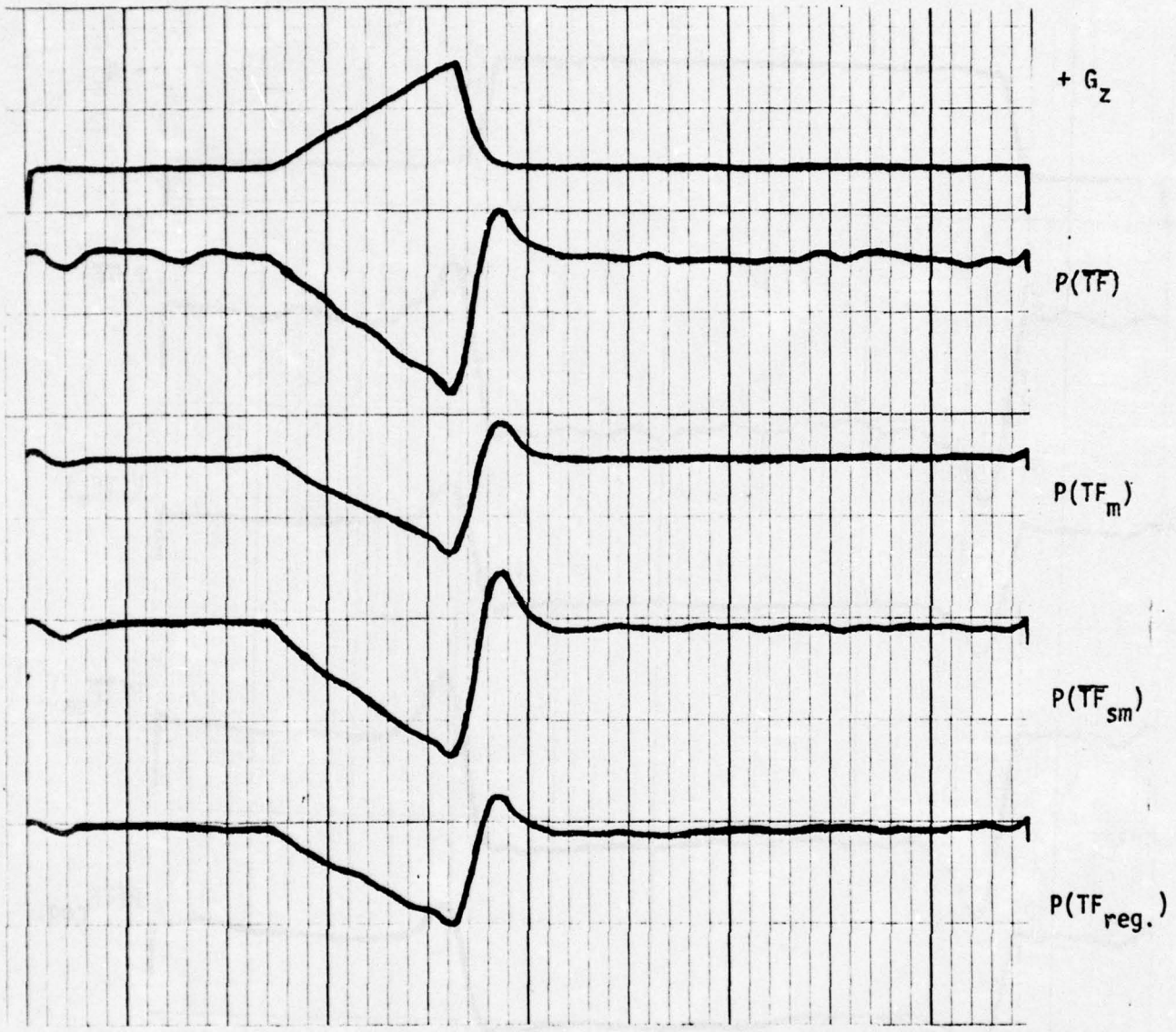
APPENDIX B

Eye-level blood pressure responses to ROR, GOR and various ACM $+G_z$ stress inputs. The responses are generated by the transfer functions $\overline{TF}$, TF_m, $\overline{TF}_{sm}$, TF_{reg}.

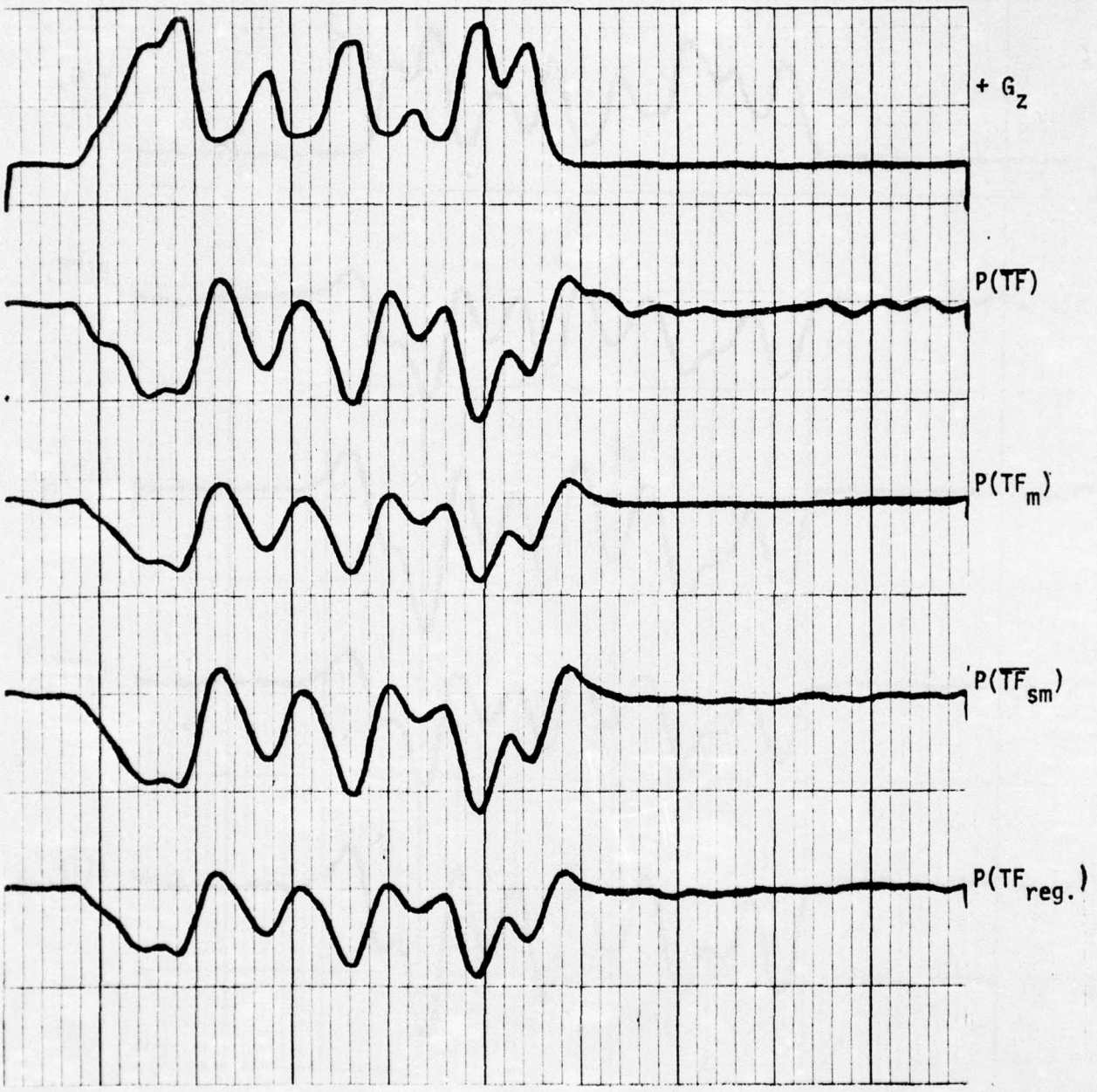
The total sampling time for all profiles was 200 seconds. The sampling rate was 1.275 samples/second.



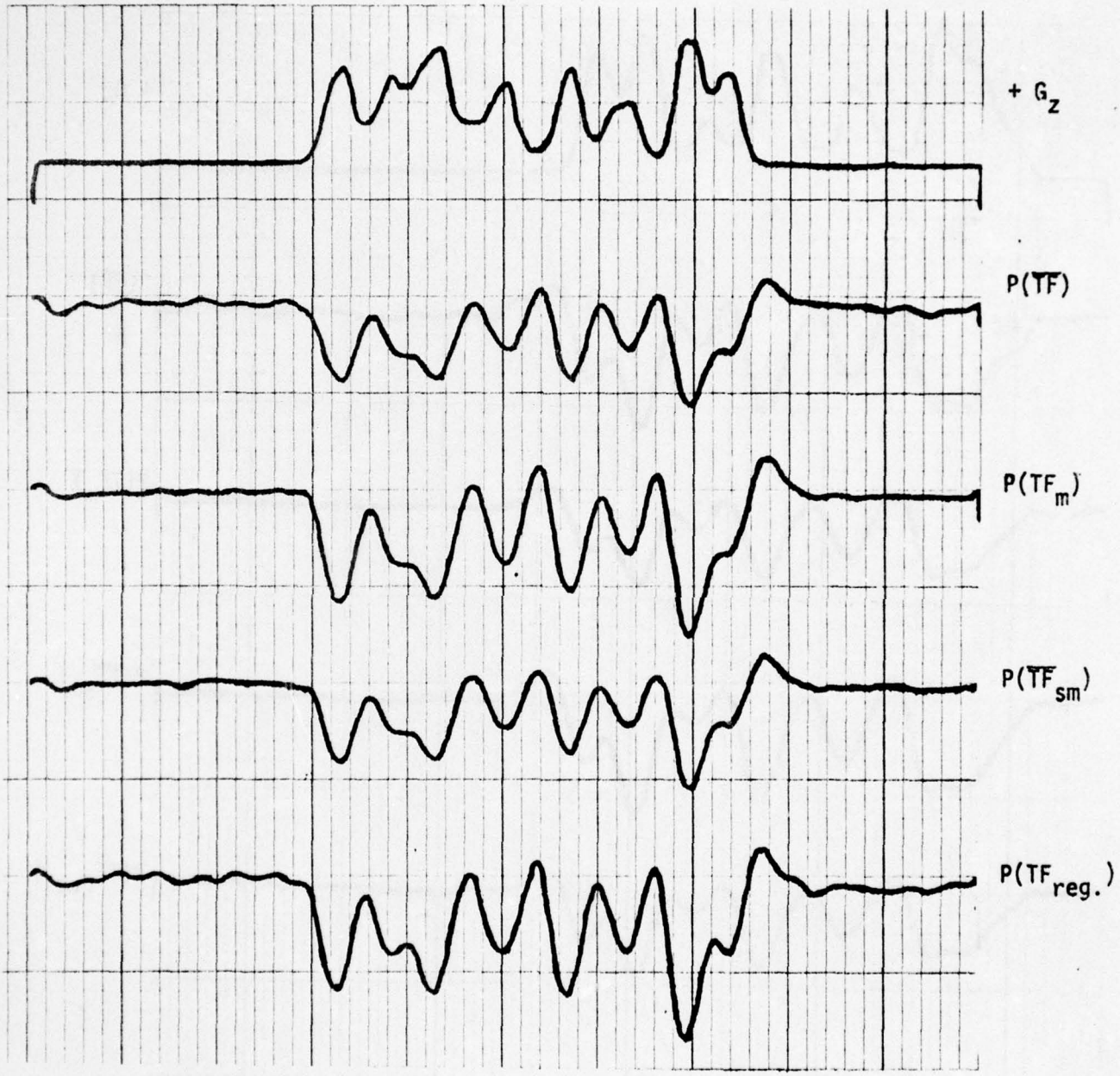
Eye-level blood pressure responses to + G_z stress inputs generated by $\overline{TF}$, TF_m, $\overline{TF}_{sm}$, $TF_{reg.}$



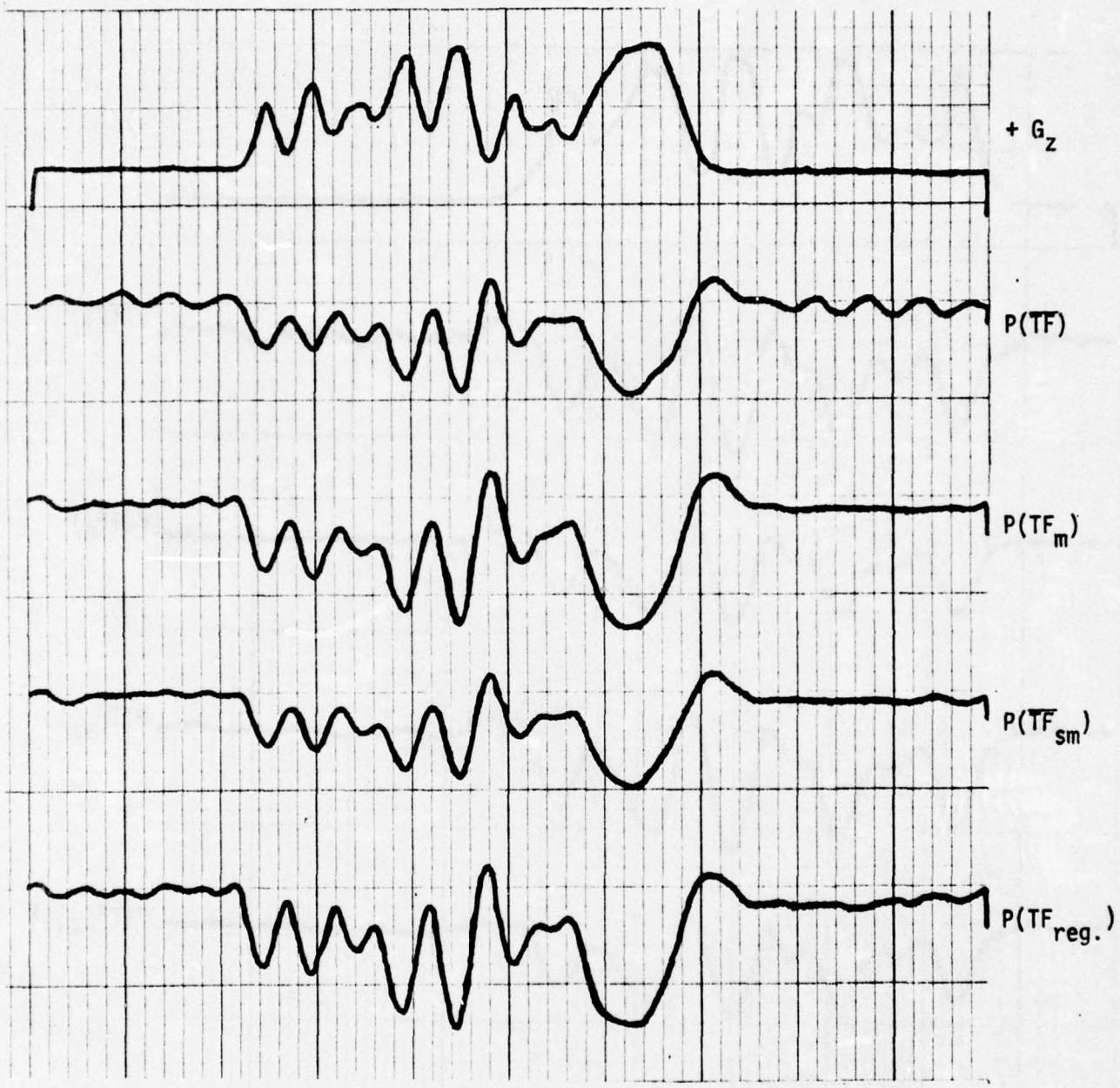
Eye-level blood pressure responses to + G_z stress inputs generated by $\overline{TF}$, TF_m, $\overline{TF}_{sm}$, $TF_{reg.}$



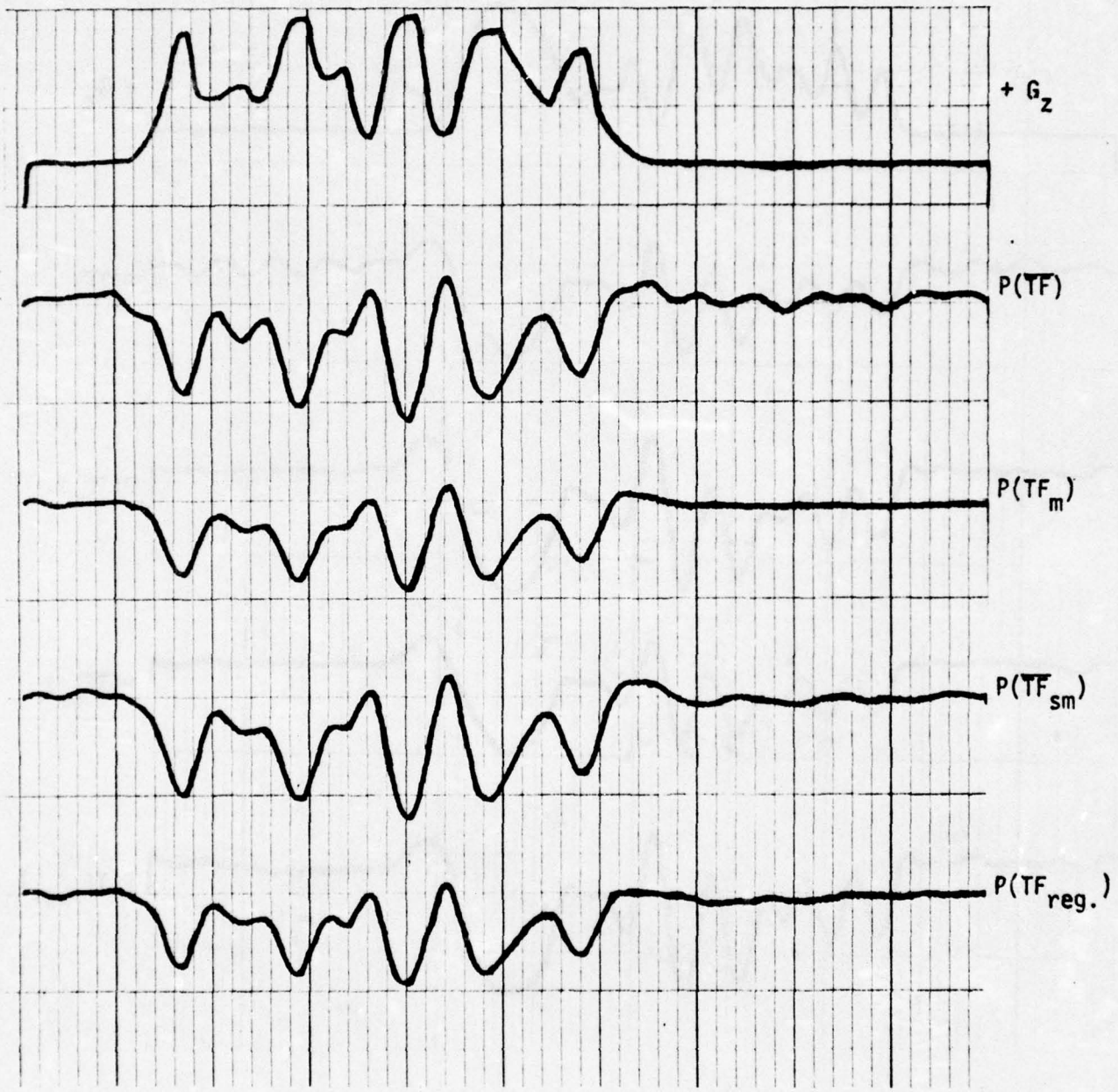
Eye-level blood pressure responses to + G_z stress inputs generated by $\overline{TF}$, TF_m, $\overline{TF}_{sm}$, $TF_{reg.}$



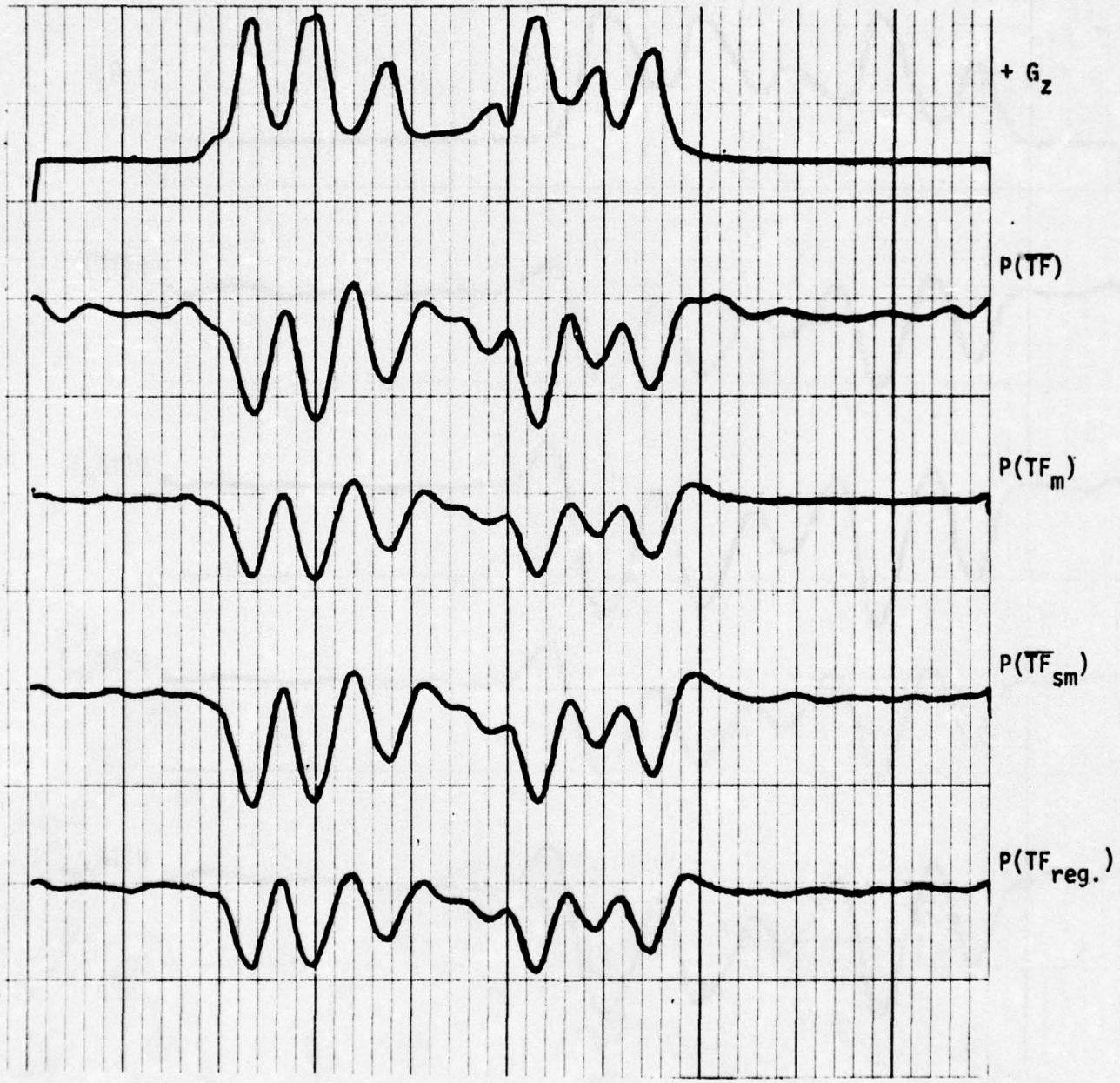
Eye-level blood pressure responses to + G_z stress inputs generated by $\overline{TF}$, TF_m, $\overline{TF}_{sm}$, $TF_{reg.}$



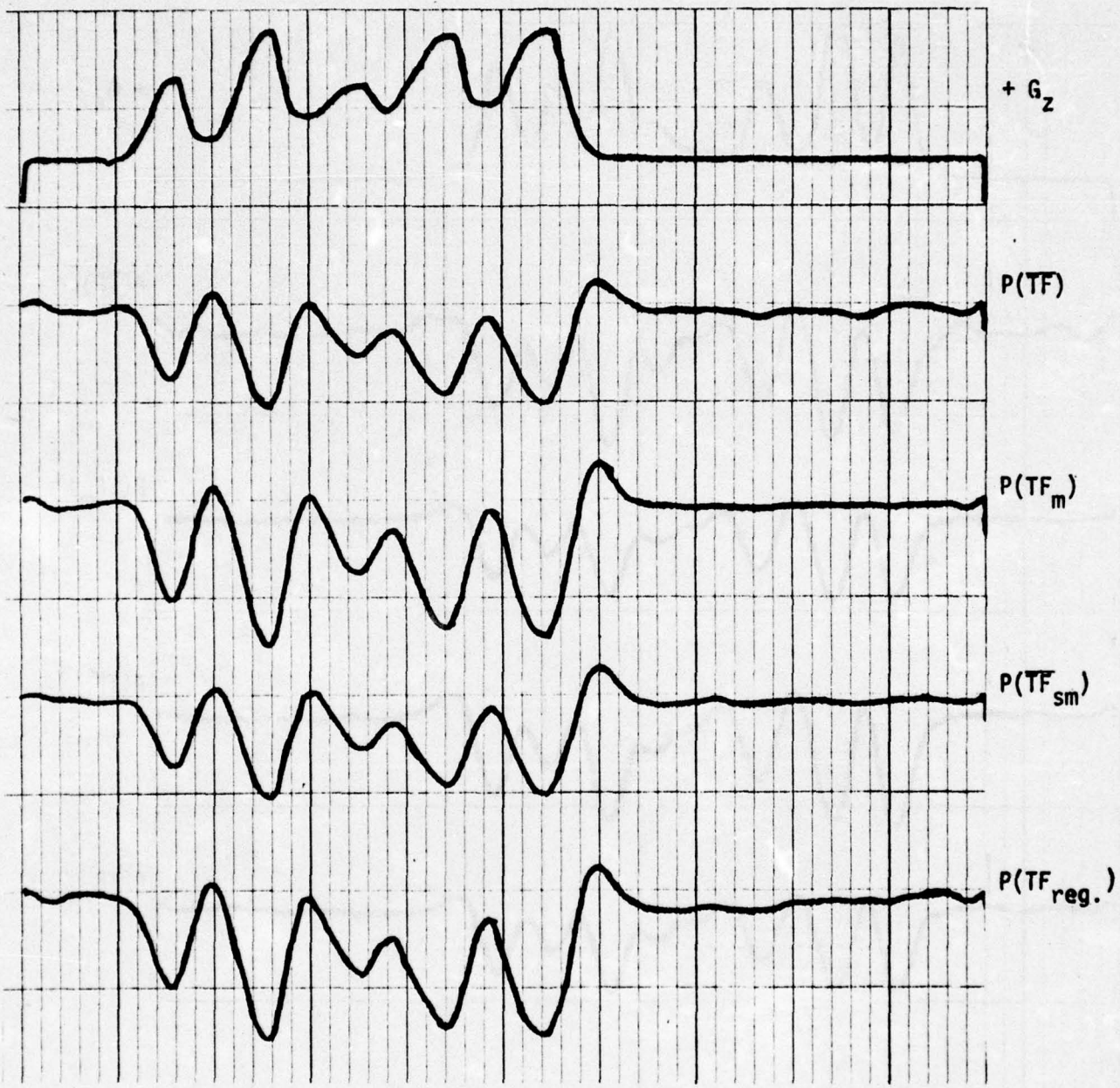
Eye-level blood pressure responses to + G_z stress inputs generated by $\overline{TF}$, TF_m, $\overline{TF}_{sm}$, $TF_{reg.}$



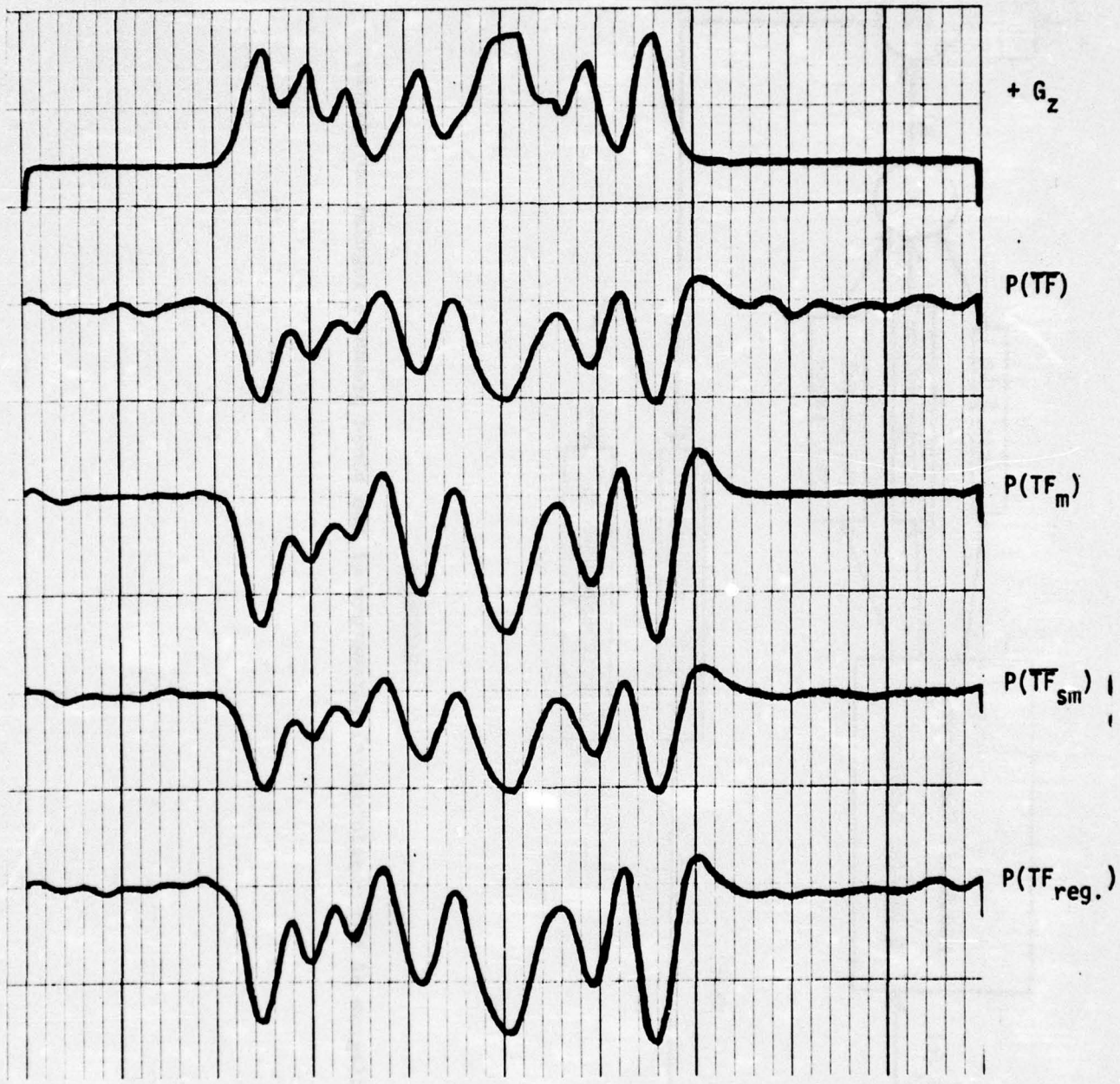
Eye-level blood pressure responses to + G_z stress inputs generated by $\overline{TF}$, TF_m, $\overline{TF}_{sm}$, $TF_{reg.}$



Eye-level blood pressure responses to + G_z stress inputs generated by $\overline{TF}$, TF_m, $\overline{TF}_{sm}$, $TF_{reg.}$



Eye-level blood pressure responses to + G_z stress inputs generated by $\overline{TF}$, TF_m, $\overline{TF}_{sm}$, $TF_{reg.}$



Eye-level blood pressure responses to + G_z stress inputs generated by $\overline{TF}$, TF_m, $\overline{TF}_{sm}$, $TF_{reg.}$

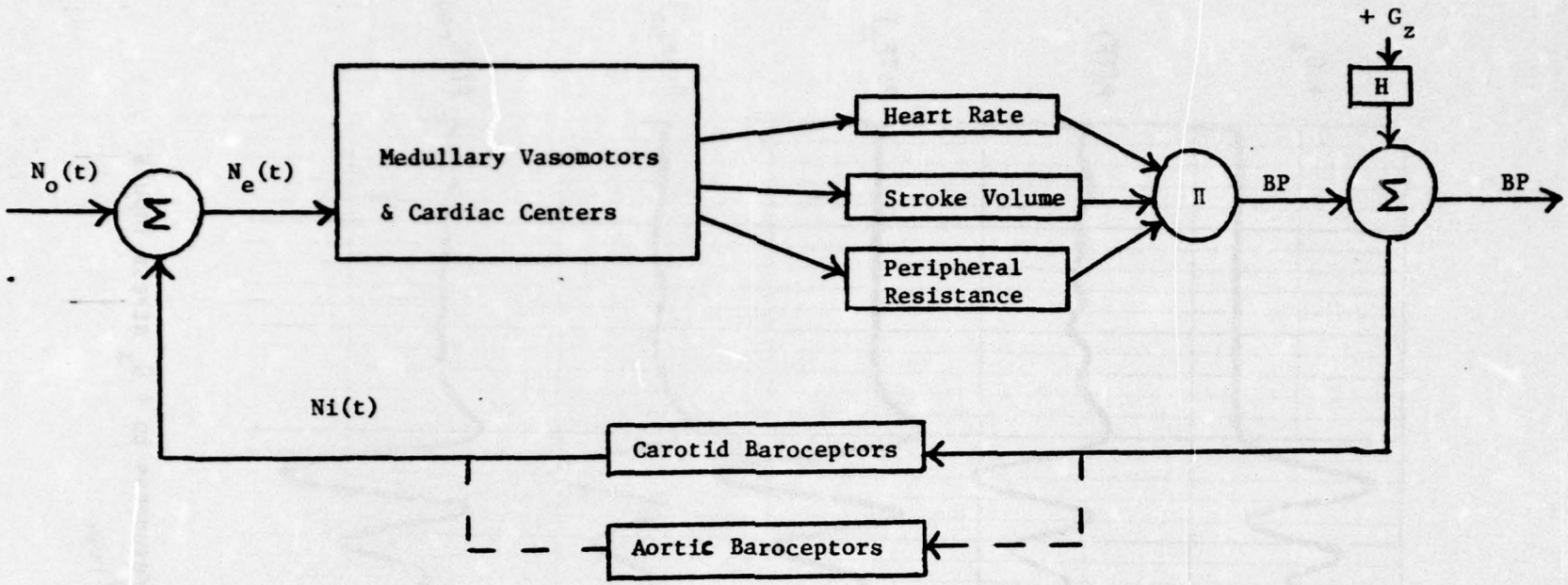


FIGURE 1

A block diagram of the physiological parameters of the blood pressure regulation system.

x	y	$\int_0^{.125} \lvert x - y \rvert^2 \, df$
$\overline{TF}$	$\overline{TF}_{sm}$	1462
$\overline{TF}$	TF_m	1365
$\overline{TF}$	TF_a	2077
$\overline{TF}$	TF_{reg}	162
$\overline{TF}_{sm}$	$\overline{TF}$	1462
$\overline{TF}_{sm}$	TF_m	582
$\overline{TF}_{sm}$	TF_a	766
$\overline{TF}_{sm}$	TF_{reg}	277
TF_{reg}	$\overline{TF}$	162
TF_{reg}	$\overline{TF}_{sm}$	277
TF_{reg}	TF_m	79
TF_{reg}	TF_a	191

TABLE 1

Frequency error analysis of the generated transfer functions

Transfer Functions	Maximum Blood Pressure Deviation (absolute)	Maximum Deviation at the Point of Minimum Blood Pressure (absolute)
$\overline{TF}$ & $\overline{TF}_{sm}$	4.10 mm. Hg.	2.03 mm. Hg.
$\overline{TF}$ & TF_m	6.40 mm. Hg.	3.07 mm. Hg.
$\overline{TF}$ & TF_a	12.67 mm. Hg.	3.11 mm. Hg.
$\overline{TF}$ & TF_{reg}	4.38 mm. Hg.	4.38 mm. Hg.
$\overline{TF}_{sm}$ & $\overline{TF}$	4.10 mm. Hg.	2.03 mm. Hg.
$\overline{TF}_{sm}$ & TF_m	7.10 mm. Hg.	7.04 mm. Hg.
$\overline{TF}_{sm}$ & TF_a	4.60 mm. Hg.	4.15 mm. Hg.
$\overline{TF}_{sm}$ & TF_{reg}	7.65 mm. Hg.	7.05 mm. Hg.
TF_{reg} & $\overline{TF}$	4.38 mm. Hg.	4.38 mm. Hg.
TF_{reg} & $\overline{TF}_{sm}$	7.65 mm. Hg.	7.05 mm. Hg.
TF_{reg} & TF_m	2.90 mm. Hg.	1.85 mm. Hg.
TF_{reg} & TF_a	4.30 mm. Hg.	3.22 mm. Hg.

TABLE 2

Response error analysis using all $+G_z$ stress profiles

1976 USAF-ASEE SUMMER FACULTY RESEARCH PROGRAM

sponsored by

The Air Force Office Scientific Research

conducted by

Auburn University and Ohio State University

Participant's Final Report

EFFECT OF RADIOFREQUENCY RADIATION (RFR) ON PERFORMANCE RETENTION OF A DELAYED RESPONSE TASK

Prepared by: Carole D. Hansult, Ph.D.

Academic Rank: Assistant Professor

Department and University: Department of Psychology
State University of New York at Binghamton

Assignment:

(Air Force Base)	Brooks AFB
(Laboratory)	USAF School of Aerospace Medicine
(Division)	Radiobiology
(Branch)	Weapons Effects Branch

USAF Research Colleague: Donald N. Farrer, Ph.D.

Date: 13 August 1976

Contract No. F44620-75-C-0031

EFFECT OF RADIOFREQUENCY RADIATION (RFR) ON PERFORMANCE AND RETENTION OF A DELAYED RESPONSE TASK

Carole D. Hansult

ABSTRACT

Through the years since the development of radar and other radiofrequency emiting equipment research has been carried out on the biologic effects of RFR. Most of the concern has been for the damaging side effects of increased body temperature after high intensity exposure. Little attention has been paid to behavioral effects or low intensity exposure.

This study investigated the effects of both thermogenic and nonthermogenic RFR upon the performance of rats learning a delayed response task. Subjects were taught to shuttle from one chamber to another while the wall between was illuminated. If they failed to change chambers or if they crossed when the wall was not illuminated they were punished with a noxious noise (100 db at 8,000 cps Hz). Once the subjects had reached criterion (10 correct trials out of 12 consecutive trials), they were tested in the apparatus in the RFR aneochoic chamber at either $5mW/cm^2$ (nonthermogenic intensity), $20mW/cm^2$ or without radiation. Each subject had a yoked control which was used to estimate simple activity levels.

Results indicate that both thermogenic and nonthermogenic radiation levels are capable of interrupting performance to a significant degree. When tested for two days after exposure, the low radiation level subjects regained performance levels by the 1st day while the high radiation level animals needed an extra day. Activity levels were not affected by any of the treatments.

The data suggest that even non-thermogenic radiation levels can be detrimental to the performance of a learned task at least in the early stages of acquisition and further suggest that some care should be taken when training personnel on RFR-emiting equipment especially if the task requires a high degree of perceptual vigilance.

ACKNOWLEDGMENT

The author would like to thank the Air Force Systems Command for the support of this summer research and to sincerely thank Mr. Fred O'Brien of Auburn University and ASEE for the administrative work which made the program function so smoothly.

The author is deeply grateful to the members of the Radiobiology Division whose constant support made the completion of this project a reality. Special thanks go to Mr. G. Carroll Brown, MSgt Ralph Detwiler, A1C Lloyd S. Gerkin, and A1C Refugio Garcia who built the apparatus and designed the electronics. Also the author wishes to thank Mr. Stewart Allen and MSgt Abram Yates for their interest and hard work at the radiation site while the experiment was in its final stages. It is important to express my gratitude to Ms. Geraldine Siebold who typed my papers for the program, to the veterinary services personnel, Dr. Jerome H. Krupp and Capt John T. Young who gave advice and carried out the histological analyses required by the study.

Finally, the author would like to thank Mr. H. C. Sutherland, Jr. of the Audiology Laboratory who gave both advice and equipment whenever needed, Dr. Phelps P. Crump from the Biometrics Division who worked at break-neck speed with less than twelve hours lead time to complete the preliminary data analyses, and my sponsor, Dr. Donald N. Farrer of the Weapons Effects Branch whose constant support of and interest in this research played a crucial part in its completion.

1. INTRODUCTION: The ancient Greeks were the first to describe the electromagnetic properties of amber and since then scientists have been drawn to investigation of the effects and uses of nonionizing radiation. Early inquiries concerned the physical aspects and practical application of radiation with very little work being investigated in the possible biologic effects of exposure. When radar and the other radiofrequency equipment were developed in World War II, however, the research emphasis was reversed (10). This is understandable since thousands of personnel were being trained to use these machines at close quarters although very little was known about side effects or safety limits. The development of nuclear power, however, overshadowed electromagnetic research. Ionizing radiation had spectacular effects both physically and biologically and concern deepened as to its safety in even minuscule doses. Basic research proliferated in these areas while interest in the physiological effects of nonionizing radiation waned.

By the early 1960's the bulk of the radiofrequency research data had increased, but was almost exclusively from high intensity exposure experiments. Although practically no information was available for low dosage level effects, most investigators nevertheless agreed that the only risk factor in exposure to radiofrequency waves was thermal insult (10, 17). Recently, however, interest in low dosage levels has intensified due to the development of new medical, industrial and domestic equipment such as the microwave oven which emit nonionizing radiation waves. Concern for the safety of the public, the worker, the patient and the environment is high.

There are two ways of studying the reactions of organisms to radio-frequency exposure. The first, as mentioned above, is to concentrate upon the biologic response of the organism. Considerable work has been done in this respect especially at higher levels of intensity (17, 18). The second approach is to observe the behavioral reaction of a subject to RFR. Very little effort has been concerned with this aspect. Thomas, Edward, Finch, Fulk and Burch In: (18) exposed rats to pulsed waves of X and S band radiation at 5, 10, 15, and 20 mW/cm^2. There was a decrement in performance in both delayed response and fixed schedule response rates after exposure at all doses. Hunt, King, and Phillips In: (18) measured the effects of constant wave exposure on exploratory activity, swimming performance and vigilance discrimination in rats and found that doses of 6.3 mW/cm^2 depressed exploration and vigilance but did not affect swimming. Dose levels of 11 mW/cm^2, however, interfered with both swimming and vigilance. Working with monkeys, Galloway (18) irradiated his subjects with 5, 10, 15, 20 and 25 mW/cm^2. He found that there were no effects on either visual discrimination performance or repeated acquisition at intensities below 15 mW/cm^2 but measurable decrements at 20 and 25 mW/cm^2. In some of the above experiments, body temperatures were raised and in some they remained normal, but it is clear that even at fairly low levels of stimulation, it is not difficult to demonstrate behavioral changes in both rats and primates.

One consideration which must be kept in mind while discussing the physiological or behavioral effects of RFR at higher intensities is its thermogenic capacity. The biologic effects of an increased core temperature

produced via exogeneous heating are well known (14, 19). In addition, the effects of externally produced heat stress on performance in humans has received some attention (1, 2, 3, 4, 5, 6). However, RFR is a unique thermogenic source and its effects upon performance or acquisition of a learned task are not well researched.

The present study seeks to begin an investigation which may help to elucidate the subtle effects of RFR exposure at thermogenic and nonthermogenic levels on a living system. Because of the brief time available for this study, only a limited inquiry may be made. The main question will address the effects of RFR on performance levels and/or learning. This has not been asked in either humans or rats for a delayed response avoidance task. It is an interesting question especially since many skilled moves require that the subject refrain from instantaneous reaction until a second factor is accounted for. Such delayed response learning is a necessary part of training in the operation, testing and maintenance of aircraft. It can mean the difference between successful mission performance and expensive (in terms of manpower and machines) delays. If an RFR exposure affects either the performance of a task or its actual neural storage, new precautions will have to be devised to monitor and counteract such changes in key personnel.

2. OBJECTIVE: The purpose of this study is to evaluate the possible detrimental effects of radiofrequency radiation on the performance and/or retention of a simple delayed response learning task. Rats will be trained to endure a noxious but not physiologically harmful noise until a "go"

signal is presented. At the signal, the subject enters a time period during which he may terminate the sound by moving to a sound chamber. If he does not, another trial will begin. If he moves during the signal off period, an even louder noise occurs from which he cannot escape.

When the task is learned, the subjects will be placed in the apparatus in graded RFR fields to produce either moderate or mild (i.e., not causing a rise in body temperature) thermal insults. Subsequently, subjects will be tested under normal circumstances in order to see whether retention as well as performance may have been affected. The resulting information is of interest since it could illuminate a possible decrement in job (task) performance and/or retention during and subsequent to exposure to RFR fields for modest increases in body temperature which are not accompanied by the overt behavioral sings of thermal stroke or heat syncope.

3. BODY OF REPORT:

Subjects. Subjects were 30 male Sprague Dawley rats over 90 days of age. They were housed in group cages, 3 or 4 to a cage and fed and watered ad lib. All animals were subjected to histological analysis after training was completed in order to identify any with otitis media.

Experimental Method. Testing was carried out in a special Plexiglass 2 room avoidance apparatus. An opening for passage allowed movement between the two chambers while an opaque sliding door kept the animal confined once it made its choice. The floor was curved to form a trough running the length of the apparatus (24 inches) in order to keep the subject oriented lengthwise to the RF waves thus maintaining equal exposure throughout testing.

The dividing wall between chambers was opaque with a single light covered by a plastic guard above the passageway on either side so that both rooms were used for the start of a new trial.

Subjects were trained on the following schedule. The trial began when a loud but not physiologically harmful white noise stimulation was presented for a total of 60 seconds. The intensity of the noise was 50 db at 8,000 Hz which is below that necessary to elicity the Pryer reflex in normal rats (13). Narrow band frequency noise was chosen because it is less damaging to the ear than pure tones and because the rat appears to be relatively unresponsive to pure tones (especially those below 10,000 Hz) due to a neuroanatomical peculiarity of the auditory system (16).

When the sound had been on for 40 seconds, the light above the door was illuminated and remained so until the noise stopped, a total of 20 seconds. At that point, if the animal had not moved to the second chamber, the door between chambers closed and a noxious narrow band noise stimulation (100 db at 8,000 Hz) was presented for 15 seconds. This level of sound was chosen because it elicits the Pryer reflex (11, 13) without exceeding the threshold for audiogenic seizures (9).

If the subject moved to the second room while the mild stimulation was on but before the signal light above the door illuminated, the door closed and the noxious sound was presented. If the subject moved through the door while the signal light was on, the mild sound terminated, the door closed and the subject received 30 seconds of time out (silence). A new trial began with the onset of the mild sound and simultaneous opening of the door between chambers. If the subject failed to move to

the second room before the light went out, the door shut and the noxious sound was presented immediately. On trials during which the subject was punished with the loud sound, an inter-trial interval of 5 seconds was observed during which no noise was presented. Such a quiet period was introduced in order to avoid auditory habituation or change of threshold (11).

Training was carried out in one-hour sessions with each subject in the apparatus for two sessions per day. Water and food deprivation, therefore, were limited to these periods. When subjects reached criterion (10 trials out of 12 correct delayed response), they were submitted to RF treatment within 24 hours. Training sessions were from 8-9, 9-10, 10-11 a.m. and 1-2, 2-3, 3-4 p.m. each day. No subject was tested at the same time every day but served randomly at 2 blocks at either 8-9 and 1-2 or 9-10 and 2-3 or at 10-11 and 3-4.

Treatment in the RF chamber will last for 1 hour per subject. Prior to the use of experimental subjects in the RF chamber, two dose levels were tested on animals of similar strain, weight and age. Previous tests at this lab on restrained rats demonstrated that an exposure of 1.6 GHz at 20 mW/cm^2 was sufficient to raise body temperature $\simeq 2^{\circ}C$ and that an exposure of 5 mW/cm^2 was well within the animals' thermoregulatory capability. In this experiment the average value for high dose subjects was 21.0 ± 0.8 mW/cm^2 and for the low dose $4.85 \pm .17$ mW/cm^2.

There were three RF treatment groups. The first received the high dose which was sufficient to raise core temperature $\sim 2^{\circ}C$ above normal. The second group received the low dose which did not significantly elevate

core temperature. The final group was run in the anechoic chamber but received no RF stimulation. This is the control group. On the day following treatment all three groups were run again on the original training schedule. Those subjects with error scores well exceeding those of the pre test days were run again daily until these scores were reduced to the expected level.

This schedule allowed for estimation of the effects of moderate RFR exposures (Group I) on performance of the delayed response task.* To assess the possible effects of moderate RFR on performance data from low RFR rats (Group II) were used for comparison. Finally, the third group served as a control for RF exposure.

Because activity levels as well as performance levels may be affected by RF fields yoked controls were employed and exposed to an apparatus almost identical to that of the experimental animals. These subjects were presented with the same stimuli as experimental subjects except that their own behavior did not control the input. Whatever the experimental subject did determined the sequela in the yoked cage. The only difference between training apparatus

---

*While Kangaroo rats can survive rectal temperatures of 40.5° - 41°C (8) and the antelope ground squirrel -- 44.4°C, the laboratory rat can survive core temperatures of 40°C but dies at 43°C. Since normal rectal temperature is 37°C (12), this study will raise body temperature to 39°C which falls comfortably below lethal levels.

was that the passageway between chambers in the yoked control equipment had no door. This was done in order to prevent excitement in any animal which happened to be passing through just as the door shut.

No surgical or drug treatment were used in this study but all incoming animals were visually checked for eardrum perforation due to otitis media and in addition, after completion of the study all subjects were submitted to a histological examination of the middle ear as a further control; but no animals demonstrated presence of infection.

4. RESULTS: Analyses of variance were carried out on the data for both activity and performance. Percent correct served as the basis for the analysis of performance among the trained subjects and average number of crossings among the yoked controls served as the basis for activity analysis.

Results of the performance ANOVAs indicate no significant differences between groups during the pre test day trial ($p > .05$). However there is a significant difference between groups during the test day trial ($p < .0002$). The data from the post-test period require clarification. Animals were tested one day post-test for comparison against pre-test performance as well as performance post-test. Although all control and low dose animals demonstrated no significant differences between groups, three of the five high dose subjects failed to perform at comparable levels. On day two post-test, however, these animals perform at the levels of other groups. If the data from day two post-test are included in the ANOVA on post-test performance there are no significant differences ($p < .09$). However if the data are analyzed using the first post-test day scores only, there is a significant ($p < .01$) difference among the three groups.

Subsequent to the analyses of variance a series of multiple t-tests were carried out on the performance data. As basis percent correct, percent incorrect (the subject ran when he should not have) and number of omissions (the subject failed to run at all) were used. Results using percent correct indicate that the differences demonstrated on test day lay between the high dose and the control ($p < .05$) and between the low dose and the control group ($p < .05$) but not between the high and low dose groups. Interestingly enough, differences become significant between the high group and the control group between 15 and 30 minutes into the test period but not between the low and control group until 30 to 45 minutes. Post-test (day one) analysis reveals significant ($p < .05$) differences between the high dose group and both low dose and control animals.

The analyses based upon incorrect responses showed no significant differences on the day before testing. On test day, however, a significant difference ($p < .05$) was demonstrated between the high dose and control groups beginning within the first 15-minute period. There were no post-test differences.

The final analyses based on omissions showed no pre-test differences, but revealed significant differences between both high dose and control groups and low dose and controls. No differences were found between experimental groups or for the post-test days.

No differences were found in activity level analyses.

5. DISCUSSION: The results demonstrate, not surprisingly, that thermal stress induced by RFR sufficient to raise body temperature $2^{o}C$ interferes to a significant degree with performance of an active avoidance

task. That thermal insult should depress learned performance in such a manner has been shown before (Galloway, 1947; Thomas, Finch, Fulk & Burch, 1974). The more interesting aspect of the results involves an indication that non-thermogenic RFR is capable of depressing performance levels as well. The statistical comparisons clearly demonstrate that this suppression in performance occurs only during, strongly suggesting that in some way RFR exposure can interrupt learned behavior even at low power levels (at least during the early stages of acquisition and at least in an active avoidance task).

Caution must be taken not to ignore the possibility that cues from the environment in the anechoic chamber plus the radiation itself might have influenced performance of experimental subjects in a way that the chamber alone without radiation did not influence the control animals. This can only be clarified fully in further studies, but the lack of effect of RFR on yoked controls' activity (if not performance) lends support to the original interpretation that RFR per se rather than a change in environmental cues depresses performance.

Therefore, whether the effect of radiation is direct (upon the neural process of retention, consolidation or recall) or indirect (interrupting the external or internal environment in a state-dependent learning situation) is crucial to the theoretical and biological aspects of the study but not to the practical outcome. The details can only be discovered in subsequent research.

It is, however, important not to underestimate the impact that these preliminary data have as an indication that there may be a period during early acquisition before a task has been learned completely wherein

performance can be significantly disrupted. The implications are clear. If further study supports this contention, perhaps personnel being trained to operate equipment which emits even non-thermogenic RFR should not be trained on the active equipment but on duplicates. When individual technical skills have reached criterion, personnel could then be transferred to their duty stations. Such a procedure might serve to increase effectiveness in an emergency situation involving inexperienced technicians. Had these persons been trained beyond the possible critical period for RFR interference before exposure to stress on the job perhaps performance could be expected to be better. Even a small improvement in the skill level which could be expected during crises might prove decisive as to final decision in training techniques.

REFERENCES:

1. Allnutt, M. F. Some behavioral manifestations of the effects of a multistress environment. Paper presented at the 4th International Symposium on Basic Environmental Probelms of Man in Space, Yveran, USSR, 1971.

2. Allnutt, M. F. and Allen, J. R. The effects of core temperature elevation and thermal sensation on performance. Ergonomics, 1973, 16, 189-196.

3. Azer, N. Z., McNail, P. E., and Leung, H. C. Effects of heat stress on performance. Ergonomics, 1972, 15, 681-691.

4. Bartlett, D. J. and Gronow, D. G. C. The effects of heat stress on mental performance. FRPC Report 846, Royal Air Force Institute of Aviation Medicine, London, England, August, 1953. AD 30-748.

5. Blockley, W. V. and Lyman, S. H. Studies of human tolerance for extreme heat. III. Mental performance under heat stress as indicated by addition and number checking test. AF Technical Report 6022, AMD, WPAFB, Ohio, October 1950.

6. Fox, R. H., Bradbury, P. A., Hampton, I.G.F., and Legg, C. F. Time judgment and body temperature. J. Experimental Psychology, 1967, 75, 88-98.

7. Crowley, D. E. Comments on Otitis Media in rats. J. of Auditory Res., 1972, 12, 125-128.

8. Dill, D. B., Adolph, E. F. and Wilber, C. G. (Eds.) Handbook of physiology: Adaptation to the environment, Vol. 4, Washington D.C.: American Physiological Society, 1964.

9. Gould, J. and Morgan, C. T. Auditory sensitivity in the rat. J. Comparative Psychology, 1942, 34, 321-329.

10. Guy, A. W. 1971 Analysis of electromagnetic fields induced in biological tissues by thermographic studies on equivalent phantom models. IEEE Trans. Microwave Theory Tech. MTT, 1971, 19, 205-214.

11. Herman, P. N. and Clock, T. D. Post-stimulatory shift of the Preyer reflex threshold in the white rat. J. Auditory Res., 1963, 3, 189-204.

12. Hudson, J. W. The role of water in the biology of the antelope ground squirrel Citellus lecurus. Univ. of Calif. Berkeley, Publications in Zoology, 1962, 64, 1-56.

13. Murphy, J. and Harris, J. D. Negligible effects of x-radiation of the head upon hearing in the rat. J. Auditory Res., 1961, 1, 117-132.

14. Newburgh, L. H. Physiology of head regulation and science of clothing. Philadelphia: W. B. Saunders Co., 1949.

15. Patton, R. A. Purlulent otitis media in albino rats susceptible to sound induced seizures. J. Psychology, 1947, 46, 64-75.

16. Price, G. R. The sensitivity of the rat ear reexamined through the cochlear microphonic. J. Auditory Res., 1970, 10, 340-348.

17. Schwan, H. P. Interaction of microwave and radiofrequency radiation with biological systems. IEEE Trans. Microwave Theory Tech. MTT, 1971, 19, 131-146.

18. Tyler, P. E. (Ed.). Biologic effects of nonionizing radiation. Ann. N.Y. Acad. Sci., 1975, 247.

19. Wang, G. H. The neural control of sweating. Madison, Wisconsin: Univ. of Wisconsin Press, 1964.

1976 USAF-ASEE SUMMER FACULTY RESEARCH PROGRAM
sponsored by
THE AIR FORCE OFFICE SCIENTIFIC RESEARCH
conducted by
AUBURN UNIVERSITY AND OHIO STATE UNIVERSITY

PARTICIPANT'S FINAL REPORT

TIME-RESOLVED FLUORESCENCE OF THE $a^3\Pi_o^+$ STATE OF BrCl

Prepared by:	John J. Wright, Ph.D.
Academic Rank:	Associate Professor
Department and University:	Department of Physics University of New Hampshire

Assignment:

(Air Force Base)	Kirtland AFB
(Laboratory)	Air Force Weapons Laboratory
(Division)	Advanced Laser Technology Div.
(Branch)	Chemical Laser Branch
USAF Research Colleague:	Capt Steven J. Davis, Ph.D.
Date:	August 13, 1976
Contract No.:	F44620-75-C-0031

TIME-RESOLVED FLUORESCENCE OF BROMINE MONOCHLORIDE

by

John J. Wright

ABSTRACT

Bromine monochloride is a potential candidate for a chemically pumped electronic transition laser. Two important parameters are the decay rate and quenching rates for various gases which may be present in the system. If the decay rate is greater than the chemical reaction rate, an inversion is unlikely, but if the decay rate is too small the system will lack sufficient gain.

This study was undertaken to determine the decay rate for the $a^3\Pi_o^+$ state of BrCl and quenching rates for BrCl, Cl_2, Br_2, He, and air. BrCl was produced by the equilibrium reaction $Br_2 + Cl_2 \rightleftarrows 2BrCl$. The $^3\Pi_o$ state was populated by an intense (100 KW) pulse from a tunable dye laser and the population as a function of time monitored by observing the fluorescence decay. Quenching rates were determined from plots of the decay rate as a function of gas pressure.

The decay rate for combined v' = o and v' = 1 levels of the $a^3\Pi_o^+$ state of BrCl is $5.4 \pm 1 \times 10^4$ sec^{-1} which corresponds to a lifetime of 18.5 ± 3 μsec. The quenching cross sections for BrCl, Cl_2, He, and air are 1×10^{-17} cm^2, 1×10^{-18}, 3×10^{-19} cm^2, and 8×10^{-18} cm^2, respectively.

INTRODUCTION:

Bromine monochloride, BrCl, is a potential candidate for an electronic transition chemically pumped laser. The excited $a^3\Pi_o^+$ state potential well is displaced from the $X^1\Sigma_g$ ground state,[1] as shown in Figure 1, so that a large population inversion is potentially possible, and BrCl can be chemically produced in the excited state[1] by the reaction $ClO_2 + Br \rightarrow BrCl + O_2$. Lastly, because of the spin forbidden nature of the $^3\Pi \rightarrow {}^1\Sigma$ transition, the decay rate of the $^3\Pi_o$ state should be less than the reaction rate, a necessary condition if an inversion is to be achieved in a chemical reaction. However, attempts to make a BrCl laser have so far been unsuccessful.[2]

One possible explanation for the failure of BrCl to lase would be too large a decay rate due either to a short lifetime, predissociation, or quenching. On the other hand, too small a radiative decay rate would prevent the system from having sufficient gain to lase since the gain is proportional to the radiative decay rate. This experiment was undertaken to determine the decay rate of the $^3\Pi_o$ state and quenching rates for various foreign gases.

A brief note about the notation is in order. The $^3\Pi_o^+$ state of BrCl has been labeled the A, B, and a states by various authors[1,3,4]

and so some confusion is apt to arise. We will use the designation $a^3\Pi_o^+$.

The experimental technique is conceptually simple: a sample cell containing BrCl is illuminated with a short pulse of laser light tuned to one of the absorption bands and the fluorescence from the excited state is monitored as a function of time to determine the effective lifetime, or decay rate. In order to study the system under controlled steady state conditions, BrCl was produced by the equilibrium reaction[5] $Br_2 + Cl_2 \rightleftarrows 2BrCl$ rather than the exothermic reaction involving ClO_2. Both Br_2 and Cl_2 have absorption bands in the wavelength range of BrCl and both have similar $^3\Pi_o \leftrightarrow {}^1\Sigma$ transitions.[6,7] Since Br_2 and Cl_2 would both be present along with BrCl, it is necessary to understand the time-resolved fluorescence of both Br_2 and Cl_2 before attacking the problem of BrCl. The decay rate for the $^3\Pi_o$ state of Br_2 in the gas phase has been previously measured[8,9] and found to be $\sim 10^6$/sec. The corresponding decay rate for Cl_2 has not been measured so our first task was to try to optically pump the $^3\Pi_o$ state of Cl_2. We were not successful at this attempt and could not observe Cl_2 fluorescence. This is not surprising since the transition is more highly forbidden than in the heavier molecule Br_2 and the Franck-Condon factors are extremely small because of the large shift between the potential wells.[10] Failure to observe Cl_2 fluorescence put us in good shape to look for BrCl fluorescence since we could now time resolve it from Cl_2 and Br_2.

Figure 1
Potential Curve for BrCl
(From Reference 1)

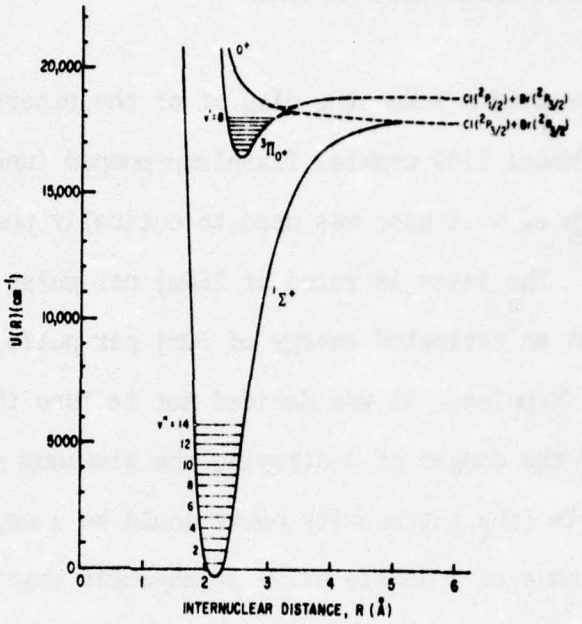
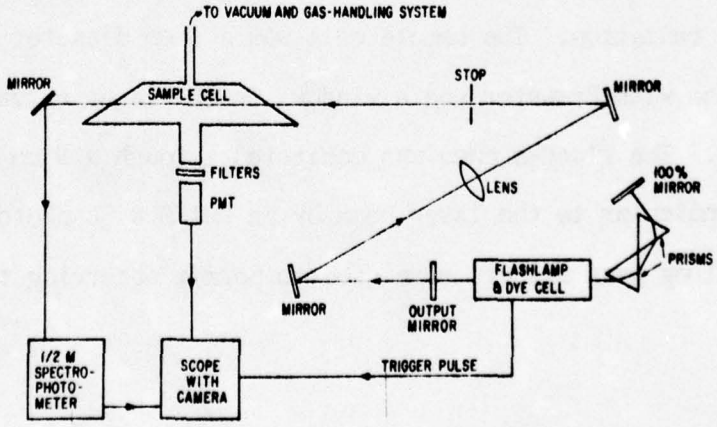


Figure 2
Block Diagram of
the Experimental
Setup



APPARATUS AND SAMPLE PREPARATION:

Figure 2 is a schematic diagram of the experimental arrangement. A Phase-R Model 1100 coaxial flashlamp-pumped tunable dye laser with a pulse width of $\sim$ .5 μsec was used to optically pump the molecules to the $^3\Pi_o$ state. The laser is rated at 250mj per pulse and was typically operated at an estimated energy of 50mj per pulse, which translates into about 100 KW/pulse. It was decided not to tune the laser with a grating because of the danger of destroying the aluminum substrate at such high power levels (the intracavity power could be a megawatt). The laser was tuned by means of a double prism arrangement which resulted in a line width of 5-10Å. The prisms were arranged so that the beam was incident on the surfaces at Brewster's angle to mimimize losses due to scattering. This resulted in a polarized laser beam. The beam was then spatially filtered by a stop and focused into the sample cell. After passing through the cell, the beam was scattered into a 1/2 meter Jarrell-Ash spectrophotometer in order to monitor the wavelength of the laser radiation. The sample cell was a 5 cm diameter Pyrex cylinder 60 cm long with Brewster angle windows on the laser entrance and exit ports. The fluorescence was monitored through a 5 cm diameter window perpendicular to the laser beam by an EMI 9684QB photomultiplier tube. Four long pass filters were used to permit observing the fluorescence

from 7000Å to 10,000Å while attenuating any scattered laser radiation below 7000Å. Each filter passed 90% of the fluorescence and attenuated the laser by 10^5. Therefore, only about 50% of the fluorescence was lost while attenuating the scattered light by 10^{20}. The transmission properties of the filters were verified by running a transmission spectrum on a Cary-14 recording spectrophotometer.

The output of the photomultiplier tube was put directly into a Tektronix 7603 oscilloscope with a 1 kΩ load resistor. The response time of the detection system was less than 100 nsec as determined by observing the response to scattered laser light. The signals were permanently recorded photographically, as shown in Figure 3, with an electronically triggered polaroid camera mounted on the oscilloscope. The fluorescence decay rate was determined from the photographs by plotting the signal amplitude as a function of time on semi-log paper as shown in Figure 3. The plots were all linear, verifying that the decay was exponential in time.

The bromine monochloride was produced by mixing Br_2 and Cl_2 gases according to the reaction

$$Br_2 + Cl_2 \rightleftarrows 2BrCl$$

with an equilibrium constant[11] K=8. Using the definition,

$$K = \frac{[BrCl]^2}{[Br_2][Cl_2]} ,$$

the equilibrium concentrations of Br_2, Cl_2, and BrCl could be determined. Table I lists the equilibrium percentages of Br_2, Cl_2, and BrCl for several initial ratios of Br_2 to Cl_2. Since the value for the equilibrium constant found in the literature varies from 6.5 to 8 at 298°K, the table shows the percentages for both. The difference is not significant, so the most recent value, K=8, was chosen throughout the experiment. The chlorine was research grade, 99.96% pure, used without further purification and the bromine was 99.96% pure and was doubly distilled on the vacuum system. Most gas mixtures were allowed to equilibriate over night.

TABLE I

Final Percentage of Total Gas Pressure for Br_2, Cl_2, and BrCl for Various Initial Ratios of Br_2 to Cl_2.

Initial Br_2:Cl_2	Final Percent of Br_2	Cl_2	BrCl	Equilibrium Constant, K
4:65	.18	88.6	11.2	8
	.22	88.6	11.2	6.5
8:65	.67	78.8	20.6	8
	.80	78.9	20.3	6.5
12:65	1.4	70.3	28.3	8
16:65	2.4	62.8	34.7	8
	2.8	63.3	33.9	6.5
24:65	4.8	50.8	44.3	8
32:65	7.7	41.7	50.6	8
	8.6	42.6	48.9	6.5
65:65	20.7	20.7	58.6	8
	22.0	22.0	56.0	6.5

Figure 3
Experimentally Observed Decay Curve with the Corresponding Semi-log Plot

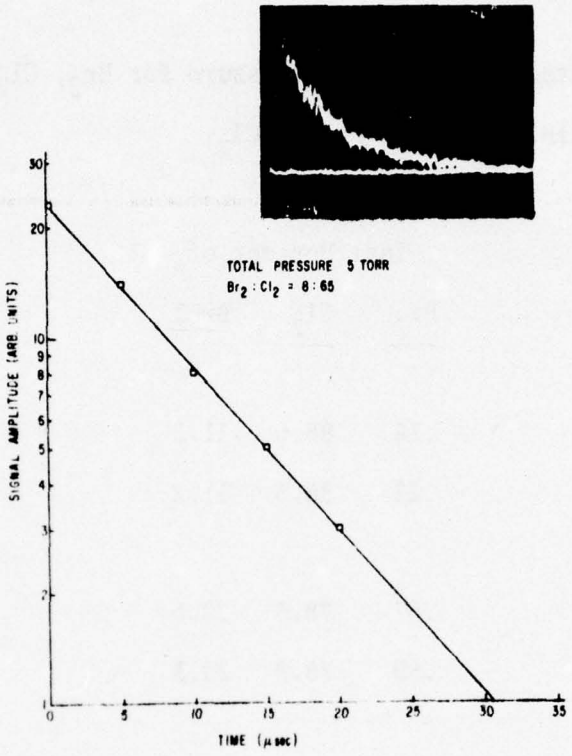
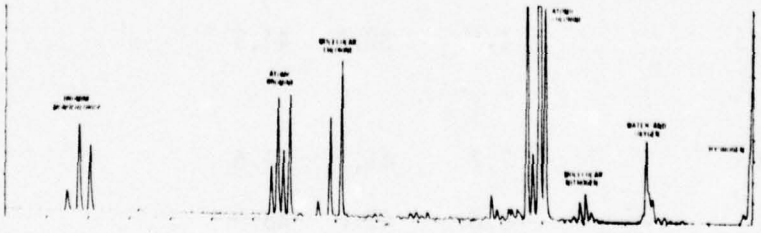


Figure 4
Mass Spectrograph of a Sample Cell Showing the Presence of BrCl



EXPERIMENT:

Because BrCl only exists in equilibrium with Cl_2 and Br_2, the experiment is inherently more complicated and "messier" than one involving a single species such as Br_2 or Cl_2. In other words, there always has to be an excess of either Cl_2 or Br_2 and both are always present to some extent, as shown in Table I. As an initial check to determine if we were actually producing BrCl, we ran a mass spectrograph on a sample mixture. The spectrograph proved the existence of BrCl in our sample cell, as shown in Figure 4. There are three BrCl peaks because there are two isotopes of bromine, ^{79}Br and ^{81}Br, and two isotopes of chlorine, ^{35}Cl and ^{37}Cl. This gives four different isotopes of BrCl; $^{79}Br^{35}Cl$, $^{79}Br^{37}Cl$, $^{81}Br^{35}Cl$, and $^{81}Br^{37}Cl$ with mass numbers of 114, 116, 116, and 118, respectively, or three different masses. The levels shown for contaminants such as N_2 and H_2O are only slightly above the background of the mass spectrometer, i.e., they are from the instrument not the sample.

With pure Cl_2 in our sample, we tuned the dye laser to several known absorption bands[7] and observed no fluorescence. Then, with pure Br_2 in the sample, we observed fluorescence which extended over the entire wavelength range of Rhodamine 6 G dye (5700-6100Å) and had a decay rate $\leq$ 1 μsec. In fact, the fluorescence was almost triangular in shape as a function of time with a full width at half maximum amplitude (FWHM) of 1 μsec. The Br_2 fluorescence line shape was almost identical

to the exciting laser pulse shape, confirming that the Br_2 observed lifetime is $\leq$ 1 μsec. When Br_2 was added to Cl_2, or vice versa, the signal character changed. The narrow Br_2 fluorescence became broadened in time with a long exponential tail. This was attributed to the presence of BrCl. The amplitude of the long exponental signal was about 20 times smaller than the short Br_2 signal at equal pressure.

There were three possibilities: BrCl emission, Cl_2 emission due to exchange collisions with excited Br_2, or Br_2 emission from the low lying and long-lived[12] $A^3\Pi_1$ state due to collisional mixing of the excited $B^3\Pi_o$ state.

We attempted to measure the wavelengths of this emission in order to identify it as due to BrCl, the BrCl emission spectrum being known.[1,4] First, we scanned a 1/4 meter Jarrell-Ash spectrophotometer but observed nothing. (Bear in mind, the time resolved fluorescence observed was with a 5 cm diameter photomultiplier tube and cut off filters so we were looking at orders of magnitude more light than with the spectrophotometer.) Next, we tried a prism spectrograph and exposed the film for 300 seconds, or 300 laser shots. (The maximum rep rate was one shot per second.) We observed nothing.

The dissociation limits of BrCl, Br_2, and Cl_2 are 5440Å, 5108Å, and 4780Å, respectively.[3,13] If the observed emission was due to optically pumped BrCl, it should not be observed for excitation wavelengths less than 5440Å. But, if the fluorescence were due to optically

pumped Br_2 for some reason, it would still be observable for wavelengths between the dissociation limits of Br_2 and BrCl. Kodak 522 dye, which lases over the range 5000Å-5400Å, was used for this investigation. What was observed were sharp short Br_2 resonances but no long-lived tail. Therefore, it seemed evident the long-lived emission was due to optically pumped BrCl.

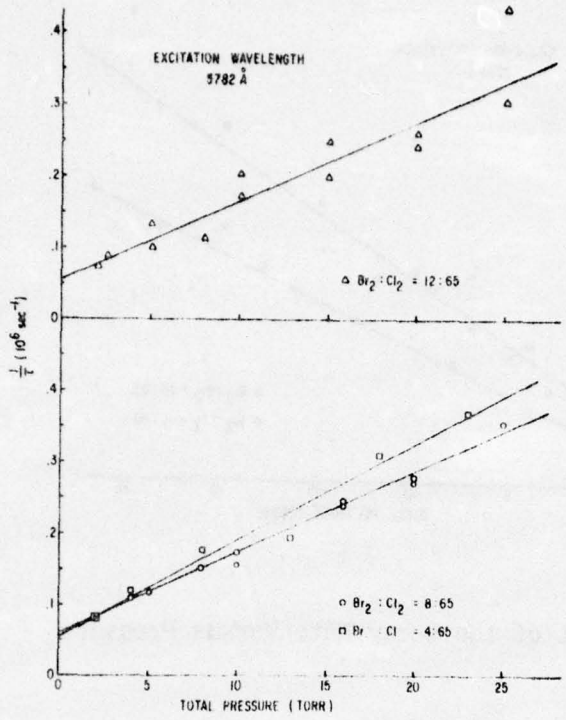
Typically, two mixes of Br_2 and Cl_2 were prepared late in the afternoon and allowed to equilibriate overnight. There was evidence, however, that this procedure was not necessary and that two hours were sufficient at pressures of 100-300 Torr for the system to equilibriate. Data was then taken, in the form of photographs, as a function of total gas pressure. Figures 5, 6, and 7 are Stern-Volmer[14] plots of the observed decay rate as a function of total gas pressure for various ratios of Br_2 to Cl_2. The excitation wavelength, 5782Å, corresponds to pumping the transition $X^1\Sigma(v''=2) \rightarrow a^2\Pi_o(v'=8)$. As the Br_2 to Cl_2 ratio increases, there is an increasing excess of Br_2 and apparently more quenching since the slopes of the curves also increase. The zero pressure intercept is the decay rate for the unperturbed molecule. The smaller the quenching, or the smaller the slope, the more accurate the intercept can be determined. For this reason, the intercept was taken as the average for the five curves with the lowest Br_2 to Cl_2 ratio. Table II summarizes the data for these five curves. The values for the slope and intercept were determined from a linear least squares fit to the data.

TABLE II

Zero Pressure Intercept and Slope for Various Mixes of Br_2 and Cl_2 at Various Excitation Wavelengths

Br_2:Cl_2	Intercept ($x10^4 sec^{-1}$)	Slope($x10^4 sec^{-1} Torr^{-1}$)	Excitation Wavelength(Å)
4:65	5.7	1.3	5782
8:65	6.0	1.1	5782
12:65	5.7	1.1	5782
16:65	5.0	1.2	5782
24:65	4.7	1.1	5782
4:65	5.4	0.9	5878
8:65	4.7	1.1	5878
8:65	5.4	0.9	6069

Figure 5
A Plot of the Observed Decay Rate Versus Pressure



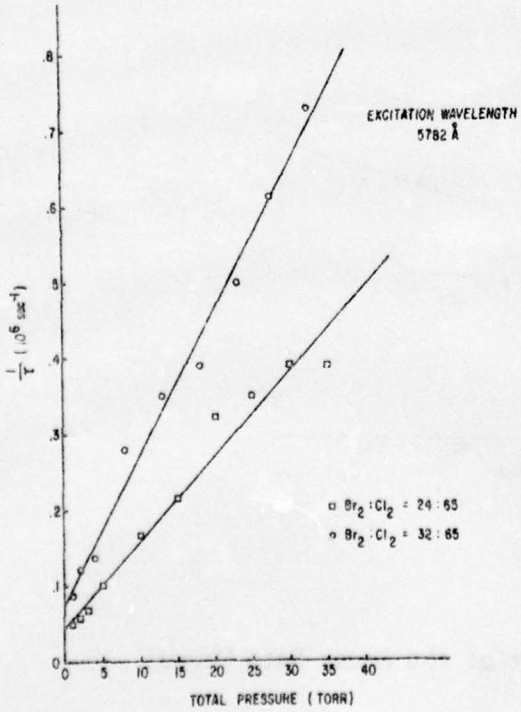


Figure 6
A Plot of the Observed Decay Rate Versus Pressure

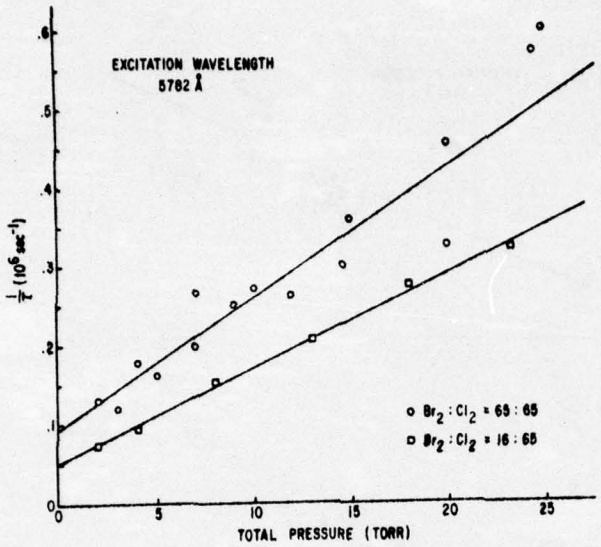


Figure 7 A Plot of the Decay Rate Versus Pressure

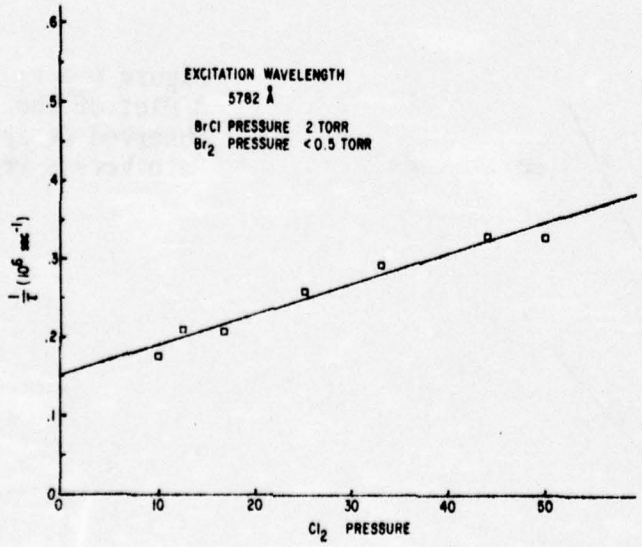


Figure 8 A Stern-Volmer Plot of the Decay Rate Versus Cl_2 Pressure

A straight average of the zero pressure intercepts gives a decay rate of $5.4 \pm .6 \times 10^4 sec^{-1}$ which corresponds to lifetime of 18.5 ± 3 μsec.

In order to determine the quenching rate for Cl_2 gas, several mixtures were made where the BrCl pressure was a constant 2 Torr (assuming equilibrium constant K=8) while varying the Cl_2 pressure and keeping the Br_2 pressure less than 0.05 Torr. Figure 8 is a Stern-Volmer plot of the decay rate as a function of Cl_2 pressure for constant BrCl pressure. The Stern-Volmer plot can be represented by the equation

$$\frac{1}{\tau} = \frac{1}{\tau_o} + \sigma_{Cl_2} (8\Pi/\mu kT)^{1/2} P_{Cl_2} ,$$

where $\frac{1}{\tau_o}$ is the decay rate at zero Cl_2 pressure (but 2 Torr BrCl pressure), σ_{Cl_2} is the cross section for Cl_2 quenching, μ is the BrCl-Cl_2 reduced mass, and P_{Cl_2} is the Cl_2 gas pressure. From the slope, $.4 \times 10^4 sec^{-1}$ $Torr^{-1}$, σ_{Cl_2} is found to be $1 \pm .25 \times 10^{-18} cm^2$. The intercept, 15.2×10^4 sec^{-1}, is the quenching rate for zero Cl_2 pressure and 2 Torr of BrCl. Previous data gave an intercept of $5.4 \times 10^4 sec^{-1}$ at zero total gas pressure. The difference, $9.8 \times 10^4 sec^{-1}$, divided by 2 Torr gives a self quenching rate for BrCl of $4.9 \times 10^4 sec^{-1} Torr^{-1}$. This translates into a self quenching cross section σBrCl of $1.5 \times 10^{-17} cm^2$. The self quenching cross section is about 15 times larger than the Cl_2

quenching cross section. Assuming the rates for Cl_2 and BrCl were now determined, we tried to determine the Br_2 quenching rate from the slopes for the various mixes, i.e., the slopes in Figures 4, 5, and 6. All of the slopes (except the 4:65 mix) including the larger ratios of 24:65, 32:65, and 65:65 are consistent with an assignment of a self quenching cross section $\sigma BrCl = 1 \pm 0.5 \times 10^{-17} cm^2$ and both Cl_2 and Br_2 quenching cross sections an order of magnitude smaller. However, a cross section for Br_2 could not be determined.

All of the preceding data was at an excitation wavelength of 5782Å. To check for a wavelength dependence of the decay rate, we changed the excitation to 5878Å which pumps the v''=2 → v'=6 band of BrCl. Figure 9 compares the slope and intercept to that obtained at 5782Å. The intercept is the same as at 5782Å within the assigned error. Two more data runs were made (but not shown in the figure) and the intercept was exactly the average of all data at 5782Å. The laser was then tuned to 6069Å to pump the v''=2 → v'=3 band. As shown in Figure 9, this data was also consistent with previous data. The failure of the decay rate to vary with excitation wavelength is consistent with the assumption that the $a^3\Pi_o$ vibrational levels are thermalized at the pressures used (1-50 Torr) and that the fluorescence is principally from the v'=0 and v'=1 levels. (That this is the case will be shown later.)

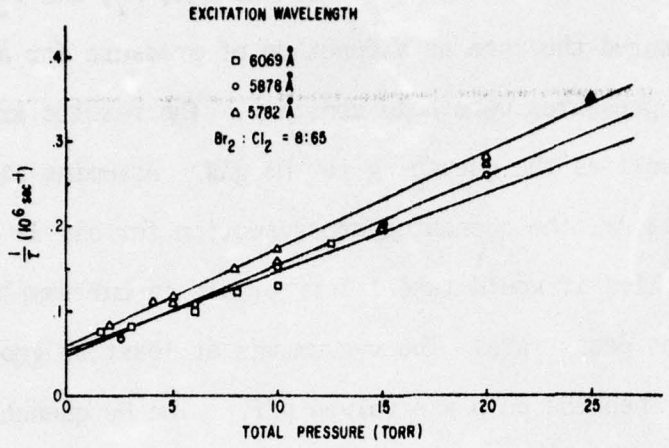


Figure 9 The Decay Rate Versus Pressure for Various Excitation Wavelengths

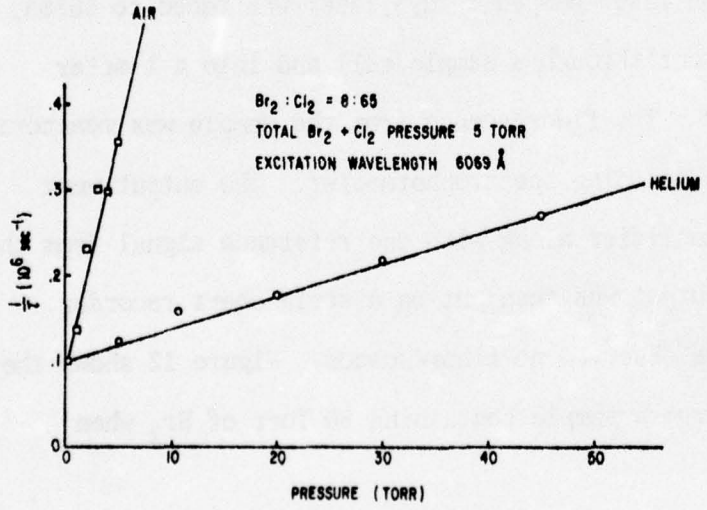


Figure 10 A Stern-Volmer Plot of the Decay Rate Versus Pressure for He and Air

To determine the effect of contaminants such as H_2O, N_2, and O_2, on the decay rate, we measured the rate as a function of pressure for air. The Br_2, Cl_2, and BrCl pressures were held constant. The results are shown in Figure 10 as well as the quenching for He gas. Assuming air to be 78% N_2, 21% O_2 and 1% Ar, the quenching cross section for air is $8 \times 10^{-18} cm^2$. This implies it would take 1 Torr of air in our sample to significantly effect the decay rate. The vacuum was at least as good as 10^{-2} Torr at all times when the pump was valved off. The He quenching cross section (σ_{He}) is $3 \times 10^{-19} cm^2$.

An auxillary experiment was done to verify that we were actually optically pumping BrCl, that the excited state vibrational levels were thermalized, and that there was no emission from Cl_2 or the long-lived $A^3\Pi_1$ state of Br_2. A schematic diagram of the apparatus is shown in Figure 11. An argon ion laser pumped cw dye laser was tuned to 5878Å, the beam was chopped, sent through a sample cell and into a 1 meter McPherson monochromator. The fluorescence from the sample was monitored by a .3 meter McPherson scanning spectrophotometer. The output went into a P.A.R. lock-in amplifier along with the reference signal from the chopper. The lock-in output was then put on a strip chart recorder. With 500 Torr of Cl_2, we observed no fluorescence. Figure 12 shows the fluorescence observed from a sample containing 50 Torr of Br_2 when

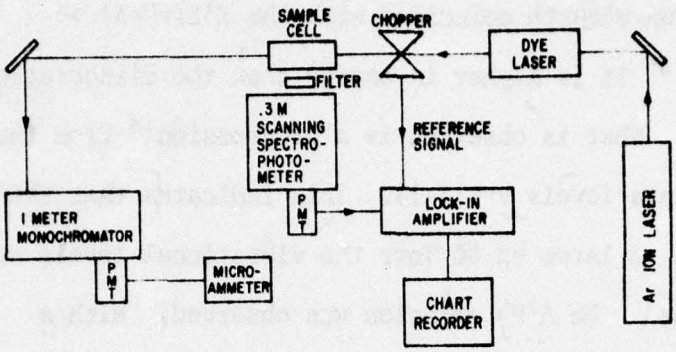


Figure 11 A Schematic Diagram of the Experimental Setup for Observing the Fluorescence Spectrum

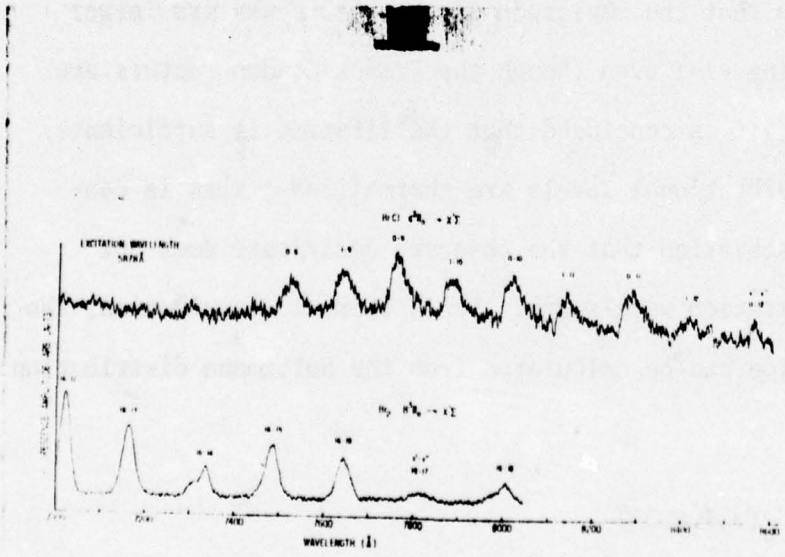


Figure 12 The Fluorescence Spectrum of Br_2 and BrCl With an Excitation at 5878Å

excited at 5878Å. This wavelength coincides with the $X^1\Sigma(v''=3) \rightarrow B^3\Pi_o(v'=16)$ transition.[15] It is higher in energy than the dissociation limit of the $A^3\Pi_1$ state. What is observed is a progression[15] from the v'=16 level to ground state levels v''=13-18. This indicates that the $B^3\Pi_o$ state decay rate is so large at 50 Torr the vibrational levels are not completely thermalized. No $A^3\Pi_1$ emission was observed. With a sample containing a 4:65 mix of Br_2 and Cl_2 at a total pressure of 276 Torr ($\sim$ 244 Torr Cl_2, 31 Torr BrCl, and .5 Torr Br_2) we observed the spectrum shown in Figure 12. The laser was still tuned to 5878Å, corresponding to pumping the v''=2 → v'=6 band of BrCl, but the emission shows progressions from v'=0 and v'=1. There are several emission lines[4] from the v'=2 and v'=3 levels which lie in the spectral range 7000-8600Å but do not appear even though they have larger Franck-Condon factors.[3] Note also that the amplitude of the v'=0 peaks are larger than the corresponding v'=1 even though the Franck-Condon factors are smaller. Therefore, it is concluded that the lifetime is sufficiently long that the $a^3\Pi_o$ vibrational levels are thermalized. This is consistent with the observation that the observed decay rate does not depend upon the excitation wavelength. For a thermal distribution, the vibrational population can be calculated from the Boltzmann distribution:[13]

$$N_v \simeq N\, e^{-G_o(v)/.6952T},$$

where $G_o(v)$ is the vibrational energy of the vth level and T is the temperature in °K. This results in 68% of the molecules in the v'=0 level with 24% and 8% in v'=1 and v'=2 levels, respectively.

The BrCl emission spectrum shown in Figure 12 is also free of Br_2 emission (and Cl_2) which is further evidence that with the pulsed laser measurements of the decay rate we were actually observing BrCl fluorescence.

SUMMARY AND CONCLUSIONS:

In summary, we have measured the combined lifetime of the v'=0 and v'=1 vibrational levels of the $a^3\Pi_o$ state of BrCl and obtained a value of 18.5 ± 3 μsec. The quenching rates for Cl_2, BrCl, He, and air are 4 x $10^3 sec^{-1}$-$Torr^{-1}$, 3.3 x $10^4 sec^{-1}$-$Torr^{-1}$, 3.8 x $10^3 sec^{-1}$-$Torr^{-1}$, and 5.3 x $10^4 sec^{-1}$-$Torr^{-1}$, respectively. In terms of cross sections, these are 1 x $10^{-18} cm^2$, 1 x $10^{-17} cm^2$, 3 x $10^{-19} cm^2$, and 8 x $10^{-18} cm^2$, respectively. The Br_2 quenching rate is small, on the order of the Cl_2 rate.

In conclusion, this experiment does not explain the failure of BrCl to lase. The decay rate is not short compared to chemical reaction rates and the quenching rates are relatively small. This does not preclude that the radiative lifetime is longer than the observed lifetime, in which case the gain of the system could be insufficient for lasing.

AKNOWLEDGEMENTS:

The author is indebted to the entire staff of the Space Laser Technology Section of the Chemical Laser Branch of the Advanced Laser Technology Division of the Air Force Weapons Laboratory for providing a cordial and helpful work environment. I am especially grateful to Capt S. Davis and Major D. Olson for providing equipment, facilities, and technical assistance. This project would not have been possible without the very dedicated and able assistance of Mr. Waldo Spates.

REFERENCES

1. M.A.A. Clyne and J.A. Coxon, Proc. R. Soc. A. 298, 424 (1967).
2. B.D. Guenther, W.S. Spates, and S.G. Hadley, Laser Digest, AFWL-TR-75-229, AFWL, Kirtland AFB, Oct 1975 (Pg 277).
3. J.A. Coxon, J. Mol. Spectrosc. 37, 39(1971); ibid 50, 142(1974).
4. S.G. Hadley, M.J. Bina, and G.D. Brabson, J. Chem. Phys. 78, 1833(1974).
5. J. Olbregts, Intern. J. of Chem. Kinetics, 6, 395(1974).
6. J.A. Horsley and R.F. Barrow, Trans. Faraday Soc. 63, 32(1967).
7. A.E. Douglas, C.K. Moeller, and B.P. Stoicheff, Can. J. Phys. 41, 1174(1963).
8. G. Capelle, K. Sakurai, and H.P. Broida, J. Chem. Phys. 54, 1728 (1971).
9. K.B. McAfee and R.S. Hozack, J. Chem. Phys. 64, 2491(1976).
10. S.N. Suchard, "Spectroscopic Data", New York, Plenum, 1976.
11. M.A.A. Clyne, P.B. Monkhouse, and L.W. Townsend, Int. J. Chem. Kinetics 8, 425(1976).
12. J.A. Coxon, J. Mole. Spectrosc. 41, 566(1972).
13. G. Herzberg, "Molecular Spectra and Molecular Structure" 1, 2nd ed. New York, Van Nostrand, 1950.
14. O. Stern and M. Volmer, Z. Physik 20, 183(1919).
15. J.A. Coxon, JQSRT 12, 639(1972).

1976 USAF-ASEE SUMMER FACULTY RESEARCH PROGRAM
sponsored by
THE AIR FORCE OFFICE SCIENTIFIC RESEARCH
conducted by
AUBURN UNIVERSITY AND OHIO STATE UNIVERSITY

PARTICIPANT'S FINAL REPORT

DYNAMIC RESPONSE OF AN ABOVEGROUND ARCH SUBJECTED TO A BLAST LOAD

Prepared by:	David Y. L. Wang
Academic Rank:	Associate Professor
Department and University:	Department of Civil Engineering University of Wisconsin - Platteville
Assignment:	
(Air Force Base) (Laboratory) (Division) (Branch)	Kirtland Air Force Base Air Force Weapons Laboratory Civil Engineering Research Division Survivability Branch
USAF Research Colleague:	M. A. Plamondon, PhD
Date:	13 August 1976
Contract No:	F44620-75-C-0031

DYNAMIC RESPONSE OF AN ARCH SUBJECTED TO A BLAST LOAD

by
David Wang

ABSTRACT

The response of an arch subjected to a blast load, currently, is assumed to be caused by a symmetrical, uniform, radial pressure corresponding to a "breathing mode" and an antisymmetrical, uniform, radial pressure corresponding to a "flexural mode" (1), (2)*. The analysis of arches based on the above assumption is approximate in nature because contributions to the arch responses due to the higher vibrational modes are neglected.

The "exact analysis" of the arch responses can be achieved by using the finite-element method. The arch is approximated by using a large number of bar-elements such that an accurate result is assured. Because of the complexity of the problem, the cost of the computing time in obtaining the exact analysis through the finite element approach is usually high and for many preliminary estimates is not required. Therefore, a simple, yet reliable simplified procedure for obtaining accurate information to determine the response of arches under blast loading needs to be formulated.

The arch, in this study, is converted to a lumped mass multidegrees of freedom system. Its responses are to be obtained by the method of "modal analysis," in which the responses in the normal modes are determined separately, and then superimposed to provide the total response. Results from this study indicate that, by selecting appropriate normal modes involved in the analysis, generally two or three at the most, an accurate arch response can be obtained.

*Numbers in the parenthesis refer to the references at the back of this report.

ACKNOWLEDGMENT

This work was sponsored by the Air Force Scientific Research Office and ASEE. The writer is grateful for their support of this summer research. The writer also wishes to express his appreciation to Mr. Fred O'Brien, Jr. of Auburn University and Dr. A. Gunther, Chief Scientist of AFWL, Kirtland Air Force Base. Their excellent administration of this project and cooperation during the course of this research has made this summer very enjoyable.

The association with Dr. M. A. Plamondon during this research has been a gratifying experience both professionally and personally. His suggestion of the project and various discussions that the writer had with him during this summer were mostly appreciated. Thanks are also due to Lt Col F. Leech, Lt Col J. Warren, and Capt J. Choate for their help and to Ms. Linda Howden who typed this report.

LIST OF FIGURES

1. Finite Element and Lumped Mass Model of the Arch
2. Modal Shapes and Its Responses for the First and the Fifth Modes
3. Modal Shapes of the Other Eight Modes
4. Comparisons of Displacements at Node 3
5. Comparisons of Moment at Node 2
6. Thrust in Element 2, Finite-Element Method
7. Comparisons of Thrust in Element 2
8. Comparisons of Thrust in Element 2
9. Shapes and Strain Energy Distributions of Normal Modes of the Arch

LIST OF TABLES

1. Pressure-Time History at the Nodes of the Blast Load

NOMENCLATURE

A	amplitude of displacement
d	nodal displacement
F	external nodal force
I	number of lumped mass
J	number of normal modes
K	number of components of the nodal displacement
[K]	stiffness matrix
[M]	mass matrix
S	stiffness of the element
R	modal response (internal forces) of free vibration
W_e	work by external forces
ϕ	amplitude ratio of nodal displacement
ω	angular frequencies of free vibration

SUBSCRIPTS

i	the ith lumped mass
j	the jth normal mode
k	the kth component of the nodal displacement

INTRODUCTION

The behavior of arches when subjected to a blast load is a complex phenomenon. The loading is difficult to determine with respect to spatial distributions and with respect to time variations. The arch responses (displacements, internal forces, and stresses) due to the blast load are also more complicated than other types of structural elements, such as beams and frames because of the curvature of its mid-plane. Exact methods such as finite-element method are possible but they are not always practical for rapid design or analysis purposes.

To simplify the effort of acquiring the arch responses, the "modal analysis" method is adopted here in this study. The arch is converted to an equivalent multidegree of freedom system with masses and external loads concentrated at the nodes. Modal equations are derived from the Lagrange's equation and they are solved numerically for each individual mode. Natural frequencies are obtained by forming a separate eignevalue problem or they can be approximated by equations established by Velestsos (3) and Wolf (4). The normalized modal shape and its corresponding modal responses at the nodes and within the element are obtained once the nodal displacement, natural frequencies, geometrical and material properties of the arch are given. The total response of the arch is then obtained by superimposing selected individual modal responses with the consideration of the nature of these individual modes.

SYSTEM AND GOVERNING EQUATIONS

A semi-circular hinged arch is modeled by six straight bar elements of equal length (figure 1). An eight bar elements model improves the results by only 1.5% while the effort in computation is increased considerably. Using the usual assumptions about the free vibration of an elastic system, the governing equation

$$[K]\{d\} = \omega^2 [M]\{d\} \qquad (1)$$

is obtained, in which [K] and [M] are stiffness and mass matrices; {d}, the nodal displacement; and ω is the natural frequency of free vibration. The modal equations are derived following the Lagrange equation (1) in which

$$\text{K. E.} = \sum_{i}^{I} 1/2\, M_i \sum_{j=1}^{J} A_j^{.2} \sum_{k=1}^{K} \phi_{ijk}^2$$

$$\text{P. E.} = \sum_{i=1}^{I} 1/2\, S_i \sum_{j=1}^{J} A_j^2 \sum_{k=1}^{K} \phi_{\Delta ijk}^2$$

$$W_e = \sum_{i=1}^{I} \sum_{j=1}^{J} A_j \sum_{k=1}^{K} F_{ik}\, \phi_{ijk}$$

where

A is the amplitude of displacement of an arbitrarily chosen mass

S is the stiffness of the elements

F is the external nodal force

I is the number of lumped mass

J is the number of normal modes

K is the number of nodal idsplacement components

ϕ_{ijk} is the amplitude ratio of nodal displacement with respect to A of the ith mass, j^{th} mode in the kth displacement component

After appropriate differentiations, modal equations

$$\ddot{A}_j + \omega_j^2 A_j = \frac{\sum_{i=1}^{I} \sum_{k=1}^{K} F_{ik}\, \phi_{ijk}}{\sum_{i=1}^{I} M_i \sum_{k=1}^{K} \phi_{ijk}^2} \qquad (2)$$

$$j = 1, 2, - - - -, J$$

are obtained. The numerator and denominator of the right side in equation (2) are generalized force and generalized mass of the equivalent system, respectively.

Equation (1) is solved by the finite element method using the "Nastran" program (5) and a CDC 7600 digital computer and equation (2) is solved numerically by Newmark's "Beta" method (1).

The material of the arch has the following properties:

$E = 3 \times 10^{10}$ P_a, Poisson's ratio = 0.15

mass density = 2.5×10^3 $\frac{kg}{m^3}$

The blast load which advances in a direction normal to the arch longitudinal axis and parallel to its base was obtained analytically. Its pressure-time history is listed in Table 1 and is obtained by a piecewise linear approximation.

RESULTS AND ITS ANALYSIS

For the given geometrical and material properties of the arch, modal shapes and their responses of free vibration of the ten modes computed from Equation (1) are shown in figures (2) and (3). A "direct transient" solution using all the normal modes as generalized coordinates and a "modal transient" solution using individual normal mode as generalized coordinates are also obtained. They are obtained by using the "Nastran" Program with the finite element approach in order to compare with results computed from Equation (2) of the equivalent multidegree system of the same load. The comparisons are made to prove or disprove the simple approach. The comparisons of the response history between these two different approaches are shown in figure 4 through figure 8 at selected nodes and bar elements. The response of the arch from the equivalent system can be computed by using the following expressions:

$$d_{ik} = \sum_{j=1}^{J} A_j \phi_{ijk} \text{ - - - (displacement)}$$

$$R_i = \sum_{j=1}^{J} A_j R_{ij} \text{ - - - (moment, shear, and thrust)} \qquad (3)$$

in which R_{ij} denotes the modal response of free vibration at node i due to the jth mode (6). The Summation covers the selected relevant modes.

The selection of appropriate normal modes in computing the responses depends a great deal on the nature of the normal modes. Normal modes, whether it be symmetrical or antisymmetrical, may be predominately flexural, predominately extensional, or the combination of both, depending on the proportion of flexural and extensional energy present in a given mode. This proportion of energy, in turn, changes with the slenderness ratio of the arch. A qualitative description of the energy proportion in a given normal mode is shown in figure 9. The vibrational modes are entirely extensional in the middle portions of the diagonal lines of the curves and entirely flexural along the horizontal segments. In the regions where the diagonal lines approaching the horizontal segments, the proportion is approximately 50-50. The displacement at nodes can be obtained by using the 1st mode only while moments at nodes should be calculated by including the first two flexural modes as indicated in figures 4 and 5. To compute the thrust within the element, 1st mode and 5th mode (breathing mode which is approximately 50% extensional from figure 9) together will approximate it to

within 20% of the exact solution at the peak loading as indicated in figure 7. Improved results can be achieved by, including in the computation, the lowest predominate extensional mode, which is the 6th mode in this particular arch. Figure 8 shows that the improved result of thrust almost matches that of the exact solution at the peak loading. Higher extensional normal modes will not improve the result further in the approximation because of its small amplitude.

CONCLUSIONS

Design of aboveground arches subjected to a blast load can be simplified by converting the structure to an equivalent multidegree system. Modal responses of free arch vibrational modes can be obtained by forming a separate eigenvalue problem. Superimposing the modal response, computed as indicated by Equation 3, for selected appropriate individual modes, will yield vital information required in the design of arches subjected to a blast load.

REFERENCES

1. Crawford, R.E., Higgins, C.J., and Bultmann, E.H., "The Air Force Manual for Design and Analysis of Hardened Structures," Civil Nuclear Systems Corporation, October 1974

2. Biggs, J. M., "Introduction to Structural Dynamics," McGraw-Hill, 1964

3. Veletsos, A.S., Austin, W.J., Pereira, C.A.L., and Wung, S.J., "Free In-Plane Vibration of Circular Arches," Journal of the Engineering Mechanics Division, ASCE, EM2, April 1972

4. Wolf, F.A., "Natural Frequencies of Circular Arches," Journal of the Engineering Mechanics Division, ASCE, ST9, Sep 1971

5. McCormick, C.W., Editor, "The Nastran User's Manual," NASA SP-222(01), COSMIC, University of Georgia, Athens, Georgia, May 1973

6. Hurty, W., Rubinstein, M. F., "Dynamics of Structures," Prentice-Hall, Inc., 1964

7. Abel, J. F., and Desai, C. S., "Introduction to the Finite-Element Method," Von Nostrand Reinhold Company, 1972

8. Thomson, W.T., "Theory of Vibration with Applications," Prentice-Hall, Inc., 1972

TABLE 1

PRESSURE-TIME HISTORY OF THE BLAST LOAD*

NODE 1					
Time	0	0.00525	0.0144	0.0275	0.0375
Pressure	0	8.276	5.345	3.103	1.897
Time	0.0475	0.152			
Pressure	1.138	0			
NODE 2					
Time	0.0005	0.006	0.0175	0.0275	0.0375
Pressure	0	7.586	4.276	2.62	1.672
Time	0.0475	0.153			
Pressure	0.966	0			
NODE 3					
Time	0.001	0.00675	0.0175	0.0275	0.0375
Pressure	0	4.565	2.235	1.304	0.635
Time	0.0475	0.153			
Pressure	0.226	0			
NODE 4					
Time	0.004	0.00625	0.0175	0.0275	0.0375
Pressure	0	2.47	0.609	0.157	-0.339
Time	0.0475	0.156			
Pressure	-0.513	0.0			
NODE 5					
Time	0.00625	0.00894	0.0125	0.0175	0.0275
Pressure	0	1.597	0.276	-0.241	-0.534
Time	0.0375	0.0494	0.0515	0.158	
Pressure	0.438	0.438	0.621	0	
NODE 6					
Time	0.00834	0.0108	0.0125	0.0181	0.0213
Pressure	0	1.103	0.441	-0.262	0.441
Time	0.0225	0.0259	0.0338	0.0415	0.0515
Pressure	1.138	0.569	0.079	0.534	0.947
Time	0.160				
Pressure	0				

*1. Time is in seconds and pressure is in Pascals x 10^5.
2. Initial time is when the shock front reaches the base (NODE 1) on the windward side of the arch.

TABLE 1 (cont'd)

PRESSURE-TIME HISTORY OF THE BLAST LOAD*

NODE 7

Time	0.01	0.0173	0.025	0.0391	0.0515
Pressure	0	2.87	1.461	0.365	1.113
Time	0.162				
Pressure	0				

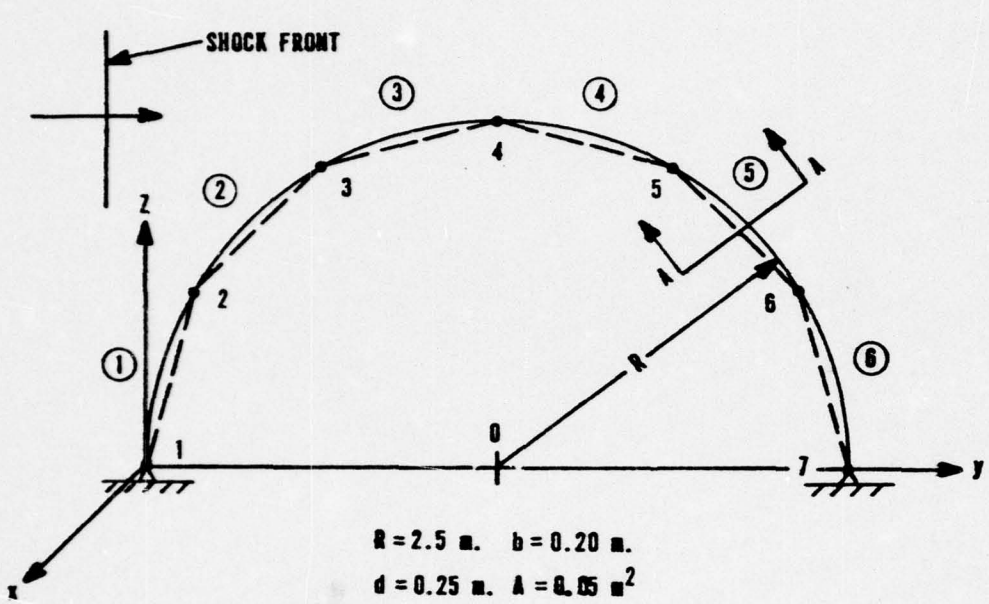


Figure 1. Model of the Arch

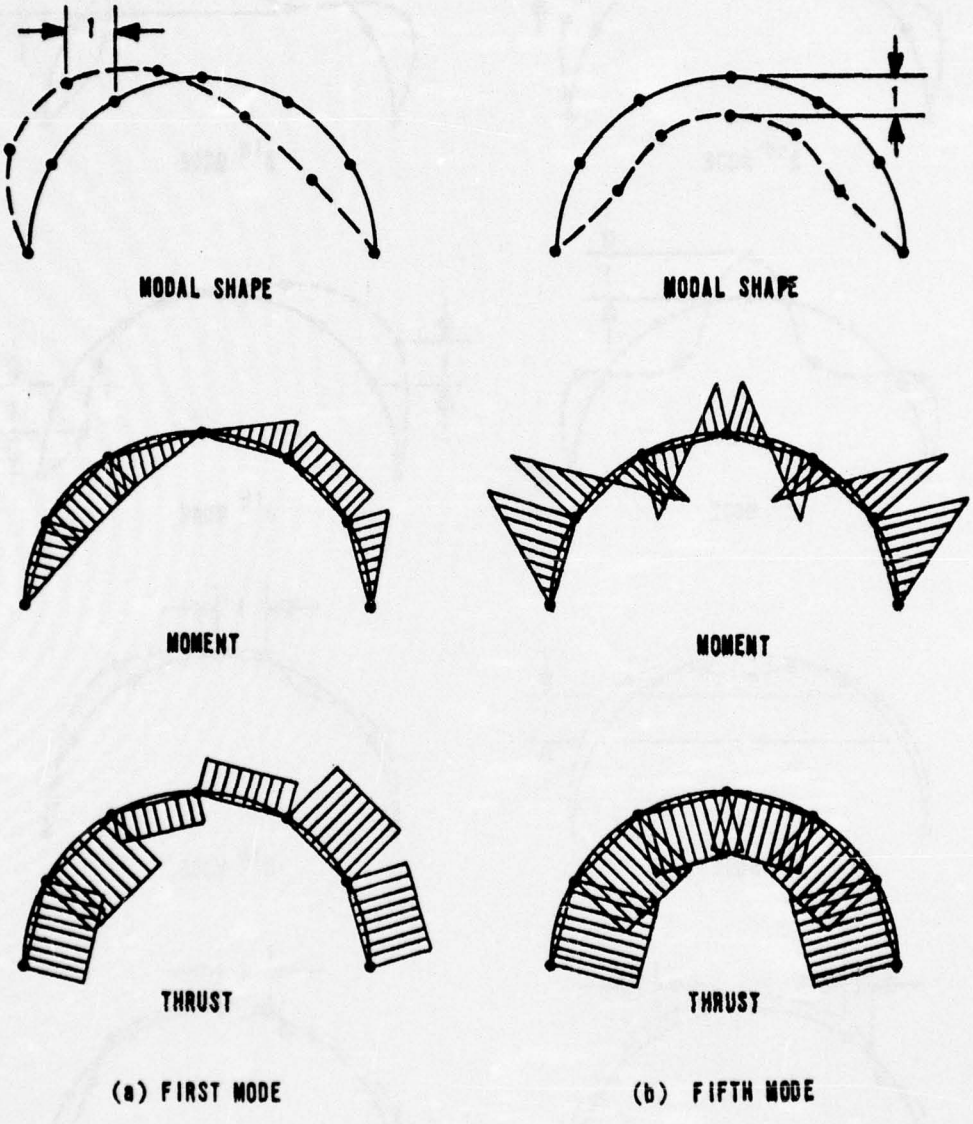


Figure 2. Typical Modal Shapes and Responses

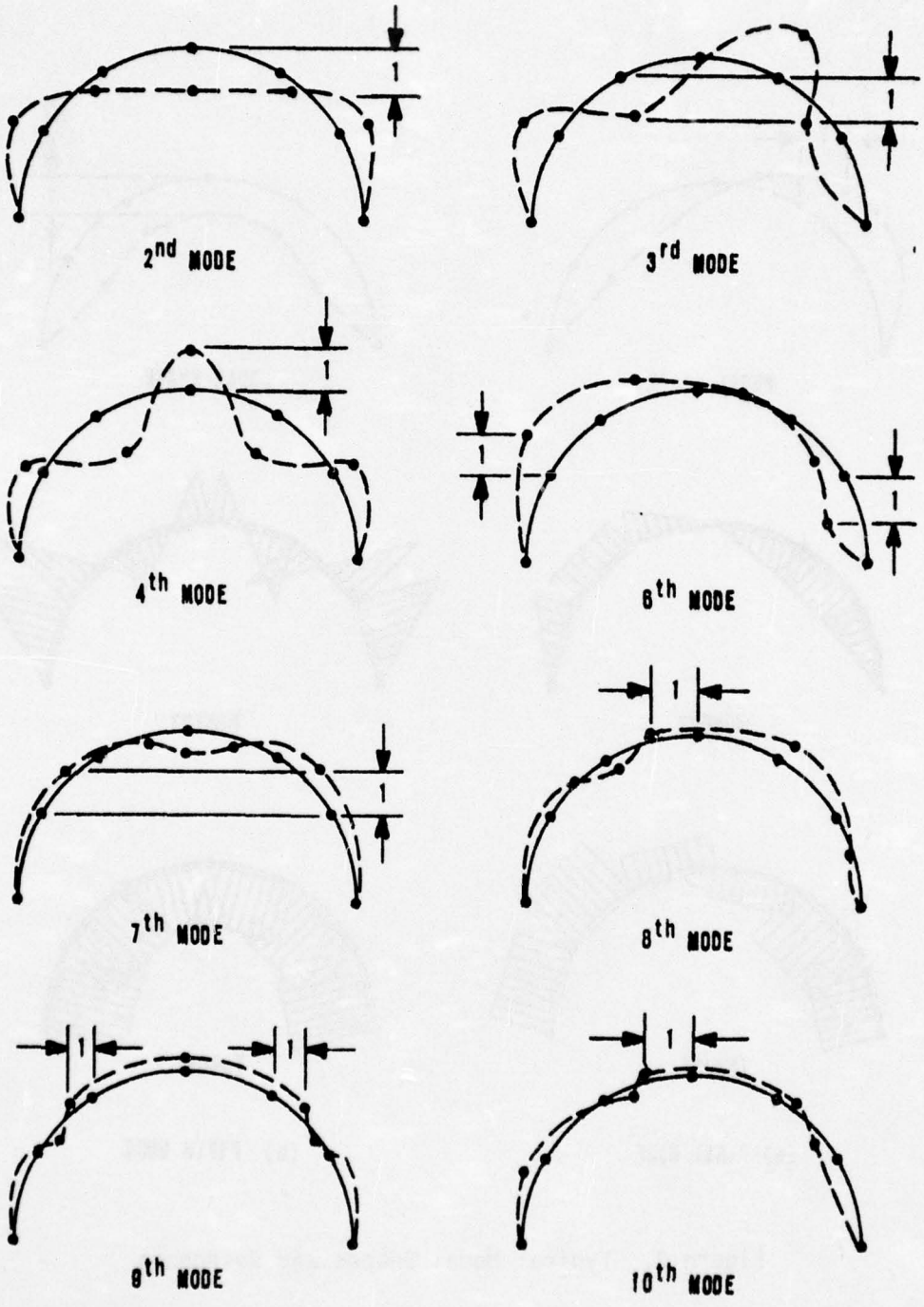


Figure 3. Modal Shapes

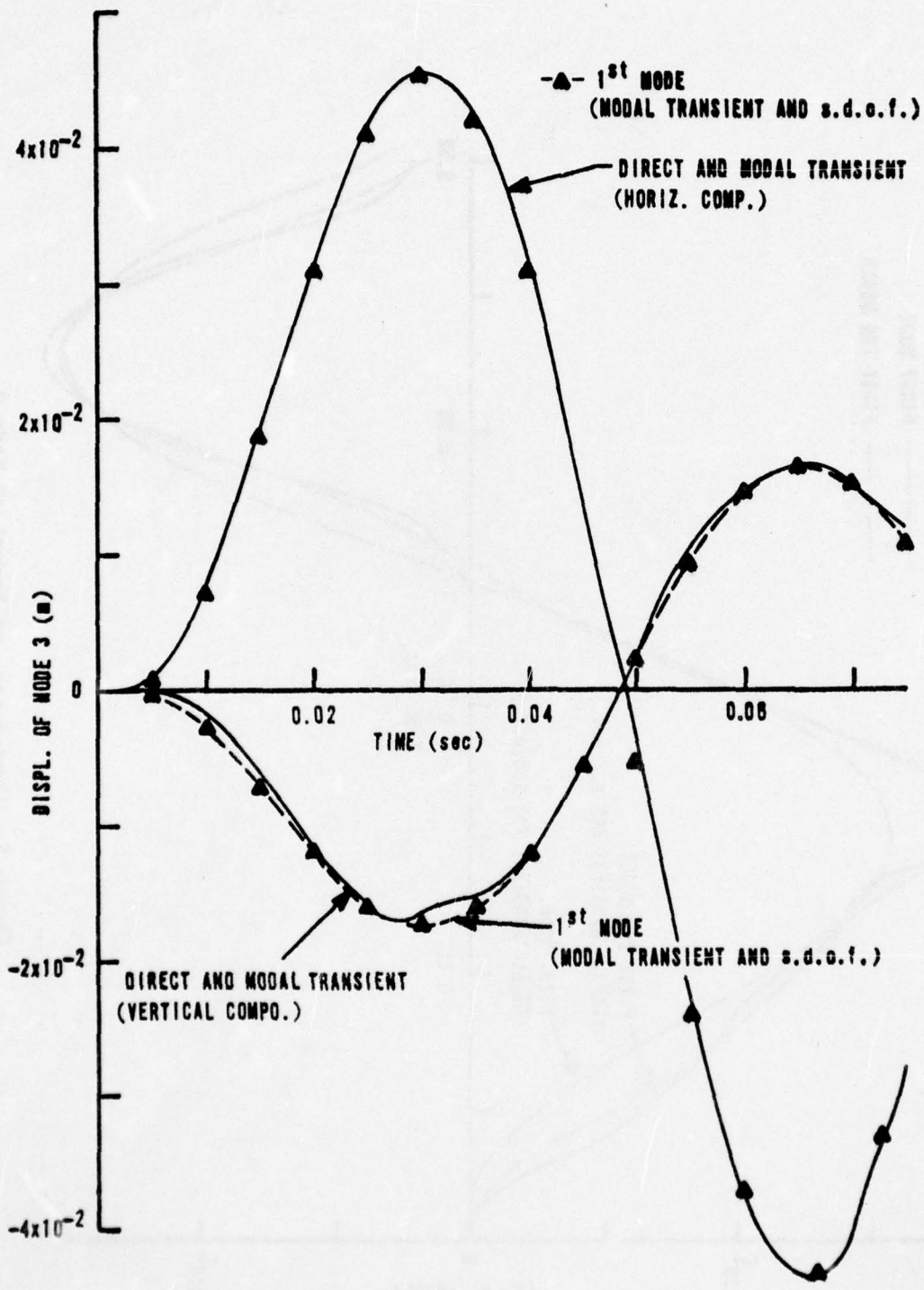


Figure 4. Comparisons of Displacement of Node 3

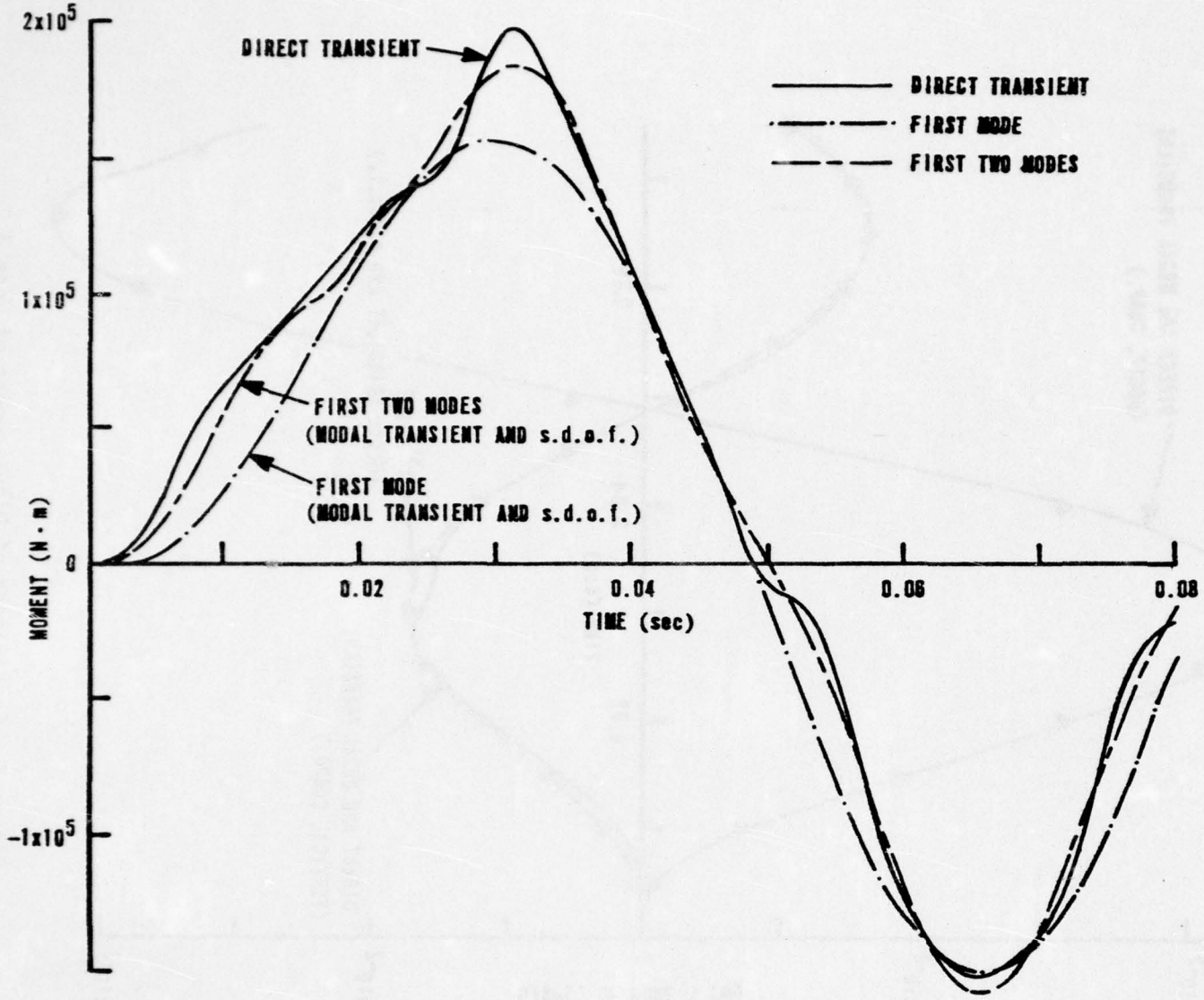


Figure 5. Comparisons of Moment at Node 2

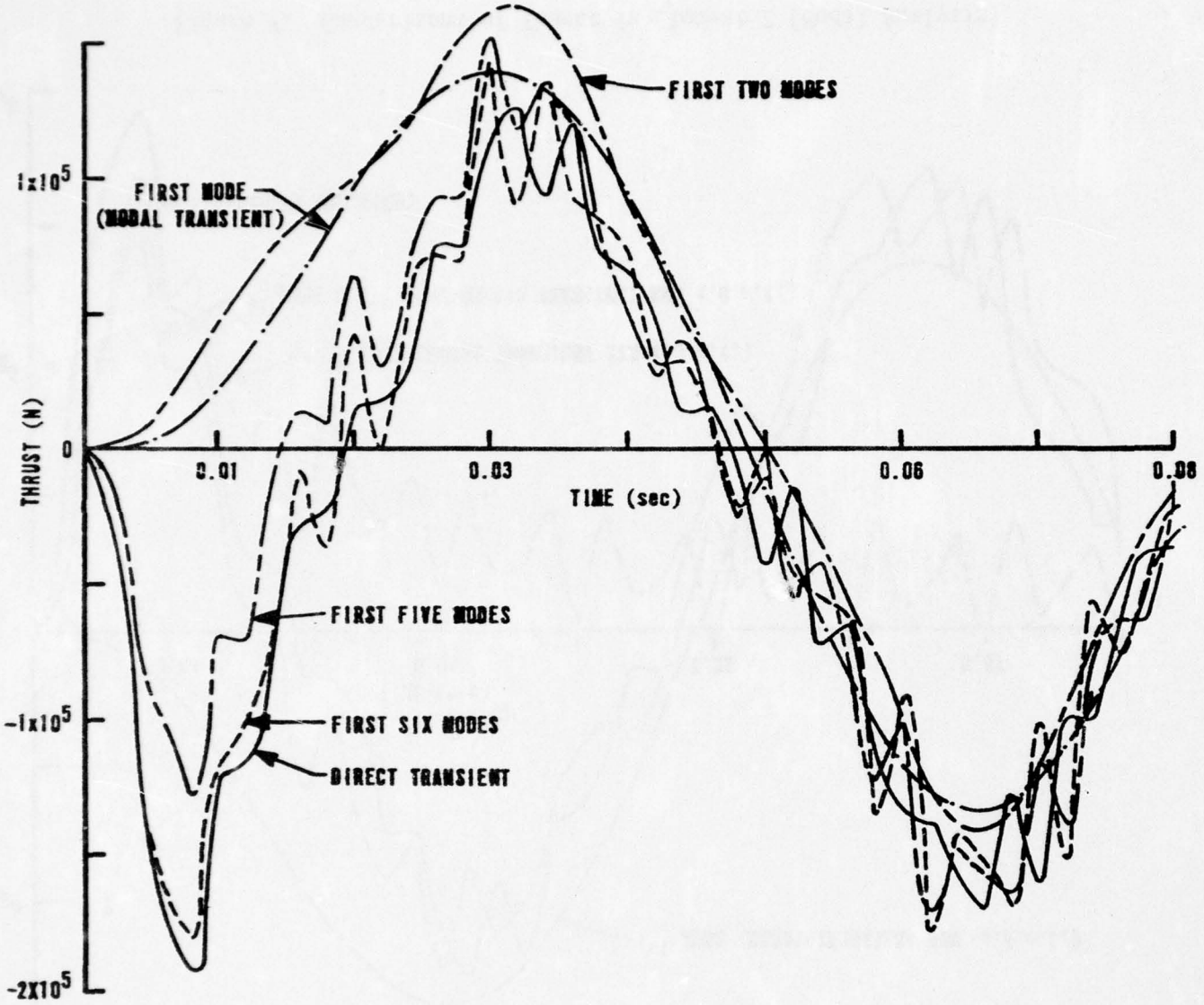
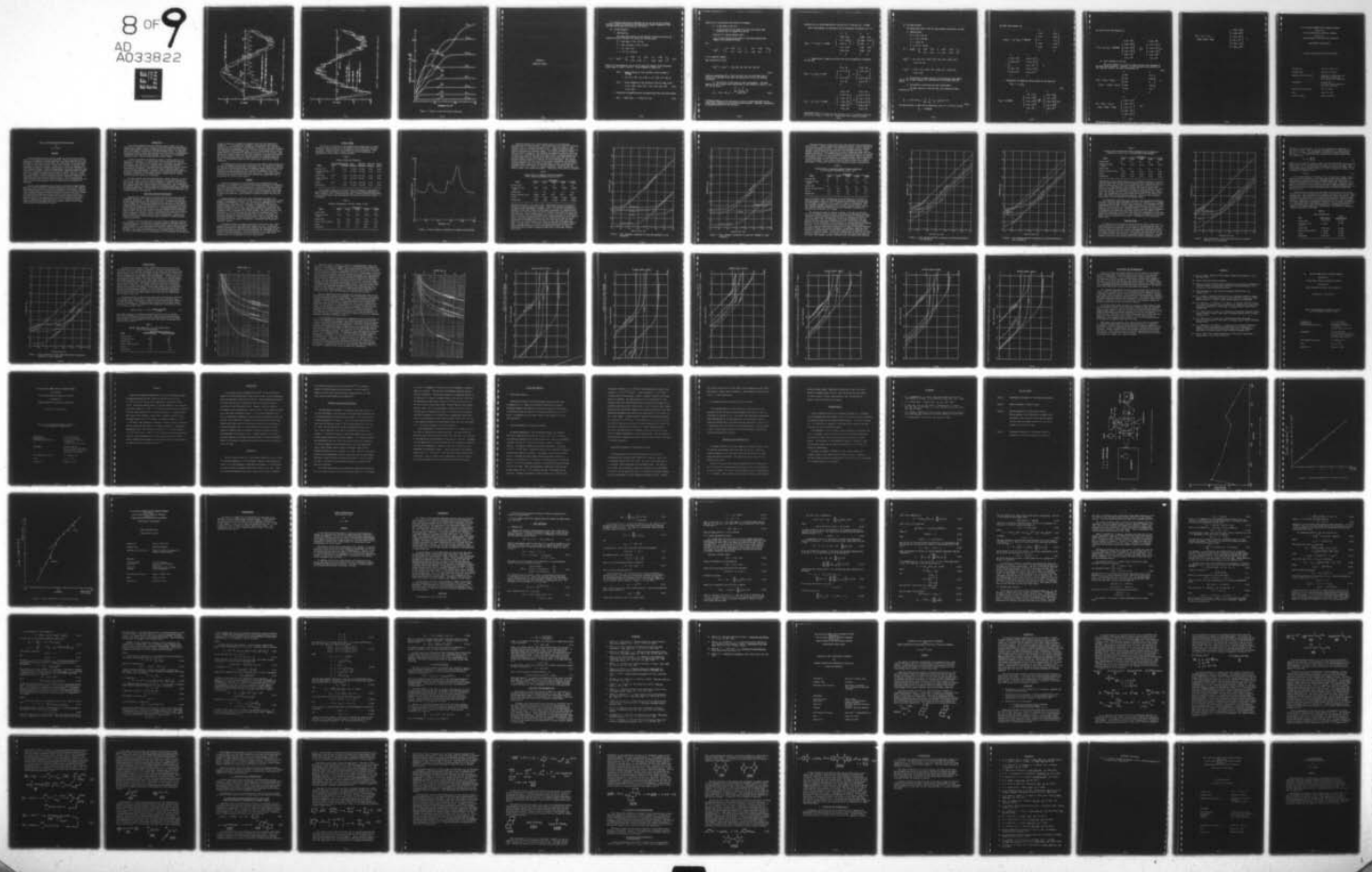


Figure 6. Comparisons of Thrust in Element 2 (Finite-Element Method)

AD-A033 822 AUBURN UNIV ALA SCHOOL OF ENGINEERING F/G 14/2
1976 USAF-ASEE SUMMER FACULTY RESEARCH PROGRAM.(U)
SEP 76 J F O'BRIEN F44620-75-C-0031
UNCLASSIFIED AFOSR-TR-76-1419 NL

8 OF 9
AD A033822



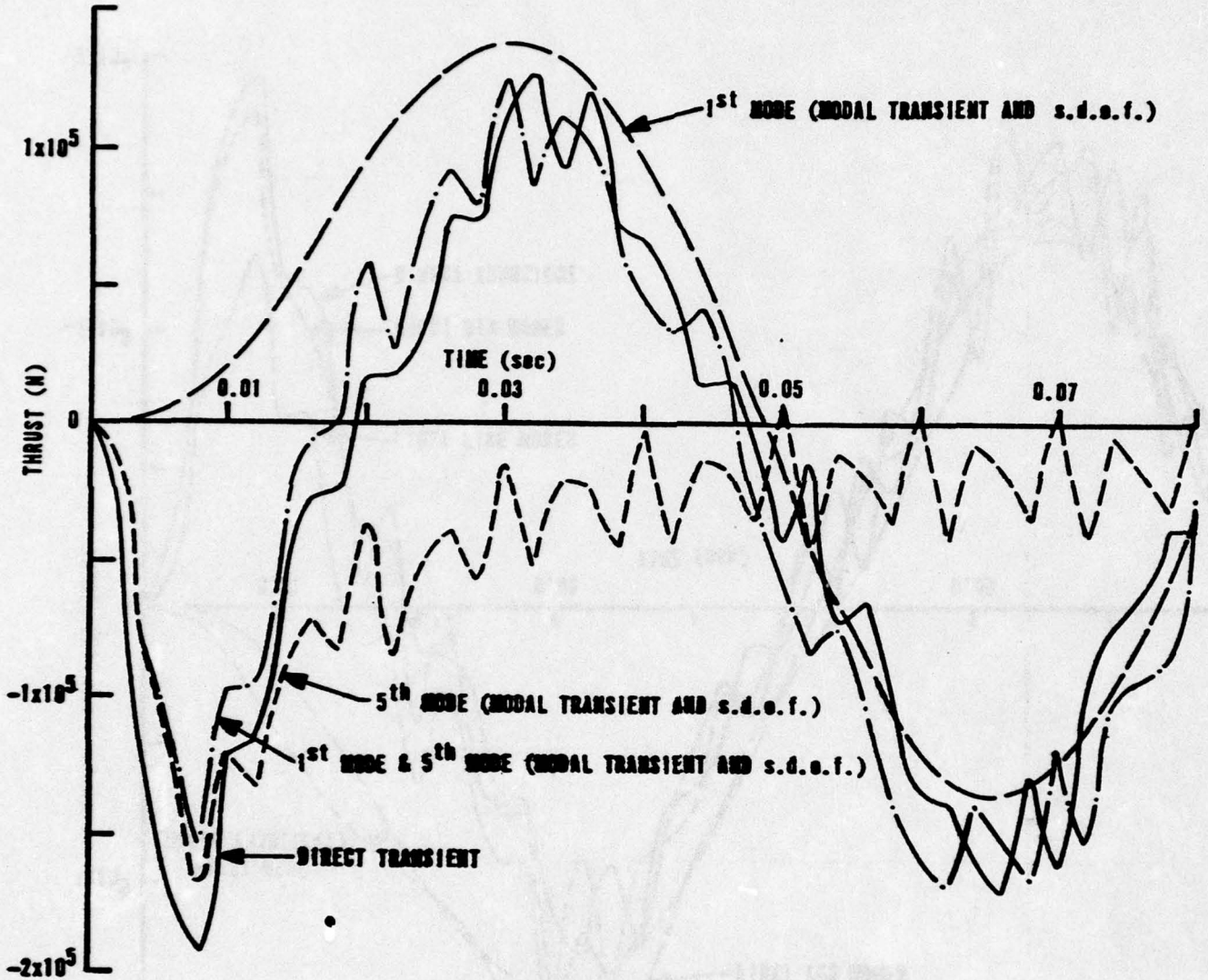


Figure 7. Comparisons of Thurst in Element 2 (Modal Analysis)

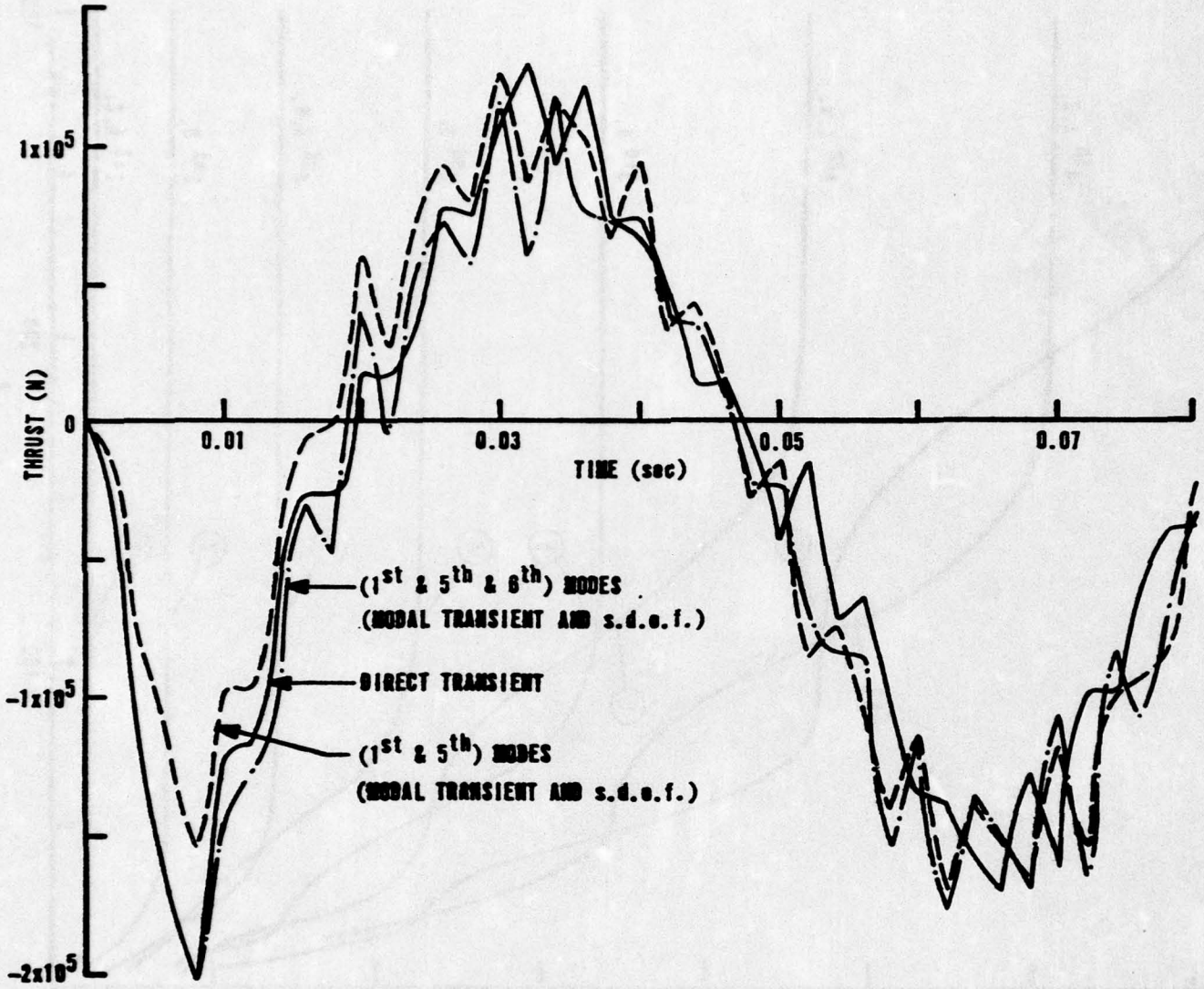


Figure 8. Comparisons of Thrust in Element 2 (Modal Analysis)

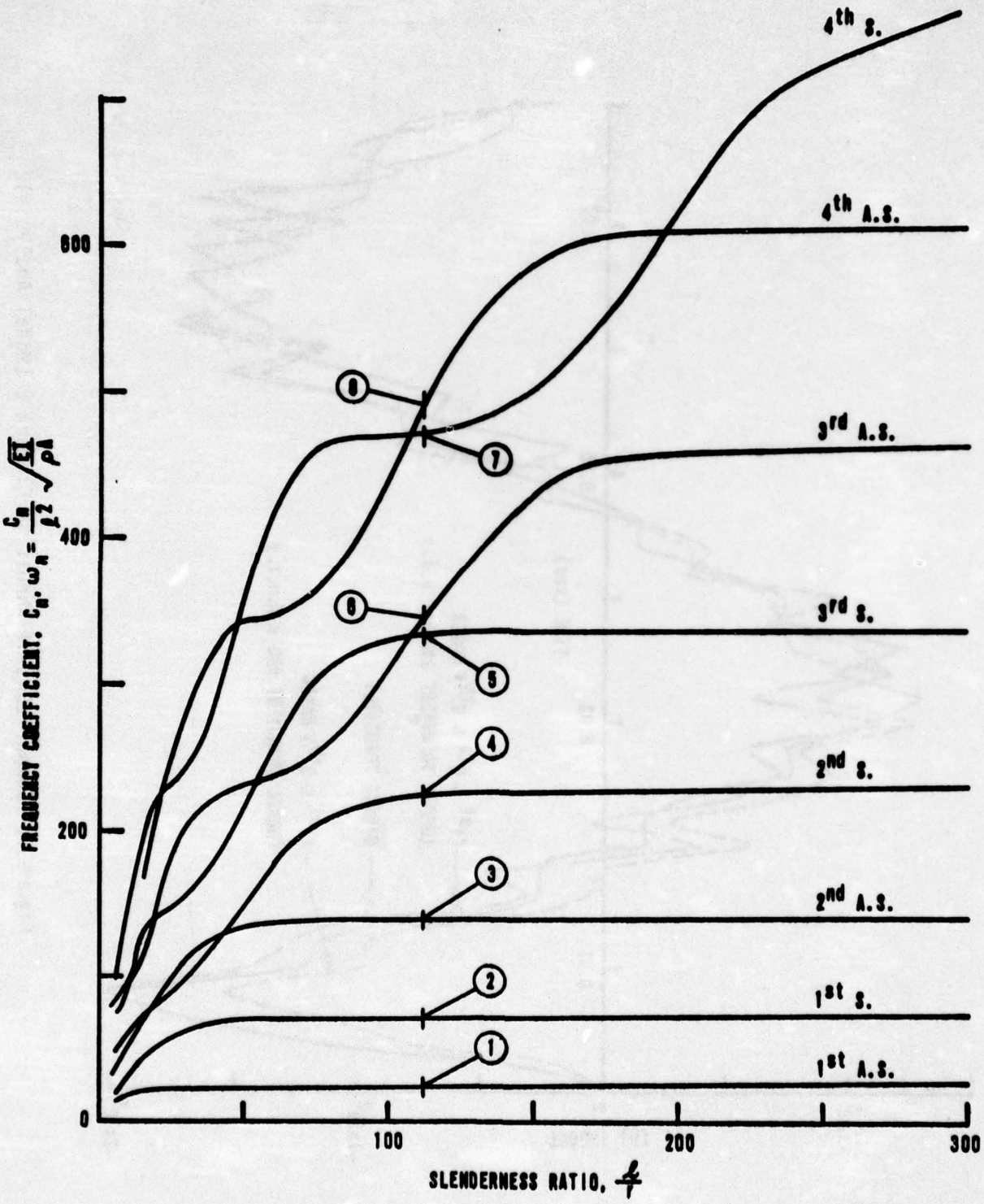


Figure 9. Frequency Curves and Energy Proportions

APPENDIX A

NUMERICAL EXAMPLE

To illustrate application of Equation (2) and (3), we use the following numerical example to demonstrate the computation of dynamic responses of the 1st mode and 5th mode of the arch at t = 0.03 sec.

A) 1st Mode Response

1. Data Required

The normal mode analysis of the "Nastran" program for solving the eigenvalue problem (Equation [1]) yields the following data:

M = Gen. Mass = 7.44×10^2 kg

k = Gen. Stiffness = 6.63×10^6 N/M

$\lambda = \omega^2 = 8.91 \times 10^3$

$f = \sqrt{\lambda} / 2\pi = 15.02$ Hz

$$\phi_1 = \{\phi_{ik}\}_1^T = \begin{Bmatrix} 0 & -0.84 & -1.0 & -0.90 & -1.0 & -0.84 & 0 \\ 0 & 0.22 & 0.38 & 0 & -0.38 & -0.22 & 0 \end{Bmatrix} \quad \text{(B-1)}$$

where ϕ_1 is the eigenvector set of the 1st mode with respect to the coordinate system shown in figure 1, and $\{A\}^T$ is the transpose of matrix $\{A\}$

$\{M_i\}^T$ = Moment response of free vibration of the 1st mode in (N-M/M$_\ell$)

= $\{0, -3.5 \times 10^6, -3.3 \times 10^6, 0, 3.3 \times 10^6, 3.5 \times 10^6, 0\}$

$\{T_i\}^T$ = Thrust response of free vibration of the 1st mode in N/M

= $\{-2.74 \times 10^6, -3.08 \times 10^6, -1.36 \times 10^6, 3.08 \times 10^6, 2.74 \times 10^6\}$ (B-2)

2. Calculation of generalized mass and generalized force load calculations

$\{F_{ik}\}$ = Nodal force = $b\,[P_i(t)l_i]\,\{\alpha_{ik}\}$ (B-2)

where $P_i(t)$ is the pressure-time history at the nodes

b is the width of the arch

l_i is the portion of arch length over which the uniform nodal pressure $P_i(t)$ is assumed to be acting

$[P_i(t)l_i]$ is a square diagonal matrix

$\{\alpha_{ik}\}$ is the direction cosine matrix of the nodal pressure with respect to the coordinate system

and

$$\{\alpha_{ik}\}^T = \begin{Bmatrix} 1.0 & 0.87 & 0.5 & 0 & -0.5 & -0.87 & -1.0 \\ 0 & -0.5 & -0.87 & -1.0 & -0.87 & -0.5 & 0 \end{Bmatrix}$$

in our numerical example.

Mass calculations (in kg)

$$\{M_i\}^T = \{\rho A l_i\}^T = \{82, 164, 164, 164, 164, 164, 82\} \qquad \text{(B-3)}$$

Substitute expressions (B-1), (B-2) and (B-3) into the right hand side of Equation (2), the generalized mass* and generalized force can be obtained accordingly.

3. Calculations of amplitude and nodal displacements. The modal equation of the 1st mode, after substitution of data obtained in steps (1) and (2), for the arch is

$$\ddot{A}_1 + 8.91 \times 10^3 A_1 = \frac{\sum_{i=1}^{7} F_{ik} \sum_{k=1}^{2} \phi_{ik}}{7.44 \times 10^2} \qquad \text{(B-4)}$$

*The Nastran program yields the numerical values of generalized mass for the normal modes considered and normalizing method selected. Therefore, computations of generalized masses are not necessary.

Equation (B-4) is solved numerically*, we have, at t = 0.03 sec, $A_1 = -0.045M$.

Nodal displacements are obtained by the 1st expression of Equation (3), i.e.,

$$\{d_{ik}\}_1 = A_1 \{\phi_{ij}\}_1 = -0.045M \begin{Bmatrix} 0 & 0 \\ -0.84 & 0.22 \\ -1.0 & 0.38 \\ -0.90 & 0 \\ -1.0 & -0.38 \\ -0.84 & -0.22 \\ 0 & 0 \end{Bmatrix} = \begin{Bmatrix} 0 & 0 \\ 0.038 & -0.01 \\ 0.045 & -0.017 \\ 0.041 & 0 \\ 0.045 & 0.017 \\ 0.038 & 0.01 \\ 0 & 0 \end{Bmatrix}$$

4. Computations of moments and thrust from the 2nd expression of Equation (3), we have

$$\{M_i\}_1 = A_1 \{M_{i1}\} = 0.45M \begin{Bmatrix} 0 \\ -3.5 \times 10^6 \\ -3.3 \times 10^6 \\ 0 \\ 3.3 \times 10^6 \\ 3.5 \times 10^6 \\ 0 \end{Bmatrix} = \begin{Bmatrix} 0 \\ 0.16 \times 10^6 \\ 0.15 \times 10^6 \\ 0 \\ -0.15 \times 10^6 \\ -0.16 \times 10^6 \\ 0 \end{Bmatrix}$$

$$\{T_i\}_1 = A_1 \{T_{i1}\} = -0.045M \begin{Bmatrix} -2.74 \times 10^6 \\ -3.08 \times 10^6 \\ -1.36 \times 10^6 \\ 1.36 \times 10^6 \\ 3.08 \times 10^6 \\ 2.74 \times 10^6 \end{Bmatrix} = \begin{Bmatrix} 0.12 \times 10^6 \\ 0.14 \times 10^6 \\ 0.61 \times 10^5 \\ -0.61 \times 10^5 \\ -0.14 \times 10^6 \\ -0.12 \times 10^6 \end{Bmatrix}$$

*Equation (B-4) is volved by the existed s.d.o.f. program modified during the summer of 1976 for lumped-mass multi-degree systems.

B) 5th mode response

Following steps taken in the 1st mode response calculations, we have

1. Required data

$M = 8.24 \times 10^2$ kg

$k = 1.31 \times 10^9$ N/M

$\lambda = 1.59 \times 10^6$

$f = \sqrt{\lambda}/2\pi = 201$ Hz

$$\phi_5 = \{\phi_{ik}\}_5^T = \begin{Bmatrix} 0 & 0.87 & 0.37 & 0 & -0.37 & -0.87 & 0 \\ 0 & -0.71 & -0.81 & -1.0 & -0.81 & -0.71 & 0 \end{Bmatrix}$$

$$\{M_{i5}\}^T = \{0,\ 1.04 \times 10^7,\ -6.23 \times 10^6,\ 4.35 \times 10^6,\ -6.23 \times 10^6,\ 1.04 \times 10^7,\ 0\}$$

$$\{T_{i5}\}^T = \{-5.37 \times 10^8,\ -4.89 \times 10^8,\ -4.68 \times 10^8,\ -4.89 \times 10^8,\ -5.37 \times 10^8\}$$

2. Calculations of generalized mass and generalized force same as that of the 1st mode response with consideration for different numerical values.

3. Calculations of amplitude and nodal displacements

The modal equation of the 5th mode, after appropriate data substitution, is

$$\ddot{A}_5 + 1.59 \times 10^6 A_5 = \sum_{i=1}^{7} \sum_{k=1}^{2} F_{ik}\ \phi_{ik}/8.24 \times 10^2 \qquad \text{(B-6)}$$

The above equation is again solved numerically, and at t = 0.03 sec, we have

$$A_5 = 0.000029M$$

The nodal displacements are

$$\{d_{ik}\}_5 = A_5 \{\phi_{ij}\}_5 = 0.000029M \begin{Bmatrix} 0 & 0 \\ 0.87 & -0.71 \\ 0.37 & -0.81 \\ 0 & -1.0 \\ -0.37 & -0.81 \\ -0.87 & -0.71 \\ 0 & 0 \end{Bmatrix}$$

$$= \begin{Bmatrix} 0 & 0 \\ 2.52 \times 10^{-5} & -2.06 \times 10^{-5} \\ 1.06 \times 10^{-5} & -2.34 \times 10^{-5} \\ 0 & -2.9 \times 10^{-5} \\ -1.06 \times 10^{-5} & -2.34 \times 10^{-5} \\ -2.52 \times 10^{-5} & -2.06 \times 10^{-5} \\ 0 & 0 \end{Bmatrix} M.$$

4. Computations of moment and thrust moments at the nodes are

$$\{M_i\}_5 = A_5 \{M_{i5}\} \qquad \text{(B-7)}$$

$$\{M_{i5}\} = 0.000029M \begin{Bmatrix} 0 & 0 \\ 1.04 \times 10^{7} & 3.02 \times 10^{2} \\ -6.23 \times 10^{6} & -1.81 \times 10^{2} \\ 4.35 \times 10^{6} & 1.26 \times 10^{2} \\ -6.23 \times 10^{6} & -1.81 \times 10^{2} \\ 1.04 \times 10^{7} & 3.02 \times 10^{2} \\ 0 & 0 \end{Bmatrix} \begin{matrix} \\ \\ \\ \\ \\ \\ \\ \end{matrix} \begin{matrix} \text{N-M} \\ \\ \\ \\ \\ \\ \\ \end{matrix}$$

$$\frac{\text{N-M}}{\text{N}}$$

The thrust within the elements are

$$\{T^i\}_5 = A_5 \{T_{i5}\} = 0.000029M \begin{Bmatrix} -5.37 \times 10^8 \\ -4.89 \times 10^8 \\ -4.68 \times 10^8 \\ -4.68 \times 10^8 \\ -4.89 \times 10^8 \\ -5.37 \times 10^8 \end{Bmatrix} \qquad \frac{N}{M} = \begin{Bmatrix} -1.56 \times 10^4 \\ -1.42 \times 10^4 \\ -1.36 \times 10^4 \\ -1.36 \times 10^4 \\ -1.42 \times 10^4 \\ -1.56 \times 10^4 \end{Bmatrix} N$$

C) Total responses of the arch

The total response of the arch is simply the sum of the responses of the modes being considered. Therefore, for the two modes being considered in this numerical example, the nodal displacements are

(B-8)

$$\{d_{ik}\} = \{d_{ik}\}_1 + \{d_{ik}\}_5 = \begin{Bmatrix} 0 \\ 0.038 \\ 0.045 \\ 0.041 \\ 0.045 \\ 0.038 \\ 0 \end{Bmatrix} \begin{Bmatrix} 0 \\ -0.01 \\ -0.017 \\ 0 \\ 0.017 \\ 0.01 \\ 0 \end{Bmatrix} M$$

t=30 ms t=30 ms t=30 ms

$$\{M_i\} = \{M_i\}_1 + \{M_i\}_5 = \begin{Bmatrix} 0 \\ 1.603 \times 10^5 \\ 1.498 \times 10^5 \\ 1.26 \times 10^2 \\ -1.502 \times 10^5 \\ -1.597 \times 10^5 \\ 0 \end{Bmatrix} N\text{-}M \quad *$$

t=30ms 5-30ms 5=30ms

*To get more accurate results, the 2nd mode should be included instead of the

$$\{T_i\} = \{T_i\} + \{T_i\}_5 =$$
$$t=30ms \quad t=30ms \quad t=30ms$$

$$\begin{Bmatrix} 1.044 \times 10^5 \\ 1.258 \times 10^5 \\ 4.74 \times 10^4 \\ -7.46 \times 10^4 \\ -1.542 \times 10^5 \\ -1.356 \times 10^5 \end{Bmatrix} \quad N$$

1976 USAF-ASEE SUMMER FACULTY RESEARCH PROGRAM

sponsored by

THE AIR FORCE OFFICE SCIENTIFIC RESEARCH

conducted by

AUBURN UNIVERSITY AND OHIO STATE UNIVERSITY

PARTICIPANT'S FINAL REPORT

OPTICAL FIBER EXPLOSION-INITIATION SYSTEM

Prepared by:	Donald A. Smith, Ph D.
Academic Rank:	Associate Professor
Department and University:	Department of Electrical and Electronics Engineering North Dakota State University
Assignment:	Kirtland AFB Air Force Weapons Laboratory Electronics Division
USAF Research Colleague:	John H. Darrah
Date:	August 6, 1976
Contract Number:	F44620-75-C-0031

OPTICAL FIBER EXPLOSION-INITIATION SYSTEM

by

D. A. Smith

ABSTRACT

A laser-initiated pulse of optical energy may be sent over an optical fiber for the purpose of initiating explosion. Energy requirements for the initiation of explosion in common materials range from 0.006 to 0.150 joule delivered in less than 10 milliseconds. For the optical system under study an energy of 0.01 joule is used. In order that a variety of optical fiber properties be taken into account, several optical fibers are considered as the propagation medium. Inherent attenuations in the fibers considered range from less than 20 dB/km to well over 1000 dB/km. Permanent-induced attenuations due to radiation range from less than 10^{-5} dB km^{-1} rad^{-1} to 5 dB km^{-1} rad^{-1} with maximum transient-induced attenuation due to radiation reaching much higher values. Sources considered are both solid-state lasers such as neodymium-glass lasers and semiconductor lasers. While the solid-state lasers are practical sources for this application, it is determined that the pulse energy of a semiconductor laser is insufficient for initiation of explosion.

Overall system requirements are utilized to determine optimum arrangements for various conditions. Optimum arrangements in both a non-radiation environment and in various radiation environments are determined. Applying a first order analysis to determine the feasibility of utilizing an optical fiber explosion-initiation system has yielded the results that such a system will operate over distances of several tens of meters after exposure to radiation doses of 10^6 to 10^8 rads if the transient effects are allowed to decay leaving only the permanent effects, but in applications where the system is subjected to high radiation doses and is required to operate shortly following irradiation while the transient effect is still large, such a system no longer appears feasible.

INTRODUCTION

Since 1970 transmission systems utilizing optical fibers have been drawing much attention for use in many military and industrial applications. Optical fibers offer a number of appealing features such as low loss, small size, light weight, high capacity, and small bending radius. In addition, since they contain no metal, they neither radiate nor pick up electromagnetic interference as do wire and cable systems. Also there are no grounding problems or short circuits associated with optical fibers.

A pulse of electrical or mechanical energy is commonly used for the initiation of explosion. An optical pulse may also be used for such an application. The purpose of this project is to investigate the feasibility of sending a laser pulse over an optical fiber to initiate explosion. Of particular interest are the capabilities and limitations of such a system when exposed to radiation. This study utilizes the measured results of several previous investigators to develop a first order analytical approach in order to investigate these capabilities and limitations and to seek performance trade-offs in the overall system. Several types of optical fibers and optical sources are considered.

The basic optical fiber explosion-initiation system consists of a pulse laser as the source, an optical fiber waveguide, and explosive material as the receiver. When the optical fiber is exposed to radiation, the radiation pulse causes luminescence and absorption within the fiber. The luminescence is a maximum during the radiation pulse and negligible thereafter. Immediately following irradiation the induced absorption is a maximum and decays with time to some permanent value. Both permanent and transient induced absorption are considered in this investigation.

EXPLOSION-INITIATION REQUIREMENTS

Properties and compositions of explosive materials have been described extensively by Bauer [1]. Explosive actuated devices can be initiated by electrical, mechanical, or laser initiator units. Information is available on many specific detonating and deflagrating devices, such as those manufactured by duPont [2]. The energy required for the initiation of explosion in common materials ranges from 0.006 joule to 0.150 joule delivered in a pulse of less than 10 milliseconds duration. The corresponding minimum peak pulse power or energy per unit time is that which will always fire the initiator. There is also a no-fire power which is a continuous power that may be applied without firing the initiator. No-fire powers range from 0.04 watts to 2.7 watts continuous in common materials. There is, therefore, a fairly broad range of all-fire and no-fire specifications available in common explosive-initiation materials.

In spite of the fact that there is a broad range of explosive specifications available, it is convenient for analysis purposes to designate typical firing requirements. In electrical initiator units a typical unit is one with a no-fire power of 1 watt continuous and an all-fire power of 25 watts peak delivered in a 1.2 millisecond pulse [1]. This is an energy of 0.03 joule in the pulse. The energy is delivered through a bridgewire with a typical area of 4×10^{-3} cm^2 resulting in an energy density of 7.5 joules/cm^2 for initiation.

An optical beam can be focused to a smaller area than that occupied by a bridgewire. It is probably not desirable to make the area much smaller, however, since at some point the reliability of explosion will decrease as the initiation area decreases. Also the quality of the focusing lens increases with decreasing required focused area. For the optical system under study an energy density of 10 joules/cm^2 applied to an area of 10^{-3} cm^2 is used. This results in a required energy of 0.01 joule delivered to the explosive material. The all-fire optical power could typically range from 1 megawatt peak for a 10 nanosecond duration pulse to 10 watts peak for a 1 millisecond duration pulse. A corresponding typical no-fire optical power would be 0.25 watts continuous.

An investigation of pyrotechnic materials which exhibit high sensitivities to laser wavelengths has been made by Mittendorf [3]. He found that a mixture of titanium, potassium perchlorate, and manganese dioxide exhibited a selective sensitivity to the 10,600Å wavelength of neodymium lasers, while a mixture of titanium, potassium perchlorate, and prussian blue exhibited a selective sensitivity to the 6943Å wavelength of the ruby laser. The energy required for ignition for these materials at their selective wavelength was found to be typically in the 0.01 joule region.

SOURCES

Solid-state lasers such as neodymium-glass and neodymium-Yag lasers operating at a wavelength of 1.06 μm and ruby lasers operating at a wavelength of 0.6943 μm are readily available that emit a pulse with sufficient energy to fulfil the explosion-initiation requirements described [4]. Such lasers are available with output pulse energy in the 1 to 100 joule region, pulse widths in the 15 nanosecond to 1 millisecond range, and pulse repetition rates from 30 pulses per second for 1 joule pulses to 4 pulses per minute for 100 joule pulses.

Radiation effects on lasers have been investigated by Compton [5]. Lasers were irradiated at dose rates of up to 2×10^{10} rads/second and to total dosages of approximately 10^7 rads. In ruby lasers the permanent effect after irradiation is a reduction in the efficienty of stimulated emission for absorbed dosages above 10^4 rads. The degree of degradation is relatively constant between 10^4 and 10^6 rads. The output energy after irradiation was restored to within 5% of the preirradiation energy after several hours. The permanent effect is therefore not a severe problem. The short-term effect is more serious. It was found that both the degree of degradation of laser efficiency and the rate of annealing depend upon the rate of pumping. No stimulated emission was observed during the first flash of the pump lamp following irradiation. During the second flash of the pump lamp the laser output was 50% of that prior to irradiation. Improvement was found with subsequent flashes.

Semiconductor lasers are appealing because of their small size, light weight, ease of pulsing, and higher pulse repetition rates. A survey of available semiconductor lasers has shown, however, that the energy available in the output pulses of such lasers is insufficient for initiation of the explosive materials discussed. The lasers feasible for this application are, therefore, the non-semiconductor type of solid-state lasers such as the neodymium-glass, the neodymium-Yag, and the ruby lasers.

OPTICAL FIBERS

The effects of radiation on the absorption and luminescence of optical fibers have been measured for a wide range of optical fibers and materials [6,7,8,9]. Several of these are considered in this investigation. Those considered, listed in Table 1 along with some of their properties, are representative of the types of fibers available.

TABLE 1

OPTICAL FIBERS AND PROPERTIES

Fiber	Indices of Refraction		Core Diameter	Cladding Thickness	Numerical Aperture	Reflectance
	Core	Cladding				
Corning 5010	1.62	1.49	1.6 mil	0.2 mil	0.63	0.06
Corning Low Loss Type B	1.5	1.49	3.3 mil	1.0 mil	0.16	0.04
Galileo K2K	1.625	1.48	2.4 mil	0.2 mil	0.66	0.06
Schott Vitreous Silica	1.5	1.48	2.6 mil	0.6 mil	0.26	0.04
Crofon	1.49	1.39	55.5 mil	0.25 mil	0.53	0.04
Polystyrene	1.5	1.39	2.7 mil	0.15 mil	0.57	0.04

The intrinsic attenuation of optical fiber is dependent on wavelength as well as material composition and purity. A typical wavelength dependence is shown in Figure 1 for a Corning low-loss fiber. Typical intrinsic attenuations of the optical fibers under consideration are shown in Table 2 for several wavelengths.

TABLE 2

INTRINSIC ATTENUATION OF OPTICAL FIBERS IN dB/M

Fiber	Wavelength				
	0.6μm	0.7μm	0.8μm	0.9μm	1.06μm
Corning 5010	1.1	1.3	1.3	1.1	1.1
Corning Low Loss Type B	0.03	0.02	0.02	0.06	0.02
Galileo K2K	0.4	0.35	0.35	0.5	0.4
Schott Vitreous Silica	0.26	0.26	0.26	0.33	0.52
Crofon	0.5	0.7	1.3	20.0	3.0
Polystyrene	1.5	1.5	1.5	20.0	3.0

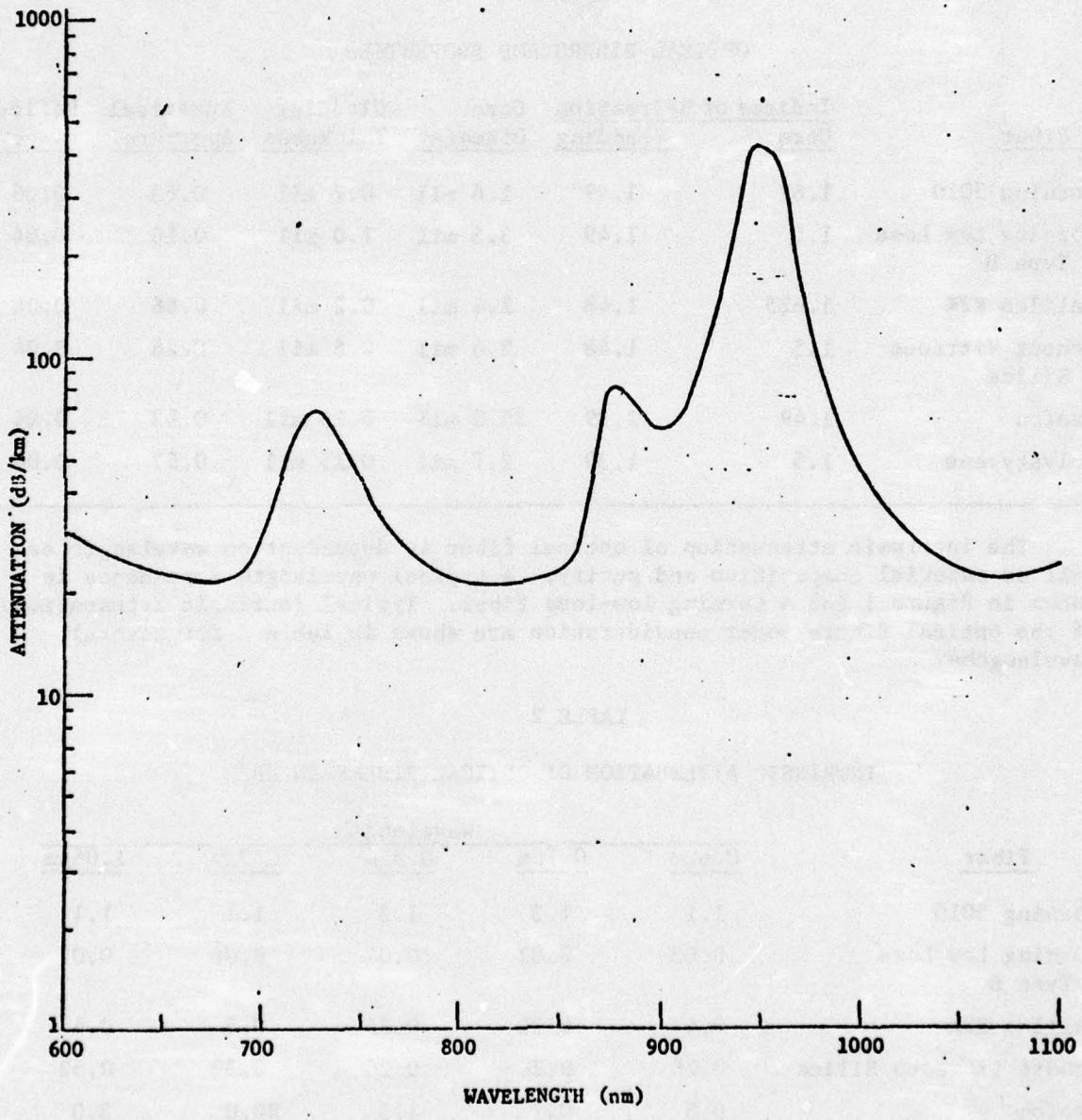


FIGURE 1. TYPICAL INTRINSIC ATTENUATION OF CORNING LOW-LOSS FIBER

Radiation exposure has a rather severe effect on the attenuation characteristics of optical fibers. This occurs both in the form of a transient absorption and of a permanent absorption [6,7]. From the nature of these measured results it is seen that there is not a simple relationship between the induced attenuation and radiation dosage. It has been determined, however, that the effects of radiation are identical for gamma-ray, electron, and X-ray radiation [6]. Although the induced attenuation due to radiation exposure may be quite complicated, it has been shown that a first order approximation may be conveniently utilized expressing the induced attenuation per unit rad of absorbed radiation dosage as a constant at a given wavelength. The permanent induced attenuation for the optical fibers under consideration was determined from measurements made by the various investigators cited. An average value of permanent induced attenuation per absorbed dosage was calculated from the measured results over a range of radiation exposures. These average values are shown in Table 3 for several wavelengths. Using these values the total permanent

TABLE 3

AVERAGE VALUES OF PERMANENT INDUCED ATTENUATION DUE TO RADIATION EXPOSURE IN dB Km^{-1} rad^{-1}

Fiber	Wavelength 0.6μm	0.7μm	0.8μm	0.9μm	1.06μm
Corning 5010	9	7	5.2	2.2	0.6
Corning Low Loss Type B	0.005	0.001	0.001	0.0008	0.0008
Galileo K2K	7.5	6.0	3.5	1.6	0.34
Schott Vitreous Silica	0.0001	$<10^{-5}$	$<10^{-5}$	$<10^{-5}$	$<10^{-5}$
Crofon	0.002	0.001	0.0002	0.0003	0.0002
Polystyrene	0.005	0.001	0.0005	0.0001	0.00006

attenuation for each of the fibers under consideration may be determined as a function of radiation absorption dosage. These total permanent attenuations are shown for two wavelengths in Figures 2 and 3. At the 0.7μm wavelength the Corning low loss, Type B fiber has the lowest attenuation for radiation doses less than 2.4×10^5 rads, while the Schott vitreous silica fiber has the lowest attenuation for larger radiation doses. At a dose of 10^8 rads the Corning low loss, the Crofon, and the Polystyrene fibers become comparable at an attenuation nearly two orders of magnitude above that of the Schott vitreous silica fiber. At the 1.06μm wavelength the Corning low loss, Type B fiber has the lowest attenuation for radiation doses less than 6.3×10^5 rads, while again the Schott vitreous silical fiber has the lowest attenuation for larger radiation doses. At doses above 4×10^6 rads, the Polystyrene and Crofon fibers have lower permanent attenuation than the Corning low loss fiber, but have an attenuation about an order of magnitude above that of the Schott vitreous silica fiber.

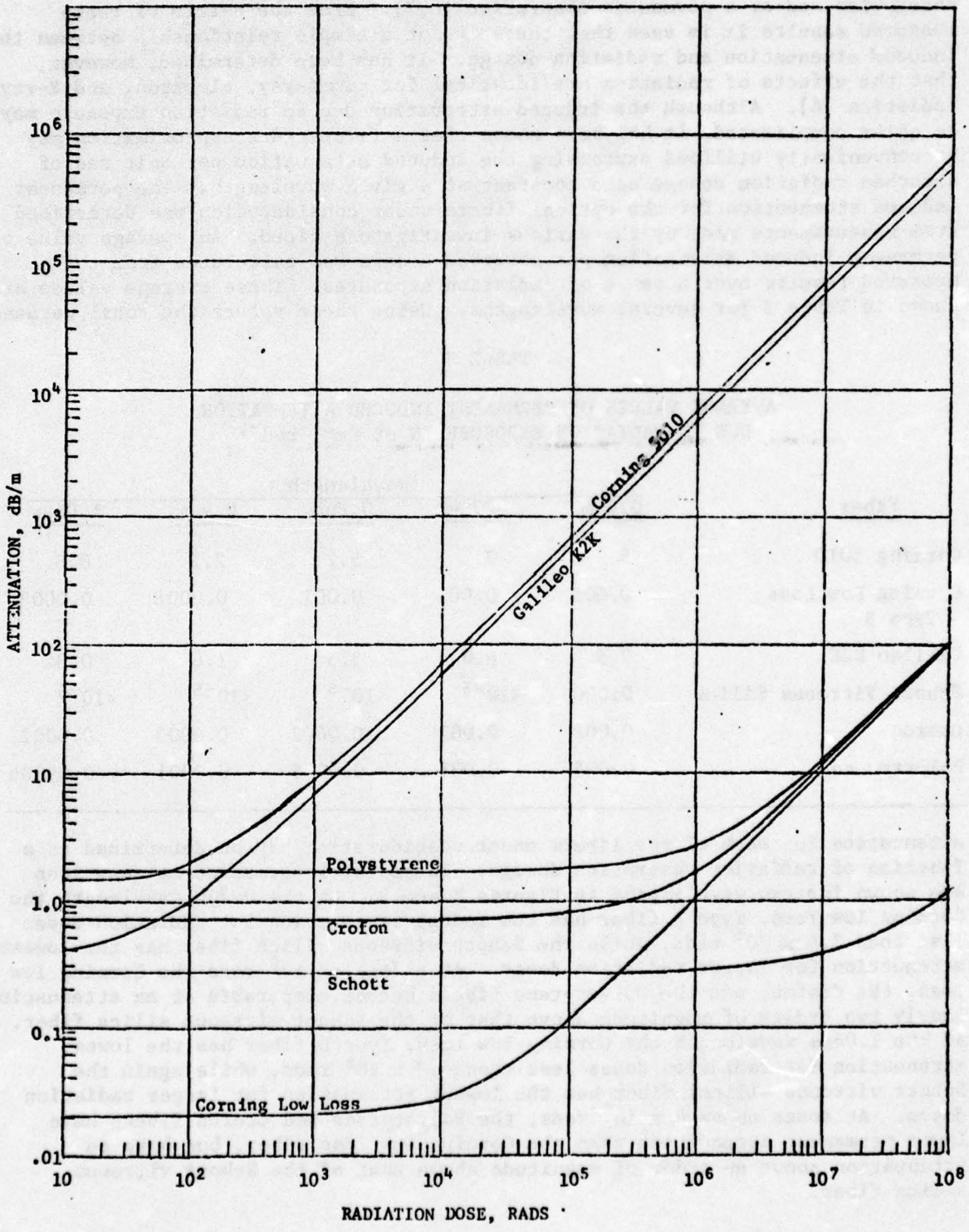


FIGURE 2. TOTAL PERMANENT ATTENUATION VS RADIATION EXPOSURE AT 0.7μm WAVELENGTH

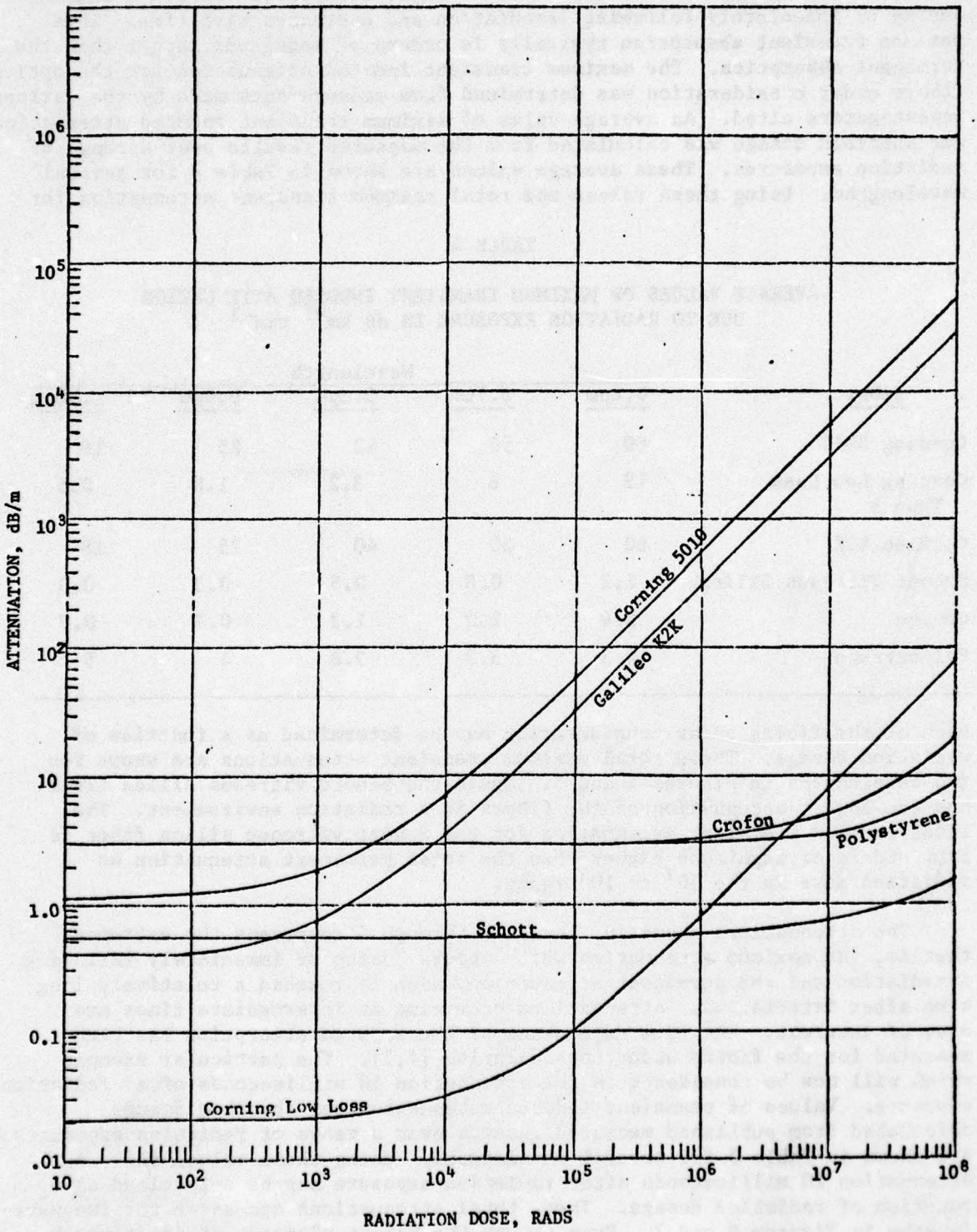


FIGURE 3. TOTAL PERMANENT ATTENUATION VS RADIATION EXPOSURE AT 1.06μm WAVELENGTH

Transient effects in optical fibers have been measured by the investigators cited [6,7,8,9]. During irradiation, luminescence occurs. This is followed by the transient absorption effect. The transient absorption reaches a maximum during or immediately following irradiation and decreases with time. This maximum transient absorption typically is orders of magnitude larger than the permanent absorption. The maximum transient induced attenuation for the optical fibers under consideration was determined from measurements made by the various investigators cited. An average value of maximum transient induced attenuation per absorbed dosage was calculated from the measured results over a range of radiation exposures. These average values are shown in Table 4 for several wavelengths. Using these values the total maximum transient attenuation for

TABLE 4

AVERAGE VALUES OF MAXIMUM TRANSIENT INDUCED ATTENUATION DUE TO RADIATION EXPOSURE IN dB km^{-1} rad^{-1}

Fiber	Wavelength 0.6μm	0.7μm	0.8μm	0.9μm	1.06μm
Corning 5010	60	50	40	25	18
Corning Low Loss Type B	12	6	3.2	1.8	0.5
Galileo K2K	60	50	40	25	18
Schott Vitreous Silica	1.2	0.8	0.5	0.3	0.3
Crofon	3.4	2.0	1.2	0.7	0.7
Polystyrene	4.3	3.3	3.8	4	5

each of the fibers under consideration may be determined as a function of radiation dosage. These total maximum transient attenuations are shown for two wavelengths in Figures 4 and 5. Again the Schott vitreous silica fiber has the lowest attenuation of the fibers in a radiation environment. The total maximum transient attenuation for the Schott vitreous silica fiber is four orders of magnitude higher than the total permanent attenuation at radiation dose in the 10^7 to 10^8 range.

The attenuations shown in Figures 2 through 5 represent the extremes, that is, the maximum attenuation which occurs during or immediately following irradiation and the permanent attenuation which is reached a relatively long time after irradiation. Attenuations occurring at intermediate times are also of interest. The time dependence of the induced absorption has been measured for the fibers under consideration [4,5]. The particular example which will now be considered is the attenuation 10 milliseconds after radiation exposure. Values of transient induced attenuation per absorbed dosage calculated from published measured results over a range of radiation exposures are shown in Table 5 for several wavelengths. Using these values the total attenuation 10 milliseconds after radiation exposure may be determined as a function of radiation dosage. These total attenuations are shown for two wavelengths in Figures 6 and 7. Even though the Schott vitreous silica fiber has the lowest total maximum transient attenuation and the lowest total permanent

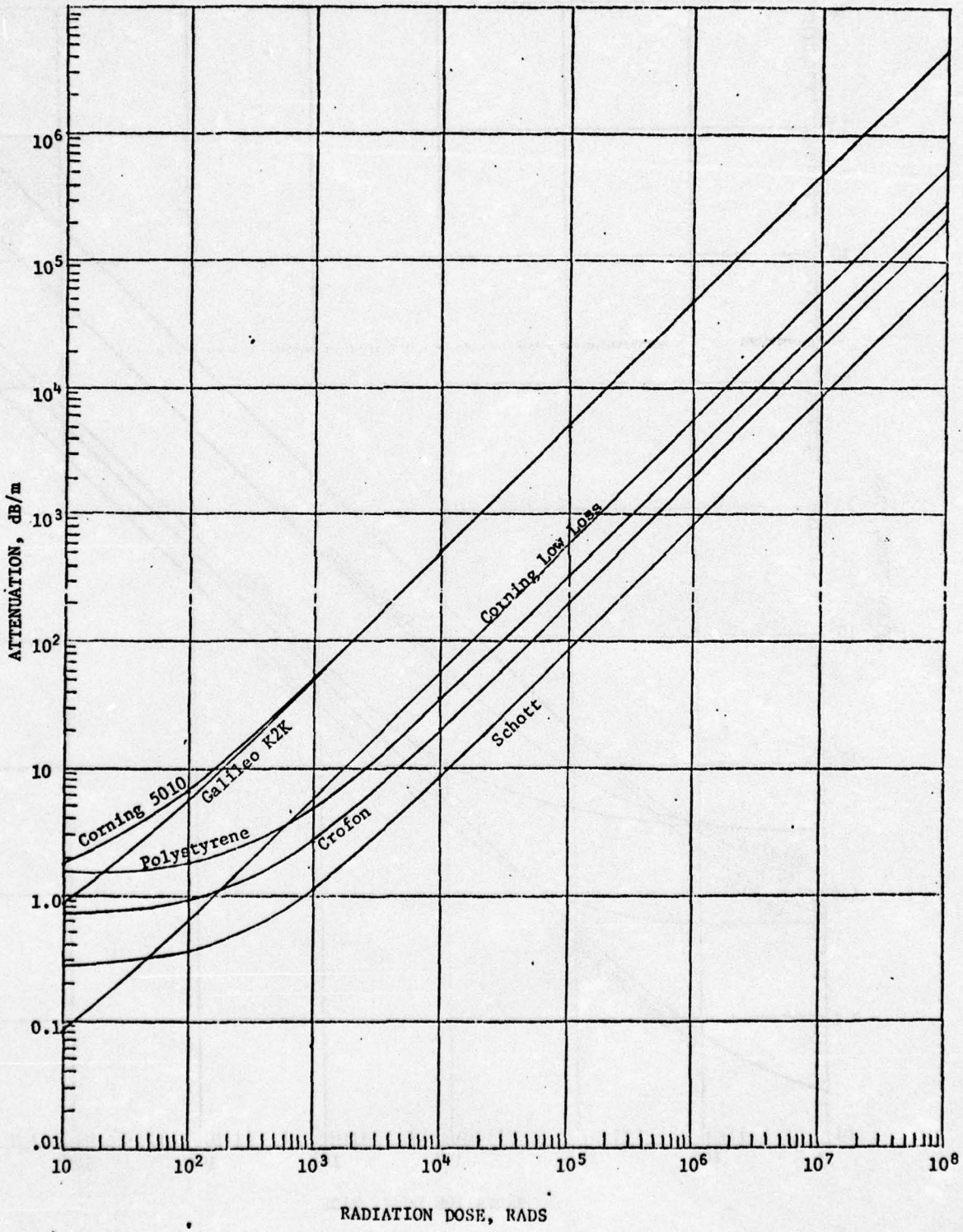


FIGURE 4. TOTAL MAXIMUM TRANSIENT ATTENUATION VS RADIATION EXPOSURE AT 0.7μm WAVELENGTH

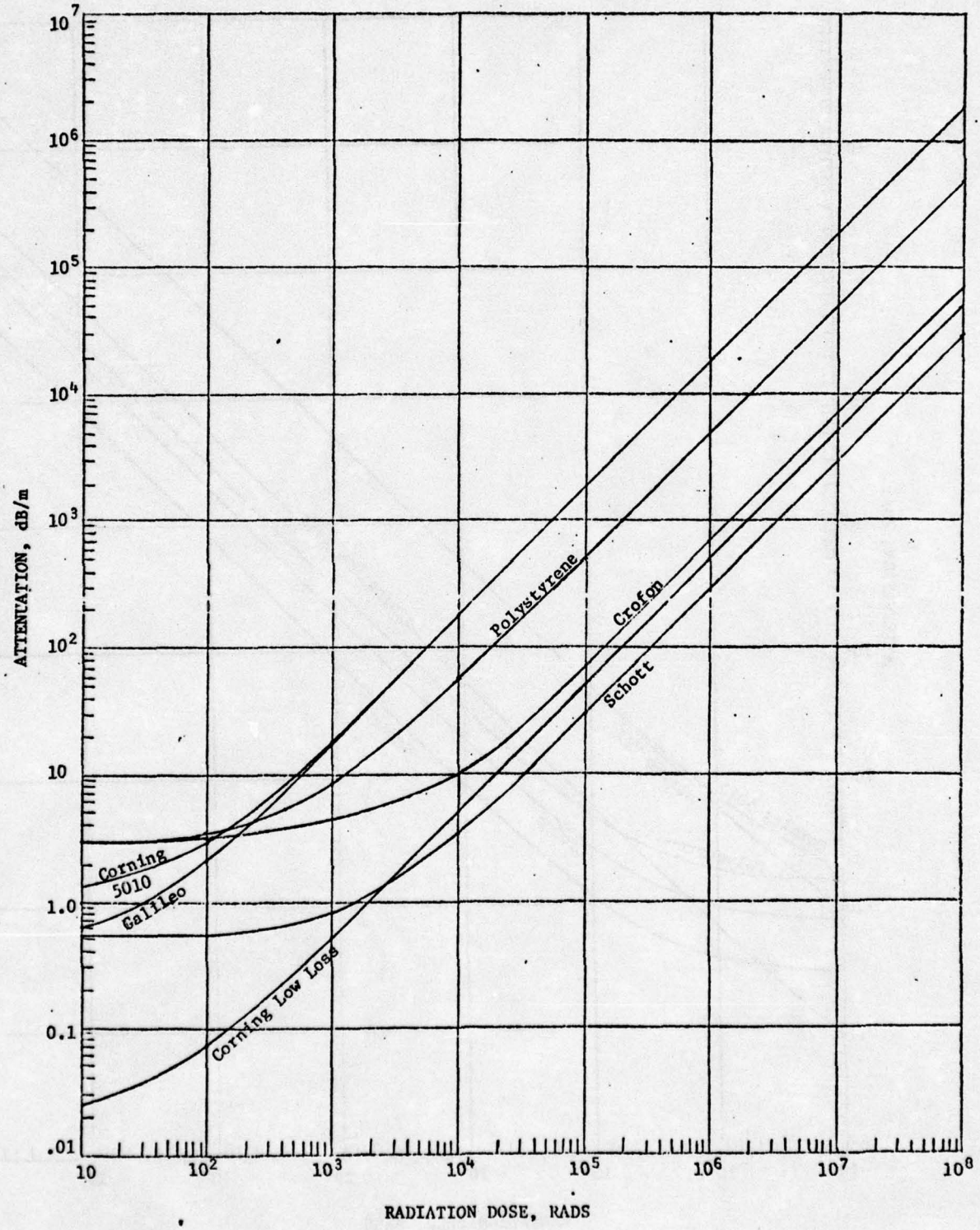


FIGURE 5. TOTAL MAXIMUM TRANSIENT ATTENUATION VS RADIATION EXPOSURE AT 1.06μm WAVELENGTH

TABLE 5

AVERAGE VALUES OF TRANSIENT INDUCED ATTENUATION DUE TO RADIATION EXPOSURE IN dB km^{-1} rad^{-1} 10 MILLISECONDS AFTER EXPOSURE

Fiber	Wavelength				
	0.6μm	0.7μm	0.8μm	0.9μm	1.06μm
Corning 5010	50	40	30	20	10
Corning Low Loss Type B	0.54	0.27	0.14	0.08	0.02
Galileo K2K	50	40	30	20	10
Schott Vitreous Silica	0.12	0.08	0.05	0.03	0.03
Crofon	0.08	0.05	0.03	0.02	0.02
Polystyrene	0.15	0.12	0.13	0.14	0.18

attenuation at high radiation doses of all the fibers considered, it does not have the lowest total attenuation 10 milliseconds after irradiation since its transient effect does not fall off as rapidly as that of some of the other fibers. At a wavelength of 0.7μm the Crofon fiber has the lowest total attenuation at high radiation doses although the Schott vitreous silica fiber is not far behind. At a wavelength of 1.06μm the Corning low loss, Type B fiber has the lowest overall total attenuation 10 milliseconds after irradiation. The attenuation of the Crofon fiber matches that of the Corning low loss, Type B fiber at high radiation exposure. Again the Schott vitreous silica fiber is not far behind in this exposure region.

At sufficiently high optical power densities the attenuation coefficient of optical fiber may become dependent upon input power density due to backward-directed, stimulated Raman and Brillouin scattering. This dependence has been investigated by Crow [10]. Using a pulsed neodymium-glass laser with a pulse-width of 1.2 milliseconds and a multimode energy of 9 joules as the source to introduce optical energy into a Corning low loss, multimode fiber, measurements of attenuation were made with input power densities up to 44 MW/cm^2. The attenuation coefficient of the fiber was found to be independent of input power density over the range measured. It will therefore be assumed in this investigation that the attenuation coefficient is independent of the input power density used.

COUPLING LOSSES

In addition to the attenuation within an optical fiber, losses occur in coupling the source to the fiber and the fiber to the explosive material. The basic coupling loss mechanisms are area mismatch, angular mismatch, packing fraction losses, and reflection losses. Area mismatch occurs when the area of the source is larger than the optical fiber bundle area and when the area of the bundle is larger than the area of the explosion-initiation area. It also occurs when there is translational misalignment between components. Angular mismatch occurs when the acceptance angle of the fiber is smaller than the

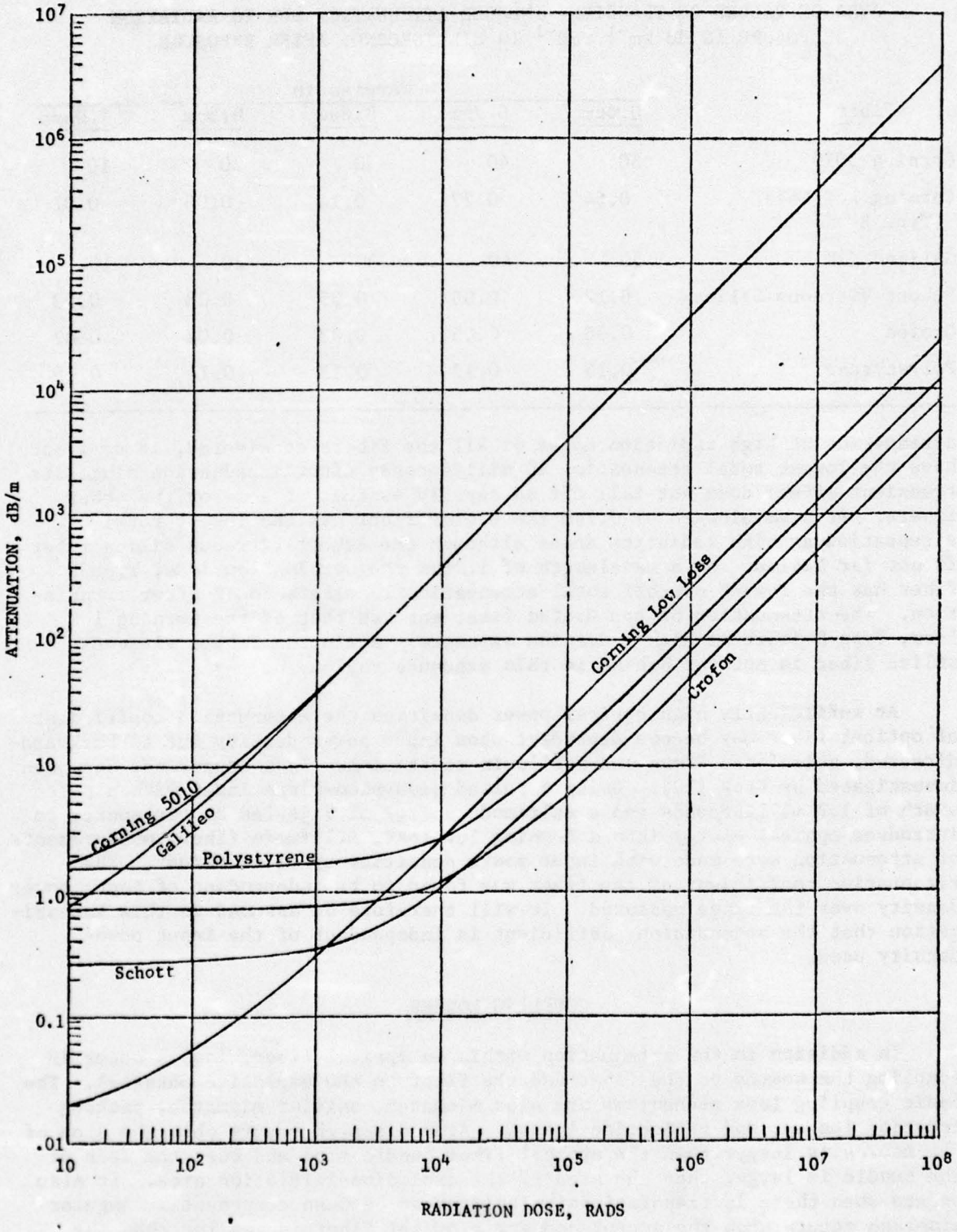


FIGURE 6. TOTAL ATTENUATION 10 MSEC AFTER IRRADIATION VS RADIATION EXPOSURE AT 0.7μm WAVELENGTH

emission angle of the source. It can also occur when the components are misaligned axially. Area and angular relationships can be traded with the use of lens systems. The best possible coupling due to area and angular relations can be determined from the conservation of radiance which yields the relationship

$$P_b \simeq P_s \frac{A_b \Omega_b}{A_s \Omega_s} \tag{1}$$

where P_b is the power that may be coupled into the fiber bundle, P_s is the power output of the source, A_s and A_b are the areas of the source and fiber bundle respectively, Ω_b is the solid angle of acceptance at the fiber bundle, and Ω_s is the solid angular spread of the source. This is limited, of course, by the conservation of energy, so that

$$P_b \leq P_s \tag{2}$$

The packing fraction is the ratio of the core areas of the fiber bundle to the total area of the bundle. This takes into account light incident on the fiber cladding and light incident on the space between the fibers which is therefore not coupled into the fibers but is instead lost. Reflection loss is due to the difference in the indices of refraction between propagation media. This can be reduced to some extent with the use of index matching material, but for this application the small improvement does not justify the additional effort and cost.

Lenses will be utilized at both the input and the output of the optical fiber in such a way as to minimize the coupling loss due to the area and angular relationships. The reflectance of the lenses will be taken into account. The reflectance per lens surface is 0.04 which when converted to decibels becomes a loss of 0.18 dB per surface or 0.36 dB for each lens used. The total input and output coupling loss, including the reflectance of the lenses, is shown for each fiber bundle under consideration in Table 6. The source is considered to be a solid-state laser of the type discussed with an output beam 10 mm in diameter with a beam divergence of 5 milliradians. The fibers are packaged in bundles as indicated in the table.

TABLE 6

TOTAL COUPLING LOSS

Fiber	Fiber Bundle	Total Coupling Loss
Corning 5010	45 mil dia.	2.7 dB
Corning Low Loss Type B	19 fiber	6.8 dB
Galileo K2K	45 mil dia.	2.3 dB
Schott Vitreous Silica	1 mm dia.	3.3 dB
Crofon	1 fiber	1.6 dB
Polystyrene	62 mil dia.	1.9 dB

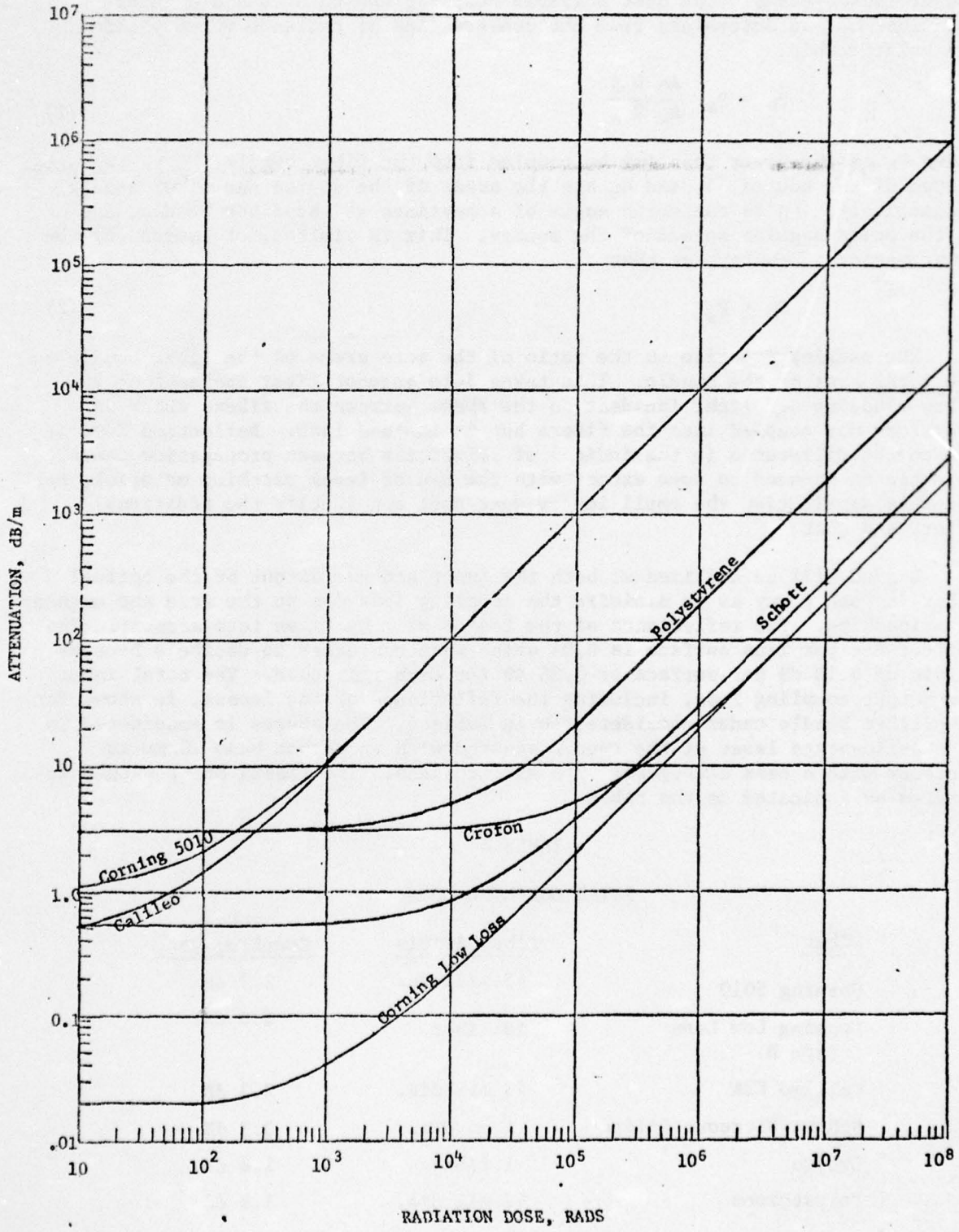


FIGURE 7. TOTAL ATTENUATION 10 MSEC AFTER IRRADIATION VS RADIATION EXPOSURE AT 1.06μm WAVELENGTH

OVERALL SYSTEM

In looking at the overall system, consideration will first be given to the system which is not exposed to radiation. The total attenuation in the system is due to the intrinsic attenuation of the fibers and the coupling loss. The Corning low loss fiber has the lowest intrinsic attenuation but also the highest coupling loss of the fibers under consideration. Figures 8 and 9 show the total system loss versus length for two wavelengths. At the 0.7μm wavelength various fibers exhibit the lowest total system loss at various lengths. For lengths less than 2 meters, the Crofon fiber system has the lowest total loss. For lengths between 2 meters and 12 meters the Galileo fiber system has the lowest total loss. For lengths between 12 meters and 15 meters the Schott vitreous silica fiber system has the lowest total loss. For lengths greater than 15 meters the Corning low loss fiber system has the lowest total loss of the fiber systems considered. At the 1.06μm wavelength the system employing the Galileo fiber exhibits the lowest total loss for lengths less than 12 meters, while for longer lengths the Corning low loss fiber system has the lowest total loss.

The maximum length of optical fiber which may be utilized for a specified source energy can be determined. As mentioned previously, available laser sources with output pulse energy in the 1 to 100 joule region may be utilized for this application. As a specific example a laser with a 10 joule output pulse will be considered. In decibels this energy may be expressed as 10 dBJ or 10 dB above 1 joule, that is

$$\text{Energy in dBJ} = 10 \log \frac{\text{Energy in joules}}{1 \text{ joule}} \qquad (3)$$

The energy required for initiation of explosion is 0.01 joule or -20 dBJ. This allows a maximum system loss of 30 dB. Deducting the coupling loss for each case shown in Table 6 and using the intrinsic attenuation of the fibers shown in Table 2 for wavelengths of 0.7μm and 1.06μm yields the maximum fiber lengths shown in Table 7.

TABLE 7

MAXIMUM FIBER LENGTH FOR A 10 JOULE SOURCE PULSE AND NO RADIATION EXPOSURE

Fiber	Maximum Length in Meters	
	0.7μm Wavelength	1.06μm Wavelength
Corning 5010	21	25
Corning Low Loss	1160	1160
Galileo K2K	79	69
Schott Vitreous Silica	103	51
Crofon	41	9.5
Polystyrene	19	9.4

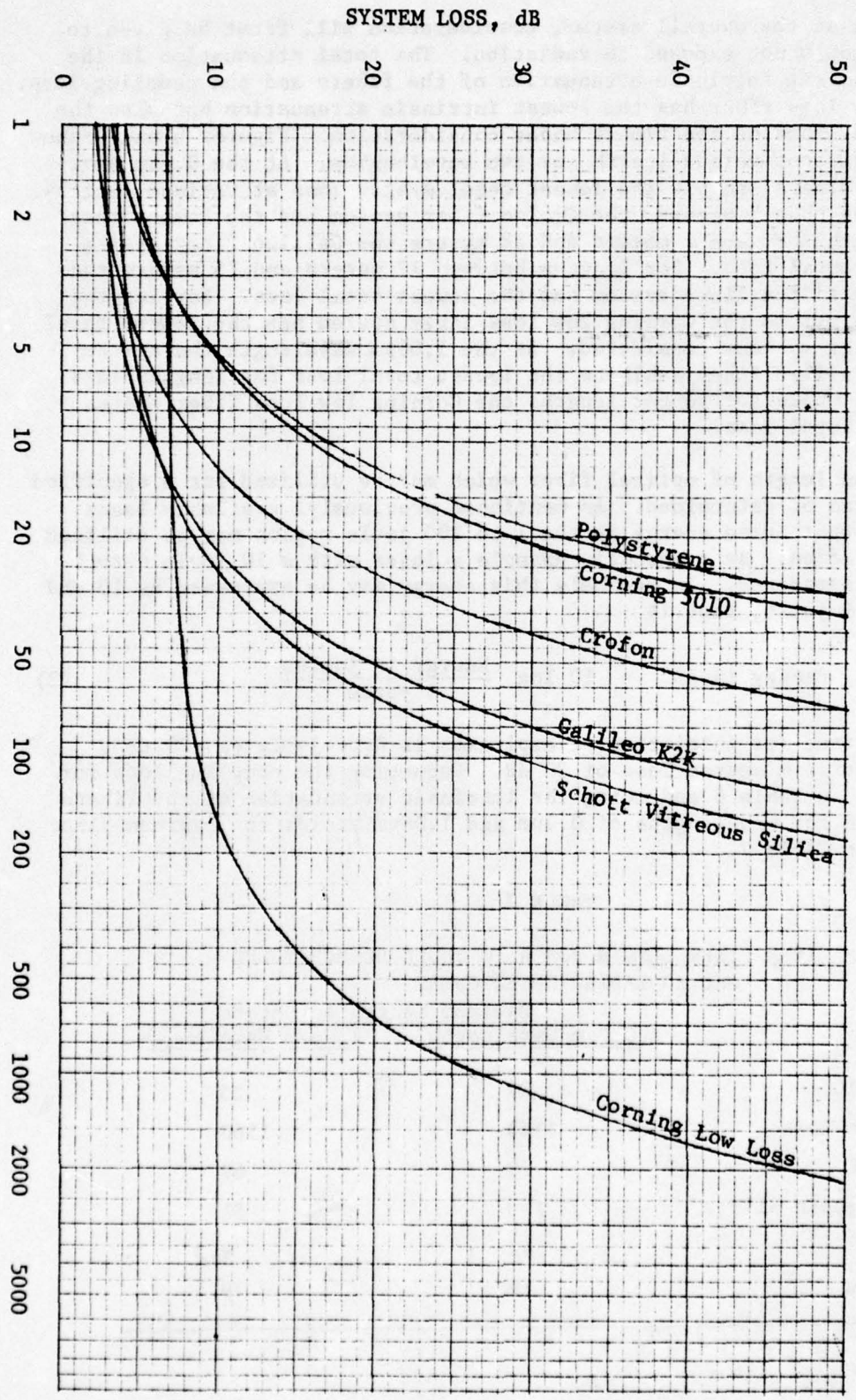


FIGURE 8. TOTAL SYSTEM LOSS VS LENGTH WITH NO RADIATION EXPOSURE FOR 0.7μm WAVELENGTH.

When the system is exposed to radiation the maximum fiber length over which the laser pulse can propagate and still deliver sufficient energy for initiation of explosion decreases. The transient effects are much more severe than the permanent effects. The permanent effect on the laser is a reduction of output energy for radiation doses above 10^4 rads to approximately 95 percent of that before irradiation. The fiber attenuation reaches its total permanent value as shown in Figures 2 and 3 for the two wavelengths under consideration. The maximum fiber length that can be utilized for initiation of explosion is shown in Figures 10 and 11 as functions of radiation dose for the two wavelengths. At both wavelengths the Corning low loss fiber yields the longest maximum length at low radiation doses while the Schott vitreous silica yields the longest maximum length at high radiation doses. These results show that an optical fiber explosion-initiation system is still feasible after the system has been exposed to radiation in applications where sufficient time lapses after the radiation exposure to allow the effects to reach their permanent values. Such time durations are typically several hours.

There are applications where initiation of explosion must occur in much shorter times after exposure to radiation. Such an application is the explosion initiation utilized for missile staging. In this situation the explosion initiation normally must occur within a time window of less than 10 milliseconds. Due to the relatively low pulse repetition rates of lasers with sufficient output energy for this application, there is not sufficient time within the time window for a second pulse to be initiated ff the first one fails. As was pointed out in the discussion of sources, the first flash of the pump lamp following irradiation often fails to produce stimulated emission. It is therefore not feasible to use a laser which is unprotected from radiation for the initiation of explosion under these restrictions. In order for the laser to be used in this case, it must be protected by radiation hardening, radiation shielding, or both.

In a system where the laser source is completely protected from radiation effects, the degradation is caused by the radiation effects on the optical fibers. For this situation maximum lengths were determined during the maximum transient attenuation and 10 milliseconds after irradiation at the two wavelengths. These results are shown in Figures 12, 13, 14, and 15 for a 10 joule pulse source. During the maximum transient absorption the maximum length is less than 10 meters for all fibers at 10^4 rads and less than 1 meter at 10^5 rads at a wavelength of 1.06μm. The lengths at these radiation doses are even shorter at the 0.7μm wavelength. The maximum lengths are somewhat improved 10 msec after irradiation. At the 1.06μm wavelength the maximum length is approximately 10 meters at 10^5 rads and 1 meter at 10^6 rads for the best performing fibers. Again the corresponding lengths are somewhat lower at the 0.7μm wavelength. If the source energy is increased to 100 joules, the maximum fiber length increases by approximately 40 percent. Even with the increased source energy and with the source completely radiation protected, this system is apparently not useful at radiation doses above 10^6 rads if it is required to operate within 10 milliseconds after irradiation.

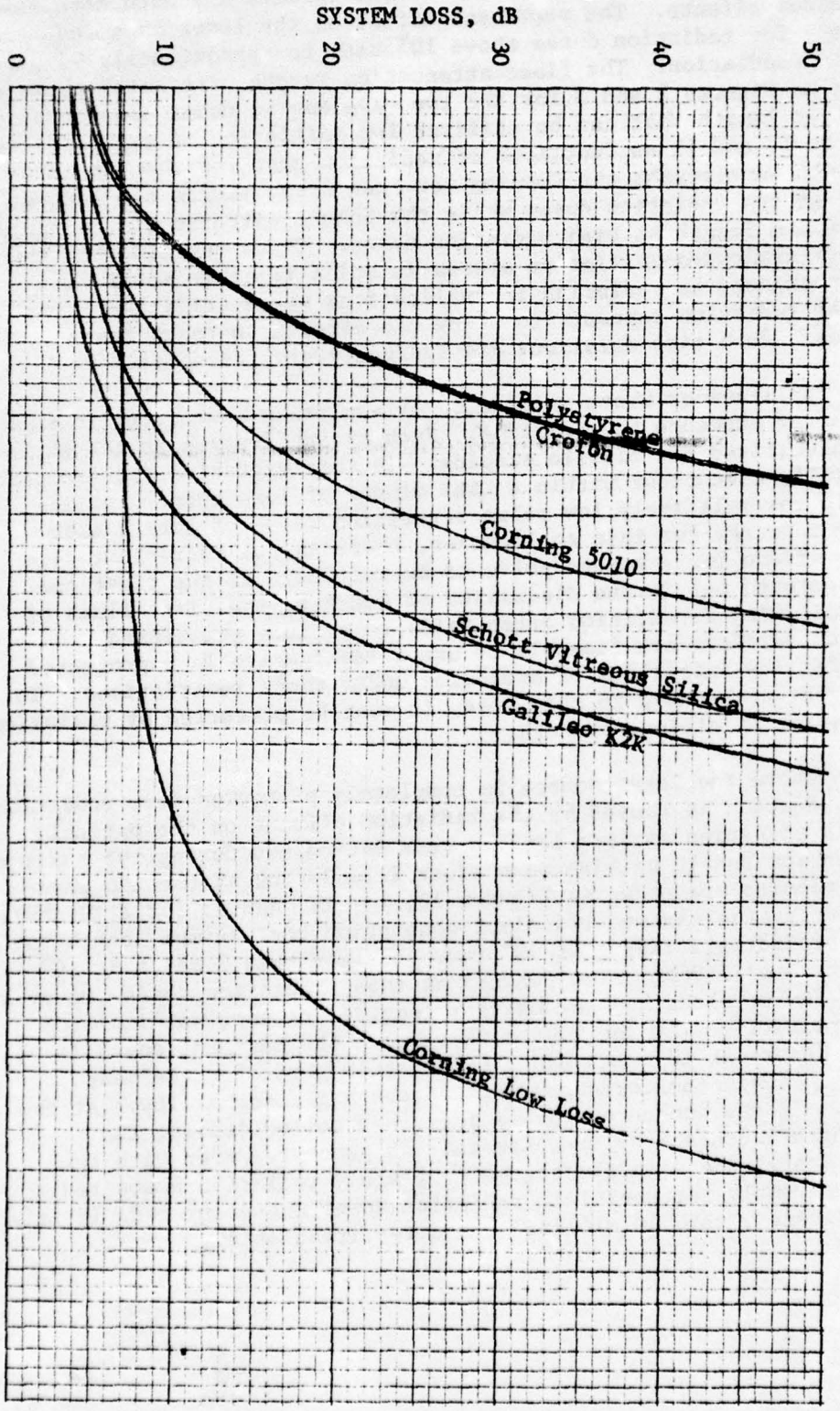


FIGURE 9. TOTAL SYSTEM LOSS VS LENGTH WITH NO RADIATION EXPOSURE FOR 1.06μm WAVELENGTH.

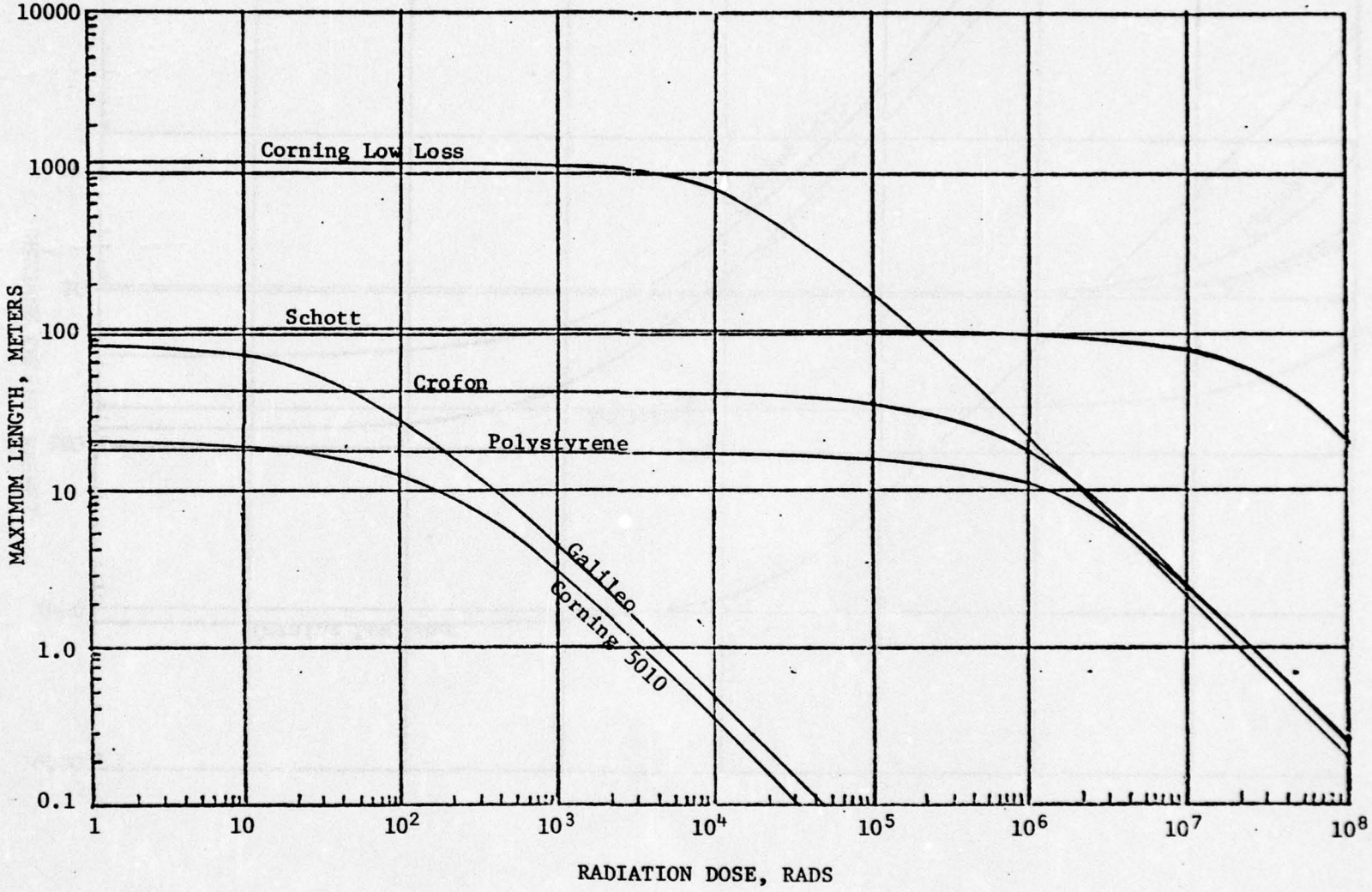


FIGURE 10. MAXIMUM FIBER LENGTH FOR PERMANENT ATTENUATION AT 0.7μm WAVELENGTH AFTER RADIATION EXPOSURE USING A 10 JOULE SOURCE

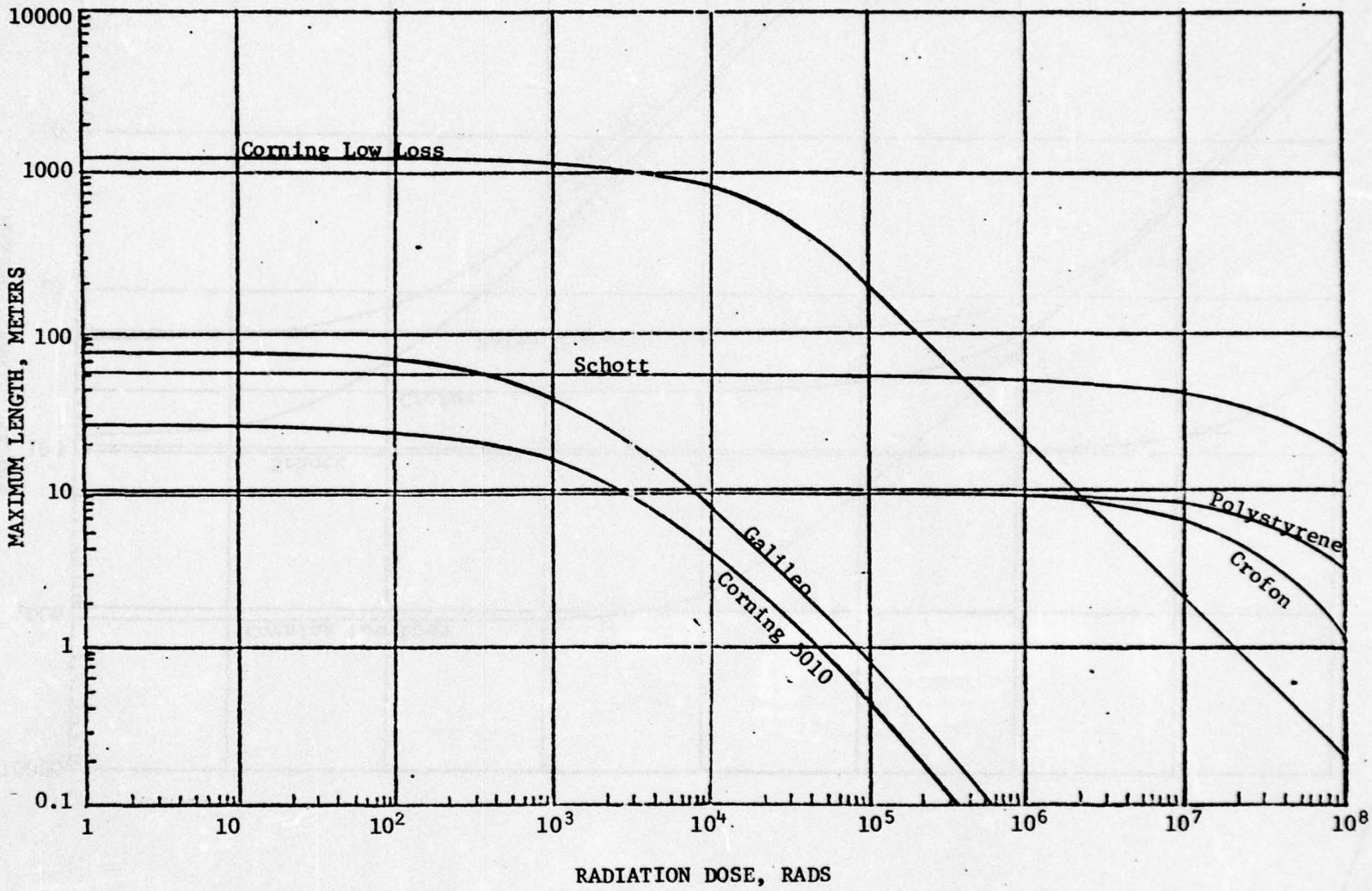


FIGURE 11. MAXIMUM FIBER LENGTH FOR PERMANENT ATTENUATION AT 1.06μm WAVELENGTH AFTER RADIATION EXPOSURE USING A 10 JOULE SOURCE

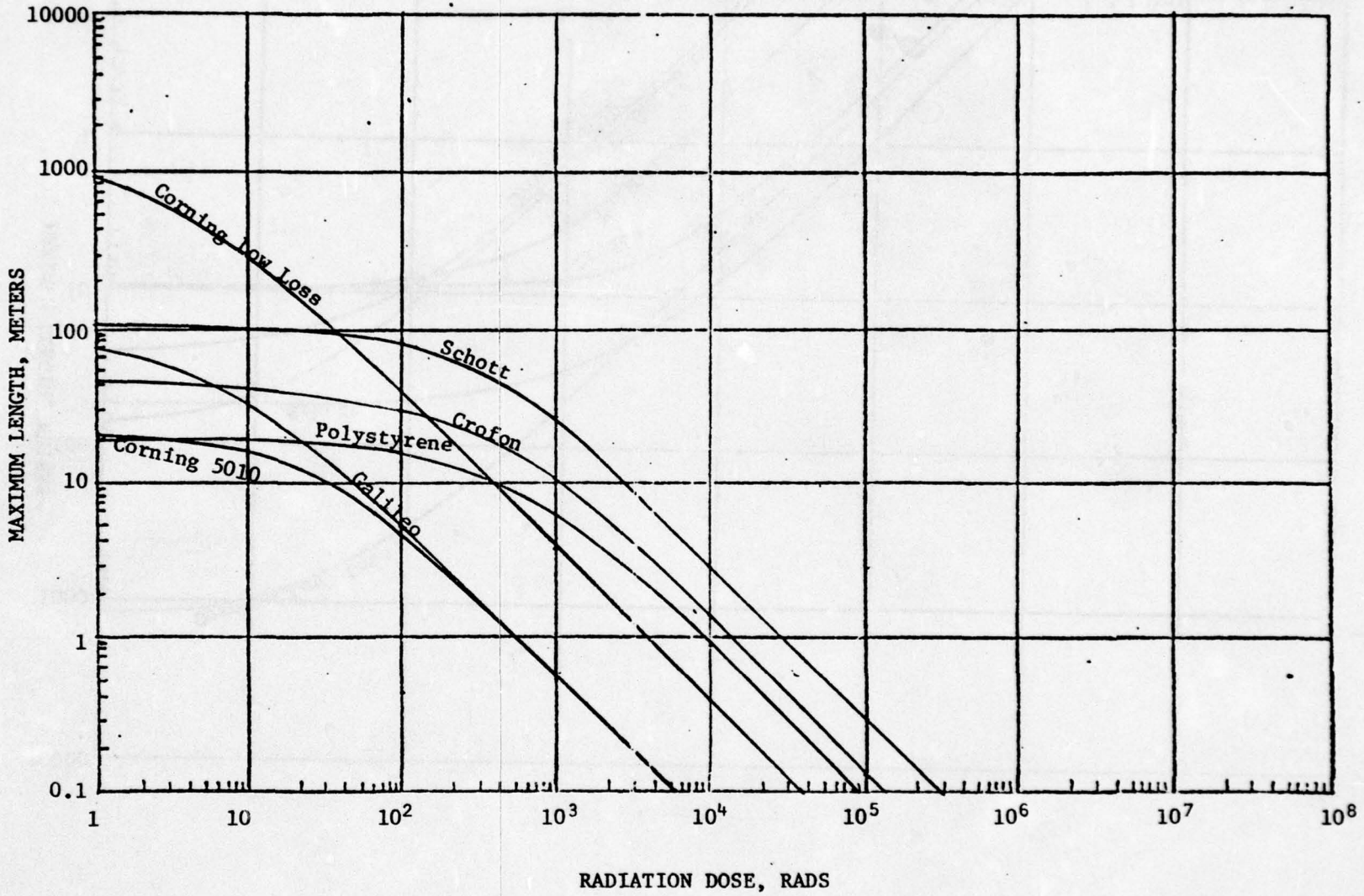


FIGURE 12. MAXIMUM FIBER LENGTH FOR MAXIMUM TRANSIENT ATTENUATION AT 0.7μm WAVELENGTH USING A 10 JOULE SOURCE

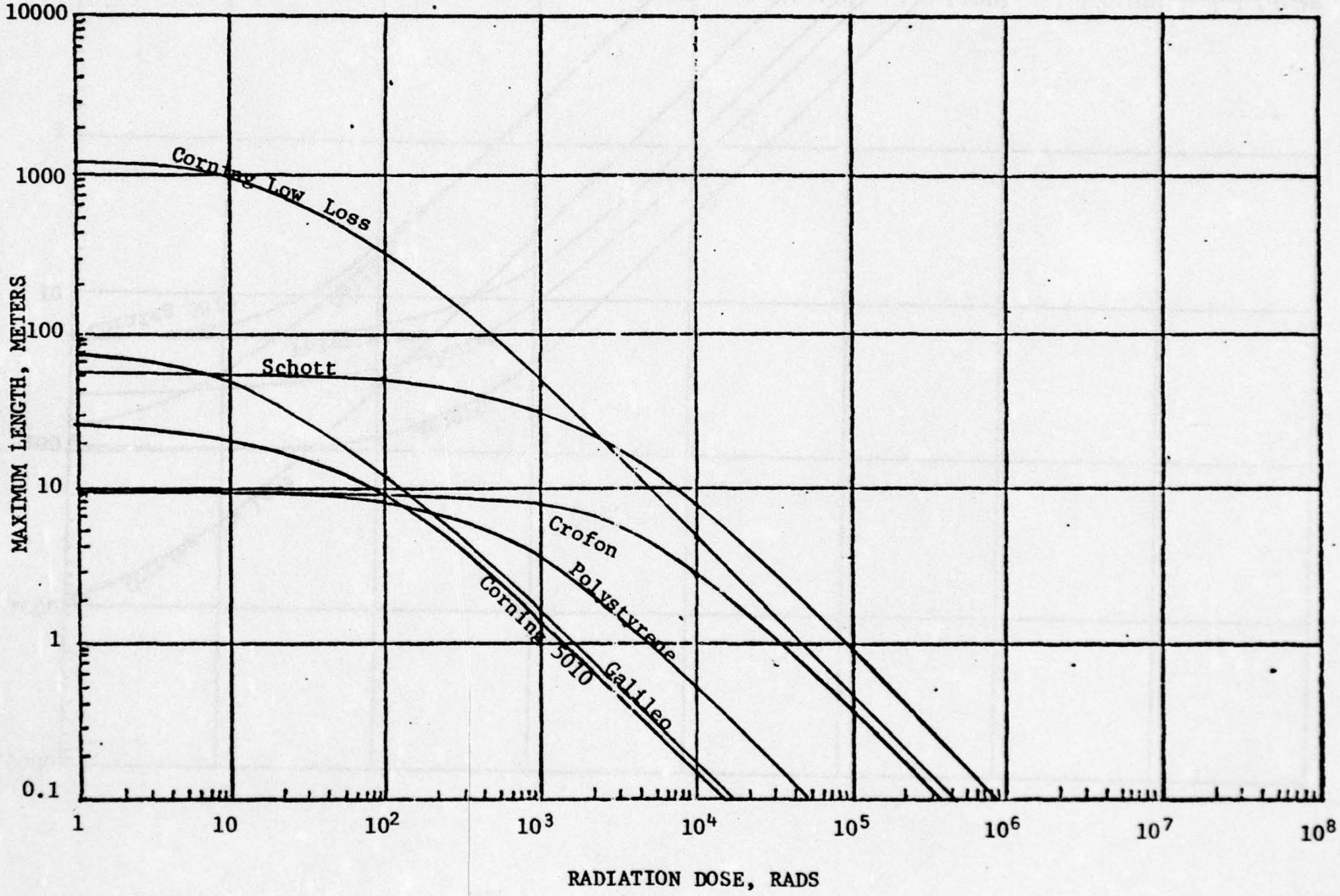


FIGURE 13. MAXIMUM FIBER LENGTH FOR MAXIMUM TRANSIENT ATTENUATION AT 1.06μm WAVELENGTH USING A 10 JOULE SOURCE

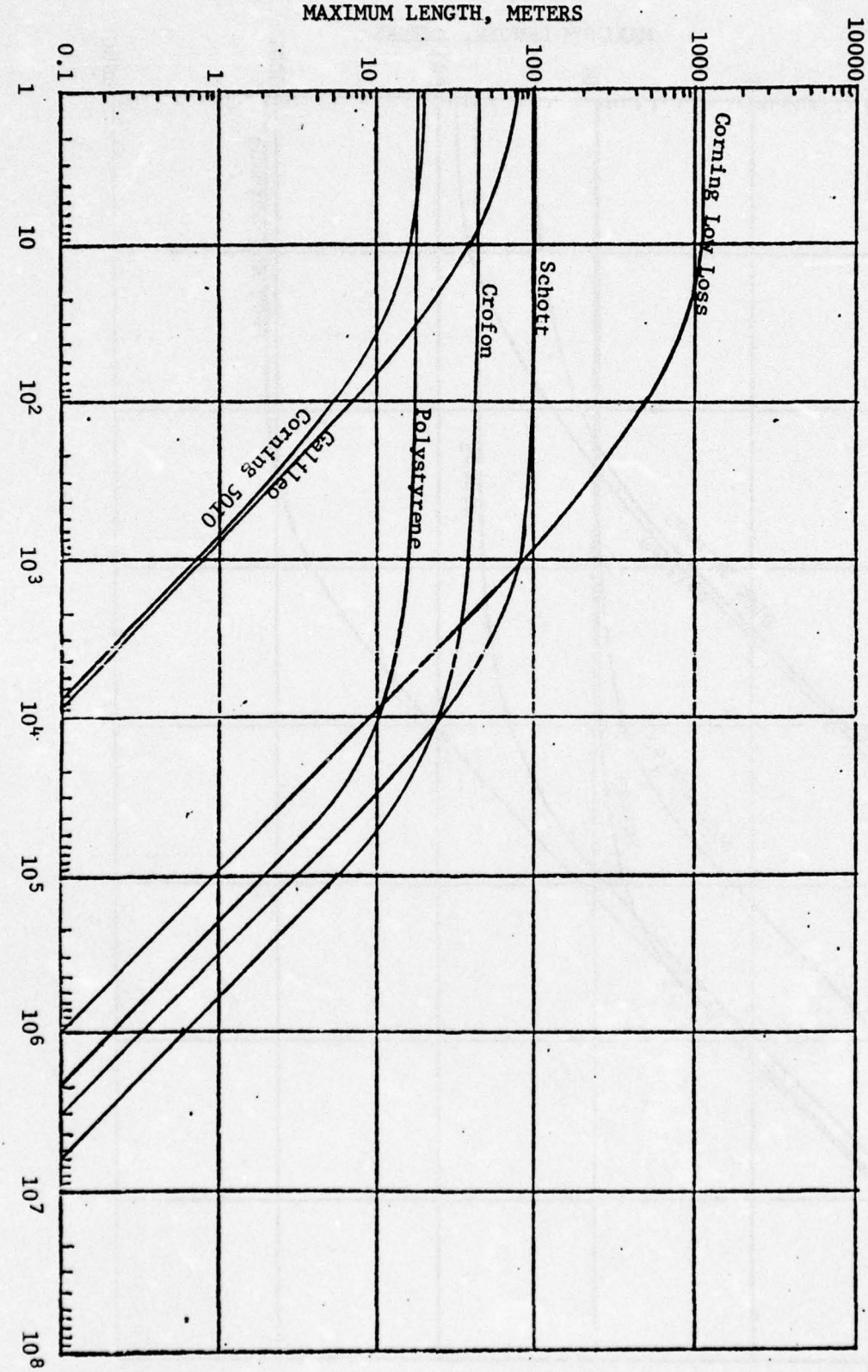


FIGURE 14. MAXIMUM FIBER LENGTH 10 MSEC AFTER IRRADIATION AT 0.7μm WAVELENGTH USING A 10 JOULE SOURCE

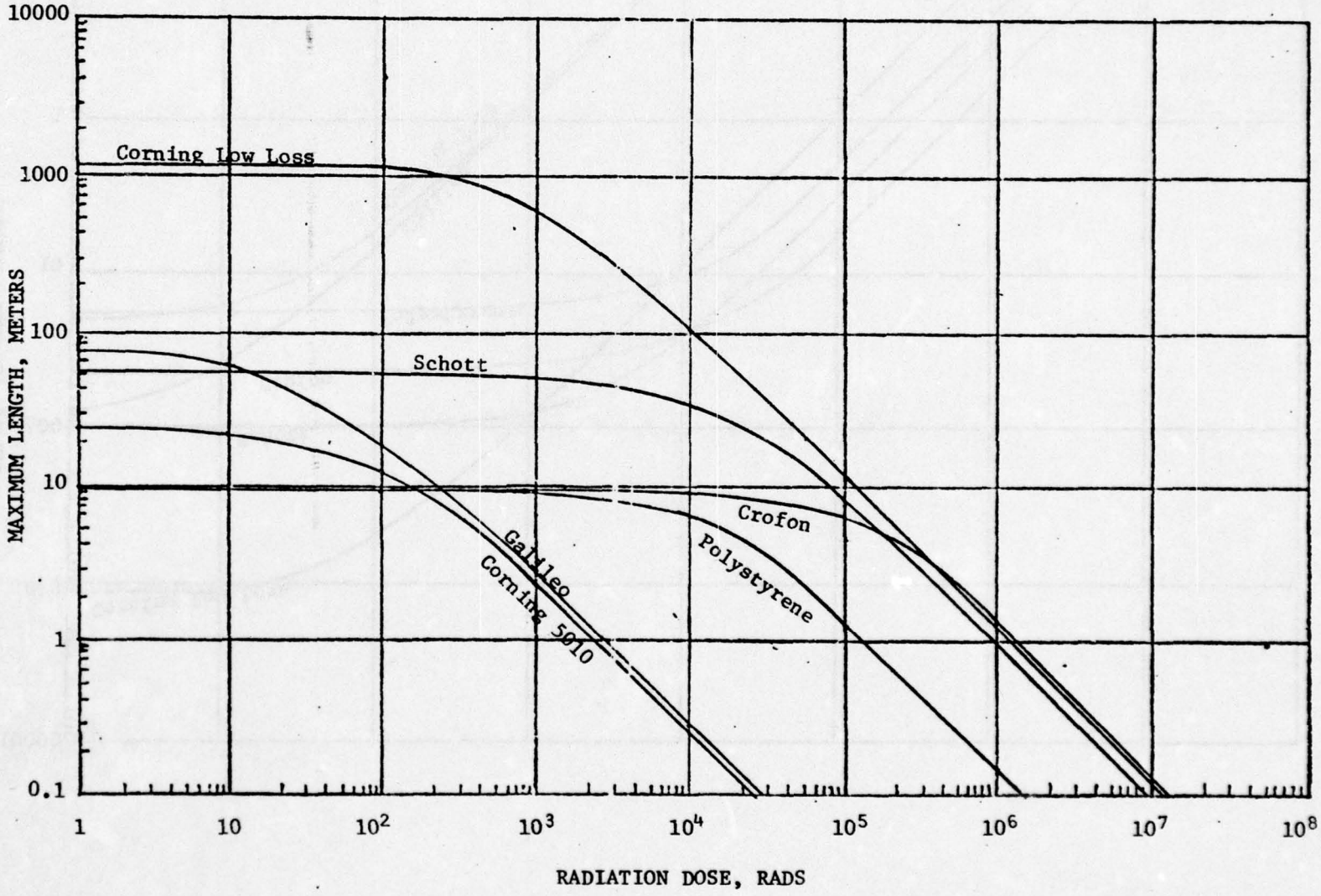


FIGURE 15. MAXIMUM FIBER LENGTH 10 MSEC AFTER IRRADIATION AT 1.06μm WAVELENGTH USING A 10 JOULE SOURCE

CONCLUSIONS AND RECOMMENDATIONS

The use of lasers and optical fibers to initiate explosion is feasible in an environment free of irradiation and in some cases in an environment subject to irradiation. There are applications, however, where such an approach is not feasible. In the radiation-free situation fiber lengths of over 1000 meters may be implemented. The optimum optical fiber depends on the length of the fiber and the wavelength of the source. Solid-state lasers such as neodymium-glass and neodymium-Yag lasers operating at 1.06μm and ruby lasers operating at 0.6943μm provide pulse energy sufficient for this application, while semiconductor lasers lack sufficient pulse energy.

In a radiation environment the Schott vitreous silica fiber is the best overall choice of fibers due to its low permanent-induced absorption and its relatively low maximum transient-induced absorption due to radiation compared to the other fibers considered. The transient-induced absorption is considerably higher than the permanent-induced absorption. The optical fiber explosion-initiation system will operate over distances of several tens of meters after exposure to radiation doses of 10^6 to 10^8 rads if the transient effects are allowed to decay leaving only the permanent effects.

It is applications where the system is subjected to high radiation doses and is required to operate shortly following irradiation while the transient effect is still large that the optical fiber explosion-initiation system no longer appears feasible. The laser source must be radiation protected through radiation hardening and shielding techniques in order for the system to operate at all. Even then, the transient-induced absorption limits the fiber length over which sufficient pulse energy to initiate explosion may be propagated. These lengths become too small to be of any use within 10 msec after exposure to radiation doses above 10^6 rads.

This approach has provided a first order analysis into the feasibility of utilizing an optical fiber explosion initiation system in a radiation environment. As more information becomes available secondary effects may be taken into account. An experimental system based on this analysis would also be useful. Surface radiation effects on the fiber ends have not been taken into account. These effects may be of sufficient significance to cause the coupling loss to increase with radiation dosage. This would further decrease the maximum fiber lengths that could be utilized.

REFERENCES

[1] Karl O. Brauer, *Handbook of Pyrotechnics*, Chemical Publishing Co., Inc., New York, 1974.

[2] DuPont Explosives Specialties Manual.

[3] Arthur W. Mittendorf, "Feasibility Study for Laser Initiation of Explosives," Picatinny Arsenal Technical Report AD 875340, Unidynamics/Phoenix, Inc., Contract No. DAAA 21-69-C-0049, May 1970.

[4] Laser Focus Buyers' Guide, Advanced Technology Publications, Inc., February 1976.

[5] P. A. Compton, "Radiation Effects on Lasers," Radiation Effects on Guided Missile Electronic Equipment, Report No. FR 63-17-173, 15 Jan-15 Jul 1963, Hughes Aircraft Co., Bureau of Naval Weapons Contract NO w63-0486-d.

[6] P. L. Mattern, L. H. Watkins, C. D. Skoog, J. R. Brandon, and E. H. Barsis, "The Effects of Radiation on the Absorption and Luminescence of Fiber Optic Waveguides and Materials," IEEE Trans. on Nuclear Science, NS-21: 81-95, December 1974.

[7] B. D. Evans and G. H. Sigel, Jr., "Permanent and Transient Radiation Induced Losses in Optical Fibers," IEEE Trans. on Nuclear Science, NS-21: 113-118, Decmeber 1974.

[8] B. D. Evans and G. H. Sigel, Jr., "Radiation Resistant Fiber Optic Materials and Waveguides," IEEE Trans. on Nuclear Science, NS-22: 2462-2467, December 1975.

[9] P. L. Mattern, L. M. Watkins, C. D. Skoog, and E. H. Barsis, "Absorption Induced in Optical Waveguides by Pulsed Electrons as a Function of Temperature, Low Dose Rate Gamma and Beta Rays, and 14 MeV Neutrons," IEEE Trans. on Nuclear Science, NS-22: 2468-2474, December 1975.

[10] John D. Crow, "Power Handling Capability of Glass Fiber Lightguides," Applied Optics, 13: 467-468, March 1974.

1976 USAF-ASEE SUMMER FACULTY RESEARCH PROGRAM

Sponsored By

THE AIR FORCE OFFICE OF SCIENTIFIC RESEARCH

Conducted By

AUBURN UNIVERSITY AND OHIO STATE UNIVERSITY

PARTICIPANT'S FINAL REPORT

DENSITY AND TEMPERATURE DEPENDENCE STUDIES OF THE THALLIUM MERCURY EXCIMER SYSTEM

Prepared By:	P. W. Chan, Ph.D.
Academic Rank:	Associate Professor
Department and University:	Department of Electrical Engineering Colorado State University
Assignment:	Kirtland AFB, NM Air Force Weapons Laboratory Advanced Laser Technology Div Electrical Laser Branch
USAF Research Colleague:	D. Drummond, Ph.D.
Date:	July 30, 1976
Contract No.	F44620-75-C-0031

1976 USAF-ASEE SUMMER FACULTY RESEARCH PROGRAM

Sponsored By

THE AIR FORCE OFFICE OF SCIENTIFIC RESEARCH

Conducted By

AUBURN UNIVERSITY AND OHIO STATE UNIVERSITY

PARTICIPANT'S FINAL REPORT

DENSITY AND TEMPERATURE DEPENDENCE STUDIES OF THE THALLIUM MERCURY EXCIMER SYSTEM

Prepared By:	P. W. Chan, Ph.D.
Academic Rank:	Associate Professor
Department and University:	Department of Electrical Engineering Colorado State University
Assignment:	Kirtland AFB, NM Air Force Weapons Laboratory Advanced Laser Technology Div Electrical Laser Branch
USAF Research Colleague:	D. Drummond, Ph.D.
Date:	July 30, 1976
Contract No.	F44620-75-C-0031

ABSTRACT

Density and temperature dependence of the thallium-mercury excimer fluorescence spectra has been studied for mercury densities from 3×10^{18} to 3×10^{19} Hg/cc and for temperatures ranging from 973°K - 1173°K. Two clearly defined regimes in density dependence are identified. For density range of 3×10^{18} - 1×10^{19} Hg/cc, the normalized fluorescence intensity varies quadratically with mercury density. The density dependence data of this quadratic regime gives a molecular formation rate constant of about 1.4×10^{-31} cm^6/sec. For density range of 1×10^{19} - 3×10^{19} Hg/cc, the fluorescence intensity increases linearly with mercury density, indicating the system is in thermal equilibrium. Temperature dependence study of the fluorescence intensity in this linear regime at 2.0×10^{19} Hg/cc from T = 973°K to 1173°K indicates that the fluorescence intensity varies exponentially as 1/T°K as predicted by quasi-static theory, confirming the system is in equilibrium and gives a well-depth of the upper $B^2\Sigma_{\frac{1}{2}}$ state to be about 4000 cm^{-1}.

INTRODUCTION

In a previous study by Drummond and Schlie[1] of the fluorescence spectra of the thallium-mercury (TlHg) excimer system, strong fluorescence bands were observed at 4590 Å and at 6560 Å. They estimated the molecular formation rate and gain at these bands and gave promising operating conditions for the TlHg excimer laser. However, since the study was performed at only one temperature (540°C) and over a limited density range due to practical limitations imposed on by the pyrex fluorescence cell used, no temperature dependence or detailed density dependence studies can be made. Such studies are important for understanding the kinetics and thermal equilibrium state of the excimer system, and for calculation of important parameters such as the well-depths of the molecular states, molecular formation rates and molecular potentials and hence the gain and performance of the excimer laser. Although some data on the TlHg molecular spectrum are available through the work of Winans and Pearce[2], details of this work are apparently unpublished and are not available to us at this time.

OBJECTIVES

Thus the primary objectives of the present investigation are to study the pressure dependence of the fluorescence intensity, and especially to identify the linear dependence regime where the system is in equilibrium, and where meaningful temperature dependence studies can be made. Using the temperature dependence data and the quasi-static theory of spectral

line broadening as expressed by Kuhn and others[3], the molecular potentials and well-depths can be calculated. From the potential energy curves for the excited and ground state molecules, the stimulated emission coefficients can be predicted[4].

APPARATUS AND EXPERIMENTAL METHODS

The experimental arrangement is essentially the same as used in (1) with the exception that fused quartz cells were used throughout and a fluorescence monitor photomultiplier was added. The complete layout is shown schematically in Figure 1. The 3776 Å pump radiation from an Osram thallium lamp was chopped at 90 Hz before entering the cell, and the signal from the cooled RCA C31034A photomultiplier (PMT) was fed into a lock-in amplifier (PAR 124A) and displayed on a strip-chart recorder. A J-Y Optical Systems 0.6 meter monochromator with a holographic grating was used for spectral analysis. The scattered light of the monochromator was very low so that no pre-filtering was necessary. The spectral response of the complete optical system was determined using a quartz-iodide standard spectral irradiance lamp (ES-7501) supplied by Eppley Lab, Inc. operated at 6.5 amps. The non-blazed holographic grating monochromator used in conjunction with the RCA C31034A PMT gave a rather flat spectral response from 4000 Å - 7000 Å as shown in Figure 2, allowing fairly accurate corrections to be made in the measured intensities.

The mercury vapor density was determined by previously determining the total weight of mercury placed in the fused quartz cell. The volume

of the cell is obtained by filling the cell with methanol and known to about $\pm$ 5% accuracy. The mercury was 99.9999% pure and the thallium used was 99.95% pure. Samples were weighed on an analytical balance to an accuracy of 0.1 mg and introduced directly into the cell, which had been preheated to 400°C under a vacuum of 10^{-6} torr for one half hour. The cell was then sealed under vacuum. The main impurity was probably thallium oxide. One of the experimental problems yet to be solved is the technique of introducing as little Tl into the cell as possible to avoid self absorption of the 5350 Å light at temperatures above 650°C, where all the fluorescence light tends to shrink to the top of the cell. A more controlled method is being developed to put just the right amount of Tl into the cell without strong self-absorption.

Before measurement of fluorescence spectrum, it is important to be sure that all the mercury has been evaporated. This was achieved by monitoring the fluorescence band at 4590 Å for each cell (i.e., for each filling density) as the temperature of the oven was increased. Initially when the mercury was not entirely evaporated, the fluorescence intensity increased with temperature. However, as soon as all the mercury was evaporated, the intensity dropped. It was found that for the highest density used (3.1×10^{19} atm/cc), 700°C was sufficient to evaporate all the mercury. Hence in studying density dependence, 700°C was used as the operating temperature which was monitored by four thermocouples.

RESULTS AND ANALYSIS

1. Fluorescence Spectrum

The principal features of the fluorescence spectrum are the same as observed in (1). Readers are referred to that work for details. Additional features were observed in the blue fluorescence band peaked at 4590 Å with eight oscillations at high mercury densities (2-3 X 10^{19} Hg/cc). No additional oscillations, however, were observed in the red band near 6560 Å.

2. Density Dependence of Fluorescence Spectrum

The density dependence of the fluorescence spectrum was studied at 700°C for a range of mercury densities from 3 X 10^{18} to 3 X 10^{19} Hg/cc. The normalized intensity ratio of the blue band with respect to the 5350 Å resonance line per cm^{-1} corrected for spectral response is shown in Figure 3. Two distinct regimes can be readily identified. From about 3 X 10^{18} - 1 X 10^{19} Hg/cc, a quadratic region of the fluorescence intensity versus mercury density is observed. This regime, also reported in reference (1), indicates the region where three-body molecular formation is dominant. At a density of 6 X 10^{18} Hg/cc. the measured spectrum indicates that 16 X 10^{-3} of the radiated intensity is in the molecular bands for the optically thin case. Hence the percentage of atoms bound into the lower excimer levels are 19.4 X 10^{-3} by taking into the ν^4 dependence of the intensity. Assuming an untrapped Tl atomic lifetime of 7 ns[5], the rate

of molecular formation is 5×10^{6} sec^{-1} and the molecular formation rate constant is 1.4×10^{-31} cm^{6} sec^{-1}. Above a density of 1×10^{19} Hg/cc a regime where the fluorescence intensity increases linearly with mercury density is observed. The identification of this linear regime is very important since this regime indicates that the upper lying states are in equilibrium with the free Tl atomic states. Since the quasi-static theory depends on this equilibrium assumption to obtain the potential curves from temperature dependence measurements, such measurements are only useful in this linear regime. A comment should be made on the data point obtained at a density of 3×10^{18} Hg/cc. At this density ($\sim$ 0.1 atm), it is still too high for the curve to go back to a linear regime where the bound TlHg population is negligible, and where free Tl atoms undergoing binary collisions with mercury atoms is dominant, producing free-free emission which is linearly proportional to the mercury density. The high value of this data point is probably due to poor signal-to-noise ratio at relatively low density of mercury.

3. Temperature Dependence of Fluorescence Spectrum

A semi-log plot of the normalized intensity ratio of the blue fluorescence band intensity versus 1000/T(°K) is shown in Figure 4 for a temperature range of 973°K to 1173°K. It can be clearly seen that it is a straight line as predicted by the Boltzmann factor. The slope of the straight line, according to quasi-static theory, gives a well-depth of 4000 cm^{-1} for the upper $B^{2}\Sigma_{\frac{1}{2}}$ state. In principle the potential energy curves can be obtained from the temperature dependent spectra. However,

due to poor signal-to-noise ratio (SNR) at high temperatures above 800°C, good spectral traces cannot be obtained. These potential curves will be given in a future publication.

4. Stimulated Emission Coefficient and Gain Estimates

The stimulated emission coefficient may be calculated using the measured spectrum and the relationship between the Einstein A and B coefficients as reported in (1). The present data essentially substantiate those reported earlier and therefore will not be discussed in detail. Suffice to mention that a stimulated emission coefficient of about 1% cm^{-1} is obtained at both the blue and red fluorescence bands. The calculation of gain is much uncertain because of lack of information regarding production and destruction processes.

CONCLUSIONS AND RECOMMENDATIONS

In summary, detailed density and temperature dependence study of the TlHg excimer fluorescence spectra have been carried out. Important kinetic parameters such as molecular formation rate constant and upper state well-depth are obtained. The complete potential curves will be obtained very shortly.

Needless to say, the most important experiment to be carried out on the TlHg system is an experimental demonstration of the lasing action of the excimer system. This work is being carried out at this laboratory by Dr. D. Drummond. Basic studies along the line of measuring life-times of

molecular states, detail theoretical calculations of the TlHg system kinetics, discharge study of the TlI salt and Hg are also much needed in order to obtain a better understanding of the Tl-Hg system and making it into an efficient laser system.

ACKNOWLEDGEMENTS

I wish to thank most heartily my research colleague, Dr. D. Drummond, for his invaluable help and guidance and for his choice of a most interesting and suitable project for the summer research program. I also wish to thank Dr. L. A. Schlie for his interest in this work and for numerous technical discussions in this and related projects.

I am indebted to Lt Col P. Tannen, Chief, Electrical Laser Branch, and to Dr. A. Guenther, Chief Scientist of the Air Force Weapons Laboratory, for providing a most cordial and helpful work environment and general support. The assistance of the secretarial staff, Mrs. Brenda St.James and Miss Becky Smith, and the laboratory assistance of Tim Gilmore are gratefully acknowledged.

The author is grateful to AFOSR, Air Force Systems Command for financial support of the summer faculty research program. Thanks are also due to ASEE and Auburn University and in particular to Mr. Fred O'Brien for his administration of the program.

REFERENCES

1. D. L. Drummond and L. A. Schlie, "The Thallium Mercury Excimer and Its Potential as a Laser", to be published in Chem. Phys. Lett. (1976).

2. J. G. Winans and W. J. Pearse, Phys. Rev. 74, 1262A (1948).

3. H. Kuhn, Phil. Mag. 18, 987 (1934); H. Margenan and W. W. Watson, Rev. Mod. Phys. 8, 22 (1936); D. R. Bates, Monthly Notices Roy. Astron. Soc. 112, 40 (1952).

4. A. V. Phelps, "Tunable Gas Lasers Utilizing Ground State Dissociation", JILA Report No. 110, University of Colorado, Boulder, Colorado (1972).

5. A. Gallagher and A. Lurio, Phys. Rev. 136, A87, (1964).

LIST OF FIGURES

Figure 1. Experimental Arrangement of Fluorescence Measurement

Figure 2. Spectral Response of Optical System

Figure 3. Density Dependence of Fluorescence Intensity
The co-ordinate is the intensity of the 4590 Å band normalized to the intensity of the 5350 Å resonance line per unit wave number corrected for the spectral response of the optical system.

Figure 4. Temperature Dependence of Fluorescence Intensity
Co-ordinate is the same as described in Figure 3.

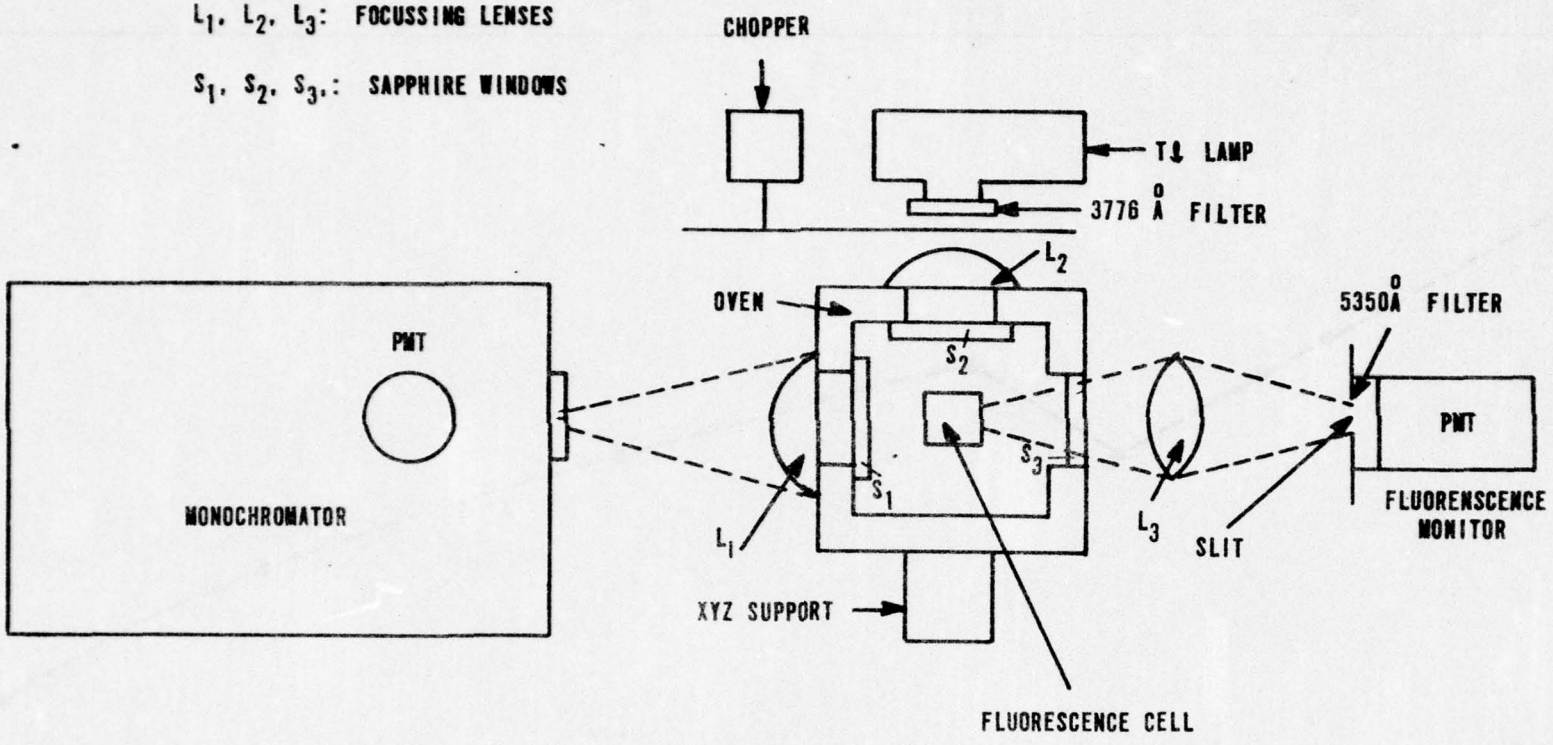


Figure 1. Experimental Arrangement of Fluorescence Measurement

FIG 1

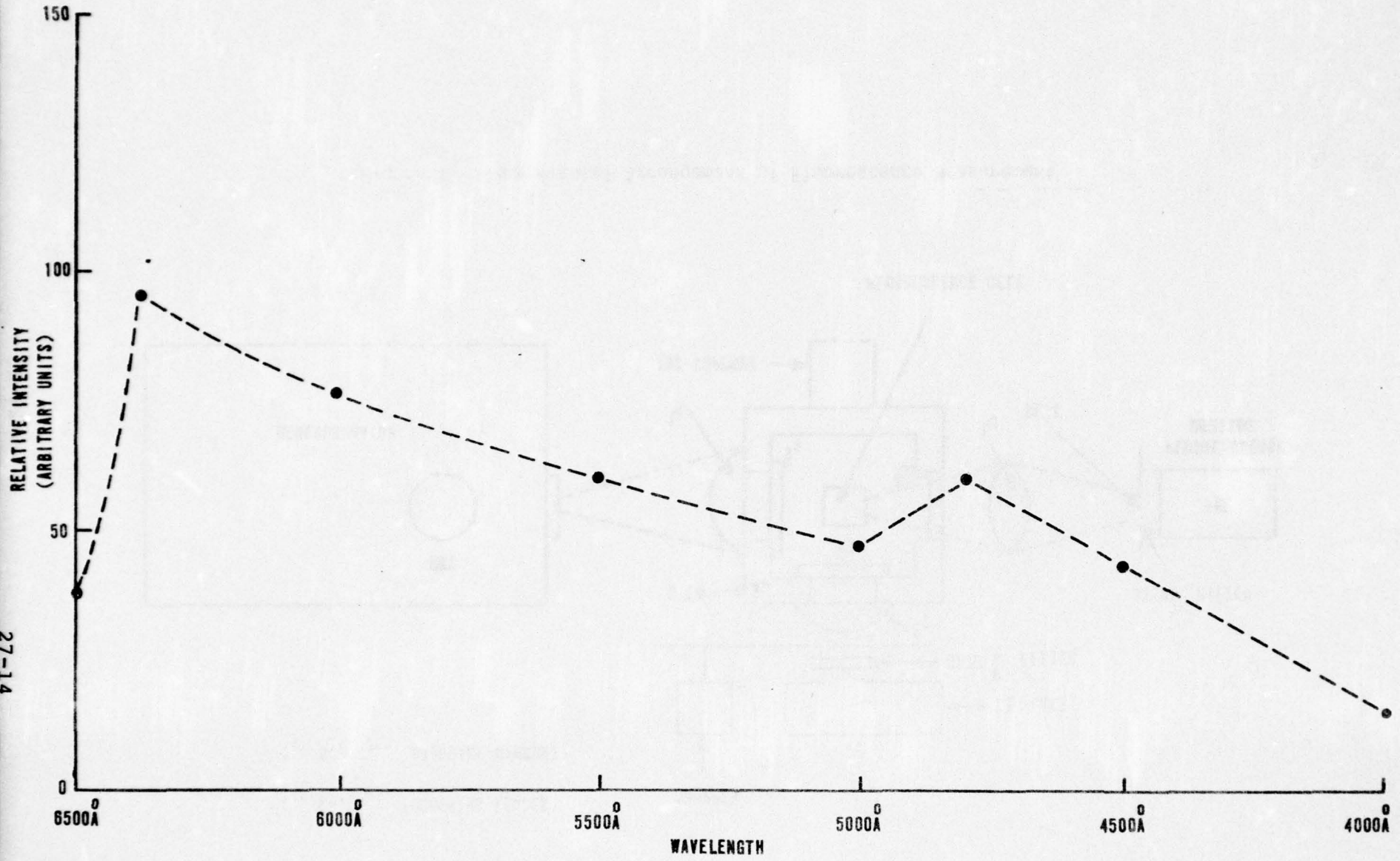


Figure 2. Spectral Response of Optical System

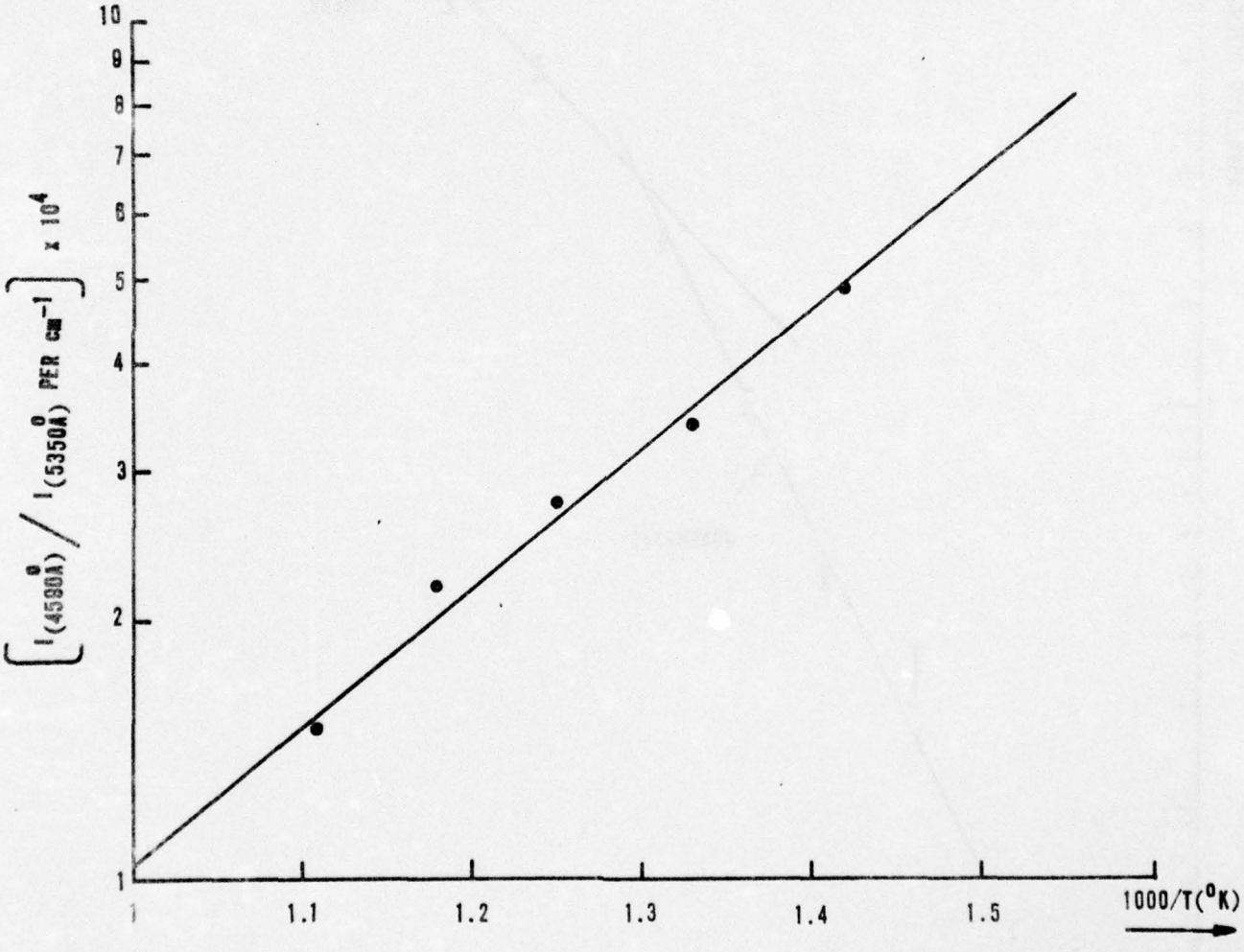


Figure 4. Temperature Dependence of Fluorescence Intensity

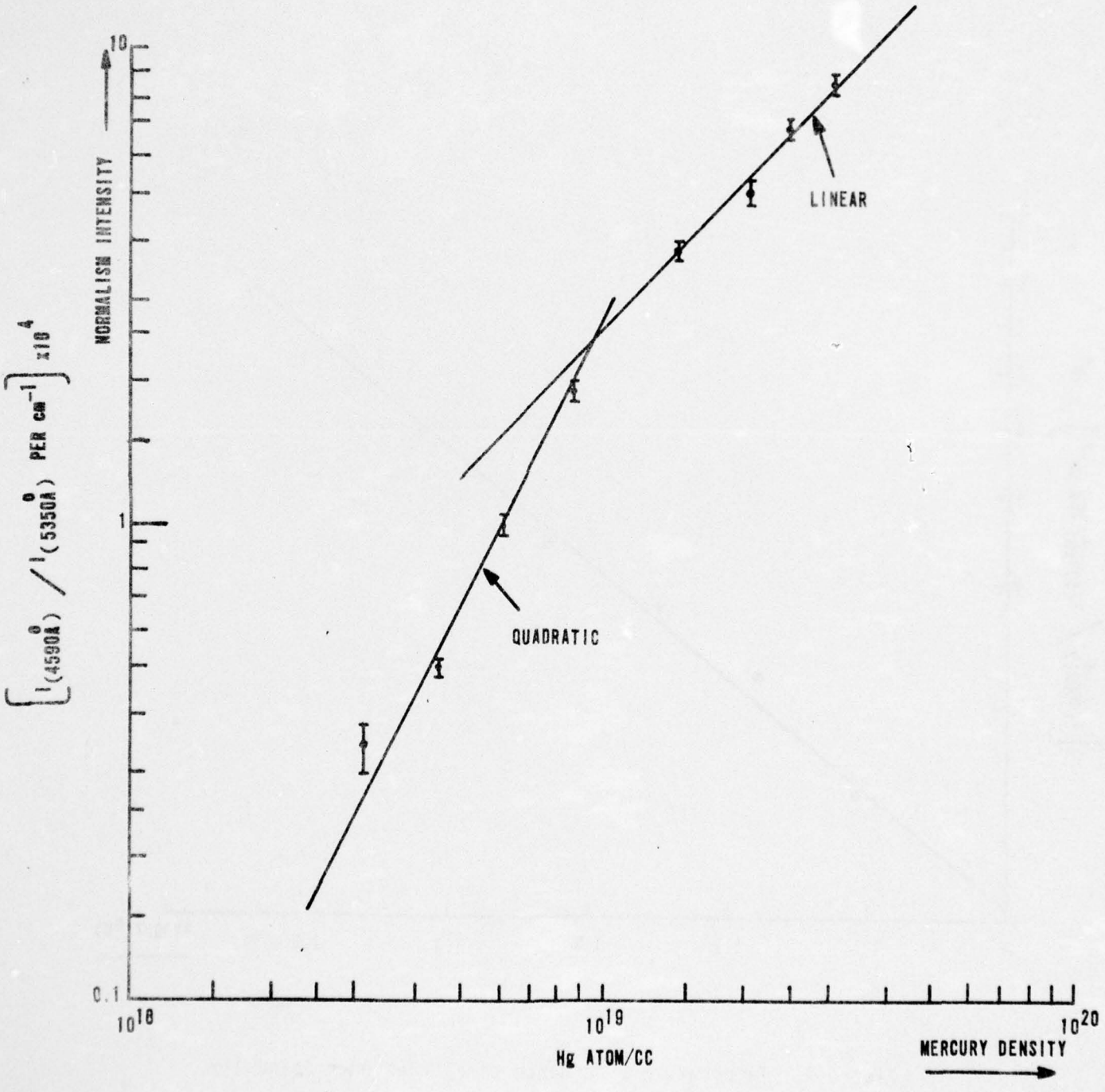


Figure 3. Density Dependence of Fluorescence Intensity

1976 USAF-ASEE SUMMER FACULTY RESEARCH PROGRAM
sponsored by
THE AIR FORCE OFFICE SCIENTIFIC RESEARCH
conducted by
AUBURN UNIVERSITY AND OHIO STATE UNIVERSITY

PARTICIPANT'S FINAL REPORT

SIGNAL PROCESSING WITH

APPLICATION TO OPTICS

Prepared by:	Craig S. Sims, Ph.D.
Academic Rank:	Associate Professor
Department and University:	School of Electrical Engineering Oklahoma State University

Assignment:

(Air Force Base) (Laboratory)	Air Force Academy Frank J. Seiler Research Laboratory
(Division) (Branch)	Aerospace-Mechanics Sciences Applied Mathematics
USAF Research Colleague:	Robert B. Asher, Ph.D.
Date:	August 27, 1976
Contract No.:	F44620-75-C-0031

ACKNOWLEDGMENT

The author is grateful for the opportunity to participate in the USAF-ASEE sponsored summer faculty research program. I wish to thank the Frank J. Seiler Research Laboratory for providing an excellent working environment, and to thank Lt Colonel Tomaskovic for his interest in the program. I also wish to thank the program director, Mr. J. Fred O'Brien, Jr. and my research colleague, Captain Robert Asher. The conversations with Dr. Asher formed the basis for most of the ideas contained in this report.

SIGNAL PROCESSING WITH APPLICATION TO OPTICS

by

C. S. Sims

ABSTRACT

In this report fixed configuration filters are derived which are thought to be applicable to the area of image processing. Two kinds of filters are suggested. One type of filter contains delayed observations, and appears to be particularly well suited to the type of cyclostationary model commonly encountered in image processing. The other type of filter suggested is a reduced order filter suitable for estimating a linear transformation of a state vector.

The objective of the fixed configuration filter design is to achieve a practical filter which will provide suboptimal performance, but be of a relatively simple structure for ease of implementation. Typically fixed configuration designs have been subject to the difficulty that one must do a large amount of off line computation to realize on line computational savings. In the filters considered here, both on and off line computational requirements are reasonable.

In addition to the filter simplification work contained in this report, some attention is also given to the area of sensitivity analysis for doubly stochastic Poisson processes. This area is studied because such processes are prevalent in the area of optics.

INTRODUCTION

The Frank J. Seiler Research Laboratory has been conducting research in the area of signal processing with application to optical processes. Image enhancement is a topic of considerable importance within this area. There has been considerable work in recent years in developing recursive estimation methods for the processing of two dimensional images [1-5]. Many of these results are suboptimal in that they deal with an averaging of a cyclostationary image process in order to obtain a tractable model [1], [2]. Other results [3], [4] can lead to improved performance at the cost of additional complexity. The optimal result in the literature is exceedingly complex as it assumes a large state vector. For a typical image, the estimation algorithm associated with such a large state vector might be too complicated for practical digital implementation. Therefore a large portion of this research has been directed towards filter simplification. The purpose of the research has been to develop fixed configuration estimators for image processing which will decrease the computational complexity required. In the course of this research, fixed configuration filters of reduced order were developed which have application to other areas such as flight systems, in addition to the application to image processing.

By far the majority of research effort was spent on the derivation of simplified filters. Some attention was also given to the area of doubly stochastic Poisson processes (DSPP), since this class of processes is prevalent in the area of optics. Frank J. Seiler Research Laboratory personnel have developed an adaptive estimation scheme for DSPP with application to adaptive optics. In order to help determine when the adaptive estimation schemes should be used, it was considered desirable to develop sensitivity equations for the analysis of mismatched estimation structures for the DSPP problem. The equations would be useful in determining reference sensitivity to erroneous parameters [6], [7]. It became evident early in the investigation of this problem that a direct approach to filter sensitivity would lead to a sensitivity matrix that is a function of the observed data. This is a severe limitation, since one would obtain different sensitivities for every experiment. The usefulness of the result would therefore be questionable. Consequently alternative definitions of sensitivity for DSPP estimation are suggested in this report.

In this report, the first section presents a number of new results in fixed configuration linear filtering pertinent to the area of image processing. These represent the main contribution of this research. In the second part of the report we indicate problems encountered in sensitivity analysis for DSPP and indicate an alternative approach to remove these difficulties.

OBJECTIVES

The objectives of this research were:

1. To derive fixed configuration filters suitable for application to image processing problems.

2. To see whether sensitivity analysis could be achieved for DSPP estimation algorithms.

1. IMAGE PROCESSING

1.1 Modeling [4]

Suppose that we have a two dimensional scalar valued random field $f(\xi,\eta)$ where ξ is a continuous horizontal variable and η is the discrete vertical variable. We assume that $f(\xi,\eta)$ is homogeneous with zero mean and factorable covariance function

$$R(\xi_1-\xi_2,\ \eta_1-\eta_2) = \alpha(\xi_1-\xi_2)\beta(\eta_1-\eta_2). \tag{1.1}$$

There is considerable justification [8-11] for the above assumption in the modeling of pictorial data. If the image is scanned one line at a time, the resulting process is sometimes called the scalar scanner [3], and is defined as

$$\begin{aligned} r(t) &= f(t,0), \quad 0 \le t \le T \\ r(t) &= f(t-kT,k), \quad kT<t\le(k+1)T, \\ &\qquad\qquad k = 1,2,\ldots,N-1. \end{aligned} \tag{1.2}$$

The process is not stationary, but is referred to as cyclostationary, having zero mean and covariance function

$$\bar{R}(t,\tau) = \begin{cases} \alpha(|t-\tau|)\beta(0), & i=j \\ \alpha(|t-\tau-(i-j)T|)\beta(i-j), & i>j \\ \alpha(|\tau-t-(j-i)T|)\beta(j-i), & i<j \end{cases} \tag{1.3}$$

for $iT<t\le(i+1)T$ and $jT<\tau\le(j+1)T$. Since f is defined on $[0,T]\times[0,N-1]$, r is defined on $[0,(N-1)T]$. Powell and Silverman [4] show that under certain conditions one can specify an output variable, $y(t)$, of a linear dynamical system having the same covariance as indicated by (1.3). In particular, if the covariance α is of the form

$$\alpha(\xi_1-\xi_2) = C_\alpha^T e^{A_\alpha|\xi_1-\xi_2|} b_\alpha \tag{1.4}$$

then a realization of $y(t)$ is given by

$$\dot{x}(t) = Fx(t) + gu(t),\ x(iT) = \gamma i \tag{1.5}$$

$$i = 0,1,2,\ldots,N-1$$

$$y(t) = \sum_{k=0}^{i} h_{i,k}\, h^T x(t-(i-k)T) \qquad (1.6)$$

$$iT<t\leq(i+1)T.$$

In (1.5) and (1.6), F, g, and h are related to C_α, A_α, and b_α in (1.4) through the state variable realization theory associated with covariance functions of the form (1.4). The terms $h_{i,k}$ are elements found from the vertical covariance function, i.e.,

$$\beta(i-j) = \sum_{k=0}^{N-1} h_{i,k}\, h_{j,k} \qquad (1.7)$$

and

$$h_{m,n} = 0 \quad \text{when} \quad m<n.$$

The term u(t) in (1.5) is zero mean white noise with covariance

$$E\{u(t)u(\tau)\} = \delta(t-\tau). \qquad (1.8)$$

The random vectors γ_i are such that

$$E\left\{\gamma_i \gamma_j^T\right\} = \begin{cases} 0 & , i\neq j \\ P_0 & , i=j \end{cases} \qquad (1.9)$$

where P_0 is the nonnegative definite solution of

$$FP_0 + P_0F^T + gg^T = 0 \qquad (1.10)$$

and γ_i is not correlated with u(t).

The proof that y(t) and r(t) have the same covariance function is contained in [4]. The details of the modeling procedure can be found in [4] and using spectral factorization procedures which may be found in the references on that topic provided in [4]. The following example may serve to clarify matters somewhat. Suppose α is of the form

$$\alpha(\xi) = ce^{-a|\xi|} \qquad (1.11)$$

where c and a are positive scalar valued constants. Then the corresponding power spectral density is

$$R_\alpha(s) = \frac{2ac}{a^2-s^2} \qquad (1.12)$$

which may be realized by the state variable model

$$\dot{x} = -ax + \sqrt{2ac}\,u \tag{1.13}$$

$$y = hx = x. \tag{1.14}$$

Hence in this case $F = -a$, $g = \sqrt{2ac}$, and $h = 1$, and these values may be used in (1.5) and (1.6). The value of P_0 can be found from (1.10) which in this case is

$$-2aP_0 + 2ac = 0 \tag{1.15}$$

which of course gives $P_0 = c$ as a solution.

1.2 A Fixed Configuration Filter

It is noted that (1.5) and (1.6) do not give a Markov realization. Therefore if the scan signal $r(t)$ and $y(t)$ are considered equivalent, and are corrupted by white noise, one cannot use Kalman Filtering to get an estimate, $\hat{f}(t)$. It is pointed out in [4] that one may obtain a Markov realization and use Kalman filtering if a vector scan is used instead of a scalar scan, but then the dimensionality of the state vector may be very large. We consider an alternative fixed configuration procedure to provide a relatively simple filter.

Consider a received signal

$$z(t) = r(t) + v(t) \tag{1.16}$$

which is considered to be equivalent to

$$z(t) = y(t) + v(t) \tag{1.17}$$

where $v(t)$ is zero mean white noise with covariance

$$E\{v(t)v(\tau)\} = R_v\,\delta(t-\tau). \tag{1.18}$$

We form the estimate

$$\hat{r}(t) = \hat{y}(t) = \sum_{k=0}^{i} h_{i,k} h^T \hat{x}\big(t-(i-k)T\big) \tag{1.19}$$

where $\hat{x}(t)$ is generated from the filter structure

$$\dot{\hat{x}}(t) = F_0(t)\hat{x}(t) + \sum_{j=0}^{i} K_j(t) z(t-jT) \tag{1.20}$$

which is used when $iT<t\leq(i+1)T$, i.e., when the filter is processing the ith row. The motivation for using (1.20) is that the observations themselves have delays in them, so it seems reasonable to design a filter with delayed driving terms.

The error, e(t) is defined as

$$e(t) \triangleq y(t) - \hat{y}(t) = \sum_{k=0}^{i} h_{i,k} h^T \tilde{x}\left(t-(i-k)T\right) \tag{1.21}$$

where

$$\tilde{x}\left(t-(i-k)T\right) \triangleq x\left(t-(i-k)T\right) - \hat{x}\left(t-(i-k)T\right). \tag{1.22}$$

In order to keep the error e well behaved, it is therefore sufficient to consider the state error $\tilde{x}$. We require that the state error $\tilde{x}(t)$ have an unbiased property, i.e.,

$$E\{\tilde{x}(t)\} = 0. \tag{1.23}$$

In achieving (1.23) it is convenient to consider the differential equation for the error. If we are operating on line i then from (1.5) and (1.20),

$$\dot{\tilde{x}} = \dot{x} - \dot{\hat{x}} = Fx + gu - F_0\hat{x} - \sum_{j=0}^{i} K_j z(t-jT) \tag{1.24}$$

where the unspecified arguments in the above and subsequent equations are at a time t. It is noted that (1.24) may be written as

$$\dot{\tilde{x}} = Fx + gu - F_0\hat{x} - \sum_{j=0}^{i} K_j v(t-jT) - \sum_{k=0}^{i} \left[\sum_{j=0}^{i-k} K_j h_{i-j,k} h^T\right] x\left(t-(i-k)T\right). \tag{1.25}$$

Substituting for $\hat{x}$ noting that $\hat{x} = x-\tilde{x}$, and grouping terms involving x(t), we obtain

$$\dot{\tilde{x}} = \left(F - F_0 - K_0 h_{i,i} h^T\right)x + F_0\tilde{x} + gu - \sum_{j=0}^{i} K_j v(t-jT) - \sum_{k=0}^{i-1} \left[\sum_{j=0}^{i-k} K_j h_{i-j,k} h^T\right] x\left(t-(i-k)T\right). \tag{1.26}$$

If we select the matrix F_0 such that

$$F_0 = F - K_0 h_{i,i} h^T \tag{1.27}$$

and also require that

$$\sum_{j=0}^{i-k} K_j h_{i-j,k} h^T = 0 \ , \ k=0,1,\ldots,i-1 \tag{1.28}$$

then (1.26) simplifies to

$$\dot{\tilde{x}} = \left(F-K_0 h_{i,i} h^T\right)\tilde{x} + gu - \sum_{j=0}^{i} K_j v(t-jT). \tag{1.29}$$

From (1.29), it is clear that

$$\frac{d}{dt} E\{\tilde{x}(t)\} = \left(F-K_0(t) h_{i,i} h^T\right) E\{\tilde{x}(t)\}. \tag{1.30}$$

Hence if

$$E\{\tilde{x}(iT)\} = 0 \tag{1.31}$$

then

$$E\{\tilde{x}(t)\} = 0 \ , \ iT \leq t < (i+1)T. \tag{1.32}$$

Since (1.32) is a desired property of the filter, we investigate (1.28). The solution for all the gains in terms of K_0 can be seen to be of the form

$$K_j = A_j K_0 \ ; \ j=1,2,\ldots,i \tag{1.33}$$

where the sequence of scalars $\{A_j\}$ can be computed recursively from the relationship

$$A_j = -\left[h_{i-j,i-j}\right]^{-1}\left[\sum_{k=0}^{j-1} A_k h_{i-k,i-j}\right]. \tag{1.34}$$

It is assumed that $A_0 = 1$ in using (1.34). In view of the above result (1.33), it is seen that (1.29) can be written as

$$\dot{\tilde{x}} = \left(F-K_0 h_{i,i} h^T\right)\tilde{x} + gu - K_0 A^* V^* \tag{1.35}$$

where

$$A^* \triangleq \left[A_0 A_1 \ldots . A_i\right] \tag{1.36}$$

and

$$V^*(t) \triangleq \begin{bmatrix} v(t) \\ v(t-T) \\ \vdots \\ v(t-iT) \end{bmatrix}. \tag{1.37}$$

The term A^*V^* is equivalent to a single input

$$V_a(t) = A^* V^*(t) \tag{1.38}$$

with zero mean, and covariance

$$E\left\{V_a(t) V_a(\tau)\right\} = R_a \delta(t-\tau) \tag{1.39}$$

where

$$R_a = A^{*T} A^* R_v = \left(\sum_{k=0}^{i} A_k^2\right) R_v. \tag{1.40}$$

The only quality that remains free at this point is the gain K_0. If $K_0(t)$ is to minimize the mean square error

$$E\left\{\tilde{x}^T(t)\tilde{x}(t)\right\} = tr\left[P(t)\right] \tag{1.41}$$

where $P(t)$ is the error covariance matrix, then it is not difficult to show that it should be selected according to

$$K_0(t) = P(t)h_{i,i}hR_a^{-1} \tag{1.42}$$

where

$$\dot{P} = \left(F-K_0h_{i,i}h^T\right)P + P\left(F-K_0h_{i,i}h^T\right)^T + gg^T + Ph_{i,i}^2hR_a^{-1}h^TP \tag{1.43}$$

and where

$$P(iT) = P_0. \tag{1.44}$$

The steps involved in obtaining the above equations for K_0 are similar to those found in [12]. From (1.27) and (1.33), it is seen that our filter is of the form

$$\dot{\hat{x}} = F\hat{x} + K_0\left[z(t) - h_{i,i}h^T\hat{x}(t) + \sum_{j=1}^{i} A_j z(t-jT)\right] \tag{1.45}$$

which operates on the ith line of data. The initial condition for (1.45) may be found from requirement (1.31), i.e.,

$$\hat{x}(iT) = E\{x(iT)\} = 0. \tag{1.46}$$

The fixed configuration filter is established, and it is appropriate to discuss its operation.

A new filter is designed, initialized, and operated for every line of data to be scanned. On line zero it is just a Kalman filter since $i = 0$ and there are no delayed observations. The size of A^* grows as the index of the line you are on grows. A new A^* is calculated for every line. Since you are scanning from left to right, the estimate is influenced only by data in the rectangular region to the left and above the estimation point. For this reason, it might be appropriate to scan and filter from a different direction and take the average of the two estimates [2]. If the dimensionality of your state vector is n and the number of lines is N, then the procedure discussed herein requires you to use N filters each of dimension n. The optimal procedure [4] requires one filter of dimension Nn. It is much easier to design and process with a large number of small order filters than with one very high order filter.

1.3 Reduced Order Filtering

If one uses the vector scan method of image processing [3], [4], one can obtain a Markov realization to model the process. The dimension of the model, and the corresponding Kalman filter is large. In this section we therefore seek to design a reduced order filtering scheme applicable when it is desired to estimate a linear transformation of a state vector which is of much smaller order than the state vector itself. Since the approach here is radically different than that of the previous section,

and since its application goes considerably beyond image processing, we do not attempt to use the same notation in this section as in the previous section. The state model and observation model are of greater generality.

The problem of optimal linear filtering has been examined from many viewpoints, including treatment within a control theoretic framework [12], [13]. Here we wish to address the problem of estimating a linear transformation of a state vector using a filter which may be of reduced order relative to the dimension of the state vector. Control methodologies are used to optimize the parameters of the filter.

Within a deterministic framework, Luenberger has shown that one may achieve considerable reduction of complexity in the state reconstruction process when only a linear combination of the state variables is required [14]. It would seem that a similar reduction in complexity should occur when the problem is stochastic. Indeed, it will become clear that this work has some relationship to observer theory, especially to treatments of observer theory which consider the stochastic nature of the problem [15].

Although the primary thrust of this section is towards the reduction of filter complexity through order reduction, it can be shown that it is even possible to reduce filter complexity in the full order case. This happens because for certain classes of problems, the Kalman filter is not the only solution, [13]. Other estimators can result in the same value for the performance measure.

The system of interest is a Markov process satisfying a linear stochastic differential equation

$$\dot{x}(t) = A(t)x(t) + w(t). \tag{1.47}$$

The observation model is also linear

$$y(t) = C(t)x(t) + v(t). \tag{1.48}$$

The state vector x is of dimension n and the observation vector y is of dimension m. It is assumed that the initial value of the state vector, $x(t_0)$, is uncorrelated with the plant noise, w(t), and the measurement noise, v(t). The noise processes are zero mean white processes, uncorrelated with each other, having covariance matrices

$$\begin{aligned} E\{w(t)w^T(\tau)\} &= Q(t)\delta(t-\tau) \\ E\{v(t)v^T(\tau)\} &= R(t)\delta(t-\tau). \end{aligned} \tag{1.49}$$

Initially, the state of the system has mean and variance

$$\begin{aligned} E\{x(t_0)\} &= \mu_0 \\ \mathrm{Var}\{x(t_0)\} &= P_0. \end{aligned} \tag{1.50}$$

The problem is to estimate a linear transformation of the state vector

$$z(t) = N(t)x(t) \tag{1.51}$$

where z is of dimension $\ell \leq n$, and presumably the $\ell \times n$ matrix, $N(t)$, is selected to indicate the part of the system which is of primary concern. The filter to be optimized is of the form

$$\dot{\hat{z}}(t) = F(t)\hat{z}(t) + K(t)y(t) + g(t) \tag{1.52}$$

where $\hat{z}$ is of dimension ℓ. The error, $e(t)$, is defined as

$$e(t) = z(t) - \hat{z}(t). \tag{1.53}$$

The deterministic vector, $g(t)$, and the filter initial condition $\hat{z}(t_0)$, are to be determined so that the filter is unbiased

$$E\{e(t)\} = 0 \quad \forall t \geq t_0. \tag{1.54}$$

Note that we do not require conditional unbiasedness which is a much stronger requirement. The matrices $F(t)$ and $K(t)$ are then to be determined so that the performance measure

$$J = E\left\{\int_{t_0}^{t_f} e^T(t)U(t)e(t)dt + e^T(t_f)Se(t_f)\right\} \tag{1.55}$$

is a minimum. It is assumed that the weighting matrix S is positive definite. The weighting matrix $U(t)$ is critical to the problem formulation, as we obtain different results depending upon whether this matrix is positive definite or zero. It can make sense to have $U(t)$ be zero, when the only time of real importance is the final time. Indeed when $U(t)$ is zero, it will be seen that performance does not depend on $F(t)$.

We shall first examine the requirements for unbiasedness. By direct substitution from (1.47), (1.48), (1.51) and (1.52), the error equation is obtained

$$\dot{e} = \left[\dot{N}+NA-FN-KC\right]x + Fe + Nw - Kv - g. \tag{1.56}$$

If $g(t)$ is selected as

$$g = \left[\dot{N}+NA-FN-KC\right]\mu \tag{1.57}$$

where $\mu(t)$ is the mean value of the system state,

$$\dot{\mu}(t) = A(t)\mu(t) \quad ; \quad \mu(t_0) = \mu_0 \tag{1.58}$$

then it is clear that taking expectation of (1.56) gives a homogeneous result

$$\frac{d}{dt} E\{e(t)\} = F(t)E\{e(t)\}. \tag{1.59}$$

Thus if $E\{e(t_0)\} = 0$, equation (1.54) is satisfied. If

$$\hat{z}(t_0) = N(t_0)\mu_0 \tag{1.60}$$

then

$$E\{e(t_0)\} = E\left\{N(t_0)x(t_0) - N(t_0)\mu_0\right\} = 0 \tag{1.61}$$

and the desired result follows. Hence (1.57) is the expression needed for $g(t)$ and (1.60) specifies the filter initial condition. Equation (1.56) can be rewritten as

$$\dot{e} = \left[\dot{N}+NA-FN-KC\right]\bar{x} + Fe + Nw - Kv \tag{1.62}$$

where $\bar{x} = x-\mu$ satisfies the linear equation

$$\dot{\bar{x}} = A\bar{x} + w. \tag{1.63}$$

Certainly $\bar{x}$ is a zero mean process having initial variance P_0. It is convenient to work with the second moment matrix associated with (1.62) and (1.63) in formulating the optimal control problem which will give the requirements for F and K.

The performance measure (1.55) can be written as

$$J = tr\left\{\int_{t_0}^{t_f} U(t)P_{ee}(t)dt + SP_{ee}(t_f)\right\} \tag{1.64}$$

where

$$P_{ee}(t) = E\left\{e(t)e^T(t)\right\}. \tag{1.65}$$

From (1.62) and (1.63), P_{ee} satisfies

$$\begin{aligned}\dot{P}_{ee} = &\left[\dot{N}+NA-FN-KC\right]P_{xe} + FP_{ee} + P_{ee}F^T \\ &+ P_{ex}\left[\dot{N}+NA-FN-KC\right]^T + NQN^T + KRK^T\end{aligned} \tag{1.66}$$

where

$$P_{ex}(t) = E\left\{e(t)\bar{x}^T(t)\right\} = P_{xe}(t)^T. \tag{1.67}$$

Using (1.62) and (1.63), it is easy to show that

$$\dot{P}_{xe} = AP_{xe} + P_{xx}\left[\dot{N}+NA-FN-KC\right]^T + P_{xe}F^T + QN^T \tag{1.68}$$

where

$$P_{xx}(t) = E\left\{\bar{x}(t)\bar{x}^T(t)\right\} \tag{1.69}$$

which satisfies the equation

$$\dot{P}_{xx} = AP_{xx} + P_{xx}A^T + Q. \tag{1.70}$$

The term P_{ex} satisfies the transpose of (1.68). Initial conditions for (1.66), (1.68), and (1.70) are

$$\begin{aligned}P_{xx}(t_0) &= P_0 \\ P_{xe}^T(t_0) = P_{ex}(t_0) &= N(t_0)P_0 \\ P_{ee}(t_0) &= N(t_0)P_0N^T(t_0).\end{aligned} \tag{1.71}$$

The matrix $P_{xx}(t)$ may be regarded as a known quantity since it is the solution to (1.70). The optimization problem may then be stated in a deterministic way, so that the matrix minimum principle is applicable [16]. The problem is to minimize (1.64) by properly selecting F and K, subject to the constraints imposed by (1.66) and (1.68). To preserve symmetry we include the transpose of (1.68) in the Hamiltonian also.

The Hamiltonian for this problem is

$$H = \mathrm{tr}\left\{UP_{ee} + \dot{P}_{ee}\Lambda_{ee}^T + \dot{P}_{xe}\Lambda_{xe}^T + \dot{P}_{ex}\Lambda_{ex}^T\right\}. \tag{1.72}$$

The equations for the Lagrange multiplier matrices are

$$\begin{aligned}\dot{\Lambda}_{ee} &= -\frac{\partial H}{\partial P_{ee}} = -\left\{U + F^T\Lambda_{ee} + \Lambda_{ee}F\right\} \\ \dot{\Lambda}_{xe} &= -\frac{\partial H}{\partial P_{xe}} = -\left\{A^T\Lambda_{xe} + \Lambda_{xe}F + \left[\dot{N}+NA-FN-KC\right]^T\Lambda_{ee}\right\}\end{aligned} \tag{1.73}$$

with terminal conditions

$$\Lambda_{ee}(t_f) = S \tag{1.74}$$

and

$$\Lambda_{xe}(t_f) = 0. \tag{1.75}$$

The matrix Λ_{ex} is just the transpose of Λ_{xe}. Setting the gradient of H with respect to K equal to zero gives a necessary condition for the optimum gain

$$K = \left[P_{ex} + \Lambda_{ee}^{-1}\Lambda_{ex}P_{xx}\right]C^TR^{-1} \tag{1.76}$$

where R and Λ_{ee} have been assumed to be nonsingular. The matrix F presents a difficulty since it appears linearly in the Hamiltonian. It is convenient to proceed as in [17] by examining that part of the Hamiltonian which depends explicitly on F, defined as

$$H^* = \mathrm{tr}\left\{F\Theta + \Theta^TF^T\right\} \tag{1.77}$$

where

$$\Theta = \left[P_{ee}-NP_{xe}\right]\Lambda_{ee} + \left[P_{ex}-NP_{xx}\right]\Lambda_{xe}. \tag{1.78}$$

Clearly what we have called Θ is just the transpose of the gradient matrix, $\partial H/\partial F$. From the initial conditions, (1.71), it may be seen that $\Theta(t_0)$ is zero. It is necessary to examine the time derivatives of Θ to determine the possible existence of a singular arc. Since different requirements will be obtained, it is convenient to examine Θ under different conditions. It is required that $\Theta(t)$ equal zero for all $t\varepsilon[t_0,t_f]$ if a singular arc is to exist.

Case 1

In this first case, it is assumed that U(t) is zero. Then it follows that

$$\dot{\Theta} = F\Theta + \Theta F + K\left[RK^T\Lambda_{ee}-CP_{xx}\Lambda_{xe}-CP_{xe}\Lambda_{ee}\right]. \tag{1.79}$$

The bracketed term in (1.79) is zero whenever K(t) is selected optimally, according to (1.76). Therefore (1.79) becomes

$$\dot{\Theta} = F\Theta + \Theta F \tag{1.80}$$

and since $\Theta(t_0)$ is zero, (1.80) assures us that $\Theta(t)$ remains zero for all $t\varepsilon[t_0,t_f]$, regardless of our choice of F. The implications of this result

are significant. In the full order case (N=I), as was pointed out in [13], the Kalman filter is just one solution, i.e., one of the optimal linear filters. This means that for final time estimation problems, one should examine other realizations of the optimum linear filter. Such realizations can be easier to implement than the Kalman filter.

Probably the most advantageous property of this singularity with respect to F is computational. If F is picked a priori, then one only needs to solve a linear two-point boundary-value problem (TPBVP), which is easy to do using linear systems theory. Alternatively one can use a procedure which leads to a Riccati equation type of solution.

Case 2

In this case N is constant but U is assumed to be positive definite. This leads to an additional term in (1.80), i.e.,

$$\dot{\Theta} = F\Theta + \Theta F - \left(P_{ee} - NP_{xe}\right)U. \tag{1.81}$$

Hence it is required that

$$P_{ee}(t) = NP_{xe}(t) \qquad \forall t\varepsilon[t_0, t_f] \tag{1.82}$$

since U is positive definite. Clearly this cannot be satisfied for arbitrary F. Thus the existence of the singular arc depends on the choice of F in this case. Defining Ω,

$$\Omega \triangleq P_{ee} - NP_{xe} \tag{1.83}$$

it is seen that

$$\dot{\Omega} = F\Omega + \Omega F^T + \left(P_{ex} - NP_{xx}\right)\left[NA - FN - KC\right] - K\left[RK^T - CP_{xe}\right]. \tag{1.84}$$

It is required that $\Omega(t)$ equal zero for all t in the interval of interest. From (1.71) is is apparent that $\Omega(t_0)$ is zero. In order for

$$\dot{\Omega} = F\Omega + \Omega F^T \tag{1.85}$$

so that $\Omega(t)$ is zero, it is sufficient that

$$NA - FN - KC = 0. \tag{1.86}$$

This leads to the result that

$$\Lambda_{ex}(t) = 0 \tag{1.87}$$

so that the gain is evaluated as

$$K(t) = P_{ex}(t)C^T(t)R^{-1}(t). \tag{1.88}$$

Clearly (1.88) implies that the last term in (1.84) is zero, and we have the desired result. Thus if F can be chosen so that (1.86) is satisfied, a singular arc exists, provided K is selected according to (1.88). Equation (1.82) has an interesting interpretation. It is easy to see that it is just the orthogonality requirement in a reduced space,

$$E\left\{\hat{z}(t)e^T(t)\right\} = 0. \tag{1.89}$$

It must be made clear that it is not always possible to satisfy (1.86) and (1.88) simultaneously, and consequently it is not always possible to have a singular arc. In such cases the problem should probably be reformulated with bounds on F, or a suboptimal solution accepted.

Case 3

In this case, N is not constant. By some fortunate cancellation (1.81) is still applicable but (1.84) is not. Equation (1.84) is replaced by

$$\dot{\Omega} = F\Omega + \Omega F^T + \left(P_{ex} - NP_{xx}\right)\left[\dot{N}+NA-FN-KC\right] - K\left[RK^T - CP_{xe}\right]. \tag{1.90}$$

It is clear that $\Omega(t)$ will be zero if

$$\dot{N} + NA - FN - KC = 0. \tag{1.91}$$

Then (1.87) and (1.88) and (1.89) are still true. To be able to solve (1.91) for F, it is necessary and sufficient that

$$\left(\dot{N}+NA-KC\right)N^{\dagger}N = \left[\dot{N}+NA-KC\right] \quad \forall t\varepsilon[t_0,t_f]. \tag{1.92}$$

The solution for F is

$$F = \left[\dot{N}+NA-KC\right]N^{\dagger} + \Gamma\left[I-NN^{\dagger}\right] \tag{1.93}$$

where $N^{\dagger}$ is a pseudo inverse of the matrix N, [18]. If NN^T is nonsingular

$$F = \left[\dot{N}+NA-KC\right]N^T\left[NN^T\right]^{-1}. \tag{1.94}$$

In Case 1, it was found that the singular arc did not specify F. In Cases 2 and 3, it is very possible that no F can be found to maintain the singular arc. Therefore it is appropriate to investigate the solution to the TPBVP when F is specified a priori. It is observed that $\Lambda_{ee}(t)$ can be precomputed in this case, and may be regarded as a known quantity. Substituting the expression for the gain (1.76) in (1.68) and (1.73) results in a linear TPBVP since $P_{xx}(t)$ and $\Lambda_{ee}(t)$ are known. Equation (1.68) becomes

$$\begin{aligned}\dot{P}_{xe} = {} & AP_{xe} + P_{xx}\left[\dot{N}+NA-FN\right]^T + P_{xe}F^T + QN^T \\ & -P_{xx}C^TR^{-1}C\left[P_{xe}+P_{xx}\Lambda_{xe}\Lambda_{ee}^{-1}\right].\end{aligned} \tag{1.95}$$

Equation (1.73) is rewritten as

$$\begin{aligned}\dot{\Lambda}_{xe} = {} & -A^T\Lambda_{xe} - \Lambda_{xe}F - \left[\dot{N}+NA-FN\right]^T\Lambda_{ee} \\ & + C^TR^{-1}CP_{xe} + C^TR^{-1}CP_{xx}\Lambda_{xe}\Lambda_{ee}^{-1}.\end{aligned} \tag{1.96}$$

Equations (1.95) and (1.96) are linear in the unknowns P_{xe} and Λ_{xe}. If Λ_{ee} is a scalar, however, things work out particularly well. Suppose F, U, and S are scalar matrices, i.e.,

$$F = fI$$
$$U = uI \tag{1.97}$$
$$S = sI.$$

Then obviously Λ_{ee} is a scalar matrix also. We can thus reposition Λ_{ee} and F in (1.95) and (1.96) obtaining the result

$$\begin{bmatrix} \dot{P}_{xe} \\ \dot{\Lambda}_{xe} \end{bmatrix} = \left[\begin{array}{c|c} G_{11} & G_{12} \\ \hline G_{21} & G_{22} \end{array}\right] \begin{bmatrix} P_{xe} \\ \Lambda_{xe} \end{bmatrix} + \begin{bmatrix} D_1 \\ D_2 \end{bmatrix} \tag{1.98}$$

where

$$\begin{aligned} G_{11} &\triangleq A + F - P_{xx}C^TR^{-1}C \\ G_{12} &\triangleq -\Lambda_{ee}^{-1}P_{xx}C^TR^{-1}CP_{xx} \\ G_{21} &\triangleq C^TR^{-1}C \\ G_{22} &\triangleq -[A^T+F-\Lambda_{ee}^{-1}C^TR^{-1}CP_{xx}] \\ D_1 &\triangleq P_{xx}[\dot{N}+NA-FN]^T + QN^T \\ D_2 &\triangleq -[\dot{N}+NA-FN]^T\Lambda_{ee}. \end{aligned} \tag{1.99}$$

With the given boundary conditions, (1.98) can be solved directly using linear systems theory. Alternatively one can find a Riccati type solution. Here we assume that Λ_{xe} can be written as

$$\Lambda_{xe} = MP_{xe} + \beta. \tag{1.100}$$

Then

$$\dot{\Lambda}_{xe} = \left[\dot{M}+MG_{11}+MG_{12}M\right]P_{xe} + MD_1 + \dot{\beta} + MG_{12}\beta$$

and

$$\dot{\Lambda}_{xe} = \left[G_{21}+G_{22}M\right]P_{xe} + G_{22}\beta + D_2. \tag{1.101}$$

If (1.100) and (1.101) are to hold for arbitrary P_{xe}, then

$$\dot{M} + MG_{11} + MG_{12}M = G_{21} + G_{22}M \tag{1.102}$$

and

$$\dot{\beta} + MD_1 + MG_{12}\beta = G_{22}\beta + D_2. \tag{1.103}$$

Since $\Lambda_{xe}(t_f) = 0$, the above equations are solved backwards in time from conditions

$$M(t_f) = 0 \tag{1.104}$$

and

$$\beta(t_f) = 0. \tag{1.105}$$

Solving the Riccati equation (1.102) and the equation for β must be done off line, as in a linear regulator problem, since the result is to be obtained by backward integration. The forward equation for P_{xe} is

$$\dot{P}_{xe} = \left(G_{11} + G_{12}M\right)P_{xe} + G_{12}\beta + D_1 \tag{1.106}$$

which is solved from the appropriate initial condition either on line or off line depending on computer requirement. The gain to be used in the filter is then

$$K = \left[P_{xe}^T + \Lambda_{ee}^{-1}\left(MP_{xe}+\beta\right)^T P_{xx}\right]C^T R^{-1}. \tag{1.107}$$

The results presented when F is specified a priori are suboptimal in general, and optimal in the situation referred to as Case 1.

In this section, we have presented some relatively simple realizations of optimal and suboptimal estimates of linear transformations of state vectors. These reduced order and full order filters are thought to be especially important because of both on and off line computational conveniences. The results should be applicable in many areas besides image processing.

2. SENSITIVITY ANALYSIS

The other area that we sought to investigate was sensitivity analysis for DSPP estimation algorithms. In the area of linear estimation theory, large scale sensitivity analysis has been developed using the matrix definition of sensitivity

$$\Gamma_i(t) = \left[V_{true}(t) - V_{assumed}(t)\right]/\Delta b_i. \tag{2.1}$$

That is, the sensitivity matrix is defined as the difference between the true error covariance matrix, and the error covariance matrix based on assumed parameter values over the difference between a true and an assumed parameter value. The equations for calculating (2.1) are presented in Sage and Melsa [6].

For DSPP problems, if one tries to use the definition given in (2.1), the problem of calculating the true and assumed error covariance matrices becomes mathematically untractable. On the other hand, if one uses conditional error covariance matrices in the sensitivity definition, it appears that one can get some approximations to the error covariance matrices. We did not pursue this approach because even in the case of correctly assumed parameters, Snyder's approximate error covariance equations couple in to the observed data [19].

There is an alternative approach which avoids the above mentioned difficulties. One can redefine the sensitivity matrix as the difference in a lower bound matrix, Σ, over the parameter difference in a way that is analogous to (2.1). The matrix Σ under certain rather general conditions [19], satisfies

$$\dot{\Sigma} = A\Sigma + \Sigma A^T + BB^T - \Sigma P \Sigma \tag{2.2}$$

and is precomputable. In (2.2), P is defined as

$$P \triangleq E\left\{\lambda^{-1}(x)\left[\frac{\partial\lambda}{\partial x}\right]\left[\frac{\partial\lambda}{\partial x}\right]^T\right\} \tag{2.3}$$

where λ, the intensity of the DSPP, is a function of a random state vector, x, and x satisfies

$$dx = Axdt + Bdw \tag{2.4}$$

where w is a Wiener process. The relationship between (2.2) and the optimum linear filtering problem is clear, and is explained in [19]. It therefore appears that one should be able to apply the sensitivity algorithms of Sage [6] with little modification. The sensitivities are then interpreted in terms of lower bound sensitivity instead of error covariance sensitivities. There is one case in which the sensitivity results described here can be interpreted in terms of the sensitivity of the error covariance matrix. In the case that λ is a linear function of x

$$\lambda = E\{\lambda\} + C^T x \tag{2.5}$$

and the optimal linear filter ([19], pg. 321) is used to obtain the estimate $\hat{x}$, then P is replaced by

$$P^* = CE^{-1}(\lambda)C^T \tag{2.6}$$

and Σ is the true error covariance matrix, i.e.,

$$E\left\{[x(t)-\hat{x}(t)][x(t)-\hat{x}(t)]^T\right\} \geq \sum(t) \tag{2.7}$$

holds with equality. In general, the usefulness of the results presented here depend to a considerable extent on how tight a bound $\Sigma(t)$ is to the error covariance matrix. There is also some question regarding whether it is allowable to use Sage's sensitivity results for linear filtering based on the fact that (2.2) corresponds to a linear filtering problem.

CONCLUSIONS AND RECOMMENDATIONS

With regard to sensitivity analysis for DSPP, it is difficult to evaluate the utility of the suggested approach at this time. It appears that an appropriate means of evaluating the lower bound method would be to use Monte Carlo simulation to see whether the lower bound is tight and whether the analytical sensitivities correspond to experimental sensitivities.

It appears that fixed configuration filtering has a definite role in the area of recursive filtering as it applies to image processing. In this area, filter simplification is of considerable importance because the dimensionality of the state vector associated with two dimensional images is very large. In this report we have derived the basic algorithms in a continuous form. It is also desirable to have discrete versions of these estimation methods. These algorithms have not been tested and compared with other approaches. Therefore it is recommended that they should be compared with other approaches from the viewpoint of performance, and with respect to the number of required calculations. It would be interesting to test the signal processing capabilities of these estimation methods on actual images.

REFERENCES

1. Nahi, N. E., and Assefi, T., "Bayesian Recursive Image Estimation," IEEE Trans. Computer, Vol. C-21, pp. 734-738, July, 1972.

2. Nahi, N. E., "Role of Recursive Estimation in Statistical Image Enhancement," Proc. IEEE, Vol. 60, pp. 872-877, July, 1972.

3. Nahi, N. E., and Franco, C. A., "Recursive Image Enhancement-Vector Processing," IEEE Trans. Comm., Vol. COM-21, pp. 305-311, April, 1973.

4. Powell, S. R., and Silverman, L. M., "Modeling of Two-Dimensional Covariance Functions with Application to Image Restoration," IEEE Trans. Auto. Contr., Vol. AC-19, pp. 8-12, Feb., 1974.

5. Habibi, A., "Two-Dimensional Bayesian Estimates of Images," Proc. IEEE, Vol. 60, pp. 878-883, July, 1972.

6. Sage, A., and Melsa, J., Estimation Theory with Applications to Communications and Control, McGraw Hill Book Co., New York, 1971.

7. Gelb, A. (editor), Applied Optimal Estimation, MIT Press, Cambridge, 1974.

8. Kretzmer, E. R., "Statistics of Television Signals," Bell Sys. Tech. J., pp. 751-763, July, 1952.

9. Franks, L. E., "A Model for the Random Video Process," Bell Sys. Tech. J., April, 1966.

10. Huang, T. S., "Subjective Effect of Two-Dimensional Pictorial Noise," IEEE Trans. Inform. Theory, Vol. IT-11, Jan., 1965.

11. Habibi, A. and Wintz, P. A., "Image Coding by Linear Transformation and Block Quantization," IEEE Trans. Comm., Vol. COM-19, pp. 50-62, Feb., 1971.

12. Athans, M., and Tse, E., "A Direct Derivation of the Optimal Linear Filter Using the Maximum Principle," IEEE Trans. Automatic Control, December, 1967.

13. Lee, J. S., "Optimal Linear Filter and its Relation to Singular Control," Proceedings of the 1970 JACC, June 22-26, 1970, Atlanta, Georgia.

14. Luenberger, D. G., "Observers for Multivariable Systems," IEEE Trans. Automatic Control, Vol. AC-11, pp. 190-197, April, 1966.

15. Tse, E., and Athans, M., "Observer Theory for Continuous Time Linear Systems," Information and Control, Vol. 22, pp. 405-434, 1973.

16. Athans, M., "The Matrix Minimum Principle," Information and Control, Vol. 11, pp. 592-606, 1968.

17. Sims, C. S., and Melsa, J. L., "A Fixed Configuration Approach to the Stochastic Linear Regulator Problem," Proceedings of the 1970 JACC, June 22-26, 1970, Atlanta, Georgia.

18. Boullion, T. L., and O'Dell, P. L., Generalized Inverse Matrices, Wiley-Interscience, New York, 1971.

19. Snyder, D. L., Random Point Processes, Wiley-Interscience, New York, 1975.

1976 USAF-ASEE SUMMER FACULTY RESEARCH PROGRAM
sponsored by
THE AIR FORCE OFFICE OF SCIENTIFIC RESEARCH
conducted by
AUBURN UNIVERSITY AND OHIO STATE UNIVERSITY

PARTICIPANT'S FINAL REPORT

SYNTHESIS OF NEW NITROALIPHATIC COMPOUNDS

AND

THERMAL DECOMPOSITION MECHANISMS OF POLYCYCLIC TRIAZOLINE COMPOUNDS

Prepared by:	William D. Closson, Ph.D.
Academic Rank:	Professor
Department and University:	Department of Chemistry State University of New York at Albany
Assignment:	
(Air Force Base) (Laboratory)	USAF Academy Frank J. Seiler Research Laboratory (AFSC)
(Division)	Energetic Materials Chemistry Division
(Branch)	Energetic Materials Research
USAF Research Colleague:	Capt Scott A. Shackelford, Ph.D.
Date:	August 13, 1976
Contract No.:	F44620-75-C-0031

SYNTHESIS OF NEW NITROALIPHATIC COMPOUNDS AND THERMAL DECOMPOSITION MECHANISMS OF POLYCYCLIC TRIAZOLINE COMPOUNDS

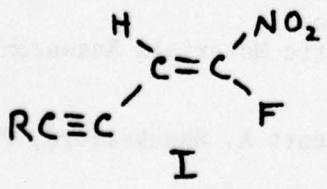
by
William D. Closson

ABSTRACT

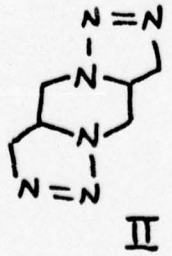
New classes of energetic compounds for use in explosive fills, solid rocket propellants, etc., are of considerable interest for the following reasons: increasing energy content and thermal and mechanical stability, and for possible replacement of nonenergetic binders, plasticizers, and crosslinking agents currently in use in these areas.

Compounds containing the acetylenic functional group as well as nitro and fluoro groups would be of interest since the triple bond not only increases the energy content but frequently increases the thermal stability of molecules in which it is present. It also allows further modification of the compound through facile addition and coupling reactions characteristic of the acetylenic group. Many attempts to synthesize one class of such compounds through SN2 reactions of acetylide salts with 2-fluoro-2,2-dinitroethyl derivatives failed but a general method for preparing the addition-elimination products (I) in reasonable yield was achieved. This is the first example of this type of reaction in polynitroaliphatic chemistry.

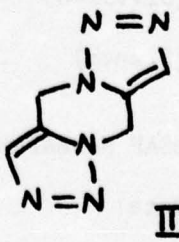
The dimer of allyl azide (II) is a shock insensitive material of considerable energy content. At about 180° it undergoes an exothermic, first order, decomposition. (Samples larger than a few milligrams frequently detonate at or below this temperature.) The kinetic parameters of this thermal decomposition are in the process of being determined and the products have been partly identified through mass spectroscopy. The aromatic analog of II (III) would very likely be more stable and more readily capable of further structural modification. Two approaches to its preparation failed.



I



II



III

INTRODUCTION

The Energetic Materials Chemistry Division of the Frank J. Seiler Research Laboratory (AFSC) (USAF Academy) maintains an active program of research on the preparation and properties of energetic materials that either are, or may be, used for explosive fills, solid rocket propellants, and related purposes. One of the more important goals of this program is to design and prepare new classes of energetic compounds that either have a greater energy content or superior stability (particularly thermal) than those currently in use. Another important goal is the development of energetic materials that could replace nonenergetic binders, plasticizers, and cross-linking agents currently used in the preparation of solid rocket propellants, etc. A third goal, or important area of research, is to achieve a thorough understanding of how energetic compounds undergo thermal degradation and to determine the products of such degradation. Thermal degradation is a serious problem with respect to explosive fills and solid propellants since it not only impairs the performance of such devices in energy terms, but also often creates corrosion problems and defects in structural stability of solid charges. Understanding the mechanism of these thermal decompositions is the first necessary step in either designing superior energetic materials or developing additives that will improve the thermal performance of current materials.

This report documents efforts involved on three separate projects in these areas. These were: 1) Synthesis of new nitroaliphatic compounds containing acetylenic groups. 2) A study of the thermal decomposition of the dimer of allyl azide and synthetic approaches to an aromatized analog of this compound. 3) Synthesis of N,N-bimaleimidyl, a potential crosslinking agent that should possess considerable stability.

OBJECTIVES

1. Development of a general synthesis of nitroaliphatic compounds containing acetylenic groups.

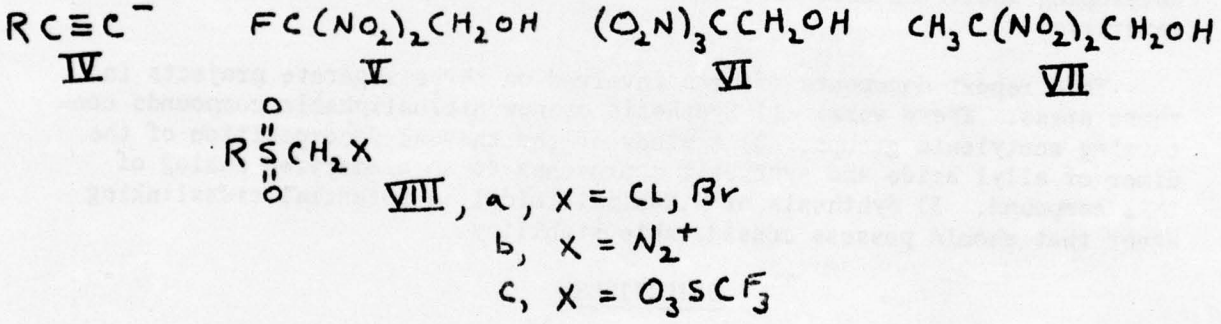
2. Determination of the mechanism of thermal decomposition of allyl azide dimer and identification of its decomposition products; preparation of the aromatic analog of allyl azide dimer.

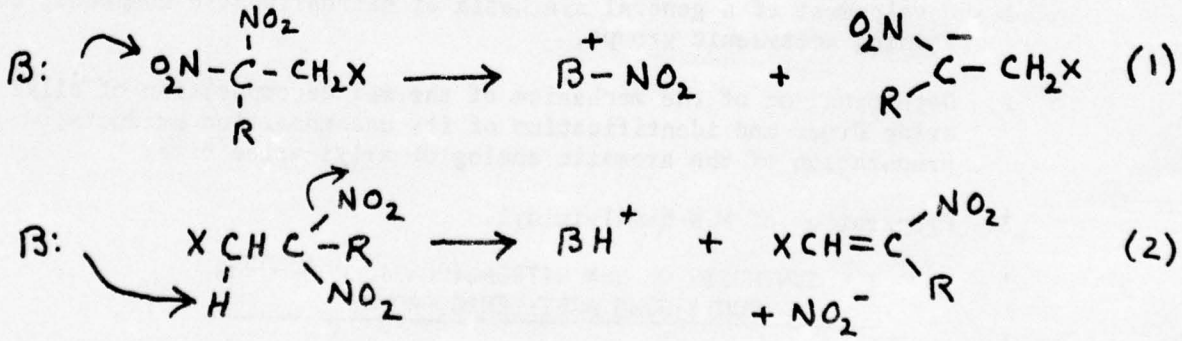
3. Preparation of N,N-bimaleimidyl.

1. SYNTHESIS OF NEW NITROALIPHATIC COMPOUNDS CONTAINING ACETYLENIC GROUPS

Compounds containing the acetylenic functional group as well as nitro and fluoro groups would be of considerable interest since the triple bond not only increases the energy content of molecules but also often increases the melting point and thermal stability as well. It also allows further modification through facile electrophilic addition and coupling reactions characteristic of the acetylenic group. Finally, the triple bond itself, or a carbon-carbon double bond easily derived from it, can serve as the locus for many types of polymerization reactions.

The simplest approach to preparation of this class of compounds would be a nucleophilic displacement reaction between acetylide anions (IV) and suitable derivatives of the readily available, highly nitrated alcohols, 2-fluoro-2,2-dinitroethanol (V), 2,2,2-trinitroethanol (VI), and 2,2-dinitro-1-propanol (VII). This approach, however, is fraught with two very serious problems. One is that all of the starting alcohols have two or more large and very electronegative substituents on the β-carbon. This seriously inhibits SN2 displacements through both steric (as in the well known case of the neopentyl system) and field effects. A well known case where the combination of these effects almost totally inhibits reaction is that of α-halosulfones (VIII).[1] Indeed, the benzenesulfonate derivative of VII has been described as being inert toward chloride or acetate ion in boiling ethanol.[2] Secondly, the nitro groups may interfere directly, either through direct attack of the nucleophile on one of the nitro groups yielding a nitro-stabilized carbanion (eq.1), or by inducing β-elimination of nitrite ion (eq.2).[3] However, recent reports that sulfones substituted at the α-position with either diazonium ion[4] (VIIIb) or triflate (VIIIc) groups[5] undergo smooth substitution reactions with certain nucleophiles,[6] and reports of some substitution reactions undergone by the tosylate of V[6] and preparation of the triflate of V[7] encouraged us to try this approach.





It was decided to concentrate initially on displacement reactions of derivatives of V since this appears to be the more stable of the three polynitroalcohols.[9] Accordingly, the tosylate, bromide, and triflate derivatives were prepared. The structures are IXa, b, and c, respectively. A plausible substrate for nucleophilic displacement in this series, the diazo compound X,

was not considered because of the treacherous nature[9] of about the only plausible precursor, 2-fluoro-2,2-dinitroethylamine.[9] The tosylate was easily prepared by the method of Adolph and Kamlet[9] and could easily be converted to the bromide by heating with lithium bromide in dimethylformamide. Steam distillation of the reaction mixture, extraction of the distillate with methylene chloride, concentration and distillation afforded pure bromide in about 65% yield. (Most of the loss is incurred during the second distillation.) This was found superior to the published method[6] in that IXb could be obtained. The triflate (IXc) was prepared as described in the literature[7] with the variation that a solution of pyridine was slowly added to a solution of V and triflic anhydride in methylene chloride at -22°.

$FC(NO_2)_2CH_2X$

IX, a, X = O_3S-(C6H4)-CH_3

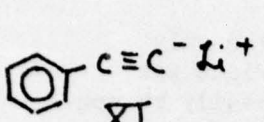
b, X = Br

c, X = O_3SCF_3

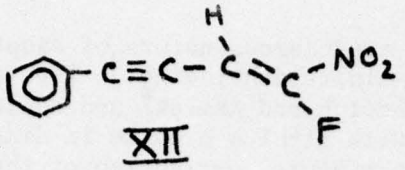
$FC(NO_2)_2CH=N_2$

X

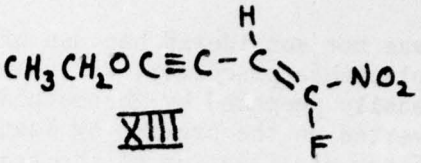
The reaction between the triflate ester (IXc) and the lithium salt of phenylacetylene (XI) was first investigated. The reaction was carried out at low temperatures in diethyl ether solution and afforded a modest yield of bright yellow solid; m.p.58.5 - -59.5°. The ir and particularly, nmr spectra, of this material quickly identified it not as a substitution product, but as an elimination-addition product with the novel structure: Z-1-fluoro-1-nitro-4-phenylbut-1-en-3-yne (XII). The mass spectrum (parent peak, m/e = 191) confirmed this. The nmr showed the vinylic proton as a doublet (J = 21 Hz) centered at about 6.8 ppm. This magnitude of coupling constant is consistent only with a <u>trans</u> arrangement of hydrogen and fluorine.[10] It was later found that this is a fairly general reaction of lithium acetylides and triflate ester IXc and two other examples of this class of enynes were prepared: Z-1-fluoro-1-nitro-4-ethoxybut-1-en-3-yne (XIII) and Z-1-fluoro-1-nitro-5-methyl-1,5-hexadien-3-yne (XIV). The usual yields under optimum conditions were in the range of 40-60%, as estimated from nmr spectra on the crude reaction mixtures. Isolation and purification, however, presented considerable difficulty, and yields of pure product were usually on the order of 30%. All of these enynes appear to polymerize quite readily on heating and attempts at distillation or sublimation usually destroyed most of the material. However, considering the wide variation in structure of the enynes prepared, their reasonable stability at ambient temperatures, and the fact that fairly pure samples can be isolated in respectable yield by simple liquid chromatography, this reaction promises to be extremely useful. Further examination of reaction variables such as temperature, concentration of reactants, mode of mixing reactants, <u>etc.</u>, and of isolation techniques, will almost certainly improve the yields.



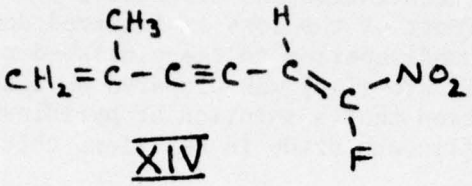
XI



XII



XIII



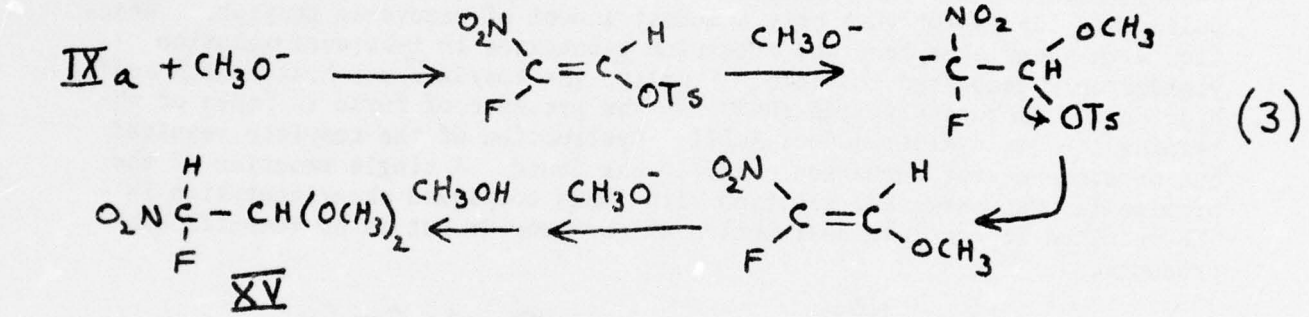
XIV

The enynes themselves probably will not be of much use as energetic materials, but attachment of more energetic groups through addition or condensation reactions should be quite feasible. The ready polymerizability of these compounds, in particular, makes their use as starting materials for the development of energetic binders, plasticizers, or crosslinking agents, appear very promising.

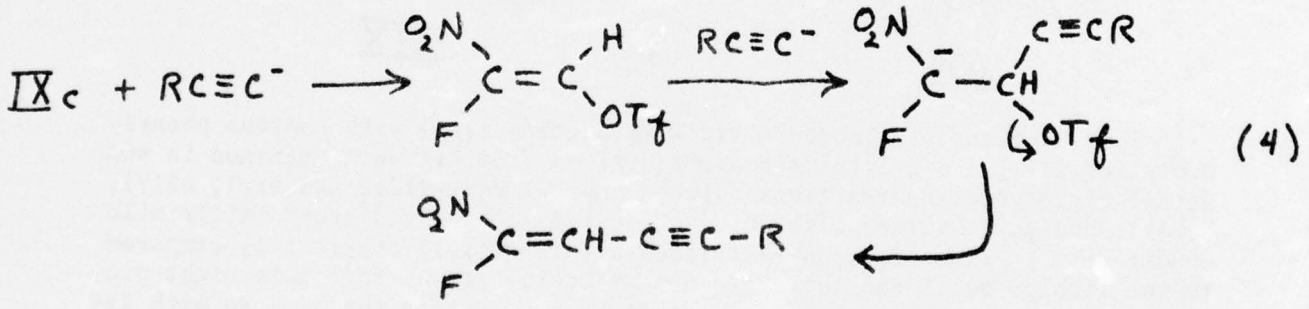
As evidence of the ease of preparation of these compounds, a typical reaction will be described in some detail. In 15 ml of dry diethyl ether 1.44 g (14.01 mmoles) of phenylacetylene was dissolved and the solution placed in a septum-sealed flask equipped with a magnetic stirrer. The solution was cooled in an ice bath, flushed with dry nitrogen, and 9.0 ml of 1.6 M butyllithium in hexane solution was added slowly via syringe. The resulting, slightly cloudy, solution was then transferred via syringe to a septum-capped dropping funnel that was also flushed with nitrogen. The dropping funnel was attached to a flask containing 2.00 g (7.0 mmoles) of 2-fluoro-2,2-dinitroethyl triflate dissolved in 20 ml of dry ether. This flask was flushed with nitrogen and then sealed with an oil bubble device. It was then cooled with stirring in a dry ice-diethyl ether bath (ca. -100°) and the phenylacetylide solution added slowly over a period of about one hour. The solution rapidly turned a red-brown color. The solution was stirred for about 2 hours while the bath was allowed to warm to room temperature. It was then poured onto a mixture of ice and saturated brine and the ether-soluble components separated in usual fashion. Drying and concentration under reduced pressure yielded 1.73 g of red-brown oil. Chromatography of this material on 13 g of 60/200 mesh silica gel using hexane as eluent yielded, from the first 250 ml fraction, 0.86 g (4.5 mmoles, 64%) of fairly pure XII. Further chromatographic purification and recrystallization afforded 0.41 g (2.14 mmoles, 30%) of material melting at 57-59°.

From the information we have thus far it is not possible to say with certainty what the mechanism of the enyne forming reaction is. The structure of the products requires that the stoichiometry of the reaction be 2 moles of acetylide to 1 mole of the triflate ester. The only reaction in the literature even vaguely similar is one described by Adolph[6] between methoxide ion in methanol and fluorodinitroethyl tosylate (IXa). The major product was 1-fluoro-1-nitro-2,2-dimethoxyethane (XV) and Adolph proposed the elimination-addition-elimination-addition mechanism shown in eq. 3. The enynes could

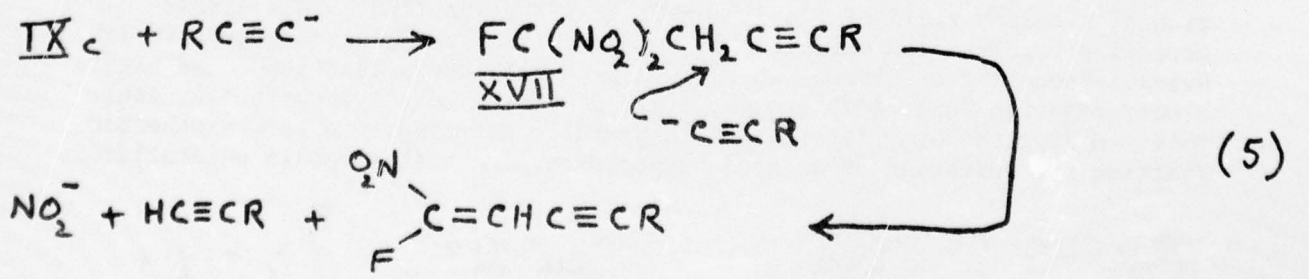
conceivably be formed by either the elimination-addition-elimination process described in eq. 4, or the substitution-elimination process shown in eq. 5. From the available information Adolph's reaction could also be taking place by a substitution-elimination process similar to eq. 5. Solution to this mechanistic puzzle is of interest not only for scientific reasons but also for the following practical ones. If the mechanism is as shown in eq. 4, it may be possible to generate the intriguing intermediate 2-fluoro-2-nitrovinyl triflate (XVI) with non-nucleophilic bases such as sodium hydride and trap it with less basic nucleophiles or possibly with conjugated dienes <u>via</u> a Diels-Alder reaction. Either trapping reaction could give rise to some very interesting classes of compounds. If the mechanism is as shown in eq. 5, it may be possible to inhibit the final elimination step and obtain the as yet unknown substitution products (XVII).



(3)

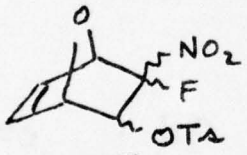


(4)

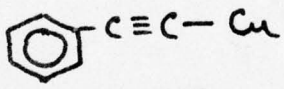


(5)

Severl other variations of this reaction were tried in hope of either improving the yield of enyne or possibly obtaining the substitution product XVII. Reaction of triflate IXc with commercially available propynyllithium in tetrahydrofuran (THF) solution failed to yield either desired product, probably because of the insolubility of this lithium salt. Reaction of IXc with lithium phenylacetylide in THF gave only traces of enyne XII, possibly because of the lesser solubility of this acetylide in THF. Complexation of lithium phenylacetylide with tetramethylethylenediamine (TMEDA) greatly improved its solubility in THF but this complexed acetylide quickly destroyed the triflate without producing any detectable amount of XII. Possibly, complexation of the acetylide increases its basicity but not its nucleophilicity. Fluorodinitroethyl tosylate (IXa) is more easily prepared than the triflate and was a needed precursor to the bromide (IXb). Several reactions of IXa were therefore examined. Reaction of the tosylate with phenylacetylene and sodium hydride in THF gave only a modest amount of recovered tosylate. Reaction with phenylacetylene and potassium t-butoxide in t-butanol solution yielded only recovered tosylate. Finally, the tosylate was heated with sodium hydride in dimethylsulfoxide (DMSO) in the presence of furan in hopes of obtaining the Diels-Alder adduct XVIII. Destruction of the tosylate resulted but no evidence for formation of XVIII was found. A single reaction of the bromide IXb was examined; reaction with TMEDA complexed phenylacetylide in THF resulted in complete destruction of the bromide but in no identifiable products.

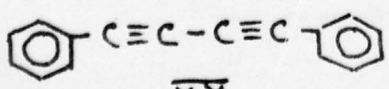


XVIII

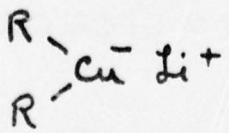


XIX

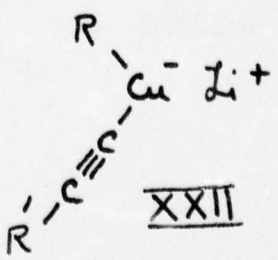
The reactions of fluorodinitroethyl bromide (IXb) with cuprous phenylacetylide (XIX) and a lithium reagent derived from XIX were examined in some detail since coupling reactions between cuprous acetylides and aryl, allyl, benzyl, and acyl halides often proceed in excellent yield under fairly mild conditions.[11] Since cuprous acetylides are relatively covalent as compared to the lithium salts and therefore not as basic, it was felt this might provide a route to the substitution product XVII. Heating the bromide with XIX in dimethylformamide (DMF) resulted in destruction of the bromide and formation of a modest yield of 1,4-diphenylbuta-1,3-diyne (XX). This almost certainly results from oxidation of the acetylide by the nitro groups in IXb. Oxidativecoupling of cuprous acetylides is a well known reaction[12] and highly electronegative functional groups, e.g., diazonium ions[13] occasionally cause this. Mixing the bromide with XIX in pyridine resulted in a very exothermic reaction and formation of a large number of products that remain unidentified.



XX



XXI



XXII

Dialkylcopper lithium species, such as XXI, readily formed from reaction of cuprous iodide with alkyllithium reagents, have recently received wide use in coupling alkyl groups to alkyl, allyl, vinyl, and even aryl iodides and bromides.[14] Mixed reagents, XXII, can also be formed through reaction of cuprous acetylides with alkyllithium in ether solution.[15] Preparation of XXII where R is n-butyl and R´ is phenyl was readily achieved, but its reaction with IXb produced only a trace of XX. Apparently, these mixed copper reagents[15] prefer to transfer the alkyl group rather than the acetylide.

Finally, a Friedel-Crafts type reaction between the bromide and phenylacetylene, catalyzed by aluminum chloride, in nitromethane solution was examined. Overnight stirring of the mixture resulted in destruction of the bromide but formation of no identifiable products.

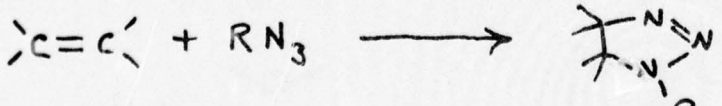
1. CONCLUSIONS AND RECOMMENDATIONS

A rapid, fairly good yield, synthesis of nitrofluoroenynes has been achieved. Further study of reaction variables and isolation techniques should improve the yields considerably. These enynes have considerable promise for use in developing new energetic binders, plasticizers, and crosslinking agents. The mechanism of the reaction is not well understood and should definitely receive further study since such knowledge could conceivably lead to methods of preparing other new classes of energetic compounds.

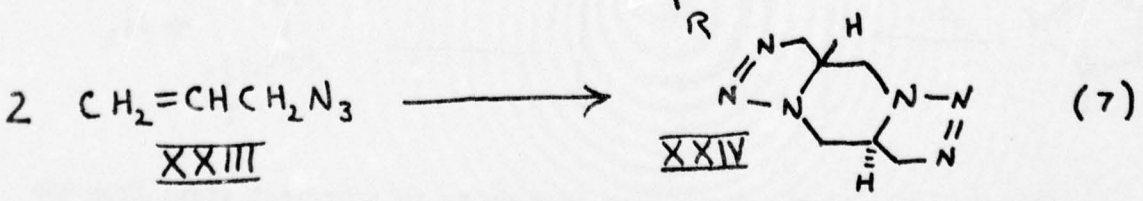
The generality of the enyne forming reaction should be further extended by testing it with triflate esters of other polynitro and polyfluoro alcohols.

2. MECHANISM OF THERMAL DECOMPOSITION OF ALLYL AZIDE DIMER AND APPROACHES TO SYNTHESIS OF ITS AROMATIC ANALOG

Some of the most well known reactions of alkyl or arylazides are their 1,3-cycloaddition reactions with carbon-carbon double and triple bonds (eq. 6). Therefore, it is not surprising that allyl azide (XXIII) undergoes a smooth dimerization reaction (eq. 7), slowly on standing, or fairly rapidly on gentle refluxing (ca. 60°). What is surprising is that at present this is the only known example of such a dimerization. All other allylic azides steadfastly resist similar condensation no matter what the conditions.



(6)



(7)

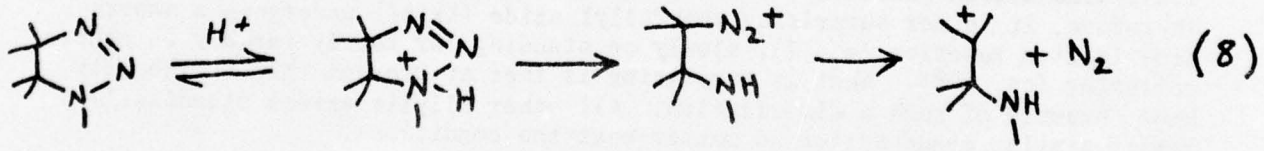
The dimer (XXIV) was first obtained by Forster and Fierz[16] in 1908 during the course of the first reported preparation of allyl azide. They noted a white, crystalline solid remaining after distillation of the azide at atmospheric pressure. At the time these workers determined its elemental composition and molecular weight, and proposed a couple of possible structures

10

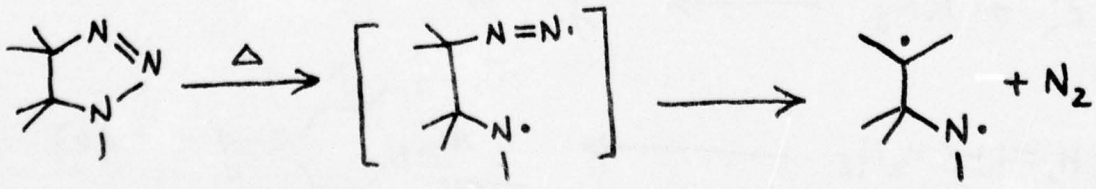
for it. In 1954, Boyer and Canter noted that one of these structures was the more likely,[17] and finally, in 1973, on the basis of a single crystal X-ray diffraction study, Pezzullo and Boyko proved it had the centrosymmetric tricyclic structure shown.[18] Its proper name, according to chemical abstracts, is 3a,4,8a,9-tetrahydro-3H,8H-bis[1,2,3]triazolo[1,5-a:1′,5′-d] pyrazine.

Preparation of the dimer is quite straightforward. Reaction of allyl chloride or bromide with sodium azide in a DMF-water mixture takes place readily on stirring at room temperature for a few hours. Addition of more water and steam distillation of the mixture yields a distillate consisting of water and quite pure allyl azide. Separation and drying with $CaCl_2$ affords the azide in 75-80% yield. Refluxing this liquid for 8-10 hrs. and cooling affords a modest (5-15%) yield of the dimer as a white, highly crystalline, solid. The unreacted azide can be easily separated by filtration or decantation and used to prepare more dimer. It is definitely inadvisable (vide infra) to reflux the azide for more than about 12 hrs. without separating the precipitated dimer from it. The dimer is rather insoluble but it can be recrystallized from methylene chloride. Its melting point, as usually determined in an open capillary, is rather variable, usually occurring with concurrent decomposition and gas evolution, somewhere between 180° and 200°.

Like most 1,2,3-triazolines, the dimer is rapidly decomposed by strong acids and even slowly by water. The likely mechanism is shown in eq. 8. The thermal decomposition of most triazolines occurs by the process shown in eq. 9, and radical intermediates are definitely involved. Some triazolines have even been recommended for use as initiators for radical catalyzed polymerization reactions. Allyl azide dimer, though, while it does decompose thermally, apparently does so by a non radical process or by a process in which intermediate radicals are rapidly converted to nonradical species. Heating the dimer in pure styrene under nitrogen does not speed the polymerization reaction, but actually inhibits the normal slow polymerization exhibited by pure styrene alone.[19]



(8)



(9)

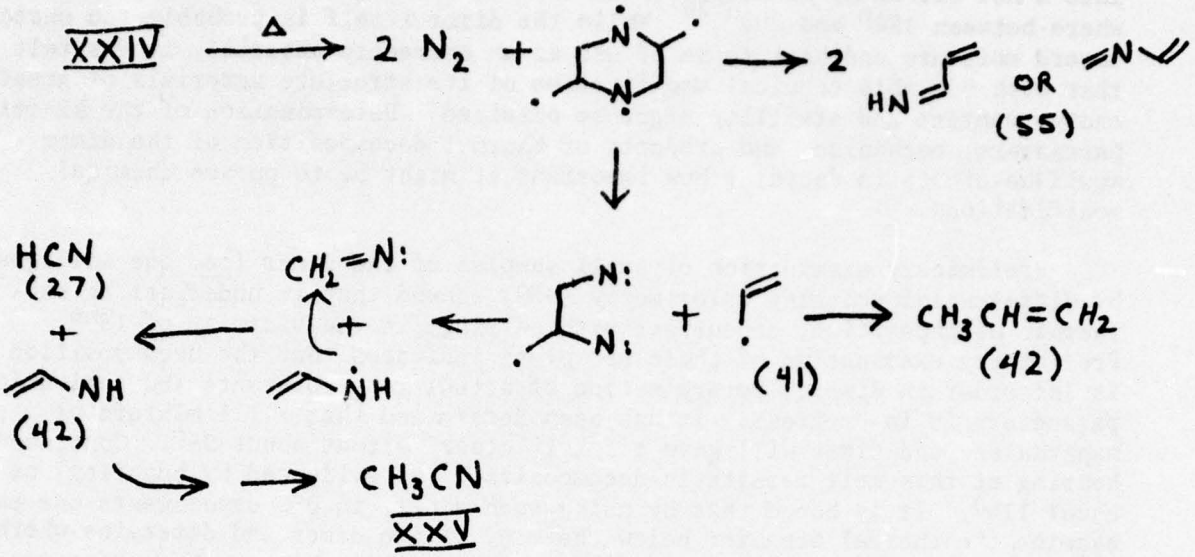
Our interest in the dimer with respect to this project stems from the fact that under certain conditions it will undergo thermal detonation but apparently has little or no shock sensitivity. (Note: Insensitivity to shock has not been carefully tested, however.) Heating of solid samples of the dimer much larger than a few milligrams, either by warming up slowly from room temperature or by rapid warming such as plunging the container

into a hot oil bath, usually results in a fairly vigorous detonation somewhere between 150° and 200°.[20] While the dimer itself is probably too unstable toward moisture and heat to be of use as an energetic material, it was felt that with suitable chemical modification of its structure materials of greater energy content and stability might be obtained. Determination of the kinetic parameters, mechanism, and products of thermal decomposition of the dimer would be of use in deciding how important it might be to pursue chemical modifications.

Preliminary examination of small samples of the dimer (ca. one milligram) by differential scanning calorimetry (DSC) showed that it undergoes an exothermic decomposition, concurrent with melting, in the vicinity of 180°. Preliminary examination of these DSC plots indicates that the decomposition is 1st order in dimer. Determination of actual rate constants and activation parameters is in progress. It has been determined that a 1:1 mixture of naphthalene and dimer will give a fairly clear melt at about 95°. Continued heating of this melt results in decomposition (as evidenced by bubbling) at about 110°. It is hoped that by using such a melt in DSC experiments one can examine the thermal behavior below the m.p. of the dimer and determine whether there is an induction period for this decomposition, whether there is a concentration effect on decomposition temperature, and determine the activation parameters much more accurately. These experiments are planned for the near future.

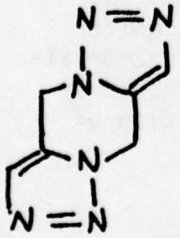
One experiment directed toward identification of the pyrolysis products has been carried out. A 4.2 mg sample of XXIV was sealed under vacuum in a glass container of about 10 ml volume. This was slowly warmed in an oil bath until it decomposed quite violently at about 200°. Examination of the gases in the closed container by mass spectroscopy revealed a sizeable peak at M/e = 41 as well as modest peaks at M/e = 27 and 57. Nitrogen was certainly present but could not be qualitatively determined because of air leakage. The material of mass 41 may be acetonitrile (XXV) and that of 27 is probably HCN. If these are correctly identified, it is rather significant that small, gaseous molecules other than N_2 are produced in the decomposition. The mass spectrum of the nonvolatile products showed a variety of peaks. The most abundant, in decreasing order, were at masses of 41, 55, 54, 42, 27, 18, 56, and 39. A little unreacted dimer (mass 166) could also be detected. The mass spectrum of allyl azide showed many of the same peaks but with quite different relative intensities. It is therefore unlikely that the decomposition of the dimer involves a preliminary cracking back to azide followed by rapid decomposition of the azide. A tentative scheme for decomposition of the dimer is outlined below.

12



Further work on more positive identification of the products is required as well as more accurate measurement of their yields before this scheme can be considered correct. A further complication that may exist is that the relatively slow thermal decomposition and the frequently observed detonation may be quite different chemical processes. An accurate product study of both reactions should answer this question. Further work is planned for the near future.

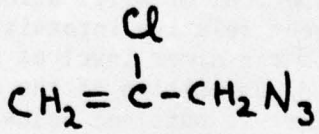
The aromatic analog of the dimer, XXVI, would be of considerable interest. The nitrogens in the triazole rings of XXVI should be essentially non-basic so this molecule should be much more stable toward moisture and acids than the azide dimer. The presence of two fairly aromatic rings should also increase thermal stability. Finally, either the carbons in the aromatic rings or the benzylic carbons in the central ring could serve as centers for attachment of energetic groups.



XXVI

$HC\equiv CCH_2N_3$

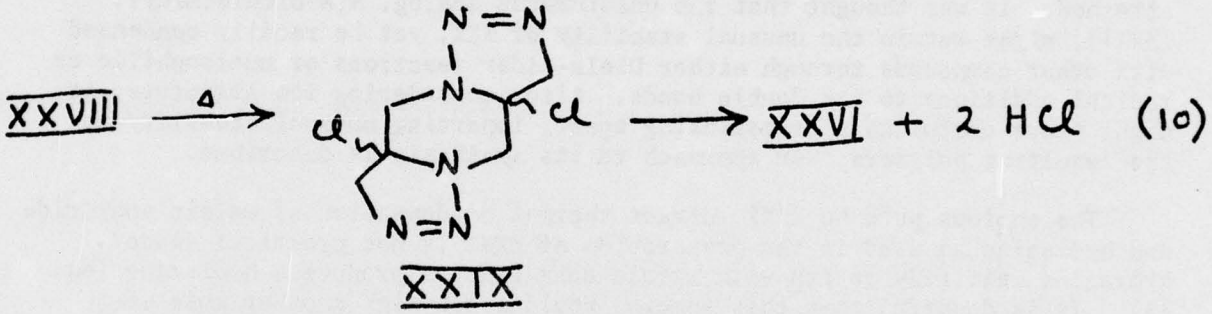
XXVII



XXVIII

Three approaches to synthesis were considered. Formally, one can consider XXVI to be the dimer of propargyl azide (XXVII). One might consider simply preparing XXVII and thermally condensing it as in the case of allyl azide. Baldwin and Coworkers, however, prepared XXVII and report that it

polymerizes at room temperature and that it "is a dangerous explosive with sensitivity greater than that of nitroglycerine."[21] This approach was not considered further. A second approach would be dimerization of β-chloroallyl azide (XXVIII). The resulting intermediate (XXIX) should rapidly lose HCl and generate XXVI (eq. 10). The β-chloroallyl azide was easily prepared in 78% yield in a manner similar to the preparation of XXIII, but neither long refluxing of the neat azide over K_2CO_3 or refluxing a solution of it in CCl_4 for several hours caused any change to occur.[4] This approach to XXVI should probably be pursued a bit further, but does not appear too promising. Finally, one could consider dehydrogenating XXIV itself. One brief experiment was carried out in this direction. Heating with elemental sulfur has been frequently used to convert nonaromatic compounds to their aromatic analogs. Two milligrams of XXIV was thoroughly mixed with 6 milligrams of powdered sulfur and a portion of it heated slowly in a m.p. capillary. Shortly after the mixture melted (ca. 120°) vigorous bubbling commenced and developed into a foaming froth. Considering the volume of gas being evolved, the dimer was probably being decomposed rather than being dehydrogenated. Molten sulfur is known to have Lewis acid properties and it probably brings about decomposition of XXIV by a mechanism similar to that shown in eq. 8.



2. CONCLUSIONS AND RECOMMENDATIONS

Allyl azide dimer undergoes an exothermic thermal decomposition at about 180° that appears to be first-order in dimer concentration. In solution in molten naphthalene the decomposition can be observed at temperatures as low as 110°. It should be quite feasible to determine the rate and activation parameters of this reaction by differential scanning calorimetry. The products of decomposition have been partially determined and a tentative mechanism for the reaction proposed. Attempts to prepare the aromatic, and potentially more useful, analog of allyl azide dimer have been unsuccessful.

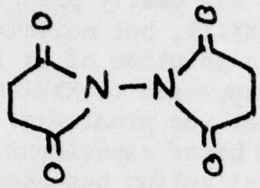
The kinetic studies on the thermal decomposition of the dimer should definitely be completed, as well as more quantitative determinations of the decomposition products. Approaches to synthesis of the aromatic analog of the dimer should continue to be explored.

3. AN APPROACH TO THE SYNTHESIS OF N,N-BIMALEIMIDYL

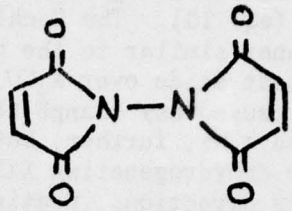
In 1963 the preparation and proof of structure of N,N-bisuccinimidyl (XXX) was reported.[22] The material melts at 310° without decomposition, is

14

quite stable toward most oxidants, and survives heating in a sealed tube at 400° for several days.[22] The compound can be prepared quite easily by simply heating a mixture of hydrazine and either succinic acid or succinic anhydride to high temperatures.



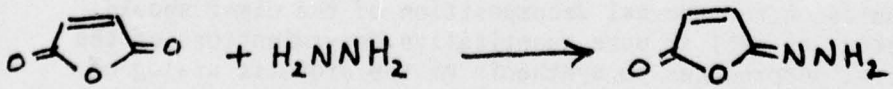
XXX



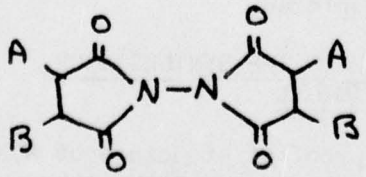
XXXI

The great stability of XXX suggests that attachment of energetic groups to such a molecule might yield new classes of energetic materials of unusually high melting point and thermal stability. Unfortunately, there are no reactive functional groups in XXX to which other molecules might be readily attached. It was thought that the unsaturated analog, N,N-bimaleimidyl, (XXXI), might retain the unusual stability of XXX, yet be readily condensed with other compounds through either Diels-Alder reactions or nucleophilic or radical additions to its double bonds. Also, considering its structure, it might prove useful as a crosslinking agent, imparting unusual stability to the resulting polymers. An approach to its synthesis is described.

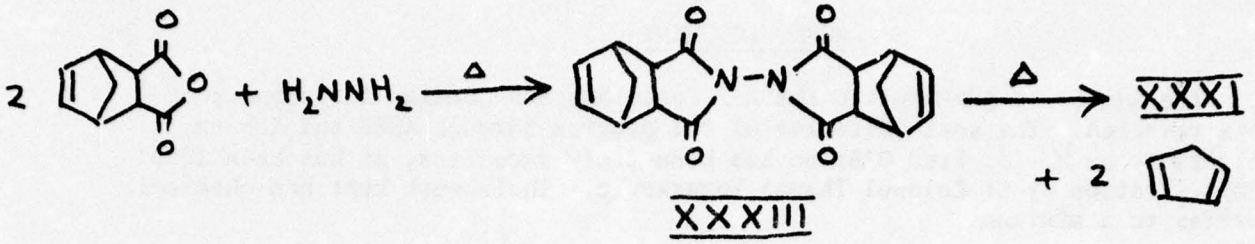
The obvious path to XXXI, direct thermal condensation of maleic anhydride and hydrazine as used in the preparation of XXX, is not practical since hydrazine initially reacts with maleic anhydride to produce a hydrazone (eq. 11). It is doubtful that this species would react with another mole of anhydride to produce structure XXXI. An alternative approach would be to prepare some saturated bi-imide (XXXII) which could be converted to XXXI in the last step of the synthetic sequence by a simple elimination reaction of the groups A and B. What appears to be an attractive synthetic sequence is outlined in eq. 12. The easily prepared adduct of cyclopentadiene and maleic anhydride[23] should react with hydrazine in about the same manner as succinic anhydride to yield the bi-imide XXXIII. At a high enough temperature XXXIII should undergo a double reverse Diels-Alder reaction to yield volatile cyclopentadiene and the desired product. The only questionable aspect of this scheme is whether the temperatures necessary for the first thermal condensation step would crack the starting material back to cyclopentadiene and some maleic acid derivative before conversion to XXXIII could be achieved.



(11)



XXXII



(12)

A single attempt at preparation of XXXI via the scheme of eq. 12 was carried out. Heating a mixture of the maleic anhydride-cyclopentadiene adduct and hydrazine at about 160° for an hour produced a viscous syrup from which a low yield of white solid could be obtained by trituration with hot CCl_4 and recrystallization from DMF-water. The material melted at about 270°, and had an nmr spectrum and mass spectrum consistent with structure XXXIII. A sample of this material (0.44 g) was placed in a sublimation apparatus and heated at 285° for 30 min. under vacuum. Most of the material simply sublimed up to a cooler portion of the apparatus, but about 20 mg of fluffy brownish solid remained in the bottom. This material did not melt below 400°, was insoluble in water, but appeared to be soluble in DMSO. It was not volatile enough to give a satisfactory mass spectrum and the limited amount of material did not give a satisfactory nmr spectrum. The material did appear to react with anthracene in DMSO solution, but again, owing to the small amounts of material available, the evidence is not very convincing. The behavior of the brownish solid is consistent with what one might expect for that of N,N-bimaleimidyl (XXXI), but the overall synthesis must be improved and larger quantities of the solid obtained before its structure can be definitely established.

3. CONCLUSIONS AND RECOMMENDATIONS

A reasonable synthetic route to the potentially useful compound N,N-bimaleimidyl has been designed and one attempt to carry it out has been made. The preparation of the bi-imide may have been achieved. Further improvement of the synthesis and proof of the structure of the compound is needed.

ACKNOWLEDGMENT

The author is grateful to the Air Force Systems Command for support of this research. The administration of the program through ASEE and Auburn University by Mr. J. Fred O'Brien has been truly excellent, as has been local administration by Lt Colonel Thomas Tomaskovic. Their work kept non-chemical worries to a minimum.

The author is indebted to all of the chemists and staff of the Frank J. Seiler Research Laboratory for providing a pleasant and helpful environment, but special thanks are due to Major Ben Loving for his cheerful encouragement and advice, to Mr. Lloyd Pflug for his superb spectroscopy service, and to Dr. Hans Reich, Mr. Fred Kibler, and Mrs. Betty Darcy for excellent assistance in ways too numerous to mention.

Finally, it should be noted that much of this work is based on ideas and insights of my research colleague, Captain Scott A. Shackelford. His constant enthusiasm, excellent advice, and vast knowledge of this area of chemistry are responsible, in large part, for the success we enjoyed. He was a splendid colleague.

REFERENCES

1. F. G. Bordwell and G. D. Cooper, J. Amer. Chem. Soc., 73, 5184 (1951); F. G. Bordwell and W. T. Brannen, Jr., ibid., 86, 4645 (1964).

2. L. W. Kissinger, T. M. Benziger, H. E. Ungnade, and R. K. Rohwer, J. Org. Chem., 28, 2491 (1963).

3. L. Zeldin and H. Schechter, J. Amer. Chem. Soc., 79, 4708 (1957).

4. J. B. F. N. Engberts and B. Zwanenburg, Tetrahedron, 24, 1737 (1968).

5. K. Hovius and J. B. F. N. Engberts, Tetrahedron Lett., 2477 (1972).

6. H. G. Adolph, J. Org. Chem., 36, 806 (1971).

7. C. D. Beard, K. Baum, and V. Grakauskas, ibid., 38, 3673 (1973).

9. H. G. Adolph and M. J. Kamlet, ibid., 34, 45 (1969).

10. R. M. Silverstein and G. M. Bassler, "Spectrometric Identification of Organic Compounds," John Wiley and Sons, Inc., N.Y., 1967, p 145.

11. C. E. Castro, R. Havlin, V. K. Honwad, A. Malte, and S. Moje, J. Amer. Chem. Soc., 91, 6464 (1969).

12. See I. D. Campbell and G. Eglinton, Org. Syn., 45, 39 (1965), and references therein.

13. R. W. Benson, unpublished observations, Dept. of Chemistry, SUNY - Albany, Albany, N.Y., 1967.

14. E. J. Corey and G. H. Posner, J. Amer. Chem. Soc., 89, 3911 (1967); ibid., 90, 5615 (1968).

15. E. J. Corey and D. J. Beames, ibid., 94, 7210 (1972).

16. M. O. Forster and H. E. Fierz, J. Chem. Soc., 93, 1178 (1908).

17. J. H. Boyer and F. C. Canter, Chem. Rev., 54, 1 (1954).

18. J. C. Pezzullo and E. R. Boyko, J. Org. Chem., 38, 168 (1973).

19. Private communication, Professor N. Invictor, Dept. of Chemistry, Brooklyn College, Brooklyn, N.Y.

20. Richard Hanauer, unpublished observations, Dept. of Chemistry, Columbia University, New York, N.Y., 1964.

21. M. G. Baldwin, K. E. Johnson, J. A. Lovinger, and C. O. Parker, J. Polym. Sci., Part B., 5, 803 (1967); Chem. Abstr., 67, 91143w (1967).

22. E. Hedaya, R. L. Hinman, and S. Theodoropulos, J. Amer. Chem. Soc., 85, 3052 (1963).

REFERENCES (Continued)

23. L. F. Fieser, "Organic Experiments," 2nd ed., Raytheon Education Co., Lexington, Mass., 1968, p. 85.

1976 USAF-ASEE SUMMER FACULTY RESEARCH PROGRAM
sponsored by
THE AIR FORCE OFFICE OF SCIENTIFIC RESEARCH
conducted by
AUBURN UNIVERSITY AND OHIO STATE UNIVERSITY

PARTICIPANT'S FINAL REPORT

ELECTRODE EROSION

IN PULSED PLASMA THRUSTERS

Prepared by:	David D. Chesak, Ph.D.
Academic Rank:	Associate Professor
Department and University:	Mathematics and Physics Department St Joseph's College
Assignment:	
(Air Force Base)	Edwards Air Force Base
(Laboratory)	Rocket Propulsion Laboratory
(Division)	Liquid Rocket Division
(Branch)	Space Propulsion Branch
USAF Research Colleague:	Franklin B. Mead, Jr.
Date:	August 20, 1976
Contract No.:	F44620-75-C-0031

ELECTRODE EROSION IN PULSED PLASMA THRUSTERS

by

D. D. Chesak

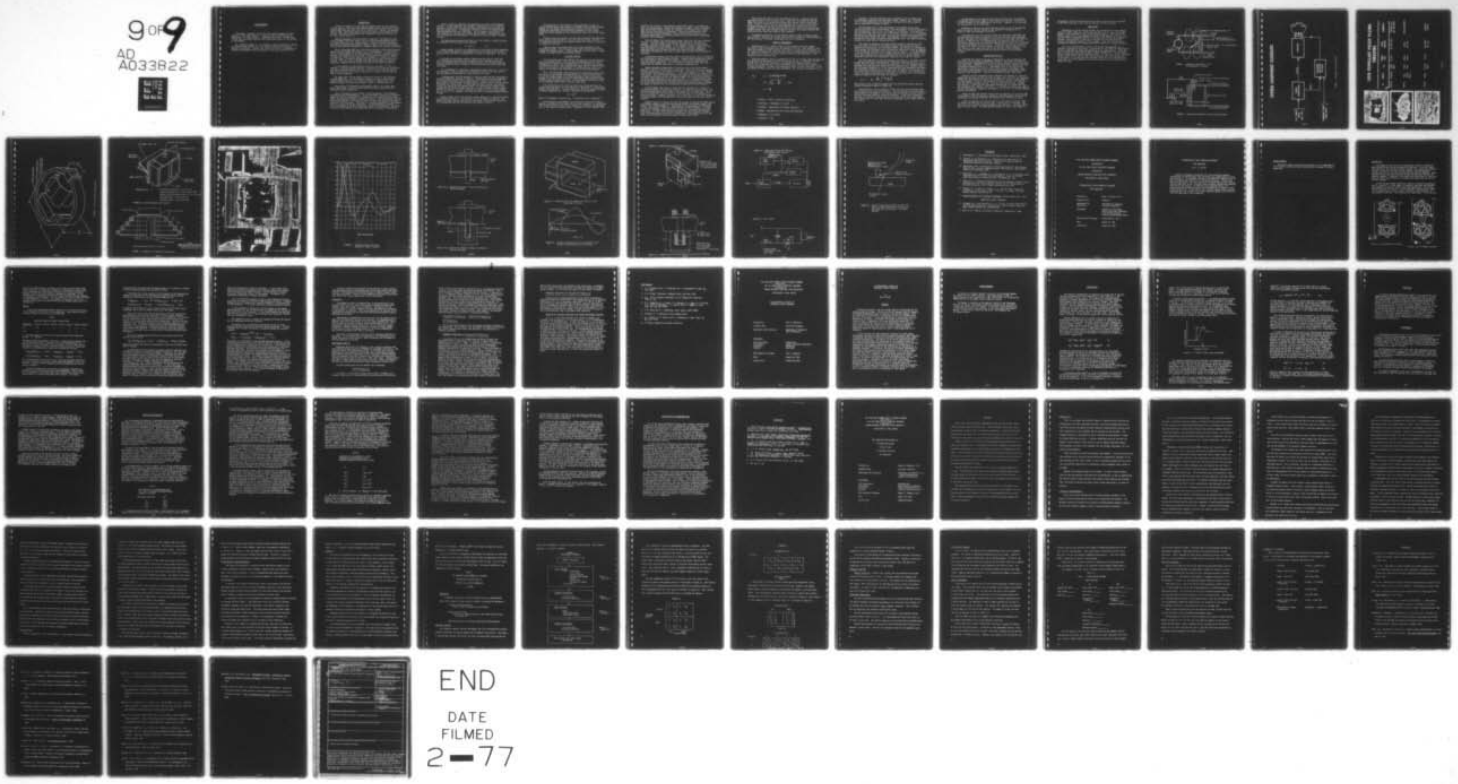
ABSTRACT

Electrode erosion in pulsed plasma, electromagnetic thrusters is a persistent problem for engineers engaged in the design of long life satellites. The most successful design utilizes Teflon as an ablative propellant and electrical energy derived from the spacecraft solar energy system. The short duration, high current pulses vaporize the electrode surfaces and cause a loss of material, especially from the anode. Fluorine interaction with the anode is suspected but there is no conclusive data to support this.

The premise of this paper is that the dwell time of the anode arc spot must be decreased and that this can be accomplished by increasing the magnetic field in the thruster chamber. Three techniques are suggested; anode reorientation, partially surrounding the anode with a magnetic core and placing Helmholtz coils around the chamber. An engineering recommendation is made for the millipound thruster which uses all three methods. Some of the pertinent specifications have been calculated and are included.

AD-A033 822 AUBURN UNIV ALA SCHOOL OF ENGINEERING F/G 14/2
1976 USAF-ASEE SUMMER FACULTY RESEARCH PROGRAM.(U)
SEP 76 J F O'BRIEN F44620-75-C-0031
UNCLASSIFIED AFOSR-TR-76-1419 NL

9 OF 9
AD A033822



END

DATE FILMED
2-77

ACKNOWLEDGMENT

The author is grateful to the Air Force Systems Command for their support of this summer research. Thanks are due to ASEE and Auburn University. Mr. Fred O'Brien, Dr. Lawrence Quinn and Dr. Richard Weiss, through their excellent planning, have contributed greatly to the success of the program.

Mr. Franklin B. Mead, Jr., the author's research counterpart, through his efforts aided enormously in the literature search and in giving patient, wise counsel. Further, the author would like to acknowledge the friendly encouragement given by everyone in the Liquid Rocket Division.

INTRODUCTION

Artificial terrestrial satellites are becoming more and more important as time goes on. Their value for communications, weather forecasting, intelligence operations and other services is inestimable. However, the monetary cost is high. Placing one vehicle in orbit can easily cost several million dollars. The high price mandates that a spacecraft serve its function for as long a time as possible.

Satellite designers are striving for a seven year life time for units to be launched in the near future. With the sophisticated hardware that is available today, this is a reasonable goal. Since solar energy converters can supply an inexhaustible supply of electric power, there is no particular limit to the time that computers and telemetry systems can continue functioning.

One of the systems that has a restricted lifetime is that which maintains proper vehicle attitude and velocity, i.e., stationkeeping. In particular, the fuel supply needed for thruster operation is limited. Compressed gas or chemical fuel thrusters do not provide a sufficiently high specific impulse. As longer and longer mission durations are planned for a specific vehicle size and weight, a trade-off between fuel supplies and other hardware must be made. Thus, until that time when in-flight refurbishment is feasible, operational capabilities and mission lifetime will be competing factors.

If the equation for the propulsive force of a thruster, $\overline{T} = \dot{M}\,\overline{U}$, is examined, it can be seen that the force is proportional to the mass expulsion rate and the thruster exhaust velocity. Since it is desirable to keep the fuel mass rate to as low a value as possible, the exhaust velocity must be made as high as possible.

The upper limit for the exhaust velocity for chemical fuel thrusters is about 5000 m/sec. The only type of thruster that has a significantly greater exhaust velocity is the electric thruster. Theoretically, some types of electric thrusters can achieve a figure of 100,000 m/sec.(1).

Since electric thrusters for stationkeeping require very modest power input levels, they can utilize solar-derived electrical energy from the spacecraft electric system bus.

Electric thrusters can be classed in three categories; electrothermal, electrostatic and electromagnetic. The electrothermal thruster uses electrical energy to raise the temperature of a propellant in a gaseous state and then expels the propellant through a conventional nozzle. The electrostatic thruster accelerates propellant in the form of ions to a very high velocity and expels these particles into space. This device is limited to operation in environments which are outside the earth's atmosphere. The electromagnetic thruster is usually considered to be one of two types, steady flow and pulsed. The latter is the principal concern of this paper and will be described in some detail.

Figure 1 shows an elementary configuration of a pulsed electromagnetic thruster. In the literature, this design is referred to as a rail thruster because of the fact that the two electrodes, the cathode and the anode, are parallel to each other. In operation, an electric arc is initiated between the electrodes and near their left ends. The arc requires the presence of some material in a gaseous state between the electrodes. Subsequently, the gas is ionized and its temperature is increased to the point where it becomes a plasma.

The equation which governs the force on a high velocity, charged particle in a magnetic field is given by the equation:

$$\overline{F} = Q\overline{V} \times \overline{B} \qquad \text{Eq. 1}$$

Simply stated, the force is proportional to the product of those components of the velocity and magnetic field vectors that are at right angles to each other and that the force is perpendicular to these two components. See Figure 1.

The force on the plasma stream is imparted by the electric field that exists between the electrodes and the magnetic field developed by the one turn loop formed by those sections of the electrodes that are conducting the electric current to the arc stream and the electron and ion motion within the arc stream.

As a consequence of the physical relationship expressed by Eq. 1, the ions and electrons in the arc stream are accelerated rapidly to the right end of the electrodes and discharged at a high velocity into space.

A somewhat more detailed diagram of a thruster which has been successfully flown on a satellite is shown in Figure 2. The propellant gases are obtained by initiating the electric arc on the surface of a block of solid Teflon. A small amount of the fluorine and carbon atoms is ablated from the Teflon surface and heated to a plasma state. A large capacitor bank furnishes the electric current for the arc and the magnetic field. An igniter plug, mounted on the cathode near the Teflon surface, supplies the initial ionization when a thrust impulse is required. The block of Teflon is pushed into the thruster chamber by a spring as it is consumed. The capacitor bank is recharged between thruster firings.

Figure 3 shows some of the thruster system voltages on a simplified diagram. The spacecraft 28 volt D.C. bus provides all of the electrical energy. The power conditioner converts the energy to two higher voltage levels; 2500 volts for the capacitor bank and 620 volts for the igniter circuitry.

The advantages of using Teflon for the propellant are that no special storage vessels are required, it ablates cleanly without forming residues on its surface that might form an electrical short circuit between the electrodes and the discharge components in the exhaust plume have little tendency to coat antennas and solar cells on the spacecraft.

Figure 4 lists the statistics of the three successful thrusters that may be used on future missions. The LES 6 has been flown, the LES 9 is flight-qualified and the millipound thruster, the largest of the three, is undergoing life tests.

Figure 5 shows the configuration of the major components of the millipound thruster. The Teflon propellant rods feed into the thruster chamber from opposite sides. Figure 6 shows this in more detail. Figure 7 shows a cut-away view of the thruster chamber.

ELECTRODE EROSION

One of the most persistent problems that electric thruster designers face is electrode erosion. Ion and electron bombardment of the solid components of a thruster can dislodge material if the particle velocity is sufficiently large. Many investigators regard radiative heat transfer from the arc stream to the electrodes to be among the most significant factors in the heating and subsequent erosion of electrode material.

Only a few researchers have recognized the concentrated energy input that occurs at the cathode and anode spots due to Joule heating (2,3). In this well known process, the plasma undergoes a severe pinch effect whereby all of the current in the arc stream enters the electrode surface through a spot of rather small area. This phenomenon can easily be seen in arc discharge devices such as mercury vapor lamps.

The constriction of the cross-sectional area of the path that the current must take results in very high current densities in a rather small volume of the electrode. The power density or electrical energy converted to thermal energy per unit volume is expressed by the equation:

$$P/V = \rho J^2$$

Where P is expressed in watts/m^3; ρ, in ohm-meters and J, amperes/m^2.

Exact values for the diameter of arc spots are difficult to obtain, however, examination of electrodes that have been subjected to high current, short duration electrical discharges shows that, typically, the degraded area is less than a millimeter across. Dethlefson (3) has cited 25×10^{10}

amp/m^2 as the critical current density, above which copper is vaporized in only a few microseconds. Fischer and Schonbach (2) show in their experiments that the critical current density for tungsten is 10^{10} amp/m^2 with current peaks lasting less than 0.1 microsecond. These two researchers have, with the aid of high speed photography, clearly established the existence of explosive erosion jets of electrode material during high current, nanosecond duration, spark discharges.

Figure 8 depicts the usual erosion pattern that occurs on the millipound thruster. The anode shows a much greater loss of material than does the cathode. A typical current pulse for this thruster exceeds 50,000 amperes and lasts more than a microsecond. If the diameter of the arc spot is 0.5 mm, then Dethlefson's critical current level is easily achieved. Operating experience with the millipound thruster with copper and with molybdenum electrodes has shown that the rates of anode loss are within the same order of magnitude.

Considerable attention has been given to the appropriate choice of materials for electrodes for the millipound thruster. Ideally, the electrode metal should have good thermal conductivity and capacity, a high melting temperature and good electrical conductivity. It is felt that the materials that have been tested have the optimum combination of desirable characteristics.

Another potential problem which is peculiar only to the Teflon-fueled thruster is that of fluorine attack on the anode. Fluorine is the most vigorous oxidizing agent known. It typically raises most other elements to their highest valence level when combined chemically. It can form compounds with some of the inert gases. In the millipound thruster, the attack on the anode by fluorine is increased significantly by the fact that the negatively charged fluorine ions are driven toward the anode by the electric field. It is conjectured that some of the fluorine combines with the anode material and is then swept into space. One could further surmise that the erosive jet action discussed above increases the amount of material that is available for interaction with the fluorine.

It would appear that there is little hope for extending the lifetime of the high performance, Teflon-fueled thruster. Yet there remains an enigma. The cathode does not suffer from erosion to the extent that the anode does. So far as can be determined, the same erosive jet action occurs at the cathode as it does at the anode. However, the metal, if it forms ions, is positively charged and is attracted back to the cathode while fluorine ions would be more likely to be repelled.

Rosebrock and his co-worker (4) cite the pressure of the particle beam against a molybdenum cathode as being 380 atmospheres whereas the pressure against the anode is only 0.029 atmospheres. They assumed a current density of 10^{10} amp/m^2 in their calculations. While the propellant was a silver filament, it is felt that similar pressure disparities exist in other arc discharges with different propellants. In view of the erosion experience with the millipound thruster, their contention that erosion jets are suppressed at the cathode but not at the anode due to difference in pressure appear to have justification.

Two factors bear heavily upon the degree of erosion. These are current magnitude and dwell time of the arc spot. Rosebrock (4) determined that the anode spot tends to lag behind the cathode spot, and well behind the plasma cloud. Knabe (5) points out that the anode spot dwells on one location until the angle between the arc and the anode decreases to a value such that the potential difference from some point on the arc with respect to the anode spot becomes greater than the breakdown potential relative to a nearer point on the anode and the arc spot then jumps to this new point.

A reasonable conclusion is that efforts should be made to enhance anode spot velocity. Reduction of current levels would be helpful in reducing erosion but the decrease in thruster performance may not be acceptable.

MAGNETIC ENHANCEMENT

Examination of Eq. 1 reveals that the force exerted upon the ionized particles is heavily dependent upon the magnetic field, $\bar{B}$. This magnetic field could be regarded as a self produced field since it arises from the current in arc stream, the lengths of the electrodes that are conducting the current to the arc spots and the strip lines that feed the current to the electrodes. This structure forms a one turn loop.

Since the magnetic field is proportional to the arc current, then consideration must be given to the manner in which this current varies. In Figure 9, it can be seen that the current waveform is an exponentially damped sinusoid. (6) This is to be expected since, from an electrical point of view, the thruster is a simple resistance, inductance and capacitance (RLC) series circuit and, if one can assume constant values for these parameters, the current is governed by Eq. 2.

Eq. 2
$$I = \frac{E \exp(-at) \sin\omega t}{L}$$

$$\omega = \sqrt{\frac{1}{LC} - \frac{R^2}{4L^2}} = 2\pi f$$

$$a = \frac{R}{2L}$$

E (volts) - initial voltage of capacitors

L (henries) - inductance of circuit

C (farads) - capacitance of storage capacitors

R (ohms) - resistance of arc stream and conductors

I (amperes) - arc current

t (seconds) - time

Obviously, since the effective loop is enlarged as the arc moves along the electrodes, resistance and inductance change. However, Eq. 2 provides a first order approximation and the curves in Figure 9 are fairly close to that of exponentially damped sinusoids.

The important point is that the magnetic flux produced by the loop follows the current curve very closely. Thus the magnetic field and consequently the electrodynamic force on the arc stream are not constant. From Figure 9, one can deduce that this force is at a high level from about 1 to 3 microseconds. Obviously, the time when this occurs will vary for different thruster dimensions but the principle remains the same: electrodynamic forces are available for accelerating the plasma only part of the discharge cycle. Gas dynamic pressures account for a good share of the motive force.

This paper is devoted to the premise that increasing the magnetic field near the anode will diminish the anode spot dwell time and thereby reduce erosion of the electrode. As a secondary benefit, any increase in the magnetic field between the electrodes should increase the longitudinal velocity component of the plasma and contribute to a greater specific impulse. In the development of the millipound thruster, little thought has been given to the magnetic field. Other major problems have required attention and until it become apparent that electrode erosion would be significant, there was little need for concern.

The first approach to improving magnetic flux density at the anode involves a minor modification of that electrode. Referring to Figures 6 and 8, it can be seen that the anode is relatively thin and wide. This configuration provides good heat flow and furnishes support for the propellant rods. However, using the Biot-Savart equation, Eq. 3, and integrating the flux components contributed by a rectangular conductor it can be shown that the magnetic flux density near the narrow side of the conductor is about twice as great as the flux density at a point the same distance away from the middle of the wide side. The conductor width was assumed to be four times its thickness.

$$\text{Eq. 3} \qquad d\bar{B} = \frac{\mu I}{4\pi} \int \frac{\sin\theta \; d\bar{l}}{r^2}$$

The results of the calculation suggest that the millipound thruster anode be rotated 90 degrees as shown in Figure 10a.

Continuing this line of reasoning, Figure 10b shows the reoriented anode with a ferrite core partly encircling it. The ferrite material provides passive reinforcement of the magnetic field and the new orientation provides a magnetic path with the least practical value of reluctance. A heat pipe is bonded to the edge of the anode to improve cooling since the ferrite core would impede heat transfer and to insure that the ferrite temperature would remain below the Curie point.

The advantages of this approach are that the operation of the thruster is unchanged and no great weight or space penalty is incurred. There will be a slight increase in the inductance of the circuit. However, it is felt that the increase will not be significant.

Dethlefson's work (3) has shown that the magnetic field can be modified across the entire thruster chamber by the addition of Helmholtz coils. Figure 11 shows the placement of the coils.

The current for the coils could be taken from the power conditioner low voltage supply and stored in capacitors till the coils need to be energized. The coil inductance and resistance in conjunction with the capacitors would be selected so when the coil is switched across the capacitors just prior to initiating a plasma pulse, the additional magnetization would be at a relatively high level throughout the thrust cycle. The equation for the coil current is the same as Eq. 2 with L and C selected so that the ringing frequency of the coil curcuit is much lower than that of the thruster ringing frequency. Figure 12 shows the relative timing and periods of the coil and thruster currents.

THRUSTER MODIFICATION

Extending the reasoning employed in Dethlefson's work and combining the features of the flux density enhancement scheme for the anode, the following is an engineering recommendation for the millipound thruster for reducing anode spot dwell time. Helmholtz coils can be incorporated with a magnetic core and a reoriented anode as shown in 13. The magnetic core is tape wound with laminations .01 mm thick of high silicon, grain oriented, transformer steel. This assures good permeability at elevated temperatures and low eddy current losses at high frequencies. The core is composed of about 2,500 layers.

Starting with the assumptions that a magnetic flux density of 1 tesla is needed near the anode and that 32 turns of copper wire (#8) could be reasonably fitted into the space at the anode, the required coil current is calculated to be 1,000 amperes. Further, the inductance is found to be 50×10^{-6} henries with the coils connected in series. The resistance will be about .03 ohms. Utilizing Eq. 2, the capacitor required to provide the coil current will be a 200 microfarad unit, charged to 525 volts. If the 620 volt supply were used to provide the electrical energy for the magnetic coil circuit, no serious problems would be anticipated.

Figure 15 shows the thruster circuit with the magnetic coil circuit added. A time delay of 100 microseconds is needed so that the magnetic field will be approaching its maximum value when the igniter starts the thruster cycle.

Figure 16 shows the coil circuit with a silicon control rectifier (SCR) to connect the capacitor to the coil when a thrust cycle is initiated. The SCR should have a minimum rating 250 amperes and 1000 volts. The diode should have a similar rating. The diode permits recovery of some of the energy in

the magnetic field and prevents excessive reverse voltage from being applied to the SCR on the second half cycle of the coil circuit transient.

CONCLUSIONS

Examination of the millipound thruster and consideration of the research results of others show that insufficient consideration has been given to the magnetic field conditions in the current thruster design. Since one of the primary factors in an electromagnetic thruster is the magnetic field and since the self field is dependent entirely on the discharge current and therefore variable, the conclusion is that the provision of a high and relatively constant supplementary magnetic field is needed. Thus all parts of the arc stream would experience a stronger acceleration and move at a higher velocity.

As a final consideration, Figure 17 illustrates the mechanism that is expected to function at the anode. As Rosebrock (4) and Knabe (5) have observed, the arc stream does not remain perpendicular to the anode surface. Since the central portion of the arc moves ahead of the electrode spots, the arc stream forms an acute angle with the electrode surface. If there is a strong transverse magnetic field in this region, then the force on the arc stream would cause it to "lay down", as it were, and thus cause the anode spot to be advanced much sooner than if it were dependent on the diminishing potential difference that Knabe has cited.

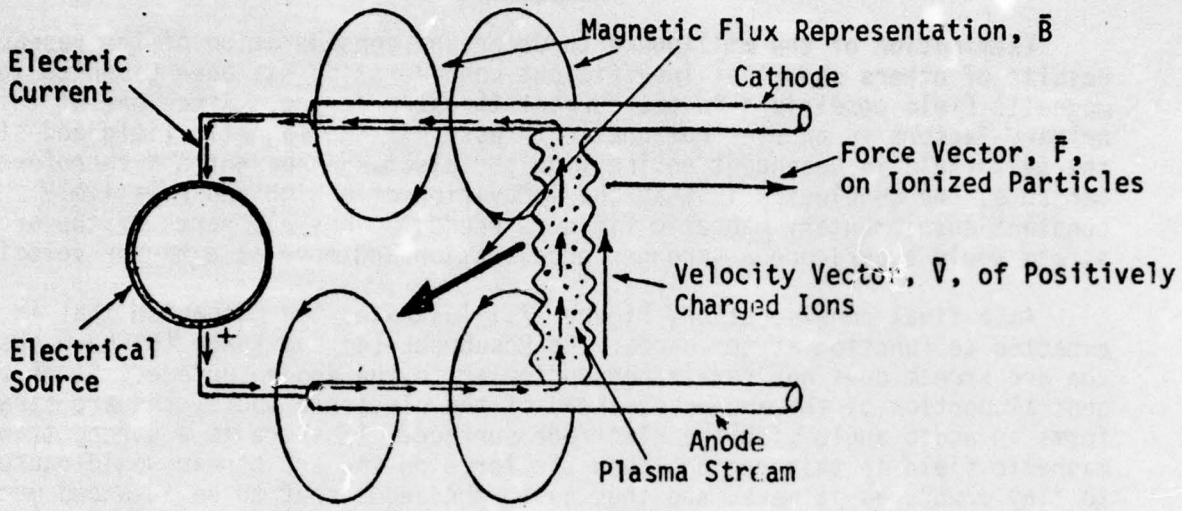


FIGURE 1. Elementary Representation of Electromagnetic Thruster

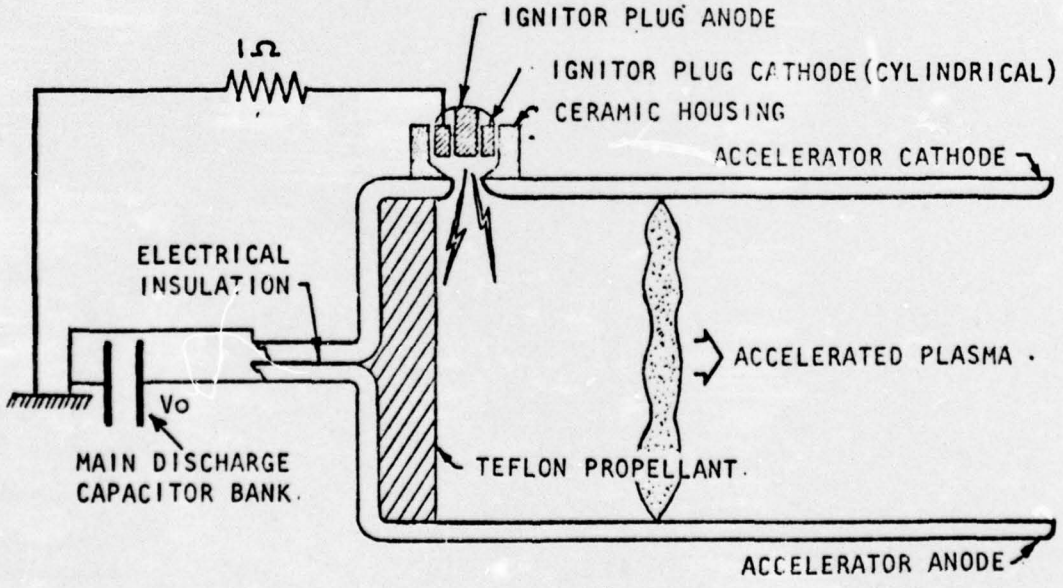


FIGURE 2. Simplified Diagram of Teflon Fueled Thruster

SYSTEM COMPONENT SCHEMATIC

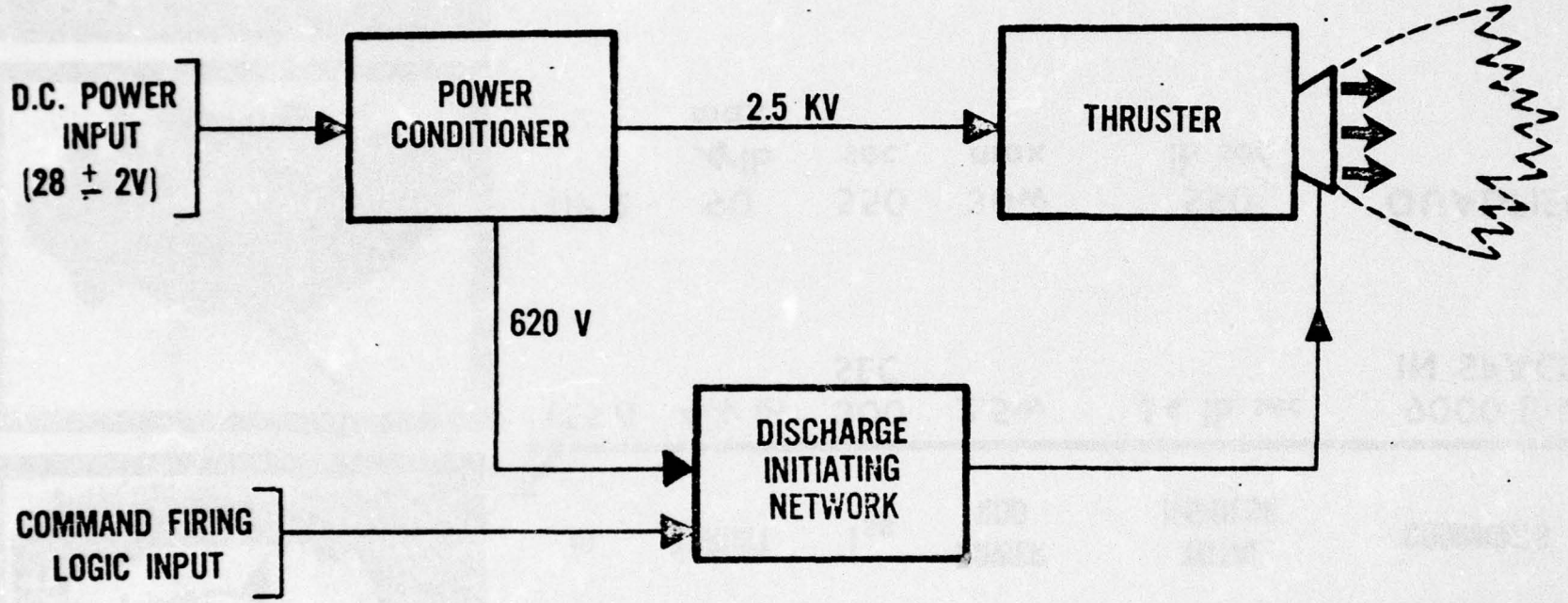
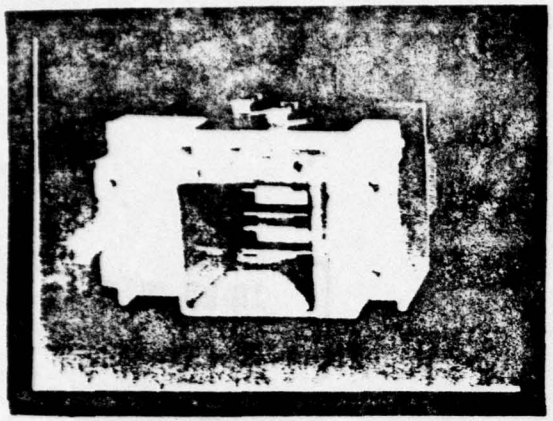
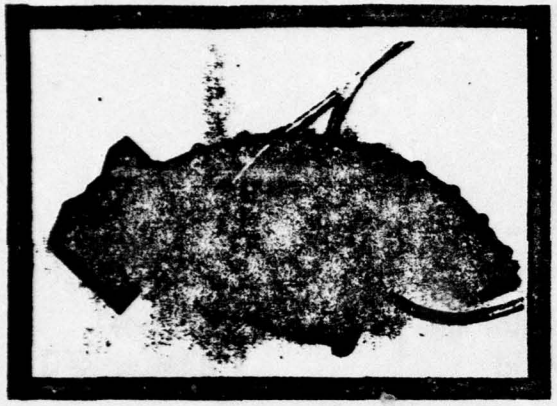
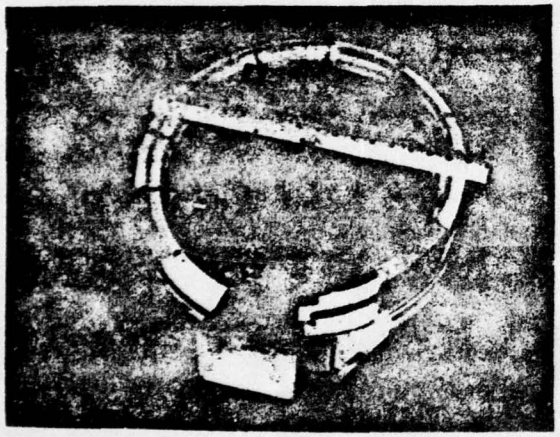


FIGURE 3. Thruster Circuit Diagram







SOLID PROPELLANT PULSED PLASMA THRUSTERS

ID	THRUST	I_{sp}	POWER RQD	TOTAL IMPULSE	COMMENTS
LES 6	4 μ lb	300 SEC	2.5w	64 lb sec	9000 hrs IN SPACE
TIP 2	90 μlb max	550 sec	30w max	550 lb sec	QUALIFIED
ADV	1mlb	1794 SEC	155w	44,850 lb sec	AFRPL EXPL.

FIGURE 4.

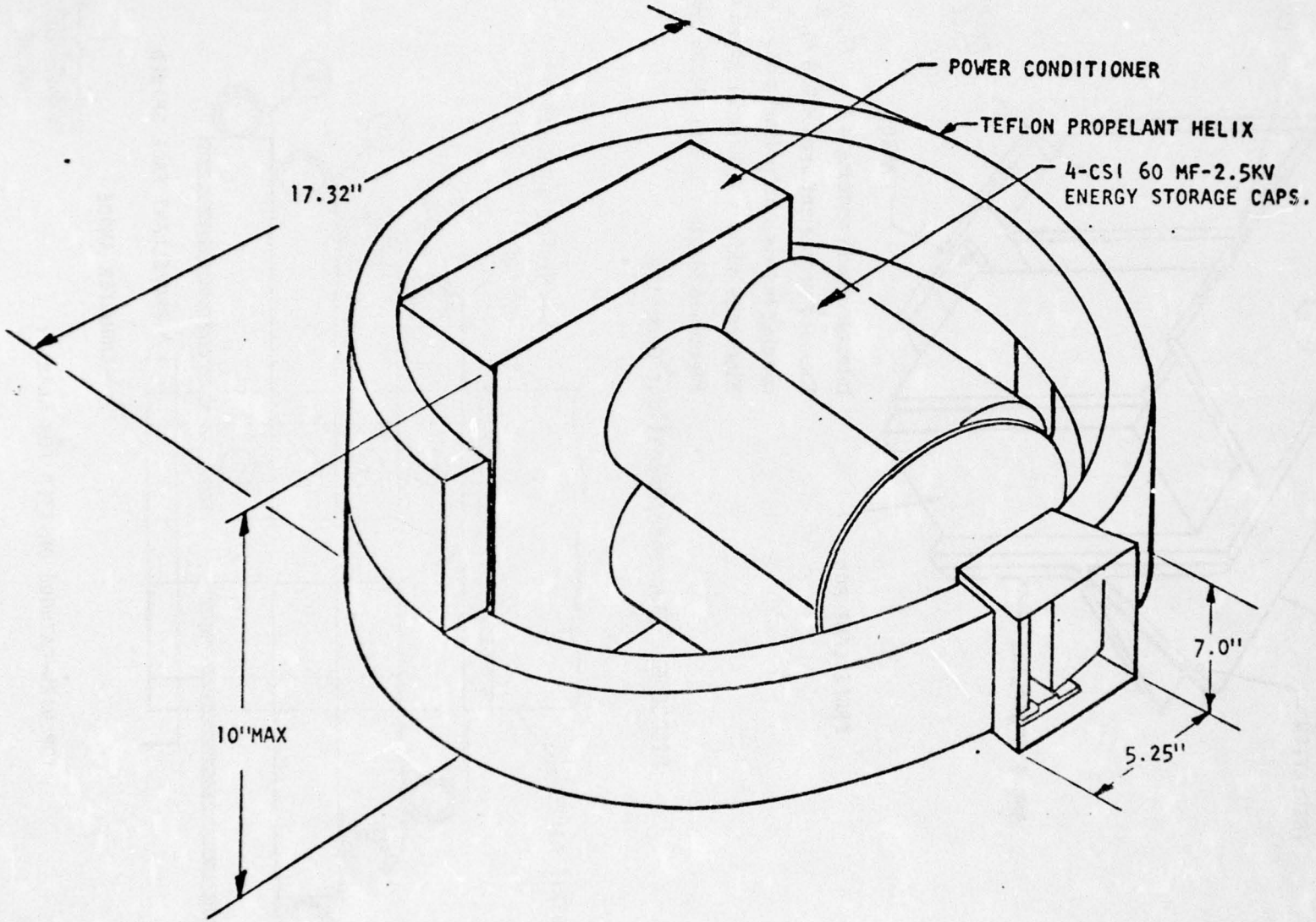
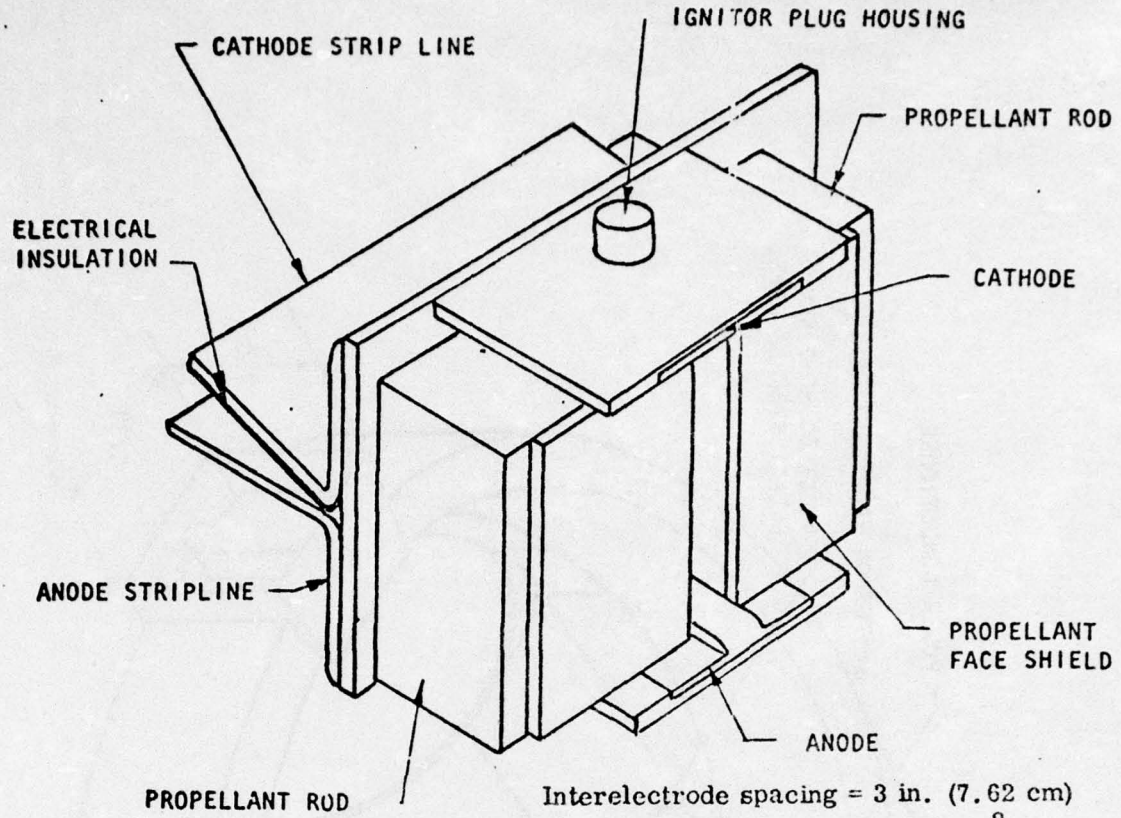


FIGURE 5. Basic Thruster Configuration



Interelectrode spacing = 3 in. (7.62 cm)
Exposed propellant area = 7.8 in.^{2} (50.3 cm^2)
Spacing between propellant rods = 0.3 in. (7.62 mm)
Electrode width = 1.5 in. (4.27 cm)
Electrode length = 1.6 in. (4.52 cm)

FIGURE 6. Electrode/Propellant Geometry

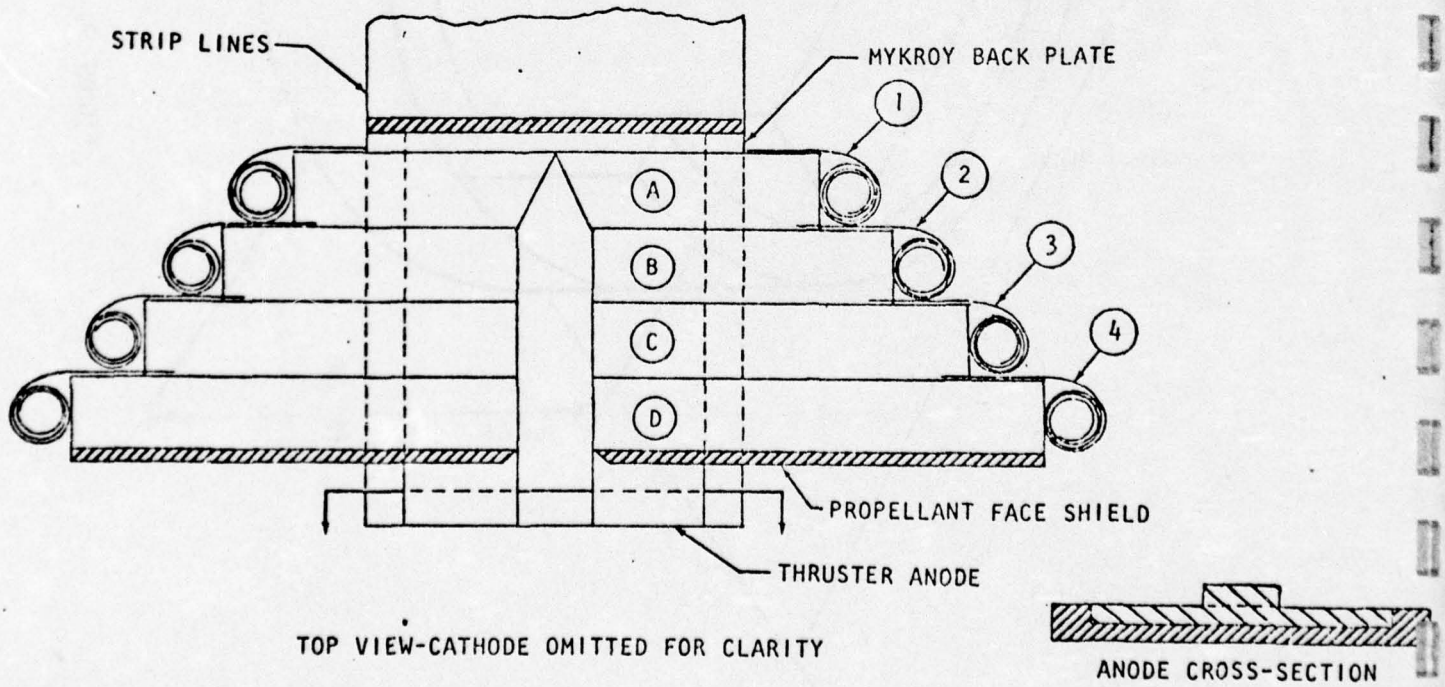


FIGURE 7. Schematic of Propellant Feed System

FIGURE 8.
Typical Electrode Erosion

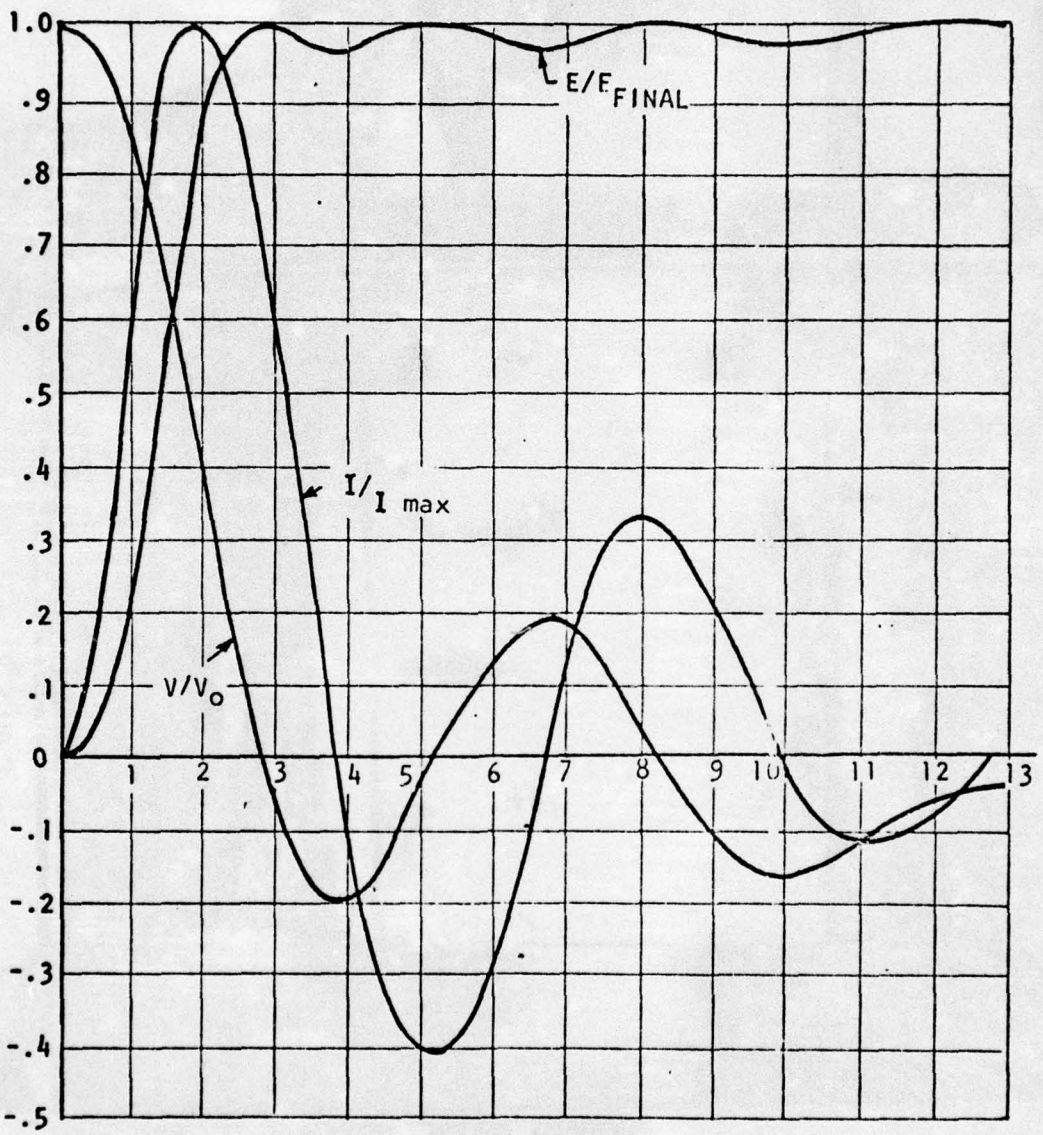


FIGURE 9. Current, Voltage and Energy Curves for Typical Thruster

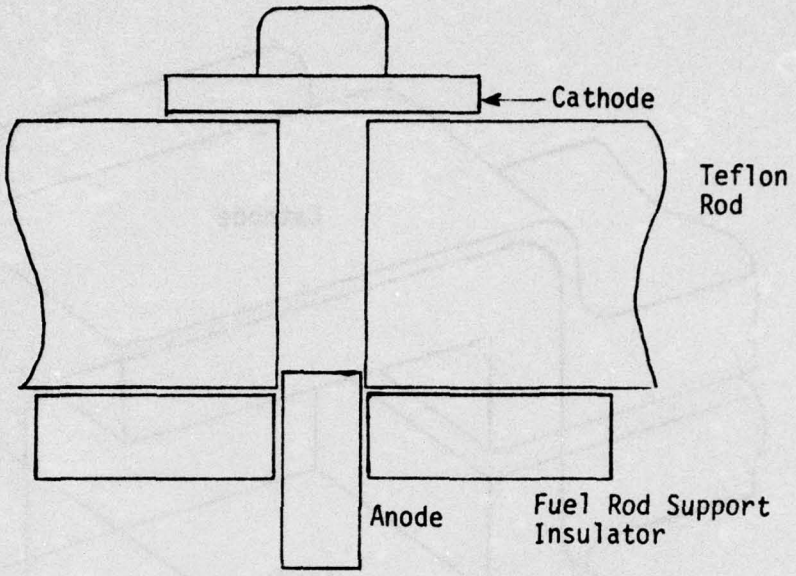


Figure 10 a) Repositioned Anode - View from Open End of Thruster Chamber

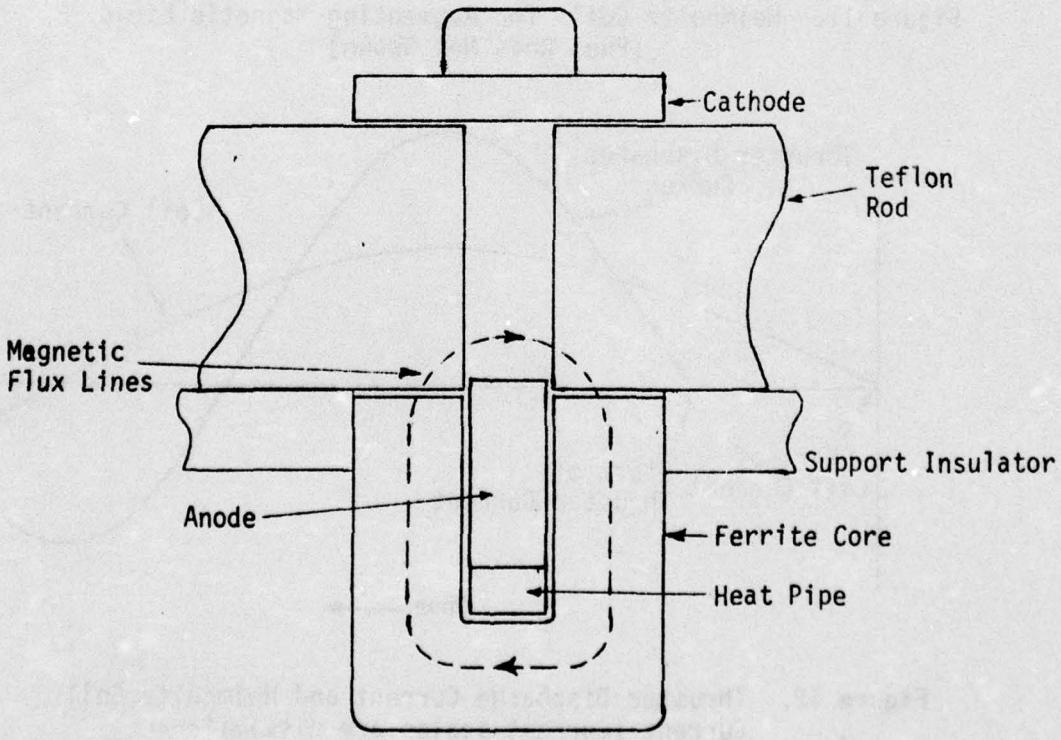


Figure 10 b) Ferrite Core Added to Enhance the Magnetic Field at the Anode

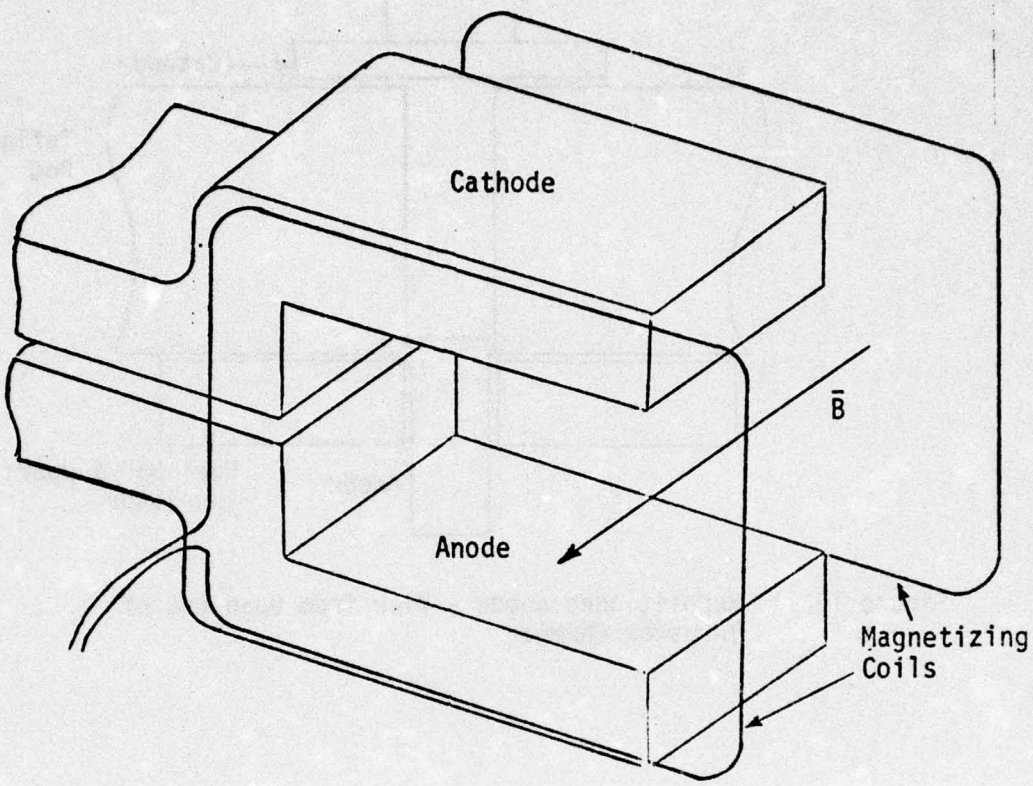


Figure 11. Helmholtz Coils for Augmenting Magnetic Field
(Fuel Rods Not Shown)

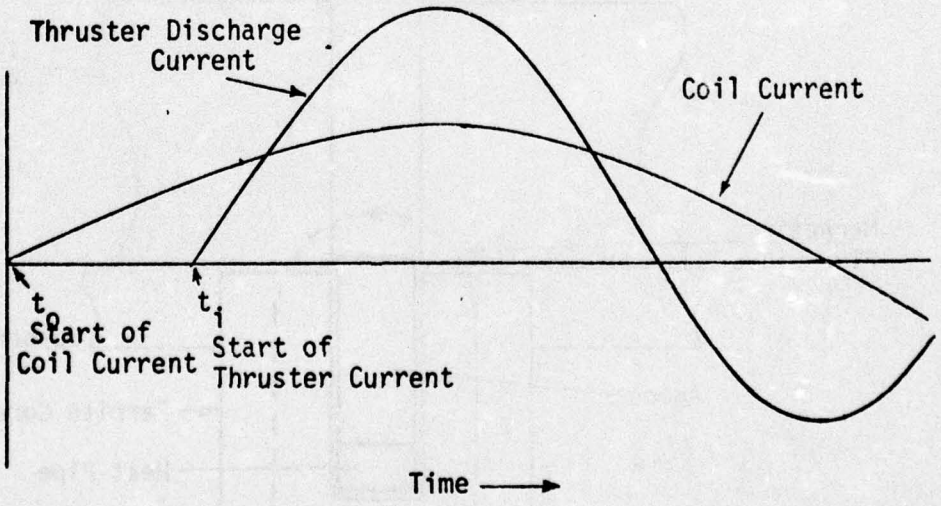
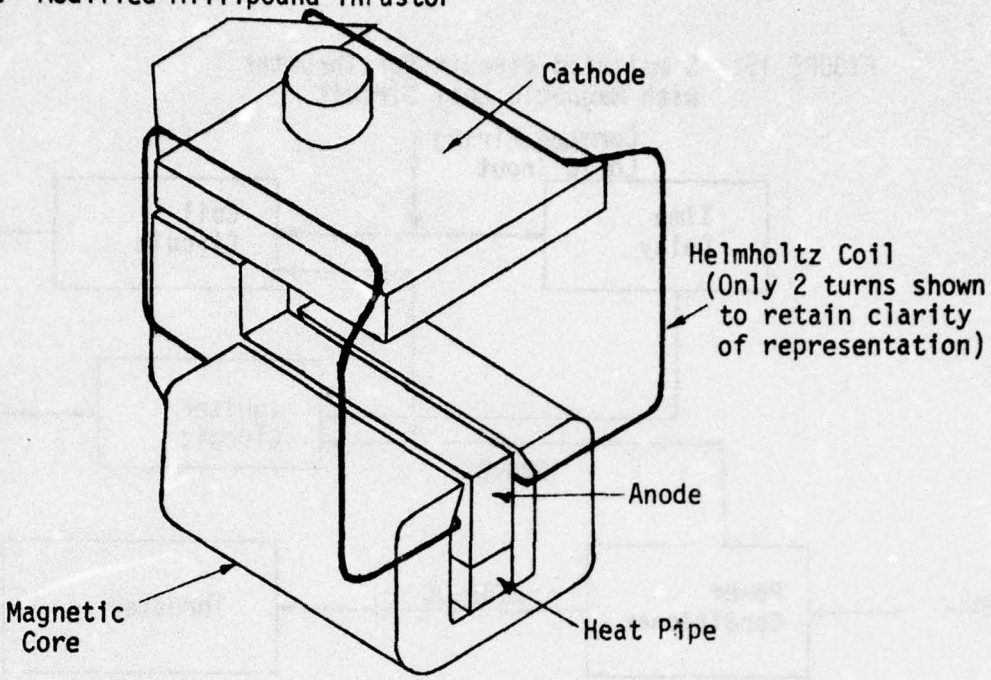


Figure 12. Thruster Discharge Current and Helmholtz Coil Current (Current scales are dissimilar)

Figure 13. Modified Millipound Thrustor



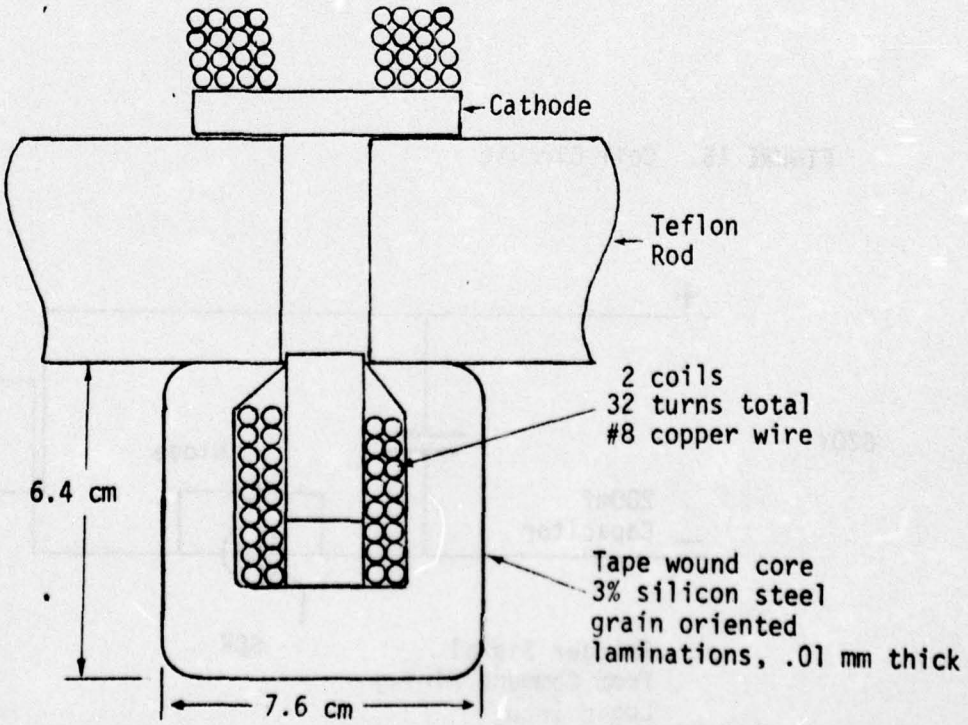


Figure 14. Cutaway View of Thruster Showing Core and Coil Positions

FIGURE 15. Simplified Circuit for Thruster with Magnetic Coil Circuit

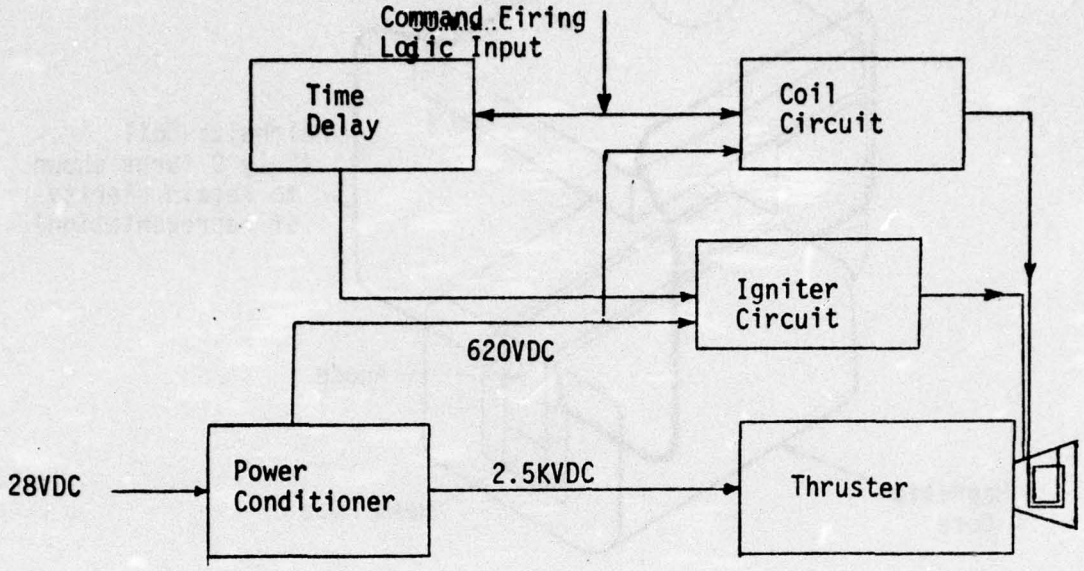
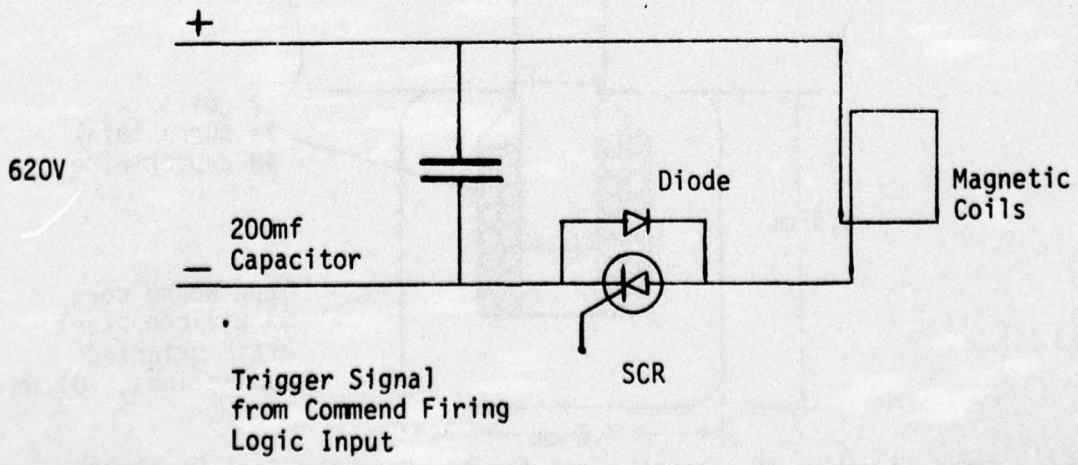


FIGURE 16. Coil Circuit



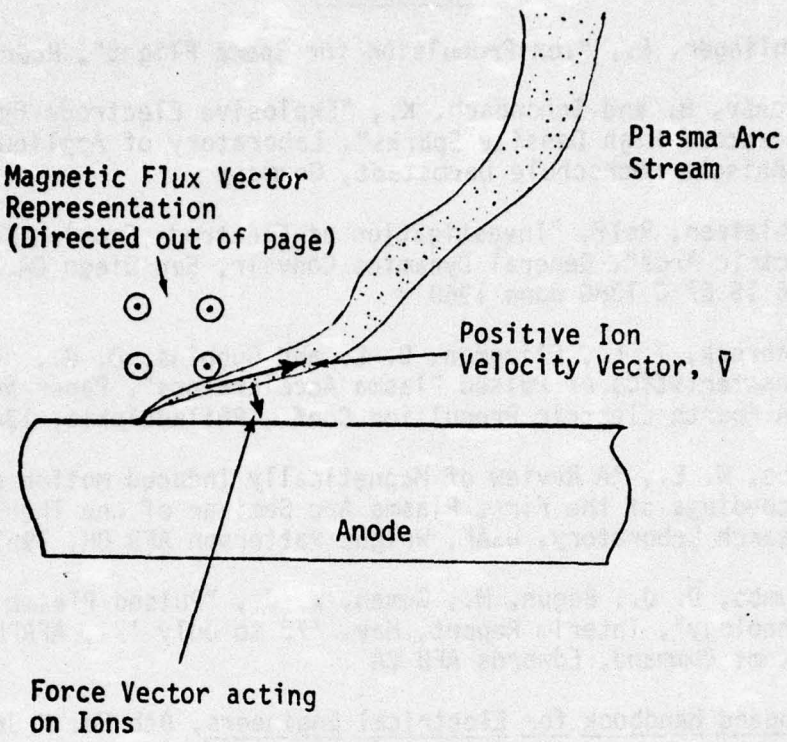


FIGURE 17. Detail Showing Force Vector on Ions with Velocity Vectors which Form an Angle of Less than 90° with Respect to the Anode Surface.

REFERENCES

1. Stuhlinger, E., "Ion Propulsion for Space Flight", McGraw-Hill, 1964

2. Fischer, H. and Schonbach, K., "Explosive Electrode Erosion in Nanosecond High Density Sparks", Laboratory of Applied Physics, Technische Hochschule Darmstadt, Germany

3. Dethlefsen, Rolf, "Investigation of Electrode Erosion in High Current Electric Arcs", General Dynamics Convair, San Diego CA. ARL 68-0112 F336 15 67 C 1386 June 1968

4. Rosebrock, T. L., Clingman, D. L. and Gubbins, D. G., "Electrode Erosion Characteristics of Pulsed Plasma Accelerators", Paper No. 64-708, AIAA Fourth Electric Propulsion Conf., Philadelphia, 1964.

5. Knabe, W. E., "A Review of Magnetically Induced Motion of Electric Arcs", Proceedings of the First Plasma Arc Seminar of the Thermo-Mechanics Research Laboratory, USAF, Wright Patterson AFB OH, 1963

6. Palumbo, D. J., Begun, M., Guman, W. J., "Pulsed Plasma Propulsion Technology", Interim Report, May, '73 to July '74, AFRPL, Air Force Systems Command, Edwards AFB CA

7. Standard Handbook for Electrical Engineers, 9th Ed. McGraw-Hill, 1957

ADDITIONAL USEFUL REFERENCES

8. Clingman, D. L. and Rosebrock, T. L., "Plasma-Electrode Phenomena of the Rail Type Accelerator", Allison Div., General Motors Corp, EDR 2277, (AFOSR Contract No. AF40(638)-864)

9. Jahn, R. G., "Physics of Electric Propulsion", McGraw-Hill, 1968

1976 USAF-ASEE SUMMER FACULTY RESEARCH PROGRAM

sponsored by

THE AIR FORCE OFFICE SCIENTIFIC RESEARCH

conducted by

AUBURN UNIVERSITY AND OHIO STATE UNIVERSITY

PARTICIPANT'S FINAL REPORT

PREPARATION OF SOLID PROPELLANT BURNING RATE MODIFIERS

Prepared by	Amos J. Leffler, Ph. D.
Academic Rank	Professor
Department and University	Department of Chemistry Villanova University
Assignment	Edwards Air Force Base Rocket Propulsion Laboratory Solid Rocket Division Propellant Development Branch
USAF Research Colleague	Claude Merrill, Ph. D.
Date	August 20, 1976
Contract No.	F44620-75-C-0031

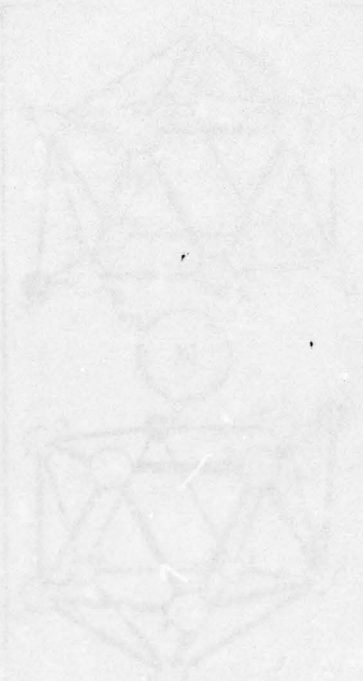
PREPARATION OF SOLID PROPELLANT BURNING RATE MODIFIERS

by A. J. Leffler

A series of compounds containing first row transition elements incorporated into boron-carbon cage structures was synthesized as burning rate modifiers. The compounds included 7,9-dicarbollide complexes and 13 vertex compounds derived from the o-carborane structure. It was found that only the Co(III), Ni(III), and Ni(IV) dicarbollides could be synthesized as described in the literature while different results were obtained with Cr(III) and Cu(III). In addition the unreported Fe(III) 7,9-dicarbollide was synthesized using a new deprotonation procedure for the carbollide(12) ion. In the case of the 13 vertex species using o-n-hexyl carborane the iron, chromium, and cobalt compounds appear to be different from that described in the literature.

Acknowledgement

The author wishes to express his gratitude to Dr. Claude Merrill for his help in getting the work started and for a number of helpful suggestions.



Introduction

The purpose of this work was to synthesize a number of transition metal dicarbollides for use as propellant additives. It is well known that certain of the transition metals, notably iron, copper, and chromium as their oxides and fluorides in small amounts, increase propellant burning rates but at the same time decrease the pressure exponent. Boron hydrides on the other hand increase the burning rates and increase the pressure exponent. Therefore it was hoped that combinations of these two materials would prove effective in increasing burning rates but not the pressure exponent.

During the past decade largely as a result of the work by Hawthorne and his coworkers[1], a large number of compounds containing boron-carbon cages bonded to transition metals, have been synthesized. Two classes, the dicarbollides and similar 13 vertex polyhedra compounds, were chosen for the present work because of their relatively simple synthesis and good chemical stability. The structures are shown below. It can be seen

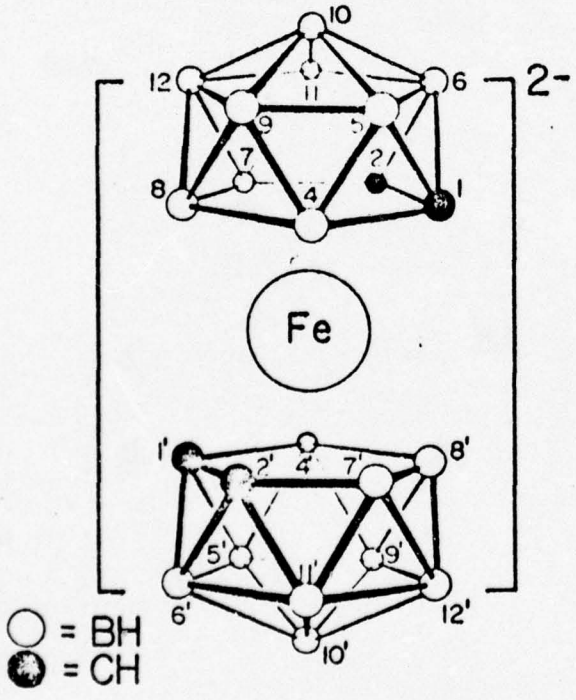


Figure 1 (a) Dicarbollide Structure

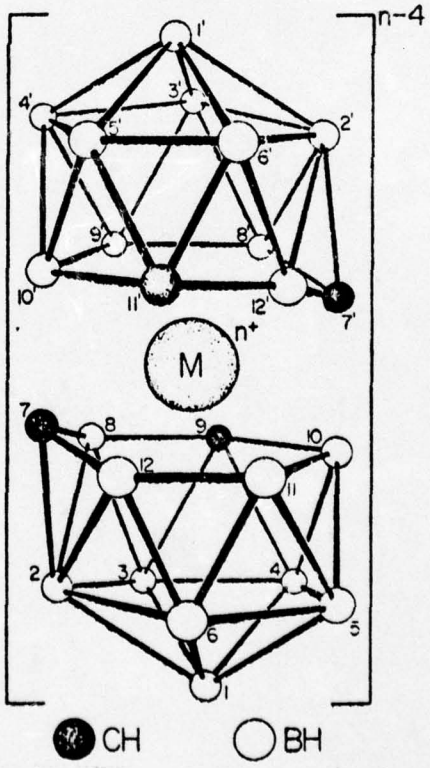


Figure 1 (b) 13 Vertex Structure

that in the carbollide(II) ion shown in 1(a) there are two carbon atoms in the open face and these may be adjacent or separated by a boron atom. Both arrangements are known and are derived from starting icosahedral boranes in which the carbon atoms are adjacent or separated. In the present work the separated structure was used since the starting compound, $K(7,9\text{-}B_9C_2H_{12})$, was available. In the synthesis of the 13 vertex structure, o-n-hexylcarborane, in which a C_6H_{13} group is attached to one of the adjacent carbon atoms, was used as the starting compound again due to its availability.

Results

It has been found experimentally that not all of the first row transition element dicarbollides can be synthesized. Shown below are those listed by Grimes[2] in his book on the Carboranes.

Table I

Reported Transition Metal Dicarbollides

Derivative	Cr(III)[a]	Mn(III)	Fe(III)	Co(III)	Ni(III)	Ni(IV)	Cu(III)
7,8	X[b]		X	X	X	X	X
7,9	X			X	X	X	

a. The roman numeral indicates the oxidation state of the transition element. b. Reported

The general reaction sequence is the same in both cases but details vary for the different metals. The first step is a deprotonation of the $B_9C_2H_{12}^-$ ion to give the carbollide ion, $B_9C_2H_{11}^{=}$. This has been carried out either in aqueous solution using 40% sodium hydroxide or nonaqueous solution, as tetrahydrofuran, using sodium hydride as the base.

$$(C_2H_5)_3NHB_9C_2H_{12} + 2\ NaOH = Na_2B_9C_2H_{11} + (C_2H_5)_3N + 2\ H_2O$$

$$(C_2H_5)_3NHB_9C_2H_{12} + 2\ NaH = Na_2B_9C_2H_{11} + (C_2H_5)_3N + 2\ H_2$$

All of the reactions can be carried out using the nonaqueous method but the aqueous method is preferable where applicable because of its convenience. Only the chromium compound must be synthesized with the nonaqueous procedure.

During the present work an alternative nonaqueous procedure was developed using potassium hydroxide in dimethoxyethane. This is based on the procedure of Jolly[3] who showed that potassium hydroxide in nonaqueous media is a much stronger base than in water. It is more

convenient than the sodium hydride method because it is simpler to dispose of the unreacted hydroxide than unreacted hydride.

The second step in the reaction is the formation of the dicarbollide complex by reaction with the corresponding transition metal chloride followed by precipitation as the tetramethylammonium ion.

$$2\ Na_2B_9C_2H_{11} + MCl_2 \xrightarrow{(Q)} Na[M(B_9C_2H_{11})_2] + 2\ NaCl + Na^+$$

$$Na[M(B_9C_2H_{11})_2] + (CH_3)_4NCl = (CH_3)_4N[M(B_9C_2H_{11})_2] + NaCl$$

In general the oxidation of the transition metal to the +3 state occurs apparently due to the much higher stability of the latter.

During the present work the 7,9 derivatives of Co(III) and Ni(III) were prepared as described by Hawthorne[4] using the aqueous procedure although the yields were lower than given in the literature. The products are air stable but it was found on one occasion that the nickel salt ignited in air after being removed from a vacuum oven. This has not been reported in the literature but may be due to catalytic amounts of transition metal ions. On another occasion a sample of tetramethylammonium carbollide, $(CH_3)_4$-$NB_9C_2H_{12}$, contaminated with Cr^{3+} ions also ignited after removal from the oven. In later preparations much more extensive washing of the products was carried out and no further difficulties were encountered.

The nickel compound described above was converted to the Ni(IV) species by the reaction:

$$(CH_3)_4N[Ni(B_9C_2H_{11})_2] + FeCl_3 = Ni(B_9C_2H_{11})_2 + FeCl_2 + (CH_3)_4NCl$$

Again this compound was found to be pyrophoric, once, but not after more careful washing.

As mentioned earlier the aqueous procedure cannot be used when the dicarbollide complex is unstable in aqueous strong base. This was found to be the case with the 7,9 chromium complex. Hawthorne[5] has reported that the chromium dicarbollide complexes formed from both the 7,8 and 7,9 carbollide(II) ions are stable in acid solution but in the present work the latter species formed a complex that appeared to hydrolyze instantly. A number of attempts were made to prepare the $[Cr(7,9\text{-}B_9C_2H_{11})_2]^-$ ion. These included both the sodium hydride and potassium hydroxide deprotonation procedures. In the former case dimethoxyethane was used as the solvent and the reaction proceeded as described in the literature in that a purple residue was left when the solvent was removed. However, when water was added as described in the procedure the solution turned blue instantly indicating hydrolysis. Apparently the 7,9 isomer is not as stable as the 7,8 species, since a number of instances of the latter being treated with water are given,

while only one mention is made of the former. It was finally found possible to isolate the complex by treating the residue with acetone and filtering off the sodium chloride. A brown residue of unknown purity was obtained by removal of the acetone. The material was immediately hydrolyzed on contact with water.

The 7,9 dicarbollide complex of Fe(III) was prepared during this work using the potassium hydroxide-dimethoxyethane procedure. Professor Hawthorne[6] has also prepared this complex although it is not described in the literature. It is water stable and relatively thermally stable.

It was attempted to prepare the Cu(III) complex by the aqueous method described for the 7,8 complex but the product was not similar to that described in the literature. A light brown material was obtained that did not correspond to the desired product even though an infrared spectrum indicated B-H bonds.

One attempt was made to prepare the manganese dicarbollide complex but only manganese dioxide was obtained.

The second class of compounds investigated are the 13 vertex metallocarboranes described by Hawthorne and his coworkers[7]. In these compounds the 12 vertex icosahedron is expanded through the reaction sequence:

$$2\ Na + o\text{-}B_{10}C_2H_{12}^{=} \xrightarrow{C_{10}H_8} 2\ Na^+ + O\text{-}B_{10}C_2H_{12}^{=}$$

$$FeCl_2 + 2\ o\text{-}B_{10}C_2H_{12}^{=} = Fe(B_{10}C_2H_{12})^{=} + 2\ Cl^-$$

The product is precipitated as the tetraethylammonium complex. In the original work o-carborane was the material used but in the present work o-n-hexylcarborane was used due to its availability. The reaction with metallic sodium went as described with a slow dissolution of the metal over about 24 hours. The addition of ferrous chloride gave a red solution rather than the purple oil described in the literature. After the tetrahydrofuran solvent was removed the residue was taken up in absolute ethanol and added to tetraethylammonium bromide in alcohol but no precipitate was formed. The change in color and solubility could be due to the presence of the n-hexyl group although it would be expected that a highly charged ionic species would not be very soluble in alcohol. The alcoholic solution was chromatographed to give a dark red solution when concentrated but blue when dilute in chloroform or ethanol. At this point the reason for the color change is unknown but may be a solvolysis effect. The final product was dark red and showed a strong B-H stretch in the infrared. It is rapidly hydrolyzed in contrast to the compound formed from o-carborane.

A similar reaction with chromium trichloride gave a brown solution that decomposed during chromatography when ethanol was used in the eluent solution. Chromatography with chloroform gave a reddish viscous liquid that may be polymeric. Again infrared showed B-H bonds and a qualitative test with silver nitrate showed very little chloride ion.

Discussion

The synthesis of the 7,9 dicarbollides is straightforward in the case of Co(III), Ni(III), and Ni(IV) species although the yields were somewhat lower than stated in the literature. The behavior of the Cr(III) complex is totally different from that described and at present no explanation is available. Both the unreported Fe(III) and the Cr(III) complexes were prepared by the potassium hydroxide deprotonation method developed in this work.

Unfortunately no determination of the purity of the products can be made since no analytical data has been received. The thermogravimetric analyses show that little weight is lost by these complexes until about 300°C except for the Ni(IV) species which sublimes about 175°C. The differential thermal analyses results for Fe(III) and Co(III) show an endotherm at 100-50°C indicating perhaps a crystal structure change. In the case of Ni(IV) an exotherm occurs at 75° and an endotherm at 200°C but no explanation for these is available.

The nature of the products from the n-hexyl carborane reactions is not known. It is possible that the presence of the n-hexylgroup could change the course of the reaction. More information will be needed before any decision can be made.

Experimental Section

Potassium carbollide, $K(7,9\text{-}B_9C_2H_{12})$, and o-n-hexyl carborane came from previous workers and were of unknown but presumably high purity. The transition metal salts were reagent grade. During this work iron(II), manganese(II), and chromium(III) chlorides were dehydrated by treatment with thionyl chloride as described in the literature[8]. Dimethoxyethane (MlM) was obtained from Aldrich Chemical Co. and distilled from calcium hydride with the fraction boiling 81-2° (3000' alt.) used. Tetrahydrofuran was Baker's reagent grade and was used as received. Cobalt tris(acetylacetonate) was obtained from Research Organic/Inorgannic Chemical Corp.

Infrared spectra were run on a Beckman IR-5 instrument.

$K[Fe(7,9\text{-}B_9C_2H_{11})_2]$

In a 500 ml. 3 neck flask equipped with stirrer, condenser, and nitrogen inlet, 26.5 g. of ground potassium hydroxide was slurried with

75 ml. of MlM. With stirring a slurry of 5.4 g. of potassium carbollide in 75 ml. of MlM was added and the mixture heated for one hour. The mixture showed a change in appearance but not in color. A solution of 6.1 g. of anhydrous ferrous chloride in 75 ml. of MlM was added dropwise through an addition funnel equipped with a by pass side arm under nitrogen flow. The mixture was stirred and heated for 1.5 additional hours and turned pink at the end of the reaction period. The solution was decanted from the residual solids and gradually turned red. On cooling a white solid gradually precipitated and was filtered off. The solvent was removed, first at atmospheric pressure and then under vacuum. The residue was taken up in 100 ml. of water, filtered, and dried in a rotary evaporator under reduced pressure. The residue was then treated with ether, filtered, and dried to give a brown product. An infrared spectrum showed a band at 2450 cm^{-1} indicating B-H bonds.

$(CH_3)_4N[Co(7,9\text{-}B_9C_2H_{11})_2]$, $(CH_3)_4N[Ni(7,9\text{-}B_9C_2H_{11})_2]$,

$Ni(7,9\text{-}B_9C_2H_{11})_2$

All of these were prepared using the aqueous procedure described in the literature[4]. As was noted in the discussion the yields of the Co(III) and Ni(III) compounds were lower than described. No explanation is presently available.

Attempted Preparation of $(C_2H_5)_4N[Cu(7,9\text{-}B_9C_2H_{11})_2]$

A mixture of 21.5 g. of triethylamine and 200 ml of water was neutralized with a slight excess of a solution of about 200 ml of hydrochloric acid in a 1 l. flask. A solution of 29.9 g. of potassium carbollide(12) in 200 ml of water was added to the triethylamine hydrochloride solution and the resultant precipitate of triethylammonium carbollide(12) filtered and sucked dry. It was then added to a solution of 123 g. of sodium hydroxide in 180 ml. of water in a 1 l. flask and the resultant solution heated and sparged with nitrogen until no more triethylamine was evolved as determined by pH paper. The solution was cooled to 0° and to it was added a solution of 44.6 g. of copper sulfate pentahydrate in about 175 ml. of water. During the addition the solution grew red and then dark green with considerable evolution of heat. However, the addition of tetraethylammonium bromide to a cooled portion gave no precipitate as described in the literature. It was noted that when additional sodium hydroxide was added to the solution it turned blue. When a portion of this solution was then treated again with tetraethylammonium bromide a brown precipitate was formed. This was dissolved in acetone and the insoluble residue filtered off. The acetone was removed to give a light brown solid. Chromatography of a portion of this material using Gelman Type S ITLC thin layer sheets using hexane-acetone eluent showed a movable yellow

portion that turned brown and stopped at the liquid front. Presumably the yellow material was converted to the brown one during the chromatographic process. At this point the nature of the product is unknown.

Attempted Preparation of $(CH_3)_4N[Cr(7,9\text{-}B_9C_2H_{11})_2]$

Using the same procedure described in the Fe(III) preparation, a solution of potassium carbollide[11] was formed from 24.6 g. of potassium hydroxide and 17.1 g. of potassium carbollide[12] in 150 ml. of MIM. The solution was then decanted from the excess potassium hydroxide and 6.9 g. of chromium trichloride added in small portions. The reaction mixture was filtered through a coarse frit and the MIM removed in vacuo. The residue was dissolved in acetone, filtered, and dried in vacuo to give a brown material that is extremely water sensitive.

Reaction of o-n-hexyl carborane with Sodium and Ferrous Chloride

In a 1 l. 3 neck flask equipped with stirrer, condenser, and nitrogen inlet was placed 8.7 g. of sodium metal, 1.1 g. of naphthalene and 650 ml. of tetrahydrofuran. To this was added 41.1 g. of o-n-hexyl carborane and the mixture heated slightly and allowed to stir for 60 hours until all of the sodium had reacted. Then 14.2 g. of ferrous chloride was added and the mixture turned red. It was stirred for 16 hours and filtered through a Celite filter aid. The tetrahydrofuran was removed by pumping to give a viscous red solution. A small portion was dissolved in absolute ethanol and added to a large excess of tetraethylammonium bromide in ethanol to give a blue solution rather than the precipitate described in the literature. The original solution in alcohol was pumped to dryness and portions were chromatographed using a 40 cm. column of SilicAR CC 4 100-200 mesh as received. The solution was placed on the column using chloroform and eluted using a 50/50 v/v chloroform absolute ethanol solution. The solution from the column was blue but turned red on evaporation to dryness to give a solid that showed bands at 2930, 2830, 2560, 1610, 1460, 1415, 1315, and 1060 cm^{-1} in the infrared as a solution in carbon tetrachloride. A flame test showed the presence of boron.

Bibliography

1. K. P. Callahan and M. F. Hawthorne, Adv. in Organometallic Chem. 14, 145 (1976).

2. R. N. Grimes, Carboranes, Academic Press, New York, 1970.

3. W. L. Jolly, Inorganic Syntheses, Vol XI, McGraw Hill, New York, 1968, p. 120.

4. M. F. Hawthorne, D. C. Young, T. D. Andrews, D. V. Howe, R. L. Pilling, A. D. Potts, M. Reintjes, L. F. Warren, and P. C. Wegner, J. Amer. Chem. Soc. 90, 896 (1968).

5. H. W. Ruhle and M. F. Hawthorne, Inorg. Chem 7, 2279 (1968).

6. Professor N. F. Hawthorne private communication.

7. D. F. Dustin, G. B. Dunks, and M. F. Hawthorne, J. Amer. Chem. Soc. 95, 1109 (1973).

8. G. Brauer, Preparative Inorganic Chemistry

1976 USAF-ASEE SUMMER FACULTY RESEARCH PROGRAM
sponsored by
THE AIR FORCE OFFICE SCIENTIFIC RESEARCH
conducted by
AUBURN UNIVERSITY AND OHIO STATE UNIVERSITY

PARTICIPANT'S FINAL REPORT

ELECTROCHEMICAL STUDIES IN ANHYDROUS LIQUID HYDRAZINE

Prepared by:	John R. Dodd Ph.D.
Academic Rank:	Assistant Professor
Department and University:	Department of Chemistry Emory University

Assignment:

(Air Force Base)	Edwards AFB
(Laboratory)	Rocket Propulsion Laboratory
(Division)	Technology
(Branch)	Chemistry

USAF Research Colleague:	John T. Nakamura
Date:	August 20, 1976
Contract No.:	F44620-75-C-0031

ELECTROCHEMICAL STUDIES IN ANHYDROUS LIQUID HYDRAZINE

by
John R. Dodd

ABSTRACT

Anhydrous hydrazine is now well-established as a monopropellant for rocket propulsion systems. The corrosivity of hydrazine and its tendency to undergo decomposition upon storage for long periods, however, limit the usefulness of hydrazine as a propellant for use in long-term space missions (7-10 years). It has been postulated in recent years that the hydrazonium ion ($N_2H_5^+$) is probably the primary corrosive species in hydrazine that is responsible for these undesirable properties. In order to further define the role of the hydrazonium ion in corrosion and to characterize the suitability of various hydrazine samples as propellants, it would be very useful to have a simple and direct analytical method for determining the level of the hydrazonium ion in hydrazine.

In this project, the electrochemical technique of single-sweep polarography was used to study the electrochemical behavior upon reduction of anhydrous hydrazine and hydrazine solutions containing various added electroactive materials. The results of an earlier feasibility study in this area indicated that the hydrazonium ion in hydrazine exhibits a well-defined polarographic reduction wave at approximately -0.7V and that consequently single-sweep polarography appeared to be feasible as a technique for the determination of the hydrazonium ion concentration in anhydrous hydrazine. In contrast, the results of further experiments in the present study indicate that the hydrazonium ion is in fact reduced at a much more negative potential (approximately -1.6V) and that this reduction occurs in a potential region where the hydrazine solvent (and/or impurities in hydrazine) undergoes decomposition to such a large extent as to prevent the observation of a well-defined wave for this reduction process. Consequently the use of simple single-sweep polarography does not appear to be feasible as an analytical method for determining the level of hydrazonium ion in anhydrous hydrazine. Differential single-sweep polarography may provide a means of overcoming the above problem and studies of anhydrous hydrazine using this latter type of polarography should be investigated in this regard.

ACKNOWLEDGEMENT

The author is sincerely grateful to the Air Force Systems Command for support of this summer research. Deep appreciation is due to Auburn University and in particular to Mr. Fred O'Brien for the excellent administration of the summer faculty research program.

The author is indebted to the Chemistry Branch of the Technology Division of the Air Force Rocket Propulsion Laboratory for providing a cordial and helpful work environment. It has been a great pleasure and a professionally gratifying experience to work with these very capable people. In particular, thanks are due to Mr. John Nakamura and Mr. Herman Martens.

INTRODUCTION

The catalytic decomposition of hydrazine has become one of the most important processes for rocket propulsion in outer space (e. g. for attitude-control rockets, etc.) The tendency for propellant-grade hydrazine to undergo decomposition[1] and to cause corrosion[1] (hydrogen embrittlement) upon storage for long periods, however, limits the usefulness of this monopropellant in long-term (7-10 years) space missions. Thus for example decomposition of hydrazine in propellant systems (which affords nitrogen, hydrogen, and ammonia gases) can lead to pressure increases within the fuel tanks severe enough to cause ruptures in the fuel system, and the corrosion process of hydrogen embrittlement can lead to ruptures in the fuel lines. Both of these events, of course, if sufficiently severe will lead to mission failure.

Several substances that are normally present as impurities in propellant-grade hydrazine are known to increase its instability and corrosivity[1]. The two most important substances in this respect are water and carbon dioxide[1]. In recent years it has been postulated[1, 2] that the primary corrosive species in liquid hydrazine is probably the hydrazonium ion ($N_2H_5^+$), which in hydrazine solution is the analogue of the well-known hydronium ion (H_3O^+) present in aqueous solutions. Both water and carbon dioxide when added to hydrazine are believed[1, 2] to be capable of affording the hydrazonium ion according to equations (1) and (2), respectively.

$$H_2O + N_2H_4 \rightleftharpoons N_2H_5^+ + OH^- \qquad (1)$$

$$CO_2 + 2N_2H_4 \rightleftharpoons N_2H_5^+ + H_2N_2HCOO^- \qquad (2)$$

Although the hydrazonium ion has been postulated to be the primary corrosive species in hydrazine, the extent to which the presence of this ion enhances the corrosivity and decomposition rate of hydrazine remains unknown. The availability of a simple and direct method for determining the level of hydrazonium ion in hydrazine would permit detailed studies to determine the influence of this ion upon the corrosivity and decomposition of hydrazine and to monitor the suitability of hydrazine samples for use in propellant systems. In this research project the use of single-sweep polarography is investigated as a possible analytical technique for determining the level of hydrazonium ion in hydrazine.

Single-sweep polarography[3] is a type of voltammetry in which the current passing through a test solution is measured as a function of the applied potential. In this electrochemical technique, a dropping mercury electrode (dme) is used as a cathode and a

mercury pool in the bottom of the polarographic cell is used as the anode. In single-sweep polarography, the complete current-voltage curve is obtained during the lifetime of a single drop of mercury falling from the dme (i. e. less than ~7 sec) using an oscilloscope to store and display the current-voltage curves.

A typical single-sweep polarogram (i. e. the measured current-voltage curve) for an electroactive species such as cadmium ion (Cd^{++}) is shown in Figure 1. In the case of a reduction process (e.g. $Cd^{++} + 2e^- \rightarrow Cd^o$) at the dme, there is a rapid increase in current at potentials sufficiently negative for the reduction process to occur. As increasingly more negative potentials are attained in a scan, the current rises further, reaches a maximum value, and then after undergoing a decrease in value, attains a steady limiting value which depends upon the rate of diffusion of the electroactive species to the dme. The curve which results excluding the baseline portion is known as a polarographic wave.

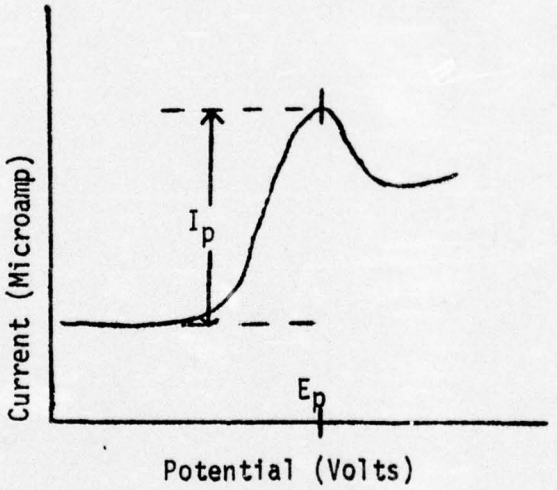


Figure 1: A typical single-sweep polarogram.

Two important quantities associated with a polarographic wave are the peak potential (Ep) and the peak current (I_p) which are illustrated in Figure 1. For a specific set of experimental conditions (solvent, temperature, etc.), the value of the peak potential is a characteristic constant for a given electroactive species. Thus, the presence or absence of a polarographic wave at the peak potential value associated with a particular electroactive species can be taken as evidence for the presence or absence of this species in a given test solution.

The peak current (I_p) of a polarographic wave is an important quantity because it is related to the concentration of the electroactive species responsible for the wave. For a species undergoing a reversible reduction in single-sweep polarography, the Randles-Sevcik

Equation[4] is applicable (equation 3) in which there is a direct proportionality between the peak current (Ip) and the concentration (C) of the electroactive species.

$$I_p = 2.687X10^5\ n^{3/2}\ A\ D^{1/2}\ v^{1/2}\ C \qquad (3)$$

In this equation, I_p is the peak current measured in microamperes (μA), n is the number of electrons involved in the reduction process, A is the surface area of the electrode (the dme in the present study) in square centimeters, D is the diffusion constant of the electroactive species in square centimeters/sec, v is the sweep rate used in obtaining the polarogram in volts/sec, and C is the concentration of the electroactive material in millimole/liter.

For reduction processes that are irreversible, the Randles-Sevcik equation is not applicable. Randles has found[4], however, that there is still an approximate direct proportionality between the measured peak current (I_p) and the concentration (C) of the electroactive species for all cases involving irreversible reductions that he investigated. It thus appears that the peak current will vary in an approximate linear fashion with concentration of the electroactive species regardless of whether the reduction process being investigated is a reversible or an irreversible one.

A study to determine the feasibility of measuring the hydrazonium ion concentration in hydrazine using single-sweep polarography was conducted last year by Whitnack[2]. Whitnack found[2] that RPL-purified anhydrous hydrazine exhibited polarographic waves at -0.73V and -1.45V (versus mercury pool) with the latter wave being of much greater intensity. Addition of hydrazonium salts ($N_2H_4 \cdot HCl$, $N_2H_4 \cdot H_2SO_4$, and $N_2H_4 \cdot 2HCl$) to anhydrous hydrazine resulted in increases in the wave heights of the waves at -0.73V and -1.45V as small quantities of the salts were added. Whitnack also found that the successive addition of small amounts of water and carbon dioxide to anhydrous hydrazine resulted in increased wave heights of the wave at -0.73V. On the basis of these results, Whitnack postulated that the wave at -0.73V is due to the reduction of the hydrazonium ion at the dme (equation 4) and that the wave at -1.45V is probably due to the reduction of H_2^+ (equation 5). Since his results suggested that the hydrazonium ion exhibits a well-defined polarographic

$$N_2H_5^+ + e^- \longrightarrow N_2H_4 + H^\bullet \qquad (4)$$

$$H_2^+ + e^- \longrightarrow H_2 \qquad (5)$$

wave at a potential that is accessible electrochemically in liquid hydrazine, Whitnack concluded[2] that single-sweep polarography should be feasible as a method of determining the hydrazonium ion concentration in hydrazine.

OBJECTIVES

In view of the above feasibility study[2], it was planned that the summer research project would involve studying the effect of various additives (selected solids, liquids, and gases) upon the hydrazonium ion concentration in anhydrous hydrazine; single-sweep polarography would be utilized to monitor the level of the hydrazonium ion. The results of our initial studies (vide infra), however, indicated that the polarographic wave at -0.73V in anhydrous hydrazine may not be due to the hydrazonium ion. Further experiments were conducted which provide strong evidence that the wave at -0.73V in hydrazine is not due to the reduction of the hydrazonium ion, and that this species is reduced at a much more negative potential. A consequence of this finding is that normal single-sweep polarography does not appear to be useful as a method for the determination of the hydrazonium ion concentration in hydrazine.

EXPERIMENTAL

The anhydrous hydrazine used in this study was obtained by distillation of propellant-grade hydrazine under nitrogen from molecular seives (Linde 3A, dried previously at 400°). Analysis of the purified hydrazine indicated a purity of 99.3%. This hydrazine was found to contain the following impurities: aniline(.040%), water (.45%), and other unspecified impurities (.1%). The specific conductivity of this purified hydrazine was measured to be 4.26×10^{-5} mhos.

The hydrazonium salts used in this study were recrystallized from water and dried overnight *in vacuo* at ~110°. Each exhibited a melting point (decomposition) in agreement with literature values. Other salts used in this study were reagent-grade chemicals which were used without further purification.

The single-sweep polarograph used in these studies is a Chemtrix Model SSP-5A polarograph equipped with a Type 105 mercury dropper. The capillary of the dme had a 7 sec drop time in distilled water (open circuit). A Hewlett-Packard Model 7047A X-Y recorder was interfaced with the polarograph and used to record polarograms on chart paper.

In a typical experiment, a 5ml quartz polarographic cell that had been oven-dried at 100° was attached while still hot to a nitrogen line

at the gas-inlet sidearm of the cell. The nitrogen gas used in all experiments was treated to remove oxygen, carbon dioxide, and water by passage through a tube of copper turnings at 450° and through tubes of magnesium perchlorate and ascarite. A polyethylene cap having a hole in its center was attached to the top of the polarographic cell. The capillary of the dme was inserted through this hole and positioned near the bottom portion of the cell.

A small amount of triple-distilled mercury was added to the bottom of the cell to serve as the mercury pool. A 1.0 ml sample of anhydrous hydrazine or a solution containing anhydrous hydrazine was added to the polarographic cell below the nitrogen blanket using a 1ml gas-tight syringe equipped with a length of small diameter teflon tubing. (A metallic syringe needle was used in earlier experiments until it was discovered to be having an undesirable effect upon the hydrazine sample.) The anhydrous hydrazine solutions were prepared and stored until used in a glove-box under nitrogen. All experiments were conducted with a nitrogen atmosphere being maintained in the polarographic cell. For test solutions containing only hydrazine as solvent, no degassing was done. Other solutions were degassed by bubbling nitrogen into the solution for at least 1 minute.

The capillary tube of the dme was positioned to give a steady dislodging of mercury drops by the drop knocker. The control setting of the drop knocker was adjusted such that the drop time was slightly shorter than the natural drop time in the potential range of interest (usually 3-5 seconds/drop). The electrode leads were connected and then checked to make sure that proper electrical contact resulted. All potentials reported are in volts relative to the mercury pool.

RESULTS AND DISCUSSION

The single-sweep polarography of anhydrous hydrazine and hydrazine solutions of hydrazonium salts was first investigated in order to determine the relative sensitivity in the peak current of the wave at -0.73V (which had been previously attributed to the hydrazonium ion) to changes in the concentration of the hydrazonium ion. Several hydrazonium salts ($N_2H_4 \cdot HCl$, $N_2H_4 \cdot H_2SO_4$, and $N_2H_4 \cdot 2HCl$) were used in this study. Each of these salts is known to behave as a strong electrolyte in anhydrous hydrazine on the basis of previous conductivity studies[5] and should undergo virtually quantitative dissociation in hydrazine solution to form an equivalent amount of the hydrazonium ion ($N_2H_5^+$) in addition to the corresponding anion. (2 equivalents of $N_2H_5^+$ in case of $N_2H_4 \cdot 2HCl$). The finding that hydrazine behaves as a highly ionizing solvent similar to water and liquid ammonia is consistent with its possessing a high dieletric constant ($\Sigma = 53$).[5]

In these initial experiments, the polarogram of anhydrous hydrazine was examined in the range of 0 to -1V and then changes in this polarogram were studied as small amounts of a hydrazonium salt were added in incremental portions. In cases where the hydrazine was brought into contact with a metal syringe needle, the resulting hydrazine sample was found to exhibit a low intensity wave at ~-.6 to -.7V. Anhydrous hydrazine not contacted with a metallic surface, however, did not exhibit any detectable polarographic wave over the potential range 0 to -1V even at the highest sensitivity setting.

In one experiment as a typical example, the anhydrous hydrazine sample was initially found to exhibit a polarographic wave at -0.58V of low intensity (I_p <1μA). (This wave presumably corresponds to the wave at -0.73V previously reported by Whitnack[2]) Addition of 3.0mg of hydrazine dihydrochloride to this hydrazine (1.0ml) afforded a wave of narrower peak width at the same potential with a slight decrease in intensity from the initial value. Addition of further amounts of $N_2H_4 \cdot 2HCl$ failed to increase the height of this wave as the data in Table 1 indicates. Similar results were obtained when $N_2H_4 \cdot HCl$ and $N_2H_4 \cdot H_2SO_4$(1-10mg) were added to anhydrous hydrazine.

Table 1

PEAK CURRENTS[a] OF POLAROGRAPHIC WAVE AT -0.58V OF HYDRAZINE DIHYDROCHLORIDE-HYDRAZINE SOLUTIONS.

Milligrams $N_2H_4 \cdot 2HCl$	I_p[b]
0	17.0
3.0	13.9
4.9	13.8
7.3	11.5
11.9	11.4

a. Polarographic settings were as follows: start potential, 0.1V; potential range, 0.5V; sensitivity, 0.2μA/division; drop time delay, 1 sec; scan time,

0.2 sec/division; recorder sensitivity, 1 volt/inch. b. Peak currents are measured in units of chart divisions (10 divisions/inch).

The above polarographic wave at -0.58V thus appears to be very insensitive to changes in the concentration of the hydrazonium ion. Addition of 3mg of $N_2H_4 \cdot 2HCl$ to 1.0ml of hydrazine corresponds to a 2.86×10^{-2}M solution of this salt. Assuming complete dissociation of this strong electrolyte in hydrazine to afford the hydrazonium ion ($N_2H_5^+$), one would expect to have a solution that is 5.72×10^{-2}M in hydrazonium ion ($N_2H_5^+$). An electroactive species present at this high concentration normally affords[3] a very intense polarographic wave in which the measured peak current varies with the concentration of the electroactive species (I_p is directly proportional to C if the Randles-Sevcik equation[4] is obeyed). In the present case, however, even at concentrations 10^{-2}M and higher in $N_2H_5^+$, the wave at -0.58V is only observed under conditions of high sensitivity (high gain), and the peak current of this wave does not vary in intensity appreciably with changing concentration of the hydrazonium ion.

In later experiments with anhydrous hydrazine that had not been exposed to a metallic syringe needle, the change in the intensity of this wave upon addition of a hydrazonium salt was qualitatively similar to the above. In this case, the anhydrous hydrazine did not initially exhibit any wave over the range of 0 to -1V under high gain (.05μA/division), and the polarogram of the anhydrous hydrazine in this range was essentially a straight line having a slight positive slope. Addition of 0.8mg of hydrazine sulfate ($N_2H_4 \cdot H_2SO_4$) afforded a barely detectable wave at -0.73V. Additions of further small portions of hydrazine sulfate increased this wave height only very slightly. After a total of 7.1mg of hydrazine sulfate had been added, the measured peak current was only 0.25μA. The above results thus suggested that perhaps the wave at approximately -0.73V is not associated with the reduction of the hydrazonium ion.

Two other possible causes might be responsible for the observed insensitivity of the wave at -0.73V to changes in the hydrazonium ion concentration. The polarograph might be very insensitive as a result of a possible malfunction of the instrument. As a second possibility, the insensitivity may be associated with the use of hydrazine as the solvent in these polarographic studies. In particular, without the presence of an added strong electrolyte in these experiments, the conductivity of the anhydrous hydrazine may be too low to permit an intense polarographic wave. In order to explore these possibilities, the polarography of cadmium ion in hydrazine solution containing an added strong electrolyte was studied as a suitable reference system, and subsequently the polarography of hydrazonium salts in hydrazine containing an added electrolyte was investigated and compared with the cadmium polarographic results.

The polarographic reduction of cadmium ion in aqueous media affords a well-defined two electron wave that is reversible. The cadmium ion (Cd^{++}) is known from Pleskov's studies[6] to be stable in anhydrous hydrazine, and thus this ion would be expected to exhibit a well-defined polarographic wave in hydrazine that might be reversible.

Solutions of cadmium chloride (10^{-3} to 10^{-7}M) in anhydrous hydrazine containing 0.5M potassium chloride were found to exhibit a single polarographic wave at -0.37V which is attributed to the reduction of Cd^{++} to Cd^{o} at the dme. A single-sweep cyclic voltammetry scan of this wave indicates that it is an essentially reversible wave. The measured peak current for this wave was found to vary with the concentration of Cd^{++} in an approximately linear manner as shown in Table 2. The wave is barely detectable for a 10^{-7}M solution of cadmium chloride in hydrazine; this concentration thus appears to be the approximate lower limit for detection of a wave in hydrazine using the instrumentation specified earlier. The fact that an electroactive species is detected at low levels (10^{-5} to 10^{-7}M) in hydrazine in this experiment rules out any problem with adequate instrument sensitivity in the above study or any peculiar problem associated with the use of hydrazine as the solvent.

Table 2

VARIATION OF PEAK CURRENT (I_p) WITH CADMIUM ION CONCENTRATION (C) IN ANHYDROUS HYDRAZINE CONTAINING 0.5M KCl.

C[a]	I_p[b]
10^{-3}	1.95×10^{1}
10^{-4}	2.42
10^{-5}	2.5×10^{-1}
10^{-6}	3.0×10^{-2}
10^{-7}	6.0×10^{-3}

a. Units are Molar. b. Measured in chart divisions.

The use of a supporting electrolyte (0.5M KCl) in anhydrous hydrazine did not result in an increase in the intensity of the wave at -0.73V observed upon the addition of a hydrazonium salt ($N_2H_4 \cdot HCl$, etc.) to hydrazine. As a typical example, the addition of 0.4mg of $N_2H_4 \cdot HCl$ to 1.0ml of anhydrous hydrazine containing 37mg of KCl (0.5M) afforded a weak

wave at -0.73V that was barely detectable. The further addition of a total of 2.2mg of $N_2H_4 \cdot HCl$ resulted in only a slight increase in the height of this wave[2] (I_p = .4 chart divisions with a sensitivity setting of .1μA/division). In sharp contrast, the addition of 0.35mg of cadmium chloride to this solution afforded an intense wave at -0.37V for the cadmium ion reduction (I_p = 31.8 divisions with a sensitivity setting of 2μA/division). These values represent a ratio of 9439 in the relative intensities of the two waves per unit concentration (ratio of I_p/C for two waves) for the case of cadmium ion reduction versus the presumed hydrazonium ion reduction.

A similar result was obtained when hydrazine sulfate was added to anhydrous hydrazine containing 0.5M KCl. Addition of 4.5mg of hydrazine sulfate to this solution afforded only a very low intensity wave at -0.68V (I_p = 0.4 chart divisions with a sensitivity setting of 0.1μA/division). In contrast, the addition of 0.25mg of cupric chloride (which is reduced immediately to Cu^+ in hydrazine) to the solution afforded an intense wave at -0.18V for reduction of Cu^+ (I_p = 27.8 chart divisions with a sensitivity setting of 1μA/division). The ratio of the relative wave intensity per unit concentration for the copper ion reduction versus the presumed hydrazonium ion reduction in this case is 12,940.

The ratio of the relative wave intensity per unit concentration of the cadmium ion reduction or cuprous ion reduction versus the presumed hydrazonium ion reduction may differ from unity as a result of these ions having different diffusion coefficients (see the Randles-Sevcik equation) and also as a result of the possible irreversible nature of the wave for the reduction of the hydrazonium ion. It seems highly unlikely though that this ratio would differ from unity by a factor of four orders of magnitude. To state this in somewhat different terms, if the hydrazonium ion were responsible for the wave at -0.73V, it should exhibit a much more intense wave by several orders of magnitude than is experimentally observed. These results thus provide strong evidence that the wave at -0.73V in the polarography of anhydrous hydrazine is not due to the reduction of the hydrazonium ion as previously postulated[2] and that this ion must be reduced at a potential more negative than -1V (since no other wave is observed in the potential range of 0 to -1V).

Studies were next conducted to determine if the hydrazonium ion exhibits an observable polarographic wave at a potential more negative than -1V. The initial studies did not include examination of this potential region in detail due to the difficulty of obtaining polarograms beyond -1V in anhydrous hydrazine. At potentials beyond -1V in hydrazine, there is a rapid increase in current with increasing negative potential which results from a broad polarographic peak at -1.9V in this solvent. In order to obtain a suitable polarogram in this region, it is necessary to lower the height

of the mercury column of the dme (a 6.5 inch mercury column was used) and to scan at a faster rate due to the short lifetimes of the mercury drops at these negative potentials.

Addition of small amounts (0.1 -1.0mg) of hydrazine hydrochloride or hydrazine sulfate to anhydrous hydrazine resulted in a much greater current at potentials beyond -1V, but no new wave was apparent when the polarogram was obtained in the normal mode. In the derivative mode, however, a shoulder appeared in the polarogram at -1.6V upon addition of small amounts (0.1-1mg) of these hydrazonium salts. This shoulder was absent in the polarogram of anhydrous hydrazine containing an equimolar amount of potassium chloride as the electrolyte. These results provide evidence that the reduction of the hydrazonium ion occurs at a more negative potential than previously thought at approximately -1.6V in anhydrous hydrazine.

Further evidence to support this viewpoint is provided by polarographic studies of hydrazonium salts in other solvents. Hydrazonium salts ($N_2H_4 \cdot HCl$, $N_2H_4 \cdot H_2SO_4$) are known[7] to dissociate completely in water to afford an equimolar amount of hydrazonium ion ($N_2H_5^+$). If the hydrazonium ion is reduced at a potential that is electrochemically accessible in water, a wave due to this species should thus be observed upon addition of a hydrazonium salt (such as $N_2H_4 \cdot HCl$) to aqueous KCl. The addition of 0.4mg of hydrazine sulfate to 1M aqueous KCl solution resulted in the appearance of a new wave at -1.82V whose intensity increases approximately linearly with the amount of $N_2H_4 \cdot H_2SO_4$ added. A similar wave was observed at -1.73V upon the addition of hydrazine hydrochloride to 1M aqueous KCl solution. The small difference in the peak potentials of the above waves appears to be real and must be attributed to the presence of two different counterions in the two cases.

The polarography of hydrazine hydrochloride in the nonaqueous solvent N, N-dimethylformamide (DMF) was examined. Addition of 0.5mg of hydrazine hydrochloride to a solution of DMF containing 0.5M tetra-n-butylammonium iodide as the supporting electrolyte afforded a wave at -1.90V, which is attributed to the hydrazonium ion.

From the above results, it thus appears that the hydrazonium ion ($N_2H_5^+$) is reduced electrochemically at a potential in the general range of -1.5 to -1.9V in a variety of solvents.

CONCLUSIONS AND RECOMMENDATIONS

All of the above experimental results taken together provide strong support for the conclusion that the hydrazonium ion ($N_2H_5^+$) in hydrazine is reduced electrochemically at a potential of approximately -1.6V, which is at a potential that is much more negative than previously thought for this reduction. It is not yet clear whan specie(s) in solutions of hydrazonium salts in anhydrous hydrazine (of the purity used in this study) is responsible for the low intensity polarographic wave at -0.73V. The results of this study, however, are not consistent with the hydrazonium ion as being the species which affords this wave in these hydrazine solutions.

In view of the above finding that the hydrazonium ion exhibits a polarographic wave at -1.6V (rather than at -0.73V), it is apparent that the use of normal single-sweep polarography for directly determining the level of this ion in hydrazine is not feasible. Because the wave for the reduction of the hydrazonium ion is superimposed upon a large background wave in this potential region (resulting from decomposition of the hydrazine solvent and/or impurities in the solvent), this wave for the hydrazonium ion reduction is not well-defined. It consequently does not appear feasible to measure peak currents for this wave accurately enough even using the derivative mode. Since the measurement of peak currents (either explicitly or implicitly)is required in the use of polarography for analytical determinations, it consequently does not appear feasible to use normal single-sweep polarography for the determination of the hydrazonium ion concentration in hydrazine.

The use of differential single-sweep polarography, however, might provide a means for overcoming the above problem. In this variation of the basic single-sweep polarographic method, a plot of the difference in current versus potential for a test solution and a reference solution (usually of known concentration) is obtained. If the background current in the potential region around -1.6V is similar for a range of concentrations of hydrazonium ion in hydrazine, then the difference polarogram recorded using this technique should provide a direct measure of the difference in hydrazonium ion concentrations between the test and reference solutions. In this case, differential single-sweep polarography should be feasible as a method for directly determining the level of hydrazonium ion in hydrazine. Further research to explore the feasibility of using differential single-sweep polarography to analyze for the hydrazonium ion in hydrazine is suggested.

15

REFERENCES

1. AFRPL-TR-69-146, Final Report, Research on Hydrazine Decomposition, Contract No. F04611-67-C-0087, Rocketdyne, a Division of North American Rockwell Corporation, Canoga Park, California, July 1969.

2. AFRPL-TR-75-47, Final Report, Feasibility of Measuring Hydrazonium Ion ($N_2H_5^+$) in Hydrazine by Polarographic Techniques, Job Order No. 304810PI, Naval Weapons Center, China Lake, California, September 1975.

3. See, for example, Single-Sweep Method, Chapter 20 by J. Vogel in Progress in Polarography, Volume 2, P. Zuman and I. M. Kolthoff, Eds., Interscience, New York (1962), p. 429-448.

4. J. E. B. Randles, Trans. Faraday Soc., 44, 327 (1948).

5. (a) Walden and Hilgert, Z. Physik. Chem., 165A,241 (1933);
(b) The Chemistry of Hydrazine, L. Audrieth and B Ogg, John Wiley and Sons, New York (1951), Chapter 10, p. 202-204.

6. W. A. Pleskow, Acta Physicochimica U.R.S.S., 13, 662 (1940).

7. Ref. 5b, p. 168.

1976 USAF-ASEE SUMMER FACULTY RESEARCH PROGRAM
sponsored by
THE AIR FORCE OFFICE SCIENTIFIC RESEARCH
conducted by
AUBURN UNIVERSITY AND OHIO STATE UNIVERSITY

PARTICIPANT's FINAL REPORT

THE TRANSFER EFFECTIVENESS OF PLATFORM MOTION AND FIELD OF VIEW IN TRAINING SELECTED UPT MANEUVERS

Prepared by:	Edward D. McDowell, Ph.D.
Academic Rank:	Assistant Professor
Department and University:	Department of Industrial and General Engineering Oregon State University
Assignment:	
(Air Force Base)	Williams AFB
(Laboratory)	Human Resources Laboratory
(Division)	Flying Training Division
(Branch)	Training Innovations Branch
USAF Research Colleague:	Edward E. Eddowes, Ph.D.
Date:	August 20, 1976
Contract No.:	F44620-75-C-0031

ABSTRACT

Most modern aircraft flight simulators attempt to provide the student pilot with both visual and motion cues. Until recently, the visual cueing was provided via the aircraft instruments exclusively. Recent technological advances have permitted cue rich extra cockpit visual scenes to be incorporated into the simulation, thus adding a new dimension to aircraft simulators.

Motion cueing has historically been provided by moving the platform on which the simulator rests. Advancements in aircraft simulator technology have permitted the development of sophisticated six degree of freedom motion platforms. The not insignificant cost of these motion platforms has been justified primarily on virtually unanimous pilot opinion that motion cues are extremely important and the belief that increased simulatory fidelity will result in increased training effectiveness.

Recent evidence has suggested, however, that this may not necessarily be true. This evidence would suggest that simulator platform motion cueing does not result in increased pilot skills that transfer to the aircraft. It has been hypothesized that this new result may be attributed to the redundancy of the motion and visual cues.

The objectives of the research program developed in this report are to specifically investigate the interaction between the visual field of view and platform motion in the Advanced Simulator for Undergraduate Pilot Training (ASUPT) using undergraduate student pilots performing selected contact and instrument maneuvers.

Introduction

There are currently two cardinal issues in flying training involving the configuration of flight simulators and their resulting training effectiveness. The first involves the degree to which simulator platform motion affects pilot skill acquisition in the simulator and its transfer to the aircraft. The dominant question is the extent to which simulator platform motion is needed to achieve effective training. A second, concomitant question involves the degree to which complex visual displays such as computer generated imagery (CGI) benefits training in the simulator and the minimum requirements for such devices to be effective.

These two questions cannot be answered independently. Since the acceleration cues provided by the simulator motion platform are essentially redundant to the cues displayed by the visual system, it may be reasonably argued that the motion cues are entirely superfluous and unnecessary when an adequate visual system is provided.

However, the converse might also be argued. In order to avoid sensory conflicts and the possible resulting pilot disorientation, it may be hypothesized that motion cueing is more important when complex visual displays are provided. Thus, the nature of the motion system visual system interaction is of some importance.

Simulator Platform Motion

A key issue in the configuration of flying training simulators is the degree to which platform motion affects skill acquisition and transfer. The dominant question is essentially the extent of platform motion needed to achieve the simulator fidelity needed in order to achieve effective training.

There are essentially four possible alternatives. First, platform motion may have a significant positive effect on flying skill acquisition and transfer. In this case the not insignificant additional cost of providing platform motion would be justified by the benefit derived by the resulting reduced simulator/flying time needed to achieve and/or maintain task proficiency. The possibility that platform motion cues positively contribute to skill acquisition, but not sufficiently to justify the additional cost involved constitute a second alternative.

Alternately, platform motion may affect neither skill acquisition or transfer, in which case it certainly could not be economically justified. Additonally, it can be argued that platform motion may lead to either slower skill acquisition or negative transfer or both, particularly with novice pilots and a rich visual display. During initial skill acquisition novice pilots are provided a multiplexity of highly redundant cues, particularly from the visual environment. Part of the initial training involves the trainee separating the redundant from the relevant cues. Since the motion cues are essentially redundant to cues obtained from the visual scene, for most maneuvers, they may confuse the novice pilot more than assist him. In addition, the motion cues are essentially a result of the pilot's control manipulation, thus they only serve as feedback confirming the control movements and do not provide additional useful information regarding the attitude or position of the aircraft.

Questions of skill transfer arise because of the possible lack of fidelity between the motion cues experienced in the simulator and those in the aircraft. Because the simulator must be physically supported, it cannot perfectly duplicate the motion cues present in the aircraft. Instead, a motion drive philosophy must be developed which attempts to produce the essential motion cues while introducing a minimum of distortion.

Unfortunately, the distortion inherent in any drive philosophy may inadvertantly provide the pilot with cues that will not be present in the aircraft. If the student pilot learns to utilize these cues to enhance his performance in the simulator, then either little or possibly negative transfer may result.

The role of the vestibular senses in manual control tasks has not been fully explored. Sheridan and Ferrell (1974) suggest that the absence of motion cues in both aircraft and automobile simulators leads to underdampening as manifest by the estimates of the operator transfer function.

The effects of roll motion cues, both alone and in conjunction with visual cues has been extensively investigated by Shirley and Young (1968). They found that the roll motion cues allowed the operator to increase their phase lead at frequencies of about 3 roll/sec and thus allow an increase in the gain for the same phase margin. This as expected, resulted in a concomitant reduction in tracking error. Cyrus (1976) has observed that the motion in the Advanced Simulator for Undergraduate Pilot Training (ASUPT) is concentrated below about 2 roll/sec, thus, roll motion cueing would not be expected to contribute to operator performance.

A number of studies have been directed toward assessing the effects of simulator platform motion. These studies, including Besco (1961), Buckout, et al, (1963) and Ruocco (1965) have generally shown simulator motion to be beneficial to pilot performance. However, these studies did not measure the transfer of training to the aircraft, but rather relied upon criteria rides in the simulator as performance measures.

Demaree, et al, (1964) have observed that motion fidelity may be significantly reduced without any appreciable decrement in performance. This is consistent with Huddleston (1966) suggestion that motion may only e necessary for the maneuvers with significant G-forces.

An interesting investigation of the effects of platform motion on a simulated landing task was reported by Bray (1973). He systematically reduced the responsiveness of a single degree of freedom of motion (vertical) platform and failed to find any significant decrement in performance, as measured by the vertical velocity at touchdown. However, when the dynamics of the aircraft being simulated were changed, such that it was only marginally stable, reduction in platform dynamics resulted in a significant reduction in pilot performance. Bray's results would tend to support the hypothesis of an interaction between simulator characteristics and the aircraft being simulated. Unfortunately, it is not clear whether this interaction is only valid for marginally stable aircraft.

Although the previous work tends to support the hypothesis that simulator motion facilitates pilot performance, a more recent study would suggest the converse. Grunzke, et al, (1976) found that experienced pilots performance in ASUPT systematically deteriorated as the number of degrees of freedom of platform motion increased from zero through three to six. This result would suggest, for at least this case, that platform motion inhibits pilot performance.

Unfortunately none of the studies cited above measured training transfer to the aircraft. The first study of the effects of platform motion on training transfer was conducted by Koonce (1974). Koonce investigated the effects of refresher instrument training in a Singer-Link GAT-2 on subsequent pilot performance. In this experiment Koonce compared two types of platform motion, sustained and washout, with a no motion control. He found that both of the motion groups performed better in the simulator than did the no motion group. Moreover, all three groups appeared to show significant and approximately equal improvement from the first to the second trial in the simulator. Surprisingly though, on the third day, when performance in the aircraft was measured, the no motion group

performed better than either of the motion groups. Although this difference was not statistically significant, the motion-aircraft simulator interaction was. This would strongly suggest the effects of simulator platform motion observed in the simulator either did not transfer to the aircraft or perhaps transferred negatively.

Koonce's results obviously and immediately reinduced all previous studies supporting simulator platform motion suspect since they did not measure transfer. It also raised the question as to how platform motion was aiding performance in the simulator.

Jacobs and Roscoe (1975) suggested that perhaps platform motion might be simply acting as an alerting rather than a directing cue. They performed a study to examine this hypothesis as well as confirm Koonce's results.

Four groups were used in Jacobs and Roscoe's study, one trained solely in the aircraft, one in a simulator with no motion, one in the simulator with normal wash-out motion and a fourth with randomly reversed wash-out motion. The results of the transfer studies indicated the normal wash-out motion was superior to the no motion cues, but the difference was not statistically significant.

All of the transfer groups performed better than the aircraft trained group in the aircraft. Although the wash-out motion group exhibited better transfer, the difference appeared to be neither statistically nor practically significant. The fact that the random motion group failed to perform as well as the wash-out motion group in the simulator would suggest that the accurate motion cues were providing directional as well as alerting information.

Visual Systems

Perhaps because the visual sense modality is more complex than the vestibular/

kinesthetic system, the questions involving visual displays tend to be more complicated than those regarding motion cueing. The utility of extra cockpit visual systems was first demonstrated by Flexman, et al, (1950). Since then, several studies, including Creelman (1955) and Payne, et al, (1954) have confirmed their worth in flying training.

The research questions involved in flight simulation can be divided into two broad categories, those involving the field of view and those involving the scene content. The scene content may be further broken down into questions regarding the utility of color displays and resolution, Chase (1970, 1971), display timing, Barnes (1970), and display scaling and content. The former of the latter two questions involve the degree to which special relationships must be preserved in the visual display.

Perhaps the most complex area of concern in visual displays is the characteristics of the display content. The multiplexity of questions involving the content may be broken down along several different lines involving the type of image generating system, CGI or model board, or point light source, and the amount of detail, such as building that need to be displayed.

The limits of the field of view needed to effectively maneuver the aircraft were explored as early as 1951 by Roscoe (1951). He showed that pilots could safely land aircraft with visual fields as small as $\pm 10°$ horizontally and vertically. However, later work, particularly Reeder and Kolnick (1969) and Armstrong (1970) have concluded the field of view may be reduced to $\pm 25°$ horizontally without adverse effects. Moran (1971) has argued that the extra cockpit visual field may be severaly limited and satisfactory performance still achieved if the pilot is familiar with the area.

The field of view, and its limits, obviously interact with both the maneuver to be flown and the experience level of the pilot. For example, Grunzke, et al,

(1976) have shown experienced pilots can perform normal overhead landings with a limited (IFS) field of view, however, there was an accompanying degradation in performance. However, it does not appear novice pilots could be successfully taught this maneuver using the limited field of view. Similarly, it does not appear possible to perform certain aerobatic maneuvers with this field of view.

Visual-Motion System Interaction

The interaction between the simulators visual and motion system is particularly interesting because of the redundant nature of the cues provided by each. Due to this redundancy, it may be hypothesized that motion cues when provided in conjunction with a rich visual environment, do not enhance training effectiveness.

In spite of its potential significance, most of the research specifically addressed toward this possible interaction between simulators visual and motion systems has been directed toward problems of pilot disorientation and simulator motion sickness induced by conflicting vestibular and visual cues.

An exception to this is an investigation of operator tracking behavior reported by Fleshman and Rich (1963). They found that visual cues initially dominate kinesthetic feedback, but that the importance of the latter increases as the operators become more experienced. This would agree with both Flexman (1966) and Briggs and Wiener's (1959) conjecture that the values of motion increases with increasing pilot experience. However, the conjectures of Flexman and Briggs and Wiener were intended for only instrument flight simulators.

Mucklor, et al, (1959) has suggested motion cues, when used in conjunction with contact cues, are more important during the initial stages of training. In a recent study Grunzke, et al, (1976) found only limited interaction between the simulator platform motion system and the range of the field of view. Experienced pilots were utilized in this study. This result might be interpreted as supporting

Muckler's position. Thus, if a platform motion visual system interaction does exist, it will probably be most pronounced for novice pilots.

Objective

One plausible explanation for the divergence in the results noted above is that simulator platform motion only affects pilot skill acquisition positively in the absence of sophisticated extra cockpit visual systems. Since Grunzke, et al, (1976) were the only researchers which utilized a visual system, this would explain why they found negative effects due to simulator platform motion while previous researchers indicated motion enhanced pilot performance. Moreover, since Grunzke's, et al, (1976) did not find a significant interaction using experienced pilots, it appears reasonable to expect that if such an interaction exists, it will be most pronounced for novice pilots.

Therefore, the objective of this research is to examine the nature of the interaction between the simulator platform motion and the pilots field of view on pilot skill acquisition and transfer. Since the maneuver performed may influence the effectiveness of platform motion as well as the visual field, the research will involve selected undergraduate pilot training (UPT), and contact and instrument flying maneuvers. The maneuvers will be selected based upon their potential interaction with either the motion or visual system.

Restated, the objective of the research is to examine the effects of simulator platform motion on skill acquisition and transfer for selected UPT maneuvers both with a field and reduced field of view.

A concomitant object is the investigation of the effects of reduced field of view on training selected UPT maneuvers. The research will be conducted using the Advanced Simulator for Undergraduate Pilot Training (ASUPT), therefore, the simulator platform motion factor will contrast ASUPT's full 6° of platform motion

with no platform motion. Likewise, ASUPT's full field of view will be contrasted with a reduced field of view.

Since the Air Force is presently in the process of acquiring new Instrument Flight Simulators (IFS) with a limited field of view, the dimensions of the IFS field of view will be used for the experimental field of view. This will permit the research results to be readily generalized. The research objectives are summarized in Table 1 below.

TABLE 1

THE TRANSFER EFFECTIVENESS OF PLATFORM MOTION AND FIELD-OF-VIEW IN TRAINING SELECTED UPT MANEUVERS (VIS-MO)

OBJECTIVES

To examine the effects of the following factors on undergraduate pilot skill acquisition and training transfer in selected UPT maneuvers.

- Simulator Platform Motion
  ASUPT's Full 6° of Motion vs. No Motion

- Visual Field-of-View
  ASUPT's Full Field-of-View vs. Restricted Field-of-View (Simulated IFS)

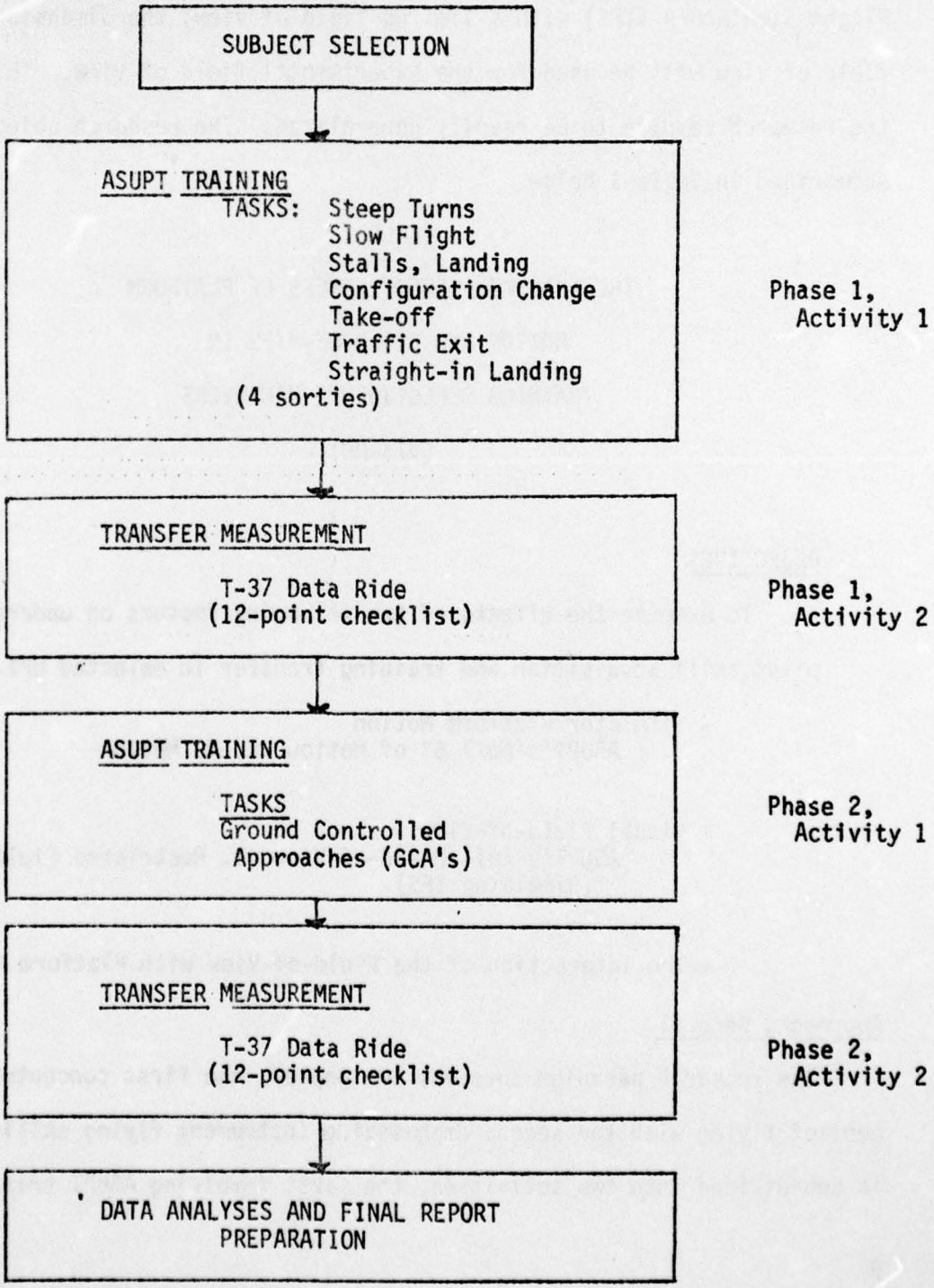
- The Interaction of the Field-of-View with Platform Motion.

Approach, General

The research paradigm involves two phases, the first concentrating on basic contact flying with the second emphasizing instrument flying skills. Each phase is sub-divided into two activities, the first involving ASUPT training and the

second the measurement of training transfer to the aircraft. This research approach is outlined in Figure 1.

FIGURE 1
EXPERIMENTAL APPROACH



The research will use only undergraduate pilots as subjects. The simulator platform motion factor will be included at two levels, no platform motion factor will be included at two levels, no platform motion and the full six-degree of freedom platform motion as defined by the ASUPT system. The visual field of view will also be included at two levels, the full ASUPT field, and a restricted field, limited to about 48° horizontally and 36° vertically. The restricted field of view is designed to simulate the IFS field of view, but will utilize computer generated images instead of a terrain model board.

The two independent factors will be crossed in the first phase of the research to create a two-squared design as illustrated in Figure 1a. Additionally, subjects will be counterbalanced with HRL/FT-DOR IPs by assigning subjects to IPs in accordance with the latin square illustrated in Figure 1b. Thus, instructor, as well as phase-activity effects may be estimated and removed.

FIGURE 1a

PLATFORM MOTION	Full Field-of-View	Limited Field-of-View
Full 6°	S_1 S_9	S_2 S_{10}
	S_5 S_{13}	S_6 S_{14}
None	S_3 S_{11}	S_4 S_{12}
	S_7 S_{15}	S_8 S_{16}

/3

FIGURE 1b

INSTRUCTOR PILOT

ACTIVITY	1	2	3	4
1	S_1-S_4	S_5-S_8	S_9-S_{12}	S_{13}-S_{16}
2	S_5-S_8	S_9-S_{12}	S_{13}-S_{16}	S_1-S_4

STATISTICAL DESIGN
PHASE I

Since Phase II involves training Ground Controlled Approaches (GCAs), only the IFS limited field-of-view will be utilized. However, the student pilots Phase I training treatment condition will be treated as an additional factor. Half the subjects from each Phase I group will receive the no-motion treatment and the remaining half, the motion treatment in Phase II, thus subjects will be assigned to motion treatment levels as illustrated in Figure 2a.

PLATFORM MOTION

FULL	NONE
S_1 - S_2	S_3 - S_4
S_5 - S_6	S_7 - S_8
S_{11}- S_{12}	S_9 - S_{10}
S_{15}- S_{16}	S_{13}- S_{14}

Figure 2a

INSTRUCTOR PILOT

ACTIVITY	1	2	3	4
1	S_9-S_{12}	S_{13}-S_{16}	S_1-S_4	S_5-S_8
2	S_{13}-S_{16}	S_1-S_4	S_5-S_8	S_9-S_{12}

STATISTICAL DESIGN - PHASE II

Subjects will also be assigned to IPs in accordance with Figure 2b, completing the contour balancing began in Phase I.

Performance in both phases will be measured by both instructor evaluation and the ASUPT automated performance measurement system. Transfer training will be measured by instructor pilot evaluations during a data ride which will immediately follow ASUPT training in both phases.

Approach, Specific

Subject Selection: Sixteen (16) subjects will be selected from the 82d Flying Training Wing Class of 77-07. No foreign students or students with over 50 hours of flying time will be used. The students will be scheduled such that Stage I ASUPT training will be completed just prior to the T-37 Syllabus Unit B1701. In Phase II, ASUPT training will be scheduled to immediately preceed T-37 Syllabus Unit I2101.

Performance Measurement

Two sets of performance measurements will be utilized during ASUPT training. Both ASUPT automated performance measurements and instructor pilot ratings will be recorded each time the students first attempts a maneuver. The IP ratings will be based upon the subjective twelve-point scale.

Terminal performance measurements will be made for each maneuver during the fourth ASUPT sortie in Phase I. This measurement will occur just prior to the Phase I data ride. The specific maneuvers to be practiced are outlined below.

Transfer measurements will be based on HRL/FT and DOR pilot ratings on the expanded 12-point scale. Data will be recorded for each of the maneuvers practiced.

/s

Experimental Factors

As ntoed above, two factors will be manipulated as part of the research paradigm. Two levels of simulator platform motion will be used. These are the full 6 of freedom platform moti n and no platform motion. Similarly, the two levels of the visual field to be used are the full ASUPT field and a reduced field simulating the Instrument Flight Simulator (IFS) field of view. The simulated IFS field of view will be created by masking out most of the ASUPT field. Computer generated images will be to generate the images as opposed to the terrain model used in the IFS.

Phase I Procedure

Each subject will receive four 0.8 hour training sessions in ASUPT during this phase. These sessions which will be referred to as syllabus units B1504A through B1507A respectively will be completed just prior to ATC syllabus P-V4A syllabus unit B2101. The collection of the first three sessions will commence with performance measurement data for all maneuvers previously practiced on that day. The remainder of each of these sessions will be used to allow the subjects time to practice. The subjects will practice each maneuver a fixed number of times during each session. The number of trials for each session and maneuver is given in Table III.

The four ASUPT sessions will commence with practice and terminate with performance measurement trials on all maneuvers practiced.

Every effort will be made, during ASUPT training, to conceal the nature of the study from the subjects. No mention of the independent factors, field of view and platform motion will be made. Both ASUPT cockpits will be utilized during Phase I of ASUPT training. However, only Cockpit B will be used for the

limited field of view subjects, with cockpit A being used exclusively for the full field of view subjects. This restriction is necessary to avoid having two full field of view subjects scheduled simultaneously. This would exceed ASUPT's capability in terms of scene content.

Additionally, the cockpit A/cockpit B schedules will be arranged such that performance measurement is not required in both cockpits simultaneously.

The content of the four phase I sessions are as outlined in Table III.

TABLE III

PHASE I - ASUPT SESSION CONTENT

ASUPT SESSIONS

I	II	III
Steep Turns (60°) _____	Steep Turns (60°) _____	Steep Turns (60°) _____
Slow Flight _____	Slow Flight _____	Slow Flight _____
Take-off _____	Take-off _____	Take-off _____
	Straight-in Landing _____	Straight-in Landing _____
		Overhead Pattern _____

IV

Steep Turns _____

Slow Flight _____

Take-off _____

Straight-in Landings _____

Overhead Pattern _____

Prior to going to the training transfer activity, the subjects will be requested not to discuss their ASUPT training with their Instructor Pilot (IP). Thus, the IP's rating student performance should be naive as to the treatment

17

each subject received in ASUPT. The data ride will be performed according to the attached scenario. This data ride will be substantiated for syllabus unit B2101. HRL/FT and DOR IP's will act as instructor pilots on this flight and will rate each maneuver on a 12-point scale on a special data form provided.

Phase II Procedures

Only the IFS field of view will be used during the second phase of the research. Half of the subjects from each Phase I group will receive a no platform motion treatment with the remaining half receiving the motion treatment during Phase I. In the analysis, the subject's treatment during Phase I will be treated as a factor, the resulting experimental design is shown in Figure .

Each subject will receive two 0.8 hr training sessions in ASUPT in Phase II. In this phasem the subject will practice general controlled approaches (GCAs) exclusively. The first GCA for the first training session and the first and last GCA for training session 2 will be measured trials. Each subject will practice exactly ten GCA's during each session. These two training sessions will be designated I1304A and I1305A and will be scheduled to just preceed ATC syllabus P-V4A-A unit I2101 which will serve as the data ride.

Again, scheduling precautions will be exercised in order to aovid conflicts in the utilization of the performance measurement system.

ATC syllabus unit I2101 will serve to measure the transfer of ASUPT training HRL/FT and DOR IP's will fly this unit and rate the subjects on the 12-point scale mentioned above. Again, students will be requested not to discuss the nature of their ASUPT training with the IP, thus the rating IPs should have no knowledge of what treatment each subject received.

Schedule of Activities

The research will be performed in accordance with the schedule shown below. This schedule is contingent upon approval of the Research Agreement by ATC and the availability of subjects from Class 77-07.

Planning	16 Aug - 13 Sept 1976
Stage I ASUPT Training	13-20 Sept 1976
Stage I Data Ride	20-27 Sept 1976
Stage I Task Freq Data Collection	20 Sept - 11 Oct 1976
Stage II ASUPT Training	8-15 Nov 1976
Stage II Data Ride	15-22 Nov 1976
Stage II Task Freq Data Collection	15 Nov - 3 Dec 1976
Data Analysis & Report Preparation	Completion - 1 March 1977

19

REFERENCES

Armstrong, B.O., Flight trials to discover whether peripheral vision is needed for landing. Royal Aircraft Establishment Technical Report 70205, 1970.

Barnes, A.G. The effect of visual threshold on aircraft control with particular reference to approach and flare simulation. British Aircraft Corporation, AIAA Visual and Motion Simulation Technology Conference, March, 1970.

Besco, R.V., The effects of cockpit vertical acceleration on a simple tracing task. (Rep. No. N.A. 61-47) Los Angeles: North American Aviation, 1961.

Bray, R.S., A study of vertical motion requirements for landing simulation. HUMAN FACTORS, Vol 15,6, 1973.

Briggs, G.E., and Wiener, E.L. Fidelity of simulation: I. Time sharing requirements and control loading as factors in transfer of training. (Tech Rep. NAVTRADEVCEN-TR-508-4, Office of Naval Training Research, 1959.

Buckhout, R., Sherman, H., Goldsmith, C.T., and Vitck, D.A. The effect of variations in motion fidelity during training on simulated low altitide flight. (Tech Rep AMRL-TR-63-108) Wright-Patterson Air Force Base, Ohio: Aerospace Medical Research Laboratory, December, 1963.

Chase, W.D. Evaluation of several T.V. display system configurations for visual simulation of the landing approach. IEEE Trans on Man-Machine Systems, Vol MMS-11, 1970.

Chase, W.D. Evaluation of several T.V. display systems for visual simulation of the landing approach. NASA Technical Note D-6274, 1971.

Creelman, J.A. Evaluation of approach training procedures. Rep. Z. Proj. NM 001-109-107, U.S. Naval School of Aviation Medicine, Pensacola, FL, 1955.

Cyrus, M. Personal Communication, Williams Air Force Base, Chandler, AZ. 1976.

Demaree, R.G., Norman, D.A., and Matheny, W.G. An Experimental Program for Relating Transfer of Training to Pilot Performance and Degree of Simulation, Naval nraining Device center, NAVTRADEVCEN TR 1388-1, 1965.

Fleishman, E.A., and Rich S. Role of kinesthetic and spatial-visual abilities in perceptual motor learning. Journal of Experimental Psychology, 66, 1963.

Flexman, R.E., Matheny, W.G., and Brown, E.L. Evaluation of School Link and Special Methods of Instruction in a Ten-Hour Private Pilot Flight-Training Program. University of Illinois Bulletin, 1950.

Flexman, R.E. Man in motion. The Connecting Link, 3, 1966.

Grunzke, P., Gray T., Irish, P., and Waters, B. Preliminary investigation of motion, visual and G-seat effects in the Advanced Simulator for Undergraduate Pilot Training (ASUPT). American Institute of Aeronautics & Astronautics Visual and Motion Simulation Conference, 1976.

Huddleston, H.F. Cockpit Motion Requirements for Flight Simulation. Royal Air Force Institute of Aviation Medicine, Farnborough, Hunts, 1966.

Jacobs, R.S., and Roscoe, S.N. Simulator Cockpit Motion and the Transfer of Initial Flight Training. 8th NTEC/Industry Conference Proceedings, 1975.

Koonce, J.M. Effects of ground-based aircraft simulator motion conditions upon prediction of pilot proficiency. University of Illinois at Urbana-Champaign, Aviation Research Laboratory, TR ARL-74-5/AFOSR-74-3, Savoy, IL, 1974.

Mucklor, F.A., Nygaard, J.E., O'Kelly, T.I., and Williams, A.C. Jr., Psychological variables in the design of flight simulators for training. (WADC Tech Rep 56-369), Wright-Patterson Air Force Base, OH, 1959.

Moran, N.P. Personal communication, 1971, as reported in visual elements in flight simulation. Report of Working Group 34, Committee on Vision, Assembly of Behavioral and Social Sciences, National Research Council, 1975.

Payne. T.A., Dougherty, D.J., Hasher, S.G., Skeen, J.R., Brown, E.L., and Williams, A.C. Jr. Improving landing performance using a contact landing trainer. (Tech Rep SPECDEVDEC 71-16-11). Office of Naval Research, Special Devices Center, 1954.

Reeder, J.P., and Kolnick, J.J. A Brief Study of Closed-Circuit Television for Aircraft Landing. NASA TN D-2185, 1964.

Roscoe, S.N. Flight by Periscope. University of Illinois Bulletin, 1951.

Ruocco, J.N., Vitole, P.A., and Benfari, R.C. Kinetic curing in simulated carrier approaches. (Tech Rep NAVTRADEVCEN-TR-1437-1). Port Washington, N.Y.: Office of Naval Research, Naval Training Device Center, April, 1965. (AD 617-689), 1965.

Sheridan, T.B., and Ferrell, W.R. MAN-MACHINE SYSTEMS: Information, Control, and Decision Models of Human Performance, MIT Press, Cambridge, Mass, 1974.

Shirley, R.S., and Young, L.R. Motion cues in man-vehicle control: Effects of roll motion cues on human operator's behavior in compensatory systems with disturbance inputs. IEEE Trans Man-Machine Systems, MMS-9, No. 4: 121-128, 1968.

UNCLASSIFIED

SECURITY CLASSIFICATION OF THIS PAGE (When Data Entered)

REPORT DOCUMENTATION PAGE	READ INSTRUCTIONS BEFORE COMPLETING FORM
1. REPORT NUMBER (18) AFOSR - TR - 76 - 1419	2. GOVT ACCESSION NO.
3. RECIPIENT'S CATALOG NUMBER	
4. TITLE (and Subtitle) (6) 1976 USAF-ASEE Summer Faculty Research Program.	5. TYPE OF REPORT & PERIOD COVERED (9) Final rept.
6. PERFORMING ORG. REPORT NUMBER	
7. AUTHOR(s) (10) J. Fred O'Brien, Jr	8. CONTRACT OR GRANT NUMBER(s) (15) F44620-75-C-0031
9. PERFORMING ORGANIZATION NAME AND ADDRESS Auburn University Engineering Extension Service Auburn, Alabama 36830	10. PROGRAM ELEMENT, PROJECT, TASK AREA & WORK UNIT NUMBERS 61102F (17) 9781-01
11. CONTROLLING OFFICE NAME AND ADDRESS Air Force Office of Scientific Research (XOP) Bldg 410 Bolling AFB, D. C. 20332	12. REPORT DATE (11) Sep 1976 13. NUMBER OF PAGES (12) 896 p.
14. MONITORING AGENCY NAME & ADDRESS (if different from Controlling Office)	15. SECURITY CLASS. (of this report) UNCLASSIFIED 15a. DECLASSIFICATION/DOWNGRADING SCHEDULE

16. DISTRIBUTION STATEMENT (of this Report)

Approved for public release; distribution unlimited.

17. DISTRIBUTION STATEMENT (of the abstract entered in Block 20, if different from Report)

18. SUPPLEMENTARY NOTES

19. KEY WORDS (Continue on reverse side if necessary and identify by block number)

Summer Faculty Research Program

20. ABSTRACT (Continue on reverse side if necessary and identify by block number)

This report represents the second years effort of an annual ten week summer research program conducted by university faculty members at selected USAF Systems Command laboratories. Program objectives are: 1) Further the research objectives of the AFSC labs; 2) Enhance the research interests and capabilities of engineering educators; 3) Stimulate continuing relations among participating faculty members and their professional peers in the AFSC labs; 4) Form the basis for continuing research of interest to the Air Force at the participant's institution.

DD FORM 1 JAN 73 1473 EDITION OF 1 NOV 65 IS OBSOLETE

UNCLASSIFIED 390 276

SECURITY CLASSIFICATION OF THIS PAGE (When Data Entered)